

# Non-Markovian Dynamics and Vibrational Spectroscopy of Hydrated Protons and Water

– Dissertation –

zur Erlangung des akademischen Grades  
eines Doktors der Naturwissenschaften (Dr. rer. nat.)  
am Fachbereich Physik der Freien Universität Berlin

vorgelegt von  
Florian Nikolas Brünig

Berlin, 2023



---

Erster Gutachter: Prof. Dr. Roland R. Netz  
Freie Universität Berlin

Zweiter Gutachter: Prof. Dr. Cecilia Clementi  
Freie Universität Berlin

Tag der Disputation: 20.10.2023





# Abstract

---

The dynamics of protons, the nuclei of hydrogen atoms, are of focal interest in chemistry and biophysics. Common examples are water splitting for hydrogen fuel production or protonation underlying the function of various essential proteins. In water or other hydrogen-rich environments, excess protons can travel rapidly over large distances by transferring between different molecules and interchanging identity with the nuclei of other hydrogen atoms. This thesis encompasses fundamental theoretical aspects of the proton-transport dynamics: the spectral signatures, the reaction kinetics and the non-Markovian nature.

The first two chapters present how the spectroscopic signatures of proton-transfer processes are predicted based on the stochastic reaction-rate time scales. The first-order linear approximation to model spectroscopic signatures is given by the harmonic vibrational motion around semi-stable configurations, the normal modes. However, the transfer motion of the excess proton between two acceptors, such as water itself, is not such a normal mode. It is rather described, according to reaction-rate theory as stochastic motion over an energy barrier. These time scales are extracted from *ab initio* simulations and related to the spectra via an analytical model.

In the third chapter, another approach for modeling spectroscopic signatures beyond the harmonic normal-mode approximation is introduced: that being the inclusion of anharmonic potential and frequency-dependent friction effects. At ambient temperature and in a liquid medium, the frequency and band shape of a vibrational mode are strongly influenced by the energetic and frictional coupling to the environment. When regarding the spectroscopic signatures of the intramolecular vibrations of water molecules in the liquid phase, both phenomena are relevant due to the strong intermolecular interactions via hydrogen bonds. The generalized Langevin equation presents an effective dynamical model, which handles arbitrary nonharmonic potential shapes in conjunction with non-Markovian time-dependent friction, and is here employed to extend the normal-mode-based description of vibrational spectra. The framework is tested on *ab initio* simulation data of water to disentangle anharmonic potential and frequency-dependent friction effects on the intramolecular dynamics.

Chapters four and five focus on aspects of reaction-rate theory, that follow from such non-Markovian memory friction models, and presumably are relevant for proton-transfer reactions. A generalized Langevin equation incorporating both time- and space-dependent friction is introduced and used to systematically study the effect of different memory friction around the minimal energy, i.e. the reactant state, and around the energy barrier at the transition state on the mean barrier-crossing times. Besides the memory friction, the effective mass and the potential shape are relevant variables of theoretical reaction-rate models. The thesis concludes with a perspective on the competition of these three effects on reaction times, which is demonstrated for pair-dissociation dynamics in water from classical molecular-dynamics simulations.



# Zusammenfassung

---

Die Dynamik von Protonen, den Kernen der Wasserstoffatome, ist ein zentrales Thema der Chemie und Biophysik. Als Beispiele gelten Wasserspaltung für die Herstellung von Wasserstoffbrennstoff oder Protonierungsdynamik, die der Funktion vieler essentieller Proteine zugrunde liegt. In Wasser oder wasserstoffreichen Umgebungen können überschüssige Protonen leicht über große Entfernungen transportiert werden: durch Sprünge zwischen den Molekülen und Austausch mit den Kernen anderer Wasserstoffatome. Diese Arbeit umfasst grundlegende theoretische Aspekte der Protonentransportdynamik: die spektralen Signaturen, die Reaktionskinetik und die nicht-Markovsche Natur.

In den ersten beiden Kapiteln wird gezeigt, wie die spektralen Signaturen des Protonentransfers mit den Zeitskalen der stochastischen Reaktionsdynamik vorhergesagt werden können. Das einfachste Modell für spektrale Signaturen ist durch die harmonische Schwingungsbewegung um metastabile Konfigurationen gegeben: die Normalmoden. Aber die Transferbewegung des Überschussprotons zwischen zwei Akzeptoren, wie zum Beispiel Wasser, ist keine solche Normalmode. Entsprechend der Rattentheorie wird sie hier als stochastische Dynamik über eine Energiebarriere beschrieben. Die entsprechenden Zeitskalen werden aus ab-initio Simulationen extrahiert und über ein analytisches Modell mit den Spektren in Beziehung gesetzt.

Im dritten Kapitel wird ein weiterer Ansatz zur Modellierung spektraler Signaturen vorgestellt: die harmonische Normalmodenapproximation wird um anharmonische Potential- und frequenzabhängige Reibungseffekte erweitert. Bei Raumtemperatur und in einem flüssigen Medium sind die Frequenz und Linienform einer Schwingungsmode stark durch Kopplung an die Umgebung beeinflusst. Beide Effekte treten in den spektralen Signaturen der intramolekularen Schwingungen von Wassermolekülen auf, da es starke intermolekulare Wechselwirkungen über Wasserstoffbrückenbindungen gibt. Die Generalisierte Langevin-Gleichung ist ein Modell für nicht-Markovsche Dynamik in allgemeinen nichtharmonischen Potentialen, welches hier verwendet wird, um die normalmodenbasierte Beschreibung von Schwingungsspektren zu erweitern. Die Methode wird hier auf ab-initio Simulationsdaten von Wasser angewendet, um die Effekte anharmonischer Potentiale und frequenzabhängiger Reibung auf die intramolekulare Dynamik zu verstehen.

Die Kapitel vier und fünf konzentrieren sich auf Aspekte der Rattentheorie, die aus Modellen mit nicht-Markovscher Memory-Reibung folgen und vermutlich für Protonentransferreaktionen relevant sind. Eine Form der Generalisierten Langevin-Gleichung, die sowohl zeit- als auch ortsabhängige Reibung enthält, wird eingeführt und verwendet, um die Effekte unterschiedlicher Memory-Reibung um die minimale Energie, d. h. den Ausgangszustand, und um die Energiebarriere herum, im Übergangszustand, auf die mittlere Reaktionszeit systematisch zu untersuchen. Zusätzlich zu der Memory-Reibung, sind auch die effektive Masse und die Potentialform relevante Variablen in theoretischen Ratenmodellen. Die Arbeit schließt mit einem Ausblick auf die Effekte dieser drei Variablen auf mittlere Reaktionszeiten, die für die Paardissoziationsdynamik in Wasser anhand klassischer Molekulardynamiksimulationen demonstriert wird.





# List of Publications

---

This cumulative thesis is comprised of the following peer-reviewed publications:

- i Florian N Brünig, Jan O Daldrop, and Roland R Netz. Pair-reaction dynamics in water : Competition of memory, potential-shape and inertial effects. *The Journal of Physical Chemistry B*, 126(49):10295-10304 (2022).  
<https://doi.org/10.1021/acs.jpcc.2c05923>
- ii Florian N Brünig, Paul Hillmann, Won Kyu Kim, Jan O Daldrop, and Roland R Netz. Proton-transfer spectroscopy beyond the normal-mode scenario. *The Journal of Chemical Physics*, 157(17):174116, (2022).  
<https://doi.org/10.1063/5.0116686>
- iii Florian N Brünig, Roland R Netz, and Julian Kappler. Barrier crossing in the presence of local memory friction : A numerical study. *Physical Review E*, 106(4):44133 (2022).  
<https://doi.org/10.1103/PhysRevE.106.044133>
- iv Florian N Brünig, Manuel Rammler, Ellen M Adams, Martina Havenith, and Roland R Netz. Spectral signatures of excess-proton waiting and transfer-path dynamics in aqueous hydrochloric acid solutions. *Nature Communications*, 13(1):4210, (2022).  
<https://doi.org/10.1038/s41467-022-31700-x>
- v Florian N Brünig, Otto Geburtig, Alexander von Canal, Julian Kappler, and Roland R Netz. Time-Dependent Friction Effects on Vibrational Infrared Frequencies and Line Shapes of Liquid Water. *The Journal of Physical Chemistry B*, 126(7):1579–1589, (2022).  
<https://doi.org/10.1021/acs.jpcc.1c09481>

Furthermore, during the doctoral research, contributions were provided to the following peer-reviewed works:

- i Achintya Kundu, Shavkat I Mamatkulov, Florian N Brünig, Douwe Jan Bonthuis, Roland R Netz, Thomas Elsaesser, and Benjamin P Fingerhut. Short-Range Cooperative Slowdown of Water Solvation Dynamics around  $\text{SO}_4^{2-}$  -  $\text{Mg}^{2+}$  Ion Pairs. *ACS Physical Chemistry Au*, 2(6):506-514 (2022).  
<https://doi.org/10.1021/acspchemau.2c00034>

- ii Yang Yang, Till Stensitzki, Luisa Sauthof, Andrea Schmidt, Patrick Piwowarski, Francisco Velazquez Escobar, Norbert Michael, Anh Duc Nguyen, Michal Szczepek, Florian N Brünig, Roland R Netz, Maria Andrea Mroginski, Suliman Adam, Franz Bartl, Igor Schapiro, Peter Hildebrandt, Patrick Scheerer, and Karsten Heyne. Ultrafast proton-coupled isomerization in the phototransformation of phytochrome. *Nature Chemistry*, 14:823–830, (2022).  
<https://doi.org/10.1038/s41557-022-00944-x>
- iii Shane Carlson, Maximilian Becker, Florian N Brünig, Kenichi Ataka, Rubén Cruz, Leixiao Yu, Peng Tang, Matej Kanduč, Rainer Haag, Joachim Heberle, Hesam Makki, and Roland R Netz. Hydrophobicity of Self-Assembled Monolayers of Alkanes: Fluorination, Density, Roughness, and Lennard-Jones Cutoffs. *Langmuir*, 37(47):13846–13858, (2021).  
<https://doi.org/10.1021/acs.langmuir.1c02187>
- iv Cihan Ayaz, Lucas Tepper, Florian N Brünig, Julian Kappler, Jan O Daldrop, and Roland R Netz. Non-Markovian modeling of protein folding. *Proceedings of the National Academy of Sciences of the United States of America*, 118(31):e2023856118, (2021).  
<https://doi.org/10.1073/pnas.2023856118>
- v Richard Schwarzl, Susanne Liese, Florian N Brünig, Fabio Laudisio, and Roland R Netz. Force Response of Polypeptide Chains from Water-Explicit MD Simulations. *Macromolecules*, 53(12):4618–4629, (2020).  
<https://doi.org/10.1021/acs.macromol.0c00138>
- vi Shane Carlson, Florian N Brünig, Philip Loche, Douwe Jan Bonthuis, and Roland R Netz. Exploring the absorption spectrum of simulated water from MHz to infrared. *The Journal of Physical Chemistry A*, 124(27):5599–5605, (2020).  
<https://doi.org/10.1021/acs.jpca.0c04063>
- vii Daniel Friedrich, Florian N Brünig, Andrew J Nieuwkoop, Roland R Netz, Peter Hegemann, and Hartmut Oshkinat. Collective exchange processes reveal an active site proton cage in bacteriorhodopsin. *Communications Biology*, 3(1):4, (2020).  
<https://doi.org/10.1038/s42003-019-0733-7>
- viii Jan O Daldrop, Julian Kappler, Florian N Brünig, and Roland R Netz. Butane dihedral angle dynamics in water is dominated by internal friction. *Proceedings of the National Academy of Sciences of the United States of America*, 115(20):5169–5174, (2018).  
<https://doi.org/10.1073/pnas.1722327115>

- ix Julian Kappler, Jan O Daldrop, Florian N Brünig, Moritz D Boehle, and Roland R Netz. Memory-induced acceleration and slowdown of barrier crossing. *The Journal of Chemical Physics*, 148(1):014903, (2018).

<https://doi.org/10.1063/1.4998239>

The following contributed publications are unrelated to this thesis:

- i Norbert Lindow, Florian N Brünig, Vincent J Dercksen, Gunar Fabig, Robert Kiewisz, Stefanie Redemann, Thomas Müller-Reichert, Steffen Prohaska, and Daniel Baum. Semi-automatic stitching of filamentous structures in image stacks from serial-section electron tomography. *The Journal of Microscopy*, 284(1):25–44, (2021).

<https://doi.org/10.1111/jmi.13039>

- ii Norbert Lindow, Stefanie Redemann, Florian N Brünig, Gunar Fabig, Thomas Müller-Reichert, and Steffen Prohaska. Chapter 3 - Quantification of three-dimensional spindle architecture. In Helder Maiato and Melina Schuh, editors, *Mitosis and Meiosis Part B*, volume 145 of *Methods in Cell Biology*, pages 45–64. Academic Press, (2018).

<https://doi.org/10.1016/bs.mcb.2018.03.012>



# Contents

---

<b>Abstract</b>	<b>v</b>
<b>Zusammenfassung</b>	<b>vii</b>
<b>List of Publications</b>	<b>ix</b>
<b>Glossary</b>	<b>xvii</b>
<b>1. Introduction</b>	<b>3</b>
1.1. Excess protons in water . . . . .	6
1.1.1. Methodology . . . . .	7
1.1.2. Excess proton structure . . . . .	12
1.1.3. Excess proton dynamics . . . . .	22
1.1.4. Nuclear quantum effects . . . . .	32
1.1.5. Excess protons in biological systems . . . . .	34
1.2. Vibrational spectroscopy . . . . .	40
1.2.1. Infrared spectrum of liquid water . . . . .	42
1.3. Reaction-rate theory . . . . .	44
1.3.1. Numerical models . . . . .	44
1.3.2. Analytical models . . . . .	46
<b>2. Conclusion and Outlook</b>	<b>49</b>
<b>3. Proton-Transfer Spectroscopy Beyond the Normal-Mode Scenario</b>	<b>53</b>
<b>4. Spectral Signatures of Excess-Proton Waiting and Transfer-Path Dynamics in Aqueous Hydrochloric Acid Solutions</b>	<b>63</b>
<b>5. Time-Dependent Friction Effects on Vibrational Infrared Frequencies and Line Shapes of Liquid Water</b>	<b>77</b>
<b>6. Barrier-Crossing Times for Different Non-Markovian Friction in Well and Barrier: A Numerical Study</b>	<b>89</b>
<b>7. Pair-Reaction Dynamics in Water: Competition of Memory Friction, Inertia and the Potential Shape</b>	<b>111</b>

<b>Appendix A. Supplementary Information:</b> Proton-Transfer Spectroscopy Beyond the Normal-Mode Scenario	123
<b>Appendix B. Supplementary Information:</b> Spectral Signatures of Excess-Proton Waiting and Transfer-Path Dynamics in Aqueous Hydrochloric Acid Solutions	155
<b>Appendix C. Supporting Information:</b> Time-Dependent Friction Effects on Vibrational Infrared Frequencies and Line Shapes of Liquid Water	209
<b>Appendix D. Supporting Information:</b> Pair-Reaction Dynamics in Water: Competition of Memory Friction, Inertia and the Potential Shape	245
<b>Appendix E. Fluctuation-Dissipation Theorem</b>	281
<b>List of Figures</b>	285
<b>Bibliography</b>	289
<b>Erklärung</b>	311
<b>Danksagung</b>	313







# Glossary

---

- AIMD** ab initio molecular dynamics
- ATR** attenuated total reflection
- BOMD** Born-Oppenheimer molecular dynamics
- BLYP** Becke, Lee, Yang and Parr
- CMD** centroid molecular dynamics
- CPMD** Car-Parinello molecular dynamics
- CP** contact pair
- DFT** density-functional theory
- EXAFS** extended X-ray absorption fine structure
- FTIR** Fourier-transform infrared
- FWHM** full width at half maximum
- GLE** generalized Langevin equation
- GH** Grote and Hynes
- HB** hydrogen bond
- HCl** hydrochloric acid
- IR** infrared
- KS** Kohn and Sham
- KSR** Krishnan, Singh and Robinson
- LE** Langevin equation
- MCTDH** multiconfiguration time-dependent Hartree
- MD** molecular dynamics
- MM** Mel'nikov and Meshkov

- MSD** mean squared displacement
- MS-EVB** multistate empirical valence bond
- MFPT** mean first-passage time
- MSD** mean squared displacement
- NM** normal-mode
- NMR** nuclear magnetic resonance
- NQE** nuclear quantum effects
- PBE** Perdew, Burke and Ernzerhof
- PMF** potential of mean force
- PGH** Pollak, Grabert and Hanggi
- RDF** radial distribution function
- RPC** ring-polymer contraction
- RPMD** ring-polymer molecular dynamics
- SCI-MS-EVB** self-consistent iterative multistate empirical valence bond
- SSP** solvent-separated pair
- TP** transition path
- TRPMD** thermostatted ring-polymer molecular dynamics
- TS** transition state
- TST** transition-state theory
- VDOS** vibrational density of states
- VSCF/VCI** vibrational self-consistent field/virtual state configuration interaction





# Introduction

---

Protons are elementary particles with electric charge  $+1e$ , in units of the elementary charge, and mass of about  $1u$ , where  $u$  denotes the atomic mass unit. Together with the electrically neutral neutrons they form the nuclei of all atoms. In contrast to neutrons, which are usually only released from the atomic nuclei upon nuclear fission, single protons are abundant in nature. That is because they appear as ionized hydrogen, the smallest and lightest chemical element, which makes up most of the matter in the universe and, together with carbon, oxygen and nitrogen, most of the organic matter [17, 18]. Naturally, excess protons play a key role in many biological and chemical processes [19, 20]. Acid-base chemistry, which essentially assesses the exchange of protons between different reactants, is fundamental to scientific and technical applications. Hence, the pH value, the hydrogen chemical potential given in terms of the concentration or rather activity of free protons, is an important scale for the characterization and quantification of chemical substances [21]. In industry, hydrogen fuel produced from renewable energy sources, for example by synthetic water oxidation, is considered to be crucial for the transition to an ecologically sustainable economy in sectors that are hard or even impossible to electrify [18, 22].

Inside proteins, the relocation of protons on short and long time scales in the complex hydrogen-bond network of amino acids and confined water molecules is believed to be critically important for protein function in various ways [23]. As examples, such ‘protonation dynamics’ are linked to i) the water-splitting redox reaction inside photosystem II as part of photosynthesis, ii) proton pumping and water synthesis in cytochrome *c* oxidase, which is part of the respiratory chain or iii) conformational transitions in phytochromes and channelrhodopsins, that exhibit enzyme regulation and light-induced signal transduction or channeling [24–27, 7].

Since the proton is the smallest atomic nucleus, it is invisible to even the most advanced experimental imaging techniques. Therefore, dielectric spectroscopic measurements that are well-established in chemistry and biophysics are often applied to probe the fast dynamics of excess protons in biological matter [28, 20, 29]. The theory to describe these measurements is historically based on vibrational normal modes, which is the linear harmonic approximation to the motion around meta-stable configurations, the local minima of the energy landscape [30]. Two nonlinear theoretical models for spectroscopy that go beyond this approach are discussed in this thesis.

At finite temperature, the motion over an energy barrier, i.e. a maximum in the energy landscape, such as encountered in the proton-transfer reaction between water

molecules or other proton acceptors, is not a vibrational normal mode. Here the process is described in terms of stochastic reaction dynamics over an effective energy barrier, which is characterized by two stochastic time scales. The barrier-crossing waiting time or mean first-passage time (MFPT) is the average time the particle waits in the reactant state on one side of the barrier before crossing over to the product state [31, 16]. The transfer-path or transition-path time is the average time of the actual crossing path of a reaction, the so-called transition path (TP) [32, 33]. The spectral signatures resulting from these stochastic time scales are derived analytically and applied to describe excess-proton transfer dynamics in chapters 3 and 4.

Furthermore, at finite temperature vibrational dynamics are affected by energetic and frictional coupling to the local environment, that give rise to homogeneous and inhomogeneous broadening and shifting of the spectroscopic signatures [30, 34]. If the frictional coupling is adiabatic, energy is dissipated on the time scale of the vibration, resulting in a so-called homogeneous broadening of vibrational bands. On the other hand, inhomogeneous broadening becomes relevant when the frictional coupling is nonadiabatic, i.e. happens on much longer time scales than the vibrational motion. In this case, the frictional force is nearly constant on the time scale of the vibration and therefore shifts the vibrational frequency. Inhomogeneous broadening of the total spectra is thus perceived when this frictional shifting, which is equivalently understood as resulting from varying inhomogeneous local environments, is time- or ensemble-averaged. These friction effects on vibrational spectra are modeled in this thesis in chapter 5 by employing the generalized Langevin equation (GLE); a generalization of the Langevin equation (LE) to time-dependent, or in this context frequency-dependent friction. Importantly, the formalism employed here handles both, homogeneous and inhomogeneous broadening, or equivalently adiabatic and nonadiabatic coupling, without any assumptions on time-scale separation, that are often applied in the literature.

Reaction-rate theory, which underlies the stochastic theory describing the proton-transfer spectral signatures, is the third major topic of this thesis. The exponential dependence of reaction times on the inverse temperature, or rather the energy-barrier height, forms the foundation of reaction rate theory [35]. Since in many biophysically relevant processes, such as proton-transfer or protein dynamics and reactions, the energy barriers are rather low, the preexponential factor then becomes relevant. Historically, the effect of the harmonic potential-shape parameters for the reactant and the transition states, i.e. the local extrema of the potential landscape, were considered first [36]. Soon after, the effects of stochastic frictional forcing and damping by the solvent molecules, so-called Brownian motion, relative to the solute mass, were shown to exhibit a complex turnover behavior between slow-downs in either the high- and low-friction limits due to different mechanisms [37]. Whenever there is no time-scale separation between the solvent degrees of freedom and the solute coordinate of interest, the Markovian assumption is violated, and the friction constant governing Brownian motion is rather a time-dependent property, the friction memory kernel [38, 39]. Ever since, reaction-rate theory has been focusing on the complex effects of time-dependent friction on the reaction rates, and how they compete with other known prefactors, such as the potential shape and the mass.

In short, the thesis is comprised of three methodological aspects: vibrational spectroscopy, non-Markovian effects and chemical reaction kinetics; that are applied to three different systems: excess protons in different environments, pure water, and pair reactions in water. The following sections of the introduction give an overview of the literature and the theoretical concepts. In chapter 3 the infrared (IR) spectral signatures and proton-transfer reaction dynamics in a water cluster, the  $\text{H}_5\text{O}_2^+$  cation, are discussed based on ab initio molecular dynamics (MD) simulations and nonlinear analytical models. In chapter 4, this analysis is transferred to decompose the excess-proton dynamics in concentrated hydrochloric acid solutions with comparison to experimental data. In chapter 5, the IR spectral line-broadening of bulk water is discussed and modeled using the GLE including non-Markovian time-dependent friction and a nonlinear potential, which is parameterized from ab initio MD data. In chapter 6, a GLE model for non-Markovian position and time-dependent friction is introduced to differentiate the effects of the well and barrier regions of a potential landscape on the mean reaction times. In chapter 7, the pair reaction dynamics of a NaCl ion pair and a pair of unpolar methane beads are analyzed using the GLE, derived from force-field MD data, and compared to previous analytical theories.



## 1.1. Excess protons in water

The structure and dynamics of excess protons in water sparked interest already two centuries ago: Grotthus hypothesized that protons move through water by rapidly hopping between water molecules, a process in which the excess proton repeatedly interchanges with water hydrogen atoms, as illustrated in Fig. 1.1 [40]. This shuttling process leads to a high mobility of protons in water compared to other ions, as confirmed in many experiments [41–45]. In attempts to understand the details of the Grotthus mechanism, the structure and dynamics of excess protons in water have been investigated in numerous studies throughout the last century, which were summarized in past reviews [46, 28, 20]. Due to its high net charge, the excess proton has a pronounced dielectric spectroscopic signature. In fact, already early IR spectroscopy experiments reported strong and broad mid-infrared signals associated with dissolved protons in acidic aqueous solutions [47, 48]. This so-called ‘continuum band’, located between the water bending and stretching bands, where only few organic molecules absorb [49–52], and the ‘acid bend band’, a blue-shifted water bending band [53–56], are well-known spectroscopic features of excess protons in water. The interpretation of the spectra of systems containing mobile protons started a debate about the equilibrium solvation structure of excess protons in water. On the one side, the Eigen state was hypothesized, corresponding to a central hydronium ion surrounded by three tightly coordinated water molecules, illustrated below in Fig. 1.2 in green [57]. On the other side, in the Zundel state, the excess proton is shared equally by two water molecules, illustrated in Fig. 1.2 in red [48]. Until today, studies argue that either the Eigen or the Zundel state is more important, often depending on whether their observable favors one or the other. Obviously, both states participate in the Grotthus mechanism, but for a complete picture, the residence and interconversion time scales need to be known.

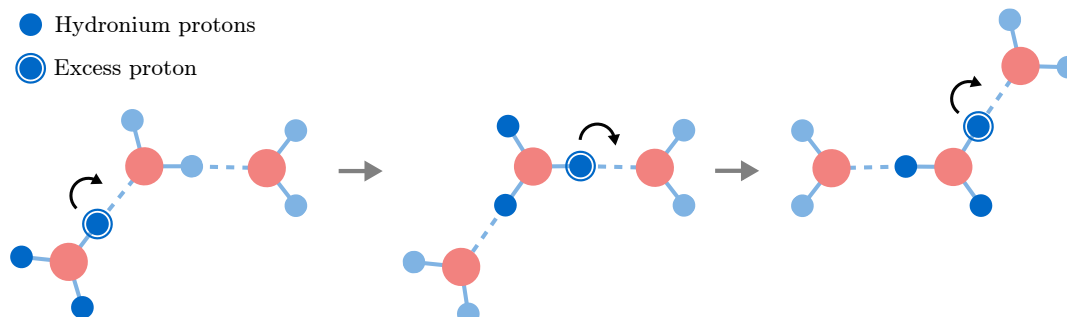


**Figure 1.1.:** Illustration of the Grotthus process of proton transport in water. An excess proton attaches to a water molecule, thereby forming a charged hydronium ion,  $\text{H}_3\text{O}^+$ . Whenever any of the three hydrogen atoms of the hydronium ion transfers to a hydrogen-bonded water molecule, a new hydronium ion is formed, while the original ion becomes again a neutral water molecule. Thus, an excess proton can transfer quickly across a chain of water molecules by exchanging identity with the hydrogen atoms of water itself during the formation of intermediate hydronium ions.

Theoretical simulation studies of excess protons in water are not unambiguous. Since the Grotthuss mechanism can be understood as a concession of fast chemical reactions between hydronium and water molecules, the efficient classical force fields are not applicable and quantum-chemical techniques, such as density-functional theory (DFT) methods, need to be applied. Until recently, such methods were computationally too expensive to address larger system sizes beyond a dozen atoms or long time scales beyond some picoseconds. To complicate the matter, the proton is the smallest atomic nucleus and hence subject to significant nuclear quantum effects (NQE) even at ambient conditions [58]. In fact simulation techniques including NQE are evolving rapidly and naturally are often applied to systems with excess protons [59–62].

More recently, the observation of characteristic IR continuum bands in biological systems whose function relies on mobile protons shifted the research focus to the role of confined water and amino acids as proton donors and acceptors in Grotthuss-like proton transfer mechanisms [63, 49, 50, 64, 52, 65, 13, 7].

### 1.1.1. Methodology

#### Experimental methods

Among experimental methods for the observation of excess protons, IR spectroscopy is the most prominent [47, 48, 66–70, 54, 71, 72, 55, 73, 56, 74–76, 52, 2]. Another prominent method that can probe excess protons directly is nuclear magnetic resonance (NMR) [77, 78, 43]. Both methods are also applied in biological systems to probe specifically excess protons, which, due to their small size and fast dynamics, are invisible to the otherwise widely used structure-resolving techniques, such as X-ray crystallography [49, 64, 52, 13, 7].

**Infrared spectroscopy** Linear IR spectroscopy relates the absorbed power of a light beam at frequency  $\omega$  to the imaginary part of the dielectric susceptibility and thereby to the autocorrelation function of the dipole moment. Many inter- and intramolecular dynamical modes are associated with changes of a local dipole moment and are therefore IR active, especially the dynamics of the charged excess protons. While strictly speaking, a spectroscopic method measures a system’s dynamics, vibrational normal modes are often well-defined for specific molecules but also super-molecular hydration configurations (further aspects of vibrational line shapes are discussed in section 1.2 and chapter 5). Due to the extremely high resolution of modern spectrometers and by tight comparison with computational quantum-chemistry methods, IR spectra are therefore often interpreted in terms of ensembles of static configurations.

IR spectra of strong acids were among the first studies that reported experimental evidence of excess proton dynamics from the characteristic spectroscopic signatures [47, 48]. More recently, pump-probe and other time-resolved IR spectroscopy methods have addressed the lifetimes of and interconversion times between various spectral regions [70, 54, 55, 73, 56, 74–76]. Studies in the THz-regime address longer time scales [79, 2] and less localized, i.e. collectively-coupled motions with the first hydration shells [71].

**Nuclear magnetic resonance** NMR spectroscopy measures the resonant Larmor frequencies of nuclear magnetic spins precessing around a strong constant external magnetic field. Therefore, only nuclei with a nuclear magnetic moment, that is with a total nonzero spin, which is the case for nuclei with an odd number of either protons or neutrons or sometimes both, are susceptible to this technique. Both, protons and deuterons, with spin one half and one respectively, are therefore NMR active. The effective magnetic field at the nucleus is usually shielded by the local electronic structure because the electronic spins are likewise reacting to the external magnetic field with an antiparallel magnetic moment. Generally, a higher local electronic density around the nucleus produces a higher ‘chemical shielding’, which reduces the effective magnetic field and likewise the NMR frequency. The relative shift to a lower frequency is called a lower ‘chemical shift’, while in this case, the chemical shielding is higher. Thus, NMR spectroscopy can be applied to probe local electronic structure around atomic nuclei and is therefore a widely used technique in biophysics and molecular chemistry. Importantly, it can be employed to measure protons directly, albeit at a lower time resolution than dielectric spectroscopic measurements.

NMR studies of excess protons in solution are reaching back almost as long as IR measurements [77, 78, 43].

### Theoretical methods

Theoretical simulation approaches for studying excess protons rely mostly on quantum-chemical methods. The quality of the quantum-chemical model usually depends on the system size and time scale that is to be addressed and then again on whether one is interested in static or dynamic properties. The most advanced models are vibrational self-consistent field/virtual state configuration interaction (VSCF/VCI) or NQE methods, and notably also electron-nuclear coupling in the multiconfiguration time-dependent Hartree (MCTDH) method, together with many-body, high-level potential energy and dipole moment surfaces, which have been applied to compute the static properties as well as IR spectra of excess protons in small water clusters [80–82, 60, 83, 84].

While these methods compare well to gas-phase experimental data, water at ambient conditions is in the liquid state. The collective, stochastic effects apparent in larger thermalized systems, such as water solutions of up to several hundred molecules, are of therefore of vital interest. Here, approximate and therefore computationally more efficient quantum-chemical methods, such as ab initio MD simulations, either as Born-Oppenheimer or Car-Parrinello MD (BOMD or CPMD), are widely applied [85–89, 61, 52, 90–94, 62]. Alternatively, classical force-field methods are augmented by heuristic models [95, 96, 53, 97] or used to sample hydration configurations that are evaluated by computationally expensive quantum-chemical techniques in post-processing [98, 99].

**Ab initio molecular-dynamics simulations** As stated above, in water and biological environments, excess protons are constantly reacting by hopping between different molecules and even exchanging identity with other hydrogen atoms. Force-field MD simulations, often called classical MD, that assume stable molecular structures and

commonly cannot address chemical reactions are therefore not applicable. Ab initio MD simulations do not rely on such force fields and molecular structure models, but solve the interatomic forces determined by quantum mechanics from first principles, i.e. by approximate solution of the Schrödinger equation for the electronic  $\mathbf{r}_i$  and nuclear  $\mathbf{R}_I$  degrees of freedom

$$i\hbar \frac{\partial}{\partial t} \Phi(\mathbf{r}_i, \mathbf{R}_I; t) = \mathcal{H} \Phi(\mathbf{r}_i, \mathbf{R}_I; t), \quad (1.1)$$

with the Hamiltonian operator  $\mathcal{H}$

$$\begin{aligned} \mathcal{H} = & - \sum_I \frac{\hbar^2}{2M_I} \nabla_I^2 - \sum_i \frac{\hbar^2}{2m_e} \nabla_i^2 \\ & + \frac{e^2}{4\pi\epsilon_0} \sum_{I < J} \frac{Z_I Z_J}{|\mathbf{R}_I - \mathbf{R}_J|} + \frac{e^2}{4\pi\epsilon_0} \sum_{i < j} \frac{1}{|\mathbf{r}_i - \mathbf{r}_j|} - \frac{e^2}{4\pi\epsilon_0} \sum_{I,i} \frac{Z_I}{|\mathbf{R}_I - \mathbf{r}_i|}, \end{aligned} \quad (1.2)$$

where  $M_I$  and  $m_e$  are the nuclear and electron masses and  $Z_I$  the atomic numbers, so that  $(eZ_I)$  are the nuclear charges.  $\epsilon_0$  is the vacuum permittivity. Since the full solution is analytically impossible to obtain and numerically demanding even for the simplest molecules, various approximations are employed to address different scientific questions.

If one is interested in nuclear dynamics, as for the case of the excess proton or IR signatures in general, an assumption of timescale separation for the dynamics of the nuclei and the electrons is useful: the Born-Oppenheimer approximation. The ab initio MD simulations used throughout this work rely on this assumption and are therefore also called Born-Oppenheimer molecular dynamics (BOMD). In this formalism, for which the introduction by Marx and Hutter [100] is followed here, only the electrons are treated quantum mechanically, while the nuclei follow classical Newtonian mechanics with the forces derived from the electronic structure. Furthermore, at the timescale of the nuclear motion, the electrons are assumed to relax instantaneously to the ground state defined by the current nuclear positions. The quantum-mechanical problem is therefore reduced at each instance of time to the ground-state solution  $\Phi_0$  of the time-independent Schrödinger equation for the electrons with energy  $E_0$  and Hamiltonian  $\mathcal{H}_e$

$$E_0 \Phi_0 = \mathcal{H}_e \Phi_0 \quad (1.3)$$

and the equations of motion for each nucleus can be formulated as

$$M_I \ddot{\mathbf{R}}_I = -\nabla_I \langle \Phi_0 | \mathcal{H}_e | \Phi_0 \rangle - \nabla_I V_{\text{nuc}}(\mathbf{R}_I), \quad (1.4)$$

where the first term on the right side is the gradient of the ground-state energy and the second term is the gradient of a Coloumb potential comprised of interactions with the

other nuclei

$$V_{\text{nuc}}(\mathbf{R}_I) = \sum_{J \neq I} \frac{Z_I Z_J}{|\mathbf{R}_I - \mathbf{R}_J|}. \quad (1.5)$$

Note, that the common convention is used and the equations are expressed in Hartree atomic units: energy is given as the Hartree energy,  $E_h = \hbar^2/(m_e a_0^2)$  and length is expressed in terms of the Bohr radius  $a_0 = 4\pi\epsilon_0 \hbar^2/(m_e e^2)$ .

A breakthrough for numerical solutions of the time-independent Schrödinger Eq. (1.3) of many-electron systems was the development of Kohn-Sham density functional theory (KS DFT). Here, the total wave function of the system  $\Phi_0$  is expanded in terms of eigenfunctions of non-interacting reference systems. This set of orthonormal single-electron functions are called the Kohn and Sham (KS) orbitals  $\phi_i$ , which together give the electronic density  $n(\mathbf{r})$  for given integer occupation numbers  $f_i$

$$n(\mathbf{r}) = \sum_i f_i |\phi_i(\mathbf{r})|^2. \quad (1.6)$$

The total energy is then the KS energy  $E^{\text{KS}}(\phi_i)$

$$E_{\text{tot}} = \langle \Phi_0 | \mathcal{H}_e | \Phi_0 \rangle \approx \min E^{\text{KS}}(\phi_i), \quad (1.7)$$

which is given by

$$E^{\text{KS}}(\phi_i) = T_s(\phi_i) + \int V_{\text{ext}}(\mathbf{r}) n(\mathbf{r}) d\mathbf{r} \quad (1.8)$$

$$+ \frac{1}{2} \int V_H(\mathbf{r}) n(\mathbf{r}) d\mathbf{r} + E_{\text{xc}}(n). \quad (1.9)$$

The first term is the kinetic energy

$$T_s(\phi_i) = \sum_i f_i \langle \phi_i | -\nabla^2 | \phi_i \rangle. \quad (1.10)$$

The second term is an external potential, in this case a Coulomb potential from the nuclear positions  $\mathbf{R}_I$  with charges  $Z_I$

$$V_{\text{ext}}(\mathbf{r}) = - \sum_I \frac{Z_I}{|\mathbf{R}_I - \mathbf{r}|}. \quad (1.11)$$

The third term is the Hartree potential, the classical electrostatic potential between the electronic densities of the different orbitals

$$V_H(\mathbf{r}) = \int \frac{n(\mathbf{r}')}{|\mathbf{r} - \mathbf{r}'|} d\mathbf{r}'. \quad (1.12)$$

The last term is the exchange–correlation energy functional  $E_{\text{xc}}(n)$ , which is often a

heuristically derived correction functional to account for the missing quantum-mechanical interactions. This term is crucial as it significantly affects the computational cost and accuracy of the simulations. The Becke, Lee, Yang and Parr (BLYP) exchange–correlation functional, used throughout this work, is a type of common GGA (generalized gradient approximation) functional that only depends on the value and the gradient of the local electronic density  $n(\mathbf{r})$  [101, 102]. The BLYP functional is heuristic and therefore strictly speaking not based on first principles, but computationally efficient and has been widely applied to study water and biological system with success, especially in combination with another heuristic correction for dispersion forces, called D3 [103].

The ground-state solution to the electronic system is found by minimization of the KS energy Eq. (1.8), which defines the KS Hamiltonian  $\mathcal{H}_e^{\text{KS}}$  in the KS equations

$$\left\{ -\frac{1}{2}\nabla^2 + V_{\text{ext}}(\mathbf{r}) + V_H(\mathbf{r}) + \frac{\partial E_{\text{xc}}[n]}{\partial \mathbf{r}} \right\} \phi_i(\mathbf{r}) = \sum \Lambda_{ij} \phi_j(\mathbf{r}) \quad (1.13)$$

$$\mathcal{H}_e^{\text{KS}} \phi_i(\mathbf{r}) = \sum \Lambda_{ij} \phi_j(\mathbf{r}), \quad (1.14)$$

where the Lagrange multipliers  $\Lambda_{ij}$  impose the orthogonality constraint between the orbitals.

For numerical solution of the KS Eqs. (1.13), the KS orbitals need to be expanded in a suitable set of basis functions. The choice of basis, in particular the number of basis functions, defines again crucially the trade-off between accuracy and computational efficiency. Typically, the valence orbitals, which define the chemical bonds, are modeled most accurately, while inner shells are featured at lower precision or even integrated into an effective nucleus with a reduced charge and a repulsive pseudopotential [104, 105]. Theoretically, Slater-type basis functions  $\sim \exp(-\zeta_j |\mathbf{r}_i - \mathbf{R}|)$ , centered at each nuclear position  $\mathbf{R}$ , are motivated from the solution of the Schrödinger equation. However, for computational application larger numbers of Gaussian-type basis functions  $\sim \exp(-\zeta_j |\mathbf{r}_i - \mathbf{R}|^2)$  are typically used, which come with analytical solutions to many integrals and Fourier-space representations. The number of different  $\zeta_j$  primitive basis functions employed to model an orbital is typically indicated in the nomenclature of a basis set. So-called polarization and diffuse functions are additional primitive basis functions for each orbital, that model far-reaching densities, for example for anions, and induced polarization. As an example, in this work the TZV2P basis set is a ‘triple-zeta valence’ basis, i.e. three basis functions, TZV, with two additional functions to account for polarization, 2P, are used to model electrons in the valence shell [106]. The orthogonality constraint in Eq. (1.13) is implied on the orbitals  $\phi_i$  but the occupation of basis functions may spread over many molecules. Localization of the electronic densities is therefore required to compute local molecular polarization. Throughout this work maximally localized Wannier functions are used, which follow as a unitary transform from the basis functions [105].

**Nuclear quantum effects** NQE are known to become relevant whenever the zero-point energy exceeds the thermal energy,  $\hbar\omega/2 > k_B T$  [58]. Thus, they generally become more important at lower temperatures, lower masses or higher frequencies. For the lightest

atomic nucleus, the proton, they may be relevant at room temperature, as has been demonstrated in numerous works [59, 60, 97, 61, 62]. Only recently, NQE simulation techniques have advanced significantly to allow to include them into established MD simulation frameworks. Based on the Trotter formalism, NQE are typically addressed by replacing each atomic nucleus by a closed-loop polymer, or ring polymer, consisting of  $P$  elementary beads and then running replica simulations. However, the required number of  $P$  increases with the maximal vibrational frequency of the system: “ $P = 32$  replicas are needed to converge simple structural properties of a system at room temperature containing O-H covalent bonds” [58]. This is the naive factor by which the computational cost of these simulations increases when compared to the case without NQE (replicas can be run in parallel though). Therefore, it remains challenging to combine these methods with ab initio MD using DFT which is already computationally very expensive, but required to model protons in aqueous environments, where formation and breaking of bonds occur constantly. Consequently, only a few works so far have introduced NQE into such simulations [61, 62], often by making additional assumptions and simplifications, for example by reducing the number of replicas  $P$ , so called ring-polymer contraction (RPC). In this rapidly emerging field, however, no general method has been established yet. Instead, each specific system requires careful optimization to allow simulation of NQE of excess protons in water with affordable additional cost.

### 1.1.2. Excess proton structure

#### The Eigen state

The Eigen state was proposed by Wicke et al. [57] as the solvation structure of excess protons in water, building on earlier works that found that excess protons attach to water molecules to form the hydronium ion,  $\text{H}_3\text{O}^+$ . The Eigen state consists of a central hydronium ion and three water molecules which are tightly hydrogen-bonded to the three hydrogen atoms of the hydronium, thus forming a  $\text{H}_9\text{O}_4^+$  complex. An illustration is given on the left in Fig. 1.2. The structure was suggested based on measurements of the molar heat capacity and molar volume, as well as earlier IR and NMR spectra of dissolved protons, from which the authors deduced ultra-fast motion of the excess proton in the local hydration environment on the order of 10 fs to 100 fs [77, 47]. In current literature, this solvation structure is supported mostly by simulation data, especially ab initio DFT and heuristic multistate empirical valence bond (MS-EVB) simulations at various levels [107, 108, 85–87, 61, 52, 92, 62]. When computing the static distribution of excess protons around water molecules in bulk, most studies find on average strong coordination to a single, but of course varying water oxygen. These distributions are significantly affected when NQE are taken into account and the excess proton is less localized due to zero-point motion and tunneling [59, 61, 109, 62]. Also experimental extended X-ray absorption fine structure (EXAFS) data supports this equilibrium structure [110]. An established concept building on the Eigen solvation structure is the so-called ‘special-pair dance’. The role of the excess proton ‘dances’ rapidly between the three candidate hydrogen atoms of the central hydronium ion, thereby forming ‘special pairs’ with the

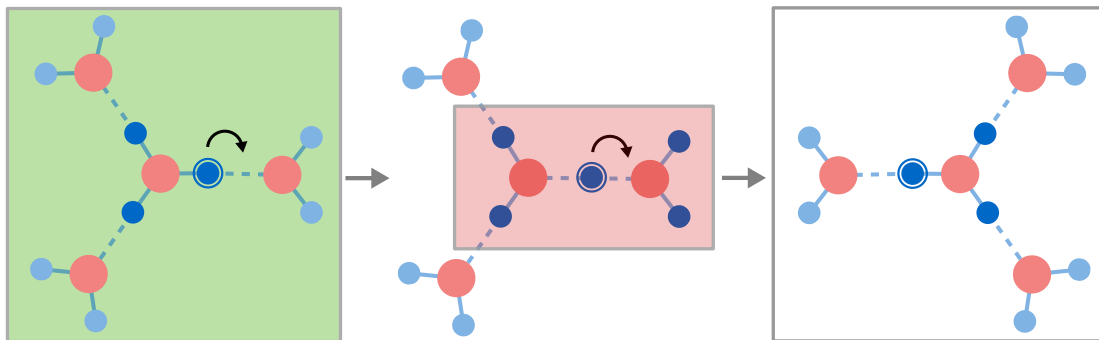


**Figure 1.2.:** Illustration of the Eigen ( $\text{H}_9\text{O}_4^+$ , green on the left) [57] and Zundel states ( $\text{H}_5\text{O}_2^+$ , red in the middle) [48] as intermediate solvation structures of the excess proton in water. The figure shows the Eigen-Zundel-Eigen transition as a model for excess-proton transport. Alternatively, the transport can be regarded as a Zundel-Eigen-Zundel transition, depending on whether the Zundel or the Eigen states are assumed to be the dominant solvation species.

according hydrogen-bonded water molecules [107, 62].

### The Zundel state

The Eigen state was soon contrasted by the Zundel state [48], in which the excess proton is symmetrically shared by two water molecules, i.e.  $\text{H}_5\text{O}_2^+$ . Interestingly, the Zundel state was also mentioned by Wicke et al. [57], following the theories by Eucken [111] and later Gierer and Wirtz [41], who suggest solvation structures of the excess proton by either two or four water molecules, of which the former case corresponds to the Zundel state.

This solvation structure was supported by the extremely high solubility of protons in water and discussed with respect to the characteristic IR spectral signatures, specifically the broad continuum between the water bend and stretch motives [48].

In a static description, the two states are mostly distinguished by the asymmetry of the excess proton localization between two water molecules. In contrast to the Eigen state, the asymmetry is small for the Zundel state. Therefore, as mentioned above, in contrast to ab initio DFT simulations with classical treatment of the nuclei, the Zundel state is supported by simulations which account for NQE because the static distributions of proton localization between two water molecules are washed out [59, 61, 62]. Furthermore, the energetically minimal proton asymmetry depends significantly on the relative distance between the two oxygen atoms [59, 92, 2, 4]. It is also notable that the Zundel state is favored when the water clusters which solvate the excess proton are confined to a two-dimensional slab or even more to one-dimensional water wires [112, 52].

Today, it is also known that the IR signatures associated with the Eigen- and Zundel-like states are indeed distinct. While the IR continuum between the water bend and stretch vibrations in the range  $2000\text{ cm}^{-1}$  to  $3000\text{ cm}^{-1}$  as well as the acid-bend mode at



1750  $\text{cm}^{-1}$  are associated with Eigen-like solvation structures, the spectral signatures at 1000  $\text{cm}^{-1}$  to 1200  $\text{cm}^{-1}$  are associated with proton-transfer motion between two water molecules, also called ‘proton-transfer mode’, in Zundel-like structures [82, 85, 54, 72, 98, 88, 99, 92, 2, 4].

Lately, the debate whether the dominant solvation structure of the excess proton in water corresponds to the Eigen or the Zundel state is converging: recent studies have demonstrated geometrically asymmetric Eigen and Zundel excess proton states in water and suggested that the distinction between those states is rather small and thus mostly semantic [55, 73, 62]. Several 2D-IR studies have identified significant lifetimes of Zundel-like states, where the excess proton fluctuates over large distances and encompasses asymmetric states that may equally well be characterized as Eigen-like and thereby relaxed strict static criteria [55, 73, 76].

Obviously, such Zundel-like and Eigen-like structures form dynamic intermediates of long-distance proton transfer events in water, as also illustrated in Fig. 1.2, where an Eigen-Zundel-Eigen transition is shown schematically. The alternative perspective is the Zundel-Eigen-Zundel transition. The general agreement is that there is fast and reversible interconversion on short time scales and that the energetic difference between the two structures is rather small, i.e. the lifetimes are also rather similar [94, 62]. A discussion of the excess-proton dynamics on short and long time scales is given in section 1.1.3.

### Concentrated acid solutions

In the following, some static properties of excess protons in concentrated hydrochloric acid (HCl) solutions are discussed, with data shown as determined from ab initio Born-Oppenheimer molecular dynamics (BOMD) simulations of BLYP-D3 DFT quality [2]. In the simulation data, excess protons are identified based on a simple geometric criterion: after assembling at each time step the water molecules for each oxygen atom with the closest two hydrogen atoms, the remaining least associated protons form hydronium ions with their respective closest water molecules. Thereby, at each time step, a total number of excess protons  $N_{\text{H}^+}$  equivalent to the number of chloride ions in the simulations is obtained.

### Radial distribution functions

Solvation structures in liquids are often analyzed in terms of spatial correlations using radial distribution functions (RDFs) of the different solutes. The RDF,  $g_{ab}(r)$ , denotes the average relative density of particles  $a$  at a distance  $r$  around particles  $b$ . The absolute density of species  $a$  at distance  $r$  to species  $b$  is then given as  $\rho_a g_{ab}(r)$  where  $\rho_a$  is the global density of species  $a$ . The RDF is computed from simulation data of two particle

species with numbers  $N_a$  and  $N_b$  and located at positions  $\mathbf{r}_i$

$$g_{ab}(r) = (N_a N_b)^{-1} \sum_{i=1}^{N_a} \sum_{j=1}^{N_b} \langle \delta(|\mathbf{r}_i - \mathbf{r}_j| - r) \rangle. \quad (1.15)$$

Average particle numbers of species  $a$  within distance  $r$  of particles of species  $b$  are obtained by integration over  $g_{ab}(r)$

$$N_{ab}(r) = \rho_a \int_0^r dr' 4\pi r'^2 g_{ab}(r'). \quad (1.16)$$

The RDF is directly related to data retrieved from EXAFS measurements [113, 114].

In Fig. 1.3A the spatial correlations of the hydronium ions and in Fig. 1.3B of the excess protons are shown as obtained from ab initio DFT MD simulation of aqueous hydrochloric acid solutions at various concentrations [2]. Comparable results for aqueous hydrochloric acid solutions were shown previously for various exchange-correlation functionals used in ab initio simulations [91] and for different self-consistent iterative multistate empirical valence bond (SCI-MS-EVB) simulations [115, 116]. Other works have regarded single excess protons dissolved in water [87].

In Fig. 1.3A the RDFs of the oxygen nuclei of the hydronium ions are shown with respect to the oxygen nuclei of other hydronium ions ( $\text{O}^+$ ) as solid lines, for the oxygen nuclei of the water molecules ( $\text{O}$ ) as broken lines, for the the excess protons ( $\text{H}^+$ ) as dashed and dotted lines and all hydrogen nuclei ( $\text{H}$ ), including excess protons, as dotted lines. Next to the trivial peaks of the dashed and dotted as well as the dotted lines at below  $1.0 \text{ \AA}$  belonging to the hydrogen nuclei which are part of the hydronium ions itself, a clear peak of the broken lines at  $d_{\text{O}^+ - \text{O}} = 2.5 \text{ \AA}$  indicates the water oxygen nuclei in the first hydration shell. A second, much smaller, peak at about  $4.20 \text{ \AA}$  indicates the water molecules in the second hydration shell of the hydronium ion. Both peaks at about  $d_{\text{O}^+ - \text{O}} = 2.5 \text{ \AA}$  and at  $4.20 \text{ \AA}$  are clearly shown in data for various exchange-correlation functionals [91], as well as the SCI-MS-EVB simulations [115, 116]. Beyond that, a decomposition of the first peak into three components has been used to support the picture of an asymmetric Eigen state [62]. Each peak is accompanied by peaks of the dotted lines at slightly larger distances, which indicate the hydrogen atoms belonging to the water molecules in the respective hydration shells. Additionally, the dotted lines show a weak and broad shoulder below roughly  $2.5 \text{ \AA}$ , the origin of which is further discussed in section 1.1.2. A slight relative maximum of the solid lines at  $d_{\text{O}^+ - \text{O}^+} = 3.00 \text{ \AA}$  but with a magnitude below one indicates a metastable solvation structure to exist between the oxygens of two hydronium ions. However, note that there is no such signature in the dashed and dotted lines, i.e. no apparent correlation with the excess proton of the nearest hydronium ion. The peak at  $d_{\text{O}^+ - \text{O}^+} = 3.00 \text{ \AA}$  was also observed by Calio et al. [116] and at  $d_{\text{O}^+ - \text{O}^+} = 3.20 \text{ \AA}$  by Xu et al. [115].

In Fig. 1.3B the RDFs of the excess protons are shown with respect to the other excess protons ( $\text{H}^+$ ) as solid lines and all hydrogen nuclei ( $\text{H}$ ), including excess protons, as broken lines. The main peak of the broken lines at  $d_{\text{H}^+ - \text{H}} = 1.8 \text{ \AA}$  indicates the mean

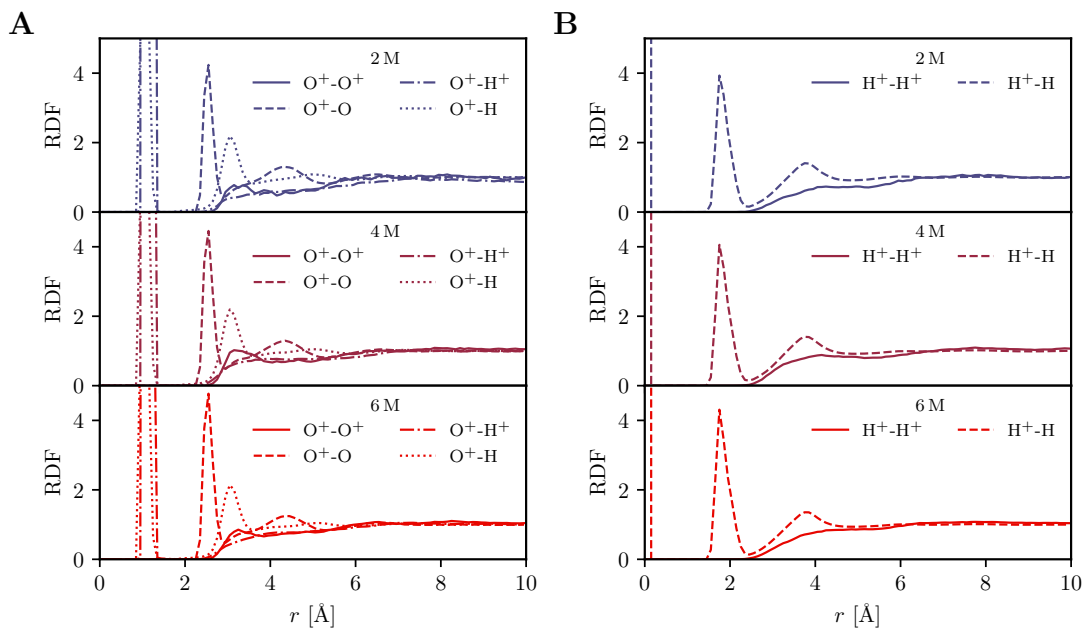


**Figure 1.3.:** Spatial correlations between the oxygen atoms of hydronium ions (A) and excess protons (B) with respect to other nuclei in terms of radial distribution functions (RDFs) as obtained from ab initio MD simulations of hydrochloric acid solutions at various concentrations. **A:** RDFs are shown for the oxygen nuclei of the hydronium ions ( $O^+$ ) as solid lines, for the oxygen nuclei of the water molecules (O) as broken lines, for the the excess protons ( $H^+$ ) as dashed and dotted lines and all hydrogen nuclei (H), including excess protons, as dotted lines. **B:** RDFs are shown for the excess protons ( $H^+$ ) as solid lines and all hydrogen nuclei (H), including excess protons, as broken lines.

distance between hydrogen atoms within the same hydronium ion. The peak shows a shoulder at around  $2.1 \text{ \AA}$  possibly related to spatial correlations between the excess proton and two hydrogen atoms in the neighboring water molecule of the  $H_5O_2^+$  complex. The second peak of the broken lines at  $3.8 \text{ \AA}$  is related to other water molecules in the first hydration shell, that form hydrogen bonds with the hydronium ion to which the excess proton is assigned. No spatial correlations are apparent in the RDFs between excess protons, shown as solid lines. In contrast to that, Xu et al. [115] observed a slight peak at  $d_{H^+-H^+} = 4.20 \text{ \AA}$ , indicative of spatial correlations between two excess protons.

In summary, the RDFs of the hydronium ions as well as of the excess protons presented in Figs. 1.3A and B indicate no spatial correlations between excess protons or hydronium ions and other excess protons. While there appears a slight relative maximum in the RDF between hydronium ions itself, this may simply be related to close-packing effects in the liquid.

In Fig. 1.4 the RDFs of the chloride counterions are shown for the three hydrochloric acid concentrations with respect to the excess protons as solid lines, all hydrogen nuclei,

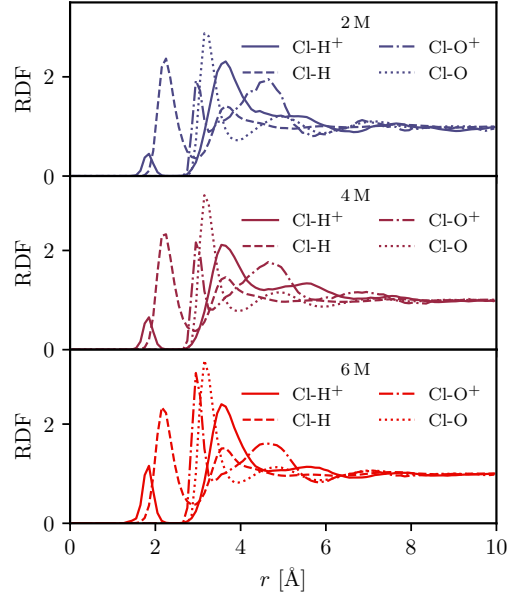


**Figure 1.4.:** Spatial correlations between the chloride counterions and other nuclei in terms of radial distribution functions (RDFs) as obtained from ab initio MD simulations of hydrochloric acid solutions at various concentrations. RDFs are shown for the excess protons ( $\text{H}^+$ ) as solid lines, all hydrogen nuclei (H), including excess protons, as broken lines, the oxygen nuclei of the water molecules (O) as dotted lines and the oxygen nuclei of the hydronium ions ( $\text{O}^+$ ) as dashed and dotted lines.

including excess protons, as broken lines, the oxygen nuclei of the water molecules as dotted lines and the oxygen nuclei of the hydronium ions as dashed and dotted lines. For all hydrochloric acid concentrations, the general features of the RDFs are comparable with only weak concentration-dependent trends. The RDFs of the excess protons around the counterions (solid lines) show two dominant peaks, a small one that is located at around  $d_{\text{Cl-H}^+} = 1.8 \text{ \AA}$  and thereby left of the major peak of the hydrogen nuclei RDFs at around  $d_{\text{Cl-H}} = 2.2 \text{ \AA}$ . This peak is important as it corresponds to excess protons coordinated directly with the counter ion, i.e. in between the chloride ion and the oxygen atom of the respective hydronium ion. This contact ion pair is considered as an important intermediate [114]. Yet, the excess protons are still part of the hydronium ion, since an even smaller distance of around  $1.4 \text{ \AA}$  would be expected for the covalent bond to the chloride atom [114]. The peak clearly increases with the hydrochloric acid concentration in Fig. 1.4, but even for the largest concentration of 6 M it remains smaller than the second and largest peak in the RDFs at about  $3.5 \text{ \AA}$ . This peak is located to the right of the first and dominant peak in the RDFs of the oxygen nuclei of the hydronium ions (dashed and dotted lines) at around  $d_{\text{Cl-O}^+} = 3.0 \text{ \AA}$ , which is slightly closer than the respective peak of all oxygen nuclei at around  $d_{\text{Cl-O}} = 3.1 \text{ \AA}$ .

All of the presented data is in good agreement with results by Baer et al. [114] from comparable ab initio simulations, who additionally show data for much higher concentrations up to 16 m ( $\sim 11.7$  M) and successfully reproduced EXAFS experimental measurements [113]. Specifically, they report  $d_{\text{Cl-O}^+} = 2.96 \text{ \AA}$  and  $d_{\text{Cl-O}} = 3.14 \text{ \AA}$  in excellent agreement with experimental EXAFS data [113]. Data comparing various exchange-correlation functionals used in the ab initio DFT simulation also consistently reproduced the results presented in Fig. 1.4 with no significant dependence (except for the PBE functional) and albeit large errors in some cases [91].

When interpreting the RDFs, the actual densities of the species need to be put into perspective. The densities of chloride ions, excess protons and hydronium ions are equal by definition. However, for the 2 M hydrochloric acid solution data set, the ratio of water molecules to chloride ions or respectively excess protons is about 24.8 and drops to 11.2 for the 4 M and 6.5 for the 6 M data sets. These numbers would have to be divided by two, assuming that water molecules are equally and exclusively solvating all chloride ions and excess protons. It is therefore evident, that for the 6 M solution, hydronium ions are necessarily residing already in the first hydration shell of the chloride ions. More precisely the average coordination numbers around the chloride ions are obtained by integration over the first peak of each RDF in Fig. 1.4 and use of Eq. (1.16). The obtained coordination numbers are reported in tab. 1.1 and are generally in good agreement with previous simulation and experimental results [114, 113]. The average number of hydronium ions in the first hydration shell of any chloride ion increases from 0.13 for 2 M to 0.52 for 6 M. Previously, Baer et al. [114] interpreted this significant increase in the coordination number with an increase of contact ion pairs, where the excess proton is shared between the hydronium oxygen and the chloride ion. However, the coordination number of the excess protons around chloride ions does not increase as much, only from 0.01 for 2 M to 0.05 for 6 M. Therefore, the excess protons of the hydronium ions in the first solvation shell of the chloride ions mostly point away from chloride ions and must be coordinated with other water molecules, rather than the chloride ions.

Taken together, this data indicates that the excess protons in aqueous hydrochloric acid solutions exclusively reside inside the water, as part of hydronium ions within this definition, and additionally within the hydronium ions mostly reside away from the chloride ions, i.e. between two oxygen atoms and not between a chloride and an oxygen atom. This holds true even for moderately high concentrations up to 6 M considered in this study, but necessarily breaks down at very high concentrations when the water is saturated with hydrochloric acid [114]. The data confirms the high solubility of excess protons in water, due to energetic but also entropic effects [116, 75]. Along these lines, according to [114] the dominant effect is the protonation of water when hydrochloric acid concentration is increased and Calio et al. [116] claimed to not observe a change in proton solvation structures for hydrochloric acid concentrations up to 3.26 M. Linear trends of IR difference spectra with respect to concentrations up to 6 M lead to similar conclusions, i.e. the correlations of two excess protons, or excess protons and chloride ions, are negligible [2].

**Table 1.1.:** Average coordination numbers  $N_{ab}(r)$  around the chloride counterions as obtained from the first peak of the RDFs in Fig. 1.4 according to Eq. (1.16).

	Cl-H <sup>+</sup> ( $r < 2.5 \text{ \AA}$ )	Cl-H ( $r < 3.0 \text{ \AA}$ )	Cl-O <sup>+</sup> ( $r < 3.5 \text{ \AA}$ )	Cl-O ( $r < 3.5 \text{ \AA}$ )
2 M	0.01	5.59	0.13	5.06
4 M	0.02	5.37	0.27	5.01
6 M	0.05	5.07	0.52	4.86
2.5 m [114]			0.17	5.82
6 m [114]			0.42	5.21
10 m [114]			0.71	4.67
16 m [114]			1.05	3.99
6 m [114, 113]			$0.7 \pm 0.2$	$5.1 \pm 0.5$
10 m [114, 113]			$1.0 \pm 0.3$	$4.8 \pm 0.5$
16 m [114, 113]			$1.6 \pm 0.3$	$4.2 \pm 0.5$

### Hydrogen-bond structure

The hydrogen bond (HB) structure of the water molecules in the first hydration shell of the excess proton has been shown to play an important role for understanding when and where the excess proton moves [87, 97, 91, 61].

**Hydrogen-bond asymmetry** Napoli et al. [61] introduced the hydrogen bond (HB) asymmetry  $\phi$  as a measure to identify the excess proton among the candidate protons in a hydronium ion. First, each water molecule is assigned a coordination number as the difference of the number of acceptor HBs minus the number of donor HBs. Then  $\phi$  is defined for each candidate proton at each time step as the coordination number of the closest neighboring water molecule minus the average of the coordination numbers of the closest water molecules of the other candidate protons of the same hydronium ion. By construction, the sum of  $\phi$  within a hydronium ion is zero. Napoli et al. [61] found that protons with strongly negative values of  $\phi$  show the typical spectral signatures associated with excess protons. This measure is also applied to the ab initio simulation data that was used for the analysis of the long time diffusion in section 1.1.3, specifically to the joint trajectories of the excess protons from which the spurious ‘special pair dance’ was removed.

Normalized distributions of  $\phi$  over the whole simulations are shown in Fig. 1.5A with mean values given in the legend. The mean values are clearly negative which suggests that this criterion agrees with the excess-proton identification scheme applied to this data set and confirms the previous observation by Napoli et al. [61]. To study the relation between HB structure and proton transfer, the trajectories are filtered in time around the transfer events, i.e. when an excess proton changes its closest oxygen. The normalized distributions of  $\phi$  values during 20 fs (40 time steps) before and after a transfer event are given in Fig. 1.5B–D as gray broken lines with mean values reported

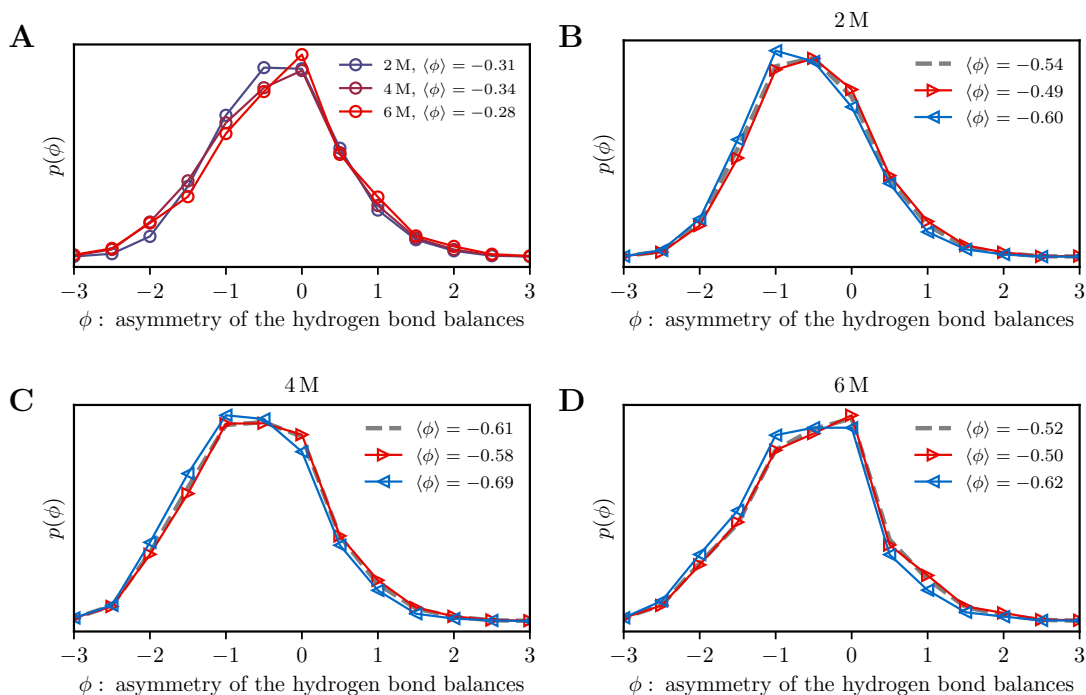


**Figure 1.5.:** Normalized distributions of the hydrogen bond asymmetries, denoted as  $\phi$ , of the excess proton trajectories from ab initio MD simulations of HCl solutions at various concentrations. See text for definition and details. Mean values of the distributions are reported in the legends. **A:** Distributions over the whole trajectories. **B–D:** Distributions of  $\phi$  during 20 fs before and after any transfer event (gray broken lines), i.e. when the excess proton changes the closest oxygen, and distributions of  $\phi$  around each uni-directional transfer event, which are split into the 20 fs before, corresponding to the donor oxygen of the proton transfer event (blue and left pointing triangles) and the 20 fs after, corresponding to the acceptor oxygen (red and right pointing triangles).

in the legends. To further elucidate the data, the same filter is applied before and after each uni-directional transfer event. Uni-directional here refers to transfer events, that are not followed by a fast return back to the original oxygen atom within the following 50 fs (100 time steps). By only regarding these uni-directional events, different HB configurations can be discriminated around the donor oxygen of the proton-transfer event, i.e. before the uni-directional transfer (shown in blue with left pointing triangles), and the acceptor oxygen, i.e. after the uni-directional transfer (shown in red with right pointing triangles), which show distinct distributions in Fig. 1.5B–D. The mean values of the distributions before a transfer are more negative than the corresponding averages in Fig. 1.5A, indicating that on average a more negative value of  $\phi$  precedes an imminent transfer event. Therefore,  $\phi$  actually seems to be a useful predictor for proton transfer.

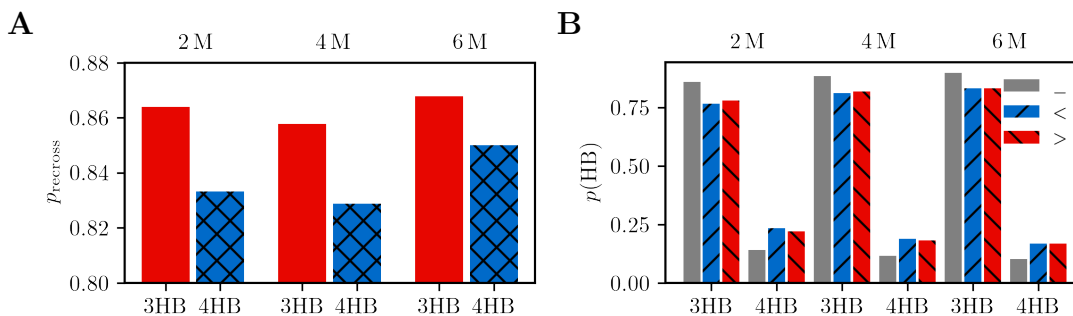


**Figure 1.6.:** Correlations between the existence of a fourth hydrogen bond of a hydronium ion (4HB) and the return probability of the excess proton, as observed in ab initio MD simulations of HCl solutions at various concentrations. **A:** Probability of the excess proton to return across the mid plane between the oxygens within the following 50 fs. **B:** Time-averaged probabilities of all hydronium ions for the fourth hydrogen bond to exist (4HB) or not (3HB), as obtained from the whole simulation (gray, no hatching) and during the 20 fs before (blue) and after (red) each uni-directional transfer event.

**The fourth hydrogen bond** Inspired by Tse et al. [87], Biswas et al. [97] and Fischer and Gunlycke [91] investigated the role of a fourth water molecule hydrogen-bonded to the hydronium ion. Presumably, its presence determines whether an excess proton would transfer to a different oxygen atom [97] and in particular whether it is likely to return to the original oxygen atom, i.e. to perform back-and-forth transfers, or not [91]. Biswas et al. [97] found a correlation between small values of the proton-sharing coordinate and a peak at 2.0 Å in the RDF between the oxygen atom of the hydronium ion and the hydrogen atoms of other water molecules in simulations of dilute hydrochloric acid solutions.

In their simulations of 1.7 M HCl solutions, Fischer and Gunlycke [91] observed a higher return probability (67 %) if the hydronium ion was coordinated with only three donor HBs as compared to four HBs (53 %), the additional one being an accepted HB from a fourth water molecule. In accordance with previous works, the fourth HB is defined to be present if the vector connecting the hydronium oxygen and the hydrogen atom of the fourth water molecule has a length of less than 2.6 Å and points at an angle of less than 35° with respect to the normal of the plane spanned by the three hydrogen nuclei of the hydronium ion [87, 91]. The probability of a return within the following 50 fs (100 time steps) upon any transfer across the mid plane between the oxygens obtained in the simulations is illustrated in Fig. 1.6A depending on whether the donor hydrogen ion is accepting a HB from a fourth water molecule (4HB, shown in blue with hatching) or not (3HB, shown in red without hatching). The data demonstrates the clear trend that the return probability is reduced if a fourth HB is present, in agreement with previous studies [91]. However, even though this correlation is discernible in the data, the mechanism does not appear to be a dominant driver for proton transfer in hydrochloric acid solutions. This follows from Fig. 1.6B, where the probability of observing the fourth



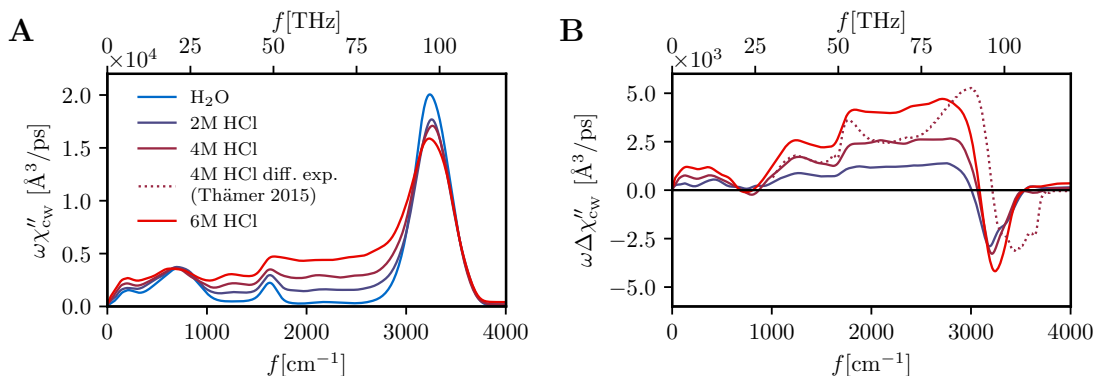


**Figure 1.7.:** **A:** IR absorption spectra obtained from ab initio MD simulations of pure water (blue solid line) and HCl solutions at various concentrations (dark purple: 2 M, purple: 4 M and red: 6 M). The spectra are divided by the water molecular number concentration  $c_w$ . **B:** Difference spectra between the three HCl spectra and the water spectrum, obtained from the spectra in A. The red dotted line shows an experimental difference spectrum of HCl at 4 M [54], rescaled in height to match the simulation results.

HB is plotted for three different time averages; the averages over the whole simulations of all hydronium ions are given in gray, the averages over the 20 fs (40 time steps) before and after each uni-directional transfer event, i.e. without return, are given in blue and red respectively. Throughout the data, the time-averaged probability of a fourth HB is only about 10–20%. Before and after uni-directional transfer events this probability is significantly increased but it is still smaller than the probability of a uni-directional transfer event happening without the presence of a fourth HB.

The data confirms that HB structure is highly correlated with the excess-proton transfer dynamics and the presented comparison with previous studies strengthens the existing hypotheses, that the HB asymmetry  $\phi$  or the fourth water molecule are useful descriptors.

### 1.1.3. Excess proton dynamics

In the following, the dynamic properties of excess protons in concentrated acid solutions are discussed, using again the data set of BLYP-D3 DFT quality [2] for illustration.

#### IR spectroscopic signatures

IR absorption spectra of hydrochloric acid solutions at various concentrations are shown in Fig. 1.7A and compared to a bulk water spectrum, all calculated from BOMD simulations [2]. By taking the properly normalized difference spectrum between the hydrochloric-acid solution spectra and the bulk water spectrum, as shown in Fig. 1.7B, the IR spectral signatures related to excess-proton dynamics are revealed. The characteristic continuum band between the water stretching and bending vibrations in the range  $2000\text{ cm}^{-1}$  to

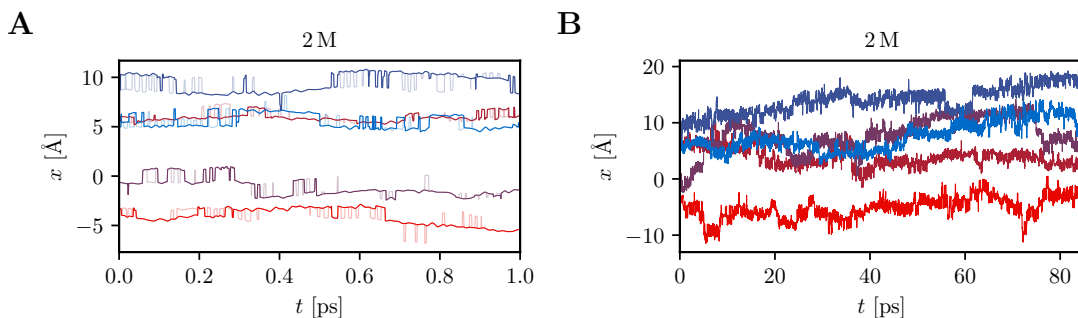


**Figure 1.8.:** Examples of five joint trajectories of excess protons in 2 M HCl solution on short (**A**) and long time scales (**B**). In A, the pale colored lines indicate the spurious jumps, resulting from the ‘special pair dance’, that are removed from the trajectories (see text for details).

$3000\text{ cm}^{-1}$  is well resolved and in addition strong bands are seen at around  $1200\text{ cm}^{-1}$ ,  $400\text{ cm}^{-1}$  and below. The difference spectra show good agreement with experimental data, shown as a red dotted line in Fig. 1.7B. The previous literature interpretation of these signatures in terms of Zundel and Eigen configurations is discussed in section 1.1.2. The interpretation in terms of the proton-transfer reaction dynamics is the topic of chapter 4.

### Long-time dynamics

For the analysis of diffusion of the excess protons on long time scales, the simple excess-proton identification scheme for static observables needs to be augmented to identify joint excess-proton trajectories throughout the whole simulation trajectory. Notably, some works instead use a center-of-excess-charge reaction coordinate to circumvent this problem [93]. Here, after identifying at each time step of the simulation a total number of  $N_{\text{H}^+}$  excess protons, the trajectories of the excess protons are stitched together to a total of  $N_{\text{H}^+}$  trajectories, each of the length of the whole simulation. The procedure obviously introduces jumps in the joint trajectories whenever an excess proton changes identity, which is a manifestation of the Grotthus process. However, rapid spurious jumps within the same hydronium ion, the ‘special pair dance’ [107, 62], are filtered from the trajectories by the following procedure: within each hydronium ion, the candidate proton that either performs the next transfer to another water molecule or is the next to be identified as an excess proton while neighboring a chloride atom, remains the excess proton (a procedure that was also used by Calio et al. [62]). Lastly, the trajectories are unwrapped over the periodic boundary conditions. Some trajectories of excess protons produced by this protocol are illustrated in Fig. 1.8A and B along a single Cartesian coordinate and on two different time scales. Additionally in Fig. 1.8A, the pale colored lines show the trajectories before removal of the ‘special pair dance’.

Such joint trajectories can be used to calculate mean squared displacements (MSDs),

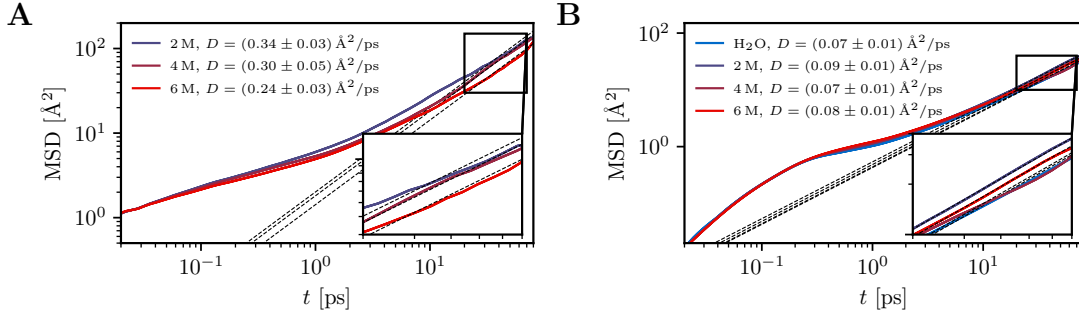


**Figure 1.9.:** MSDs (mean squared displacements) in the lab frame,  $\langle |\mathbf{r}(t) - \mathbf{r}(0)|^2 \rangle$ , of the excess protons (**A**) and the oxygen atoms (**B**) computed from the simulation trajectories of HCl solutions at three different concentrations. In B, the MSD of the oxygen atoms in the pure-water simulations is shown as well. Errors of the mean are indicated by the line widths and taken from standard deviations computed over the individual excess-proton and oxygen-atom joint trajectories. Linear fits are shown as black broken lines, which are fitted in the long time regimes, 20 ps to 80 ps, the range that is also shown enlarged in the insets.

$\langle |\mathbf{r}(t) - \mathbf{r}(0)|^2 \rangle$ , of the excess protons on long time scales. The MSDs averaged over all excess protons are shown in Fig. 1.9A for simulations of hydrochloric acid solutions at three different concentrations and compared to the MSDs computed for the oxygen atoms representative of the water molecules in Fig. 1.9B. In general, the MSD is expected to show inertial scaling,  $\text{MSD} \sim t^2$ , for short time scales and diffusive scaling,  $\text{MSD} \sim t$ , for long time scales. Both regimes are well visible in Fig. 1.9B for the oxygen atoms. For the excess protons the inertial regime is perturbed by the jumps in the joint trajectories, caused by changes of the excess-proton identities.

The diffusion constant  $D$ , which is an experimentally observed quantity, is related to the MSD by

$$D = \frac{1}{6t} \langle |\mathbf{r}(t) - \mathbf{r}(0)|^2 \rangle, \quad (1.17)$$

and computed by a least-square fit of the slopes in the diffusive regime between 20 ps to 80 ps. The diffusion constants are reported in the legends of Figs. 1.9A and B with statistical errors from the linear fits.

To access the accuracy of these diffusion constants, the focus is first put on the values for the oxygen atoms. Within the error the same diffusion constant of about  $D_{\text{O}} = 0.08 \text{ \AA}^2/\text{ps}$  is obtained in all four simulations. While this value is significantly smaller than the experimental value of  $D_{\text{O}} = 0.23 \text{ \AA}^2/\text{ps}$  [117, 118], it is well known that specifically the BLYP exchange-correlation functional in this simulation approach produces too small diffusion constants. In agreement with these results, various studies of water utilizing ab initio MD together with the BLYP exchange-correlation functional, reported diffusion constants in the range of  $0.04 \text{ \AA}^2/\text{ps}$  to  $0.11 \text{ \AA}^2/\text{ps}$  for comparable

setups to these, as reviewed recently [119].

Note that in experiments the excess proton diffusion constant is known to be strongly concentration and temperature dependent [45]. In the dilute limit, the experimental diffusion constant of the excess proton,  $D_{\text{H}^+} = 0.94 \text{ \AA}^2/\text{ps}$ , is much higher than the experimental diffusion constant of water by a factor of  $D_{\text{H}^+}/D_{\text{O}} = 4.1$ , an observation that corroborates Grotthus' hypothesis [44]. However, this factor drops to about 3.0 at 2 M and 1.5 at 6 M [45]. This trend was qualitatively captured in self-consistent iterative multistate empirical valence bond (SCI-MS-EVB) simulations of hydrochloric acid solutions [115, 116]. Both studies obtained values between  $D_{\text{H}^+} = 0.2 \text{ \AA}^2/\text{ps}$  to  $0.3 \text{ \AA}^2/\text{ps}$  around 1 M and  $D_{\text{H}^+} = 0.15 \text{ \AA}^2/\text{ps}$  to  $0.20 \text{ \AA}^2/\text{ps}$  around 3 M, compared to a value of  $D_{\text{H}^+} = 0.37 \text{ \AA}^2/\text{ps}$  in the dilute limit (one excess proton in 256 waters) [97]. While a similar trend is also indicated in the present data, the errors are too large to draw definite conclusions. The obtained diffusion constants for the excess protons,  $D_{\text{H}^+} = 0.24 \text{ \AA}^2/\text{ps}$  to  $0.34 \text{ \AA}^2/\text{ps}$ , are smaller than the experimental value. However, the ratios  $D_{\text{H}^+}/D_{\text{O}} = 0.34/0.09 = 3.8 \pm 0.8$  for 2 M,  $D_{\text{H}^+}/D_{\text{O}} = 0.30/0.07 = 4.3 \pm 1.3$  for 4 M and  $D_{\text{H}^+}/D_{\text{O}} = 0.24/0.08 = 3.0 \pm 0.8$  for 6 M, that is observed in the presented data, seem in satisfactory agreement with experiments. Similar ab initio simulation setups for a single excess proton in a box of water molecules obtained diffusion constants of  $D_{\text{H}^+} = 0.3 \text{ \AA}^2/\text{ps}$  to  $0.6 \text{ \AA}^2/\text{ps}$  [87] and of  $D_{\text{H}^+} = 0.3 \text{ \AA}^2/\text{ps}$  to  $0.8 \text{ \AA}^2/\text{ps}$  [94]. A study employing Car-Parinello molecular dynamics (CPMD) simulations of 1.7 M HCl solutions and the Perdew, Burke and Ernzerhof (PBE) exchange-correlation functional found  $D_{\text{H}^+} = 0.9 \text{ \AA}^2/\text{ps}$  to  $1.1 \text{ \AA}^2/\text{ps}$  compared to  $D_{\text{O}} = 0.04 \text{ \AA}^2/\text{ps}$  to  $0.07 \text{ \AA}^2/\text{ps}$  for the water molecules [91]. An older study of a single excess proton in a box of 64 water molecules using CPMD with the BLYP functional obtained  $D_{\text{H}^+} = 0.05 \text{ \AA}^2/\text{ps}$  to  $0.08 \text{ \AA}^2/\text{ps}$  compared to  $D_{\text{O}} = 0.02 \text{ \AA}^2/\text{ps}$  to  $0.06 \text{ \AA}^2/\text{ps}$  for the water molecules [120]. It is noteworthy, that the inclusion of nuclear quantum effects in simulations has been shown to significantly increase the obtained excess-proton diffusion constants closer to the experimentally observed values [97, 121].

To conclude, the accurate estimation of diffusion constants for the excess proton remains challenging, which is seen from the wide spread of results obtained in previous studies. The results presented here for the diffusion constants appear reasonable when compared to previously reported values and specifically the ratios  $D_{\text{H}^+}/D_{\text{O}} = 3.0$  to  $4.3$  are in good agreement with experiment.

### Short-time dynamics

The mean proton-transfer rate is at the heart of research on excess protons solvated in water, as it is the relevant microscopic time scale that determines the macroscopic large diffusion obtained by the Grotthus process, which is not governed by vehicular diffusion of the oxygens but by exchange of the excess-proton identity. The mean transfer rate is the inverse of the waiting time of a stochastic barrier-crossing process, that is not to be confused with the transfer-path time of the actual transition over the barrier.

Agmon [46] gives a summary of early experimental results, suggesting a mean proton-transfer time of 1.5 ps obtained in NMR studies [43], which is believed to be correlated with the hydrogen bond rearrangement and water reorientation dynamics on the time scales of 1 ps to 2 ps determined from a number of other experiments. These time scales seem to contrast more recent experimental results from 2D IR spectroscopy, that report interconversion between different proton hydration structures, i.e. Eigen and Zundel-like structures, on time scales of around 100 fs and less [122, 55, 74]. On the other hand, Carpenter et al. [56] write, “the hydrated proton bend displays fast vibrational relaxation and spectral diffusion timescales of 200 – 300 fs, however, the transient absorption anisotropy decays on a remarkably long 2.5 ps timescale, which matches the timescale for hydrogen bond reorganization in liquid water”. Arguing that the latter would be an upper bound, they infer “the transfer of excess protons in water [...] is an activated process with a timescale of 1 – 2 ps.” Kundu et al. [74] confirm that “during the lifetime of the  $\text{H}_5\text{O}_2^+$  motif, that is on the order of 1 ps, the proton undergoes fluctuating large-amplitude motions exploring essentially all possible positions between the flanking water molecules”. Yuan et al. [90] measure a concentration-dependent ‘proton hopping time’ in HCl solutions using 2D IR chemical exchange spectroscopy with a methyl thiocyanate probe and extrapolate a time of 1.6 ps for the dilute limit.

It transpires, that two time scales determine the distribution of proton-transfer waiting times, which was confirmed in various simulation studies and interpreted as stemming from either back-and-forth or uni-directional proton transfer, respectively, in the literature sometimes referred to as ‘reversible’ and ‘irreversible’ proton transfer. Napoli et al. [61] point out that while they find a frequency-correlation time of  $(1.4 \pm 0.3)$  ps “corresponding to the pump ( $3150 \text{ cm}^{-1}$ ) and probe ( $1760 \text{ cm}^{-1}$ ) frequencies used in [54]”, the auto-correlation of the proton asymmetry actually decays on time scales of less than 100 fs with a second slower component of  $(0.8 \pm 0.1)$  ps. Fischer et al. [123] find the time scale of proton ‘hopping’ to be around 0.5 ps, including back-and-forth events, and deduce a time scale of 2.5 ps for uni-directional events in a later study [91]. Calio et al. [116] extract two timescales of about 400 fs to 500 fs and 1.3 ps to 2.3 ps for the concentrations 0.43 M to 3.26 M from fits to the long-lived anisotropy decays, which the authors argue “can correlate experimental time constants to irreversible proton transfer”. In a follow-up study Calio et al. [62] report three timescales of about 10 – 17 fs, 320 – 490 fs and 2.3 – 3.2 ps for the concentrations 0.22 M to 0.43 M from fits to the anisotropy decay of the excess-proton dynamics projected on the axis of the two closest oxygen atoms, with a slight acceleration to the values 12 – 15 fs, 83 – 270 fs and 1.4 ps when nuclear-quantum effects are considered. Roy et al. [92] find a time scale of 1 – 2 ps for uni-directional proton transfer between two water molecules in 2 M HCl solutions employing two-dimensional transition state theory and Marcus theory of ion pairing. This number increases significantly to 2 – 4 ps in 8 M HCl solutions. Arntsen et al. [94] report time constants of the excess-proton identity auto-correlation function, which is elaborated on further below. They find a values of 184 fs, but after eliminating back-and-forth events from the data the time scale increases to 1.69 ps. Furthermore, a couple of studies point out that the long time scale of proton transport increases significantly with concentration [75, 92].

**Table 1.2.:** Collection of proton-transfer time scales in water at 300 K reported in the literature from experiment (upper section) and theory (lower section).

	method	conc. [M]	time
Meiboom [43]	NMR		1.5 ps
Woutersen and Bakker [122]	2D IR	5	<0.1 ps
Dahms et al. [55]	2D IR	<1	<0.1 ps
Thämer et al. [54]	2D IR	4	>0.48 ps
Carpenter et al. [56]	2D IR	2	<2.5 ps
Kundu et al. [74]	2D IR	1	<0.1 ps
			1 ps
Yuan et al. [90]	2D IR chemical exchange	dilute limit	1.6 ps
Fischer et al. [123]	DFT CPMD	1.7	0.5 ps
Fischer and Gunlycke [91]	DFT CPMD	1.7	2.5 ps
Calio et al. [116]	MS-EVB	0.43 – 3.26	0.4 – 0.5 ps
			1.2 – 2.3 ps
Calio et al. [62]	MS-EVB, DFT BOMD	0.22 – 0.43	10 – 17 fs
			0.3 – 0.5 ps
			2.3 – 3.2 ps
	+ NQE		12 – 15 fs
			0.83 – 0.27 ps
			1.4 ps
Arntsen et al. [94]	DFT BOMD		0.184 ps
			1.69 ps
Roy et al. [92]	DFT BOMD	2	1 – 2 ps
	DFT BOMD	8	2 – 4 ps

A summary of the reported values is given in Tab. 1.2. It transpires that the separation in back-and-forth and uni-directional events is important to distinguish two time scales in the broad distributions of proton-transfer times. For stochastic barrier-crossing processes of highly inertial or non-Markovian coordinates and furthermore for low energy barriers, it is well established that barrier-crossing events exhibit large numbers of subsequent back-and-forth events, due to the slow dissipation of the energy required for the initial barrier-crossing event [35, 124, 125, 16, 92, 4]. Such events appear especially important with regard to proton-transfer processes and their spectral signatures [2, 4].

**Identity auto-correlation functions** To describe the long time scales of excess-proton diffusion observed in the anisotropy decay of 2D IR experiments [54, 56], correlation times of the excess-proton identity have proven useful. Inspired by previous work [86, 94, 62], the auto-correlation functions of the excess-proton and hydronium-oxygen identities are calculated from joint trajectories of the excess protons as have been used for the analysis of the long-time diffusion properties described in 1.1.3. Following this protocol, the excess protons are given as the remaining protons after the water molecules are assembled for each oxygen atom with the closest two hydrogen atoms at each time step of the simulation. Hydronium ions are defined by an excess proton together with the water molecule of the closest oxygen atom. Therefore, at each time step a total number of excess protons  $N_{\text{H}^+}$ , as well as hydronium ions, equivalent to the number of chloride ions in the simulation, is obtained. The trajectories are then stitched together to give  $N_{\text{H}^+}$  trajectories, each of the length of the whole simulation, for the excess protons and hydronium oxygens, respectively. Following Arntsen et al. [94], rapid back-and-forth fluctuation of hydronium-oxygen identities is ‘filtered out’ from the trajectories by the following procedure. Whenever along a trajectory the identity changes from one oxygen atom to another, it is checked whether the identity returns to the original nucleus within 0.5 ps. If it returns without passing to a third nucleus in between, the identity remains with the original nucleus as if the identity did not change throughout this time. For the excess-proton identities this criterion does not suffice since the identity often fluctuates between three candidates within one hydronium ion. Rather the same procedure as also detailed in section 1.1.3 and similar to Calio et al. [62] is used to ‘filter out’ the rapid back-and-forth fluctuation of excess-proton identities, i.e. the ‘special pair dance’: The candidate proton that either performs the next transfer to another water molecule or is the next to be identified as an excess proton while neighboring a chloride atom, remains the excess proton. These procedures define sets of trajectories from which the fast identity fluctuations are ‘filtered out’. The identity auto-correlation functions are then calculated for excess-proton and hydronium-oxygen identities on both sets of trajectories, ‘filtered’ and ‘unfiltered’.

The identity auto-correlation function is here defined as

$$c(t) = \frac{\langle h(t)h(0) \rangle - \langle h \rangle^2}{\langle h \rangle - \langle h \rangle^2}, \quad (1.18)$$

where  $h(t)$  is one if an excess proton or hydronium oxygen atom has the same identity,

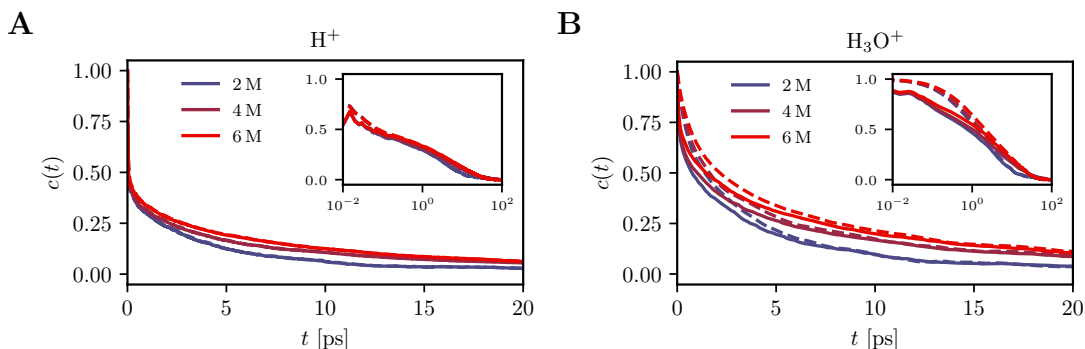


**Figure 1.10.:** Identity auto-correlation functions Eq. (1.18) of the excess protons (**A**) and hydronium oxygens (**B**) obtained from ab initio MD simulations of HCl solutions at various concentrations. The correlation functions are computed from unfiltered (solid colored lines) and filtered trajectories (broken colored lines), see text for details. The data is shown on a logarithmic time axis in the insets.

i.e. is the same nucleus, as at  $t = 0$ , otherwise  $h(t)$  is zero. In this definition the identity auto-correlation function is designed to reach unity for  $t = 0$  and to decay to zero for long times and is thereby slightly different compared to previous work [126, 86, 94]. Additionally, the continuous identity auto-correlation function is given as [94, 62]

$$C(t) = \frac{\langle H(t)H(0) \rangle}{\langle H \rangle}, \quad (1.19)$$

where  $H(t)$  is one as long as an excess proton or hydronium oxygen atom continuously has the same identity for the entire time interval  $[0, t]$  and zero otherwise.

The excess-proton and hydronium-oxygen identity auto correlations obtained according to Eq. (1.18) are given in Figs. 1.10A and B with the same data shown on a logarithmic time axis in the insets. Auto-correlation functions of the filtered trajectories are shown as broken colored lines for the three hydrochloric acid solutions at various concentrations while the auto-correlation functions of the unfiltered trajectories are shown as solid colored lines. The curves decay on multiple time scales. All show remarkable long-time behavior beyond several picoseconds, indicating that proton as well as hydronium identity is correlated over very long times scales, which occurs from looping of identities over several different nuclei [86]. As expected, the two types of data from filtered or unfiltered trajectories converge in these long time regimes. Both, the excess-proton identity auto correlations in Fig. 1.10A and the hydronium identities in Fig. 1.10B show a clear concentration dependence, with longer decay times for higher concentrations. On short time scales the excess-proton identity auto correlations largely decay within 0.1 ps to a value of 0.5, whereas the hydronium identity auto correlations decay to a value of 0.5 only after about 1 ps to 2 ps. Furthermore, a slight peak in the hydronium identity auto-correlation of the unfiltered trajectories (solid colored lines in Fig. 1.10B) at about



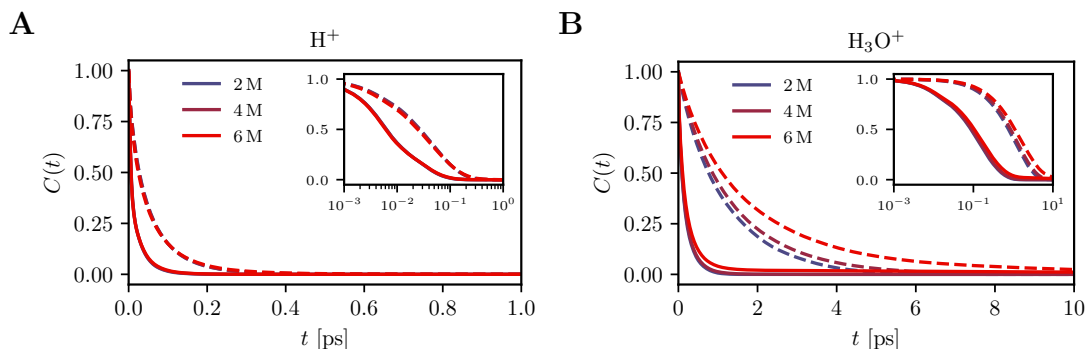


**Figure 1.11.:** Continuous identity auto-correlation functions Eq. (1.19) of the excess protons (a) and hydronium oxygens (b) obtained from ab initio MD simulations of HCl solutions at various concentrations. The correlations functions are computed from filtered (solid colored lines) and unfiltered trajectories (broken colored lines), see text for details. The data is shown on a logarithmic time axis in the insets.

0.025 ps indicates back-and-forth transfer of the excess proton in the transient  $\text{H}_5\text{O}_2^+$  cluster occurring at about twice the transfer-path time,  $\tau_{\text{TP}} = 12.6$  fs to 14.3 fs, which is related to the  $1200\text{ cm}^{-1}$  proton-transfer-path IR spectral signature [2]. Similarly, a peak in the excess-proton identity auto correlations of the unfiltered trajectories (solid colored lines in Fig. 1.10A) at about 0.010 ps indicates the time scale of excess-proton rattling within a single hydronium ion, referred to as ‘special pair dance’ in the literature [107, 62].

Next, to focus on the fast time scales of the correlations, the continuous identity auto-correlation functions according to Eq. (1.19) of the excess protons and of the hydronium oxygens are given in Figs. 1.11A and B with the same data shown on logarithmic time axes in the insets. Again, the data is shown in each plot as computed from filtered (broken colored lines) and unfiltered trajectories (solid colored lines). Note, that for the computation of these continuous identity auto correlations, configurations where the excess proton is located between the oxygen atom and a chloride ion are excluded. These configurations obviously produce spurious long-time auto correlations but have been analyzed to make up only 5% of the total trajectory lengths of all excess protons even at the concentration of 6 M, which is discussed in detail in section 1.1.2. The excess-proton continuous identity auto correlations decay fully within 0.3 ps and the hydronium-oxygen identity continuous auto-correlations within 10 ps. Comparing to the data presented in Fig. 1.10A and B, the hydronium identity auto correlations in Fig. 1.11B show again a clear concentration dependence, with longer decay times for higher concentrations. In contrast, such a dependence is not visible for the excess-proton identity auto correlations in Fig. 1.11A.

The time scales of the hydronium continuous identity auto correlations have been interpreted to be consistent with the time scales of the anisotropy decay observed in 2D IR experiments [56, 94]. Fits to these auto correlations with the sum of two decaying

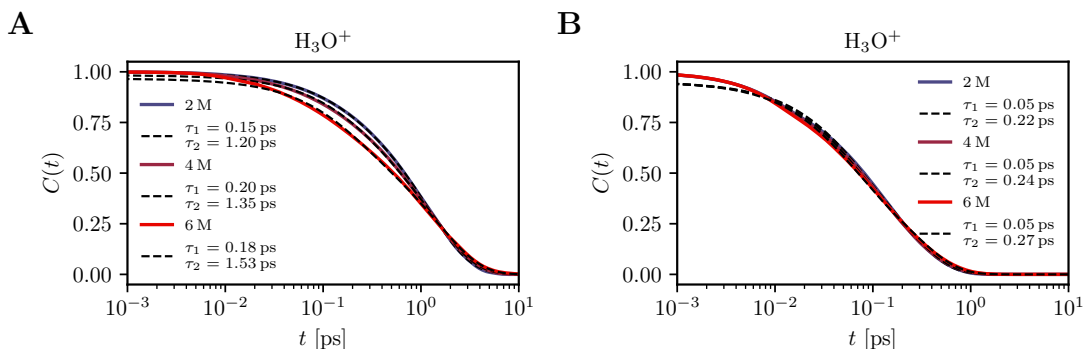


**Figure 1.12.:** Continuous identity auto-correlation functions Eq. (1.19) of the hydronium oxygens obtained from ab initio MD simulations of HCl solutions at various concentrations (already shown in Fig. 1.11B). The correlation functions are computed from filtered (**A**) and unfiltered trajectories (**B**), see text for details. Each curve is fitted to a sum of two decaying exponentials with the time scales reported in the legends and shown as black broken lines.

exponentials are therefore given as broken black lines, together with the original data from Fig. 1.11B repeated as solid colored lines in Fig. 1.12A (for the filtered trajectories) and B (for the unfiltered trajectories). The long time-scales of the bi-exponential fits to the correlations of the filtered trajectories, shown in 1.12A, reach from 1.2 ps to 1.53 ps, increasing with concentration. These time scales match the time scales reported for uni-directional proton transfer rather well (see Tab. 1.2). With regard to the results reported in section 1.1.3, where the long-time diffusion constants are found to be too small by a factor of about four when compared to experiment, one would expect the time scales for uni-directional proton transfer to be longer by the same factor. However, the present analysis excludes configurations involving chloride ions, which presumably are characterized by longer decay times. The diffusion constants on the other hand would have to be split in vehicular diffusion, due to translation of hydronium ions, and the jump diffusion, due to uni-directional proton transfer, to allow for a better comparison to the time scales of the auto correlations.

The long time-scales of the bi-exponential fits to the continuous hydronium identity auto correlations of the unfiltered trajectories, shown in Fig. 1.12b, reach from 0.22 ps to 0.27 ps, increasing with concentration. They can be interpreted as the mean proton-transfer waiting times [2], that however are dominated by back-and-forth fluctuations. In case that back-and-forth motion of the excess-protons between two oxygen atoms within 0.5 ps are filtered from the trajectories, the continuous hydronium identity auto correlation in Fig. 1.12a decays on time scales that match experimental spectroscopic anisotropy decays and have been interpreted as uni-directional proton transfer.

### 1.1.4. Nuclear quantum effects

Apart from the challenging computational demand, the estimation of dynamical properties, such as spectroscopic quantities or time-correlation functions, from MD simulations addressing NQE remains a “challenging problem” [58]. Strictly speaking, treating NQE on the basis of the Trotter formalism is only valid for static observables.

So far, to obtain dynamical properties, NQE simulations are mostly propagated using either CMD or RPMD. Note, that both are based on ring polymers though and do not consider correlations between nuclei and electrons, thus relying on the Born-Oppenheimer approximation. In fact, “the formal justification of both CMD and RPMD does not involve a hierarchy of well-controlled approximations starting from the full quantum mechanical expression for the various time correlation functions. Because one cannot identify or compute terms that are neglected by these methods, it is hard to systematically address their known artifacts, which becomes particularly problematic at low temperatures or when calculating the nonlinear operators encountered in many types of spectroscopy” [58]. Thus, it is not surprising that IR spectra obtained from different NQE methods may vary significantly, see Fig. 1.13, taken from reference [60], which shows IR spectra for the  $\text{H}_5\text{O}_2^+$  cation in vacuum obtained from different NQE simulation techniques.

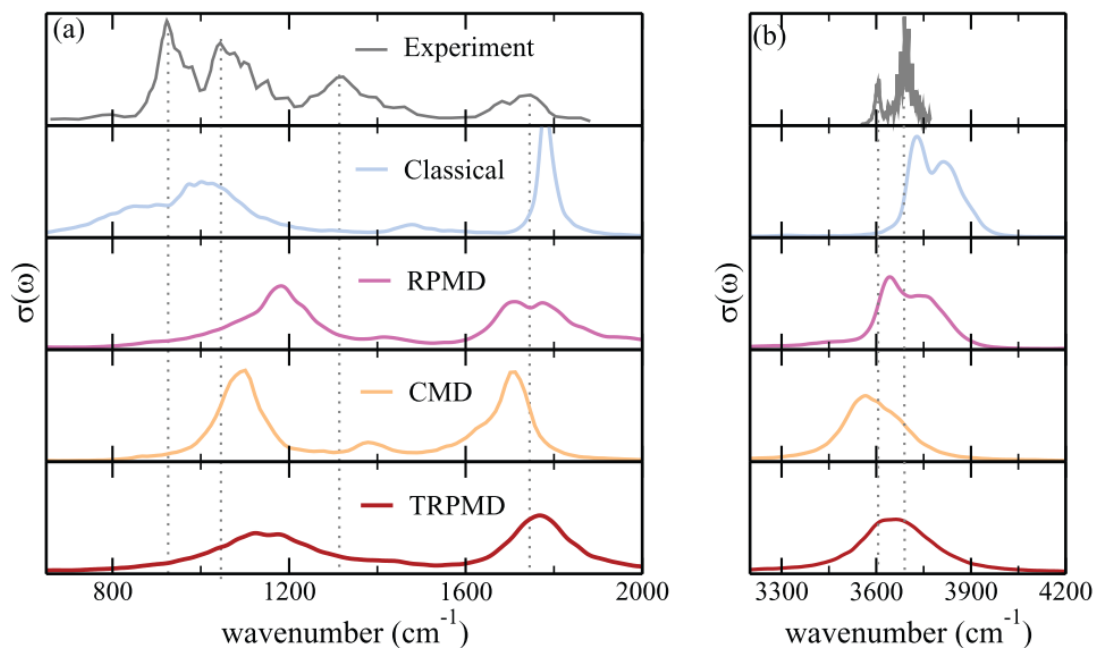


**Figure 1.13.:** IR spectra for the Zundel cation in gas phase,  $\text{H}_5\text{O}_2^+$ , for various NQE simulation techniques (ring-polymer molecular dynamics (RPMD), centroid molecular dynamics (CMD) and thermostatted ring-polymer molecular dynamics (TRPMD)). Reprinted from Rossi, M., Ceriotti, M. & Manolopoulos, D. E. *J. Chem. Phys.* 140, 234116 (2014), with the permission of AIP Publishing.

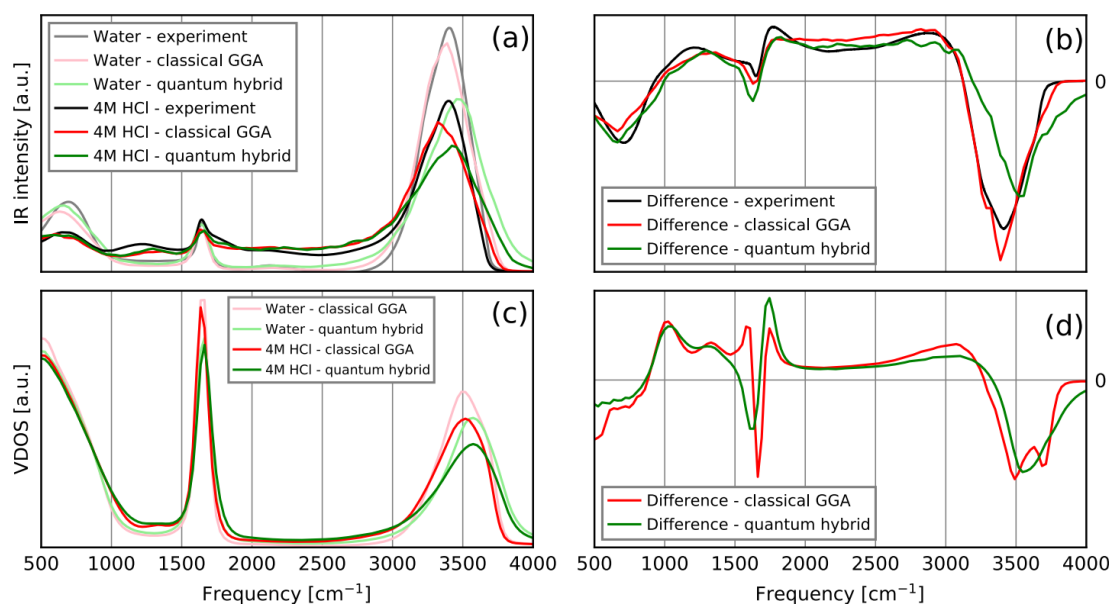


**Figure 1.14.:** IR and vibrational density of states (VDOS) spectra and difference spectra for 4M HCl solution from experiment and ab initio molecular dynamics simulations with quantum and classical nuclei. Reprinted from Napoli, J. A., Marsalek, O. & Markland, T. E. *J. Chem. Phys.* 148, 222833 (2018), with the permission of AIP Publishing.

Similarly, diffusion coefficients are known to be vastly affected [97].

To date, only a single study of aqueous hydrochloric acid solution shows IR spectra obtained from ab initio MD simulations based on DFT which in addition attempts to model NQE [61]. The study achieves this by making relatively drastic simplifications, for example performing RPC to a single bead and compare to data with larger ring polymers only for a single observable. Still, the authors perform most of their analysis, which focuses on the hydrogen-bond dynamics, based on the classical trajectories. The study is important here as it compares IR spectra as obtained with and without NQE for a similar DFT model. The spectra taken from the publication, including also a comparison to experimental data, are given in Fig. 1.14. The qualitative and quantitative differences between the absolute as well as the difference spectra obtained with and without NQE are virtually nonexistent, except for high frequencies of the regime of the OH stretch vibration around  $3300\text{ cm}^{-1}$ . Interestingly, the data obtained without NQE appears to be in better agreement with the experimental data overall, which of course could be due to cancellation of errors. Notably, the study finds large deviations between simulations with and without NQE for the mean distribution of the excess proton positions along a proton sharing coordinate. While this strong effect of NQE is known for a long time [59], the actual dynamics do not seem to be drastically changed, which is seen by the good overall agreement of the spectra. This is also seen from the IR difference spectra reported in another study, comparing spectra with and without NQE for two versions

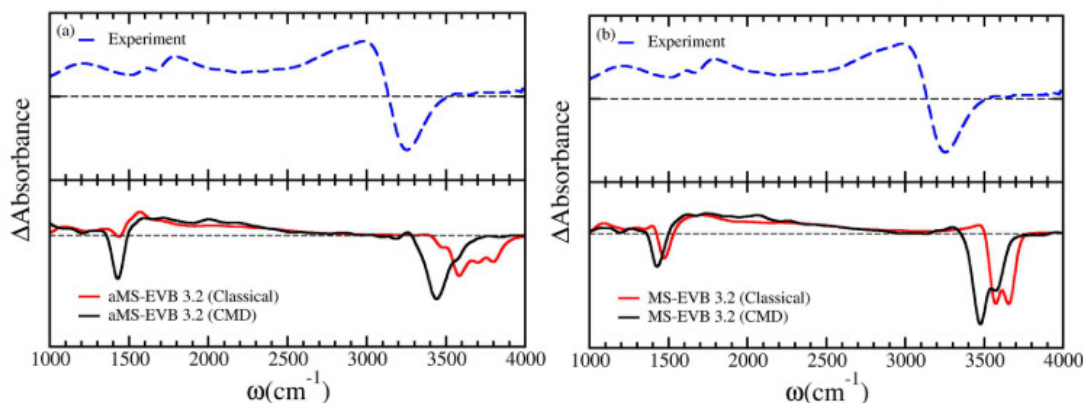


**Figure 1.15.:** IR difference spectra obtained from classical and CMD trajectories of (a, left) aMS-EVB 3.2 and (b, right) MS-EVB 3.2 simulations of 1 HCl aqueous system along with the experimental attenuated total reflection (ATR) difference spectrum. Reprinted with permission from Biswas, R., Tse, Y. L. S., Tokmakoff, A. & Voth, G. A. *J. Phys. Chem. B* 120, 1793 (2016). Copyright 2016 American Chemical Society.

of the multistate empirical valence bond (MS-EVB 3.2) model for the hydrated excess proton [97]. The spectra taken from [97] are shown in Fig. 1.15 and likewise do not differ much with and without NQE.

Another recent study performed simulations of a single hydrochloric acid pair in water using DFT and attempting to account for NQE [62]. They addressed static properties using a computationally very expensive path-integral simulation with  $P = 30$  beads for 32 ps and dynamical properties by RPC simulations with a reference potential that was obtained using machine learning techniques. From this study, it transpires that either extensive computational resources or advanced methods with possibly uncontrolled approximations are still required to address NQE in high-level quantum-chemical MD simulations.

### 1.1.5. Excess protons in biological systems

The functioning of several widely studied proteins depends on the dynamics of protons. Examples include the pumping of protons to build electrochemical gradients in bacteriorhodopsin [63, 49, 24, 50, 52, 13] or cytochrome c oxidase [127, 128, 27], the transport of protons from the water-splitting reaction center in photosystem II [129, 25, 130, 26], the proton-coupled isomerization of phytochromes [131–133, 7] and viral proton channels, so-called viroporins, that are targeted in drug design [134, 135].

The study of the dynamics of the small and fast-moving protons is especially difficult in the complex protein environment. IR spectroscopy, which, due to its high resolution and sensitivity, is an established experimental method in the field of biophysics, is also used to probe proton dynamics in these systems. However, as discussed above, the spectral signatures of proton transport are rather broad [52, 2, 4] and the high resolution

of IR spectroscopy cannot be exploited. By difference spectroscopy it is possible to distinguish these signatures from the broad background of the protein [49, 50, 64, 52], but the localization of the protons in the protein and the resulting signatures often requires guidance by simulations [51, 65]. Time-resolved IR spectroscopy adds another dimension to the data and therefore aids the interpretation of these signals [131, 7].

In proteins, proton transport also happens in a Grotthuss mechanism which differs from bulk solution because it involves proton-accepting side chains and confined water molecules [24, 136]. Such scenarios are nowadays also modeled using ab initio MD simulations [137, 52, 65, 13, 7].

### Proton transfer between amino-acid side chains

Model systems for studying the excess proton localization and dynamics in the vicinity of a typical proton-accepting side chain in a protein, are pairs of deprotonated carboxyl molecules, as commonly assumed in a protein environment, with water molecules and an excess proton in between. Such systems have recently been studied in ab initio MD simulations, the results of which are summarized in Figs. 1.16 and 1.17 [13, 7].

The first model system depicted in Fig. 1.16C, with one water molecule between a pair of carboxylates, is a typical proton-storage site [65, 7]. It agrees well with the crystal structure of bacteriorhodopsin, shown in Fig. 1.16A and B, which shows a water molecule located right in between the head groups of the aspartate side chains D85 and D212 [13].

Suitable coordinates for analyzing the proton localization are given by the oxygen-oxygen distances  $R_{O_C O_W}$  and an asymmetry coordinate for the hydrogen atoms,  $R_{O_C H} - R_{O_W H}$ , similar to the coordinates used for excess protons in bulk or gas-phase water clusters [59, 2, 4]. Since in this model system the role of the excess proton is fluctuating rapidly, the asymmetry coordinate is always computed for all three hydrogen atoms near the water oxygen,  $O_W$ , with respect to the carboxylic oxygen,  $O_C$  of either carboxyl molecule, that produces the smallest absolute asymmetry. This description is useful as it treats all hydrogen atoms interchangeably and does not double count different pairs of oxygen atoms.

Example trajectories of  $R_{O_C H}$  for the three central hydrogen atoms are shown in Fig. 1.16D. It is well visible in the time course that always two of the three protons produce a small value of  $R_{O_C H}$ , and one being closer to a carboxylic oxygen, one being slightly closer to the water oxygen. As soon as one of these protons changes its asymmetry and moves closer to the water, the other one moves closer to the carboxylic oxygen. The free energy of  $R_{O_C H} - R_{O_W H}$  shows in Fig. 1.16D a  $\sim 2.5 k_B T$  barrier separating an excess-proton localization near a carboxylic oxygen and the water oxygen.

A second model system with two water molecules mimics a water cluster near the chromophore of bacteriophytochrome Agp2, that is proposed to transiently store a mobile excess proton [7]. The model system consists of two carboxylate molecules, two water molecules and an excess proton as shown in Fig. 1.17A. The total charge amounts to -1 e. The carbon atoms are constrained at a fixed mutual distance of 7.4 Å, which corresponds to the distance between the carboxylic side chains of propB and propC of the chromophore taken from the crystal structure [133]. The water oxygen atoms

## 1. Introduction

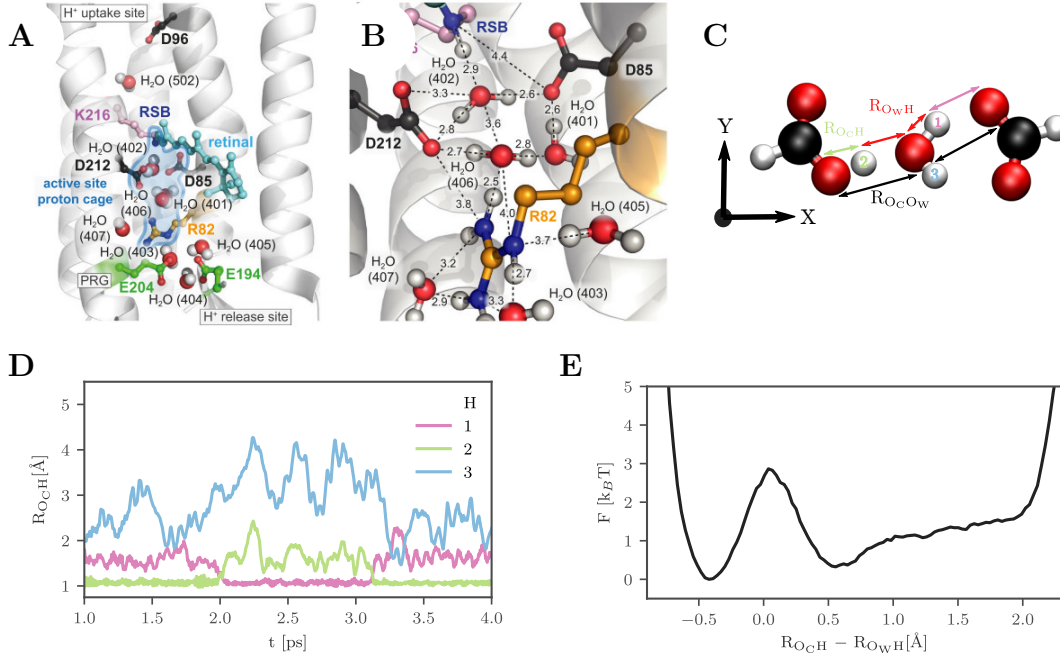


**Figure 1.16.:** **A, B:** Illustration of the proposed active-site proton cage near the chromophore of bacteriorhodopsin. Reprinted from Ref. [13], used under Creative Commons CC-BY license (<http://creativecommons.org/licenses/by/4.0/>). **C:** Snapshot from the ab initio MD simulation of a water molecule and an excess proton in between two carboxylate molecules. The reaction coordinate for the proton transfer between the two carboxylates is the distance between carboxyl group and water oxygen  $R_{O_cO_w}$  and and the excess proton's relative asymmetry to these oxygens  $R_{O_cH} - R_{O_wH}$ . **D:** Example trajectories of the  $R_{O_cH}$  distances of the three central hydrogen atoms in the system. The proton transfer is well visible as a fast jump process by which protons 1 and 2 exchange **E:** The free energy of the asymmetry coordinate  $R_{O_cH} - R_{O_wH}$  shows an effective barrier height of about  $3 k_B T$  for proton transfer between the two carboxyl group via a Grotthus mechanism.

are constraint by a quadratic potential in Y and Z direction,  $k(y^2 + z^2)$ , illustrated in Fig. 1.17, to model the confining effect inside the protein. Since the realistic confinement strength is not known, simulations at three different strengths were performed at  $k = 0.0, 0.4, 4.0 k_B T / \text{\AA}^2$ , where  $k_B T$  is the thermal energy.

IR spectra of this toy model system for different confining strengths are shown in Fig. 1.17B. All systems show a much higher IR intensity along the X axis than in the YZ plane. The signals in the YZ plane are mostly independent of the confining strengths  $k$ . Clear bands reside at 500, 800 and around 1000 to 1200  $\text{cm}^{-1}$ , that are associated with the modulated OC vibrations. In addition, broad features appear between 2500  $\text{cm}^{-1}$  and 3500  $\text{cm}^{-1}$  for  $\text{H}_2\text{O}$  (and between 1500  $\text{cm}^{-1}$  and 2500  $\text{cm}^{-1}$  for  $\text{D}_2\text{O}$ ), that are associated

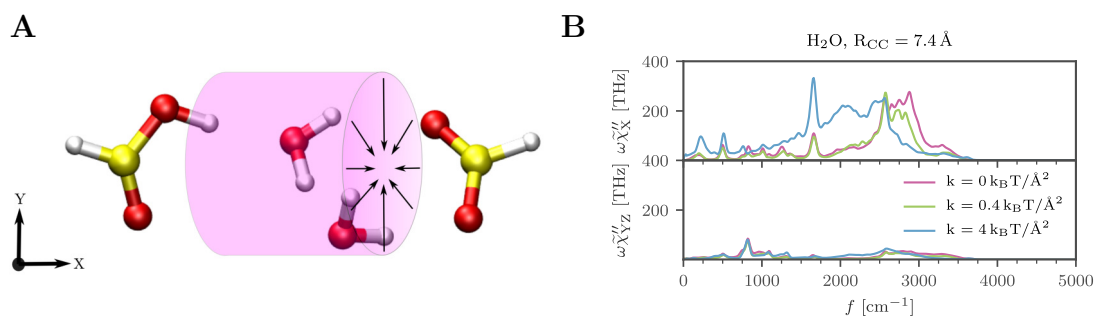


**Figure 1.17.:** **A:** Snapshot from the ab initio MD simulation of an excess proton and two water molecules that are located in between a pair of carboxylate molecules. The pink cylinder illustrates the confining potential acting on the water oxygen nuclei, which is centered on the axis connecting the carbon atoms. The carbon atoms are fully constrained in the MD simulations. **B:** IR spectra of the model system shown in Figure S13a along different axes for different confining strengths ( $k$  in  $k_B T / \text{\AA}^2$ ) of the water molecules. For each figure, IR spectra along the X axis connecting the fully constrained carbon atoms of the carboxylates are shown in the upper panel and IR spectra in the YZ plane in the lower panel. Reprinted from Ref. [7], used under Creative Commons CC-BY license (<http://creativecommons.org/licenses/by/4.0/>).

with modulated OH (and OD) stretching vibrations. The relatively stronger signal along the X axis on the other hand heavily depends on the confining potential. While for the two weakly confined cases (red and green lines) the broad features between  $2500 \text{ cm}^{-1}$  and  $3500 \text{ cm}^{-1}$  for  $\text{H}_2\text{O}$  (and between  $1500 \text{ cm}^{-1}$  and  $2500 \text{ cm}^{-1}$  for  $\text{D}_2\text{O}$ ) resemble the ones in the YZ plane, the signature is clearly different for the strongly confined case (blue line). Here a broad continuum band appears in the  $1700 \text{ cm}^{-1}$  to  $2500 \text{ cm}^{-1}$  range for  $\text{H}_2\text{O}$  and between  $1300 \text{ cm}^{-1}$  and  $2000 \text{ cm}^{-1}$  for  $\text{D}_2\text{O}$ , likely connected to a proton delocalization. The data shows that an excess proton exchange between two carboxylate molecules with two water molecules in between, as suggested by the crystal structure of Agp2 of the carboxylic side chains of propB and propC, is possible at the ps time scale, if the water molecules are confined to the central axis by a cylindrical confining potential. A confining potential is obviously necessary to model the protein environment in this simplified model system, it is however difficult to estimate the realistic potential strength.

These toy-model simulations serve as a guidance for generally understanding the effect of confinement on water-mediated proton transfer dynamics between carboxylate molecules and its spectral signature, specifically the appearance of a continuum band in the  $1700 \text{ cm}^{-1}$  and  $2000 \text{ cm}^{-1}$  range for both  $\text{H}_2\text{O}$  and  $\text{D}_2\text{O}$  under confinement.

It is also possible to observe proton transfer in ab initio MD simulations of more complex systems which model the protein environment more closely. This has been demonstrated for a different extended water cluster that is proposed to transiently store a mobile excess proton in bacteriophytochrome Agp2, and which consists of one side of



the chromophore including ring C and ring D, side chains H278 and Y165, that were each truncated at the ring and three water molecules TW1, TW2 and W6 [7]. An illustration is given in Fig. 1.18. The system models the scenario of a deprotonated ring D and is therefore setup with a neutral deprotonated ring D, but also an excess proton and thus a total charge of 1 e. The excess proton is initially placed between water molecule TW2 and the carboxylic side chain of ring C of the chromophore, which was found by initial equilibration to be a meta-stable configuration.

The IR spectra are averaged over three non-equilibrium simulations for H<sub>2</sub>O, five non-equilibrium simulations for D<sub>2</sub>O and all dimensions. The resulting spectra are shown in Fig. 1.18B for both, H<sub>2</sub>O and D<sub>2</sub>O, as red lines and compared to average IR spectra computed from the reference simulations, in which the keto group is protonated, shown as blue lines. A comparison of the IR spectra clearly shows that the non-equilibrium simulations exhibit a continuum band between 1700 cm<sup>-1</sup> to 3000 cm<sup>-1</sup> for H<sub>2</sub>O (and between 1800 cm<sup>-1</sup> and 2200 cm<sup>-1</sup> for D<sub>2</sub>O), which are not visible in the IR spectra of the reference simulations. In conclusion, the ab initio MD simulations of the two model systems of water clusters near the chromophore of Agp2, each show a mobile excess proton and related continuum bands in the IR spectra for both, H<sub>2</sub>O and D<sub>2</sub>O, that are of comparable magnitude. The continuum bands reach approximately between the bands of the respective water bending and stretching vibrations, i.e. between 1700 cm<sup>-1</sup> to 3000 cm<sup>-1</sup> for H<sub>2</sub>O (and between 1300 cm<sup>-1</sup> to 2200 cm<sup>-1</sup> for D<sub>2</sub>O).

The ab initio MD simulation results of these model systems illustrate how proton dynamics in biological systems may be mediated by hydrogen-bond networks of confined water molecules and proton-accepting protein side chains. The energy barriers for proton transfer in the models systems, which are based on realistic scenarios in a protein, are not too large, on the order of a few  $k_B T$ , and the dynamics can be resolved by these types of simulations. The related IR spectral signatures that are experimentally accessible show distinct features, such as the continuum band.

As for the first model system, the data supported experimental evidence that excess-proton exchange near the Schiff base of the chromophore in bacteriorhodopsin is possible in the equilibrated dark-state at ambient temperature, which hints to an active-site proton cage.

In context of the experimental data presented in [7], the ab initio MD simulations of the model systems two or three do not exclude either one as being the preferred system for transient proton storage near the chromophore in bacteriophytochrome Agp2. It is rather the contrary, both clusters present plausible candidates that confirm the experimentally observed transient IR spectra.

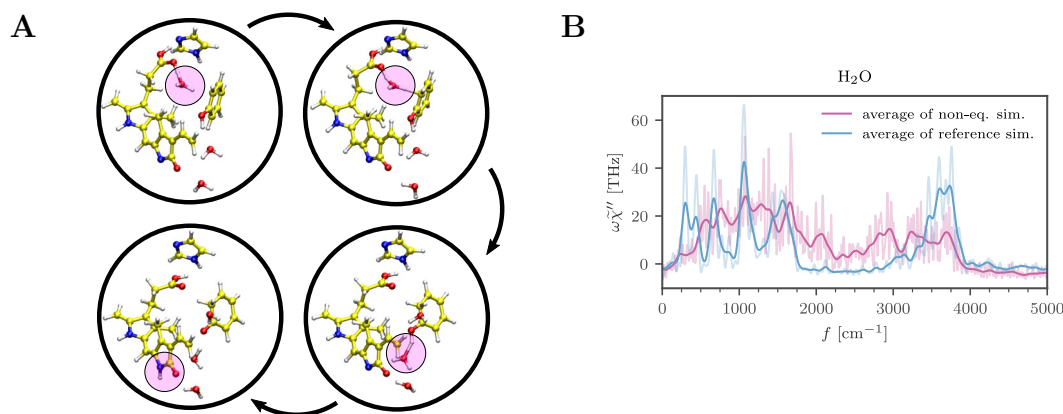


**Figure 1.18.:** **A:** Snapshots from the ab initio MD simulations of a proposed water cluster near the chromophore of Agp2, including one side of the chromophore with ring C and ring D, side chains H278 and Y165, that were each truncated at the ring, three water molecules TW1, TW2 and W6 (see Fig. 1 of Ref. [7]) and an excess proton, so that the total charge amounts to 1 e. The pink circle illustrates the location of the excess proton during the course of the non-equilibrium simulations. A number of constraints is applied to model the confining effect inside the protein. The heavy atoms of the chromophore and H278 are fully constrained, except for the carboxylic side chain at ring C. Furthermore the water oxygen atoms are constraint by a weak quadratic potential in all dimensions,  $k(x^2 + y^2 + z^2)$ , with  $k = 0.04 k_B T / \text{\AA}^2$ . Furthermore, for Y165, the oxygen atom of the hydroxyl group and the carbon atom of the phenyl ring that connects to the back bone of the protein are constrained by such a quadratic potential with  $k = 0.04 k_B T / \text{\AA}^2$ . A small number of simulations of this non-equilibrium system are performed for each, H<sub>2</sub>O and D<sub>2</sub>O, under NVT conditions at 300 K using a simulation time step of 0.5 fs. All show a transfer of the excess proton to Y165 as a Grotthus process within the first 5 ps, in some simulations the excess proton is further transferred to the nitrogen atom of the keto group at ring D. Interestingly, in some simulations, Y165 is protonated at the phenyl ring, before the proton from the hydroxyl group is released, which probably presents another meta-stable state. Each simulation is run for about 5 ps to 7.5 ps or until the keto group at ring D is protonated, which is considered the meta-stable reference configuration. The first 0.1 ps are truncated for initial fast equilibration. **B:** IR spectra of the model system shown in Figure S13b. The IR spectra are averaged over three non-equilibrium simulations for H<sub>2</sub>O, five non-equilibrium simulations for D<sub>2</sub>O and all dimensions. Reprinted from Ref. [7], used under Creative Commons CC-BY license (<http://creativecommons.org/licenses/by/4.0/>).

## 1.2. Vibrational spectroscopy

Linear vibrational spectroscopy measures the power absorbed by a system subject to an external field  $\vec{F}(t)$ , oscillating at frequency  $\omega = 2\pi f$ . The measured quantity is then the imaginary part of the susceptibility,  $\omega\tilde{\chi}''(\omega)$ . According to the fluctuation-dissipation relation, which is derived in supplement E, the absorbed power is proportional to the equilibrium fluctuations of an observable  $a(t)$  coupling to the field  $\vec{F}(t)$  in the Hamiltonian [138]. In the case of IR spectroscopy the external field is the electric field of the incoming light beam and the observable is the system's dipole moment.

Thus, to model the IR spectroscopic response of a system, one usually attempts to model the fluctuations of the system's dipole moment [30]. Of course, if suitable simulation data with sufficiently high time resolution is available, the most direct way is to determine the fluctuations from unperturbed equilibrium simulations [139]. The Wiener-Kintchine theorem provides an efficient and numerically stable approach to estimate the fluctuations from the Fourier transform of the observable [140]. However, this is a computationally demanding approach since force-field MD simulations are usually insufficient and quantum-mechanical methods are needed.

Alternatively, as mentioned already in the previous section, an efficient model are normal modes, i.e. harmonic approximations to the dynamics around energetically minimal states, which can be estimated directly from the stiffness of these states along all  $3N$  spatial dimensions [30]. Obviously, normal modes become exact in the zero-temperature limit, when this linear approximation to the dynamics is valid. At elevated temperature, these harmonic normal modes are mainly affected by two different effects. On the one hand, nonlinear potential effects beyond the harmonic approximation become relevant and on the other hand, line broadening occurs as a result of coupling to the thermal environment. It shall be noted that in the following only nonlinear potential effects are considered and not nonlinear response which is also a common perspective taken in the literature with respect to multidimensional or time-resolved spectroscopy.

Line broadening is commonly accounted for by using effective line-shape, or band-shape, functions that are fitted to the data at hand. The common choice is the Lorentzian line shape which is derived from the response of the damped harmonic oscillating dipole moment  $p(t)$  with mean  $\langle p \rangle = qL$ , where  $q$  is the charge and  $L$  a length scale, as

$$\tilde{\chi}(\omega) = \frac{q^2}{V\epsilon_0} \frac{k - m\omega^2 + i\gamma\omega}{(k - m\omega^2)^2 + \gamma^2\omega^2}, \quad (1.20)$$

where  $k_B T$  is the thermal energy,  $V$  is the system volume,  $\epsilon_0$  is the vacuum permittivity,  $m$  is the mass and  $k$  is the stiffness of the harmonic potential  $U(p) = kp^2/2$ . The normal-mode frequency  $\omega_{\text{NM}} = \sqrt{k/m}$  is the position of the maximum of the function. The friction constant  $\gamma$  is the linear frictional damping coefficient of the damped oscillator

and determines the line width. Eq. (1.20) can be rewritten as

$$\tilde{\chi}(\omega) = \frac{q^2}{V\epsilon_0 m} \frac{\omega_{\text{NM}}^2 - \omega^2 + i\gamma m^{-1}\omega}{(\omega_{\text{NM}}^2 - \omega^2)^2 + \gamma^2 m^{-2}\omega^2} \quad (1.21)$$

$$\approx \frac{q^2}{V\epsilon_0 m \omega_{\text{NM}}} \frac{2(\omega_{\text{NM}} - \omega) + i\gamma m^{-1}}{4(\omega_{\text{NM}} - \omega)^2 + \gamma^2 m^{-2}}, \quad (1.22)$$

where the near-resonance approximations  $\omega \approx \omega_{\text{NM}}$  and  $\omega_{\text{NM}}^2 - \omega^2 \approx 2\omega_{\text{NM}}(\omega_{\text{NM}} - \omega)$  are used [34]. The imaginary part of Eq. (1.22) is identified as the normalized Lorentzian function [30]

$$\mathcal{L}(\omega_0 - \omega, \beta) = \frac{1}{\pi} \frac{\beta}{(\omega_0 - \omega)^2 + \beta^2}, \quad (1.23)$$

with a maximal value of  $2/(\pi\beta)$  at  $\omega_{\text{NM}}$  and a full width at half maximum (FWHM) of  $2\beta$ , so that

$$\omega \tilde{\chi}''(\omega) = \frac{q^2 \pi}{2V\epsilon_0 m} \mathcal{L}(\omega_{\text{NM}} - \omega, \gamma/(2m)). \quad (1.24)$$

Note, that the Lorentzian function becomes the Dirac delta function in the frictionless limit  $\beta \rightarrow 0$ .

In the overdamped limit,  $m \rightarrow 0$ , the previous approximations are not valid, but rather, starting from Eq. (1.20), defining  $\tau_\gamma = \gamma/k$ , and using  $k = k_B T/L^2$ , one obtains the Debye line-shape function [141]

$$\tilde{\chi}(\omega) = \frac{q^2 L^2}{V\epsilon_0 k_B T} \frac{k + i\tau_\gamma \omega}{1 + \tau_\gamma^2 \omega^2}, \quad (1.25)$$

which is useful to model slow processes in the GHz regime, such as the well-known Debye peak of water at around 20 GHz [142, 143, 12].

In addition to the frictional broadening discussed above, the effective harmonic stiffness  $k$  may also fluctuate in a varying local environment. The previous equations remain valid in the limit of homogeneous line-broadening, i.e. when the broadening due the friction  $\gamma$  is larger than the broadening due to the variance in  $k$ . This broadening is therefore expected for strongly damped vibrations, i.e. with a fast energy exchange with the environment, and in homogeneous media. Another limit, referred to as inhomogeneous line-broadening occurs when the variance in  $k$  is large compared to the frictional broadening, which is expected for weakly damped vibrations with slow energy exchange in inhomogeneous media. Then the individual Lorentzian modes can be modeled to first order as Gauss-distributed around a mean value  $\omega^*$  [30],

$$\omega \chi''(\omega) = \frac{q^2 \pi}{2V\epsilon_0 m} \int d\omega' g(\omega', \omega^*) \mathcal{L}(\omega' - \omega, \beta), \quad (1.26)$$

where  $g(\omega, \omega_0) = \exp[-\ln(2)(\omega - \omega_0)^2/\beta^2]\sqrt{\ln(2)/\pi}/\beta$  is the normalized Gaussian distribution, written for a FWHM of  $2\beta$  analogous to the Lorentzian function above. This convolution is called the Voigt shape, which in the limit of weak damping  $\gamma \rightarrow 0$ , becomes simply the Gaussian line shape

$$\omega\chi''(\omega) = \frac{q^2\pi}{2V\epsilon_0m}g(\omega, \omega^*). \quad (1.27)$$

It shall be noted that a Gaussian line shape is also experimentally observed in gas-phase spectra due to the Doppler effect, where it is therefore called Doppler broadening [30].

Since especially the estimation of the molecular friction  $\gamma$  is difficult, in practice these line shape functions mostly present heuristic but efficient models. However, recent developments in parameterization of the GLE, which is introduced in detail in section 1.3.1, allow for accurate estimation of molecular friction from MD simulation data. In the GLE, molecular friction is expressed as a time-dependent memory friction kernel  $\Gamma(t)$  and the response for a harmonic potential is given as [1]

$$\omega\tilde{\chi}''(\omega) = \frac{q^2}{V\epsilon_0} \frac{\omega^2 \operatorname{Re}\tilde{\Gamma}^+(\omega)}{\left|k - m\omega^2 - i\tilde{\Gamma}^+(\omega)\omega\right|^2}, \quad (1.28)$$

where  $\Gamma^+(\omega)$  denotes the single-sided Fourier-transformed friction kernel. When comparing the denominator to the one in Eq. (1.20), it transpires that the real part of  $\Gamma^+(\omega)$  acts like homogeneous frictional line-broadening, while the imaginary part acts like a correction to the harmonic stiffness  $k$  as expected for inhomogeneous line broadening. This line shape function therefore handles both inhomogeneous and homogeneous line broadening and by numerical evaluation of the GLE also nonlinear potential effects can be addressed.

### 1.2.1. Infrared spectrum of liquid water

The experimental IR spectrum of liquid water given in Fig. 1.19 as a black broken line is comprised of four dominant bands. A spectrum from ab initio MD simulations of BLYP-D3 quality of 256 water molecules in a periodic box, representative of bulk water, is shown for comparison as a blue solid line. The data set is discussed in detail in chapter 5, where it is employed to analyze the frequency-dependent friction of the water vibrational modes and its effect on the line shape. The assignment of the peak at around  $1650 \text{ cm}^{-1}$  as the water bending and the broad peak centered at  $3300 \text{ cm}^{-1}$  as the water stretching band is straightforward when regarding the gas phase normal modes of a single water molecule (vertical gray broken lines). Note the significant shift compared to the gas phase and the different band widths which are explained as part of the analysis in chapter 5. The broad peak centered at  $600 \text{ cm}^{-1}$  is associated with librational motion of water molecules and the peak at around  $150 \text{ cm}^{-1}$  with the stretching of hydrogen bonds [144–146, 12].

Previous effort in modeling the bulk-water IR spectrum is extensive but has proven

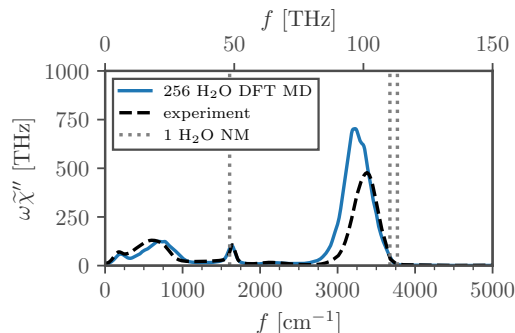


**Figure 1.19.:** IR absorption spectra obtained from ab initio MD simulations of pure water (blue solid line, BLYP-D3 quality) and normal modes calculated from a single water molecule on the same level (vertical gray broken lines) [1]. The black broken line shows an experimental spectrum [198].

difficult due to a number of complex effects. While simple assignment of the few bands of bulk water is easy when compared to the few gas-phase normal modes of the comparably simple single water molecule, these modes are strongly coupled across several molecules in the bulk phase and quantitative models for the line shape need to account for this [147–155]. Many works therefore rely on computationally expensive quantum-chemical ab initio MD methods for simulating bulk water and calculating spectroscopic properties (such as the BOMD data shown in Fig. 1.19) [144, 156, 145, 157, 119, 158–161, 12, 162, 1].

Alternatively, several works have attempted to optimize the representation of water molecules in classical MD simulations with respect to the spectral properties [163–166] or with great success by including many-body interactions [167–172].

Also, mixed quantum-classical approaches have been used, where an ensemble of configurations is sampled from force-field MD and the spectroscopic properties are then evaluated on a more complex quantum-chemical level [173, 174, 151, 175, 176], among which the classical dipole and fluctuating-frequency approximations can be differentiated [177, 178].

Beyond that, Fermi-resonance between the water bend and stretch vibrations [179] and NQE [180, 181, 172] are known to affect the line shapes and have been addressed.

Line shape models based on the GLE have also previously gained some attention [182–188] but only new parameterization methods allow to account for both anharmonic potential and frequency-dependent friction simultaneously [1].

The complex nature of vibrational lifetimes, which are closely related to molecular friction and vibrational coupling between different molecules and modes, have been the focus of several experimental time-dependent and multidimensional IR studies [189–197, 162], which present further benchmarks for computational studies and inspiration for future models.

### 1.3. Reaction-rate theory

Covalent and non-covalent reactions in solution are relevant in almost all biological processes as well as technical applications. As such the mean turnover rate from reactants to products is arguably the most important observable in such processes, as it determines the time scales that balance the complex reaction chains and circles in biological systems or simply the efficiency of large-scale technical applications. The analytical prediction of such mean reaction rates has a long history in theoretical chemistry, reaching back to Arrhenius [199], who stated the exponential dependence of the reaction rate on the free energy barrier height separating reactants and products along a reaction coordinate.

In solution, the stochastic random forces and frictional damping induced by the solvent particles on the reacting solutes result in stochastic Brownian motion [200], which is modeled by the Langevin equation [201] and determines an important prefactor to the aforementioned exponential scaling. Kramers [37] first explored the inverse scaling of the prefactor in opposite limits of the friction constant, known since as Kramers' turnover.

To complicate the matter, low-dimensional models of reaction dynamics tend to break down whenever the solvent influence is critical, and therefore even for the simplest reactions in solution, constant-friction models along a single reaction coordinate appear insufficient [5]. However, due to their large number, it is not practical to include solvent molecules explicitly in the model and effective descriptions remain necessary. This issue has in the past been addressed by searching for more suitable reaction coordinates and proposing higher dimensional representations [202, 203]. By linear projection, a higher dimensional representation can be brought back to a one-dimensional dynamical model, the generalized Langevin equation (GLE) [38, 39] including a time convolution with a kernel function, known as the memory friction kernel. Therefore, instead of searching for an explicit high-dimensional representation, a suitable model including a memory kernel appears to be more accurate and more general. The parameterization of memory kernels from time series data is an active field of research [204–206, 15], also in the application to chemical reaction dynamics [124, 207–209]. A crucial advantage of the memory friction model is its generality. A lot of effort has been put into the development of analytic rate theories for the generalized Langevin equation, including inertial and memory friction effects, and therefore the precise prediction of mean reaction rates can be performed based on a largely reduced set of parameters [210, 211, 16, 212, 213, 3].

#### 1.3.1. Numerical models

Numerical simulations of thermally activated stochastic motion, also known as Brownian motion, of a reaction coordinate  $x(t)$  is most effectively performed with the Langevin equation (LE), which is given in the overdamped form as [201]

$$\gamma\dot{x}(t) = -\nabla U(x) + F_R(t), \quad (1.29)$$

where  $\gamma$  is the friction coefficient and  $U(x)$  an arbitrary potential shape.  $F_R(t)$  is a stochastic random force, which has zero mean  $\langle F_R(t) \rangle = 0$  and is correlated according to

$\langle F_R(t)F_R(t') \rangle = 2b\delta(t-t')$ . In case of  $b = k_B T \gamma$ , the equation fulfills the fluctuation-dissipation relation and therefore describes a system at equilibrium. The equation is conveniently derived by linear projection on the primary coordinate of an infinite number of independent degrees of freedom describing the solvent particles and then assuming a time-scale separation between the fast coupled degrees of freedom and the primary coordinate, i.e. by absorbing the fast solvent coordinates into the effective random force and frictional damping terms [214]. For the free case, i.e. for  $U(x) = 0$ , the mean-squared displacement (MSD),  $\langle [x(t) - x(0)]^2 \rangle = 2Dt$ , where  $D = k_B T / (\gamma L^2)$  is the diffusion constant and  $L$  a length scale, is a topical result of statistical physics [215, 216].

The overdamped LE can also be derived for a position-dependent friction profile  $\gamma(x)$  [217]

$$\gamma(x)\dot{x}(t) = -\nabla U(x) - \frac{k_B T \nabla \gamma(x)}{2\gamma(x)} + F_R(x, t). \quad (1.30)$$

For the time correlation of the random force  $F_R(x, t)$  follows  $\langle F_R(x, t)F_R(x, t') \rangle = 2b(x)\delta(t-t')$ , which for  $b(x) = k_B T \gamma(x)$  fulfills the fluctuation-dissipation relation. An in general position-dependent friction profile  $\gamma(x)$  has been widely applied to model for example the dynamics of drug diffusion [218], protein dynamics [219, 220] and also pair reactions [221, 222]. However, be aware of the appearance of a drift term  $k_B T \nabla \gamma(x) / (2\gamma(x))$  in Eq. (1.29) in case of position-dependent friction,  $\nabla \gamma(x) \neq 0$ .

If inertial effects are relevant, the non-overdamped, or inertial, version of the LE is given as [217]

$$m\ddot{x} = -\gamma(x)\dot{x}(t') - \nabla U[x(t)] + F_R(x, t), \quad (1.31)$$

where the random force  $F_R(t)$  likewise has zero mean  $\langle F_R(t) \rangle = 0$  and is correlated according to  $\langle F_R(x, t)F_R(x, t') \rangle = 2b(x)\delta(t-t')$ , where again  $b(x) = k_B T \gamma(x)$  fulfills the fluctuation-dissipation relation.

If a time-scale separation between the solvent degrees of freedom and the primary coordinate is not given, the GLE follows from the same projection scheme [39, 38]

$$m\ddot{x} = - \int_0^t \Gamma(t-t')\dot{x}(t')dt' - \nabla U[x(t)] + F_R(t), \quad (1.32)$$

which is exact in case of a harmonic,  $U[x(t)] = kx^2/2$ , or no potential,  $U(x) = 0$ . The given GLE Eq. (1.32) is valid if the correlation between the velocity and the random force  $\langle v(t)F_R(t') \rangle$  is independent of  $x$  [223]. In this equation, instead of a friction constant  $\gamma$ , a time-dependent friction memory kernel  $\Gamma(t)$  couples to the velocity in a time convolution. Due to the dependence on past states, this is a non-Markovian model in contrast to the previous two LEs, Eqs. (1.29) and (1.31). For the random force  $F_R(t)$ , zero mean  $\langle F_R(t) \rangle = 0$  and a correlation according to  $\langle F_R(t)F_R(t') \rangle = k_B T \Gamma(t-t')$  is required to fulfill the fluctuation-dissipation relation. In case of a non-linear potential  $U[x(t)]$ , the GLE Eq. (1.32) has been applied successfully to model dihedral dynamics [15], protein



dynamics [8], pair reactions [5] and even vibrational line shapes [1].

Note, that the three Eqs. (1.29)–(1.32) are expected to give consistent results in the respective limits. The Markovian limit, where memory effects are negligible, is obtained in the zero limit of all time scales in the memory kernel  $\Gamma(t)$ , so that  $\Gamma(t) \rightarrow 2\gamma\delta(t)$  and the friction constant  $\gamma$  therefore corresponds to the integral over the memory kernel  $\gamma = \int_0^\infty \Gamma(t)dt$ . Then, Eq. (1.32) reduces to the Markovian LE Eq. (1.31). Likewise in the overdamped Markovian limit, when inertial effects are negligible compared to the friction, i.e.  $m/\gamma$  is smaller than the relevant time scale of the system, the Markovian LE Eq. (1.31) reduces to the overdamped Markovian LE Eq. (1.29).

For application, efficient parameterization and evaluation techniques are furthermore required. All parameters in Eqs. (1.31)–(1.32) can in principle be derived directly from the time series of the reaction coordinate  $x(t)$  sampling the equilibrium ensemble. The mass is obtained from the equipartition theorem  $m = k_B T / \langle \dot{x}^2(t) \rangle$  and the potential is taken to be the free energy as obtained from the distribution function  $g(x)$  via  $U(x) = -k_B T \log(g(x))$ . The friction constant  $\gamma$  is usually estimated from MSDs, which is also presented in section 1.1.3. The estimation of position-dependent friction profiles  $\gamma(x)$  is more complex, but can be achieved for example from MFPTs as discussed in section 1.3.2. The parameterization of the memory friction kernel  $\Gamma(t)$  is certainly the most difficult and remains an active field of research [204–206, 15, 8, 224–227]. Here, a parameter-free extraction using a Volterra equation is applied, as detailed in previous works [8, 1].

For evaluation of the model, the GLE Eq. (1.32) can be solved efficiently using a Markovian embedding, which requires the memory kernel to be parameterized as a sum of exponentially decaying and oscillating components [228, 186, 229, 1]

$$\Gamma(t) = \sum_{i=0}^n \frac{\gamma_i}{\tau_i^e} e^{-t/\tau_i^e} + \sum_{i=0}^l a_i e^{-t/\tau_i^o} \left[ \cos(\omega_i t) + \frac{1}{\tau_i^o \omega_i} \sin(\omega_i t) \right]. \quad (1.33)$$

The generalization of the non-Markovian GLE Eq. (1.32) to include position-dependent friction effects is more difficult and attempts reach back to Zwanzig [230]. In chapter 6, a model with locally independent memory friction is introduced [3], which has the striking advantage that it has a simple corresponding Markovian embedding and therefore the analytical and numerical treatments are straightforward.

### 1.3.2. Analytical models

Analytical predictions for barrier-crossing dynamics in a viscous environment reach back to Kramers [37], who derived different friction-dependent prefactors to the Arrhenius law in the opposing inertia-dominated and overdamped regimes. The well-known Kramers turnover between these regimes was only later fully covered in a theory by Mel'nikov and Meshkov (MM) [231]. A memory-induced acceleration compared to the overdamped Kramers limit was first explored by Grote and Hynes (GH) [210], which competes with a slow down in the long memory-time limit [211, 16, 212, 3].

The transition-state theory (TST) escape rate [36] appears in several of the rate theories that are considered in the following. According to TST, assuming a harmonic potential well for the reactant state, the mean escape time of an undamped particle is given as [36]

$$\tau_{\text{TST}} = \frac{2\pi}{\omega_{\min}} e^{\beta U_0}, \quad (1.34)$$

where  $U_0$  denotes the potential-barrier height,  $\beta^{-1} = k_B T$  is the thermal energy, and the well frequency  $\omega_{\min} = \sqrt{U''_{\min}/m}$  contains the curvature  $U''_{\min} := U''(x_{\min})$  at the minimum  $x_{\min}$  of the potential well from which the particle escapes.

Kramers considered the escape from a potential well for a particle undergoing Brownian motion, as described by the LE Eq. (1.31) with position-independent friction  $\gamma$ , for both the limits of medium-to-high friction, and low friction [37]. For the medium-to-high friction regime, he obtained

$$\tau_{\text{Kr}}^{\text{hf}} = \left[ \left( \frac{\gamma^2}{4m^2} + \omega_{\max}^2 \right)^{1/2} - \frac{\gamma}{2m} \right]^{-1} \omega_{\max} \tau_{\text{TST}}, \quad (1.35)$$

while in the low-friction limit, he derived

$$\tau_{\text{Kr}}^{\text{lf}} = \frac{m}{\gamma \beta U_0} e^{\beta U_0}, \quad (1.36)$$

where the barrier frequency  $\omega_{\max} = \sqrt{-U''_{\max}/m}$  contains the curvature  $U''_{\max} := U''(x_{\max})$  at the barrier top  $x_{\max}$ . Note the opposite scaling of both equations with respect to the friction constant  $\gamma$ : While for medium-to-high friction  $\tau_{\text{Kr}}^{\text{hf}} \sim \gamma$ , for low friction  $\tau_{\text{Kr}}^{\text{lf}} \sim \gamma^{-1}$ . The bridging of these asymptotic limits, the so-called Kramers' turnover, was a long-standing problem in statistical mechanics.

Mel'nikov and Meshkov [231] (MM) derived a solution to the Kramers' problem which is valid for all values of the friction, and hence connects the two expressions eqs. (1.35), (1.36). The Mel'nikov and Meshkov (MM) result is given by

$$\tau_{\text{MM}} = A^{-1}(\Delta) \left[ \left( \frac{\gamma^2}{4m^2} + \omega_{\max}^2 \right)^{1/2} - \frac{\gamma}{2m} \right]^{-1} \omega_{\max} \tau_{\text{TST}}, \quad (1.37)$$

$$A(\Delta) = \exp \left[ \frac{2}{\pi} \int_0^{\frac{\pi}{2}} \ln \left[ 1 - e^{-\Delta/[4 \cos^2(x)]} \right] dx \right], \quad (1.38)$$

$$\Delta = 2\sqrt{2} \frac{\gamma}{\sqrt{m}} \beta \int_{-\sqrt{2}L}^0 \sqrt{U_0 - U(x)} dx. \quad (1.39)$$

While both Kramers' and MM theory consider Markovian dynamics, that correspond to numerical results from the LE Eq. (1.31), Grote and Hynes (GH) [210] developed a theory for the mean first-passage time under influence of memory, hence non-Markovian

## 1. Introduction

---

effects. Their expression for the case where the dynamics in the potential well relax fast, and only memory effects on the barrier are relevant, is given by

$$\tau_{\text{GH}} = \frac{\omega_{\text{max}}}{\lambda} \tau_{\text{TST}}, \quad (1.40)$$

where  $\tilde{\Gamma}(\lambda)$  denotes the Laplace-transformed memory friction kernel  $\Gamma(t)$  at the barrier top, and the real reactive frequency,  $\lambda > 0$ , is the solution of the equation

$$\lambda = \frac{\omega_{\text{max}}^2}{\lambda + \tilde{\Gamma}(\lambda)/m}. \quad (1.41)$$

For example, for a single memory time scale, i.e. the exponential kernel  $\Gamma(t) = \gamma e^{-t/\tau}/\tau$ , the frequency  $\lambda$  is given as the single positive solution of the cubic equation

$$\lambda^3 + \frac{\lambda^2}{\tau} + \left( \frac{\gamma}{m\tau} - \omega_{\text{max}}^2 \right) \lambda = \frac{\omega_{\text{max}}^2}{\tau}. \quad (1.42)$$

Note that, either in the inertial,  $m \rightarrow \infty$ , or the long memory limit,  $\tau \rightarrow \infty$ , it follows  $\lambda = \omega_{\text{max}}$  and GH theory collapses onto the TST result,  $\tau_{\text{GH}} = \tau_{\text{TST}}$  in Eq. (1.40). Furthermore, in the Markovian limit, i.e. for delta-correlated friction,  $\Gamma(t) = 2\gamma\delta(t)$  and  $\tilde{\Gamma}(\lambda) = \gamma$ , it follows  $\lambda = (\gamma^2/(4m^2) + \omega_{\text{max}}^2)^{1/2} - \gamma/(2m)$ , which results in  $\tau_{\text{GH}} = \tau_{\text{Kr}}^{\text{hf}}$ , the Kramers high-friction result in Eq. (1.35).

In the overdamped Markovian limit, the Fokker-Planck equation for a distribution  $P(x, t)$  is most suitable for analytical and numerical calculations,

$$\frac{\partial}{\partial t} P(x, t) = \frac{\partial}{\partial x} \left[ \frac{\beta^{-1}}{\gamma(x)} e^{-\beta U(x)} \frac{\partial}{\partial x} \left[ P(x, t) e^{\beta U(x)} \right] \right], \quad (1.43)$$

since it handles arbitrary potential shapes  $U(x)$  and even position-dependent friction  $\gamma(x)$ . An exact expression for  $\tau_{\text{MFP}}$  between initial  $x_i$  and final positions  $x_f$  can then be derived [31]

$$\tau_{\text{MFP}}(x_i, x_f) = \beta \int_{x_i}^{x_f} dq' \gamma(x') e^{\beta U(x')} \int_{x_{\text{min}}}^{x'} dx e^{-\beta U(x)}. \quad (1.44)$$

Eq. 1.44 can be inverted and thereby used to estimate a position-dependent friction profile  $\gamma(x)$  from measured values of  $\tau_{\text{MFP}}$  [220, 221]. Determined by a different approach, position-dependent friction profiles  $\gamma(x)$  have reproduced the non-equilibrium dissociation dynamics of the NaCl ion pair [222]. However, it has been shown recently that memory effects may give rise to spurious spatially dependent profiles when the GLE is mapped on Markovian models [8, 5].

## Conclusion and Outlook

---

The present thesis reveals the spectroscopic signatures related to non-Markovian effects and reaction kinetics that are shown to occur for hydrated excess protons and in water itself. Beyond that, reaction kinetics themselves are subject to non-Markovian effects even for the simplest pair reactions in water such as NaCl dissociation. The intriguing insights gained into these various systems fundamental to chemistry and biophysics are achieved in close conjunction with significant methodological advances.

In the first part of the thesis, the excess-proton dynamics and vibrational signatures in water are interpreted in terms of nonlinear stochastic reaction dynamics. Specifically, the framework is presented as applied to excess-proton dynamics in between two water molecules, i.e. in an isolated cluster in chapter 3, and to the dynamics in concentrated hydrochloric acid solutions in chapter 4. It is shown that in both systems the excess-proton spectra along the direction of proton transfer between two water molecules are nearly proportional to the total IR spectra of the systems, which are experimentally accessible. Thus, the total spectra report on the proton-transfer dynamics and in turn the analysis of these dynamics is useful to interpret characteristic signatures in the total IR spectra, namely the so-called continuum band between the water bend and stretch bands, as well as a strong feature at around  $1100\text{ cm}^{-1}$ . By a combination of trajectory and spectral decomposition, these well-known signatures are assigned to different stochastic time scales of the proton-transfer reaction from one water molecule to another, which in bulk water is an elementary step in the long-range Grotthuss transport of excess protons. Following reaction-rate theory, the stochastic time scales of proton transfer are the transfer-waiting time, defined as the mean first-passage time, which is the average time the proton stays with one water molecule between distinct transfer events; and the transfer-path time, which is the duration of an actual transfer event. In addition to these two time scales, vibrational bands result from the dynamics of the proton while waiting near a water molecule, which are quasi-harmonic oscillations around a fluctuating potential minimum and can therefore be modeled as normal modes of an ensemble of states. These normal modes of the excess proton are the fastest contribution of the dynamics and give rise to the continuum band, which is broad because of the strong fluctuation of the effective potential. The transfer-path time of the actual proton transfer on the other hand gives rise to the spectral signature at  $1100\text{ cm}^{-1}$ . The waiting time scale is comparably longer, and the associated signature is therefore expected at lower frequencies in the THz regime, for which experimental evidence was found. In addition to the decomposition, the IR line shapes of the nonlinear spectral contributions for waiting

## 2. Conclusion and Outlook

---

and transfer-path dynamics are derived analytically in chapter 3. The good agreement of the analytical theory with the decomposed spectra confirms that the characteristic time scales of each process can be inferred from the spectral signatures.

In the second part, in chapter 5, the vibrational spectrum of bulk water is modeled using the GLE containing a time-dependent friction memory kernel and a nonlinear potential, which inherently treats homogeneous and inhomogeneous line-broadening effects without assumptions of time scale separation. It is shown that the GLE self-consistently reproduces the vibrational spectra of the bending and stretching vibrations of water molecules in the liquid phase. By comparing to data of single water molecules in gas phase, the hydration effect of the bulk liquid can be decomposed in static potential and dynamic friction effects. It is concluded that while both the bending and stretching mean potentials of water are softened in bulk when compared to gas phase, which results in a red shift of the vibrations, this effect is partially compensated by a blue shift due to time-dependent friction acting on the vibrations. For the stretching band a net red shift remains but for the bending band the frictional blue shift overcompensates the potential red shift. The observed shifts has previously been interpreted only in terms of potential effects, which is an inconsistent interpretation when compared to the static ensemble energetics.

In the third part, the implications of non-Markovian effects on the stochastic time scales of chemical reactions are discussed. First, in chapter 6, the scaling of the mean reaction time, the mean first-passage time or barrier-crossing time, is analyzed for a model combining position- and time-dependent friction. The model is employed to compare the effects of different non-Markovian friction on the potential barrier and in the potential well. It is found, that whenever the dynamics in the potential well are overdamped and Markovian, the barrier-dynamics dominantly determine the barrier-crossing time, which in case of long non-Markovian memory friction can result in acceleration, in accordance with predictions by Grote and Hynes. If, on the other hand, the dynamics in the potential well are energy-diffusion limited, meaning that inertial or non-Markovian memory effects are relevant, the well-dynamics dominate the barrier-crossing time rather independently of the dynamics on the barrier. However, for this case, a small speed-up in case of an overdamped Markovian barrier is found, which has not previously been observed and notably behaves opposite to the acceleration predicted by Grote and Hynes.

At last, in chapter 7, the competing effects of memory friction, inertia, and the effective potential shape on pair reaction dynamics are discussed. By extracting all parameters of the GLE, namely the friction memory kernel, the effective mass and the nonlinear pair potential, directly and unambiguously from data obtained in MD simulations of typical pair reactions in water, the validity of the GLE model is demonstrated. Beyond that, the effect of these different physically relevant parameters on the mean reaction times is evaluated independently which is not possible in MD simulations. The analysis is presented for the dissociation dynamics of the NaCl ion pair and a pair on nonpolar methane beads in water. For both systems, the importance of non-Markovian memory effects is demonstrated, which speed up the dissociation reactions by a factor of two compared to the Markovian limit. The effective mass on the other hand leads to a

---

slow-down of the dynamics by a similar factor when compared to the overdamped limit. The effect of the potential shape is analyzed by comparing numerical simulations to different analytical results which assume harmonic approximations to the potential, notably the Kramers' and Grote and Hynes's theories. Nonlinearities in the potential shape are thereby found to slow-down reactions, which, when this effect cancels with memory-associated acceleration, may spark the wrong conclusion that a Markovian harmonic theory, i.e. the Kramers theory, describes the system's dynamics faithfully and that the Markovian and harmonic approximations would be correct.

To conclude, several new methods for the analysis and modeling of complex biophysical systems were developed in this thesis and successfully applied in different profound scenarios with elucidating results. Clearly, these developments and findings motivate a number of potential future projects.

The decomposition of spectral signatures of stochastic reaction dynamics, developed with respect to the excess-proton dynamics in water in chapters 3 and 4, can possibly be applied to gain valuable insight into the vibrational spectra of other systems. Importantly, since vibrational spectra are usually accessible much easier in experiment than, for example, the reaction times, the presented theory and methods can help to explicate their relation and distinguish the spectroscopically equivalent Debye signatures of overdamped dynamics. The ion-pairing dynamics discussed in chapter 7, which are obviously susceptible to dielectric spectroscopic measurements, potentially present an interesting system to apply these techniques. Of course, with recent developments in simulating NQE, more realistic dynamical data of excess protons is becoming available, which calls for the adaption of the presented methods and theories to the delocalized nature of the quantum excess proton.

Since in chapter 5 the GLE is proven to self-consistently reproduce the vibrational spectra of the water intramolecular modes, it would be interesting to apply the framework to interpret different kinds of shifts that are known when molecules are placed in different environments, for example, such as different solvents or a protein environment, where characteristic shifting of vibrational modes has previously been observed. With the large number of water models available, it will also be interesting to compare the frequency-dependent friction among them to further understand the robustness of both the water models and the friction profiles. Likewise, since the broad spectral signature of the continuum band is associated with the dynamics of excess protons, the analysis can possibly be applied here to decompose potential- and friction-induced line-shape effects. In turn, the same accurately parametrized GLE may also be used to build dynamical models for proton transfer.

The application of the GLE for modeling reaction dynamics is successfully shown for NaCl and methane dissociation dynamics in water in chapter 7. It may thus be introduced in coarse-grained models of such systems and extended to other pairing dynamics or other kinds of reactions. Preliminary results show that position-dependent memory friction, as for example handled by the type of GLE introduced in chapter 6, may be a promising model for protein folding or the dissociation dynamics of water molecules.

## 2. Conclusion and Outlook

---

The GLE model for position- and time-dependent friction, introduced in chapter 6, has the advantage over alternative models that it has a simple Markovian embedding and is therefore easily evaluated numerically. In order to make it applicable for modeling complex systems, a parametrization method needs to be developed. Several methods exist for similar kinds of GLEs, for example the one applied in chapters 5 and 7, which provide promising starting points for parametrization of the presented model.

Beyond that, the GLE model introduced in chapter 6 obviously calls for some extensions and thus sparks ideas for the future development of Markovian embeddings. For example, the currently independent local heat baths with corresponding local non-Markovian friction kernels could be coupled, which is motivated by the underlying physical picture and would introduce a controllable tuning between local and position-independent memory friction.

In chapters 6 and 7 the GLE is explored to gain insight into the scaling of the mean reaction time in terms of the mean first-passage time. The second time scale that characterizes the reaction dynamics is the transition-path time of the actual transfer path which is receiving increasing attention, especially in nonequilibrium scenarios such as single-molecule experiments on protein folding. It will be interesting to apply the GLE in the same way to understand the scaling of the transition-path time with respect to non-Markovian friction memory, inertia and the potential shape.

# Proton-Transfer Spectroscopy Beyond the Normal-Mode Scenario

---

3

by Florian N. Brünig, Paul Hillmann, Won Kyu Kim, Jan O. Daldrop, and Roland R. Netz

**Contributions:** F.N.B. and R.R.N. conceived the theory and designed the simulations. F.N.B. performed the ab initio MD simulations and analyzed the data. P.H. performed the quantum-mechanical zero-point calculations. W.K.K. contributed to the transfer-path-shape theory. All authors discussed the results, analyses and interpretations. F.N.B. and R.R.N. wrote the paper with input from all authors.

**Bibliographic information:** This chapter has previously been published in the *Journal of Chemical Physics* by the American Institute of Physics (AIP) as open access under the Creative Commons CC BY licence (<http://creativecommons.org/licenses/by/4.0/>) [4].

<https://doi.org/10.1063/5.0116686>



# Proton-transfer spectroscopy beyond the normal-mode scenario

Cite as: J. Chem. Phys. 157, 174116 (2022); doi: 10.1063/5.0116686

Submitted: 29 July 2022 • Accepted: 26 September 2022 •

Published Online: 7 November 2022



View Online



Export Citation



CrossMark

Florian N. Brünig,<sup>1</sup> Paul Hillmann,<sup>1</sup> Won Kyu Kim,<sup>2</sup> Jan O. Daldrop,<sup>1</sup> and Roland R. Netz<sup>1,a)</sup>

## AFFILIATIONS

<sup>1</sup>Department of Physics, Freie Universität Berlin, 14195 Berlin, Germany

<sup>2</sup>School of Computational Sciences, Korea Institute for Advanced Study, Seoul 02455, Republic of Korea

<sup>a)</sup>Author to whom correspondence should be addressed: [rnetz@physik.fu-berlin.de](mailto:rnetz@physik.fu-berlin.de)

## ABSTRACT

A stochastic theory is developed to predict the spectral signature of proton-transfer processes and is applied to infrared spectra computed from *ab initio* molecular-dynamics simulations of a single  $\text{H}_5\text{O}_2^+$  cation. By constraining the oxygen atoms to a fixed distance, this system serves as a tunable model for general proton-transfer processes with variable barrier height. Three spectral contributions at distinct frequencies are identified and analytically predicted: the quasi-harmonic motion around the most probable configuration, amenable to normal-mode analysis, the contribution due to transfer paths when the proton moves over the barrier, and a shoulder for low frequencies stemming from the stochastic transfer-waiting-time distribution; the latter two contributions are not captured by normal-mode analysis but exclusively reported on the proton-transfer kinetics. In accordance with reaction rate theory, the transfer-waiting-contribution frequency depends inversely exponentially on the barrier height, whereas the transfer-path-contribution frequency is rather insensitive to the barrier height.

© 2022 Author(s). All article content, except where otherwise noted, is licensed under a Creative Commons Attribution (CC BY) license (<http://creativecommons.org/licenses/by/4.0/>). <https://doi.org/10.1063/5.0116686>

## I. INTRODUCTION

The transfer dynamics of excess protons in the aqueous environment is central to many biochemical processes,<sup>1</sup> but despite substantial work, even for acidic water, a complete kinetic model that would describe all spectral features encompassing the low THz and infrared (IR) regimes remains elusive. Typically, the discussion is based on two idealized proton-transfer intermediates, namely the  $\text{H}_5\text{O}_2^+$  Zundel cation, where two water molecules symmetrically point their oxygens to the excess proton,<sup>2</sup> and the Eigen cation, where hydronium  $\text{H}_3\text{O}^+$  is formed and solvated by three water molecules.<sup>3</sup> Accordingly, proton diffusion in water is portrayed as a stochastic succession of these two states, where the excess proton switches during diffusion: It is a defect that diffuses rather than a specific proton, which explains the high proton mobility in water.<sup>4,5</sup>

An intensely debated question concerns the relative stability and abundance of the Eigen and Zundel forms in acidic water.<sup>6–10</sup> Several experimental 2D IR studies suggest the Zundel form dominates the proton-transfer spectroscopic signature in bulk

water.<sup>8,9,11–14</sup> From *ab initio* molecular-dynamics (AIMD) work, it was concluded that an excess proton in bulk liquid water is predominantly present in the Eigen state and that the Zundel form plays the role of a relatively short-lived transfer or barrier state.<sup>15–17</sup> As the separation between the two water oxygen atoms that flank the excess proton decreases, the relative stability changes and eventually the Zundel form becomes preferred over the Eigen form,<sup>18</sup> it transpires that excess proton and water motion are dynamically coupled. As a consequence, proton transfer from one water molecule to a neighboring one not only involves motion of the proton but also of the flanking water molecules and even further water neighbors, making the kinetics highly collective.<sup>7,10,13,14,16,19–23</sup>

In isolated  $\text{H}_5\text{O}_2^+$  clusters, the subject of this paper, and protonated water wires the situation is different from bulk: Experimental<sup>8,24–27</sup> and theoretical<sup>19,20,28–33</sup> work demonstrated that the oxygen–oxygen distance is decreased and the Zundel form is more stable than the hydronium form. By chemical modifications of two proton acceptors in gas-phase clusters, proton-transfer energy barriers of variable heights could be demonstrated.<sup>34</sup> Proton-transfer barriers also exist inside proteins, where amino-acid

side chains that act as proton donors can be located at variable separations.<sup>35–38</sup> Thus, energetic barriers for proton transfer exist in a variety of systems and produce characteristic spectroscopic signatures that fundamentally go beyond the established normal-mode picture, as we show in this paper.

The excess proton has a high net charge and during a transfer event covers significant distances over short times; consequently, IR linear and nonlinear spectroscopy are very suitable methods to detect proton-transfer events and have been applied to bulk acidic solutions,<sup>2</sup> acidic water clusters,<sup>34</sup> gas-phase ions,<sup>39</sup> and proteins.<sup>40</sup> While spectra computed from dynamical simulations encompass nonlinear dynamics and do not employ a normal-mode approximation, the interpretation of simulated spectra is typically based on normal modes, with notable extensions to include anharmonic and frequency-dependent friction effects.<sup>41–43</sup> Also the interpretation of experimental spectra is traditionally based on normal-mode analysis around one or multiple local energy minima, where the normal-mode frequency  $f_{\text{NM}}$  defines a vibrational time scale according to  $\tau_{\text{NM}} = 1/f_{\text{NM}}$ . However, if a barrier exists, two additional time scales emerge, the transfer-waiting time  $\tau_{\text{TW}}$ , which is the time the proton waits in one minimum before it transfers,<sup>44–46</sup> and the transfer-path (TP) time  $\tau_{\text{TP}}$ , which is the time the actual transfer over the barrier takes.<sup>47–51</sup>

In this paper, we show by a combination of stochastic theory and *ab initio* molecular-dynamics (AIMD) simulations that the normal-mode, the transfer-waiting, and the TP time scales, which together characterize the transfer-waiting kinetics, leave distinct and characteristic spectroscopic traces. As a specific example, we consider a  $\text{H}_5\text{O}_2^+$  cation in gas phase. In order to probe different proton-transfer barrier heights, we constrain the separation between the two water oxygen atoms at variable fixed distances, which is applicable to proteins and other systems where proton-accepting residues are positioned at well-defined distances.<sup>35–37</sup> While the transfer-waiting time depends exponentially on the barrier height  $U_0$  as  $\tau_{\text{TW}} \sim e^{U_0/k_B T}$ ,<sup>44,46</sup> the normal-mode time scale  $\tau_{\text{NM}}$  is determined by the stiffness of the effective harmonic potential  $k$  and the effective mass  $m$  according to  $\tau_{\text{NM}} = 2\pi\sqrt{m/k} \sim 1/\sqrt{U_0}$ , and the TP time depends logarithmically on  $U_0$  as  $\tau_{\text{TP}} \sim \ln(U_0/k_B T)/U_0$ .<sup>49–51</sup> From the different functional dependencies on  $U_0$ , one expects a not too low barrier heights  $\tau_{\text{NM}} \sim \tau_{\text{TP}} < \tau_{\text{TW}}$ . Indeed, for an oxygen–oxygen distance of  $R_{\text{OO}} = 2.64 \text{ \AA}$ , which in our AIMD simulations of the  $\text{H}_5\text{O}_2^+$  cation leads to a moderate effective barrier height of  $U_0 = 2.0 k_B T$ , the normal-mode spectroscopic contributions lie between 1000 and 2000  $\text{cm}^{-1}$ , the TP contribution turns out to be a rather well-defined band centered around 800  $\text{cm}^{-1}$ , and since the waiting-time distribution is rather broad, the transfer-waiting contribution forms a continuum band below 500  $\text{cm}^{-1}$  that reaches deep into the GHz range, in agreement with experimental THz absorption measurements.<sup>52,53</sup>

Our AIMD results show that the broad low-frequency transfer-waiting spectral contribution crucially depends on the barrier height, controlled by the relative distance of the water molecules sharing the excess proton. In contrast, the TP spectral contribution shifts only slightly with barrier height, in agreement with recent theoretical and experimental findings.<sup>49–51</sup> Isotope exchange of the excess proton, on the other hand, affects the TP contribution but not the waiting-time contribution, as we predict by stochastic theory. In summary, we show that the spectroscopic signature of proton barrier crossing

reflects transfer-waiting statistics as well as TP kinetics and, in particular, cannot be modeled by a succession of normal modes located across the barrier. Our results also apply to experimental systems with fluctuating barrier heights, such as acidic water, as recently considered by a combined theoretical/experimental study.<sup>53</sup> We show that the spectrum of unconstrained  $\text{H}_5\text{O}_2^+$  can be quite accurately reproduced by Boltzmann averaging of spectra of constrained systems; thus, all of the features we see in our constrained simulations are also expected in experimental systems where the proton acceptor separation can fluctuate.

Our simulations are performed at the Born–Oppenheimer level with classically treated nuclei. Nuclear-quantum zero-point motion has been shown to lead to an increased proton density at the barrier, which is typically interpreted as a signature of a decreased barrier height,<sup>10,15,16,28,54</sup> but for large enough barriers, such nuclear-quantum effects are not expected to eliminate the spectroscopic features we predict, as discussed in the [supplementary material](#), Sec. I. Furthermore, electron-nuclear quantum-mechanical coupling has been shown to be relevant for protonated systems<sup>30</sup> but is challenging to include within the framework of our stochastic theory and therefore, left for future work.

## II. RESULTS AND DISCUSSION

We perform AIMD simulations of a single  $\text{H}_5\text{O}_2^+$  cation with a total trajectory length of 5 ns for several constrained oxygen separations as well as for unconstrained oxygens (see Sec. III A for details). Suitable reaction coordinates are the oxygen–oxygen distance  $R_{\text{OO}}$  and the excess-proton distance from the oxygen midpoint position,  $d = \frac{1}{2}(R_{\text{O,H}} - R_{\text{O,H}})_x$ , projected onto the  $x$ -axis that connects the two oxygens, as illustrated in Fig. 1(a). The two-dimensional free energy in Fig. 1(d), calculated from the probability distribution of unconstrained simulations according to  $U(R_{\text{OO}}, d) = -k_B T \ln p(R_{\text{OO}}, d)$ , demonstrates that the global minimum of the free energy is located around  $R_{\text{OO}} = 2.40 \text{ \AA}$ , and  $d = 0$ . This is the symmetric Zundel state, where the excess proton is symmetrically shared by the oxygens.<sup>2</sup> For  $R_{\text{OO}} > 2.55 \text{ \AA}$ , a double-well free-energy landscape along  $d$  appears, which indicates a preferred localization of the excess proton near one water molecule, analogous to the Eigen state in bulk water.<sup>3</sup> The excess proton trajectory for constrained  $R_{\text{OO}} = 2.64 \text{ \AA}$  in Fig. 1(b) is typical for the thermally activated barrier crossing of a weakly damped massive particle<sup>46</sup> and involves a moderate barrier height of  $U_0 = 2.0 k_B T$ , as seen in the corresponding free-energy profile in Fig. 1(c). Most of the time, the excess proton is part of a  $\text{H}_3\text{O}^+$  molecule and vibrates in one of the two free-energy minima with an oscillation time described by the normal-mode time  $\tau_{\text{NM}} = 17 \text{ fs}$  [inset Fig. 1(b)], while from time to time the proton suddenly crosses the barrier, the mean time of such a TP is  $\tau_{\text{TP}} = 25 \text{ fs}$  [inset Fig. 1(b)]. The longest time scale is the transfer-waiting time, which for  $R_{\text{OO}} = 2.64 \text{ \AA}$  is  $\tau_{\text{TW}} = 440 \text{ fs}$ . In Fig. 1(e), we show as a grey solid line the absorption spectrum of the unconstrained  $\text{H}_5\text{O}_2^+$  cation for an electric field along  $x$ , the oxygen separation direction, calculated from the entire nuclear and electronic polarizations (see Sec. III A). It shows, in addition to the OH stretch and HOH bend bands at 3400 and 1800  $\text{cm}^{-1}$ , respectively, a prominent feature at 1000  $\text{cm}^{-1}$ , which is the Zundel normal mode, where the excess proton vibrates in a rather soft potential produced by the two flanking water molecules (see the [supplementary material](#), Secs. II and III, for

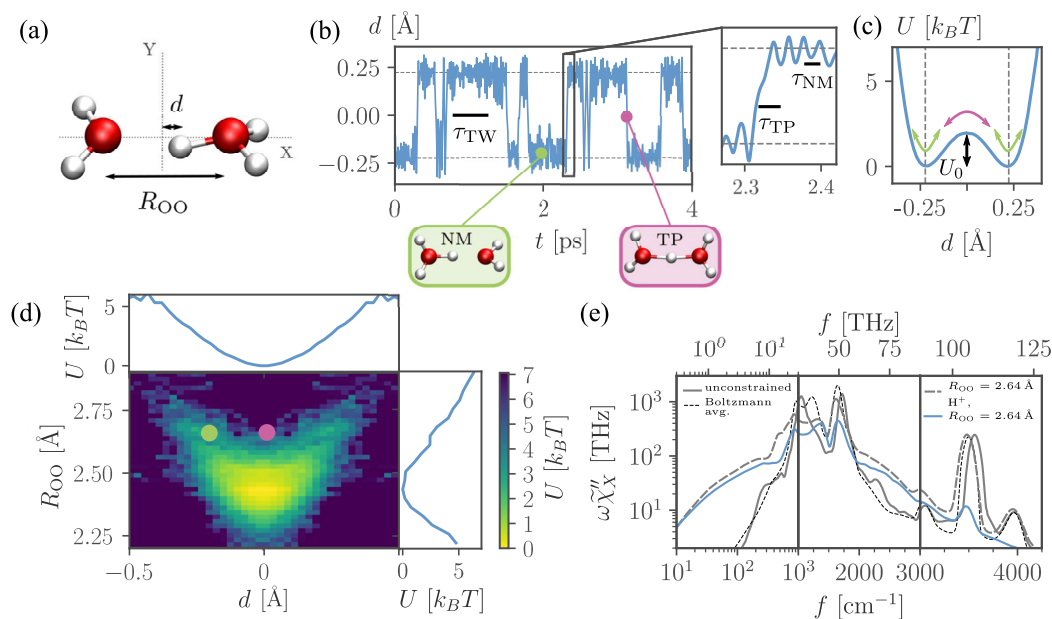


**FIG. 1.** *Ab initio* molecular-dynamics (AIMD) simulations of the  $\text{H}_5\text{O}_2^+$  cation. (a) The oxygen–oxygen separation  $R_{\text{OO}}$  and the proton distance from the oxygen midpoint along the  $x$  axis, named  $d$ , describe the excess-proton dynamics. (b) The excess proton trajectory for fixed  $R_{\text{OO}} = 2.64 \text{ \AA}$  visualizes the transfer-waiting time  $\tau_{\text{TW}}$  as well as the normal-mode time  $\tau_{\text{NM}}$  and the transfer-path (TP) time  $\tau_{\text{TP}}$  (see the inset). Selected snapshots show structures at the free-energy minimum and at the barrier top. (c) Free-energy profile for fixed  $R_{\text{OO}} = 2.64 \text{ \AA}$ , extracted from constrained simulations. (d) 2D free-energy landscape in terms of  $R_{\text{OO}}$  and  $d$  from unconstrained simulations. (e) Absorption spectra for an E field along the  $x$  axis where  $\omega = 2\pi f$ . The grey solid line shows the total (i.e., nuclear + electronic) spectrum of the unconstrained system, compared with the Boltzmann average of constrained systems (black broken line). The grey broken line shows the total spectrum for constrained  $R_{\text{OO}} = 2.64 \text{ \AA}$ , compared to the spectrum of only the excess proton (blue line, multiplied by a factor of 2). Note the change of scales at  $f = 1000 \text{ cm}^{-1}$  and  $f = 3000 \text{ cm}^{-1}$ .

a literature overview). The spectrum for the constrained system with  $R_{\text{OO}} = 2.64 \text{ \AA}$ , grey broken line, displays a band at  $800 \text{ cm}^{-1}$  and a very broad shoulder that extends down to the lowest frequencies. As we show in this paper, these two spectral features stem from proton TPs and proton transfer-waiting-time stochastics, respectively, and are the only spectroscopic contributions that reflect the actual proton-transfer kinetics. Interestingly, the spectral contribution of only the excess proton for fixed  $R_{\text{OO}} = 2.64 \text{ \AA}$  (blue solid line, multiplied by a factor of 2) is almost identical to the full spectrum (gray broken line), so we conclude that the IR spectrum is predominantly caused by proton motion and can thus be used to investigate excess-proton dynamics (more details are given in the [supplementary material](#), Sec. IV). In fact, the spectrum of the unconstrained system (gray solid line) agrees well with the free-energy-weighted Boltzmann average over constrained spectra with different  $R_{\text{OO}}$  values (black broken line, see the [supplementary material](#), Sec. V, for details), indicating that the absorption spectrum can be understood from decoupled proton and oxygen dynamics. Our simulation model with constrained oxygen–oxygen separation is thus also a tool to decompose and, thereby, understand unconstrained system spectra (a finding that is obvious only for static observables<sup>55</sup>).

In order to distinguish transfer-waiting, TP and normal-mode spectral contributions, the proton trajectory  $d(t)$  is decomposed according to  $d(t) = d_{\text{TW}}(t) + d_{\text{TP}}(t) + d_{\text{NM}}(t)$ , as illustrated in [Fig. 2\(a\)](#) for  $R_{\text{OO}} = 2.64 \text{ \AA}$ . The transfer-waiting part  $d_{\text{TW}}(t)$

describes two-state kinetics with instantaneous transfers when the trajectory last crosses a free-energy minimum at  $d_{\text{TW}}^* = \pm 0.22 \text{ \AA}$ . The TP contribution  $d_{\text{TP}}(t)$  consists of transfer trajectories between last and first crossing the free-energy minima, including recrossings where the proton shuttles repeatedly back and forth between the minima. Recrossings are rather frequent for the low friction experienced by the proton<sup>46</sup> (see the [supplementary material](#), Sec. VI), a threefold recrossing event is seen in the proton trajectory in [Fig. 2\(a\)](#) at  $t = 0.6 \text{ ps}$ . Finally, the normal-mode part  $d_{\text{NM}}(t)$  comprises the trajectory remainder.

[Figure 2\(b\)](#) shows in blue the simulated excess-proton spectrum decomposed into its three components according to  $\tilde{\chi}'' = \tilde{\chi}''_{\text{B}} + \tilde{\chi}''_{\text{TP}} + \tilde{\chi}''_{\text{NM}}$ , the red broken lines show theoretical predictions (which will be explained further below). Trajectory decomposition in the time domain creates spectral cross contributions, which are relatively small, as shown in the [supplementary material](#), Secs. VII and VIII, and are added to  $\tilde{\chi}''_{\text{NM}}$ . The transfer-waiting spectrum  $\tilde{\chi}''_{\text{TW}}$  in [Fig. 2\(b2\)](#) displays a pronounced low-frequency shoulder, which reflects the transfer-waiting-time distribution. The TP spectrum  $\tilde{\chi}''_{\text{TP}}$  in [Fig. 2\(b3\)](#) is a rather well defined band at  $800 \text{ cm}^{-1}$ . Even though the time fraction the excess proton spends on TPs is only 16% for  $R_{\text{OO}} = 2.64 \text{ \AA}$ , the spectral contribution is significant due to the large and quick charge displacement: The proton transfer velocity of roughly  $v_{\text{TP}} = 2d_{\text{TP}}^*/\tau_{\text{TP}} = 0.44 \text{ \AA}/25 \text{ fs} = 1.8 \times 10^3 \text{ m/s}$  is slightly larger than the proton thermal velocity of  $v_{\text{th}} = \sqrt{k_{\text{B}}T/m_{\text{p}}}$

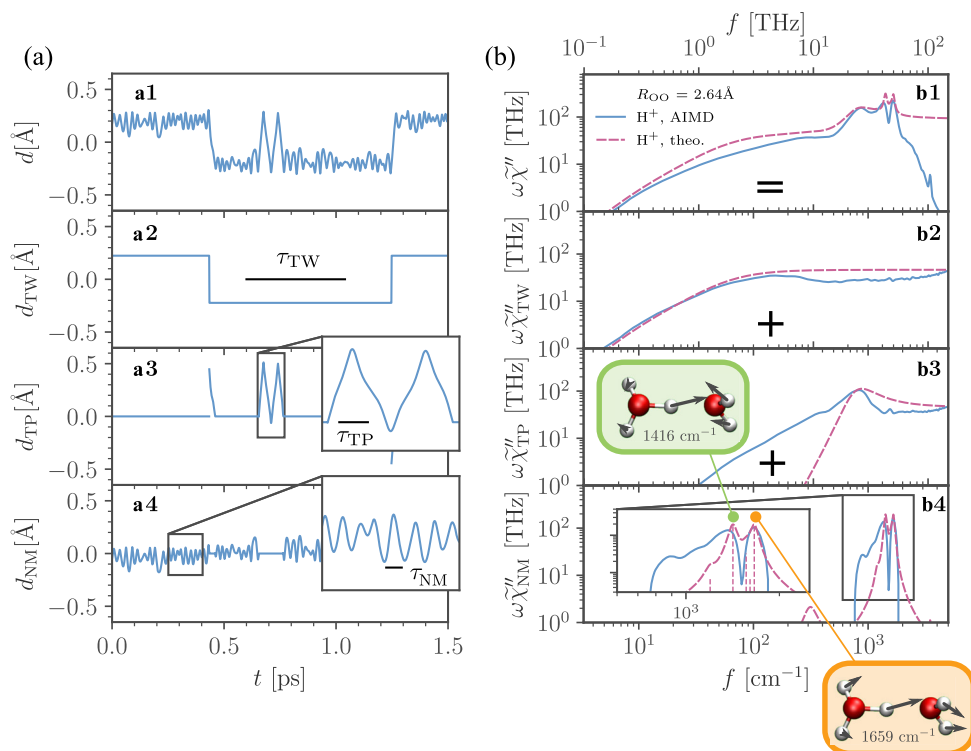


**FIG. 2.** AIMD simulations of a  $\text{H}_5 \text{O}_2^+$  cation with constrained  $R_{\text{OO}} = 2.64 \text{ \AA}$ . (a) Decomposition of the excess-proton trajectory  $d(t)$  into the two-state transfer-waiting contribution  $d_{\text{TW}}(t)$ , the TP contribution  $d_{\text{TP}}(t)$  and the remaining normal-mode contribution  $d_{\text{NM}}(t)$ . (b) Blue solid lines show the simulated excess-proton spectrum  $\omega\tilde{\chi}''$  and its decomposition into the transfer-waiting  $\omega\tilde{\chi}''_{\text{TW}}$ , the TP  $\omega\tilde{\chi}''_{\text{TP}}$  and the normal-mode contribution  $\omega\tilde{\chi}''_{\text{NM}}$ . The red broken lines in (b2) and (b3) show the corresponding theoretical predictions according to Eqs. (1) and (5). The red broken line in (b4) shows the normal-mode spectrum including friction-induced line broadening. The snapshots illustrate the two dominant normal modes at  $1416$  and  $1659 \text{ cm}^{-1}$ .

$= 1.5 \times 10^3 \text{ m/s}$ , where  $m_p = 1.7 \times 10^{-27} \text{ kg}$  is the proton mass. This confirms previous findings that TPs correspond to the high-energetic part of the Maxwell-Boltzmann ensemble, i.e., the excess proton initiates a TP only when its kinetic energy is significantly above average.<sup>56</sup> The normal-mode spectrum  $\tilde{\chi}''_{\text{NM}}$  in Fig. 2(b4) consists of two main peaks.

We will now present analytic theories for each simulated spectral contribution shown in Figs. 2(b2)–2(b4). A stochastic two-state process has the spectrum

$$\omega\tilde{\chi}''_{\text{TW}}(\omega) = \frac{2q^2 d_{\text{TW}}^{*2}}{V\epsilon_0 k_B T} \text{Re} \left( \frac{\omega^2 \tilde{q}_{\text{TW}}(\omega)}{1 - \tilde{p}_{\text{TW}}(\omega)^2} \right) \quad (1)$$

and depends on the Fourier-transformed transfer-waiting-time distribution  $\tilde{p}_{\text{TW}}(\omega)$  and the survival distribution  $\tilde{q}_{\text{TW}}(\omega)$ , which is defined as  $q_{\text{TW}}(t) = \int_t^\infty p_{\text{TW}}(t') dt'$ , the positions of the free-energy minima  $\pm d_{\text{TW}}^*$ , the excess proton charge  $q = e$  and the system volume  $V$  (see the supplementary material, Sec. IX, for a detailed derivation). Using  $d_{\text{TW}}^* = 0.22 \text{ \AA}$  and bi-exponential fits for  $p_{\text{TW}}(t)$  to the simulation data in Fig. 4(c),  $\omega\tilde{\chi}''_{\text{TW}}(\omega)$  according to Eq. (1) (red broken line) matches the simulation data (blue solid line) in Fig. 2(b2) very well without any fitting parameters. For a single-exponential waiting-time distribution,  $p_{\text{TW}}(t) = \tau_{\text{TW}}^{-1} \exp(-t/\tau_{\text{TW}})$ , Eq. (1) simplifies to

$$\omega\tilde{\chi}''_{\text{TW}}(\omega) = \frac{2q^2 d_{\text{TW}}^{*2}}{V\epsilon_0 k_B T} \frac{\tau_{\text{TW}} \omega^2}{(4 + \tau_{\text{TW}}^2 \omega^2)}, \quad (2)$$

which shows that the spectrum is identical to an overdamped harmonic oscillator with a corner frequency  $\omega_{\text{TW}}^* \sim 1/\tau_{\text{TW}}$  (see the supplementary material, Sec. X, for details). For large frequencies,  $\omega\tilde{\chi}''_{\text{TW}}$  is constant and proportional to the transfer-waiting rate,  $\omega\tilde{\chi}''_{\text{TW}} \sim 1/\tau_{\text{TW}}$ , for small frequencies  $\omega\tilde{\chi}''_{\text{TW}} \sim \tau_{\text{TW}} \omega^2$ .

The TP spectral contribution depends on the TP shape. The ensemble of all 2829 TPs observed in the simulations for  $R_{\text{OO}} = 2.64 \text{ \AA}$  is shown in Fig. 3(a) (gray lines), together with the mean TP (blue solid line) obtained by position averaging. The path-integral saddle-point prediction for the TP shape over a parabolic barrier,<sup>51</sup>

$$d_{\text{TP}}(t) = d_{\text{TW}}^* \left[ e^{t/\kappa} - e^{-t/\kappa} \right] / \mathcal{N} \quad (3)$$

(red dotted line), matches the simulated mean TP shape very well ( $\mathcal{N}$  is a normalization constant). In the supplementary material, Sec. XI, it is shown that Eq. (3) corresponds to the exact mean TP shape in the high-barrier limit.<sup>50</sup> The fitted characteristic time  $\kappa = d_{\text{TW}}^{*2} \gamma / (2U_0) = 6.5 \text{ fs}$  depends on the effective friction coefficient  $\gamma$  acting on the proton as it moves over the barrier. A straight line (black broken line) also describes the simulated mean TP shape quite well. Figure 3(b) shows the TP-time distribution of all TPs (green triangles) together with a decomposition into single (non-recrossing, blue squares) and multiple (recrossing, red dots) TPs, where the TP time  $\tau_{\text{TP}}$  is defined by the turning points of the TPs. It is seen that multiple TPs that consist of recrossing trajectories are significantly faster than single TPs, which reflects that recrossing

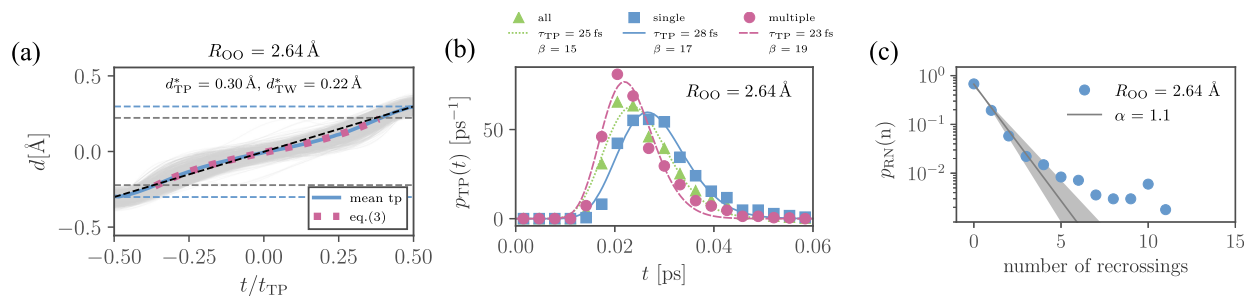


**FIG. 3.** TP statistics. (a) Ensemble of all 2829 proton TPs for constrained  $R_{OO} = 2.64 \text{ \AA}$  (gray lines) as a function of the rescaled time  $t/t_{TP}$ , where  $t_{TP}$  is the individual TP time. The horizontal blue broken lines indicate the mean TP terminal positions  $\pm d_{TP}^*/2$ , defined by the TP turning points, while horizontal grey dashed lines indicate the free-energy minima  $\pm d_{TW}^*/2$ . The simulated mean TP (blue line) agrees well with the path-integral prediction Eq. (3) (red dotted line). The straight black broken line also approximates the TP shape quite well. (b) Time distribution  $p_{TP}(t)$  of all TPs (green triangles) and a decomposition into single (non-recrossing, blue squares) and multiple (recrossing, red dots) TPs together with fits according to Eq. (4). (c) Recrossing-number probability distribution  $p_{RN}(n)$  compared to an exponential fit  $p_{RN}(n) = (1 - e^{-\alpha})e^{-\alpha n}$ , the confidence interval  $\alpha \pm 20\%$  is shown by grey lines.

protons have a higher kinetic energy and, thereby, tend to rebound back over the barrier. Fits according to the Erlang distribution,<sup>57</sup>

$$p_{TP}(t) = \frac{t^{\beta-1}}{(\beta-1)!} \left( \frac{\beta}{\tau_{TP}} \right)^{\beta} e^{-\beta t/\tau_{TP}}, \quad (4)$$

are shown as lines. In Fig. 3(c) the simulated recrossing-number distribution  $p_{RN}(n)$  is compared to an exponential fit with a decay constant  $\alpha = 1.1$ , 40% of all TPs are single transfer events,  $n = 0$ , while the remaining 60% TPs are part of multiple events with  $n > 0$ .

Combining the TP time distribution  $p_{TP}(t)$  in the infinitely sharp limit  $\beta \rightarrow \infty$ , the exponential recrossing-number distribution  $p_{RN}(n)$  and approximating the TP shape as a straight line, the analytical result for the TP spectral contribution [red broken line in Fig. 2(b3)] is derived in the supplementary material, Sec. XII, and is given as

$$\omega \tilde{\chi}_{TP}''(\omega) = \frac{d_{TP}^*{}^2 q^2}{V \epsilon_0 k_B T \tau_{TW}} \frac{64 \omega^2 \tau_{TP}^2}{\pi^4 (\pi + \omega \tau_{TP})^2} \times \frac{e^{\alpha} \omega^2 \tau_{TP}^2}{2 \cosh(\alpha) - 2 + (\pi - \omega \tau_{TP})^2}, \quad (5)$$

it matches the simulation data (blue solid line) around the maximum quite well. In the comparison, the mean time of recrossing TPs  $\tau_{TP} = 23 \text{ fs}$  from Fig. 3(b) is used, which is shown to be the dominating time scale in the supplementary material, Sec. XII. Interestingly, the TP spectrum Eq. (5) is a product of a Debye and a Lorentzian line shape, both with the same characteristic frequency  $f_{TP} = 1/(2\tau_{TP})$ , which explains its relative sharpness.

The remaining normal-mode contribution  $\tilde{\chi}_{NM}''$  in Fig. 2(b4) is obtained by harmonic analysis of the minimal energy structure, including line broadening from frictional damping (red broken line). The two dominant normal modes around  $1416$  and  $1659 \text{ cm}^{-1}$ , which correspond to in-phase and out-of-phase coupled vibrations of the excess protons with the hydrogens of the distant water,

are illustrated in Fig. 2(b4) (see Sec. III A and the supplementary material, Sec. III, for details).

In Fig. 2(b1), the simulated excess-proton spectrum (blue solid line) is compared to the sum of the theoretical transfer-waiting, TP, and normal mode predictions (red broken line); the agreement is good (except for very high frequencies), which demonstrates that Eqs. (1) and (5) together with the normal-mode analysis allow us to quantitatively describe excess-proton transfer spectra.

The excess-proton spectra in Fig. 4(a1) vary significantly for different values of  $R_{OO}$ . The excess-proton free energies from simulations in Fig. 4(b) demonstrate that the three systems exhibit high, moderate, and low barriers. Very pronounced is the change of the low-frequency shoulder of the transfer-waiting contribution in Fig. 4(a2), which moves to lower frequencies and becomes weaker with growing barrier height and is well captured by the theoretical predictions Eq. (1) (black broken lines), using bi-exponential fits to the transfer-waiting distributions in Fig. 4(c). Equation (2) demonstrates that the spectral differences are due to less frequent transfers as the barrier height increases. The simulated mean transfer-waiting time  $\tau_{TW}$  in the inset of Fig. 4(c) exponentially increases with the barrier height  $U_0$ , as expected for thermally activated barrier crossing.<sup>44,46</sup> On the other hand, the frequency of the TP spectral contribution in Fig. 4(a3) shifts very little for different  $R_{OO}$ , which is well-captured by Eq. (5) (black broken lines) and reflects the weak dependence of the TP time  $\tau_{TP}$  on the barrier height in the inset of Fig. 4(c), in agreement with the predicted logarithmic dependence of  $\tau_{TP}$  on the barrier height.<sup>49</sup>

Figure 4(d) compares the IR spectrum of the excess proton (blue solid line) in the  $\text{H}_5\text{O}_2^+$  cation to the normal-mode spectrum, including frictional line broadening (grey broken line, see the supplementary material, Sec. III, for details) for fixed  $R_{OO} = 2.40 \text{ \AA}$ , the barrier-less global minimum of the unconstrained  $\text{H}_5\text{O}_2^+$  cation. The good agreement highlights that the barrier-less Zundel state is well described by a normal-mode analysis. This is in contrast to the results for larger values of  $R_{OO}$  in Fig. 4(a), where a finite barrier exists and the transfer-waiting and TP spectral signatures dominate over the normal-mode contribution.

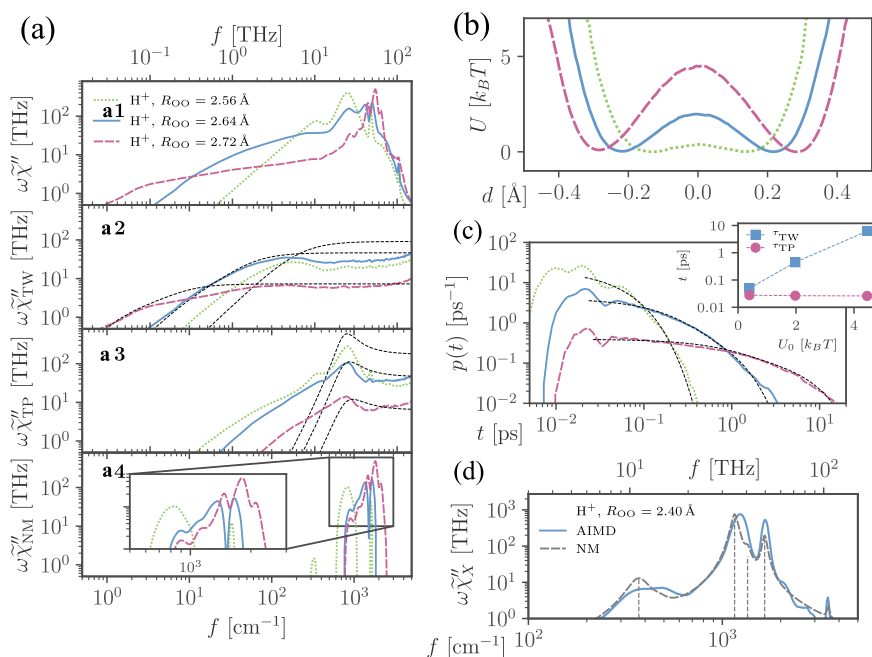


**FIG. 4.** Decomposition of the excess-proton spectra for various constrained  $R_{OO}$ . (a) AIMD spectra are shown as colored lines and theoretical predictions are shown for the transfer-waiting contribution, Eq. (1), in (a2) and for the TP contribution, Eq. (5), in (a3) as thin black broken lines. (a4) shows the normal-mode contributions. See the [supplementary material](#), Sec. XIII, for details. (b) Proton free energies landscapes extracted from simulation trajectories. (c) Transfer-waiting time distributions together with bi-exponential fits (black broken lines). The inset shows the mean transfer-waiting times  $\tau_{TW}$  and the mean TP times  $\tau_{TP}$  as a function of the free-energy barrier height  $U_0$ . (d) IR spectrum of the excess proton (blue solid line) in the  $H_5O_2^+$  cation with a fixed  $R_{OO} = 2.40$  Å compared to the normal-mode spectrum including frictional line-broadening (grey broken line). Vertical grey broken lines denote the dominant normal modes.

### III. CONCLUSIONS AND DISCUSSION

In contrast to traditional normal-mode-based approaches to proton-transfer spectroscopy, which consider proton vibrations around energy minima, we here investigate the spectrum of a proton as it actually makes the move from one energy minimum to another. While the normal-mode frequencies are on the harmonic-approximation level determined by the positive curvature of the energy landscape and by the effective mass, two fundamentally different time scales govern the barrier-crossing absorption spectrum: the mean time the proton waits in a potential minimum before it crosses the barrier, the transfer-waiting time, and the mean time it takes the proton to actually move over the barrier once it has left the potential minimum, the so-called transfer-path (TP) time. While the TP time distribution is rather narrow, which leads to a well-defined TP band, the transfer-waiting times are broadly distributed, which leads to a wide spectral absorption down to low frequencies. Recent experimental studies on hydrochloric acid solutions in the THz regime indeed observed broad absorption that, by comparison with AIMD simulations, could be attributed to proton motion.<sup>52,53</sup>

The AIMD simulations of single  $H_5O_2^+$  cations reveal a high similarity between excess-proton-only spectra and spectra from all nuclei and electronic polarizations. This emphasizes the impact of proton-transfer processes on experimentally measured spectra and allows us in turn to develop a stochastic spectral theory based on excess-proton motion only. The excess-proton transfer between two water molecules depends strongly on the separation of the two water oxygens. For oxygen–oxygen separations  $R_{OO} \geq 2.5$  Å, a barrier crossing is involved, whereas for closer separations the proton is rather located directly in between the two water molecules. It should be noted, though, that nuclear quantum effects significantly increase the probability to finding the proton in the barrier

position, which is typically interpreted as an indication that the effective barrier height is reduced. This means that the effective barrier heights could be smaller in the presence of nuclear quantum effects.

An H/D isotope exchange of the excess proton does not shift the low-frequency transfer-waiting signature, as shown in the [supplementary material](#), Sec. XIV, which is expected since the excess-proton barrier crossing is a friction-dominated process and mass plays only a minor role, as discussed in the [supplementary material](#), Sec. XV. In contrast, TP and normal-mode signatures show isotope effects, which suggests how to experimentally distinguish barrier crossing from the other spectral contributions. For the normal-mode spectral contribution the isotope effect is well known (see Sec. X in the [supplementary material](#)), the mass-dependence of the TP spectral contribution is rather subtle and depends on the stochastic mass-friction balance (see Sec. XV in the [supplementary material](#)).

The spectroscopic signatures of proton transfer are most pronounced along the transfer direction, as shown in Sec. V in the [supplementary material](#), thus dichroic spectroscopic measurements of oriented samples<sup>33,38</sup> would be most suitable to observe the features discussed in this paper.

### A. Methods

The Born–Oppenheimer AIMD simulations of the  $H_5O_2^+$  cation were performed with the CP2K 4.1 software package using a doubly polarizable triple-zeta basis set for the valence electrons, dual-space pseudopotentials, the BLYP exchange–correlation functional and D3 dispersion correction.<sup>58–60</sup> The simulation box size was  $10 \times 10 \times 10$  Å<sup>3</sup> and the cutoff for the plane-wave representation was 400 Ry. For each constrained system, 20 ps simulations with a time step of 0.5 fs were performed under NVT conditions

at 300 K by coupling all atoms to a CSVR thermostat with a time constant of 100 fs, which has been shown to be exceptionally good for preserving vibrational dynamics.<sup>61</sup> Consequently, a number of independent simulations with a time step of 0.25 fs were performed under NVE conditions starting from different snapshots of the NVT data,  $12 \times 20$  ps for the systems with  $R_{OO} \leq 2.5$  Å and  $\geq 20 \times 60$  ps for the systems with  $R_{OO} \geq 2.5$  Å,  $20 \times 90$  ps for  $R_{OO} = 2.72$  Å. Even though the time step was chosen to be very small, some systems did not preserve energy during the NVE simulation due to unfavorable starting conditions and the small number of degrees of freedom. These systems were excluded from further analysis. The data for systems with constrained oxygen atoms stem from NVE simulations, totaling in simulation time 240–1800 ps for each system. In the case of the unconstrained system, the oxygen atoms were only constrained in the  $yz$ -plane. Nevertheless, the NVE simulations were less stable due to large spatial fluctuations along  $x$ . For this system, NVT simulations with a total simulation time of 20 ps were performed.

Linear response theory relates the dielectric susceptibility  $\chi(t)$  to the equilibrium autocorrelation of the dipole moment  $C(t) = \langle \mathbf{p}(t)\mathbf{p}(0) \rangle$ , reading in Fourier space

$$\tilde{\chi}(\omega) = \frac{1}{V\epsilon_0 k_B T} \left( C(0) - i\frac{\omega}{2} \tilde{C}^+(\omega) \right), \quad (6)$$

with system volume  $V$ , thermal energy  $k_B T$ , and vacuum permittivity  $\epsilon_0$ . IR spectra can therefore be calculated straight-forwardly from sufficiently sampled trajectories of the AIMD simulation data using Eq. (6) and the Wiener-Kintchin relation, derived in the [supplementary material](#), Sec. XVI. Quantum corrections have previously been addressed,<sup>62</sup> but they were not applied here. The dipole moments were obtained after Wannier-center localization of the electron density at a time resolution of 2 fs. The power spectra were smoothed using Gaussian kernels with widths that are logarithmically increasing from  $20 \text{ cm}^{-1}$  centered at  $f = 20 \text{ cm}^{-1}$  to  $100 \text{ cm}^{-1}$  centered at  $f = 5000 \text{ cm}^{-1}$ . All presented spectra were scaled by the volume of two water molecules,  $V = 0.060 \text{ nm}^3$ , which follows from the density of water at atmospheric pressure and 300 K,  $\rho = 0.99 \text{ g/ml}$ . The normal-mode analysis was performed using the implementation in CP2K 4.1 by diagonalizing the Hessian of energetically optimal structures for the same system parameters as in the AIMD simulations. The normal modes were obtained as the Eigenvectors of the Hessian, the Eigenvalues are the frequencies. A projection of the Eigenvectors onto the excess-proton coordinate gave their spectral contributions. Line broadening resulted from frictional damping with the same fitted friction coefficient  $\gamma = 16 \text{ u/ps}$  for all normal modes (see the [supplementary material](#), Sec. X, for details).

## SUPPLEMENTARY MATERIAL

See the [supplementary material](#) for detailed derivations, analysis procedures, additional data, and discussion.

## ACKNOWLEDGMENTS

We gratefully acknowledge support by the DFG (Grant No. SFB 1078), project C1, and computing time on the HPC clusters at the physics department and ZEDAT, FU Berlin. W.K.K. acknowledges

the support by a KIAS Individual Grant (No. CG076001) at Korea Institute for Advanced Study.

## AUTHOR DECLARATIONS

### Conflict of Interest

The authors have no conflicts to disclose.

## Author Contributions

F.N.B. and R.R.N. conceived the theory and designed the simulations. F.N.B. performed the AIMD simulations and analyzed the data. P.H. performed the quantummechanical zero-point calculations. W.K.K. contributed to the transfer-path-shape theory. All authors discussed the results, analyses and interpretations. F.N.B. and R.R.N. wrote the paper with input from all authors.

**Florian N. Brünig:** Conceptualization (equal); Data curation (lead); Formal analysis (equal); Investigation (equal); Methodology (equal); Software (lead); Visualization (lead); Writing – original draft (equal); Writing – review & editing (equal). **Paul Hillmann:** Formal analysis (supporting); Software (supporting); Visualization (supporting); Writing – original draft (supporting). **Won Kyu Kim:** Formal analysis (supporting); Visualization (supporting); Writing – original draft (supporting). **Jan O. Daldrop:** Conceptualization (supporting); Supervision (supporting). **Roland R. Netz:** Conceptualization (equal); Funding acquisition (lead); Project administration (lead); Supervision (lead); Writing – original draft (equal); Writing – review & editing (equal); Formal analysis (equal); Investigation (equal); Methodology (equal).

## DATA AVAILABILITY

The data that support the findings of this study are available from the corresponding author upon request.

## REFERENCES

- 1 D. Marx, "Proton Transfer 200 Years after von Grothuss: Insights from Ab Initio Simulations," *ChemPhysChem* **7**, 1848–1870 (2006).
- 2 G. Zundel and H. Metzger, *Z. Phys. Chem* **58**, 225 (1968).
- 3 E. Wicke, M. Eigen, and T. Ackermann, *Z. Phys. Chem.* **1**, 340 (1954).
- 4 M. Tuckerman, K. Laasonen, M. Sprik, and M. Parrinello, *J. Phys. Chem.* **103**, 150 (1995).
- 5 T. C. Berkelbach, H.-S. Lee, and M. E. Tuckerman, *Phys. Rev. Lett.* **103**, 238302 (2009).
- 6 D. Asthagiri, L. R. Pratt, and J. D. Kress, *Proc. Natl. Acad. Sci. U. S. A.* **102**, 6704 (2005).
- 7 C. A. Daly, L. M. Streaker, Y. Sun, S. R. Pattenaude, A. A. Hassanali, P. B. Petersen, S. A. Corcelli, and D. Ben-Amotz, *J. Phys. Chem. Lett.* **8**, 5246 (2017).
- 8 F. Dahms, B. P. Fingerhut, E. T. J. Nibbering, E. Pines, and T. Elsaesser, *Science* **357**, 491 (2017).
- 9 W. B. Carpenter, J. A. Fournier, N. H. C. Lewis, and A. Tokmakoff, *J. Phys. Chem. B* **122**, 2792 (2018).
- 10 P. B. Calio, C. Li, and G. A. Voth, *J. Am. Chem. Soc.* **143**, 18672 (2021).
- 11 M. Thämer, L. De Marco, K. Ramasesha, A. Mandal, and A. Tokmakoff, *Science* **350**, 78 (2015).
- 12 J. A. Fournier, W. B. Carpenter, N. H. C. Lewis, and A. Tokmakoff, *Nat. Chem.* **10**, 932 (2018).

- <sup>13</sup>A. Kundu, F. Dahms, B. P. Fingerhut, E. T. J. Nibbering, E. Pines, and T. Elsaesser, *J. Phys. Chem. Lett.* **10**, 2287 (2019).
- <sup>14</sup>W. B. Carpenter, Q. Yu, J. H. Hack, B. Dereka, J. M. Bowman, and A. Tokmakoff, *J. Chem. Phys.* **153**, 124506 (2020).
- <sup>15</sup>D. Marx, M. E. Tuckerman, J. Hutter, and M. Parrinello, *Nature* **397**, 601 (1999).
- <sup>16</sup>J. A. Napoli, O. Marsalek, and T. E. Markland, *J. Chem. Phys.* **148**, 222833 (2018).
- <sup>17</sup>S. Roy, G. K. Schenter, J. A. Napoli, M. D. Baer, T. E. Markland, and C. J. Mundy, *J. Phys. Chem. B* **124**, 5665 (2020).
- <sup>18</sup>T. Komatsuzaki and I. Ohmine, *Chem. Phys.* **180**, 239 (1994).
- <sup>19</sup>W. Kulig and N. Agmon, *Nat. Chem.* **5**, 29 (2013).
- <sup>20</sup>R. Biswas, W. Carpenter, J. A. Fournier, G. A. Voth, and A. Tokmakoff, *J. Chem. Phys.* **146**, 154507 (2017).
- <sup>21</sup>H. Wang and N. Agmon, *J. Phys. Chem. A* **121**, 3056 (2017).
- <sup>22</sup>T. K. Esser, H. Knorke, K. R. Asmis, W. Schöllkopf, Q. Yu, C. Qu, J. M. Bowman, and M. Kaledin, *J. Phys. Chem. Lett.* **9**, 798 (2018).
- <sup>23</sup>S. A. Fischer and D. Gunlycke, *J. Phys. Chem. B* **123**, 5536 (2019).
- <sup>24</sup>K. R. Asmis, N. L. Pivonka, G. Santambrogio, M. Brümmer, C. Kaposta, D. M. Neumark, and L. Wöste, *Science* **299**, 1375 (2003).
- <sup>25</sup>J. M. Headrick, E. G. Diken, R. S. Walters, N. I. Hammer, R. A. Christie, J. Cui, E. M. Myshakin, M. A. Duncan, M. A. Johnson, and K. D. Jordan, *Science* **308**, 1765 (2005).
- <sup>26</sup>T. L. Guasco, M. A. Johnson, and A. B. McCoy, *J. Phys. Chem. A* **115**, 5847 (2011).
- <sup>27</sup>F. Dahms, R. Costard, E. Pines, B. P. Fingerhut, E. T. J. Nibbering, and T. Elsaesser, *Angew. Chem., Int. Ed.* **55**, 10600 (2016).
- <sup>28</sup>M. E. Tuckerman, D. Marx, M. L. Klein, and M. Parrinello, *Science* **275**, 817 (1997).
- <sup>29</sup>J. Sauer and J. Döbler, *ChemPhysChem* **6**, 1706 (2005).
- <sup>30</sup>O. Vendrell, F. Gatti, and H.-D. Meyer, *J. Chem. Phys.* **127**, 184303 (2007).
- <sup>31</sup>F. Agostini, R. Vuilleumier, and G. Ciccotti, *J. Chem. Phys.* **134**, 084303 (2011).
- <sup>32</sup>M. Rossi, M. Ceriotti, and D. E. Manolopoulos, *J. Chem. Phys.* **140**, 234116 (2014).
- <sup>33</sup>J. O. Daldrop, M. Saita, M. Heyden, V. A. Lorenz-Fonfria, J. Heberle, and R. R. Netz, *Nat. Commun.* **9**, 311 (2018).
- <sup>34</sup>C. T. Wolke, J. A. Fournier, L. C. Dzugas, M. R. Fagiani, T. T. Odbadrakh, H. Knorke, K. D. Jordan, A. B. McCoy, K. R. Asmis, and M. A. Johnson, *Science* **354**, 1131 (2016).
- <sup>35</sup>S. Wolf, E. Freier, M. Potschies, E. Hofmann, and K. Gerwert, *Angew. Chem., Int. Ed.* **49**, 6889 (2010).
- <sup>36</sup>R. Tripathi, H. Forbert, and D. Marx, *J. Phys. Chem. B* **123**, 9598 (2019).
- <sup>37</sup>D. Friedrich, F. N. Brünig, A. J. Nieuwkoop, R. R. Netz, P. Hegemann, and H. Oshkinat, *Commun. Biol.* **3**, 4 (2020).
- <sup>38</sup>Y. Yang, T. Stensitzki, L. Sauthof, A. Schmidt, P. Piwowarski, F. Velazquez Escobar, N. Michael, A. D. Nguyen, M. Szczepek, F. N. Brünig, R. R. Netz, M. A. Mroginski, S. Adam, F. Bartl, I. Schapiro, P. Hildebrandt, P. Scheerer, and K. Heyne, *Nat. Chem.* **14**, 823 (2022).
- <sup>39</sup>R. J. Saykally, *Science* **239**, 157 (1988).
- <sup>40</sup>A. Barth, *Biochim. Biophys. Acta - Bioenerg.* **1767**, 1073 (2007).
- <sup>41</sup>M. Park, I. Shin, N. J. Singh, and K. S. Kim, *J. Phys. Chem. A* **111**, 10692 (2007).
- <sup>42</sup>F. Agostini, R. Vuilleumier, and G. Ciccotti, *J. Chem. Phys.* **134**, 084302 (2011).
- <sup>43</sup>F. N. Brünig, O. Geburtig, A. von Canal, J. Kappler, and R. R. Netz, *J. Phys. Chem. B* **126**, 1579 (2022).
- <sup>44</sup>H. A. Kramers, *Physica* **7**, 284 (1940).
- <sup>45</sup>G. Williams, *Chem. Rev.* **72**, 55 (1972).
- <sup>46</sup>J. Kappler, J. O. Daldrop, F. N. Brünig, M. D. Boehle, and R. R. Netz, *J. Chem. Phys.* **148**, 014903 (2018).
- <sup>47</sup>G. Hummer, *J. Chem. Phys.* **120**, 516 (2004).
- <sup>48</sup>P. Faccioli, M. Sega, F. Pederiva, and H. Orland, *Phys. Rev. Lett.* **97**, 108101 (2006).
- <sup>49</sup>H. S. Chung, J. M. Louis, and W. A. Eaton, *Proc. Natl. Acad. Sci. U. S. A.* **106**, 11837 (2009).
- <sup>50</sup>W. K. Kim and R. R. Netz, *J. Chem. Phys.* **143**, 224108 (2015).
- <sup>51</sup>P. Cossio, G. Hummer, and A. Szabo, *J. Chem. Phys.* **148**, 123309 (2018).
- <sup>52</sup>D. Decka, G. Schwaab, and M. Havenith, *Phys. Chem. Chem. Phys.* **17**, 11898 (2015).
- <sup>53</sup>F. N. Brünig, M. Rammner, E. M. Adams, M. Havenith, and R. R. Netz, *Nat. Commun.* **13**, 4210 (2022).
- <sup>54</sup>C. Schran and D. Marx, *Phys. Chem. Chem. Phys.* **21**, 24967 (2019).
- <sup>55</sup>M. Sprik and G. Ciccotti, *J. Chem. Phys.* **109**, 7737 (1998).
- <sup>56</sup>J. O. Daldrop, W. K. Kim, and R. R. Netz, *Europhys. Lett.* **113**, 18004 (2016).
- <sup>57</sup>D. R. Cox and H. D. Miller, *The Theory of Stochastic Processes* (CRC Press, 1977).
- <sup>58</sup>J. Hutter, M. Iannuzzi, F. Schiffmann, and J. Vandevondele, *Wiley Interdiscip. Rev.: Comput. Mol. Sci.* **4**, 15 (2014).
- <sup>59</sup>R. A. Kendall, T. H. Dunning, and R. J. Harrison, *J. Chem. Phys.* **96**, 6796 (1992).
- <sup>60</sup>S. Grimme, J. Antony, S. Ehrlich, and H. Krieg, *J. Chem. Phys.* **132**, 154104 (2010).
- <sup>61</sup>G. Bussi, D. Donadio, and M. Parrinello, *J. Chem. Phys.* **126**, 014101 (2007).
- <sup>62</sup>R. Ramírez, T. López-Ciudad, P. Kumar P, and D. Marx, *J. Chem. Phys.* **121**, 3973 (2004).





# Spectral Signatures of Excess-Proton Waiting and Transfer-Path Dynamics in Aqueous Hydrochloric Acid Solutions

---

4

by Florian N. Brünig, Manuel Rammler, Ellen E. Adams, Martina Havenith, and Roland R. Netz

**Contributions:** F.N.B. and R.R.N. conceived the theory and designed the simulations. F.N.B. performed the ab initio MD simulations. F.N.B. and M.R. analyzed the data and designed the figures. E.A. and M.H. carried out the THz measurements and analyzed the data. All authors discussed the results, analyses, and interpretations. F.N.B., M.H., and R.R.N. wrote the paper with input from all authors.

**Bibliographic information:** This chapter has previously been published in *Nature Communications* by Springer Nature as open access under the Creative Commons CC BY licence (<http://creativecommons.org/licenses/by/4.0/>) [2].

<https://doi.org/10.1038/s41467-022-31700-x>

# Spectral signatures of excess-proton waiting and transfer-path dynamics in aqueous hydrochloric acid solutions

Florian N. Brüning <sup>1</sup>, Manuel Rammler <sup>1</sup>, Ellen M. Adams<sup>2</sup>, Martina Havenith<sup>2</sup> & Roland R. Netz <sup>1</sup>✉

The theoretical basis for linking spectral signatures of hydrated excess protons with microscopic proton-transfer mechanisms has so far relied on normal-mode analysis. We introduce trajectory-decomposition techniques to analyze the excess-proton dynamics in *ab initio* molecular-dynamics simulations of aqueous hydrochloric-acid solutions beyond the normal-mode scenario. We show that the actual proton transfer between two water molecules involves for relatively large water-water separations crossing of a free-energy barrier and thus is not a normal mode, rather it is characterized by two non-vibrational time scales: Firstly, the broadly distributed waiting time for transfer to occur with a mean value of 200–300 fs, which leads to a broad and weak shoulder in the absorption spectrum around  $100\text{ cm}^{-1}$ , consistent with our experimental THz spectra. Secondly, the mean duration of a transfer event of about 14 fs, which produces a rather well-defined spectral contribution around  $1200\text{ cm}^{-1}$  and agrees in location and width with previous experimental mid-infrared spectra.

<sup>1</sup>Freie Universität Berlin, Department of Physics, 14195 Berlin, Germany. <sup>2</sup>Ruhr-Universität Bochum, Department of Physical Chemistry II, 44780 Bochum, Germany. ✉email: [rnetz@physik.fu-berlin.de](mailto:rnetz@physik.fu-berlin.de)

The motion of excess protons in aqueous solution is fundamental for many biological and chemical processes. The excess-proton diffusivity is significantly higher compared to other monovalent cations in water<sup>1,2</sup>, since the excess proton exchanges its identity with water hydrogens during the diffusion process<sup>3,4</sup>. Grotthus hypothesized a similar process over two centuries ago<sup>5,6</sup>, but a detailed understanding of the proton-transfer dynamics between water or other molecules remains difficult to date due to the multitude of time scales involved and the only indirect experimental evidence.

Infrared (IR) spectroscopy in the THz and mid-IR regimes is a powerful tool to explore the ultrafast dynamics of water and aqueous ion solutions. For example, the prominent absorption peak around 200 cm<sup>-1</sup> of bulk water is dominated by first-solvation-shell dynamics, whereas motion involving the second solvation shell contributes most significantly below 80 cm<sup>-1</sup> (2.4 THz)<sup>7,8</sup>. Furthermore, so-called ‘rattling’ modes for strongly hydrated ions lead to characteristic absorption features, while for weakly hydrated ions vibrationally induced charge fluctuations are dominant<sup>9,10</sup>, as suggested by dissecting simulation spectra into contributions from different solvation shells<sup>11,12</sup>.

IR spectroscopy has proven particularly useful for the study of the ultrafast dynamics of the excess proton in aqueous solution<sup>13,14</sup>. Due to their low pH value, aqueous hydrochloric acid (HCl) solutions are perfect model systems to study excess-proton dynamics, since HCl dissociates readily in water and gives rise to a large number of highly mobile protons that are only weakly coordinated with neutralizing chloride ions and therefore behave as if added in excess. The characteristic continuum band in the IR absorption spectrum, located between the water-bending mode around 1650 cm<sup>-1</sup> and the water-stretching mode around 3300 cm<sup>-1</sup>, has long been known and led to the hypothesis of the Zundel state, i.e., two water molecules symmetrically sharing the excess proton<sup>15</sup>. This model has been challenged by a contrasting picture, the Eigen state, which is a hydronium ion caged symmetrically by three water molecules<sup>16</sup>. Ever since these idealized structures have been proposed, their relative stability has been controversially debated<sup>13,17–27</sup>. It is now known that neither the idealized Zundel nor the Eigen states are realistic structural representations and that the excess proton mostly resides slightly asymmetrically shared between two water molecules, in the ‘special pair’ state, which geometrically can be interpreted as a ‘distorted Zundel’ state or a ‘distorted Eigen’ state<sup>20,23,24,26–28</sup>.

While simulations can reproduce most experimental spectroscopic signatures, the understanding of the proton transfer mechanism requires model building based on and guided by simulations. It is generally accepted that proton transfer involves consecutive transitions between states that can be viewed as more Eigen-like and more Zundel-like and have fast interconversion times<sup>24,26,29</sup>. That the excess proton diffusion involves the crossing of free-energetic barriers follows from the experimentally known Arrhenius behavior of the excess-proton conductivity<sup>28,30–32</sup>. Similar to the above-mentioned discussion on the relative stability of the Eigen and Zundel states, it remains debated whether the Zundel state is the transition state between two Eigen states or the opposite is the case, i.e., whether the Eigen state is the transition state between two Zundel states<sup>23,24,27</sup>. Theoretical models for the spectroscopic signatures of the hydrated proton motion so far relied on normal-mode calculations and have explained many aspects of experimental linear absorption<sup>33–35</sup> as well as 2D IR spectra<sup>25,26</sup>. However, normal modes by construction cannot deal with the thermally activated transfer of an excess proton over a free-energy barrier, since this corresponds to an unstable mode with a negative free-energy curvature along the transfer reaction coordinate<sup>36</sup>. It is clear that

such proton-barrier-transfer events will make a sizable spectroscopic contribution, since they involve fast motion of a highly charged object over relatively large distances. From this follows that an excess-proton transition state, which corresponds to a free energy maximum and thus occurs with a small probability, nevertheless can make a dominant contribution to the spectrum, which would lead to characteristic differences between experimental spectra and normal-mode theory predictions. Indeed, it has been noted that the normal-mode spectra computed from instantaneous configurations do not explain all experimental spectral signatures associated with the excess proton in water<sup>19,25–27</sup>, in particular of the proton-transfer dynamics<sup>37</sup>. It was recently shown that proton transfer in the H<sub>5</sub>O<sub>2</sub><sup>+</sup> cationic complex gives rise to two distinct spectroscopically relevant time scales that cannot be captured by normal-mode analysis<sup>38</sup>.

In general, the transfer of a particle with mass  $m$  over an energy barrier with negative curvature  $k < 0$  corresponds to an unstable mode. The dynamics of such a barrier-crossing is not characterized by a vibrational time scale, which according to a harmonic oscillator model could erroneously be written as  $\tau \simeq \sqrt{m/|k|} \simeq \sqrt{mL^2/U_0}$ , where  $U_0$  is the barrier height and  $L$  is the barrier width, but rather by two other time scales, namely the mean transfer-waiting time  $\tau_{\text{TW}}$  and the mean transfer-path time  $\tau_{\text{TP}}$ .  $\tau_{\text{TW}}$  is the average waiting time before a transfer event occurs and  $\tau_{\text{TP}}$  is the average time of the actual transfer path over the energy barrier. The former one scales exponentially with the barrier height  $U_0$ ,  $\tau_{\text{TW}} \sim \exp(U_0/k_B T)$ <sup>36,39</sup>, whereas the latter one scales logarithmically with the barrier height  $U_0$ ,  $\tau_{\text{TP}} \sim \log(U_0/k_B T)$ <sup>40–43</sup>. In essence, it is not clear with current theoretical methodology what the spectroscopic signature of excess-proton transfer events in aqueous solutions is and whether the continuum band stems just from vibrations in metastable states or whether transfer reactions over barriers are involved. Thus, a theoretical approach that is complementary to normal modes and can handle proton-transfer events that involve free-energy barriers is needed.

In this study, we investigate the excess-proton dynamics in aqueous HCl solutions at ambient conditions using ab initio molecular dynamics (MD) simulations at the Born–Oppenheimer level and experimental THz/Fourier-transform infrared (THz/FTIR) measurements. Our simulated IR difference absorption spectra compare well to our experimental data in the THz regime as well as to literature data in the mid-IR regime. By projecting the excess-proton dynamics onto the two-dimensional coordinate system spanned by the proton position along the axis connecting the two closest water oxygens  $d$  and the oxygen distance  $R_{\text{OO}}$ <sup>44,45</sup>, the excess-proton trajectories and their spectral signatures are subdivided into three contributions with distinct time scales, as illustrated in Fig. 1a. The fastest time scale,  $\tau_{\text{NM}}$ , reflects vibrations when the excess proton transiently forms a solvated H<sub>3</sub>O<sup>+</sup> molecule which is asymmetrically solvated in a special pair. It is well captured by a normal-mode description and has been amply discussed in literature<sup>19,25,26,37,46</sup>. The other two spectral signatures, stemming from proton transfer events, are the focus of this study. The associated time scales  $\tau_{\text{TW}}$  and  $\tau_{\text{TP}}$  are directly obtained from our simulated excess proton trajectories using a multidimensional path analysis. While the transfer-waiting time  $\tau_{\text{TW}}$  of aqueous proton-transfer events has been studied recently<sup>47</sup>, the identification of both  $\tau_{\text{TW}}$  and  $\tau_{\text{TP}}$  in simulated and experimental spectra is a main result of this work. We find a mean transfer-waiting time of  $\tau_{\text{TW}} = 200\text{--}300$  fs depending on HCl concentration, which in our experimental THz spectra shows up as a broad weak shoulder around 100 cm<sup>-1</sup>, that is partially overlaid by the absorption due to rattling chloride anions at about 150 cm<sup>-1</sup><sup>9,11</sup>. The mean transfer-path time, from simulations obtained as  $\tau_{\text{TP}} = 14$  fs, produces a spectroscopic signature

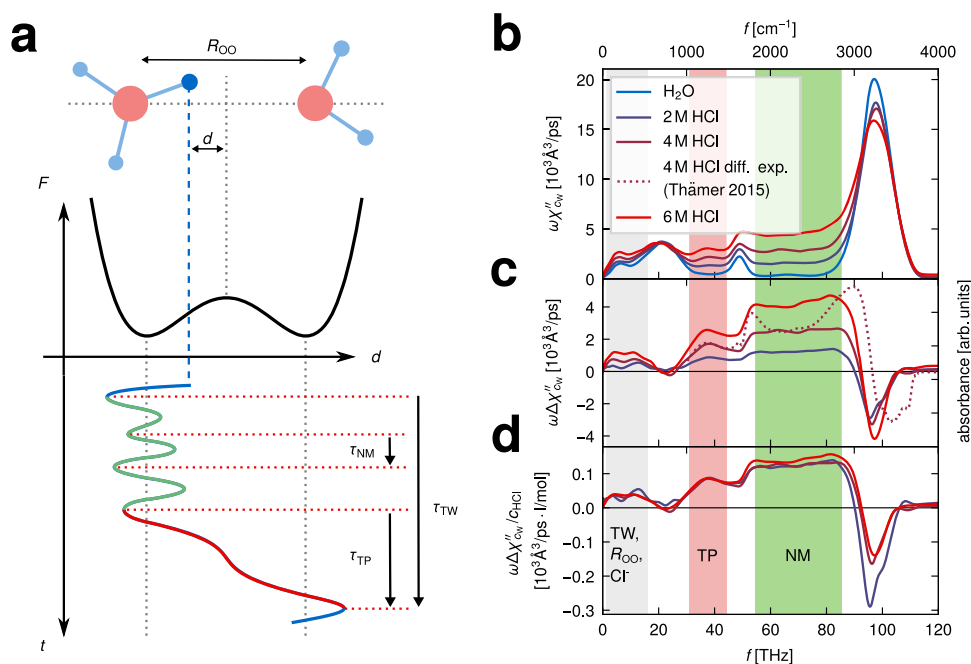


**Fig. 1 Time scales of excess-proton dynamics and simulated absorption spectra.** **a** Schematic trajectory of an excess proton that transfers between two water molecules, together with a schematic free energy profile  $F(d)$  that exhibits a barrier and is representative of a relatively large oxygen-oxygen separation  $R_{OO}$ . Three time scales characterize the proton trajectory, the normal-mode vibrational period of the solvated transient  $H_3O^+$ ,  $\tau_{NM}$ , the transfer-path time,  $\tau_{TP}$  and the transfer-waiting time,  $\tau_{TW}$ , where  $\tau_{TW} > \tau_{TP} > \tau_{NM}$ . An animation is shown online <https://fu-berlin.eu.vbrickrev.com/sharevideo/df2d94a4-6e7f-499a-a256-17d73b6124e4>. **b** Infrared (IR) absorption spectra obtained from ab initio molecular dynamics (MD) simulations of pure water (blue solid line) and hydrochloric acid (HCl) solutions at various concentrations (dark purple: 2 M, purple: 4 and red: 6 M). The spectra are divided by the water molecular number concentration  $c_W$ . **c** Difference spectra between the three HCl spectra and the water spectrum, obtained from the spectra in **b**. The purple dotted line shows an experimental difference spectrum of HCl at 4 M<sup>14</sup>, rescaled in height to match the simulation results. **d** The simulated difference spectra (as shown in **c**) divided by the HCl concentrations  $c_{HCl}$ . Three distinct spectral regions are shaded in different colors, that are identified with different excess-proton dynamic processes: transfer waiting (TW, gray), transfer paths (TP, red), and normal modes (NM, green). The transfer-waiting time is close to the chloride-ion ( $Cl^-$ ) rattling time and the oxygen vibrational time in local  $H_5O_2^+$  complexes that is described by the  $R_{OO}$  coordinate.

around  $1200\text{ cm}^{-1}$ , which is well captured in experimental mid-IR spectra<sup>14,20,23,24,26</sup>. Note that in our simulations the proton transfer becomes barrier-less for small water separation and thus includes the highly anharmonic normal-mode vibration of Zundel-like configurations, which have already been analyzed theoretically<sup>19,25,37,46</sup>. In the THz regime our experimental difference spectra show an additional prominent peak around  $300\text{--}400\text{ cm}^{-1}$ , in good agreement with our simulation data, which is demonstrated to be caused by the coupling of the excess-proton motion to the relative oscillations of the two flanking water molecules in transient  $H_5O_2^+$  complexes. Proton transfer events between water molecules are frequently followed by a few immediate back-and-forth transfer events, which is a consequence of non-Markovian effects<sup>48</sup> that have to do with the slowly changing solvation structure around the excess proton. Although these transfer events are therefore not always productive in the sense that they lead to large-scale diffusion of the excess proton, they nevertheless give rise to pronounced experimental spectroscopic signatures and therefore need to be included in the analysis.

## RESULTS

**Infrared and THz spectra of HCl solutions.** Within linear spectroscopy, the energy absorption rate of incident light with frequency  $f = \omega/(2\pi)$  is proportional to the imaginary part of the dielectric susceptibility and given by  $\omega\chi''(\omega)$ . IR power spectra are obtained from ab initio MD simulations of water (blue solid line) and HCl solutions at three concentrations between 2 and 6 M

(purple to red solid lines) and are shown in Fig. 1b. The spectra are divided by the water molecular number concentration  $\omega\chi''_W = \omega\chi''/c_W$ . Simulation details are provided in the “Methods” section. All IR spectra show the characteristic features of pure water spectra, which are the prominent OH-stretching peak around  $3300\text{ cm}^{-1}$ , the HOH-bending mode around  $1650\text{ cm}^{-1}$  and librational modes in the far IR regimes between  $200$  and  $800\text{ cm}^{-1}$ . The IR spectra of HCl solutions additionally show a broad continuum between the bending and the stretching peaks, from  $2000$  to  $3000\text{ cm}^{-1}$ , and a broad peak at around  $1200\text{ cm}^{-1}$ , both of which are commonly interpreted as to reflect the excess-proton dynamics<sup>14,23,49</sup>. Furthermore, additional features are observed below  $800\text{ cm}^{-1}$ , that are shown in Fig. 2 in comparison to our experimental THz spectra and will be discussed further below.

The simulated difference spectra in Fig. 1c (solid lines) clearly demonstrate three distinct regions (color shaded), that relate to distinct time scales of the excess-proton dynamics and will in this work be identified as transfer-waiting (TW, gray), transfer-path (TP, red) and normal-mode contributions (NM, green). We obtain rather good agreement with the experimental difference spectrum for 4 M HCl<sup>14</sup>, which was scaled to match the height of the simulated IR  $1200\text{ cm}^{-1}$  peak, see Supplementary Fig. 5 for a comparison of different experimental data. Our simulated 4 M difference spectrum in Fig. 1c does not reproduce the local maximum of the experimental difference spectra around  $1750\text{ cm}^{-1}$ , which is interpreted as the acid-bend band, i.e., a blue shift of the bending mode in  $H_3O^+$  compared to water, and also not the shape of the experimental acid-

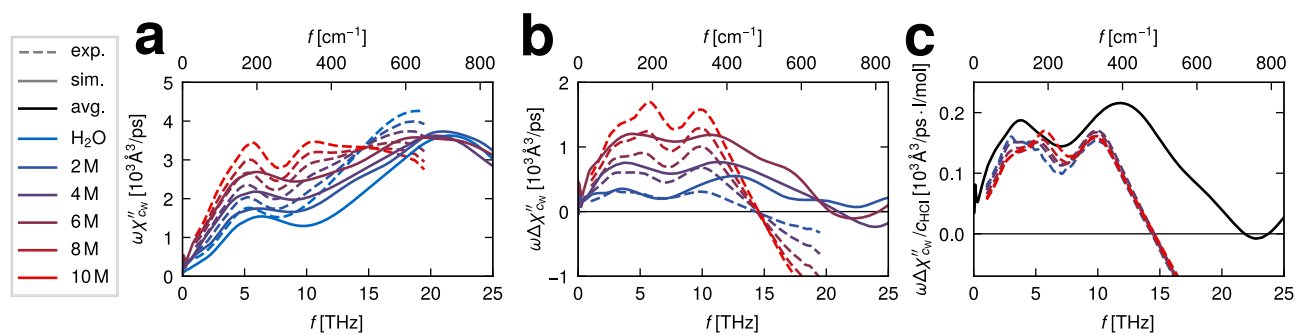


**Fig. 2 Experimental absorption spectra.** **a** Experimental THz/Fourier-transform infrared (THz/FTIR) absorption spectra of HCl solutions at various concentrations (colored broken lines for 2 M to 10 M), compared to literature data of pure water<sup>74</sup> (blue broken line). The experimentally measured extinction spectra have been converted into energy absorption spectra using the Kramers–Kronig relation, no amplitude adjustment is used in the comparison with the ab initio spectra (solid lines). **b** Experimental and ab initio molecular dynamics (MD) difference spectra derived from the results given in **a** and plotted in the respective colors and line styles. **c** The experimental difference spectra (shown in **b**) are divided by the HCl concentration  $c_{\text{HCl}}$  (colored broken lines) and compared to the average of the simulated difference spectra after dividing by  $c_{\text{HCl}}$  (black solid line).

stretch signature around  $3000\text{ cm}^{-1}$ <sup>14,19,20,23,50</sup>. The reason for this disagreement is unclear, we note that the normalization of spectra when calculating difference spectra is a subtle issue, see Supplementary Note 3 for a discussion.

Figure 1d shows that the three simulated HCl difference spectra divided by the HCl concentrations  $c_{\text{HCl}}$  are nearly indistinguishable. This clearly indicates that the spectroscopic features are due to single-proton dynamics and that collective proton effects as well as proton-chloride coupling effects, which would scale non-linearly in the HCl concentration, are minor. This is an important finding and justifies our theoretical analysis of single excess-proton motion in this work.

In order to investigate the intermolecular vibrational dynamics of water, solvated protons, and chloride ions, we experimentally measure THz absorption spectra for HCl concentrations of 2 M, 4 M, 6 M, 8 M, and 10 M. For quantitative comparison with our simulation data, the experimentally measured extinction spectra are converted into energy absorption spectra using the Kramers–Kronig relation, details are described in the “Methods” section and in Supplementary Methods 1. The experimental THz/FTIR spectra are shown in Fig. 2a in the range  $0\text{--}650\text{ cm}^{-1}$  (colored broken lines) together with a literature spectrum of pure water (blue broken line) and are compared to the available simulated spectra (solid lines). Again, all experimental and simulated spectra are divided by the respective water concentration  $c_w$ . One notes the good agreement between the experimental and simulation spectra below  $400\text{ cm}^{-1}$ , which is noteworthy since the spectral amplitudes are not rescaled or adjusted. However, the reason of the disagreement for larger wave numbers is not clear. All spectra show a prominent peak at  $200\text{ cm}^{-1}$ . Difference spectra of the experimental data with respect to the pure water spectrum are shown in Fig. 2b (broken lines) and again compared to the available simulated difference spectra (solid lines). Two peaks dominate the difference spectra, one around  $150\text{--}200\text{ cm}^{-1}$  and one around  $300\text{--}400\text{ cm}^{-1}$ . The experimental difference spectra scale linearly with HCl concentration, which is demonstrated in Fig. 2c, where the difference spectra are divided by the HCl concentrations  $c_{\text{HCl}}$ . For comparison, the simulated difference spectra divided by  $c_{\text{HCl}}$ , already presented in Fig. 1d, are averaged over the three HCl concentrations and shown as a black solid line. The linear scaling of the experimental spectra with HCl concentration reconfirms that the difference spectra are related to single-ion behavior and that collective ion effects are negligible, in agreement with previous observations<sup>13,14</sup>. In essence, two different processes at  $150\text{--}200\text{ cm}^{-1}$  and  $300\text{--}400\text{ cm}^{-1}$  are clearly indicated by our experimental and simulated spectra and

will be interpreted by our spectral trajectory-decomposition techniques. In the remainder we analyze exclusively the 6 M solution, which provides the best proton statistics.

**Excess-proton trajectories and spectra.** Excess protons constantly change their identity as they move through the HCl solution. Each identity change introduces a spurious discontinuity in the excess-proton trajectory, which does not actually correspond to charge transport and therefore is spectroscopically irrelevant. In order to extract continuous excess-proton trajectories from our simulations, we use a dynamic criterion as illustrated in Fig. 3a (that our extracted excess-proton trajectories are spectroscopically meaningful we will a posteriori demonstrate by comparison of spectra calculated from excess proton trajectories with spectra calculated from the complete simulation system). Each proton is assigned to its closest oxygen atom at each time step. Whenever three protons are assigned to the same oxygen, thereby forming a hydronium ion, all of them are registered as excess-proton candidates. That means, for the generation of continuous excess-proton trajectories, we do not select the hydrogen with the largest separation from the oxygen, which would lead to fast switching of the excess proton identity, the so-called ‘special pair dance’ of hydronium with its surrounding water molecules<sup>27,51</sup>. Rather, if during the simulation an excess-proton candidate becomes assigned to a different oxygen and thus transfers to a neighboring water, it is selected as an excess proton for the entire time during which it was part of any hydronium ion<sup>27</sup>. Note that the spectral effects of the rattling of the excess-proton candidates within one hydronium ion, i.e., the ‘special pair dance’, are in some of our calculations below included by taking into account the flanking water molecules in the calculation of spectra, but do not show significant spectral signatures. Excess protons that are coordinated with a chloride anion as the second nearest neighbor are neglected from our analysis. This does not influence our excess-proton spectra, since even for the highest acid concentration of 6 M, only 5% of all configurations are of this type, as demonstrated in Supplementary Table 3. Note, however, that the fraction of protons coordinated with chloride ions increases significantly at higher concentrations<sup>52</sup>. Our procedure for calculating continuous excess-proton trajectories is discussed in further detail in Supplementary Methods 2.

The excess-proton trajectories are described by the two-dimensional coordinate system defined within local transient  $\text{H}_5\text{O}_2^+$  complexes consisting of the excess proton and its two nearest water molecules, as illustrated in the right part of Fig. 3a. The coordinates are the instantaneous distance between the two

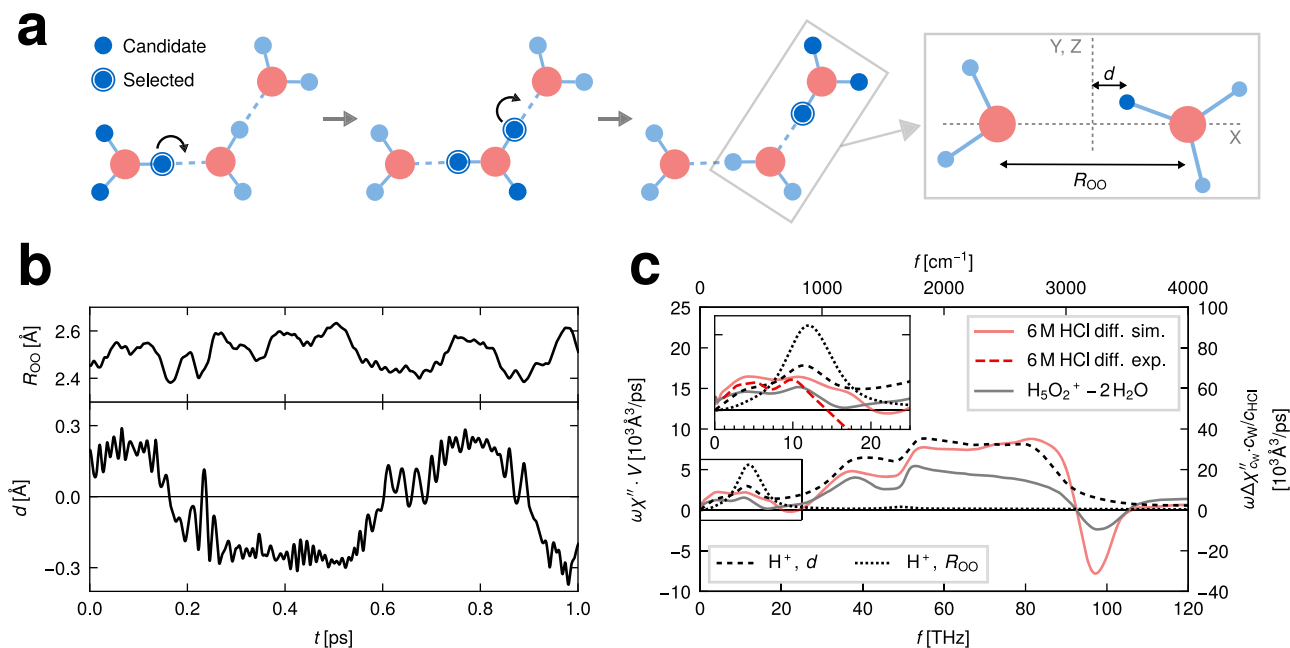


**Fig. 3 Excess-proton trajectories and spectra.** **a** Illustration of the method used to extract continuous excess-proton trajectories from ab initio molecular dynamics (MD) simulations. From the three protons in a hydronium ion, the one that will later transfer to a neighboring water is identified as excess proton. To the right the coordinates  $d$  and  $R_{OO}$  are defined. **b** Example trajectories of the  $d$  and  $R_{OO}$  coordinates. **c** Power spectra of the  $d$  and  $R_{OO}$  coordinates are shown as broken and dotted black lines, respectively (vertical axis on the left). Also shown are the simulated difference spectrum of the 6 M HCl solution, divided by the HCl concentration  $c_{\text{HCl}}$  and multiplied by the water concentration  $c_{\text{W}}$  (red solid line), and the simulated difference spectrum between a transient  $\text{H}_5\text{O}_2^+$  complex in HCl solution and two hydrogen-bonded water molecules in pure water (gray solid line), using the vertical axis on the right. The inset shows a zoom into the THz regime, which additionally shows our 6 M experimental THz/FTIR difference spectrum (red broken line).

oxygen atoms  $R_{OO}$  and the excess proton's distance from the midplane  $d^{45}$ . The state for  $d = 0$ , where the excess proton is in the middle between the oxygens, will be later used to define the transition state of the proton transfer between the two flanking water molecules. Figure 3b shows an example excess-proton trajectory from our ab initio MD simulations in terms of the  $R_{OO}$  and  $d$  coordinates. While the motion along the two coordinates is strongly correlated, as we will show later, the  $d$  trajectory shows fast oscillatory components that are much weaker in the  $R_{OO}$  trajectory.

The power spectra of the excess-proton trajectories, averaged over all excess protons in the solution, are shown in Fig. 3c for the  $d$  coordinate as a black broken line and for the  $R_{OO}$  coordinate as a black dotted line, in the calculations we assume a bare charge of 1 e for the excess proton (left axis). We compare with the simulated difference spectrum of the 6 M HCl solution (red solid line), which is multiplied by the water concentration  $c_{\text{W}}$  and divided by HCl concentration  $c_{\text{HCl}}$  and thus is normalized per excess proton (right axis). The qualitative agreement between the two spectra (black broken and red solid lines) is very good up to an overall scaling factor of roughly four, which reflects polarization enhancement due to neighboring water molecules. The good agreement indicates that the difference spectrum of an HCl solution is proportional to the spectrum of the highly IR-active excess proton in terms of its coordinate  $d^{47}$ . In other words, the HCl-solution difference spectrum reports on the excess-proton motion relative to the two flanking water oxygens and can therefore be used to investigate proton-transfer dynamics. In turn, the analysis of excess-proton trajectories allows to reveal the microscopic mechanism causing the signatures of HCl-solution difference spectra, which is a central validation of the trajectory-decomposition technique used in our study. In contrast, the dynamics of  $R_{OO}$ , i.e., the vibrations of the water molecules in the  $\text{H}_5\text{O}_2^+$  complex, black dotted line in Fig. 3c, gives rise to a single

spectral feature around  $400\text{ cm}^{-1}$ , which turns out to be present also in the simulated and experimental HCl-solution spectra, as will be discussed below.

To check for the effect of the two water molecules that flank the excess proton on the difference spectrum, we also calculate the IR spectrum of transient  $\text{H}_5\text{O}_2^+$  complexes, as done previously<sup>22,53</sup> and presented in more detail in Supplementary Fig. 11. To construct a difference spectrum, we subtract from the  $\text{H}_5\text{O}_2^+$  spectrum the spectrum of hydrogen-bonded water-molecule pairs obtained from the pure-water ab initio MD simulation. The resulting difference spectrum in Fig. 3c (gray solid line, right scale) is reduced by a factor of roughly two compared to the difference spectrum of the entire HCl solution (red solid line) but otherwise agrees in shape rather nicely. Compared to the spectrum of the isolated excess proton (broken line, left scale) we observe an amplification by a factor of roughly two, but no essential spectral shape change. We conclude that the flanking water molecules and in particular the ‘special pair dance’ with further solvating water molecules does not modify the spectrum of the excess proton in an essential way. The amplification of the complete HCl-solution difference spectrum compared to the  $\text{H}_5\text{O}_2^+$  difference spectrum (red and gray solid lines, respectively) we rationalize by polarization enhancement effects of water molecules that solvate the  $\text{H}_5\text{O}_2^+$  complex.

A few spectral contributions that are not included in the excess proton power spectrum (black broken line in Fig. 3c) deserve mentioning: (i) Dynamics orthogonal to the connecting axis of the oxygens are shown to be small in Supplementary Fig. 11. (ii) The chloride motion is shown below to contribute only slightly and at low frequencies to the spectrum. (iii) The translation and rotation of the internal  $\text{H}_5\text{O}_2^+$  coordinate system relative to the lab frame is in Supplementary Figs. 12 and 13 shown to only give a small spectral contribution. We thus conclude that the IR difference spectrum between HCl solutions and pure water

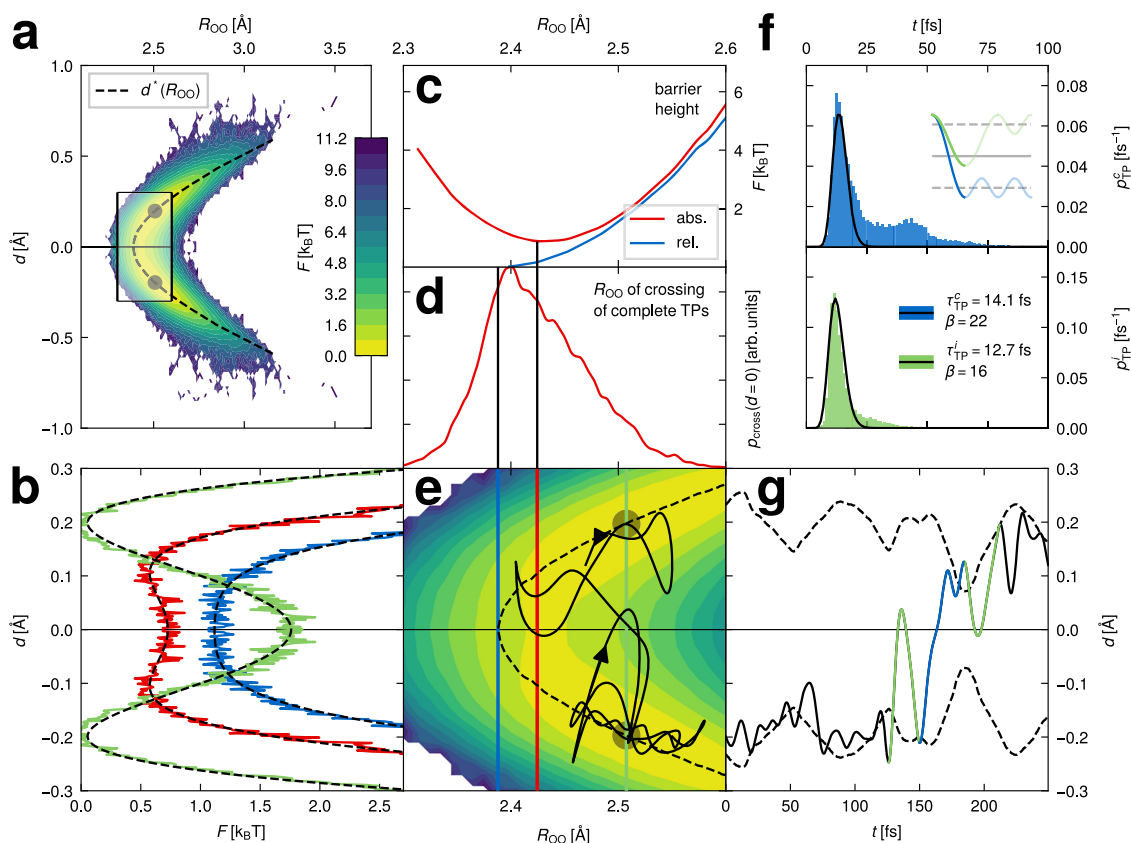


**Fig. 4 2D excess-proton trajectory analysis.** **a** The two-dimensional (2D) free energy of the excess protons in 6 M HCl solution for the  $(d, R_{OO})$  coordinates defined in the inset of Fig. 3a. The shaded area is enlarged and shown in e. The gray dots denote the positions of the global minima of the 2D free energy. The minima for fixed  $R_{OO}$ , i.e., the most likely proton locations,  $d^*(R_{OO})$ , are indicated by a black broken line. **b** Cuts through the free energy in a for  $R_{OO} = 2.39 \text{ \AA}$ , where the barrier just vanishes (blue solid line),  $R_{OO} = 2.42 \text{ \AA}$ , where the absolute barrier height is minimal (red solid line) and  $R_{OO} = 2.51 \text{ \AA}$ , for which the global minima of the 2D free energy are obtained (green solid line). **c** The absolute free energy at  $d = 0$  (red solid line) and the barrier height relative to the minima at fixed  $R_{OO}$  located at  $d^*(R_{OO})$  (blue solid line). **d** Distribution of  $R_{OO}$  positions at which complete transfer paths cross the  $d = 0$  midplane. **e** Zoom into the free energy shown in a. The vertical colored lines indicate the cuts through the free energy shown in b. An example trajectory from the ab initio molecular dynamics (MD) simulation is shown as a black solid line. **f** Path-duration distributions of complete (blue, times defined from  $d^*$  to  $-d^*$ ) and incomplete transfer paths (green, times defined from  $d^*$  to  $d = 0$ ). Fits according to Eq. (1) are shown as black solid lines. **g** Time course of the example trajectory along  $d$ , same as shown in e, with complete and incomplete transfer paths indicated as blue and green lines, respectively. The two branches of the  $R_{OO}$ -dependent minimal energy position  $d^*[R_{OO}(t)]$  are shown as black broken lines.

reports very faithfully on the excess-proton dynamics, apart from an overall amplification factor.

**2D excess-proton trajectory analysis.** Figure 4a shows the two-dimensional (2D) free energy for 6 M HCl obtained from the negative logarithm of the distribution function of the continuous excess-proton trajectories as a function of the coordinates  $d$  and  $R_{OO}$ , a blow up of the shaded area is given in Fig. 4e. By definition, the free energy is symmetric with respect to the midplane at  $d = 0$ , which separates two global minima at  $R_{OO} = 2.51 \text{ \AA}$  and  $d = \pm 0.2 \text{ \AA}$ . These minima, highlighted as gray dots in Fig. 4a, correspond to states where the excess proton is asymmetrically shared between the two flanking water molecules. The transition between these minima, i.e., the proton transfer, is, therefore, a barrier-crossing process in the two-dimensional plane spanned by  $R_{OO}$  and  $d$ .

Figure 4b shows cuts through the free energy for constant  $R_{OO}$  along  $d$ , each fitted to a quartic expression  $F(d) = F_{d=0}(1 + \gamma_2 d^2 + \gamma_4 d^4)$  shown as black broken lines. Details are reported in Supplementary Methods 3. For negative  $\gamma_2$ , two minima at  $d^* = \pm \sqrt{-\gamma_2/(2\gamma_4)}$  are separated by a barrier at  $d = 0$ , which correspond to the optimal proton asymmetry for a given value

of  $R_{OO}$  and are determined by the parabolic function  $d^*(R_{OO})$ , which is plotted as a black broken line in Fig. 4a, e. The cuts in Fig. 4b are shown for  $R_{OO} = 2.39 \text{ \AA}$ , where the barrier just vanishes (blue solid line),  $R_{OO} = 2.42 \text{ \AA}$ , where the absolute barrier height is minimal and which contains the transition state in the  $d$ - $R_{OO}$  plane at  $d = 0$  (red solid line), and  $R_{OO} = 2.51 \text{ \AA}$ , which contains the global minima of the 2D free energy (green solid line).

The absolute free energy at  $d = 0$  is plotted in Fig. 4c as a red solid line and compared to the barrier height relative to the  $R_{OO}$ -dependent minima at  $d^*(R_{OO})$  (blue solid line). The minimal absolute barrier free energy of  $0.9 k_B T$  (red line), located at  $R_{OO} = 2.42 \text{ \AA}$ , defines the transition state; for  $R_{OO} = 2.51 \text{ \AA}$ , for which the most probable excess-proton state is obtained, the barrier has a moderate absolute height of  $1.8 k_B T$ , suggesting that proton transfer is not excluded for this value of  $R_{OO}$ . Note that for  $R_{OO} < 2.39 \text{ \AA}$  the relative barrier height vanishes and thus a symmetrically shared excess proton is most likely.

Next, to decompose the excess proton trajectories into segments where the excess proton moves around the local free energy minima and where a transfer across the midplane happens, transfer-path start and end points need to be defined. For this we use the most likely proton location  $d^*(R_{OO})$  (black



broken lines in Fig. 4a, e, g). The start of a transfer path is thus defined as the last crossing of  $d^*(R_{OO})$  on one side of the midplane at  $d=0$  and the end of a transfer path as the first crossing of  $d^*(R_{OO})$  on the other side of the midplane at  $d=0$ . The transfer paths are slightly extended forward and backward in time to the points where the velocity along  $d$  vanishes, the so-called turning points, in order to be consistent with the analytical theory presented in<sup>38</sup>. An example trajectory is shown in Fig. 4e (thin black line) in the  $(d, R_{OO})$  plane, the corresponding time-dependent position  $d$  is given in Fig. 4g, where the transfer path is highlighted in blue. Many transfer attempts are unsuccessful and lead to incomplete transfer paths, where the excess proton crosses the mid-plane  $d=0$  but does not reach to the minimal free energy state  $d^*(R_{OO})$  on the other side. Two incomplete transfer paths are shown in green in Fig. 4g and for consistency are also extended to their turning points. Transfer-path-time distributions are given in Fig. 4f; with our definitions used, incomplete transfer paths turn out to be slightly faster. In total, there are about as many incomplete ( $n=14877$ ) as complete transfer paths ( $n=14357$ ), meaning that about half of all excess protons reaching the midplane  $d=0$  actually transfer from one water molecule to the other. The main peaks in the distributions are fitted by the Erlang distribution<sup>54–56</sup>

$$p_{TP}(t) = \frac{t^{\beta-1}}{(\beta-1)!} \left( \frac{\beta}{\tau_{TP}} \right)^{\beta} e^{-\beta t/\tau_{TP}}, \quad (1)$$

with the mean transfer-path time defined by  $\tau_{TP}$ , shown as black solid lines in Fig. 4f, the fit parameters are given in the legend.

The distribution of transition states in Fig. 4d, i.e., the  $R_{OO}$  position at which complete transfer paths cross the midplane at  $d=0$ , is rather broad and peaks slightly below  $R_{OO} = 2.42 \text{ \AA}$ , the most probable excess-proton position at  $d=0$ . Most paths, in fact, 77%, cross for  $R_{OO} > 2.39 \text{ \AA}$ , i.e., for values of  $R_{OO}$  where a barrier along the  $d$  coordinate is present. This means that the dominant mechanism for proton transfer is not one where the proton waits until the oxygen-oxygen separation  $R_{OO}$  reaches small values so that the remaining barrier along  $d$  is small or absent. Rather, protons cross the  $d=0$  midplane for a broad distribution of oxygen-oxygen separations  $R_{OO}$  and by doing so overcome substantial free-energy barriers. This reverberates that a normal-mode analysis cannot account for all aspects of proton transfer in HCl solutions.

**Spectral signatures of proton transfer.** In order to dissect the excess-proton spectrum in Fig. 3c (black broken line) into contributions that have to do with proton-transfer events and those that do not, the excess-proton trajectories  $d(t)$  are decomposed into three parts according to

$$d(t) = d_{TW}(t) + d_{TP}(t) + d_{NM}(t). \quad (2)$$

To illustrate this decomposition, Fig. 5a shows part of an example excess-proton trajectory,  $d(t)$  (black line), together with the most likely excess-proton positions  $d^*[R_{OO}(t)]$  (thin gray lines); the deviations between the black and gray lines visualize excess-proton motion relative to the oxygen it is bound to. We define the transfer-waiting contribution to the excess-proton trajectory as  $d_{TW}(t) \equiv d^*[R_{OO}(t)]$  projected onto the closer branch of  $d^*[R_{OO}(t)]$ , shown as a blue solid line in Fig. 5b. Thereby,  $d_{TW}(t)$  reflects the proton transfer jumps and also contains the water motion. The transfer-path contribution  $d_{TP}(t)$  in Fig. 5c (red solid line) is defined as  $d_{TP}(t) = d(t) - d_{TW}(t)$  during complete and incomplete transfer paths (as defined in Fig. 4e, g) and is zero elsewhere, it describes the excess-proton motion during transfer processes. Finally, by subtracting  $d_{TW}(t)$  and  $d_{TP}(t)$  from  $d(t)$ , we are left with the oscillations around  $d^*[R_{OO}(t)]$  when the excess

proton is not undergoing a transfer, which constitutes the normal-mode contribution  $d_{NM}(t)$  in Fig. 5d (green solid line). Different or more detailed excess-proton trajectory decompositions are certainly conceivable, the usefulness of the present scheme follows from its spectral decomposition properties.

In Fig. 5e the excess-proton spectrum, (black solid line) is decomposed as

$$\omega\chi'' = \omega\chi''_{TW} + \omega\chi''_{TP} + \omega\chi''_{NM}. \quad (3)$$

The power spectra of the transfer-waiting,  $\chi''_{TW}$  (blue line), and transfer-path contributions,  $\chi''_{TP}$  (red line), are computed from the  $d_{TW}(t)$  and  $d_{TP}(t)$  trajectories using the Wiener-Kintchine theorem (see “Methods” section for details). All cross-correlation contributions are included in the normal-mode contribution,  $\chi''_{NM}$  (green line).

The normal-mode spectrum  $\omega\chi''_{NM}$  in Fig. 5e accounts for the continuum band located between 2000 and 3000  $\text{cm}^{-1}$ , it is in fact amenable to normal-mode analysis<sup>19,25,27</sup> but by construction does not include the proton-transfer dynamics. The range of the dominant normal-mode time scales included in  $\omega\chi''_{NM}$ ,  $\tau_{NM} = 11\text{--}17$  fs, follows from the spectral width of the continuum band, taken to be  $f = 2000\text{--}3000 \text{ cm}^{-1}$  in Fig. 5e, via  $\tau_{NM} = 1/f$ .

The transfer-path spectrum  $\omega\chi''_{TP}$  in Fig. 5e shows a pronounced peak around 1200  $\text{cm}^{-1}$ . An analytical model calculation shows that the peak in the transfer-path spectrum is related to the mean transfer-path time as  $f_{TP} = 1/(2\tau_{TP})$ <sup>38</sup>. Taking the results from the fits in Fig. 4f, yielding  $\tau_{TP} = 14.1$  fs for complete and  $\tau_{TP}^i = 12.7$  fs for incomplete transfer paths, we predict  $f_{TP}^c = 1170 \text{ cm}^{-1}$  and  $f_{TP}^i = 1300 \text{ cm}^{-1}$ , indicated in Fig. 5e as vertical lines and which bracket the transfer-path peak very nicely.

The transfer-waiting spectrum  $\omega\chi''_{TW}$  in Fig. 5e exhibits a peak around 400  $\text{cm}^{-1}$ , a shoulder around 100  $\text{cm}^{-1}$  and a slow decay for lower frequencies. The peak around 400  $\text{cm}^{-1}$  (12 THz) is caused by oscillations of the oxygen-oxygen separation,  $R_{OO}$ , which couple to the proton position  $d$  via the most likely proton position  $d^*[R_{OO}(t)]$ ; in simple terms, the proton vibrates with the water molecule it is bound to. The oxygen vibrational time scale  $\tau_{R_{OO}} = 86$  fs, indicated in Fig. 5b, follows from the peak of the power spectrum of  $R_{OO}$  around 400  $\text{cm}^{-1}$ , which is plotted in the lower panel of Fig. 5e and agrees perfectly with the peak in  $\omega\chi''_{TW}$ . This peak is in fact also well visible in our experimental THz/FTIR difference spectra, shown again in Fig. 6a as a broken red line for a 6 M HCl solution, the dotted red line shows the corresponding simulated difference spectrum. Note that this translational vibration of two water oxygens in the transient  $\text{H}_5\text{O}_2^+$  complex is about twice as fast as the translational vibration of two hydrogen-bonded water molecules in pure water, which gives rise to the well-known IR signature around 200  $\text{cm}^{-1}$ , shown as a blue solid line in Fig. 6b obtained from pure-water simulations<sup>12</sup>. This frequency shift is the reason why the water-vibration peak appears prominently in the difference spectra in Fig. 6a.

The shoulder in  $\omega\chi''_{TW}$  around 100  $\text{cm}^{-1}$  is related to the transfer waiting time  $\tau_{TW}$ , which is the average time between two consecutive complete proton-transfer events, as predicted from an analytically solvable barrier-crossing model<sup>38</sup>. In Fig. 5f we show distributions of the transfer-waiting first-passage times, i.e., distributions of the time difference between crossing the most likely proton position  $d^*[R_{OO}(t)]$  on one side of the midplane  $d=0$  and crossing  $d^*[R_{OO}(t)]$  on the other side of the midplane  $d=0$  for the first time, for the three HCl concentrations. The distributions are essentially exponential in nature, which means that transfer events occur at a roughly constant rate and reflects the stochastic nature of the excess-proton transfer process in this

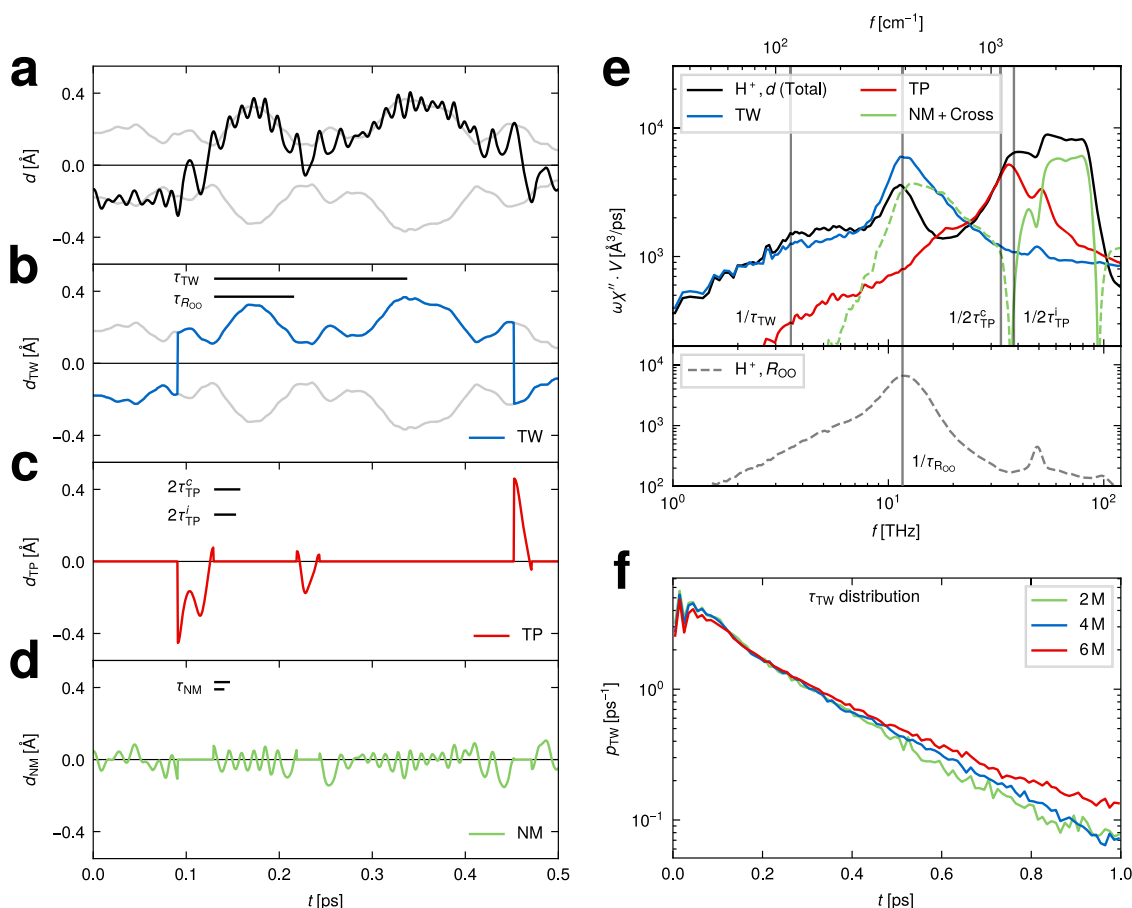


**Fig. 5 Spectral signatures of proton transfer.** **a–d** Decomposition of an excess-proton trajectory  $d(t)$  (black solid line in **a**) into transfer-waiting  $d_{TW}$  (blue solid line in **b**), transfer-path  $d_{TP}$  (red solid line in **c**) and normal-mode contributions  $d_{NM}$  (green solid line in **d**). The time course of the  $R_{OO}$ -dependent most likely proton positions at  $d'[R_{OO}(t)]$  are shown as thin gray solid lines in (**a** and **b**). **e** IR spectrum of the excess-proton motion projected onto  $d$ , shown as a black solid line, and IR spectra of the contributions shown in **a–c** in the respective color (the green broken line denotes negative values). The power spectrum of the  $R_{OO}$  coordinate is shown as a gray broken line in the lower panel. The inverse of the characteristic time scales  $\tau_{TW}$ ,  $\tau_{R_{OO}}$ ,  $2\tau_{TP}^c$  and  $2\tau_{TP}^i$  are shown as thin vertical solid gray lines. **f** Distributions of the transfer-waiting first-passage times of excess protons, see main text for details.

reduced one-dimensional description. The mean of these first-passage distributions defines the transfer-waiting time  $\tau_{TW}$ , which is given in Table 1 and increases with rising HCl concentration. This indicates that hydronium ions have a slightly longer life time at higher HCl concentrations. In contrast, both complete and incomplete transfer-path times interestingly show no dependence on the HCl concentration. The inverse of the transfer-waiting time  $\tau_{TW} = 280$  fs for 6 M, which is shown in Fig. 5e as a vertical line, is located at  $120 \text{ cm}^{-1}$  (3.5 THz) and corresponds well to the position of the shoulder in  $\omega\chi''_{TW}$ , which confirms the connection between the transfer-waiting time and the spectroscopic signature around  $100 \text{ cm}^{-1}$  that is predicted by analytical theory<sup>38</sup>. We note that the total length of the continuous proton-transfer trajectories are roughly twice as long as the mean transfer-waiting times, meaning that typically a few back-and-forth proton-transfer events occur in each trajectory (see Supplementary Note 7 for more details).

The characteristic time scales of each contribution, i.e., the transfer-waiting time  $\tau_{TW} = 280$  fs, the water-oxygen vibrational time  $\tau_{R_{OO}} = 86$  fs, the transfer-path times  $\tau_{TP}^c = 14.1$  fs and  $\tau_{TP}^i = 12.7$  fs and the normal-mode times  $\tau_{NM} = 11$ –17 fs are unambiguously extracted from the simulations and characterize both the trajectory contributions in the time domain in Fig. 5a–d, where they are included as horizontal black bars, and also the different spectral contributions in Fig. 5e.

We comment on the subtle spectral features in the range  $1400$ – $1800 \text{ cm}^{-1}$  in Fig. 5e, where small but distinct peaks are revealed in the different spectral contributions. The transfer-waiting contribution (blue line) peaks at about  $1650 \text{ cm}^{-1}$ , hinting to a weak coupling to an unperturbed water bending mode of the flanking water molecules. The transfer-path contribution (red line) peaks at  $1750 \text{ cm}^{-1}$ , the location of the experimental acid bend signature, which suggests that the acid bend couples particularly to the transfer path motion of the excess proton. Note, that even though the acid bend is primarily produced by the excess-proton motion orthogonal to the  $d$  coordinate, this contribution to the isotropic spectrum is largely compensated by motion of the flanking water molecules, as shown in Supplementary Fig. 11. The normal-mode contribution (green line) peaks around  $1500 \text{ cm}^{-1}$ , consistent with previously calculated normal-mode spectra of Eigen-like solvated proton structures<sup>25</sup>. We thus see that our trajectory-decomposition technique also allows to disentangle the various normal-modes obtained for the solvated excess-proton complex.

So far we have concentrated on the excess-proton spectral contribution and not discussed the chloride contribution. The decomposition of the total simulated 6 M HCl spectrum in Fig. 6b (red solid line) into the chloride contribution (green solid line, including all cross correlations) and the remainder (gray solid line) demonstrates a prominent chloride peak around  $150 \text{ cm}^{-1}$ , which

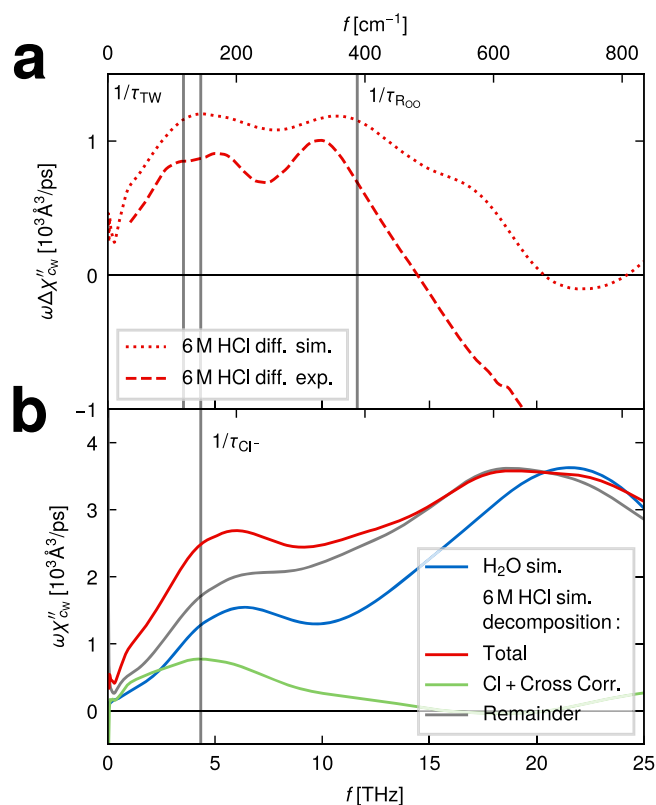


**Fig. 6** Absorption spectra in the THz regime. **a** Experimental THz/Fourier-transform infrared (THz/FTIR) difference spectra of 6 M HCl solution (red broken line) compared to the difference spectrum from ab initio molecular dynamics (MD) simulations (red dotted line). **b** The simulated 6 M HCl spectrum (red solid line) is decomposed into a chloride-ion contribution (green solid line, including cross correlations) and the remainder (gray solid line). For comparison the simulated pure-water spectrum (blue solid line) is also shown.

**Table 1** Characteristic time scales of excess-proton transfer dynamics.

conc.	2 M	4 M	6 M
$\tau_{\text{TW}}$ [fs]	208 ± 6	229 ± 4	283 ± 4
$\tau_{\text{Cl}^-}$ [fs]	241 ± 3	249 ± 3	231 ± 3
$\tau_{\text{Roo}}$ [fs]	81 ± 3	82 ± 2	86 ± 2
$\tau_{\text{TP}}^+$ [fs]	14.08 ± 0.08	14.34 ± 0.05	14.10 ± 0.04
$\tau_{\text{TP}}^-$ [fs]	12.65 ± 0.09	12.80 ± 0.05	12.74 ± 0.05
$\tau_{\text{NM}}$ [fs]	(11 ± 1) – (17 ± 1)		

The standard errors of the transfer-waiting time  $\tau_{\text{TW}}$  and the transfer-path times  $\tau_{\text{TP}}^+$  and  $\tau_{\text{TP}}^-$  are estimated from the variances of the fitted distributions. The errors of the normal-mode times  $\tau_{\text{NM}}$ , the oscillation time of the two flanking water molecules  $\tau_{\text{Roo}}$  and the rattling time of chloride ions  $\tau_{\text{Cl}^-}$  are estimated from the resolution of the underlying spectra.

translates to a corresponding time scale of  $\tau_{\text{Cl}^-} = 185$  ps and is due to the rattling of a chloride in its hydration cage<sup>9,10</sup>. This peak is also seen in the simulated difference spectrum in Fig. 6a (red dotted line) and is slightly shifted to larger frequencies in the experimental difference spectrum (red broken line). At 100–200  $\text{cm}^{-1}$  the remainder contribution in Fig. 6b (gray solid line) is significantly stronger than the pure-water spectrum (blue line), indicating that a process related to excess-proton motion significantly contributes in this wavenumber range. We suggest that this process is the excess-proton transfer-waiting contribution, which in Fig. 5e is shown to produce a broad shoulder around 100  $\text{cm}^{-1}$ .

While the generally good agreement between our simulated and experimental spectra supports our chosen simulation methodology, it is clear that our classical treatment of nuclei motion is a drastic approximation and therefore some of the agreement might be due to fortuitous cancellation of errors. Interestingly, previous studies found no significant differences between IR spectra computed from simulations with and without nuclear quantum effects below 3000  $\text{cm}^{-1}$ <sup>34,35,55</sup>, which might suggest that quantum-mechanical zero-point motion influences the excess-proton dynamics less than the instantaneous excess-proton distribution. We discuss quantum nuclear effects and basis set issues in the “Methods” section and Supplementary Note 1. Furthermore, we also compare our simulation results for radial distribution functions<sup>28,33,52,56,57</sup> (Supplementary Note 4) and proton diffusion coefficients<sup>28,33,58–60</sup> (Supplementary Note 8) with previous reports and discuss other observables that have been used in literature to characterize excess-proton transfer dynamics, such as identity correlation functions<sup>27,58,61</sup> (Supplementary Note 7), the hydrogen-bond asymmetry around hydronium ions<sup>35</sup> and the number of hydrogen bonds hydronium ions participate in<sup>34,57,59</sup> (Supplementary Note 9).

## Discussion

We show that the spectroscopic signature of proton-transfer dynamics between two water molecules in hydrochloric acid (HCl) solutions can be investigated by trajectory decomposition into transfer-waiting (characterized by the time scale  $\tau_{\text{TW}}$ ), transfer-path (characterized by  $\tau_{\text{TP}}$ ) and normal-mode contributions (characterized by  $\tau_{\text{NM}}$ ). The decomposition is performed in the two-dimensional coordinate system that is spanned by the excess-proton position and the oxygen-oxygen distance of the two flanking water molecules and operates both in the time domain as well as in the frequency domain. The coupling of the excess-proton motion to the relative oscillations of the two flanking water molecules produces a fourth spectral proton-dynamics contribution (characterized by  $\tau_{\text{Roo}}$ ). The dynamics of each of the four contributions are described by distinct time scales with the ordering  $\tau_{\text{TW}} > \tau_{\text{Roo}} > \tau_{\text{TP}} > \tau_{\text{NM}}$  and therefore contribute with distinct peaks to the excess-proton IR spectrum. Due to the high proton charge, the excess-proton spectrum, and due to correlation effects with the neighboring water molecules in particular the excess-proton motion along the axis connecting the oxygens, contributes significantly to the IR difference spectrum of HCl. Our experimental THz/FTIR difference spectra resolve the slowest time scales,  $\tau_{\text{TW}}$  and  $\tau_{\text{Roo}}$ , of which the former one is overlaid by an additional spectral contribution due to rattling of the chloride ions, characterized by yet another time scale  $\tau_{\text{Cl}^-}$ , which is close to  $\tau_{\text{TW}}$ . Mid-IR experimental difference spectra from literature on the other hand are compatible with our predicted spectra associated with the  $\tau_{\text{TP}}$  and  $\tau_{\text{NM}}$  time scales.

In contrast to the transfer-path time  $\tau_{\text{TP}}$ , the transfer-waiting time  $\tau_{\text{TW}}$  shows a weak dependence on the HCl concentration. Possible reasons include ionic screening and repulsion effects between neighboring excess protons, but also entropic effects due to the reduced number of accepting water molecules have been discussed<sup>28,32,62</sup>. This is consistent with experimental results showing a decrease of the excess-proton diffusivity with increasing HCl concentration<sup>60</sup>, which is reproduced in our simulations (see Supplementary Fig. 19). One should note that the transfer-waiting times in local transient  $\text{H}_5\text{O}_2^+$  complexes include back-and-forth proton-transfer events, which do not contribute to the long-time excess-proton diffusion<sup>28,33,58,59,63</sup> but nevertheless have a pronounced spectroscopic signature<sup>38</sup>.

Our results nicely complement recent normal-mode calculations. We find that the continuum band stems from normal-

mode vibrations of less symmetric, i.e., more Eigen-like, configurations of the excess proton, which are strongly influenced by the oxygen-oxygen separation  $R_{OO}$ <sup>14,19,25,26</sup>. On the other hand, our transfer-path signature, which is dominated by a broad absorption around  $1200\text{ cm}^{-1}$ , shows striking similarity with normal-mode spectra computed for more symmetric, i.e., more Zundel-like, configurations of the excess proton<sup>14,19,25,26</sup>. It is not implausible that normal modes for small separations of the two flanking water molecules show similar spectroscopic signatures as the transfer paths we extract from our simulation trajectories. Yet, in a normal-mode picture the interconversion between the metastable Zundel-like and Eigen-like excess-proton states cannot be explained consistently, even though the importance of this process for a complete description of the mid-IR signatures was acknowledged several times<sup>14,24–26,35</sup>. In fact, the broad distribution of this interconversion time scale is demonstrated by the transfer-waiting time distribution and also gives rise to a distinct spectral signature, that we identify in the THz regime.

A recent study employing similar simulation techniques has decomposed the proton power spectra with respect to the proton asymmetry coordinate and thereby reached similar conclusions to ours: Eigen-like configurations give rise to the continuum band while Zundel-like configurations dominantly contribute around  $1200\text{ cm}^{-1}$ <sup>47</sup>. That study also determined the proton-transfer time scale using two-dimensional transition state theory and Marcus theory of ion pairing and finds this time scale to be concentration dependent, in agreement with our and previous observations.

In summary, in many theoretical treatments, only normal modes of meta-stable or stable states are assumed to produce spectral contributions. Any spectral mode is therefore interpreted as being due to a meta-stable state, consequently, broad spectral modes are often interpreted as reflecting a wide collection of normal modes with slightly different frequencies. In this paper, we show that transfer and barrier-crossing events of charged particles as well as transfer paths create spectral features by a mechanism that is very different from a normal-mode picture and that these spectral features are broadened by the stochastic nature of the transfer dynamics<sup>38</sup>. In fact, the strength or frequency of a spectral feature does not allow to tell whether it is caused by normal-mode oscillations in a stable or meta-stable state or whether it is caused by transfer or barrier-crossing dynamics.

## Methods

**Computational methods: ab initio molecular dynamics simulations.** The Born–Oppenheimer ab initio MD simulations of pure water and HCl solutions at three different concentrations were performed with the CP2K 7.1 software package using a polarizable double-zeta basis set for the valence electrons, optimized for small molecules and short ranges (DZVP-MOLOPT-SR-GTH, with the exception of the chloride anions, that were modeled including diffuse functions in the aug-DZVP-GTH basis set), dual-space pseudopotentials, the BLYP exchange-correlation functional, and D3 dispersion corrections<sup>64–68</sup>. The cutoff for the plane-wave representation was 400 Ry. The system parameters are summarized in Table 2.

Before production, each system was equilibrated in classical MD simulations for 200 ps under NPT conditions at atmospheric pressure and 800 ps under NVT conditions at 300 K, using the GROMACS 2020.5 software<sup>69</sup> with the SPC/E water

model<sup>70</sup>. The force fields for  $\text{Cl}^-$  and  $\text{H}_3\text{O}^+$  were taken from<sup>71</sup>. The ab initio MD simulations were subsequently performed using a time step of 0.5 fs under NVT conditions at 300 K by coupling the system to a CSVR thermostat with a time constant of 100 fs<sup>72</sup>.

Dipole moments were obtained after Wannier-center localization of the electron density at a time resolution of 2 fs or 4 fs. At each time step, the Wannier centers were assigned to the closest oxygen or chloride ion. Water molecules were assembled by assigning each proton to the closest oxygen nucleus, thereby forming either water or hydronium ions. For the hydronium ions, all protons were treated as excess-proton candidates and further processed based on a dynamical criterion as discussed in the main text and Supplementary Methods 2. The dipole moments  $\mathbf{p}$  follow as a sum over the respective position vectors  $\mathbf{r}_i$  and charges  $q_i$  ( $q = 2e$  for Wannier centers, and reduced core charges for nuclei),  $\mathbf{p} = \sum_i q_i \mathbf{r}_i$  for the whole or desired sub systems.

Linear response theory relates the dielectric susceptibility  $\chi(t)$  to the equilibrium autocorrelation of the dipole moment  $C(t) = \sum_D \langle \mathbf{p}(t) \mathbf{p}(0) \rangle$ , reading in Fourier space

$$\chi(\omega) = \frac{1}{Vk_B T \epsilon_0 D} \left( C(0) - i \frac{\omega}{2} \tilde{C}^+(\omega) \right), \quad (4)$$

with system volume  $V$ , thermal energy  $k_B T$ , vacuum permittivity  $\epsilon_0$  and  $D$  being the number of Cartesian dimensions of the polarization vector  $\mathbf{p}$ . IR spectra can therefore be calculated straight-forwardly from sufficiently sampled trajectories of the ab initio MD simulation data using Eq. (4) and the Wiener–Kintchine relation, derived in Supplementary Methods 4 as

$$C(t) = \frac{1}{2\pi(L_t - t)} \int_{-\infty}^{\infty} d\omega e^{-i\omega t} \tilde{\mathbf{p}}(\omega) \tilde{\mathbf{p}}^*(\omega), \quad (5)$$

where  $\tilde{\mathbf{p}}(\omega)$  is the Fourier-transformed dipole-moment trajectory with length  $L_t$  and the asterisk denotes the complex conjugate. Alternatively, for charged subsystems, as in the case of the chloride ions, the computation using the time derivative of the polarization, i.e., the current  $\mathbf{j} = \frac{d}{dt} \mathbf{p}(t)$ , is preferable

$$C(t) = \frac{1}{2\pi(L_t - t)} \int_{-\infty}^{\infty} d\omega \frac{e^{-i\omega t}}{\omega^2} \tilde{\mathbf{j}}(\omega) \tilde{\mathbf{j}}^*(\omega). \quad (6)$$

Quantum corrections have previously been addressed<sup>73</sup>, but were not applied here.

Since the Wannier-center localization time step  $\Delta t_{WC} = 4\text{ fs}$  is larger than the original simulation time step  $\Delta t = 0.5\text{ fs}$ , the analysis is performed on two types of trajectories stemming from the same simulations: one set of trajectories containing the electronic degrees of freedom and another set of trajectories of higher time resolution but only containing nuclei positions. This higher resolution data is used for the calculation of excess-proton spectra and kinetics.

All spectra were smoothed by a convolution with a Gaussian kernel of varying width, depending on their respective resolution. We used a standard deviation of 55, 20, and  $50\text{ cm}^{-1}$  for bulk spectra, the  $\text{H}_5\text{O}_2^+$  complex difference spectrum in Fig. 3c and excess-proton spectra, respectively. Experimental data was smoothed using a standard deviation of  $3\text{ cm}^{-1}$ .

To address the quality of the chosen basis set, shorter simulations at 6 M were performed using the non-short range basis set (DZVP-MOLOPT-GTH) as well as a triple-zeta doubly polarizable (TZV2P-GTH) basis set. Spatial correlations in the data are compared in Supplementary Fig. 9. While the coordination of excess protons with chloride ions slightly increases when the more elaborate basis sets are used, no significant differences in correlations between excess protons and oxygen nuclei are found, which are the focus of this study.

**Experimental methods: THz absorption measurements.** THz spectroscopic measurements in the  $30\text{--}650\text{ cm}^{-1}$  frequency range were done with a commercial Fourier Transform spectrometer (Bruker Vertex 80v, Germany) equipped with a mercury light source and a liquid helium cooled bolometer detector (Infrared Laboratories, Germany). Spectra result from an average of 128 scans with a resolution of  $2\text{ cm}^{-1}$ . The liquid sample cell is composed of diamond windows (Diamond Materials GmbH, Germany) in which a Kapton spacer of approximately  $13\text{ }\mu\text{m}$  was placed between the windows to fix the sample thickness. The exact thickness of the sample cell was determined from the etaloning pattern of the empty sample cell. The temperature of the sample was held constant at  $20.0 \pm 0.2\text{ }^\circ\text{C}$  by an external chiller. The measured frequency-dependent extinction coefficient,  $\alpha_{\text{solution}}(\omega)$ , is determined using the Beer–Lambert law

$$\alpha_{\text{solution}}(\omega) = \frac{1}{d} \ln \left( \frac{I_{\text{water}}(\omega)}{I_{\text{solution}}(\omega)} \right) + \alpha_{\text{water}}(\omega), \quad (7)$$

where  $d$  is the sample thickness,  $I_{\text{water}}(\omega)$  and  $I_{\text{solution}}(\omega)$  are the experimental transmitted intensities of the water reference and the sample.  $\alpha_{\text{water}}(\omega)$  is the extinction coefficient of bulk water and is taken from literature<sup>74</sup>. The extinction coefficient  $\alpha(\omega)$  is converted to the absorption spectrum, proportional to the imaginary part of the dielectric susceptibility  $\chi''(\omega)$ , by fitting the spectra and performing a Kramers–Kronig transform as presented in Supplementary Methods 1.

**Table 2 Parameters of the ab initio molecular dynamics simulations.**

Conc.	0 M	2 M	4 M	6 M
$V_{\frac{1}{3}}$	19.73 Å	20.25 Å	20.25 Å	20.23 Å
$N_{\text{H}_2\text{O}}$	256	258	244	224
$N_{\text{H}^+}, N_{\text{Cl}^-}$	0	10	20	30
$\tau$	201 ps	52 ps	84 ps	84 ps
$\Delta t_{WC}$	2 fs	4 fs		

The difference absorption spectra of HCl solutions with respect to pure water and normalized with respect to the water concentration are given by

$$\omega \Delta \chi''_{\text{CW}}(\omega) = \frac{1}{c_{\text{W}}} \omega \chi''_{\text{solution}}(\omega) - \frac{1}{c_{\text{W}}^0} \omega \chi''_{\text{water}}(\omega), \quad (8)$$

where  $c_{\text{W}}$  and  $c_{\text{W}}^0$  are the concentration of water in the aqueous HCl solutions and bulk water, respectively, determined from the solution density at room temperature.

## Data availability

The datasets generated and analyzed during the current study are available from the corresponding author on request.

Received: 5 October 2021; Accepted: 22 June 2022;

Published online: 21 July 2022

## References

- Marx, D. Proton transfer 200 years after Von Groththuss: Insights from ab initio simulations. *ChemPhysChem* **7**, 1849 (2006).
- Agmon, N. et al. Protons and hydroxide ions in aqueous systems. *Chem. Rev.* **116**, 7642 (2016).
- Tuckerman, M., Laasonen, K., Sprik, M. & Parrinello, M. Ab initio molecular dynamics simulation of the solvation and transport of hydronium and hydroxyl ions in water. *J. Phys. Chem.* **103**, 150 (1995).
- Berkebach, T. C., Lee, H. S. & Tuckerman, M. E. Concerted hydrogen-bond dynamics in the transport mechanism of the hydrated proton: A first-principles molecular dynamics study. *Phys. Rev. Lett.* **103**, 238302 (2009).
- de Groththuss, C. Mémoire - Sur la décomposition de l'eau et des corps qu'elle tient en dissolution à l'aide de l'électricité galvanique. *Ann. Chim.* **58**, 54 (1806).
- Agmon, N. The Groththuss mechanism. *Chem. Phys. Lett.* **244**, 456 (1995).
- Heyden, M. et al. Dissecting the THz spectrum of liquid water from first principles via correlations in time and space. *Proc. Natl. Acad. Sci. USA* **107**, 12068 (2010).
- Heyden, M. et al. Understanding the origins of dipolar couplings and correlated motion in the vibrational spectrum of water. *J. Phys. Chem. Lett.* **3**, 2135 (2012).
- Schwaab, G., Sebastiani, F. & Havenith, M. Ion hydration and ion pairing as probed by THz spectroscopy. *Angew. Chem. - Int. Ed.* **58**, 3000 (2019).
- Balos, V. et al. Macroscopic conductivity of aqueous electrolyte solutions scales with ultrafast microscopic ion motions. *Nat. Commun.* **11**, 1611 (2020).
- Schienenbein, P., Schwaab, G., Forbert, H., Havenith, M. & Marx, D. Correlations in the solute-solvent dynamics reach beyond the first hydration shell of ions. *J. Phys. Chem. Lett.* **8**, 2373 (2017).
- Carlson, S., Brüning, F. N., Loche, P., Bonthuis, D. J. & Netz, R. R. Exploring the absorption spectrum of simulated water from MHz to infrared. *J. Phys. Chem. A* **124**, 5599 (2020).
- Decka, D., Schwaab, G. & Havenith, M. A THz/FTIR fingerprint of the solvated proton: Evidence for Eigen structure and Zundel dynamics. *Phys. Chem. Chem. Phys.* **17**, 11898 (2015).
- Thämer, M., De Marco, L., Ramasesha, K., Mandal, A. & Tokmakoff, A. Ultrafast 2D IR spectroscopy of the excess proton in liquid water. *Science* **350**, 78 (2015).
- Zundel, G. & Metzger, H. Energiebänder der tunnelnden Überschuss-Protonen in flüssigen Säuren. Eine IR-spektroskopische Untersuchung der Natur der Gruppierungen  $\text{H}_5\text{O}_2^+$ . *Zeit. Phys. Chem.* **58**, 225 (1968).
- Wicke, E., Eigen, M. & Ackermann, T. Über den Zustand des Protons (Hydroniumions) in wäßriger Lösung. *Zeit. Phys. Chem.* **1**, 340 (1954).
- Komatsuzaki, T. & Ohmine, I. Energetics of proton transfer in liquid water. I. Ab initio study for origin of many-body interaction and potential energy surfaces. *Chem. Phys.* **180**, 239 (1994).
- Esser, T. K. et al. Deconstructing prominent bands in the terahertz spectra of  $\text{H}_7\text{O}_3^+$  and  $\text{H}_9\text{O}_4^+$ : Intermolecular modes in Eigen clusters. *J. Phys. Chem. Lett.* **9**, 798 (2018).
- Biswas, R., Carpenter, W., Fournier, J. A., Voth, G. A. & Tokmakoff, A. IR spectral assignments for the hydrated excess proton in liquid water. *J. Chem. Phys.* **146**, 154507 (2017).
- Dahms, F., Fingerhut, B. P., Nibbering, E. T., Pines, E. & Elsaesser, T. Large-amplitude transfer motion of hydrated excess protons mapped by ultrafast 2D IR spectroscopy. *Science* **357**, 491 (2017).
- Kulig, W. & Agmon, N. Deciphering the infrared spectrum of the protonated water pentamer and the hybrid Eigen-Zundel cation. *Phys. Chem. Chem. Phys.* **16**, 4933 (2014).
- Kulig, W. & Agmon, N. A 'clusters-in-liquid' method for calculating infrared spectra identifies the proton-transfer mode in acidic aqueous solutions. *Nat. Chem.* **5**, 29 (2013).
- Fournier, J. A., Carpenter, W. B., Lewis, N. H. & Tokmakoff, A. Broadband 2D IR spectroscopy reveals dominant asymmetric  $\text{H}_5\text{O}_2^+$  proton hydration structures in acid solutions. *Nat. Chem.* **10**, 932 (2018).
- Kundu, A. et al. Hydrated excess protons in acetonitrile/water mixtures: Solvation species and ultrafast proton motions. *J. Phys. Chem. Lett.* **10**, 2287 (2019).
- Yu, Q., Carpenter, W. B., Lewis, N. H. C., Tokmakoff, A. & Bowman, J. M. High-level VSCF/VCI calculations decode the vibrational spectrum of the aqueous proton. *J. Phys. Chem. B* **123**, 7214 (2019).
- Carpenter, W. B. et al. Decoding the 2D IR spectrum of the aqueous proton with high-level VSCF/VCI calculations. *J. Chem. Phys.* **153**, 124506 (2020).
- Calio, P. B., Li, C. & Voth, G. A. Resolving the structural debate for the hydrated excess proton in water. *J. Am. Chem. Soc.* **143**, 18672 (2021).
- Calio, P. B., Li, C. & Voth, G. A. Molecular origins of the barriers to proton transport in acidic aqueous solutions. *J. Phys. Chem. B* **124**, 8868 (2020).
- Woutersen, S. & Bakker, H. J. Ultrafast vibrational and structural dynamics of the proton in liquid water. *Phys. Rev. Lett.* **96**, 138305 (2006).
- Loewenstein, A. & Szöke, A. The activation energies of proton transfer reactions in water. *J. Am. Chem. Soc.* **84**, 1151 (1962).
- Luz, Z. & Meiboom, S. The activation energies of proton transfer reactions in water. *J. Am. Chem. Soc.* **86**, 4768 (1964).
- Carpenter, W. B., Lewis, N. H., Fournier, J. A. & Tokmakoff, A. Entropic barriers in the kinetics of aqueous proton transfer. *J. Chem. Phys.* **151**, 034501 (2019).
- Xu, J., Izvekov, S. & Voth, G. A. Structure and dynamics of concentrated hydrochloric acid solutions. *J. Phys. Chem. B* **114**, 9555 (2010).
- Biswas, R., Tse, Y. L. S., Tokmakoff, A. & Voth, G. A. Role of presolvation and anharmonicity in aqueous phase hydrated proton solvation and transport. *J. Phys. Chem. B* **120**, 1793 (2016).
- Napoli, J. A., Marsalek, O. & Markland, T. E. Decoding the spectroscopic features and time scales of aqueous proton defects. *J. Chem. Phys.* **148**, 222833 (2018).
- Williams, G. The use of the dipole correlation function in dielectric relaxation. *Chem. Rev.* **72**, 55 (1972).
- Wang, H. & Agmon, N. Reinvestigation of the infrared spectrum of the gas-phase protonated water tetramer. *J. Phys. Chem. A* **121**, 3056 (2017).
- Brünig, F. N., Hillmann, P., Kim, W. K., Daldrop, J. O. & Netz, R. R. Proton-transfer spectroscopy beyond the normal-mode scenario. Preprint at <https://arxiv.org/abs/2109.08514> (2021).
- Kramers, H. Brownian motion in a field of force and the diffusion model of chemical reactions. *Physica* **7**, 284 (1940).
- Hummer, G. From transition paths to transition states and rate coefficients. *J. Chem. Phys.* **120**, 516 (2004).
- Chung, H. S., Louis, J. M. & Eaton, W. A. Experimental determination of upper bound for transition path times in protein folding from single-molecule photon-by-photon trajectories. *Proc. Natl. Acad. Sci. USA* **106**, 11837 (2009).
- Kim, W. K. & Netz, R. R. The mean shape of transition and first-passage paths. *J. Chem. Phys.* **143**, 224108 (2015).
- Cossio, P., Hummer, G. & Szabo, A. Transition paths in single-molecule force spectroscopy. *J. Chem. Phys.* **148**, 123309 (2018).
- Huggins, M. L. 50 years of hydrogen bond theory. *Angew. Chem. - Int. Ed.* **10**, 147 (1971).
- Marx, D., Tuckerman, M. E., Hutter, J. & Parrinello, M. The nature of the hydrated excess proton in water. *Nature* **397**, 601 (1999).
- Wolke, C. T. et al. Spectroscopic snapshots of the proton-transfer mechanism in water. *Science* **354**, 1131 (2016).
- Roy, S. et al. Resolving heterogeneous dynamics of excess protons in aqueous solution with rate theory. *J. Phys. Chem. B* **124**, 5665 (2020).
- Kappler, J., Daldrop, J. O., Brüning, F. N., Boehle, M. D. & Netz, R. R. Memory-induced acceleration and slowdown of barrier crossing. *J. Chem. Phys.* **148**, 014903 (2018).
- Daldrop, J. O. et al. Orientation of non-spherical protonated water clusters revealed by infrared absorption dichroism. *Nat. Commun.* **9**, 311 (2018).
- Carpenter, W. B., Fournier, J. A., Lewis, N. H. & Tokmakoff, A. Picosecond proton transfer kinetics in water revealed with ultrafast IR spectroscopy. *J. Phys. Chem. B* **122**, 2792 (2018).
- Markovitch, O. et al. Special pair dance and partner selection: Elementary steps in proton transport in liquid water. *J. Phys. Chem. B* **112**, 9456 (2008).
- Baer, M. D., Fulton, J. L., Balasubramanian, M., Schenter, G. K. & Mundy, C. J. Persistent ion pairing in aqueous hydrochloric acid. *J. Phys. Chem. B* **118**, 7211 (2014).
- Daly, C. A. et al. Decomposition of the experimental Raman and infrared spectra of acidic water into proton, special pair, and counterion contributions. *J. Phys. Chem. Lett.* **8**, 5246 (2017).

54. Cox, D. R. & Miller, H. D. *The Theory of Stochastic Processes* (CRC Press, 1977).
55. Markland, T. E. & Ceriotti, M. Nuclear quantum effects enter the mainstream. *Nat. Rev. Chem.* **2**, 0109 (2018).
56. Fullton, J. L. & Balasubramanian, M. Structure of hydronium ( $\text{H}_3\text{O}^+$ )/chloride ( $\text{Cl}^-$ ) contact ion pairs in aqueous hydrochloric acid solution: A Zundel-like local configuration. *J. Am. Chem. Soc.* **132**, 12597 (2010).
57. Fischer, S. A. & Gunlycke, D. Analysis of correlated dynamics in the Grothuss mechanism of proton diffusion. *J. Phys. Chem. B* **123**, 5536 (2019).
58. Arntsen, C., Chen, C., Calio, P. B., Li, C. & Voth, G. A. The hopping mechanism of the hydrated excess proton and its contribution to proton diffusion in water. *J. Chem. Phys.* **154**, 194506 (2021).
59. Tse, Y. L. S., Knight, C. & Voth, G. A. An analysis of hydrated proton diffusion in ab initio molecular dynamics. *J. Chem. Phys.* **142**, 014104 (2015).
60. Dippel, T. & Kreuer, K. D. Proton transport mechanism in concentrated aqueous solutions and solid hydrates of acids. *Solid State Ionics* **46**, 3 (1991).
61. Hassanali, A., Giberti, F., Cuny, J., Kühne, T. D. & Parrinello, M. Proton transfer through the water gossamer. *Proc. Natl. Acad. Sci. USA* **110**, 13723 (2013).
62. Yuan, R. et al. Tracking aqueous proton transfer by two-dimensional infrared spectroscopy and ab initio molecular dynamics simulations. *ACS Cent. Sci.* **5**, 1269 (2019).
63. Fischer, S. A., Dunlap, B. I. & Gunlycke, D. Correlated dynamics in aqueous proton diffusion. *Chem. Sci.* **9**, 7126 (2018).
64. Kendall, R. A., Dunning, T. H. & Harrison, R. J. Electron affinities of the first-row atoms revisited. Systematic basis sets and wave functions. *J. Chem. Phys.* **96**, 6796 (1992).
65. VandeVondele, J. et al. Quickstep: Fast and accurate density functional calculations using a mixed Gaussian and plane waves approach. *Comput. Phys. Commun.* **167**, 103 (2005).
66. VandeVondele, J. & Hutter, J. Gaussian basis sets for accurate calculations on molecular systems in gas and condensed phases. *J. Chem. Phys.* **127**, 114105 (2007).
67. Grimme, S., Antony, J., Ehrlich, S. & Krieg, H. A consistent and accurate ab initio parametrization of density functional dispersion correction (DFT-D) for the 94 elements H-Pu. *J. Chem. Phys.* **132**, 154104 (2010).
68. Kühne, T. D. et al. CP2K: An electronic structure and molecular dynamics software package - Quickstep: Efficient and accurate electronic structure calculations. *J. Chem. Phys.* **152**, 194103 (2020).
69. Abraham, M. J. et al. GROMACS: High performance molecular simulations through multi-level parallelism from laptops to supercomputers. *SoftwareX* **1-2**, 19 (2015).
70. Berendsen, H. J. C., Grigera, J. R. & Straatsma, T. P. The missing term in effective pair potentials. *J. Phys. Chem.* **91**, 6269 (1987).
71. Bonthuis, D. J., Mamatkulov, S. I. & Netz, R. R. Optimization of classical nonpolarizable force fields for  $\text{OH}^-$  and  $\text{H}_3\text{O}^+$ . *J. Chem. Phys.* **144**, 104503 (2016).
72. Bussi, G., Donadio, D. & Parrinello, M. Canonical sampling through velocity rescaling. *J. Chem. Phys.* **126**, 014101 (2007).
73. Ramírez, R., López-Ciudad, T., Kumar P, P. & Marx, D. Quantum corrections to classical time-correlation functions: Hydrogen bonding and anharmonic floppy modes. *J. Chem. Phys.* **121**, 3973 (2004).
74. Bertie, J. E. & Lan, Z. Infrared intensities of liquids XX: The intensity of the OH stretching band of liquid water revisited, and the best current values of the optical constants of  $\text{H}_2\text{O}(l)$  at 25 °C between 15,000 and  $1\text{ cm}^{-1}$ . *Appl. Spectrosc.* **50**, 1047 (1996).

## Acknowledgements

We gratefully acknowledge computing time on the HPC clusters at the physics department and ZEDAT, FU Berlin, as well as the computational resources provided by the North-German Supercomputing Alliance (HLRN) under project bep00068 (R.R.N.). This work was funded by the Deutsche Forschungsgemeinschaft (DFG) under Germany's Excellence Strategy - EXC 2033 - 390677874 - RESOLV (M.H.) and via grants SFB 1078, project C1 (R.R.N.) and SFB 1349, project C4 (R.R.N.). Funding by the European Research Council (ERC) is acknowledged via Advanced Grant 695437 THz Calorimetry (M.H.) and Advanced Grant 835117 NoMaMemo (R.R.N.).

## Author contributions

F.N.B. and R.R.N. conceived the theory and designed the simulations. F.N.B. performed the ab initio MD simulations. F.N.B. and M.R. analyzed the data and designed the figures. E.A. and M.H. carried out the THz measurements and analyzed the data. All authors discussed the results, analyses, and interpretations. F.N.B., M.H., and R.R.N. wrote the paper with input from all authors.

## Funding

Open Access funding enabled and organized by Projekt DEAL.

## Competing interests

The authors declare no competing interests.

## Additional information

**Supplementary information** The online version contains supplementary material available at <https://doi.org/10.1038/s41467-022-31700-x>.

**Correspondence** and requests for materials should be addressed to Roland R. Netz.

**Peer review information** *Nature Communications* thanks the anonymous reviewers for their contribution to the peer review of this work. Peer reviewer reports are available.

**Reprints and permission information** is available at <http://www.nature.com/reprints>

**Publisher's note** Springer Nature remains neutral with regard to jurisdictional claims in published maps and institutional affiliations.



**Open Access** This article is licensed under a Creative Commons Attribution 4.0 International License, which permits use, sharing, adaptation, distribution and reproduction in any medium or format, as long as you give appropriate credit to the original author(s) and the source, provide a link to the Creative Commons license, and indicate if changes were made. The images or other third party material in this article are included in the article's Creative Commons license, unless indicated otherwise in a credit line to the material. If material is not included in the article's Creative Commons license and your intended use is not permitted by statutory regulation or exceeds the permitted use, you will need to obtain permission directly from the copyright holder. To view a copy of this license, visit <http://creativecommons.org/licenses/by/4.0/>.

© The Author(s) 2022



# Time-Dependent Friction Effects on Vibrational Infrared Frequencies and Line Shapes of Liquid Water

---

5

by Florian N. Brünig, Otto Geburtig, Alexander von Canal, Julian Kappler, and Roland R. Netz

**Contributions:** F.N.B. and R.R.N conceived the theory and designed the simulations. F.N.B. performed the ab initio simulations. F.N.B., O.G. and A.v.C. performed the GLE simulations. F.N.B., O.G. and A.v.C. analyzed the data. All authors discussed the results, analyses, and interpretations. F.N.B. and R.R.N. wrote the paper with input from all authors.

**Bibliographic information:** This chapter has previously been published in the *Journal of Physical Chemistry B* by the American Chemical Society (ACS) as open access under the Creative Commons CC BY-NC-ND licence (<http://creativecommons.org/licenses/by-nc-nd/4.0/>) [1].

<https://doi.org/10.1021/acs.jpcb.1c09481>



# Time-Dependent Friction Effects on Vibrational Infrared Frequencies and Line Shapes of Liquid Water

Florian N. Brünig, Otto Geburtig, Alexander von Canal, Julian Kappler, and Roland R. Netz\*

Cite This: *J. Phys. Chem. B* 2022, 126, 1579–1589

Read Online

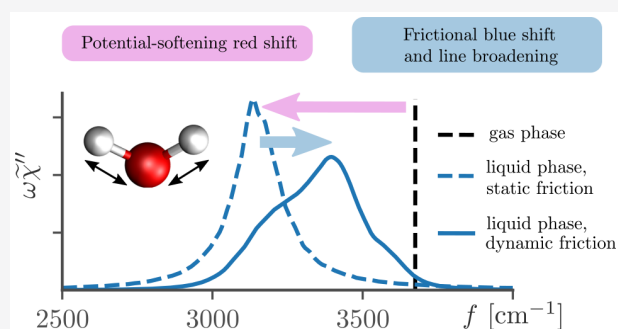
ACCESS |

Metrics & More

Article Recommendations

Supporting Information

**ABSTRACT:** From ab initio simulations of liquid water, the time-dependent friction functions and time-averaged nonlinear effective bond potentials for the OH stretch and HOH bend vibrations are extracted. The obtained friction exhibits not only adiabatic contributions at and below the vibrational time scales but also much slower nonadiabatic contributions, reflecting homogeneous and inhomogeneous line broadening mechanisms, respectively. Intermolecular interactions in liquid water soften both stretch and bend potentials compared to the gas phase, which by itself would lead to a red-shift of the corresponding vibrational bands. In contrast, nonadiabatic friction contributions cause a spectral blue shift. For the stretch mode, the potential effect dominates, and thus, a significant red shift when going from gas to the liquid phase results. For the bend mode, potential and nonadiabatic friction effects are of comparable magnitude, so that a slight blue shift results, in agreement with well-known but puzzling experimental findings. The observed line broadening is shown to be roughly equally caused by adiabatic and nonadiabatic friction contributions for both the stretch and bend modes in liquid water. Thus, the quantitative analysis of the time-dependent friction that acts on vibrational modes in liquids advances the understanding of infrared vibrational frequencies and line shapes.



## INTRODUCTION

The OH stretch band in liquid water is significantly red-shifted and broadened compared to the gas-phase spectrum, while the HOH bend frequency is in fact slightly blue-shifted when going from gas to the liquid phase.<sup>1</sup> The broadening of the OH stretch band in liquid water is typically rationalized by a combination of homogeneous and inhomogeneous effects.<sup>2,3</sup> Inhomogeneous line broadening is associated with different hydrogen-bonding environments of individual OH bonds, which in the limit when the hydrogen-bonding pattern changes more slowly than the OH vibrational period and in the presence of nonlinearities in the OH bond potential produce vibrational frequencies that vary over time.<sup>4–6</sup> Homogeneous line broadening reflects the fast coupling of OH bonds to their neighboring water molecules, mostly via hydrogen bonding, which reduces the vibrational lifetime because the vibrational energy is quickly transported to neighboring molecules and thus dissipated into collective modes.<sup>7</sup> Indeed, the vibrational lifetime of the OH stretch is very short (of the order of 190 fs<sup>8,9</sup>) and thus only 19 times longer than the OH-stretch vibrational period itself (of the order of 10 fs). The experimentally observed red shift of the OH stretch band is usually rationalized by strong hydrogen bonding in liquid water, which extends and thereby softens the OH bond<sup>2,3</sup> (in fact, the relationship between the hydrogen-bond strength, the OH bond length and the red shift of the stretch band has been amply and partly controversially discussed in literature<sup>5,10–12</sup>).

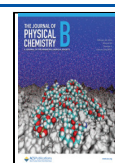
According to such reasoning, the rather small frequency shift of the water bending mode when going from gas to liquid water could be argued to imply that the bond angle potential is only weakly perturbed by the liquid water environment and thus that the coupling of bend vibrations to the hydration environment is weak. This interpretation is puzzling though, because the vibrational lifetime of the water bending mode in liquid water is rather short (around 170 fs<sup>13,14</sup>) and thus only 8.5 times longer than the vibrational period of 20 fs, an even smaller ratio than for the stretch mode. The short bend vibrational lifetime reflects quick energy dissipation into librational modes,<sup>15–17</sup> which in turn can be rationalized by efficient multiphonon energy relaxation based on the excitation of librational overtones in liquids.<sup>18</sup>

Time-dependent or, equivalently, frequency-dependent friction arises whenever the dynamics of a many-particle system is described in a low-dimensional reaction-coordinate space,<sup>19–25</sup> and its relevance for infrared (IR) spectra was clearly demonstrated in the past.<sup>26–31</sup> All friction contributions

Received: November 2, 2021

Revised: January 7, 2022

Published: February 15, 2022



that decay faster or similarly as the vibrational period stem from adiabatic solvent degrees of freedom and account for dissipation into intra- and intermolecular degrees of freedom (including vibrational overtones);<sup>32–35</sup> these friction contributions dominate the vibrational energy relaxation and lead to homogeneous line broadening. Friction contributions that decay much slower than the vibrational time scale describe the slowly changing nonadiabatic hydration environment and in conjunction with nonlinear bond potentials induce inhomogeneous line broadening, as our results explicitly demonstrate. Of course, there is no clear-cut separation between adiabatic and nonadiabatic solvent relaxation modes,<sup>36–39</sup> prompting for a time-scale bridging framework to treat the dynamic coupling of molecular vibration modes and their environment. In fact, the frequency-dependent friction function, which appears in the generalized Langevin equation (GLE), is the appropriate framework to account for all these effects, with the only drawback that nuclear quantum effects can at the current level of the formalism not be included without making additional approximations. Only recently developed extraction methods that account for nonlinearities<sup>40</sup> allow obtaining these time-dependent friction functions from ab initio molecular dynamics (aiMD) simulations and with high enough accuracy; this we self-consistently demonstrate by deriving vibrational spectra from numerical simulations of the GLE that are virtually indistinguishable from the vibrational spectra directly obtained from aiMD simulation trajectories.

In this paper, we address the puzzle posed by the different line shifts of the water stretch and bend modes by analyzing the vibrational water dynamics in terms of the time-averaged nonlinear bond potentials (as a function of the bond length for the OH stretch and the bond angle for the HOH bend) and the corresponding time-dependent friction functions, which are extracted from extensive aiMD simulations for 256 H<sub>2</sub>O molecules. In particular, we show that the slight blue shift of the water bend mode when going from gas to the liquid phase is not caused by a stiffening of the bend potential, which would explain the blue shift,<sup>1</sup> but rather by the time dependence of the friction acting on bending vibrations. We find that the liquid environment in fact significantly softens the time-averaged bond potentials, and it does so quite similarly for the stretch and bend modes. Neglecting the frequency dependence of the friction, both stretch and bend bands would thus be expected to be red-shifted by comparable amounts when going from gas to the liquid phase, in stark contrast to the experimental finding.<sup>1</sup> It turns out that nonharmonic bond-potential effects are rather unimportant for the band position and thus cannot explain this puzzling finding. Likewise, frequency-independent friction shifts the bands insignificantly and only increases the line width, in agreement with expectations.<sup>4</sup> In contrast, the frequency dependence of the friction is crucial and not only leads, in conjunction with nonlinearities in the bond potentials, to inhomogeneous line broadening but also gives rise to pronounced blue shifts for both stretch and bend bands. The mechanism for this blue shift is very general,<sup>26</sup> as we analytically demonstrate. The compensation of the potential red shift and the friction blue shift is incomplete for the stretch band but almost perfect for the bend band, so the stretch band exhibits a significant net red shift from gas to liquid, while the bend band shows only a slight blue shift in both experiments and simulations. The absence of a significant frequency shift of the bend mode does by no means imply that bend vibrations couple less to their

environment than stretch vibrations (as has been demonstrated previously<sup>15–17</sup>); rather, it is the subtle balance of the potential and friction contributions to the line shift, which both are caused by interactions with the liquid environment, that is different for the stretch and bend bands. We conclude that the coupling of water stretch and bend vibrations to other intra- and intermolecular degrees of freedom, as quantified by the time-averaged bond potentials and friction functions, is of similar strength, which explains their similar vibrational life times, although their frequency shifts are rather different, which we rationalize by a subtle difference of the compensatory potential and friction effects. The spectral blue shift due to frequency-dependent friction is a very general mechanism; it transpires that the concept of frequency-dependent friction is important for advancing the understanding of vibrational spectroscopy.

## SYSTEM, SPECTRA, AND MODEL

We primarily analyze aiMD simulations of 256 H<sub>2</sub>O (and D<sub>2</sub>O for comparison) molecules in the liquid phase at 300 K that neglect nuclear quantum effects. Figure 1A compares the

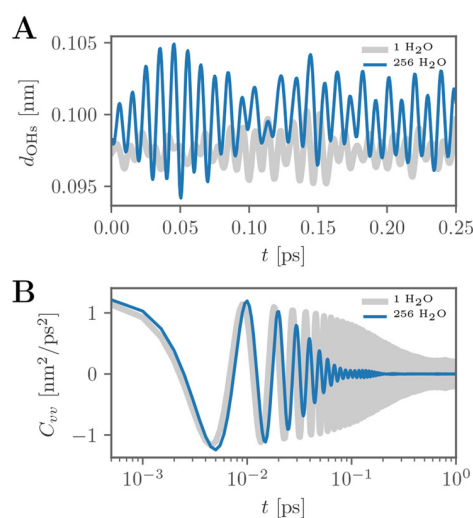


**Figure 1.** (A) Trajectory of the OH bond length, averaged over both OH bonds in a single water molecule, from ab initio molecular dynamics (aiMD) simulations of one H<sub>2</sub>O in the gas phase (gray line) and for 256 H<sub>2</sub>O molecules in the liquid phase (blue line), both at 300 K. (B) Corresponding velocity autocorrelation functions.

trajectories of the mean OH bond length of a single H<sub>2</sub>O molecule in liquid H<sub>2</sub>O (blue line) and in the gas phase (gray line), both at 300 K (see Methods for simulation details). The increase of the mean and the variance of the bond length in the liquid phase compared to the gas phase is clearly visible, which reflects the shift and softening of the OH bond potential due to hydrogen bonding in the liquid phase. The slow fluctuations of the oscillation amplitude reflect vibrational energy relaxations that occur over about 100 fs in the liquid phase (pure dephasing due to fluctuations of the vibrational frequency<sup>41,42</sup> is not easily visible in the time domain). Similarly, the bond-length velocity autocorrelation function (VACF) in Figure 1B demonstrates a significantly faster decay and thus a decreased vibrational lifetime in the liquid phase. Although the OH-stretch absorption spectrum is (apart from electronic and collective effects) straightforwardly related to the OH bond-

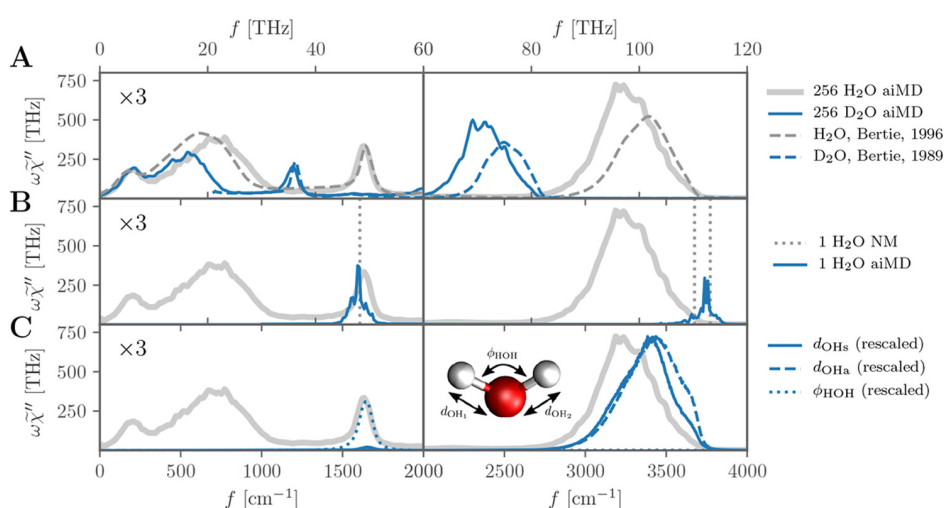


**Figure 2.** Absorption spectra of aiMD simulations at 300 K of 256 H<sub>2</sub>O molecules are shown as gray solid lines in panels A–C. The spectra up to 2000 cm<sup>-1</sup> are multiplied by a factor three. (A) Comparison to aiMD spectra for liquid D<sub>2</sub>O (blue solid line) and experimental data (obtained for 298 K), shown as a gray broken line for H<sub>2</sub>O<sup>43</sup> and a blue broken line for D<sub>2</sub>O.<sup>44</sup> (B) Comparison to aiMD simulations of a single H<sub>2</sub>O (blue solid line). The normal-mode frequencies of a single H<sub>2</sub>O are shown as vertical dotted lines. (C) Comparison to power spectra of the symmetric stretch,  $d_{\text{OHs}}$  (blue solid line); antisymmetric stretch,  $d_{\text{OHa}}$  (blue broken line); and bend mode vibrations,  $\phi_{\text{HOH}}$  (blue dotted line), which are averaged over all molecules and rescaled to match the absorption spectrum.

length VACF via Fourier transformation, it turns out that a careful analysis of the molecular vibrations in terms of the GLE reveals interesting information on the mechanisms that determine the vibrational frequencies and line shapes.

Linear IR spectroscopy experiments measure the absorbed power of light at angular frequency  $\omega = 2\pi f$ , which is proportional to the imaginary part of the dielectric susceptibility  $\tilde{\chi}''(\omega)$ . Linear-response theory relates  $\tilde{\chi}''(\omega)$  to the total dipole-moment autocorrelation (see section I of the Supporting Information), allowing IR spectra to be calculated from equilibrium simulations.<sup>45,46</sup> Figure 2A compares the IR absorption spectrum from aiMD simulations of liquid H<sub>2</sub>O (gray solid line) and D<sub>2</sub>O (blue solid line) with corresponding experimental data (gray and blue broken lines, respectively). One discerns the stretch band (around 3300 cm<sup>-1</sup> for H<sub>2</sub>O and 2400 cm<sup>-1</sup> for D<sub>2</sub>O in the aiMD results) and the bend band (at 1650 cm<sup>-1</sup> for H<sub>2</sub>O and 1200 cm<sup>-1</sup> for D<sub>2</sub>O). The librational absorption band is produced by a large number of different intermolecular vibrational modes<sup>47</sup> that are dominated by rotational vibrations of water molecules in their hydrogen-bond environment (around 700 cm<sup>-1</sup> for H<sub>2</sub>O and 550 cm<sup>-1</sup> for D<sub>2</sub>O) and by translational vibrations of water molecules against each other around 200 cm<sup>-1</sup> for both H<sub>2</sub>O and D<sub>2</sub>O. The agreement between the absorption spectra from aiMD simulations, which fully account for electronic and nuclear polarizations, and from experiments is good, which suggests that the chosen simulation method is well-suited for modeling IR spectra, although the agreement is known to be partly due to a cancellation of approximations in the employed density functional theory (DFT) and the neglect of nuclear quantum effects.<sup>48,49</sup> Molecular simulations of liquids including nuclear quantum effects have rather recently become feasible, mostly via centroid and ring-polymer molecular dynamics (MD) techniques.<sup>50</sup> Unfortunately, the projection techniques we apply on the classical nuclear trajectories from our aiMD simulations are not available on the quantum level; therefore, the analysis we do in this paper can currently not be done for quantum systems without additional drastic and uncontrolled

approximations. Nevertheless, the interplay of potential and frequency-dependent friction effects we explore in this paper presumably is not modified by nuclear quantum effects in a fundamental way, so that the conclusions we draw with regard to the importance of frequency-dependent friction effects should remain valid even beyond our classical treatment of the nuclei.

Figure 2B compares simulated liquid H<sub>2</sub>O (gray) and single H<sub>2</sub>O (blue solid line) spectra at 300 K. The single-water spectrum shows sharp peaks which perfectly coincide with the normal-mode frequencies of a single water molecule (vertical dotted lines, computed on the same DFT level as the aiMD simulations) at 1607, 3675, and 3772 cm<sup>-1</sup>, which are within 20 cm<sup>-1</sup> of the experimental values 1594.7, 3657.1, and 3755.9 cm<sup>-1</sup>.<sup>51,52</sup> Note that the OH-stretch band consists of two modes, namely, the low-frequency symmetric mode, where both OH bonds vibrate in phase, and the high-frequency antisymmetric mode, where the OH bonds vibrate out of phase, which do not clearly separate in the liquid spectrum. The symmetric stretch mode in the gas phase shows a much smaller intensity than the antisymmetric stretch mode, in agreement with experiment,<sup>52</sup> which is caused by electronic polarization effects. The OH-stretch peak in the liquid is significantly red-shifted and enhanced compared to gas phase, which is typically rationalized by the softening of the OH bond potential and the constructive collectivity of OH-stretching vibrations in the liquid (see section II in the Supporting Information);<sup>2,3,53</sup> the significant enhancement is noteworthy, because one could expect the friction acting on the OH bond to be much stronger in the liquid and thus to reduce the vibrational amplitude. In contrast, the HOH-bending mode in the liquid is slightly blue-shifted and not enhanced, which can be rationalized by collective effects that are slightly destructive (see section II in the Supporting Information). All these effects are fully accounted for by the frequency-dependent friction acting on the different vibrational modes, as explained below.

The vibrational modes of a water molecule can be described by the bond angle  $\phi_{\text{HOH}}$  and the symmetric and antisymmetric

stretch distances,  $d_{\text{OHs}} = (d_{\text{OH1}} + d_{\text{OH2}})/2$  and  $d_{\text{OHa}} = (d_{\text{OH1}} - d_{\text{OH2}})/2$ , where the two OH bond distances in a water molecule are denoted as  $d_{\text{OH1}}$  and  $d_{\text{OH2}}$ , which are all based on the nuclear positions in the aiMD simulations, as illustrated in the inset in Figure 2C. The power spectra of these three vibrational modes, averaged over all water molecules in the liquid, are shown in Figure 2C ( $\phi_{\text{HOH}}$  as dotted,  $d_{\text{OHs}}$  as solid, and  $d_{\text{OHa}}$  as broken blue lines) and compared to the absorption spectrum from the total dipole moment. The agreement of the line frequencies and shapes is quite good, except that the absorption spectrum is red-shifted compared to the  $d_{\text{OHs}}$  and  $d_{\text{OHa}}$  vibrational spectra. This red shift is due to dipolar correlations between neighboring water molecules (as mentioned above and discussed in detail in section II in the Supporting Information) and also due to electronic polarization effects, as shown in section III in the Supporting Information. The  $d_{\text{OHs}}$  and  $d_{\text{OHa}}$  spectra overlap significantly, with a small red shift of the  $d_{\text{OHs}}$  spectrum relative to the  $d_{\text{OHa}}$  spectrum, in accordance with previous observations.<sup>54</sup> The vibrational spectrum of the  $\phi_{\text{HOH}}$  mode overlaps perfectly with the spectrum from the total (nuclear and electronic) dipole moment, which is due to the fact that the bending angle vibrations of neighboring water molecules are only weakly (and in fact anti-) correlated, as shown in section II in the Supporting Information.<sup>53</sup> We conclude that the absorption spectrum calculated from the total system polarization (including nuclear and electronic polarization from all water molecules and their correlations) match the power spectra based on the single-water nuclear-coordinate-based vibrational modes rather faithfully. This good agreement lies at the heart of the common interpretation of IR absorption spectra in terms of molecular vibrations; it also validates our approach, because it means that the conclusions from our GLE analysis, which in the present formulation can be applied only on one-dimensional reaction coordinates that are derived from nuclear positions, can also be used to interpret simulated and experimental absorption spectra.

In the following, we will analyze the dynamics of different water vibrational modes based on the one-dimensional GLE<sup>55,56</sup>

$$m\ddot{x}(t) = - \int_0^t \Gamma(t-t')\dot{x}(t')dt' - \nabla U[x(t)] + F_R(t) \quad (1)$$

which contains an in-general nonharmonic time-independent potential  $U(x)$  that corresponds to a free energy as it results from integrating out all other degrees of freedom except  $x(t)$ . The memory kernel  $\Gamma(t)$  describes the time-dependent friction acting on the fluctuating variable  $x(t)$ , which can be the bond angle ( $\phi_{\text{HOH}}$ ), the symmetric stretch distance ( $d_{\text{OHs}}$ ), or the antisymmetric stretch distance ( $d_{\text{OHa}}$ ). The random force  $F_R(t)$  has zero mean  $\langle F_R(t) \rangle = 0$  and fulfills the fluctuation–dissipation relation  $\langle F_R(t)F_R(t') \rangle = k_B T \Gamma(t-t')$ . The GLE approach as introduced by Mori and Zwanzig in the 1960s is an exact projection of the full dynamics of a multiparticle system onto a reduced set of coordinates. Given a one-dimensional trajectory  $x(t)$  from the aiMD simulations, the effective mass  $m$ , the potential  $U(x)$ , and the friction function  $\Gamma(t)$  are uniquely determined and can be accurately extracted,<sup>40</sup> as described in sections IV and V in the Supporting Information. It follows that all intra- and intermolecular interaction effects on the molecular vibration dynamics are accurately taken into account: as a crucial test of

the validity of the GLE in the formulation of eq 1, of our extraction methods, and of our simulation methods of the GLE, we will further demonstrate below that the GLE accurately reproduces the vibrational mode spectra calculated directly from the aiMD simulations. Therefore, our description of the vibrational dynamics of a water molecule in the liquid phase via the GLE is accurate, or, more strictly speaking, it accurately reproduces the vibrational dynamics obtained in our ab initio simulations.

For a harmonic potential,  $U(x) = kx^2/2$ , the vibrational power spectrum that follows from the GLE eq 1 can be given in closed form as (see section VI in the Supporting Information)

$$\omega\tilde{\chi}''(\omega) = \frac{\omega^2 \text{Re}\tilde{\Gamma}(\omega)}{|k - m\omega^2 - i\tilde{\Gamma}(\omega)\omega|^2} \quad (2)$$

where the frequency-dependent friction is obtained by a single-sided Fourier transform  $\tilde{\Gamma}(\omega) = \int_0^\infty dt e^{i\omega t}\Gamma(t)$ . In the limit of frequency-independent friction  $\tilde{\Gamma}(\omega) = \gamma$ , this yields the standard Lorentzian line shape<sup>57</sup> (see section VII in the Supporting Information)

$$\omega\tilde{\chi}''(\omega) = \frac{\omega^2\gamma}{(k - m\omega^2)^2 + \gamma^2\omega^2} \quad (3)$$

which will be shown below to give only a poor account of our simulated vibrational spectra. Nonharmonic potentials are parametrized as

$$U(x) = \frac{k}{2}(x - x_0)^2 + \frac{k_3}{3}(x - x_0)^3 + \frac{k_4}{4}(x - x_0)^4 \quad (4)$$

where  $x_0$  is the position of the minimum of  $U(x)$ . Vibrational spectra in the presence of nonharmonic potentials are obtained from numerical simulations of the GLE using a parametrized friction function of the form<sup>58–60</sup>

$$\Gamma(t) = \sum_{i=0}^n \frac{\gamma_i}{\tau_i} e^{-t/\tau_i} + \sum_{i=0}^l a_i e^{-t/\tau_i} \left[ \cos(\omega_i t) + \frac{1}{\tau_i \omega_i} \sin(\omega_i t) \right] \quad (5)$$

consisting of  $n$  exponentially decaying components with time scales  $\tau_i$  and friction coefficients  $\gamma_i$  as well as  $l$  oscillating and decaying components with amplitudes  $a_i$ , oscillation frequencies  $\omega_i$ , and decay time scales  $\tau_i^0$  (see sections VIII–X in the Supporting Information for details).

## METHODS

All Born–Oppenheimer aiMD simulations are performed with the CP2K 4.1 software package using a contracted double- $\zeta$  basis set for the valence electrons, optimized for small molecules and short ranges (DZVP-MOLOPT-SR-GTH), dual-space pseudopotentials, the BLYP exchange–correlation functional, D3 dispersion correction, and a cutoff for the plane-wave representation set to 400 Ry.<sup>61–63</sup> A time step of 0.5 fs is used under *NVT* conditions at 300 K by coupling all atoms to a CSVR thermostat with a time constant of 100 fs.<sup>64</sup> The bulk systems contain 256 molecules subject to periodic boundary conditions in a cubic cell of size (1.9734 nm)<sup>3</sup>, corresponding to densities of 996.4 kg/m<sup>3</sup> for H<sub>2</sub>O and 1107.8 kg/m<sup>3</sup> for D<sub>2</sub>O. The total trajectory lengths of the liquid systems are 230 ps for H<sub>2</sub>O and 130 ps for D<sub>2</sub>O. Simulations of a single H<sub>2</sub>O molecule, representing the gas phase data, are performed in the *NVE* ensemble with 47 initial configurations sampled from a

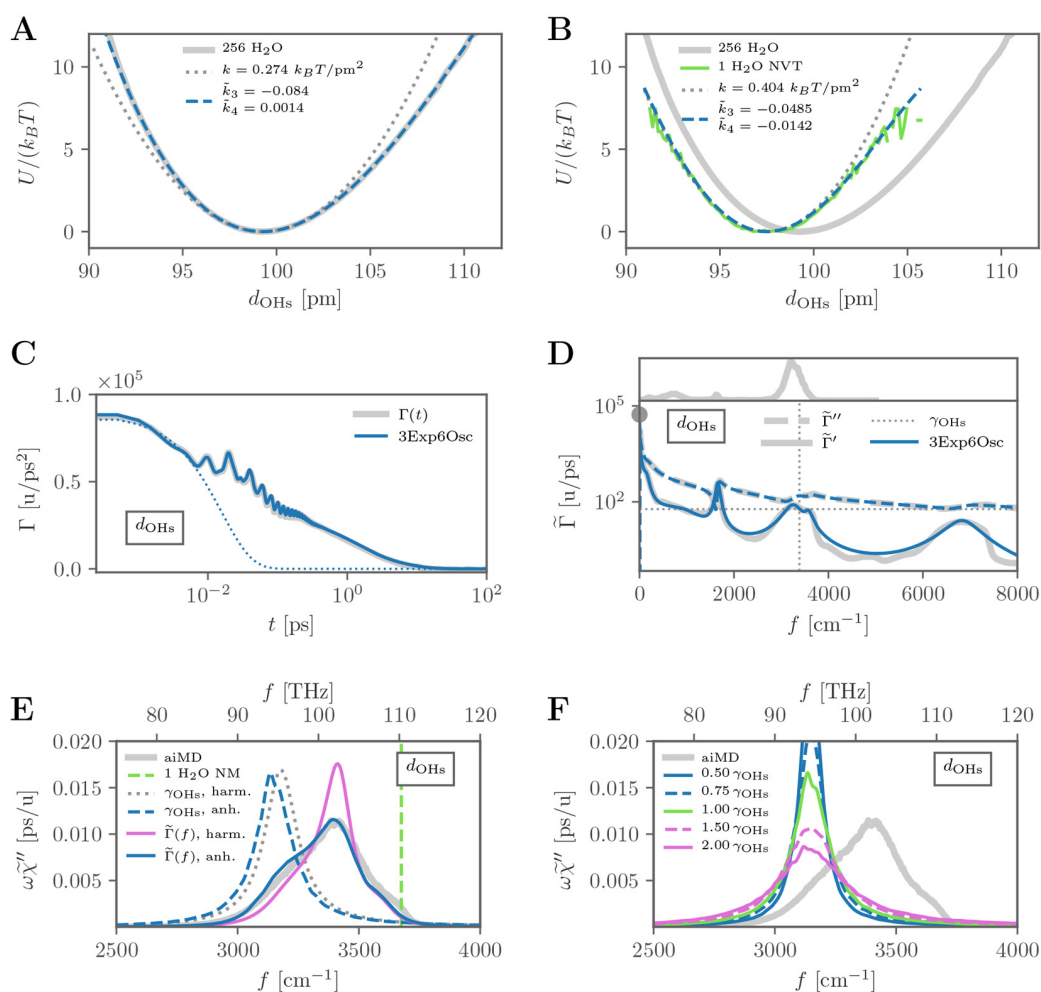


**Figure 3.** Results for the symmetric stretch coordinate  $d_{\text{OHs}}$  from aiMD simulations. (A) Potential  $U(d_{\text{OHs}})$  for 256  $\text{H}_2\text{O}$  in the liquid phase (gray solid line) compared to the nonharmonic fit according to eq 4 (blue broken line) and the harmonic part (gray dotted line). (B) Potential  $U(d_{\text{OHs}})$  for a single  $\text{H}_2\text{O}$  molecule in the gas phase (green solid line) compared with the nonharmonic fit according to eq 4 (blue broken line) and the harmonic part (gray dotted line). The liquid-phase potential (gray solid line) is shown for comparison. (C and D) Friction as a function of time and frequency (gray lines) compared with the fit according to eq 5 (blue lines). Real and imaginary parts in panel D are shown as solid and broken lines, respectively; the spectrum on top is the full absorption spectrum from aiMD. The blue dotted line in panel C shows a single exponential with decay time  $\tau = 10$  fs; the dotted horizontal line in panel D shows the constant real friction  $\gamma_{\text{OHs}} = \tilde{\Gamma}'(f_{\text{OHs}})$  evaluated at the symmetric OH stretch vibrational frequency  $f_{\text{OHs}} = 3390 \text{ cm}^{-1}$ . The gray circle denotes the static friction  $\tilde{\Gamma}'(0)$ . (E) Vibrational power spectrum  $\omega\tilde{\chi}''$  (gray solid line) compared to models of varying complexity: normal mode of single  $\text{H}_2\text{O}$  (broken vertical line), Lorentzian with harmonic potential and constant friction  $\gamma_{\text{OHs}}$  (gray dotted line), nonharmonic potential and constant friction  $\gamma_{\text{OHs}}$  (blue broken line), harmonic potential and frequency-dependent friction  $\tilde{\Gamma}(f)$  (purple solid line), and nonharmonic potential and frequency-dependent friction  $\tilde{\Gamma}(f)$  (blue solid line). (F) Vibrational power spectrum  $\omega\tilde{\chi}''$  using the nonharmonic potential and different values of the constant friction  $\gamma$ , where  $\gamma_{\text{OHs}} = \tilde{\Gamma}'(f_{\text{OHs}})$  is the friction evaluated at the symmetric OH stretch vibrational frequency. The gray solid line is the spectrum from aiMD simulations.

25 ps *NVT* simulation using an individual thermostat with a time constant of 10 fs for each atom. The *NVE* simulations are each run for 10 ps with a time step of 0.25 fs. The distributions of their initial configurations sample well the equilibrium distributions as shown in section XI of the [Supporting Information](#).

Linear response theory relates the dielectric susceptibility  $\chi(t)$  to the equilibrium autocorrelation of the dipole moment  $C(t) = \langle \mathbf{p}(t)\mathbf{p}(0) \rangle$ , reading in Fourier space<sup>65</sup> (see section I in the [Supporting Information](#))

$$\tilde{\chi}(\omega) = \frac{1}{V\epsilon_0 k_B T} \left( C(0) - i \frac{\omega}{2} \tilde{C}^+(\omega) \right) \quad (6)$$

with system volume  $V$ , thermal energy  $k_B T$ , and vacuum permittivity  $\epsilon_0$ . IR absorption spectra can therefore be calculated straight-forwardly from sufficiently long trajectories from aiMD simulation data using eq 6 and the Wiener–Khinchine relation,<sup>53,66</sup> derived in section XII in the [Supporting Information](#). Quantum corrections have previously been addressed, but are not applied here.<sup>67</sup> The molecular dipole moments are obtained after Wannier-center localization of the electron density at a time resolution of 2 fs. The Wannier centers are assigned to the molecule of the nearest oxygen, which always results in exactly four Wannier centers per water molecule. A charge of  $-2e$  is assigned to each Wannier center, which together with the nuclear charges, reduced by the electronic charges of the inner shells, allows for

the calculation of the dipole moment. The power spectra are smoothed using a Gaussian kernel with width  $10\text{ cm}^{-1}$ . The normal-mode analysis is performed for an energetically minimal configuration of a single  $\text{H}_2\text{O}$  using the implementation in CP2K 4.1 and the same ab initio model as for the aiMD simulation.

## RESULTS AND DISCUSSION

We start with a discussion of the symmetric stretch mode  $d_{\text{OHs}}$ . The potential (which actually corresponds to a free energy)  $U(d_{\text{OHs}})$  from the aiMD simulations for liquid water (gray solid line) is in Figure 3A compared with a nonharmonic fit according to eq 4 (blue broken line); the harmonic contribution is shown as a gray dotted line. The comparison of the liquid and gas-phase bond potentials in Figure 3B shows that the minimum of the potential (i.e., the most probable OH bond length) increases from  $x_0 = 97.50\text{ pm}$  in the gas phase to  $x_0 = 99.25\text{ pm}$  in the liquid; at the same time the harmonic force constant decreases from  $k/k_{\text{B}}T = 0.404\text{ pm}^{-2}$  in the gas phase to  $k/k_{\text{B}}T = 0.274\text{ pm}^{-2}$  in the liquid. This softening of the potential is due to elongation of the bond, caused by hydrogen bonding in the liquid, and will in the absence of frequency-dependent friction effects be shown to induce a pronounced spectral red shift. Furthermore, the potential nonharmonicity increases, as can be seen by comparing the reduced cubic potential coefficient in the liquid phase  $\tilde{k}_3 = k_3/k_{\text{B}}T(k/k_{\text{B}}T)^{-3/2} = -0.0840$  with the value in the gas phase  $\tilde{k}_3 = -0.0485$ .

The time-dependent friction function for the symmetric stretch mode  $\Gamma(t)$  extracted from aiMD simulations (gray line in Figure 3C) shows multiexponential decay characterized by relaxation times from a few femtoseconds to many picoseconds, which is appreciated by comparison with a single-exponential function with decay time  $\tau = 10\text{ fs}$  (dotted blue line, the logarithmic time axis should be noted). This in particular means that  $\Gamma(t)$  accounts for solvent relaxations that are equally fast (adiabatic) and slower (nonadiabatic) compared to the OH vibrational period of about  $10\text{ fs}$ ; one thus expects homogeneous as well as inhomogeneous line broadening to occur, as indeed borne out by our analysis below. The oscillations that appear in  $\Gamma(t)$  at around  $10\text{--}250\text{ fs}$  reflect the dissipative coupling of symmetric stretch vibrations to antisymmetric stretch as well as higher-harmonic bend and librational modes. This is illustrated by the real and imaginary frequency-dependent friction components  $\tilde{\Gamma}'(\omega) + i\tilde{\Gamma}''(\omega) = \int_0^\infty dt e^{i\omega t} \Gamma(t)$  in Figure 3D (solid and broken gray lines, respectively), which exhibit maxima at the OH-stretching and HOH-bending frequencies and also at their higher harmonics.

The friction function thus accounts for the frequency-dependent vibrational energy dissipation of a given vibrational mode within a water molecule as well as into the surrounding water and in particular accounts for resonances between different vibrational modes and their overtones. The resonances contained in the friction function thus are equivalent to Fermi resonances,<sup>32–35</sup> which typically arise in a quantum formulation and in our classical description are caused by nonlinear intra- and intermolecular couplings in the multidimensional potential landscape that describes the nuclear vibrations. Also non-Condon effects, which arise because of modifications of the transition dipole moment of a vibrational mode due to time-dependent changes of the solvation environment of a molecule,<sup>36</sup> are included via the

interplay of the potential  $U(d_{\text{OHs}})$  and the time-dependent friction function  $\Gamma(t)$ . Interestingly, the symmetric stretch shows a much stronger frictional damping at the characteristic frequency of the bending mode than the antisymmetric stretch mode, shown in section XIII of the Supporting Information, which points to a stronger dissipative coupling of bending vibrations with symmetric than with antisymmetric stretch vibrations.

For simulations of the GLE, which are necessary for the analysis of the coupling between nonlinearities in the potential and frequency-dependent friction, we fit  $\tilde{\Gamma}'(\omega)$  by the expression eq 5 with a sum of three exponential and six oscillating functions, see section VIII of the Supporting Information for details. The fit shown in blue in Figure 3C,D describes the simulated friction function equally well in the time as well as in the frequency domain.

The vibrational spectrum of the  $d_{\text{OHs}}$  mode directly extracted from aiMD simulations is shown in Figure 3E as a gray solid line. The simplest possible model for a vibrational line shape is the Lorentzian model eq 3 for a harmonic potential and a constant, frequency-independent friction. Using  $k/k_{\text{B}}T = 0.274\text{ pm}^{-2}$  from the harmonic fit in Figure 3A and the friction  $\gamma_{\text{OHs}} = \tilde{\Gamma}'(f_{\text{OHs}})$  in Figure 3D at the stretch vibrational frequency  $f_{\text{OHs}} = 3390\text{ cm}^{-1}$ , we obtain the gray dotted line in Figure 3E. Compared to the normal-mode frequency of the gas phase, denoted by a vertical green broken line, the Lorentzian is significantly red-shifted by about  $500\text{ cm}^{-1}$ ; the width of the Lorentzian reflects homogeneous line broadening due to adiabatic solvent friction that is described by the frequency-independent constant  $\gamma_{\text{OHs}}$ . Note that the Lorentzian is considerably red-shifted and narrower compared to the spectrum extracted from the aiMD simulation (gray line). Interestingly, the friction  $\gamma_{\text{OHs}}$  that acts at the vibration frequency  $f_{\text{OHs}}$  is about 2 orders of magnitude smaller than the friction in the static limit  $f = 0$ , as seen in Figure 3D, which explains why the stretch vibrational dynamics shown in Figure 1A is rather weakly damped. The vibrational power spectrum in the presence of the full nonharmonic potential  $U(d_{\text{OHs}})$  and constant friction  $\gamma_{\text{OHs}}$ , obtained from numerical simulations of the memoryless Langevin equation (blue broken line, see section IX in the Supporting Information for details), is only slightly red-shifted with respect to the Lorentzian obtained for a harmonic potential, which is expected based on perturbation theory.<sup>4</sup> We conclude that nonlinearities in the potential have for constant friction only an insignificant influence on the line frequency and shape. The peak frequency of a Lorentzian does not depend on the value of the constant friction  $\gamma$  (see section XIV in the Supporting Information), which is approximately true also in the presence of the nonharmonic potential  $U(d_{\text{OHs}})$ , as demonstrated in Figure 3F where spectra from numerical simulations for varying  $\gamma$  are compared. We next check for the influence of time-dependent friction on the spectrum. For a harmonic potential and for frequency-dependent friction, the spectrum is determined analytically by eq 2 and shown in Figure 3E as a purple solid line. A significant blue shift compared to the results for constant friction is obtained, so that the position of the spectrum agrees very well with the simulated spectrum, while the line shape is too narrow. The blue shift can be understood based on simple and rather general analytic arguments, as shown below. The spectrum obtained from the GLE in the presence of the nonharmonic potential  $U(d_{\text{OHs}})$  and time-dependent friction  $\Gamma(t)$ , shown by the blue solid line in Figure 3E (here numerical

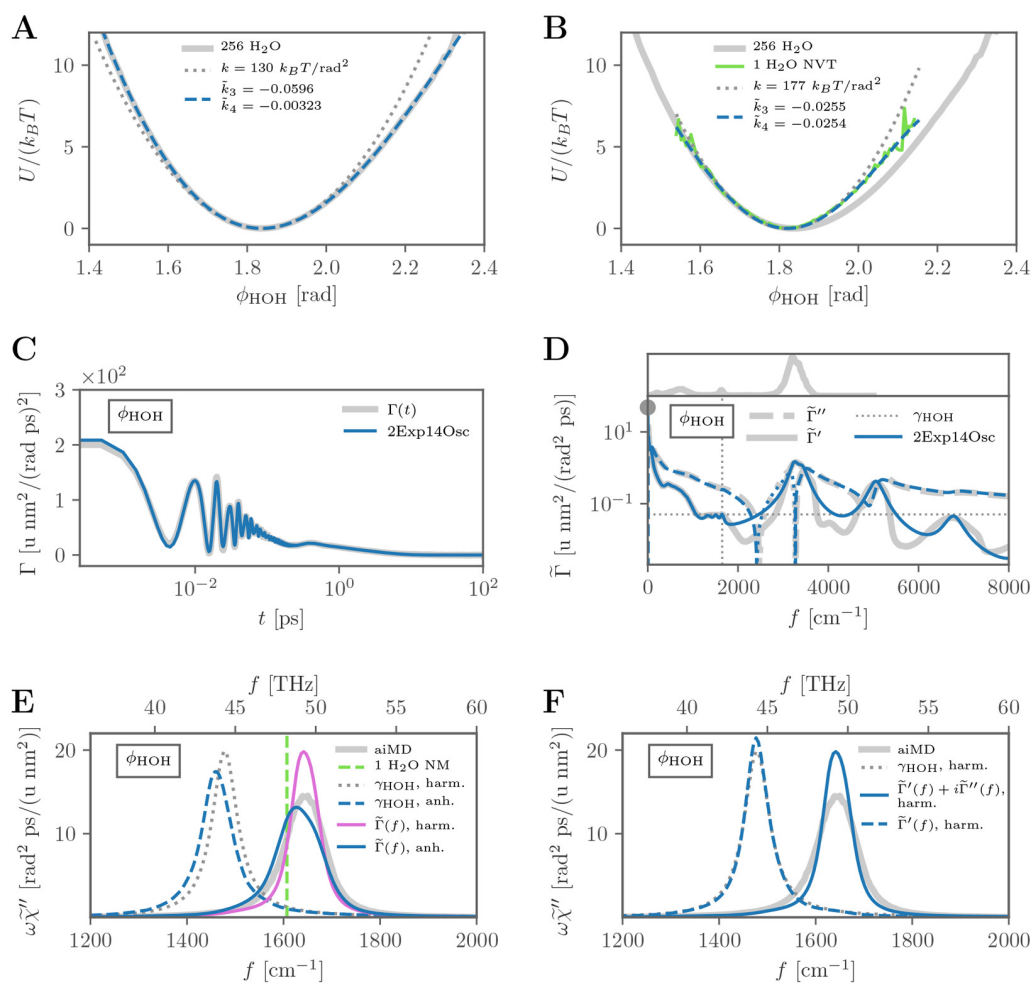


**Figure 4.** Results for the bend coordinate  $\phi_{\text{HOH}}$  from aiMD simulations. (A) Potential  $U(\phi_{\text{HOH}})$  for 256  $\text{H}_2\text{O}$  molecules in the liquid phase (gray solid line) compared to the nonharmonic fit according to eq 4 (blue broken line) and the harmonic part (gray dotted line). (B) Potential  $U(\phi_{\text{HOH}})$  for a single  $\text{H}_2\text{O}$  molecule in the gas phase (green solid line) compared with the nonharmonic fit according to eq 4 (blue broken line) and the harmonic part (gray dotted line). The liquid-phase potential (gray solid line) is shown for comparison. (C and D) Friction as a function of time and frequency (gray lines) compared with the fit according to eq 5 (blue lines). Real and imaginary parts in panel D are shown as solid and broken lines; dotted lines denote negative values of the imaginary part; the spectrum on top is the full absorption spectrum from aiMD. The dotted horizontal line in panel D shows the constant real friction  $\gamma_{\text{HOH}} = \tilde{\Gamma}'(f_{\text{HOH}})$  evaluated at the bend vibrational frequency  $f_{\text{HOH}} = 1650 \text{ cm}^{-1}$ . The gray circle denotes the static friction  $\tilde{\Gamma}''(0)$ . (E) Vibrational power spectrum  $\omega\tilde{\chi}''$  (gray solid line) compared to models of varying complexity: normal mode of single  $\text{H}_2\text{O}$  (broken vertical line), Lorentzian with harmonic potential and constant friction  $\gamma_{\text{HOH}}$  (gray dotted line), nonharmonic potential and constant friction  $\gamma_{\text{HOH}}$  (blue broken line), harmonic potential and frequency-dependent friction  $\tilde{\Gamma}(f)$  (purple solid line), and nonharmonic potential and frequency-dependent friction  $\tilde{\Gamma}(f)$  (blue solid line). (F) Vibrational power spectrum  $\omega\tilde{\chi}''$  using the harmonic potential part and the constant friction  $\gamma_{\text{HOH}}$  (gray dotted line), the real frequency-dependent friction only  $\tilde{\Gamma}'(f)$  (blue broken line), and the real and imaginary frequency-dependent friction  $\tilde{\Gamma}'(f) + i\tilde{\Gamma}''(f)$  (blue solid line). The gray solid line is the spectrum from aiMD simulations.

simulations are employed), is significantly broadened compared to the results obtained for a harmonic potential and time-dependent friction  $\Gamma(t)$  (purple line). This reflects the effects of inhomogeneous line broadening,<sup>4</sup> i.e., the effects of a slowly varying hydration environment of a vibrating bond that elongates or compresses the bond length in conjunction with a nonlinear bond potential, and reproduces the spectrum extracted from the aiMD simulations (gray line) almost perfectly; in fact, inhomogeneous line broadening is quite substantial and accounts for 52% of the total line broadening. This means that the GLE, when used in conjunction with the properly extracted nonharmonic time-averaged potential  $U(d_{\text{OH}_2})$  and time-dependent friction  $\Gamma(t)$ , reproduces the system dynamics very well, which is not guaranteed in general

because the projection onto the GLE neglects nonlinear friction effects.<sup>31</sup>

The  $\phi_{\text{HOH}}$  water bending coordinate is analyzed analogously: The bend angle potential  $U(\phi_{\text{HOH}})$  in Figure 4A extracted from aiMD simulations (gray line) includes significant nonquadratic contributions as appreciated by a comparison of the nonharmonic fit (blue broken line) with the harmonic part (dotted line) and as witnessed by the magnitude of the reduced cubic and quartic fit parameters  $\tilde{k}_3 = -0.0596$  and  $\tilde{k}_4 = k_4/k_B T(k/k_B T)^{-2} = -0.00323$ . Different from the situation for the stretch potential, the liquid environment shifts the most probable bending angle only very slightly. Nevertheless, the potential is softened considerably, as is seen by a comparison of the shape and fit parameters of the gas and liquid-phase potentials  $U(\phi_{\text{HOH}})$  in Figure 4B, which can be

rationalized by the fact that attractive electrostatic interactions, which are predominant for strongly correlated polar liquids such as water, exhibit negative curvature throughout their entire interaction range. The time-dependent friction  $\Gamma(t)$  extracted from the simulations in Figure 4C (gray line) shows a broad decay but more pronounced oscillations compared to the stretch vibrations in Figure 3C. The fit (blue solid line) to the simulated real frequency-dependent friction  $\tilde{\Gamma}'(f)$  (gray solid line) in Figure 4D requires two exponential and 14 oscillatory functions to describe the simulated data satisfactorily, see section VIII in the Supporting Information for details. The dissipative damping is significantly more pronounced at stretch frequencies around 3400  $\text{cm}^{-1}$  and at the overtones of the bending around 3300  $\text{cm}^{-1}$  and around 4950  $\text{cm}^{-1}$  than at the bending fundamental around 1650  $\text{cm}^{-1}$  itself, indicative of the nonlinear coupling between different modes and overtones (where it should be noted that coupling of bend vibrations to higher-frequency modes and overtones are reduced when quantum effects are properly included<sup>16</sup>).

The vibrational spectrum of the  $\phi_{\text{HOH}}$  coordinate from the aiMD simulations is shown in Figure 4E as a gray solid line and is weakly blue-shifted from the gas-phase normal mode (vertical green broken line), which is a surprising fact and will be explained now by compensatory potential and friction effects. The spectrum from the Lorentzian model eq 3 (gray dotted line) using only the harmonic potential part of  $U(\phi_{\text{HOH}})$  and the frequency-independent friction  $\gamma_{\text{HOH}} = \tilde{\Gamma}'(f_{\text{HOH}})$ , obtained at the bending peak at  $f_{\text{HOH}} = 1650 \text{ cm}^{-1}$  (horizontal broken line in Figure 4D), is significantly red-shifted and is not modified much by including the non-harmonic potential contributions (blue broken line). Upon including the complex frequency-dependent friction  $\tilde{\Gamma}(f)$  but only the harmonic part of  $U(\phi_{\text{HOH}})$ , the purple line is obtained, which is blue-shifted with respect to the constant-friction case and reaches the frequency of the simulated curve but is too narrow. Including the complex frequency-dependent friction  $\tilde{\Gamma}(f)$  and also the full nonharmonic potential  $U(\phi_{\text{HOH}})$ , the GLE (indicated by the blue line) rather accurately reproduces the position and width of the simulated spectrum. In agreement with our stretch-vibration results in Figure 3E, we detect considerable inhomogeneous line broadening (amounting to 47% of the total line broadening) from the comparison of the results with and without nonharmonic potential contributions in the presence of frequency-dependent friction. In contrast to the stretch–vibration results, we see that the blue shift induced by including the frequency dependence of the friction almost exactly cancels the red shift due to the softening of the bond potential in the liquid phase, which means that the frequency dependence of  $\tilde{\Gamma}(f)$  close to the characteristic bend-mode frequency is more pronounced compared to the stretch mode. It transpires that the fine details of the frequency dependence of the friction at the vibrational frequency determine vibrational line shape and position, which we now analyze in more detail.

It turns out that the imaginary and real parts of the frequency-dependent friction influence the line position and shape quite differently.<sup>26</sup> This is illustrated in Figure 4F by comparing spectra using only the harmonic part of the potential for constant friction (gray dotted line), for purely real frequency-dependent friction  $\tilde{\Gamma}'(f)$  (blue broken line), and for friction that contains both real and imaginary frequency-dependent parts  $\tilde{\Gamma}'(f) + i\tilde{\Gamma}''(f)$  (blue solid line), note that for purely imaginary friction the spectrum according to eq 2

exhibits a singularity and thus is not shown. It is in fact the imaginary part  $\tilde{\Gamma}''(f)$  that gives rise to the blue shift, as is now explained by a simple analytical argument.

For this we consider a single-exponential memory function  $\Gamma(t) = \gamma\tau^{-1} \exp(-t/\tau)$ . The single-sided Fourier transform is given as  $\tilde{\Gamma}(\omega) = \int_0^\infty dt e^{i\omega t} \Gamma(t) = \gamma/(1 - i\tau\omega)$  with the asymptotic limits  $\tilde{\Gamma}(\omega) \simeq \gamma(1 + i\omega\tau)$  for small  $\omega$  and  $\tilde{\Gamma}(\omega) \simeq i\gamma/(\omega\tau)$  for large  $\omega$ ; both deviations from the zero-frequency limit  $\tilde{\Gamma}(\omega \rightarrow 0) \simeq \gamma$  turn out to be imaginary, which already hints at why the imaginary part of the friction determines the line position, as demonstrated in Figure 4F. A general form that contains both asymptotic limits is given by  $\tilde{\Gamma}(\omega) \simeq \gamma + ia\omega + ib/\omega$ , where  $a = \gamma\tau$  and  $b = 0$  for small  $\omega$  and  $a = 0$  and  $b = \gamma/\tau$  for large  $\omega$ . By inserting this asymptotic form into eq 2, the Lorentzian line shape eq 3 is recovered but with an effective mass  $m_{\text{eff}} = m - a$  and an effective potential curvature  $k_{\text{eff}} = k + b$ . The vibrational frequency turns out to be

$$\omega_0 = \sqrt{\frac{k_{\text{eff}}}{m_{\text{eff}}}} = \sqrt{\frac{k + b}{m - a}} \quad (7)$$

and in fact increases both in the small and large frequency limits, because  $a$  and  $b$  are positive constants for single-exponential memory. Thus, a blue shift of the vibrational frequency is very generally expected for frequencies where the frequency-dependent friction is described by the asymptotic form  $\tilde{\Gamma}(\omega) \simeq \gamma + ia\omega + ib/\omega$  with positive  $a$  and  $b$ . In fact, this functional form is able to describe the stretch and band friction functions rather accurately around the stretch and band frequencies, respectively, as inspection of Figures 3D and 4D shows. In other words, frequency-dependent friction can lead to a blue shift of a vibrational band irrespective of whether the imaginary friction function decreases or increases in the vicinity of the vibrational band.

The full width at half-maximum of a Lorentzian is given as  $\gamma/m_{\text{eff}} \simeq \gamma/(m - a)$ ; thus, the line width is, within the harmonic approximation, predicted to slightly increase for the stretch band (because  $\tilde{\Gamma}''(f)$  slightly increases at the stretch vibrational frequency in Figure 3D and thus  $a$  is positive) but to stay rather constant for the bend band (because  $\tilde{\Gamma}''(f)$  slightly decreases at the bend vibrational frequency Figure 4D and thus  $a$  presumably is small and dominated by  $b$ ). These predictions are in good agreement with the results shown in Figures 3E and 4E for the scenario of a harmonic potential and friction-dependent friction (purple lines). Clearly, the exact line shape and position are determined by the interplay of nonlinearities of the potential and frequency-dependent friction, which can be accessed only by simulations or perturbation theory, but the simple harmonic model discussed here allows appreciation of part of the mechanisms at play.

## CONCLUSIONS

Frequency-independent friction, which reflects the fast adiabatic dissipative channels available for a specific vibrational mode, modifies the vibrational spectral line width via homogeneous line broadening but not the line position. This is strictly true for a harmonic potential but holds approximately even in the presence of nonharmonic potential contributions, as we demonstrate in Figure 3F. On the other hand, the full frequency dependence of the friction, which in particular accounts for the slower solvent relaxation processes, gives rise to a spectral blue shift and additional line broadening. The latter reflects what is typically called inhomogeneous line



broadening. In contrast, softening of the bond potential in the liquid environment, which is due to hydrogen bonding and hydration interactions, gives rise to a red shift. Therefore, we find that the line shapes and positions of the bend and stretch bands in liquid water can be interpreted in terms of the compensatory effects of frequency-dependent friction and harmonic as well as nonharmonic potential contributions. For stretch vibrations, the bond softening dominates and therefore the stretch vibration is red-shifted when going from gas to liquid water. For bend vibrations the potential-induced red shift and the friction-induced blue shift almost exactly compensate. This of course does not imply that the coupling of bend vibrations to the hydrating liquid environment is weaker than for stretch vibrations, as one might naively guess from only looking at the frequency shifts. Rather, the contrary is true. It turns out that it is the imaginary part of the frequency-dependent friction that gives rise to the blue shift, in line with previous arguments.<sup>28</sup> The situation is rather complex, though, because the effects due to the frequency-dependency of the friction and due to nonlinearities in the potential do not decouple.

Our methodology is different from previous approaches to describe the infrared line shapes of water<sup>6,68</sup> because we deploy the time-averaged bond potential as it naturally emerges via the projection formalism used to derive the GLE. This in particular means that in our approach, inhomogeneous line broadening enters via the time-dependent friction function, not via a time-dependent bond potential, as in previous theories.

The GLE framework we use to derive the time- or frequency-dependent friction function is not constrained to nuclear reaction coordinates that describe the vibrations of a single molecule, which forms the topic of this paper. Rather, electronic polarization degrees of freedom can be included as well and also collective effects that stem from dipolar correlations between neighboring molecules can be accounted for by suitable reaction coordinates. Likewise, it would be interesting to model Raman spectra, which reveal a perspective on the vibrational molecular modes that is very different from IR spectroscopy.<sup>69</sup>

As mentioned before, our ab initio simulations neglect nuclear quantum effects, owing to the fact that methods to extract friction functions from path-integral simulations are not yet available. This approximation presumably is permissible in the present context, as we target the general compensatory effects the liquid environment has on bond potentials and the bond friction function, which should not be fundamentally changed by nuclear quantum effects. This is corroborated by results by Marsalek and Markland,<sup>49</sup> who reported a red shift of the OH peak by about 200 cm<sup>-1</sup> and of the HOH bend peak by about 50 cm<sup>-1</sup> upon inclusion of nuclear quantum effects in their simulations, which are somewhat smaller than the shifts due to potential and frequency-dependent friction effects we find here. Nonetheless, in the future, it would be highly desirable to develop techniques that would allow extracting GLE parameters from path integral simulations<sup>48,49</sup> and from mixed quantum/classical approaches.<sup>32,34,70</sup>

## ■ ASSOCIATED CONTENT

### SI Supporting Information

The Supporting Information is available free of charge at <https://pubs.acs.org/doi/10.1021/acs.jpcc.1c09481>.

Detailed derivations, analysis procedures, additional data, and discussion (PDF)

## ■ AUTHOR INFORMATION

### Corresponding Author

Roland R. Netz – Freie Universität Berlin, 14195 Berlin, Germany; [orcid.org/0000-0003-0147-0162](https://orcid.org/0000-0003-0147-0162); Email: [rnetz@physik.fu-berlin.de](mailto:rnetz@physik.fu-berlin.de)

### Authors

Florian N. Brüning – Freie Universität Berlin, 14195 Berlin, Germany

Otto Geburtig – Freie Universität Berlin, 14195 Berlin, Germany

Alexander von Canal – Freie Universität Berlin, 14195 Berlin, Germany

Julian Kappler – Freie Universität Berlin, 14195 Berlin, Germany

Complete contact information is available at: <https://pubs.acs.org/10.1021/acs.jpcc.1c09481>

### Notes

The authors declare no competing financial interest.

## ■ ACKNOWLEDGMENTS

We thank M. Bonn, W. Eaton and T. Elsaesser for enjoyable and useful discussions and comments. We gratefully acknowledge support by the Deutsche Forschungsgemeinschaft (DFG) Grants SFB 1078 and SFB 1114; the MaxWater initiative from the Max Planck Society; the European Research Council (ERC) Advanced Grant NoMaMemo Grant No. 835117; computing time on the HPC cluster at ZEDAT, FU Berlin; and the computational resources provided by the North-German Supercomputing Alliance (HLRN) under project bep00068.

## ■ REFERENCES

- (1) Falk, M. The frequency of the HOH bending fundamental in solids and liquids. *Spectrochim. Acta Part A Mol. Spectrosc.* **1984**, *40*, 43–48.
- (2) Bakker, H. J.; Skinner, J. L. Vibrational spectroscopy as a probe of structure and dynamics in liquid water. *Chem. Rev.* **2010**, *110*, 1498–1517.
- (3) Perakis, F.; De Marco, L.; Shalit, A.; Tang, F.; Kann, Z. R.; Kühne, T. D.; Torre, R.; Bonn, M.; Nagata, Y. Vibrational spectroscopy and dynamics of water. *Chem. Rev.* **2016**, *116*, 7590–7607.
- (4) Oxtoby, D. W.; Levesque, D.; Weis, J. J. A molecular dynamics simulation of dephasing in liquid nitrogen. *J. Chem. Phys.* **1978**, *68*, 5528–5533.
- (5) Møller, K. B.; Rey, R.; Hynes, J. T. Hydrogen bond dynamics in water and ultrafast infrared spectroscopy: A theoretical study. *J. Phys. Chem. A* **2004**, *108*, 1275–1289.
- (6) Auer, B. M.; Skinner, J. L. IR and Raman spectra of liquid water: Theory and interpretation. *J. Chem. Phys.* **2008**, *128*, 224511.
- (7) Woutersen, S.; Bakker, H. J. Resonant intermolecular transfer of vibrational energy in liquid water. *Nature* **1999**, *402*, 507–509.
- (8) Lock, A. J.; Bakker, H. J. Temperature dependence of vibrational relaxation in liquid H<sub>2</sub>O. *J. Chem. Phys.* **2002**, *117*, 1708–1713.
- (9) Cowan, M. L.; Bruner, B. D.; Huse, N.; Dwyer, J. R.; Chugh, B.; Nibbering, E. T.; Elsaesser, T.; Miller, R. J. Ultrafast memory loss and energy redistribution in the hydrogen bond network of liquid H<sub>2</sub>O. *Nature* **2005**, *434*, 199–202.
- (10) Badger, R. M. A relation between internuclear distances and bond force constants. *J. Chem. Phys.* **1934**, *2*, 128–131.

- (11) Mikenda, W. Stretching frequency versus bond distance correlation of O–D(H) ... Y (Y = N, O, S, Se, Cl, Br, I) hydrogen bonds in solid hydrates. *J. Mol. Struct.* **1986**, *147*, 1–15.
- (12) Boyer, M. A.; Marsalek, O.; Heindel, J. P.; Markland, T. E.; McCoy, A. B.; Xantheas, S. S. Beyond Badger's rule: The origins and generality of the structure-spectra relationship of aqueous hydrogen bonds. *J. Phys. Chem. Lett.* **2019**, *10*, 918–924.
- (13) Ashihara, S.; Huse, N.; Espagne, A.; Nibbering, E. T.; Elsaesser, T. Vibrational couplings and ultrafast relaxation of the O–H bending mode in liquid H<sub>2</sub>O. *Chem. Phys. Lett.* **2006**, *424*, 66–70.
- (14) Van Der Post, S. T.; Hsieh, C.-S. S.; Okuno, M.; Nagata, Y.; Bakker, H. J.; Bonn, M.; Hunger, J. Strong frequency dependence of vibrational relaxation in bulk and surface water reveals sub-picosecond structural heterogeneity. *Nat. Commun.* **2015**, *6*, 8384.
- (15) Ashihara, S.; Huse, N.; Espagne, A.; Nibbering, E. T.; Elsaesser, T. Ultrafast structural dynamics of water induced by dissipation of vibrational energy. *J. Phys. Chem. A* **2007**, *111*, 743–746.
- (16) Rey, R.; Ingrassio, F.; Elsaesser, T.; Hynes, J. T. Pathways for H<sub>2</sub>O bend vibrational relaxation in liquid water. *J. Phys. Chem. A* **2009**, *113*, 8949–8962.
- (17) Yu, C.-C. C.; Chiang, K.-Y. Y.; Okuno, M.; Seki, T.; Ohto, T.; Yu, X.; Korepanov, V.; Hamaguchi, H.-o. o.; Bonn, M.; Hunger, J.; et al. Vibrational couplings and energy transfer pathways of water's bending mode. *Nat. Commun.* **2020**, *11*, 5977.
- (18) Ma, A.; Stratt, R. M. Multiphonon vibrational relaxation in liquids: Should it lead to an exponential-gap law? *J. Chem. Phys.* **2004**, *121*, 11217–11226.
- (19) Lange, O. F.; Grubmüller, H. Collective Langevin dynamics of conformational motions in proteins. *J. Chem. Phys.* **2006**, *124*, 214903.
- (20) Horenko, I.; Hartmann, C.; Schütte, C.; Noe, F. Data-based parameter estimation of generalized multidimensional Langevin processes. *Phys. Rev. E* **2007**, *76*, 016706.
- (21) Darve, E.; Solomon, J.; Kia, A. Computing generalized Langevin equations and generalized Fokker-Planck equations. *Proc. Natl. Acad. Sci. U. S. A.* **2009**, *106*, 10884–10889.
- (22) Lesnicki, D.; Vuilleumier, R.; Carof, A.; Rotenberg, B. Molecular hydrodynamics from memory kernels. *Phys. Rev. Lett.* **2016**, *116*, 147804.
- (23) Deichmann, G.; Van der Vegt, N. F. Bottom-up approach to represent dynamic properties in coarse-grained molecular simulations. *J. Chem. Phys.* **2018**, *149*, 244114.
- (24) Jung, G.; Hanke, M.; Schmid, F. Generalized Langevin dynamics: construction and numerical integration of non-Markovian particle-based models. *Soft Matter* **2018**, *14*, 9368–9382.
- (25) Meyer, H.; Voigtmann, T.; Schilling, T. On the dynamics of reaction coordinates in classical, time-dependent, many-body processes. *J. Chem. Phys.* **2019**, *150*, 174118.
- (26) Metiu, H.; Oxtoby, D. W.; Freed, K. F. Hydrodynamic theory for vibrational relaxation in liquids. *Phys. Rev. A* **1977**, *15*, 361–371.
- (27) Whitnell, R. M.; Wilson, K. R.; Hynes, J. T. Vibrational relaxation of a dipolar molecule in water. *J. Chem. Phys.* **1992**, *96*, 5354–5369.
- (28) Tuckerman, M.; Berne, B. J. Vibrational relaxation in simple fluids: Comparison of theory and simulation. *J. Chem. Phys.* **1993**, *98*, 7301–7318.
- (29) Gnanakaran, S.; Hochstrasser, R. M. Vibrational relaxation of HgI in ethanol: Equilibrium molecular dynamics simulations. *J. Chem. Phys.* **1996**, *105*, 3486–3496.
- (30) Joutsuka, T.; Ando, K. Vibrational spectroscopy and relaxation of an anharmonic oscillator coupled to harmonic bath. *J. Chem. Phys.* **2011**, *134*, 204511.
- (31) Gottwald, F.; Ivanov, S. D.; Kühn, O. Applicability of the Caldeira-Leggett model to vibrational spectroscopy in solution. *J. Phys. Chem. Lett.* **2015**, *6*, 2722–2727.
- (32) Lawrence, C. P.; Skinner, J. L. Vibrational spectroscopy of HOD in liquid D<sub>2</sub>O. VI. Intramolecular and intermolecular vibrational energy flow. *J. Chem. Phys.* **2003**, *119*, 1623–1633.
- (33) Ramasesha, K.; De Marco, L.; Mandal, A.; Tokmakoff, A. Water vibrations have strongly mixed intra- and intermolecular character. *Nat. Chem.* **2013**, *5*, 935–940.
- (34) Kananenka, A. A.; Skinner, J. L. Fermi resonance in OH-stretch vibrational spectroscopy of liquid water and the water hexamer. *J. Chem. Phys.* **2018**, *148*, 244107.
- (35) Matt, S. M.; Ben-Amotz, D. Influence of intermolecular coupling on the vibrational spectrum of water. *J. Phys. Chem. B* **2018**, *122*, 5375–5380.
- (36) Schmidt, J. R.; Corcelli, S. A.; Skinner, J. L. Pronounced non-Condor effects in the ultrafast infrared spectroscopy of water. *J. Chem. Phys.* **2005**, *123*, 044513.
- (37) De Marco, L.; Carpenter, W.; Liu, H.; Biswas, R.; Bowman, J. M.; Tokmakoff, A. Differences in the vibrational dynamics of H<sub>2</sub>O and D<sub>2</sub>O: Observation of symmetric and antisymmetric stretching vibrations in heavy water. *J. Phys. Chem. Lett.* **2016**, *7*, 1769–1774.
- (38) Carpenter, W. B.; Fournier, J. A.; Biswas, R.; Voth, G. A.; Tokmakoff, A. Delocalization and stretch-bend mixing of the HOH bend in liquid water. *J. Chem. Phys.* **2017**, *147*, 084503.
- (39) Ojha, D.; Karhan, K.; Kühne, T. D. On the hydrogen bond strength and vibrational spectroscopy of liquid water. *Sci. Rep.* **2018**, *8*, 16888.
- (40) Daldrop, J. O.; Kappler, J.; Brünig, F. N.; Netz, R. R. Butane dihedral angle dynamics in water is dominated by internal friction. *Proc. Natl. Acad. Sci. U. S. A.* **2018**, *115*, 5169–5174.
- (41) Stenger, J.; Madsen, D.; Hamm, P.; Nibbering, E. T.; Elsaesser, T. Ultrafast vibrational dephasing of liquid water. *Phys. Rev. Lett.* **2001**, *87*, 027401.
- (42) Chuntunov, L.; Kumar, R.; Kuroda, D. G. Non-linear infrared spectroscopy of the water bending mode: Direct experimental evidence of hydration shell reorganization? *Phys. Chem. Chem. Phys.* **2014**, *16*, 13172–13181.
- (43) Bertie, J. E.; Lan, Z. Infrared intensities of liquids XX: The intensity of the OH stretching band of liquid water revisited, and the best current values of the optical constants of H<sub>2</sub>O(l) at 25°C between 15,000 and 1 cm<sup>-1</sup>. *Appl. Spectrosc.* **1996**, *50*, 1047–1057.
- (44) Bertie, J. E.; Ahmed, M. K.; Eysel, H. H. Infrared intensities of liquids. 5. Optical and dielectric constants, integrated intensities, and dipole moment derivatives of H<sub>2</sub>O and D<sub>2</sub>O at 22°C. *J. Phys. Chem.* **1989**, *93*, 2210–2218.
- (45) Silvestrelli, P. L.; Bernasconi, M.; Parrinello, M. Ab initio infrared spectrum of liquid water. *Chem. Phys. Lett.* **1997**, *277*, 478–482.
- (46) Heyden, M.; Sun, J.; Funkner, S.; Mathias, G.; Forbert, H.; Havenith, M.; Marx, D. Dissecting the THz spectrum of liquid water from first principles via correlations in time and space. *Proc. Natl. Acad. Sci. U. S. A.* **2010**, *107*, 12068–12073.
- (47) Schulz, R.; von Hansen, Y.; Daldrop, J. O.; Kappler, J.; Noé, F.; Netz, R. R. Collective hydrogen-bond rearrangement dynamics in liquid water. *J. Chem. Phys.* **2018**, *149*, 244504.
- (48) Habershon, S.; Markland, T. E.; Manolopoulos, D. E. Competing quantum effects in the dynamics of a flexible water model. *J. Chem. Phys.* **2009**, *131*, 024501.
- (49) Marsalek, O.; Markland, T. E. Quantum dynamics and spectroscopy of ab Initio liquid water: The interplay of nuclear and electronic quantum effects. *J. Phys. Chem. Lett.* **2017**, *8*, 1545–1551.
- (50) Markland, T. E.; Ceriotti, M. Nuclear quantum effects enter the mainstream. *Nat. Rev. Chem.* **2018**, *2*, 0109.
- (51) Fraley, P. E.; Narahari Rao, K. High resolution infrared spectra of water vapor:  $\nu_1$  and  $\nu_3$  band of H<sub>2</sub><sup>18</sup>O. *J. Mol. Spectrosc.* **1969**, *29*, 348–364.
- (52) McClatchey, R. A.; Benedict, W. S.; Clough, S.; Burch, D.; Calfee, R. F.; Fox, K.; Rothman, L. S.; Garing, J. S. AFCRL atmospheric absorption line parameters compilation. *Environ. Res. Pap.* **1973**, *434*, 1–78.
- (53) Carlson, S.; Brünig, F. N.; Loche, P.; Bonthuis, D. J.; Netz, R. R. Exploring the absorption spectrum of simulated water from MHz to infrared. *J. Phys. Chem. A* **2020**, *124*, 5599–5605.

(54) Zhang, C.; Guidoni, L.; Kühne, T. D. Competing factors on the frequency separation between the OH stretching modes in water. *J. Mol. Liq.* **2015**, *205*, 42–45.

(55) Zwanzig, R. Memory effects in irreversible thermodynamics. *Phys. Rev.* **1961**, *124*, 983–992.

(56) Mori, H. Transport, collective motion, and Brownian motion. *Prog. Theor. Phys.* **1965**, *33*, 423–455.

(57) *Infrared and Raman spectroscopy: Methods and applications*; Schrader, B., Ed.; Wiley-VCH: New York, 1995.

(58) Marchesoni, F.; Grigolini, P. On the extension of the Kramers theory of chemical relaxation to the case of nonwhite noise. *J. Chem. Phys.* **1983**, *78*, 6287–6298.

(59) Morrone, J. A.; Markland, T. E.; Ceriotti, M.; Berne, B. J. Efficient multiple time scale molecular dynamics: Using colored noise thermostats to stabilize resonances. *J. Chem. Phys.* **2011**, *134*, 014103.

(60) Lee, H. S.; Ahn, S. H.; Darve, E. F. The multi-dimensional generalized Langevin equation for conformational motion of proteins. *J. Chem. Phys.* **2019**, *150*, 174113.

(61) Hutter, J.; Iannuzzi, M.; Schiffmann, F.; Vandevondele, J. CP2K: Atomistic simulations of condensed matter systems. *Wiley Interdiscip. Rev. Comput. Mol. Sci.* **2014**, *4*, 15–25.

(62) VandeVondele, J.; Hutter, J. Gaussian basis sets for accurate calculations on molecular systems in gas and condensed phases. *J. Chem. Phys.* **2007**, *127*, 114105.

(63) Grimme, S.; Antony, J.; Ehrlich, S.; Krieg, H. A consistent and accurate ab initio parametrization of density functional dispersion correction (DFT-D) for the 94 elements H-Pu. *J. Chem. Phys.* **2010**, *132*, 154104.

(64) Bussi, G.; Donadio, D.; Parrinello, M. Canonical sampling through velocity rescaling. *J. Chem. Phys.* **2007**, *126*, 014101.

(65) Kubo, R. Statistical-mechanical theory of irreversible processes. I. General theory and simple applications to magnetic and conduction problems. *J. Phys. Soc. Jpn.* **1957**, *12*, 570–586.

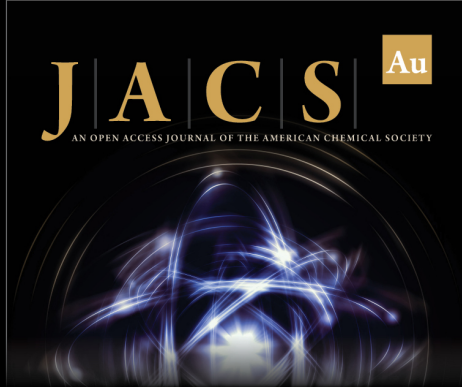
(66) Wiener, N. Generalized harmonic analysis. *Acta Math.* **1930**, *55*, 117–258.

(67) Ramírez, R.; López-Ciudad, T.; Kumar P, P.; Marx, D. Quantum corrections to classical time-correlation functions: Hydrogen bonding and anharmonic floppy modes. *J. Chem. Phys.* **2004**, *121*, 3973–3983.

(68) Ni, Y.; Skinner, J. L. IR and SFG vibrational spectroscopy of the water bend in the bulk liquid and at the liquid-vapor interface, respectively. *J. Chem. Phys.* **2015**, *143*, 014502.


(69) Torii, H. Time-domain calculations of the polarized Raman spectra, the transient infrared absorption anisotropy, and the extent of delocalization of the OH stretching mode of liquid water. *J. Phys. Chem. A* **2006**, *110*, 9469–9477.


(70) Medders, G. R.; Paesani, F. Infrared and raman spectroscopy of liquid water through "first-principles" many-body molecular dynamics. *J. Chem. Theory Comput.* **2015**, *11*, 1145–1154.



**JACS** Au  
AN OPEN ACCESS JOURNAL OF THE AMERICAN CHEMICAL SOCIETY

Editor-in-Chief  
**Prof. Christopher W. Jones**  
Georgia Institute of Technology, USA

**Open for Submissions** 

pubs.acs.org/jacsau  ACS Publications  
Most Trusted. Most Cited. Most Read.

# Barrier-Crossing Times for Different Non-Markovian Friction in Well and Barrier: A Numerical Study

---

# 6

by Florian N. Brünig, Roland R. Netz, and Julian Kappler

**Contributions:** F.N.B., R.R.N., and J.K. conceived the theory and designed the simulations. F.N.B. and J.K. performed simulations. F.N.B. analyzed the data. All authors discussed the results, analyses, and interpretations. F.N.B. and J.K. wrote the paper with input from all authors.

**Bibliographic information:** This chapter has previously been published in *Physical Review E* by the American Physical Society (APS) as open access under the Creative Commons CC BY licence (<http://creativecommons.org/licenses/by/4.0/>) [3].

<https://doi.org/10.1103/PhysRevE.106.044133>

**Barrier-crossing times for different non-Markovian friction in well and barrier: A numerical study**Florian N. Brüning<sup>1</sup>, Roland R. Netz<sup>1</sup>, and Julian Kappler<sup>2,\*</sup><sup>1</sup>*Department of Physics, Freie Universität Berlin, 14195 Berlin, Germany*<sup>2</sup>*Department of Applied Mathematics and Theoretical Physics, Centre for Mathematical Sciences, University of Cambridge, Wilberforce Road, Cambridge CB3 0WA, United Kingdom*

(Received 3 May 2022; accepted 21 July 2022; published 24 October 2022)

We introduce a generalized Langevin model system for different non-Markovian effects in the well and barrier regions of a potential, and use it to numerically study the barrier-crossing time. In the appropriate limits, our model interpolates between the theoretical barrier-crossing-time predictions by Grote and Hynes (GH), as well as by Pollak *et al.*, which for a single barrier memory time can differ by several orders of magnitude. Our model furthermore allows one to test an analytic rate theory for space-inhomogeneous memory, which disagrees with our numerical results in the long well-memory regime. In this regime, we find that short barrier memory decreases the barrier-crossing time as compared to long barrier memory. This is in contrast with the short well-memory regime, where both our numerical results and the GH theory predict an acceleration of the barrier crossing time with increasing barrier memory time. Both effects, the “Markovian-barrier acceleration” and GH “non-Markovian-barrier acceleration,” can be understood from a committor analysis. Our model combines finite relaxation times of orthogonal degrees of freedom with a space-inhomogeneous coupling to such degrees and represents a step towards more realistic modeling of reaction coordinates.

DOI: [10.1103/PhysRevE.106.044133](https://doi.org/10.1103/PhysRevE.106.044133)**I. INTRODUCTION**

Many physical systems are comprised of large numbers of interacting degrees of freedom. A standard approach towards understanding dynamics in such systems is to define a low-dimensional reaction coordinate, motivated by the phenomenon to be investigated, and to construct an effective model for the dynamics of this reaction coordinate [1–10]. Hereby, the orthogonal degrees of freedom are subsumed into an effective heat bath, which interacts with the reaction coordinate [1–4]. One is then typically interested in the long-time dynamics of the reaction coordinate and in particular rare events such as barrier-crossing phenomena characterized by mean first-passage times (MFPTs),  $\tau_{\text{MFP}}$  [7,11–18]. Systems where this approach has been applied are molecules in solution, which show conformational transitions, for example, protein folding [7,19–22], chemical reactions, where the reaction coordinate characterizes the transition from reactants to products [13,23–28], and vibrational spectroscopy [29,30].

If the dissipative coupling between reaction coordinate and heat bath is assumed linear, the dynamics is described by an approximate version of the generalized Langevin equation (GLE), with memory effects due to the finite relaxation time of the heat bath [2,31]. However, in many physical sys-

tems the dissipative interaction between reaction coordinate and heat bath depends nonlinearly on the current state of the reaction coordinate [3]. For example, a small molecule traversing a membrane separating two different fluids, as illustrated in Fig. 1(a), clearly interacts with different orthogonal degrees of freedom, namely, fluid or membrane molecules, depending on where it is currently located. As a second example, a reaction coordinate describing the folding of a protein is expected to experience different friction depending on whether the protein is unfolded or folded. Even for a single confined solute particle in a fluid, the nonlinear dissipative interaction of the particle and its surrounding fluid molecules leads to confinement-dependent memory effects [32]; for colloidal particles in a viscoelastic fluid, such nonlinear solute-solvent interactions have been observed experimentally [33].

The first analytical relation between the friction magnitude and the barrier-crossing time was derived by Kramers [11]. Kramers considered the memoryless, i.e., Markovian, Langevin equation with homogeneous friction magnitude. He showed that, while in the high-friction limit  $\tau_{\text{MFP}}$  scales linearly with the friction, in the low-friction scenario  $\tau_{\text{MFP}}$  scales linearly with the inverse of the friction magnitude. The crossover between these two asymptotic results was eventually bridged by a theory due to Melnikov and Meshkov [15] (MM), which is valid for all values of the friction magnitude.

For the scenario where there is no timescale separation between heat bath and reaction coordinate, so that non-Markovian memory effects are relevant, the first theory to describe barrier-crossing times is due to Grote and Hynes (GH) [13]. In their theory, only the local memory effects in the barrier region are taken into account, and away from the barrier region the reaction coordinate is assumed Markovian.

\*Corresponding author: [jkappler@posteo.de](mailto:jkappler@posteo.de)

Published by the American Physical Society under the terms of the [Creative Commons Attribution 4.0 International](https://creativecommons.org/licenses/by/4.0/) license. Further distribution of this work must maintain attribution to the author(s) and the published article's title, journal citation, and DOI.

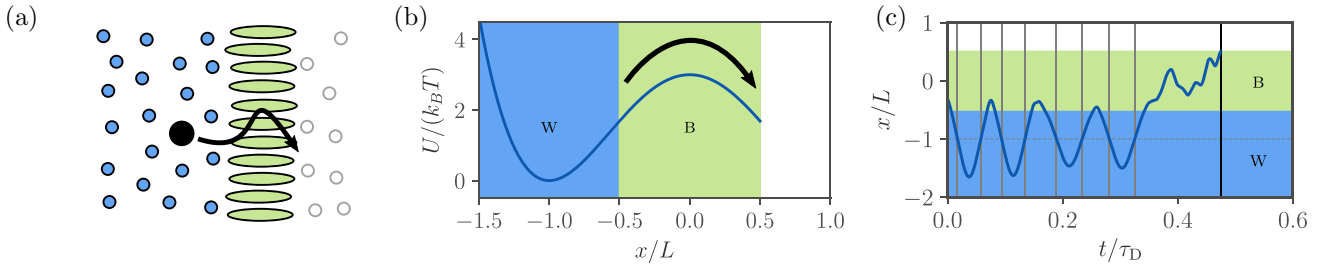


FIG. 1. (a) The dynamics of a particle diffusing through a membrane, separating different solvent species, serves as an illustrative example for space-inhomogeneous friction effects. (b) The truncated quartic potential Eq. (5) is used to model barrier-crossing dynamics. The colors indicate regions  $X_i$  with different local friction. (c) Example trajectory, simulated using single-exponentially decaying locally coupled memory-friction components, Eq. (6), with  $\tau_W/\tau_D = 1$  and  $\tau_B/\tau_D = 0.01$ , that together form the friction kernel of Eq. (2). The coupling function  $\chi_i(x)$  is given by Eq. (3) for the regions  $X_i$ , also shown in (b). The mean first-passage time (MFPT),  $\tau_{\text{MFP}}$ , for barrier crossing is defined as the average of all time differences between crossings of the well bottom at  $x/L = -1$  (shown as vertical gray solid lines) to the escape at the boundary at  $x/L = 0.5$  (shown as a vertical black solid line).

For the case of homogenous memory effects throughout the well and barrier regions, Pollack, Grabert, and Hänggi (PGH) derived  $\tau_{\text{MFP}}$ , which for long memory scales quadratically with the memory time, so that the former can exceed the latter by orders of magnitude [34]. For the special case of a single-exponential memory function, the quadratic scaling of  $\tau_{\text{MFP}}$  with memory time was also derived analytically from a harmonic approximation, and a simple heuristic formula which reproduces the results of the PGH theory was proposed [35]. Importantly, for systems with long memory, the predictions of the barrier-crossing time by the PGH and GH theories differ by many orders of magnitude. Evidently it is crucial whether the coupling between reaction coordinate and heat bath is linear throughout well and barrier region (homogeneous friction) or nonlinear and thus different in well and barrier region (space-inhomogeneous friction) [35,36].

For homogeneous friction, there exist numerical studies of barrier crossing considering both single-timescale memory [7,35,37–39], as well as the implications of several memory timescales [21,40]. Models incorporating space-inhomogeneous friction have so far mostly been studied in the double limit where inertial and memory effects are negligible and can thus be modeled via an overdamped Langevin equation [41] or the equivalent Fokker-Planck equation [42,43]. However, this limit is subtle, as non-Markovian memory effects can generate spurious space-inhomogeneous friction if interpreted in terms of a Markovian model [22]. For space-inhomogeneous memory friction magnitude with a single homogeneous timescale, some works observed significant deviations of  $\tau_{\text{MFP}}$  in both analytic theory and simulations when compared to the space-homogeneous case [44–46]. The implications of space-inhomogeneous memory timescales in the well and barrier regions on the global barrier-crossing dynamics have so far been addressed only by an analytical model [47–49] which bridges the GH and PGH scenarios in certain limits. However, this model has never been challenged by numerical simulations.

We here present a model system to study space-inhomogeneous friction memory times and magnitudes, which in the appropriate parameter regimes reproduces the predictions of both the PGH and GH theory. Our model is

based on the nonlinear Zwanzig model [3,48]. Importantly, while the model makes certain simplifying assumptions that are not guaranteed to hold for general systems, it allows us to study under which conditions  $\tau_{\text{MFP}}$  is determined dominantly by the memory friction either in the well or in the barrier region. Specifically, we consider a reaction coordinate subject to a potential well, bounded by a moderate barrier on one side, as illustrated in Fig. 1(b). In the well and barrier regions the reaction coordinate is locally coupled to independent heat baths, each with a single finite and in general different relaxation time. This local coupling leads to space-inhomogeneous single-exponential memory in the reaction coordinate, and by independently varying the memory effects in the well and barrier region we disentangle the effects of space-inhomogeneous memory times,  $\tau_W$  for the well and  $\tau_B$  for the barrier, and friction magnitudes,  $\gamma_W$  and  $\gamma_B$ , on the barrier-crossing time. By comparing results of numerical simulations to the rate theories of the GH theory [13] and PGH theory [34] (for which we for simplicity use our previously derived heuristic formula [21]), with the latter evaluated using either the well or barrier friction, we are able to infer which theory describes the numerical results, and whether the barrier-crossing time depends dominantly on the well or barrier friction.

We present the results of our numerical study in two parts. First, we discuss the Markovian regime, for which memory effects in both the well and barrier regions are negligibly small, i.e.,  $\tau_B$  and  $\tau_W$  are much smaller than the diffusive timescale  $\tau_D = \gamma L^2/(k_B T)$ , given by the friction constant  $\gamma$ , a length scale  $L$  and thermal energy  $k_B T$ . The dynamics in this regime are thus dependent only on inertial effects, which, strictly speaking, are Markovian only if both instantaneous position and velocity are used for defining a configuration. By labeling inertial effects as Markovian, we demarcate such inertial effects from non-Markovian effects due to coupling of the principle coordinate with hidden heat bath degrees of freedom. In our model inertial effects are characterized by the inertial timescale for the different friction magnitudes,  $\tau_{m,B} = m/\gamma_B$  or  $\tau_{m,W} = m/\gamma_W$ . We find that whenever the well dynamics is in the high-friction regime,  $m/\gamma_W \ll \tau_D$ , then the barrier-crossing time is determined by the barrier top friction. If then, the barrier top is also in the high-friction

regime,  $m/\gamma_B \ll \tau_D$ ,  $\tau_{\text{MFP}}$  is described by Kramers' theory [11], evaluated using the friction magnitude at the barrier top. If, instead, the barrier dynamics is in the low-friction regime,  $m/\gamma_B > \tau_D$ , while  $\gamma_B$  and  $\gamma_W$  are not too different, then the MM theory [15] or PGH theory [34], evaluated using the barrier parameters, describes the numerically obtained barrier-crossing times. On the other hand, if the dynamics in the well is in the low-friction regime,  $m/\gamma_W > \tau_D$ , then  $\tau_{\text{MFP}}$  is described by the PGH theory or MM theory, both evaluated using the well parameters, which therefore dominates the global barrier-crossing dynamics.

In the second part we discuss the non-Markovian regime, where memory effects in either well or barrier regions are relevant, i.e., either  $\tau_B$  or  $\tau_W$  is of at least similar order as the diffusive timescale  $\tau_D$ . For simplicity we keep the friction magnitudes equal,  $\gamma_B = \gamma_W$ , and consider the high-friction regime by imposing  $m/\gamma_B = m/\gamma_W \ll \tau_D$ . Analogous to the previous case, we find that whenever the well dynamics is in the Markovian regime,  $\tau_W \ll \tau_D$ , then the barrier-crossing time is determined by the barrier top friction. If then again, the barrier top is also in the Markovian regime,  $\tau_B \ll \tau_D$ ,  $\tau_{\text{MFP}}$  is described by Kramers' theory [11], evaluated using the friction parameters for the barrier top. If, instead, memory effects in the barrier region are relevant, then the GH theory [13] agrees with the numerically obtained barrier-crossing times. In contrast, if the well memory is long,  $\tau_W > \tau_D$ ,  $\tau_{\text{MFP}}$  is described by the PGH theory using the well parameters. While then in general  $\tau_{\text{MFP}}$  is rather independent of the barrier friction, Markovian barrier dynamics lead to a speed up of  $\tau_{\text{MFP}}$  as compared to a barrier region with long memory. This speedup, which we term the ‘‘Markovian-barrier acceleration,’’ is not captured by any presently available rate theory, but can be understood from a committor analysis, analogous to the ‘‘non-Markovian-barrier acceleration’’ already predicted by the GH theory.

The remainder of this paper is organized as follows. In Sec. II we first introduce the space-inhomogeneous memory model we consider. In Sec. III we then compare numerical simulations of our model to rate-theory predictions. We first consider the short-memory limit and subsequently study how local memory effects modify  $\tau_{\text{MFP}}$ . In our concluding Sec. IV we provide a table which summarizes our results.

## II. MODEL

We consider a reaction coordinate  $x$  and  $N$  noninteracting heat baths with finite relaxation dynamics [3,48]; for  $x \in X_i$ , the reaction coordinate couples linearly to the  $i$ th heat bath. As we show in Appendix A 1, integrating out the bath degrees of freedom then leads to a GLE

$$m\ddot{x}(t) = - \int_0^t dt' \Gamma[t-t', x(t), x(t')] \dot{x}(t') - \partial_x U[x(t)] + \eta[x(t), t], \quad (1)$$

which is a generalization of the model proposed by Zwanzig [3].  $U[x(t)]$  is a potential landscape, and the space- and time-

dependent friction kernel  $\Gamma[t-t', x(t), x(t')]$  is given as

$$\Gamma[t-t', x(t'), x(t)] = \sum_{i=1}^N \chi_i[x(t)] \Gamma_i(t-t') \chi_i[x(t')], \quad (2)$$

where the purely time-dependent components  $\Gamma_i$  describe the internal relaxation dynamics of reservoir  $i$ , and the dimensionless functions  $\chi_i$ , defined by

$$\chi_i(x) = \begin{cases} 1 & \text{if } x \in X_i, \\ 0 & \text{if } x \notin X_i, \end{cases} \quad (3)$$

describe the coupling of the reaction coordinate  $x$  to reservoir  $i$ . The terms in Eq. (2) have a simple intuitive interpretation: at any past time  $t'$ , the reaction coordinate  $x$  perturbs reservoir  $i$  via the coupling strength  $\chi_i[x(t')]$ ; this perturbation relaxes in the heat bath for a duration  $t-t'$  as described by  $\Gamma_i(t-t')$ , and finally couples back to the reaction coordinate at the time  $t$  via  $\chi_i[x(t)]$ .

As we show in Appendix A 2, the random force fulfills the fluctuation-dissipation relation

$$\beta \langle \eta[x(t), t] \eta[x(t'), t'] \rangle = \Gamma[t-t', x(t), x(t')], \quad (4)$$

where  $\beta^{-1} = k_B T$  is the thermal energy with  $k_B$  the Boltzmann constant and  $T$  the absolute temperature.

For our numerical simulations we consider barrier crossing in the quartic potential

$$U(x) = U_0 \left[ \left( \frac{x}{L} \right)^2 - 1 \right]^2, \quad (5)$$

with a length scale  $L$  and barrier height  $\beta U_0 = 3$  (we show some results with varying barrier heights in Appendix C 2). To systematically study the effect of space-inhomogeneous memory on  $\tau_{\text{MFP}}$ , we consider  $N = 2$  independent heat baths with coupling regions in the well,  $X_W/L = (-\infty, -0.5)$ , and on the barrier,  $X_B/L = [-0.5, 0.5)$ , as illustrated in Fig. 1(b). For the resulting two memory kernels  $\Gamma_W$  and  $\Gamma_B$ , we consider single-exponential kernels,

$$\Gamma_i(t) = \frac{\gamma_i}{\tau_i} e^{-t/\tau_i}, \quad (6)$$

with friction magnitudes  $\gamma_i$  and relaxation timescales  $\tau_i$ , where  $i \in \{W, B\}$ . This means that the particle interacts with two independent heat baths, each of which relaxes according to a single exponential.

As we show in Appendix A 3, Eq. (1) with local memory Eq. (2) can be cast into dimensionless form by introducing a diffusion timescale  $\tau_D = \beta \gamma L^2$  with  $\gamma = \sum_i \gamma_i$ , and an inertial timescale  $\tau_m = m/\gamma$ . With the potential (5) and a given barrier height  $\beta U_0$ , the system is then specified by four dimensionless parameters which we choose to be the dimensionless inertial timescale  $\tau_m/\tau_D$ , the dimensionless local memory times  $\tau_i/\tau_D$ ,  $i \in \{W, B\}$ , and one of the two relative friction magnitudes  $\gamma_i/\gamma$ ,  $i \in \{W, B\}$ . To transform dimensionless results to physical dimensions, the temperature  $T$ , the length scale  $L$ , and the sum  $\gamma$  of the local friction magnitudes additionally need to be specified. To simulate the dimensionless formulation of Eqs. (1), (2), and (4), we use a Markovian embedding whereby we explicitly simulate the dynamics in the reservoirs, as detailed in Appendix A 3.

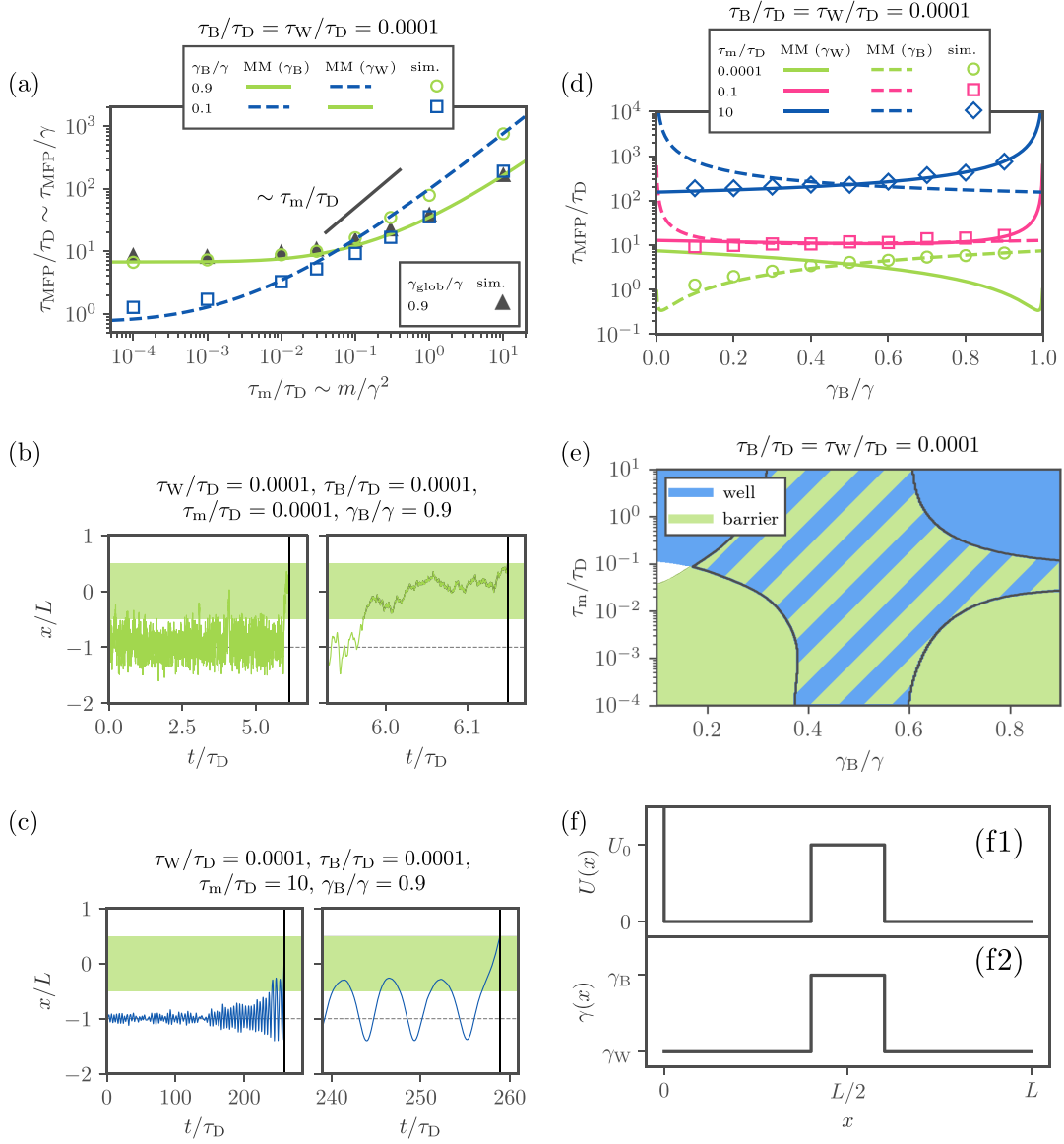


FIG. 2. MFPT,  $\tau_{\text{MFPT}}/\tau_D$ , for different barrier memory friction,  $\Gamma_B(t) = \gamma_B e^{-t/\tau_B}/\tau_B$  and well memory friction,  $\Gamma_W(t) = \gamma_W e^{-t/\tau_W}/\tau_W$ , obtained from numerical simulations (data points) and compared with analytical predictions given by Mel'nikov and Meshkov [15] (MM, solid and broken lines). The data are shown for various inertial timescales  $\tau_m/\tau_D$  and equal memory times in the Markovian limit,  $\tau_B/\tau_D = \tau_W/\tau_D = 10^{-4}$ . (a)  $\tau_{\text{MFPT}}/\tau_D$  plotted over the inertial timescale  $\tau_m/\tau_D$  for different ratios of the barrier to total friction magnitude  $\gamma_B/\gamma$ . The predictions by MM are shown for the effective barrier-friction parameters given by  $\gamma_B$  and for the effective well-friction parameters given by  $\gamma_W$ . The black triangles denote simulations with space-homogeneous friction. (b, c) Example trajectories from simulations. (d)  $\tau_{\text{MFPT}}/\tau_D$  plotted over  $\gamma_B/\gamma$  for various  $\tau_m/\tau_D$ . The predictions by MM are shown for the effective barrier-friction parameters as broken lines and for the effective well-friction parameters as solid lines. (e) Contour plot of agreement of the simulation results with the theoretical predictions. The color denotes whether the simulated  $\tau_{\text{MFPT}} \in [2/3 \tau_{\text{theo}}, 3/2 \tau_{\text{theo}}]$ , where  $\tau_{\text{theo}}$  is calculated using MM theory and either the effective well- or barrier-friction parameters. The hatching indicates that both theoretical predictions agree with the simulated data. White denotes that neither predictions agrees within the tolerance. (f) Model potential (f1) and friction profile (f2) used to study the effect of the barrier friction on  $\tau_{\text{MFPT}}$  in the high-friction Markovian regime. For this model  $\tau_{\text{MFPT}}$  is exactly predicted by Eq. (8).

In analogy to previous works, we define various limits by comparison of respective timescales with the diffusive timescale  $\tau_D$ . For example the Markovian limit where memory effects are negligible is obtained for  $\tau_i < \tau_D$ , and the high-friction limit where inertial effects are negligible is obtained for  $\tau_m < \tau_D$  [21,35,40]. However, since the local friction in region  $i$ ,  $\gamma_i$ , is only part of the total friction  $\gamma$ , which is used to

define  $\tau_D$ , a condition  $\tau_i \ll \tau_D$  does not automatically ensure the expected limit in region  $i$ . Rather, a condition involving the local diffusive timescale,  $\tau_{D,i} \equiv \beta L^2 \gamma_i$ , needs to be used, namely,  $\tau_i/\tau_{D,i} \equiv \tau_i/\tau_D (\gamma/\gamma_i) \ll 1$ . Similarly, inertial effects are locally relevant for  $\tau_{m,i}/\tau_{D,i} \equiv \tau_m/\tau_D (\gamma/\gamma_i)^2 \gtrsim 1$ , where  $\tau_{m,i} \equiv m/\gamma_i$ . While the distinction between  $\tau_{m,i}$ ,  $\tau_{D,i}$  and  $\tau_m$ ,  $\tau_D$  is important if  $\gamma_i$  is significantly smaller than  $\gamma$ , for most



of the parameter combinations we consider in the main text, all  $\gamma_i$  are of similar order as their sum  $\gamma$ .

Since we are interested in evaluating the barrier-crossing time starting from the well region  $X_W$ , we restart the simulation once the particle crosses the right boundary at  $x/L = 0.5$ , which we consider a successful escape. At each restart, we draw the initial position from an approximate Boltzmann distribution around the well minimum, i.e., we draw a Gaussian random variable  $x(0)$  with  $\langle x(0)/L \rangle = -1$  and  $\langle [x(0)/L + 1]^2 \rangle = k_B T / [L^2 U''(-L)] = k_B T / (8U_0)$ . Similarly, we draw the initial velocity  $\dot{x}(0)$  from its equilibrium distribution, i.e., a Gaussian random variable with  $\langle \dot{x}(0) \rangle = 0$  and  $\langle \dot{x}^2(0) \rangle = k_B T / m$ . The initial conditions for the heat bath variables we subsequently draw from their respective Boltzmann distributions, as detailed in Appendix A 2.

In Fig. 1(c) we show an example trajectory, simulated using long memory in the well and short memory on the barrier, for which different dynamics in the different regions are clearly observed: While in the well region the trajectory oscillates weakly-damped around the potential minimum, on the barrier the trajectory is more akin to overdamped diffusive dynamics. Figure 1(c) furthermore illustrates how we compute  $\tau_{\text{MFP}}$  from observed time differences between crossings of the well minimum and the escape at  $x/L = 0.5$ . That this is a reliable method for calculating  $\tau_{\text{MFP}}$  has been shown before [35].

In the main text, we compare our numerical results to the GH [13], MM [15], and PGH theory [34], where instead of the latter we use a heuristic formula [35] in practice. The GH theory accounts only for barrier memory friction, which is why we always evaluate it using the barrier memory kernel; the theory assumes fast equilibration within the well, and does not depend on the well friction explicitly. Both the Markovian MM and non-Markovian PGH theory assume homogeneous friction. We therefore evaluate these theories using either the local parameters  $\gamma_i$ ,  $\tau_i$  of the well or barrier region. This allows us to infer not only which rate theory describes the barrier-crossing dynamics in which regime, but also which region (well or barrier) dominantly determines the global  $\tau_{\text{MFP}}$ . In Appendix B we summarize the equations used to calculate predictions for all rate theories considered in the main text. In the main text, we do not compare our numerical simulations to the analytical rate theory for space-inhomogeneous memory friction due to Krishnan *et al.* [48]. The reason for this is twofold: First, by comparing to the widely used GH and PGH theories, we are able to assess which local dynamics dominate the global  $\tau_{\text{MFP}}$ . Second, as we show in Appendix C 4, the theoretical predictions by Krishnan *et al.* [48] do not capture the ‘‘Markovian-barrier acceleration’’ regime, which we prominently discuss below and which we quantify using the PGH predictions.

### III. RESULTS

In order to decouple Markovian inertial effects and non-Markovian memory effects we analyze both scenarios independently. For this we first consider the Markovian limit,  $\tau_B/\tau_D, \tau_W/\tau_D \ll 1$ , and vary  $\tau_m/\tau_D$ , and second the high-friction limit,  $\tau_m/\tau_D \ll 1$ , with varying  $\tau_B/\tau_D$  and  $\tau_W/\tau_D$ .

#### A. Markovian friction dynamics

We now consider the Markovian limit for both well and barrier. In Fig. 2(a) we show the rescaled  $\tau_{\text{MFP}}/\tau_D$  as a function of the rescaled inertial time  $\tau_m/\tau_D$ . For reference, we include numerical results from a GLE with a homogeneous single-exponential memory kernel with memory time  $\tau_{\text{glob}}/\tau_D = 10^{-4}$  and a single friction magnitude  $\gamma_{\text{glob}} = 0.9\gamma$  (chosen as to coincide with the light green solid line, as explained further below) [35]; the resulting  $\tau_{\text{MFP}}$  are shown in Fig. 2(a) as black triangles, and clearly show the Kramers turnover between high-friction dynamics for  $\tau_m/\tau_D \ll 1$ , where  $\tau_{\text{MFP}}$  scales as  $\sim \gamma$ , and low-friction dynamics for  $\tau_m/\tau_D \gg 1$ , where  $\tau_{\text{MFP}}$  scales as  $\sim m/\gamma$  [11,15,35].

Figure 2(a) furthermore shows numerical results for the space-inhomogeneous memory model Eqs. (1) and (2) for  $\tau_B/\tau_D = \tau_W/\tau_D = 10^{-4}$  and the two values  $\gamma_B/\gamma = 0.1, 0.9$ . For  $\gamma_B/\gamma = 0.1$  we have  $\gamma_W/\gamma = 0.9$ , so that the friction in the well is almost one order of magnitude larger as compared to the friction in the barrier region. Conversely, for  $\gamma_B/\gamma = 0.9$  the friction in the well,  $\gamma_W/\gamma = 0.1$ , is almost one order of magnitude smaller as compared to the friction in the barrier region. While in the high-friction regime  $\tau_m/\tau_D \ll 1$ , the results for  $\gamma_B/\gamma = 0.9$  (light green circles; barrier friction much larger than well friction) agree well with the global memory friction data (black triangles), in the low-friction regime  $\tau_m/\tau_D \gg 1$ , it is  $\tau_{\text{MFP}}$  for  $\gamma_B/\gamma = 0.1$  (dark blue squares; well friction much larger than barrier friction) that is comparable to the global memory friction result. This indicates that for high friction,  $\tau_{\text{MFP}}$  is dominated by the barrier friction, whereas for low friction  $\tau_{\text{MFP}}$  is dominated by the well friction.

The crossover between barrier-dominated  $\tau_{\text{MFP}}$  to well-dominated  $\tau_{\text{MFP}}$  observed in Fig. 2(a) is further confirmed by comparing the numerical data to predictions of the MM theory for Markovian barrier crossing, which is based on homogeneous friction. In Fig. 2(a) we show the predictions of MM theory, evaluated using either the well friction  $\gamma_W$  or the barrier friction  $\gamma_B$ . Note that because of the symmetry in the used parameters, the light green solid line represents both the MM prediction for  $\gamma_B/\gamma = 0.9$ , and evaluation using the barrier friction, as well as the MM prediction for  $\gamma_B/\gamma = 0.1$ , and evaluation using the well friction. On the other hand, the dark blue broken line represents the opposite parameter choice in both scenarios. We observe that, while in the high-friction limit  $\tau_m/\tau_D \ll 1$ , the simulated  $\tau_{\text{MFP}}$  agree with the MM predictions evaluated at the barrier region, for low friction  $\tau_m/\tau_D \gg 1$  the numerical data are described by the MM theory evaluated at the well.

That for the Markovian high-friction scenario,  $\tau_{\text{MFP}}$  is dominated by the barrier friction, follows from a simple analytical model. In the high-friction Markovian limit  $\tau_{\text{MFP}}$  to start at  $x_0$  and reach  $x_f$  in a potential  $U(x)$  and for space-inhomogeneous friction  $\gamma(x)$  is derived exactly from the Fokker-Planck equation as [43]

$$\tau_{\text{MFP}}(x_0, x_f) = \beta \int_{x_0}^{x_f} dx \gamma(x) e^{\beta U(x)} \int_{x_L}^x dx' e^{-\beta U(x')}, \quad (7)$$

where  $x_L < x_0$  is a lower reflecting boundary. To study the effect of barrier friction on  $\tau_{\text{MFP}}$ , we consider the model illustrated in Fig. 2(f): a simplified flat potential  $U(x)$ , which

features a reflecting boundary at  $x = 0$  and a step barrier of height  $U_0$ , width  $B$  and friction  $\gamma_B$  located at position  $x = L/2$ . Outside of the potential barrier, the friction is  $\gamma_W$ . Considering  $x_0 = x_L = 0$  and  $x_f = L$ ,  $\tau_{\text{MFP}}$  is calculated from Eq. (7) to be

$$\tau_{\text{MFP}}^{0 \rightarrow L} = \beta \frac{L^2}{2} \gamma_W + \beta \frac{LB}{2} (\gamma_B - \gamma_W) + \beta \frac{B(L-B)}{2} (1 - e^{-\beta U_0}) (\gamma_B e^{\beta U_0} - \gamma_W). \quad (8)$$

In the high-barrier limit, where  $\beta U_0 \gg 1$ , Eq. (8) is dominated by an expression which contains only the barrier friction  $\gamma_B$ :

$$\tau_{\text{MFP}}^{0 \rightarrow L} \approx \beta \gamma_B \frac{B(L-B)e^{\beta U_0}}{2}. \quad (9)$$

This result explains why the  $\tau_{\text{MFP}}$  in the high-friction scenario is determined by the barrier friction.

Example trajectories, comparing the cases of Markovian high-friction dynamics ( $\tau_m/\tau_D = 10^{-4}$ ), where  $\tau_{\text{MFP}}$  is determined by the barrier friction, and Markovian low-friction dynamics ( $\tau_m/\tau_D = 10$ ), where  $\tau_{\text{MFP}}$  is determined by the well friction, are shown in Figs. 2(b) and 2(c). While the trajectory in Fig. 2(b) generally exhibits dynamics reminiscent of Markovian high-friction Langevin dynamics around the well and also in the barrier region, differences in the lengths of persistent motion due to the vastly different local friction magnitudes are clearly visible. The trajectory in Fig. 2(c) shows oscillations within the wells and long residence times, which are typical of inertia-dominated stochastic dynamics [35].

Figure 2(d) shows the numerical  $\tau_{\text{MFP}}$ , plotted as a function of the relative barrier friction  $\gamma_B/\gamma$  for various values of the rescaled inertial time  $\tau_m/\tau_D$ . Again, while for high friction,  $\tau_m/\tau_D = 10^{-4}$ , the simulated data agree with the MM theory evaluated using the barrier friction (light green broken line), for large  $\tau_m/\tau_D = 10$  the numerical results agree with the predictions using the well friction (dark blue solid line). We observe that for the parameters considered, the rescaled  $\tau_{\text{MFP}}/\tau_D$  always increases monotonously with  $\gamma_B/\gamma$ , indicating that increasing barrier friction while decreasing well friction slows down barrier-crossing. The analytical MM theory shows nonmonotonicities for the case of high total friction,  $\tau_m/\tau_D = 10^{-4}$ , but very unequal friction magnitudes in well and barrier regions,  $\gamma_i/\gamma \ll 1$ , i.e., to the far right and left of Fig. 2(d). This is discussed in detail in Appendix C 1.

Figure 2(e) illustrates for which parameters the simulated  $\tau_{\text{MFP}}$  is described by the theoretical predictions of MM theory, evaluated for either the well- or barrier-friction parameters. The figure again clearly shows that for high-friction dynamics,  $\tau_m/\tau_D \ll 0.1$ ,  $\tau_{\text{MFP}}$  is determined by the barrier friction, whereas for low-friction dynamics, the well friction determines  $\tau_{\text{MFP}}$ . The hatched area shows the overlap where both predictions calculated using well or barrier friction agree with the simulated  $\tau_{\text{MFP}}$ . Obviously, in the crossover between barrier- and well-dominated friction, where  $\gamma_B \approx \gamma_W$ , the rate theories produce similar results when evaluated using barrier or well friction; see also Fig. 2(d). This is because for  $\gamma_B/\gamma \approx 0.5$ , we have  $\gamma_W/\gamma = (\gamma - \gamma_B)/\gamma \approx 0.5$ , so that the effective friction magnitudes in well and barrier region, and hence the predictions of MM theory, which depend on the effective local friction, are similar.

To summarize Figs. 2(a)–2(e), in the Markovian (short memory) limit, the rescaled  $\tau_{\text{MFP}}$  is for high-friction dynamics determined by the barrier friction, whereas for low-friction dynamics it is determined by the well friction. The former effect is illustrated by the analytical result Eq. (9), while the latter is intuitively understood from the concept of energy diffusion. For low-friction dynamics the energy exchange between the reaction coordinate and the heat bath is weak and therefore the energy to cross the potential barrier is only slowly built up in the well region. This process is dominated by the well dynamics and leads to a slow-down of the global barrier-crossing times. Since slow energy diffusion is also apparent for long memory times, a similar effect is observed in the discussion of the non-Markovian dynamics in the following.

## B. Non-Markovian friction dynamics

In Fig. 3 we investigate the memory-time dependence of  $\tau_{\text{MFP}}$ . For this, we consider a constant inertial timescale in the high-friction limit,  $\tau_m/\tau_D = 10^{-4}$ , and identical friction magnitudes for the two reservoirs,  $\gamma_W/\gamma = \gamma_B/\gamma = 0.5$ , while varying the well- and barrier-friction timescales,  $\tau_W/\tau_D$  and  $\tau_B/\tau_D$ . We compare our numerical results to analytical predictions based on both the GH theory [13], which we evaluate using the barrier-friction parameters  $\tau_B, \gamma_B$  and which is hence independent of the well parameters, and PGH theory [34] (for which we in practice use a heuristic formula [21]), which we evaluate for both the well parameters  $\tau_W, \gamma_W$  or the barrier parameters  $\tau_B, \gamma_B$ .

In Fig. 3(a) we show the rescaled  $\tau_{\text{MFP}}$  as a function of the barrier memory time  $\tau_B/\tau_D$  for various fixed well memory times  $\tau_W/\tau_D$ . For short barrier memory,  $\tau_B/\tau_D \ll 0.1$ , the dynamics on the barrier top is Markovian and the numerical  $\tau_{\text{MFP}}$  are independent of  $\tau_B/\tau_D$ . If additionally also the memory in the well is short,  $\tau_W/\tau_D \ll 0.1$ , we are in the Markovian high-friction limit. While, as we have already discussed in the context of Fig. 2(a), in this limit the barrier-crossing time is determined by the barrier friction, the PGH theory evaluated with well friction (black solid line) agrees with the PGH theory evaluated with barrier friction (colored solid lines) and GH theory (black broken line; always evaluated at barrier friction); this is because we have equal friction magnitudes in well and barrier. While in the double limit of high friction and short well memory  $\tau_W/\tau_D \leq 0.01$ , all theories describe the numerical data (shown as circle and square markers) as long as  $\tau_B/\tau_D \ll 0.01$ , for  $\tau_B/\tau_D \gtrsim 0.01$ , both the GH theory and numerical results display an acceleration (as compared to the Markovian limit  $\tau_B/\tau_D \rightarrow 0$ ); we refer to this as GH “non-Markovian-barrier acceleration.” That the GH theory describes this acceleration regime is expected because it was derived assuming fast equilibration within each well, which is in line with the high-friction Markovian dynamics inside the well for  $\tau_m/\tau_D = 10^{-4}$ ,  $\tau_W/\tau_D \leq 0.01$ . We note that in the limit of  $\tau_B/\tau_D \rightarrow \infty$ , the GH theory agrees with the predictions of transition state theory [13]. For high-friction dynamics with short well memory,  $\tau_{\text{MFP}}$  is thus determined by the barrier friction and described by the GH theory.

On the other hand, for long memory in the well,  $\tau_W/\tau_D \geq 1$ , the numerical  $\tau_{\text{MFP}}$  (dark purple diamonds and dark blue

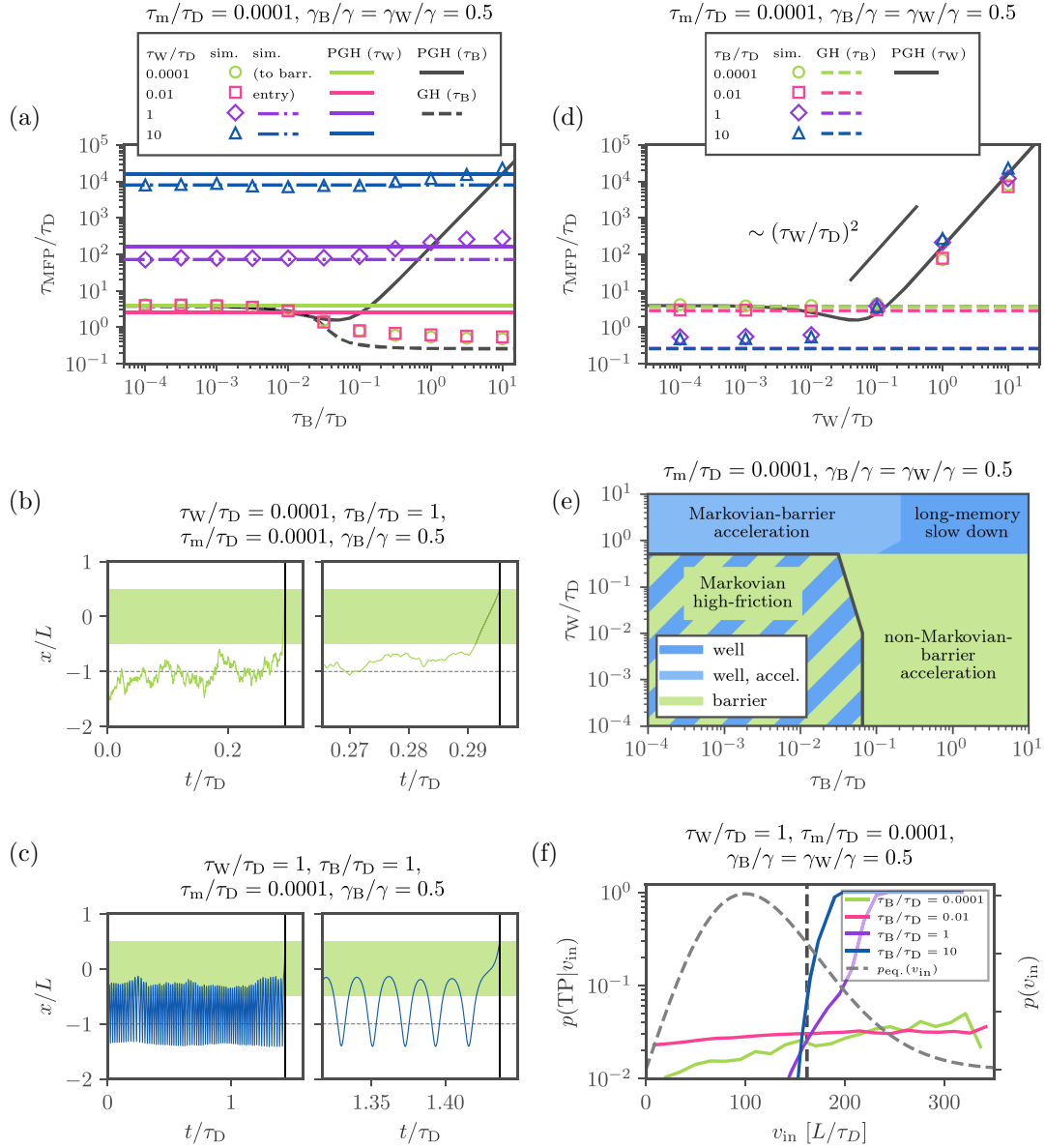


FIG. 3. MFPT,  $\tau_{\text{MFP}}/\tau_D$ , for different barrier memory friction,  $\Gamma_B(t) = \gamma_B/\tau_B e^{-t/\tau_B}$  and well memory friction,  $\Gamma_W(t) = \gamma_W/\tau_W e^{-t/\tau_W}$ , from numerical simulations (data points) compared with analytical predictions given by Grote and Hynes [13] (GH, broken lines) and Pollak *et al.* [34] (PGH, solid lines, evaluated using the heuristic formula [21]). The data are shown for various barrier-friction  $\tau_B/\tau_D$  and well-friction times  $\tau_W/\tau_D$ , constant inertial timescale in the high-friction limit  $\tau_m/\tau_D = 10^{-4}$ , and equal friction magnitudes  $\gamma_B/\gamma = \gamma_W/\gamma = 0.5$ . (a)  $\tau_{\text{MFP}}$  plotted over the barrier-friction time  $\tau_B/\tau_D$  (data points). The theories are shown for the respective barrier-friction time in black and in the case of the PGH theory for the well-friction time as colored lines. Simulated  $\tau_{\text{MFP}}$  to reach the barrier entry at  $x/L = -1/2$  are shown as colored dash-dotted lines. (b, c) Example trajectories from simulations for the barrier-dominated and GH-predicted limit (b) and the well-dominated PGH-predicted limit (c). (d)  $\tau_{\text{MFP}}$  plotted over the well-friction time  $\tau_W/\tau_D$  (data points). The theories are shown for the respective well-friction time in black and in the case of the GH theory for the barrier-friction time as colored broken lines. (e) Contour plot of agreement of the simulation results with the theoretical predictions. The color denotes whether the simulated  $\tau_{\text{MFP}} \in [1/3 \tau_{\text{theo}}, 3 \tau_{\text{theo}}]$ , where  $\tau_{\text{theo}}$  is calculated using either the GH theory with the barrier-friction parameters or the PGH theory with the well-friction parameters. The hatching indicates that both theoretical predictions agree with the simulated data. The light blue area denotes the “Markovian-barrier acceleration” of the PGH prediction for which we define  $\tau_{\text{theo,MBA}} = 0.2 \tau_{\text{theo,PGH}}$ . (f) Committor  $p(\text{TP}|v_{in})$  for transition paths crossing the barrier region plotted over the initial velocity  $v_{in}$  upon entering the barrier region for various barrier-friction times  $\tau_B/\tau_D$  and constant well-friction time  $\tau_W/\tau_D = 1$  and inertial time  $\tau_m/\tau_D = 10^{-4}$ . The velocity related to the difference in potential energy relative to the barrier top is plotted as a vertical black broken line. The flux-weighted equilibrium velocity distribution  $p_{eq}(v_{in})$  is plotted as a gray broken line on a linear scale.

triangles) are comparable to the predictions of the PGH theory evaluated with the well parameters, and even for a Markovian barrier,  $\tau_B/\tau_D \ll 1$ , disagree considerably with the GH theory (which indicates a breakdown of the assumption of fast equilibration within the well inherent to the GH theory). In contrast to the Markovian-well scenario, for long well memory  $\tau_{\text{MFP}}$  is thus determined by the well dynamics. Interestingly, in the long-well-memory regime,  $\tau_W/\tau_D \geq 1$ , the observed  $\tau_{\text{MFP}}$  show a slight acceleration for small barrier-memory times  $\tau_B/\tau_D \lesssim 0.1$ , as compared to the predictions by the PGH theory and the numerical results for  $\tau_B/\tau_D \gg 0.1$ . We here refer to this acceleration due to short barrier memory as “Markovian-barrier acceleration,” which notably behaves opposite as a function of  $\tau_B$  as compared to GH “non-Markovian-barrier acceleration,” as we discuss further below.

Figures 3(b) and 3(c) show example trajectories where  $\tau_{\text{MFP}}$  is determined by barrier or well friction. For the trajectory shown in Fig. 3(b)  $\tau_{\text{MFP}}$  is determined by the barrier friction, and we observe high-friction Markovian dynamics within the well and a direct transition path upon entering the barrier region. The trajectory with well-friction-determined  $\tau_{\text{MFP}}$ , Fig. 3(c), on the other hand shows a long residence time in the well, and multiple attempts entering the barrier region before crossing over the barrier top, that are associated with energy-diffusion, i.e., memory- or inertia-dominated trajectories [35].

In Fig. 3(d) we show the numerical  $\tau_{\text{MFP}}$  as function of the well memory time  $\tau_W/\tau_D$ , for several constant values of the barrier memory time  $\tau_B/\tau_D$ . We again compare to theoretical predictions based on the PGH and GH theories. Similar to Fig. 3(a) we see that for short well memory,  $\tau_W/\tau_D \ll 0.1$ ,  $\tau_{\text{MFP}}$  becomes independent of the well memory time so that the dynamics is governed by the barrier. If additionally the barrier memory time is short,  $\tau_B/\tau_D \ll 0.1$ , then  $\tau_{\text{MFP}}$  is described by both the PGH (evaluated in the well) and GH theory. Increasing the barrier memory time  $\tau_B/\tau_D$  then leads to an acceleration of barrier crossing as we discussed in Fig. 3(a), and as described by the GH theory [leftmost data points in Fig. 3(d)]. For any value of the barrier memory  $\tau_B/\tau_D$ , we observe that as the well memory is increased, for  $\tau_W/\tau_D \gtrsim 1$  an asymptotic long-memory regime with  $\tau_{\text{MFP}} \sim \tau_W^2$  is reached [35], which is well described by the PGH theory evaluated at the well. Increasing the well memory time  $\tau_W/\tau_D$  thus has both a qualitatively and quantitatively very different effect from increasing the barrier memory time  $\tau_B/\tau_D$  where, as demonstrated in Fig. 3(a),  $\tau_{\text{MFP}}$  slightly increases/decreases (depending on  $\tau_W/\tau_D$ ) and then becomes independent of  $\tau_B/\tau_D$ .

Figure 3(e) summarizes the agreement of the simulated high-friction  $\tau_{\text{MFP}}$  with the PGH theory, evaluated on well parameters, and the GH theory, which is always evaluated using the barrier parameters. We see that once the well memory becomes relevant, i.e., for  $\tau_W/\tau_D \gtrsim 0.1$ ,  $\tau_{\text{MFP}}$  is approximately described by PGH theory evaluated at the well. The “Markovian-barrier acceleration” regime appears if memory in the well is relevant, but in the barrier region the memory time is short, i.e., for  $\tau_B/\tau_D \ll 1$ ,  $\tau_W/\tau_D \gtrsim 1$ , and is shown as light blue. If well memory effects are negligible, i.e., for  $\tau_W/\tau_D \ll 0.1$ , but memory effects are relevant in the barrier

region,  $\tau_B/\tau_D \gg 0.1$ , then GH theory describes the numerical results. If memory effects are negligible for both well and barrier region,  $\tau_W/\tau_D \ll 1$  and  $\tau_B/\tau_D \ll 0.1$ , then we are in the Markovian limit, where the barrier friction  $\gamma_B$  determines  $\tau_{\text{MFP}}$ . That in this regime both GH theory (evaluated at the barrier region) and PGH theory (evaluated at the well region) describe the numerical  $\tau_{\text{MFP}}$ , as indicated by the hatching, can be rationalized by the fact that we use the same friction magnitude for well and barrier,  $\gamma_B = \gamma_W$ .

### C. Markovian-barrier acceleration

In order to gain intuition about the “Markovian-barrier acceleration” regime, i.e., the slight barrier-crossing speed-up observed for  $\tau_W/\tau_D \gtrsim 1$ ,  $\tau_B/\tau_D \ll 1$  in Figs. 3(a) and 3(d), we perform a committor analysis, the results of which are shown in Fig. 3(f). The committor shown in the figure is defined as the probability to be on a transition path through the barrier region, and plotted as a function of the initial velocity with which the particle enters the barrier region,  $v_{\text{in}}$ . For comparison, the flux-weighted equilibrium velocity probability density,  $p_{\text{eq.}}(v) \propto v \exp[-mv^2/(2k_B T)]$  [50,51], is given as a gray broken line. Furthermore, we show as a vertical black broken line the threshold velocity  $v_t$  with which an undamped particle entering the barrier region crosses over the barrier top, so that  $mv_t^2/2 = U_0 - U(x = -L/2) = 7U_0/16$ , and hence  $v_t = \sqrt{7U_0/(8m)}$ .

For short memory in the barrier region,  $\tau_B/\tau_D \ll 1$ , the committor is relatively small and only very slightly increases with larger initial velocities (the light green and light red solid lines), indicating that the kinetic energy is quickly dissipated in the barrier region and the probability to perform a transition is approximately independent of the velocity with which the particle enters the barrier region. For long barrier memory  $\tau_B/\tau_D \geq 1$ , the committor remains almost zero for velocities  $v_{\text{in}} \lesssim v_t$ , indicating that many trajectories that enter the barrier region will simply roll back into the well region. They initially do not have enough kinetic energy to cross the barrier top and the energy exchange with the barrier heat bath is not fast enough to gain the missing energy. At  $v_t$ , the committor starts to increase sharply and saturates at a value of 1, which means that virtually every trajectory that enters the barrier region with at least this kinetic energy performs a transition through the barrier region. This is consistent with a weak energy exchange of heat bath and reaction coordinate in the barrier region, where a trajectory traverses the barrier top only if initially it has enough kinetic energy to reach there.

The physical picture for the “Markovian-barrier acceleration” regime is hence that for short barrier memory time the energy exchange between reaction coordinate and barrier heat bath is fast; this means that for high-friction Markovian barrier dynamics, a large fraction of particles entering the barrier region (without enough energy to cross the barrier top) is able to obtain the missing energy from the barrier heat bath, which leads to a decrease in  $\tau_{\text{MFP}}$  with decreasing barrier memory time. Interestingly, as can be seen in Fig. 3(a), this effect changes  $\tau_{\text{MFP}}$  in the opposite way as the “non-Markovian-barrier acceleration” predicted by the GH theory, and reproduced by our numerical model in the limit of high-friction Markovian dynamics in the well.

Nevertheless, the mechanisms behind both regimes are similar and can each be understood from the committor analysis shown in Fig. 3(f). “Non-Markovian-barrier acceleration” profits from the fact that in the case of long barrier memory fast initial velocities, i.e.,  $v_{in} \gtrsim v_r$  [to the right of the vertical black broken line in Fig. 3(f)], always lead to a direct transition. In case of short well memory, the initial velocities  $v_{in}$  of subsequent barrier crossing attempts are only weakly correlated, allowing for the assumption made by the GH theory that the equilibrium velocity distribution is sampled equally at any attempt. Consequently the high-velocity tail of the equilibrium distribution of  $v_{in}$  is visited more frequently over time compared to the long well memory case, where the initial velocity changes rather slowly for consecutive attempts, due to the weak coupling to the well heat bath. On the other hand, in the limit of long well memory the “Markovian-barrier acceleration” profits from the fact, that in the case of slow initial velocities, i.e., to the left of the vertical black broken line, and short barrier memory, there is still a small chance that a transition over the barrier occurs. This leads to a slightly faster  $\tau_{MFP}$  when compared to the case that all the energy to reach the barrier top needs to be accumulated from the well heat bath.

This analysis furthermore suggests a simple way to quantify the “Markovian-barrier acceleration”:  $\tau_{MFP}$  over the barrier is mainly determined by  $\tau_{MFP}$  to reach the barrier region for the first time. Subsequently, a successful transition of the barrier region happens relatively quickly. On the contrary, for long barrier memory  $\tau_{MFP}$  over the barrier is determined by the time to reach the barrier top. In Fig. 3(a) we therefore also compare  $\tau_{MFP}$  to reach the barrier entry at  $x/L = -0.5$  (dark purple and dark blue dash-dotted lines) and  $\tau_{MFP}$  over the barrier to reach at  $x/L = 0.5$  (the data coincide with the dark purple and dark blue solid lines), both evaluated from simulations with a global memory friction assuming the well friction parameters. As expected, the former coincide with the data of the “Markovian-barrier acceleration” regime correctly, while the later coincide with the data in the case of long barrier memory.

A comparison of all presented simulation data with the global analytical rate theory for local memory effects by Krishnan *et al.* [48] is shown in Appendix C4. Their theory performs well in some regimes of the parameter space, correctly interpolates between predictions by GH and PGH and therefore intrinsically determines whether the dynamics are well or barrier dominated. However, in certain parameter regimes, including the “Markovian-barrier acceleration” regime, major deviations from the numerical results are observed. This is due to instabilities of the perturbation theory inherent to the analytical approach, in fact, the authors themselves state that predictions in this parameter regime should be validated by simulations, as we have done here.

#### IV. CONCLUSIONS

We study a model for barrier crossing with different well and barrier memory friction times and magnitudes. By comparing extensive numerical simulations of this model to the GH theory (which takes into account memory friction in the barrier region) and the PGH theory (which does not take into

TABLE I. Summary of the regimes observed when varying single-exponential barrier and well memory friction, and the respective applicable rate theories with the dominant preexponential scaling factors. The GH reactive frequency  $\lambda$  is defined in Appendix B1. The table is approximately valid while the barrier and well friction magnitudes remain within one order of magnitude. Some effects for very different friction magnitudes in well and barrier are discussed in Appendix C1.

		Well		
		Markovian high friction	Markovian low friction	Long memory
Barrier	Markovian high friction	Barrier dominated Kramers, GH, PGH MM $\tau_{MFP} \sim \gamma_B$	Well dominated	Well dominated PGH (Markovian-barrier acceleration) $\tau_{MFP} \sim \tau_W^2/\gamma_W$
	Markovian low friction	Barrier dominated PGH MM $\tau_{MFP} \sim m/\gamma_B$	PGH MM $\tau_{MFP} \sim m/\gamma_W$	Well dominated PGH $\tau_{MFP} \sim \tau_W^2/\gamma_W$
	Long memory	Barrier dominated GH (non-Markovian -barrier acceleration) $\tau_{MFP} \sim \lambda^{-1}(\gamma_B, \tau_B)$		

account space-inhomogeneous memory), we identify in which region of the model parameter space the barrier-crossing time, in terms of the mean first-passage time,  $\tau_{MFP}$ , is determined by the well memory or the barrier memory, respectively.

The memory friction around the barrier top determines  $\tau_{MFP}$  only if the dynamics in the well is in the Markovian high-friction regime. In this case  $\tau_{MFP}$  is described by GH theory if non-Markovian effects on the barrier are present, and instead by MM theory if Markovian low-friction effects dominate the barrier dynamics while the friction magnitudes in well and barrier are comparable.

If the dynamics in the well is in the so-called energy-diffusion regime, i.e., either dominated by inertia effects,  $\tau_{m,W}/\tau_{D,W} \gtrsim 1$ , or because of long memory in the well,  $\tau_W/\tau_{D,W} \gtrsim 1$ , then the rate-limiting step is obtaining enough energy from the well heat bath to make a barrier-crossing attempt. In this scenario,  $\tau_{MFP}$  is described by the PGH theory evaluated for the well parameters. In this regime, high friction on the barrier top slightly diminishes  $\tau_{MFP}$ ; this “Markovian-barrier acceleration” is due to the strong interaction between reaction coordinate and heat bath in the barrier region, which enables particles that enter the barrier region without enough energy for a barrier crossing to gain the missing energy in the barrier region and make it over the top. Interestingly, the same mechanism leads to a slow-down in the case of a Markovian well, where the “non-Markovian-barrier acceleration” correctly predicted by the GH theory happens in the limit of long barrier memory, not short barrier memory. This contrast highlights the complex interplay between barrier friction and well friction. The different regimes, and which theory needs to be evaluated where in order to describe the corresponding  $\tau_{MFP}$ , are summarized in Table I. The table

allows one to quickly infer which aspect of the dynamics of a reaction coordinate determines the timescales of rare events, and will help researchers identify the appropriate rate theory for a given system.

While theoretical works often incorporate only either space-inhomogeneous friction magnitudes or homogeneous time-dependent memory friction [7–10,21,34,35,40–43], reaction coordinates in physical systems with nonlinear interactions may in general exhibit both effects simultaneously. Our model system therefore represents a step towards more realistic coarse-grained descriptions of reaction coordinates. To parametrize a GLE with both space-inhomogeneous memory friction time and magnitude, such as the one presented in this work, from time series data, an extension of methods established for homogeneous memory can be considered [7,52,53]. Furthermore, there are several relevant extensions of our model system. First, an interaction between the different coupling heat baths could be included, as in a physical system the orthogonal degrees of freedom are in general not isolated from each other. Second, it will be interesting to consider the nonequilibrium scenario where the interaction between reaction coordinate and orthogonal degrees of freedom does not originate from an interaction potential; this scenario has been studied before for homogeneous friction [54].

Quantum effects are not incorporated in the present model, but quantum projection methods have previously been discussed [55,56]. Within the Born-Oppenheimer approximation classical barrier crossing dynamics would essentially be modified by two effects: reduction of the effective barrier height due to zero-point motion and competition of the classical barrier-crossing rate with the tunneling rate [14,16]. Beyond the Born-Oppenheimer approximation, nonadiabatic effects such as electronic transitions between different energy surfaces would require multistate modeling [57].

#### ACKNOWLEDGMENTS

We gratefully acknowledge support by the Deutsche Forschungsgemeinschaft (DFG) grant SFB 1078, by the European Research Council under the Horizon 2020 Programme, ERC Grants Agreement No. 740269 and No. 835117, by the Royal Society through grant RP1700, and computing time on the HPC clusters at the Physics Department and at ZEDAT, FU Berlin.

F.N.B., R.R.N., and J.K. conceived the theory and designed the simulations. F.N.B. and J.K. performed simulations. F.N.B. analyzed the data. All authors discussed the results, analyses, and interpretations. F.N.B. and J.K. wrote the paper with input from all authors. The authors declare no competing interests.

#### APPENDIX A: GENERALIZED LANGEVIN EQUATION WITH SPACE-INHOMOGENEOUS MEMORY FRICTION

##### 1. Formulation of the GLE in a Markovian embedding

In the present section we show that the GLE with space-inhomogeneous memory, Eq. (1) from the main text, is equivalent to a  $N + 1$ -dimensional dynamical system, in which the reaction coordinate  $x(t)$  is coupled to  $N$  auxil-

iary degrees of freedom ( $y_1(t), \dots, y_N(t)$ ), which we refer to as the heat bath. We assume that each of the  $y_i$  obeys an overdamped Langevin equation with random force  $F_i(t)$  and friction magnitude  $\gamma_i$ . In analogy to the derivation by Zwanzig [3], we assume that the reaction coordinate is coupled to the heat bath via a nonlinear potential  $U_{\text{hb}}(x, y_1, \dots, y_N) = \sum_{i=1}^N k_i [f_i(x) - y_i]^2 / 2$ , where hb stands for heat bath,  $k_i$  determines the coupling strength between  $x$  and  $y_i$ , and the functions  $f_i$  will be used to obtain a space-inhomogeneous coupling between reaction coordinate and reservoir  $i$ . The total potential  $U_{\text{tot}}$  experienced by the dynamical system ( $x(t), y_1(t), \dots, y_N(t)$ ) is then given as a sum

$$U_{\text{tot}}(x, y_1, \dots, y_N) = U(x) + U_{\text{hb}}(x, y_1, \dots, y_N), \quad (\text{A1})$$

where  $U(x)$  is the double-well potential (5). The equations of motion for  $x(t)$  and the  $y_i(t)$  are then given by

$$m\ddot{x}(t) = - \sum_{i=1}^N k_i \{f_i[x(t)] - y_i(t)\} \partial_x f_i[x(t)] - (\partial_x U)[x(t)], \quad (\text{A2})$$

$$\gamma_i \dot{y}_i(t) = k_i \{f_i[x(t)] - y_i(t)\} + F_i(t). \quad (\text{A3})$$

The random forces  $F_i$  are Gaussian white noise with zero mean,  $\langle F_i(t) \rangle = 0$ , and covariances  $\langle F_i(t) F_j(t') \rangle = 2\gamma_i k_B T \delta_{ij} \delta(t - t')$ , so that the Langevin Eq. (A3) obeys the fluctuation-dissipation relation. To obtain a GLE for only the reaction coordinate  $x(t)$ , we eliminate the degrees of freedom  $y_i(t)$  in Eq. (A2). For this, we use the formal solution of Eq. (A3), which is given by

$$\begin{aligned} y_i(t) &= y_i(0) e^{-t/\tau_i} + \tau_i^{-1} \int_0^t dt' e^{-(t-t')/\tau_i} f_i[x(t')] \\ &+ \int_0^t dt' e^{-(t-t')/\tau_i} \frac{F_i(t')}{\gamma_i} \\ &= \{y_i(0) - f_i[x(0)]\} e^{-t/\tau_i} + f_i[x(t)] \\ &- \int_0^t dt' e^{-(t-t')/\tau_i} \partial_x f_i[x(t')] \dot{x}(t') \\ &+ \int_0^t dt' e^{-(t-t')/\tau_i} \frac{F_i(t')}{\gamma_i}, \end{aligned} \quad (\text{A4})$$

where we define the relaxation time of reservoir  $i$  as  $\tau_i = \gamma_i / k_i$ . Substituting the formal solution for  $y_i(t)$  into Eq. (A2), we obtain

$$m\ddot{x}(t) = - \int_0^t \Gamma[t - t', x(t), x(t')] \dot{x}(t') dt' - \partial_x U[x(t)] + \eta[x(t), t] \quad (\text{A6})$$

with the space-inhomogeneous memory function

$$\begin{aligned} \Gamma[t - t', x(t), x(t')] &= \sum_{i=1}^N \frac{\gamma_i}{\tau_i} \partial_x f_i[x(t)] e^{-(t-t')/\tau_i} \partial_x f_i[x(t')], \end{aligned} \quad (\text{A7})$$

and the random force

$$\begin{aligned} \eta[x(t), t] = & - \sum_{i=1}^N \frac{\gamma_i}{\tau_i} \partial_x f_i[x(t)] e^{-t/\tau_i} \{f_i[x(0)] - y_i(0)\} \\ & + \sum_{i=1}^N \frac{1}{\tau_i} \int_0^t dt' \partial_x f_i[x(t')] e^{-(t-t')/\tau_i} F_i(t'). \end{aligned} \quad (\text{A8})$$

How the coupling of the reaction coordinate to reservoir  $i$  varies with  $x(t)$  is determined by the function  $f_i[x(t)]$ . To obtain an on-off coupling depending on the value of  $x(t)$ , as used in Eqs. (2) and (3), we choose functions

$$f_i(x) = \begin{cases} x, & x \in X_i \\ \min(X_i), & x < \min(X_i) \\ \max(X_i), & x \geq \max(X_i), \end{cases} \quad (\text{A9})$$

where  $X_i$  is a spatial domain, which we assume to be a single interval, within which  $x(t)$  couples to reservoir  $i$ . With this definition, the spatial derivative of  $f_i$  is the coupling function,

$$(\partial_x f_i)(x) = \chi_i(x) := \begin{cases} 1, & x \in X_i \\ 0, & x \notin X_i, \end{cases} \quad (\text{A10})$$

so that Eqs. (A2) and (A3) couple  $x(t)$  and  $y_i(t)$  if and only if  $x(t) \in X_i$ , equivalent to a local memory kernel in that regime; cf. Eq. (A7). Note that, strictly speaking, the derivative  $\partial_x f_i$  is not single-valued at the two points,  $x = \min(X_i)$ ,  $\max(X_i)$ ; since the probability that the reaction coordinate takes either one of these values is zero, this is not an issue.

To simulate the GLE (1), we always use the equivalent formulation in terms of a dimensionless version of the Markovian system of Eqs. (A2) and (A3), given in Appendix A 3.

## 2. Generalized fluctuation-dissipation relation

We now show that the memory kernel (A7) and the random force (A8) obey the generalized fluctuation-dissipation relation

$$\langle \eta[x(t), t] \eta[x(t'), t'] \rangle = k_B T \Gamma[x(t), x(t'), t - t']. \quad (\text{A11})$$

To compute the autocorrelation on the left-hand side of Eq. (A11) for all times  $t, t'$ , and not just for times larger than the longest initial relaxation time  $\max_i \{\tau_i\}$  of the heat bath, we need to specify initial conditions  $y_i(0)$  for the auxiliary variables, which appear in Eq. (A8). For this we assume that, for given  $x(0)$ , the  $y_i(0)$  are distributed according to the Boltzmann distribution pertaining to the potential  $U_{\text{hb}}$ , so that  $y_i(0) - f_i[x(0)]$  are given by a Gaussian distribution with zero mean and variance  $\langle \{y_i(0) - f_i[x(0)]\}^2 \rangle = k_B T \tau_i / \gamma_i$ . With this initial condition, the autocorrelation of the noise  $\eta[x(t), t]$  follows as

$$\begin{aligned} & \langle \eta[x(t), t] \eta[x(t'), t'] \rangle \\ &= \sum_{i=1}^N \left( \frac{\gamma_i}{\tau_i} \right)^2 \chi_i[x(t)] \chi_i[x(t')] e^{-(t+t')/\tau_i} \langle \{f_i[x(0)] - y_i(0)\}^2 \rangle \\ &+ \sum_{i=1}^N \frac{1}{\tau_i^2} \int_0^t dt'' \int_0^{t'} dt''' \chi_i[x(t'')] \chi_i[x(t''')] \\ &\times e^{-(t-t''+t'-t''')/\tau_i} \langle F_i(t'') F_i(t''') \rangle. \end{aligned}$$

$$\begin{aligned} &= \sum_{i=1}^N k_B T \frac{\gamma_i}{\tau_i} \chi_i[x(t)] \chi_i[x(t')] e^{-(t+t')/\tau_i} \\ &+ \sum_{i=1}^N \frac{1}{\tau_i^2} \chi_i[x(t)] \chi_i[x(t')] e^{-(t+t')/\tau_i} \\ &\times \int_0^t dt'' \int_0^{t'} dt''' e^{(t''+t''')/\tau_i} 2\gamma_i k_B T \delta(t'' - t''') \\ &= \sum_{i=1}^N k_B T \frac{\gamma_i}{\tau_i} \chi_i[x(t)] \chi_i[x(t')] e^{-(t+t')/\tau_i} \\ &+ \sum_{i=1}^N 2k_B T \frac{\gamma_i}{\tau_i^2} \chi_i[x(t)] \chi_i[x(t')] e^{-(t+t')/\tau_i} \\ &\times \int_0^{\min(t, t')} dt'' e^{2t''/\tau_i} \\ &= \sum_{i=1}^N k_B T \frac{\gamma_i}{\tau_i} \chi_i[x(t)] \chi_i[x(t')] e^{-|t-t'|/\tau_i}. \end{aligned} \quad (\text{A12})$$

By comparing the result (A12) with the memory kernel (A7), we observe that the generalized fluctuation-dissipation relation Eq. (A11) holds.

## 3. Dimensionless formulation of the GLE

In the present section, we give the dimensionless version of both the GLE (1), as well as the equivalent Markovian system Eqs. (A2) and (A3). This in particular makes explicit how many independent parameters the GLE model has.

Using the typical length scale  $L$  of the potential Eq. (5), and the thermal energy  $k_B T \equiv \beta^{-1}$  as energy scale, we define the diffusive time,  $\tau_D = \beta L^2 \gamma$ , which is the typical time a freely diffusing particle with friction constant  $\gamma = \sum_i \gamma_i$  needs to travel a distance  $L$  in a flat potential landscape. We furthermore define the inertial timescale  $\tau_m = m/\gamma$ , on which inertia is dissipated.

Using the scales  $L, \tau_D, \tau_m, \beta$ , we rewrite the coupled Langevin Eqs. (A2) and (A3) in dimensionless form as

$$\begin{aligned} \frac{\tau_m}{\tau_D} \ddot{\tilde{x}}(\tilde{t}) = & - \sum_{i=1}^N \frac{\gamma_i}{\gamma} \frac{\tau_D}{\tau_i} \{ \tilde{f}_i[\tilde{x}(\tilde{t})] - \tilde{y}_i(\tilde{t}) \} \partial_{\tilde{x}} \tilde{f}_i[\tilde{x}(\tilde{t})] \\ & - (\partial_{\tilde{x}} \tilde{U})[\tilde{x}(\tilde{t})], \end{aligned} \quad (\text{A13})$$

$$\dot{\tilde{y}}_i(\tilde{t}) = \frac{\tau_D}{\tau_i} \{ \tilde{f}_i[\tilde{x}(\tilde{t})] - \tilde{y}_i(\tilde{t}) \} + \sqrt{\frac{\gamma}{\gamma_i}} \tilde{F}_i(\tilde{t}), \quad (\text{A14})$$

where  $\tilde{t} := t/\tau_D$ ,  $\tilde{x}(\tilde{t}) := x(\tau_D \tilde{t})/L$ ,  $\dot{\tilde{x}}(\tilde{t}) = \tau_D \dot{x}(\tau_D \tilde{t})/L$ ,  $\ddot{\tilde{x}}(\tilde{t}) = \tau_D^2 \ddot{x}(\tau_D \tilde{t})/L$  are dimensionless time, position, velocity and acceleration.  $-(\partial_{\tilde{x}} \tilde{U})(\tilde{x})$  is the dimensionless deterministic force corresponding to the quartic potential (5) and given by

$$-(\partial_{\tilde{x}} \tilde{U})(\tilde{x}) = -4\tilde{U}_0(\tilde{x}^2 - 1)\tilde{x} \quad (\text{A15})$$

with dimensionless barrier height  $\tilde{U}_0 := \beta U_0$ .

The dimensionless coupling between reaction coordinate and heat bath is given by  $\tilde{f}_i(\tilde{x}) := f_i(L\tilde{x})/L$ , so that

$$\tilde{f}_i(\tilde{x}) = \begin{cases} \tilde{x}, & \tilde{x} \in \tilde{X}_i \\ \min(\tilde{X}_i), & \tilde{x} < \min(\tilde{X}_i) \\ \max(\tilde{X}_i), & \tilde{x} \geq \max(\tilde{X}_i) \end{cases}, \quad (\text{A16})$$

where  $\tilde{X}_i = X_i/L$ , so that

$$(\partial_{\tilde{x}} \tilde{f}_i)(\tilde{x}) = \tilde{\chi}_i(\tilde{x}) = \begin{cases} 1, & \tilde{x} \in \tilde{X}_i \\ 0, & \tilde{x} \notin \tilde{X}_i \end{cases}. \quad (\text{A17})$$

The dimensionless random forces  $\tilde{F}_i(\tilde{t}) = L/(k_B T) \sqrt{\gamma/\gamma_i} F_i(t)$  are Gaussian white noise with zero mean, and covariances  $\langle \tilde{F}_i(\tilde{t}) \tilde{F}_j(\tilde{t}') \rangle = 2\delta_{ij} \delta(\tilde{t} - \tilde{t}')$ .

As in Appendix A 1, we formally solve Eq. (A14), and substitute the result into Eq. (A13), to obtain the dimensionless GLE

$$\frac{\tau_m}{\tau_D} \ddot{\tilde{x}}(\tilde{t}) = - \int_0^{\tilde{t}} \tilde{\Gamma}[\tilde{t} - \tilde{t}', \tilde{x}(\tilde{t}), \tilde{x}(\tilde{t} - \tilde{t}')] \dot{\tilde{x}}(\tilde{t}') d\tilde{t}' - (\partial_{\tilde{x}} \tilde{U})(\tilde{x}(\tilde{t})) + \tilde{\eta}[\tilde{x}(\tilde{t}), \tilde{t}], \quad (\text{A18})$$

with the dimensionless space-inhomogeneous memory kernel

$$\begin{aligned} & \tilde{\Gamma}[\tilde{t} - \tilde{t}', \tilde{x}(\tilde{t}), \tilde{x}(\tilde{t}')] \\ &= \sum_{i=1}^N \frac{\gamma_i}{\gamma} \frac{\tau_D}{\tau_i} \tilde{\chi}_i[\tilde{x}(\tilde{t})] \tilde{\chi}_i[\tilde{x}(\tilde{t}')] \exp\left[-\frac{\tau_D}{\tau_i}(\tilde{t} - \tilde{t}')\right], \end{aligned} \quad (\text{A19})$$

and the dimensionless random force  $\tilde{\eta}[\tilde{x}(\tilde{t}), \tilde{t}] := \beta\eta[x(t), t]/L$ . Instead of explicitly eliminating the heat-bath variables, Eqs. (A18) and (A19), can also be obtained by directly recasting Eqs. (A6) and (A7), in dimensionless form. Similarly to Eq. (A11), the dimensionless memory kernel  $\tilde{\Gamma}$  and random force  $\tilde{\eta}$  obey the generalized fluctuation-dissipation theorem

$$\langle \tilde{\eta}[\tilde{x}(\tilde{t}), \tilde{t}] \tilde{\eta}[\tilde{x}(\tilde{t}'), \tilde{t}'] \rangle = \tilde{\Gamma}[\tilde{t} - \tilde{t}', \tilde{x}(\tilde{t}), \tilde{x}(\tilde{t}')]. \quad (\text{A20})$$

## APPENDIX B: RATE THEORIES

### 1. Formulas for rate theories considered in the main text

In the present section we recall the formulas used to evaluate the various rate theories we consider in the main text.

#### a. Transition-state theory

While we do not explicitly show results from transition-state theory (TST) [58] in the main text, the TST escape rate appears in several of the rate theories we consider. According to TST, for a parabolic free-energy in the reactant state, the mean escape time is given as [58]

$$\tau_{\text{TST}} = \frac{2\pi}{\omega_{\min}} e^{\beta U_0}, \quad (\text{B1})$$

where as before  $U_0$  denotes the barrier height,  $\beta^{-1} = k_B T$  is the thermal energy, and the well frequency  $\omega_{\min} = \sqrt{U''_{\min}/m}$  contains the curvature  $U''_{\min} := U''(x_{\min})$  at the minimum  $x_{\min}$  of the potential well from which the particle escapes.

#### b. Kramers' theory

Kramers considered the escape from a potential well for a particle described by the Markovian inertial Langevin equa-

tion, for both the limits of medium-to-high friction, and low friction [11]. For the medium-to-high friction regime he obtained

$$\tau_{\text{Kr}}^{\text{hf}} = \left[ \left( \frac{\gamma^2}{4m^2} + \omega_{\max}^2 \right)^{1/2} - \frac{\gamma}{2m} \right]^{-1} \omega_{\max} \tau_{\text{TST}}, \quad (\text{B2})$$

while in the low-friction limit, he derived

$$\tau_{\text{Kr}}^{\text{lf}} = \frac{m}{\gamma \beta U_0} e^{\beta U_0}, \quad (\text{B3})$$

where the barrier frequency  $\omega_{\max} = \sqrt{-U''_{\max}/m}$  contains the curvature  $U''_{\max} := U''(x_{\max})$  at the barrier top  $x_{\max}$ . Note the opposite scaling of both equations with respect to the friction constant  $\gamma$ : While for medium-to-high friction it holds that  $\tau_{\text{Kr}}^{\text{hf}} \sim \gamma$ , for low friction we have  $\tau_{\text{Kr}}^{\text{lf}} \sim \gamma^{-1}$ .

#### c. Mel'nikov and Meshkov theory

Mel'nikov and Meshkov [15] (MM) derived a solution to the Kramers' problem which is valid for all values of the friction, and hence bridges the two asymptotic expressions Eqs. (B2) and (B3). The MM result is given by

$$\tau_{\text{MM}} = A^{-1}(\Delta) \left[ \left( \frac{\gamma^2}{4m^2} + \omega_{\max}^2 \right)^{1/2} - \frac{\gamma}{2m} \right]^{-1} \omega_{\max} \tau_{\text{TST}}, \quad (\text{B4})$$

$$A(\Delta) = \exp \left[ \frac{2}{\pi} \int_0^{\frac{\pi}{2}} \ln[1 - e^{-\Delta/[4 \cos^2(x)]}] dx \right], \quad (\text{B5})$$

$$\Delta = 2\sqrt{2} \frac{\gamma}{\sqrt{m}} \beta \int_{-\sqrt{2}L}^0 \sqrt{U_0 - U(x)} dx. \quad (\text{B6})$$

#### d. Grote and Hynes theory

While both Kramers' and Mel'nikov and Meshkov theory consider Markovian dynamics, Grote and Hynes [13] developed a theory for the mean first-passage time,  $\tau_{\text{MFP}}$ , under the influence of memory effects. Their expression for the case where the dynamics in the potential well relax fast, and only memory effects on the barrier are relevant, is given by

$$\tau_{\text{GH}} = \frac{\omega_{\max}}{\lambda} \tau_{\text{TST}}, \quad (\text{B7})$$

where  $\tilde{\Gamma}(\lambda)$  denotes the Laplace-transformed memory friction kernel  $\Gamma(t)$  at the barrier top, and the real reactive frequency  $\lambda > 0$  is given as the solution of the equation

$$\lambda = \frac{\omega_{\max}^2}{\lambda + \tilde{\Gamma}(\lambda)/m}. \quad (\text{B8})$$

Thus, for a single exponential kernel  $\Gamma(t) = \gamma e^{-t/\tau}$ ,  $\lambda$  is calculated from the cubic equation

$$\lambda^3 + \frac{\lambda^2}{\tau} + \left( \frac{\gamma}{m\tau} - \omega_{\max}^2 \right) \lambda = \frac{\omega_{\max}^2}{\tau}. \quad (\text{B9})$$

Note that, either in the inertial,  $m \rightarrow \infty$ , or in the long memory limit,  $\tau \rightarrow \infty$ , it follows that  $\lambda = \omega_{\max}$  and the GH theory collapses onto the transition-state theory result,  $\tau_{\text{GH}} = \tau_{\text{TST}}$  in Eq. (B7).

Furthermore, in the case of instantaneous, i.e., delta-correlated friction,  $\Gamma(t) = 2\gamma\delta(t)$  and  $\tilde{\Gamma}(\lambda) = \gamma$ , it follows



$\lambda = (\gamma^2/(4m^2) + \omega_{\max}^2)^{1/2} - \gamma/(2m)$ , which results in  $\tau_{\text{GH}} = \tau_{\text{Kr}}^{\text{hf}}$ , the Kramers high-friction result in Eq. (B2).

### e. Heuristic formula

In our previous work we constructed a heuristic formula that agrees with both the theory by Pollak *et al.* [34] (PGH) and numerical simulations of  $\tau_{\text{MFP}}$  in the double-well potential Eq. (5), and a GLE with a global single-exponential memory kernel with friction magnitude  $\gamma$  and memory time  $\tau$  [21,35]. Using the diffusive and inertial timescales  $\tau_D = \gamma\beta L^2$  and  $\tau_m = m/\gamma$ , the heuristic formula is given by

$$\frac{\tau_{\text{emp.}}}{\tau_D} = \frac{e^{\beta U_0}}{\beta U_0} \left[ \frac{\pi}{2\sqrt{2}} \left( 1 + 10\beta U_0 \frac{\tau}{\tau_D} \right)^{-1} + \frac{\tau_m}{\tau_D} + 2\sqrt{\beta U_0 \frac{\tau_m}{\tau_D}} + 4\beta U_0 \frac{\tau^2}{\tau_D^2} \right]. \quad (\text{B10})$$

## 2. Evaluation of rate theories for a space-inhomogeneous memory kernel

Whenever we evaluate a rate theory for the effective friction parameters of a region, we use the respective regional friction and memory parameters, or equivalently  $\tau_i$ ,  $\tau_{D,i} = L^2\beta\gamma_i$ ,  $\tau_{m,i} = m/\gamma_i$ . On the other hand, in plots we always rescale the  $\tau_{\text{MFP}}$  as well as the parameters using the diffusive- and inertial times  $\tau_D = L^2\beta\gamma$ ,  $\tau_m = m/\gamma$ , which correspond to the total friction magnitude  $\gamma = \sum_i \gamma_i$ . In the present section we state the relevant relations between these local and global timescales.

The relation between the local and global diffusive and inertial timescales is given by

$$\tau_{D,i} = L^2\beta\gamma_i = \frac{\gamma_i}{\gamma} L^2\beta\gamma = \frac{\gamma_i}{\gamma} \tau_D, \quad (\text{B11})$$

$$\tau_{m,i} = \frac{m}{\gamma_i} = \frac{\gamma}{\gamma_i} \frac{m}{\gamma} = \frac{\gamma}{\gamma_i} \tau_m, \quad (\text{B12})$$

so that

$$\frac{\tau_{m,i}}{\tau_{D,i}} = \left( \frac{\gamma}{\gamma_i} \right)^2 \frac{\tau_m}{\tau_D}, \quad (\text{B13})$$

$$\frac{\tau_{D,i}}{\tau_i} = \frac{\gamma}{\gamma_i} \frac{\tau_D}{\tau_i}, \quad (\text{B14})$$

$$\frac{\tau_{\text{MFP}}}{\tau_{D,i}} = \frac{\gamma}{\gamma_i} \frac{\tau_{\text{MFP}}}{\tau_D}. \quad (\text{B15})$$

Therefore, if we want to calculate  $\tau_{\text{MFP}}/\tau_D$  for region  $i$  using a rate theory for globally homogeneous friction, we have to evaluate

$$\frac{\tau_{\text{MFP}}}{\tau_D} = \frac{\gamma_i}{\gamma} \frac{\tau_{\text{MFP}}}{\tau_{D,i}} \Bigg|_{(\gamma/\gamma_i)^2 \tau_m/\tau_D, (\gamma/\gamma_i) \tau_i/\tau_D}, \quad (\text{B16})$$

where the first argument  $(\gamma/\gamma_i)^2 \tau_m/\tau_D$  is the argument for the dimensionless inertial timescale  $\tau_m/\tau_D$  in the rate theory, and the second argument  $(\gamma/\gamma_i) \tau_i/\tau_D$  is the argument for the dimensionless single-exponential memory  $\tau_i/\tau_D$  in the rate theory.

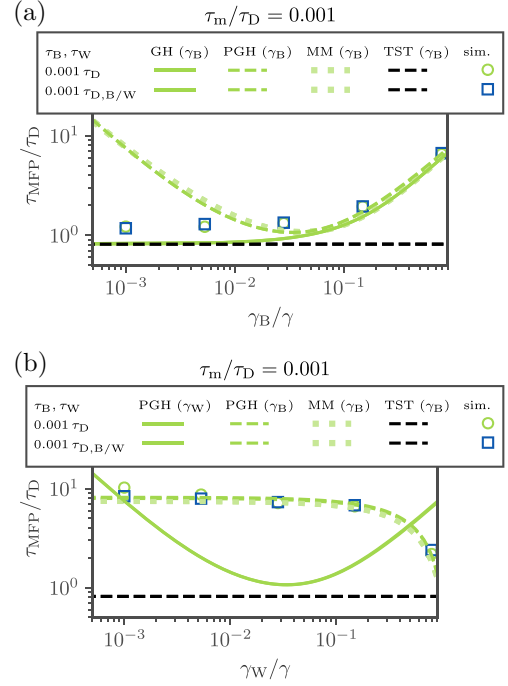


FIG. 4. MFPT,  $\tau_{\text{MFP}}/\tau_D$ , for various single-exponential barrier- and well-memory friction parameters, compared with analytic predictions given by Grote and Hynes [13] [GH, solid line in (a)], Mel'nikov and Meshkov [15] (MM, dotted lines), Pollak *et al.* [34] (PGH, evaluated using the heuristic formula [21]), and transition-state theory (TST, black broken lines). The numerical data are shown for equal barrier and well-friction times,  $\tau_B/\tau_D = \tau_W/\tau_D = 10^{-3}$ , and the inertial timescale is fixed in the high-friction regime  $\tau_m/\tau_D = 10^{-3}$ . Dark blue square markers denote data for which the local friction timescales are kept constant,  $\tau_B/\tau_{D,B} = \tau_W/\tau_{D,W} = 10^{-3}$ , instead of the global ones. (a) Results for the limit  $\gamma_B/\gamma \ll 1$ , the limit of Markovian low friction on the barrier. (b) Results for the limit  $\gamma_W/\gamma \ll 1$ , the limit of Markovian low friction in the well.

## APPENDIX C: FURTHER COMPARISONS OF NUMERICAL DATA WITH RATE THEORIES

### 1. Very unequal friction coefficients in well and barrier regions

In Fig. 2(d) above we show both the well- and barrier-evaluated MM predictions for high friction,  $\tau_m/\tau_D = 10^{-4}$ . Both curves show a nonmonotonic behavior as a function of the barrier friction magnitude  $\gamma_B/\gamma$ : Whereas the barrier-evaluated MM theory displays a minimum at small  $\gamma_B/\gamma$ , the well-evaluated MM prediction for  $\tau_{\text{MFP}}$  becomes minimal at  $\gamma_B/\gamma$  close to 1. We here investigate these two limits in detail by performing simulations for both  $\gamma_B/\gamma \ll 1$  and  $1 - \gamma_B/\gamma = \gamma_W/\gamma \ll 1$ . We show the results in Fig. 4, where we consider an inertial timescale of  $\tau_m/\tau_D = 10^{-3}$  and equal friction timescales in the well and barrier,  $\tau_B/\tau_D = \tau_W/\tau_D = 10^{-3}$ .

In Fig. 4(a) we consider the limit  $\gamma_B/\gamma \ll 1$ , i.e., the limit of Markovian low friction on the barrier. While the MM and PGH theories, both evaluated for the barrier friction parameters, show a nonmonotonic trend (namely the Kramers turnover), the numerical  $\tau_{\text{MFP}}$  (light green circles) levels off to

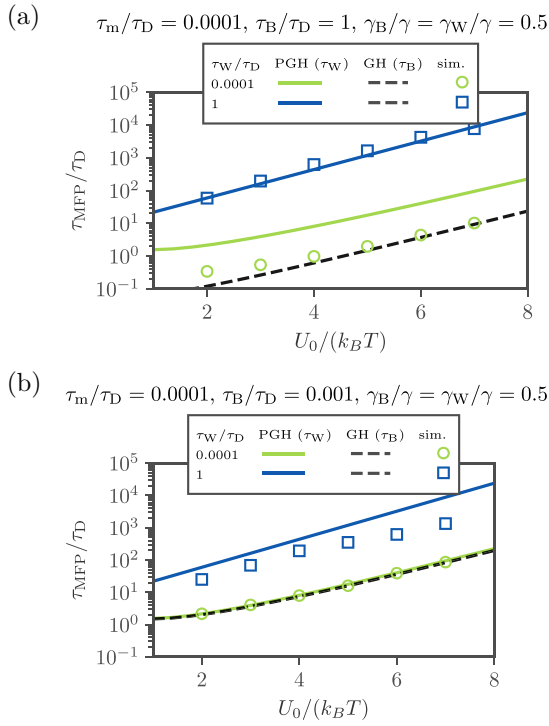


FIG. 5. MFPT,  $\tau_{MFP}/\tau_D$ , for various single-exponential barrier- and well-friction parameters, shown as a function of the barrier height  $\beta U_0$ . The numerical data are shown for two well-friction times,  $\tau_W/\tau_D = 10^{-4}$  and  $\tau_W/\tau_D = 1$ , fixed barrier-friction time  $\tau_B/\tau_D = 1$  (a) and  $\tau_B/\tau_D = 10^{-3}$  (b), always for equal friction constants  $\gamma_B/\gamma = \gamma_W/\gamma = 1/2$ . The inertial timescale is fixed in the high-friction regime  $\tau_m/\tau_D = 10^{-4}$ . For comparison, predictions by Grote and Hynes [13] (GH, broken lines) and Pollak *et al.* [34] (PGH, solid lines, evaluated using the heuristic formula [21]) are also shown.

a constant for small  $\gamma_B/\gamma$ , with a value close to the prediction of transition-state theory (black broken line). This limit is also correctly recovered by the GH theory evaluated for the barrier friction parameters (light green solid line). Therefore, for  $\gamma_B/\gamma \ll 1$ , the GH theory outperforms MM theory and PGH theory. This is in contrast to the results shown in the main text in Figs. 2(a), 2(d), and 2(e), where the local friction magnitudes are considered to be within one order of magnitude, and the well-friction evaluated MM theory describes the numerical data correctly.

We discuss the opposite limit  $\gamma_W/\gamma \ll 1$  in Fig. 4(b). Here the numerical  $\tau_{MFP}$  (light green circles) is consistent with both the MM and PGH theories, evaluated using the barrier parameters, and markedly different from the predictions of transition-state theory and the PGH theory evaluated using the well parameters. The agreement of barrier-evaluated theories and the numerical data indicates that the system is described by the Kramers high-friction limit. At first sight this might seem surprising, because for  $\gamma_W/\gamma \ll 1$  the local dynamics in the well is clearly underdamped, as for  $\gamma_W/\gamma = 10^{-3}$  we have  $\tau_{m,W}/\tau_{D,W} = 10^3$ . However, since for  $\gamma_W/\gamma \ll 1$  we have  $\tau_{D,W} \ll \tau_{D,B}$ , even though the mean time a particle in the well needs to reach the barrier is a large multiple of  $\tau_{D,W}$ , this time

may still be much smaller than the time to diffusively cross the barrier (which depends on  $\tau_{D,B}$ ). Therefore, for  $\gamma_W/\gamma \ll 1$ , even though the well dynamics is in the energy diffusion limit, the crossing over the barrier can still be the rate-limiting step of the escape process.

Furthermore, we note that in both Figs. 4(a) and 4(b), for the lowest value of the local friction magnitude  $\gamma_i/\gamma = 10^{-3}$ , the local friction times,  $\tau_i/\tau_{D,i} = 1$ , are not anymore in the Markovian limit. To exclude local non-Markovian effects influencing the shown  $\tau_{MFP}$ , we also show numerical data for constant local friction times,  $\tau_B/\tau_{D,B} = \tau_W/\tau_{D,W} = 10^{-3}$  (dark blue squares) in Figs. 4(a) and 4(b). These data are almost identical to the data at constant  $\tau_B/\tau_D, \tau_W/\tau_D$ , so we conclude that non-Markovian effects remain negligible for the parameter regime shown.

## 2. Variation of barrier height

In the main text, we consider numerical results and rate theories for the barrier height  $\beta U_0 = 3$ . In Fig. 5 we compare numerical results for barrier heights ranging from  $\beta U_0 = 2$  to  $\beta U_0 = 7$  to rate-theory predictions, and find that conclusions drawn in the main text remain true also for larger barrier heights.

While in Fig. 5(a) we show results for non-Markovian barrier dynamics  $\tau_B/\tau_D = 1$ , in Fig. 5(b) we consider a barrier with Markovian dynamics,  $\tau_B/\tau_D = 0.001$ . For both subplots we use  $\gamma_W/\gamma = \gamma_B/\gamma = 0.5$ , i.e., an equal partitioning of the total friction magnitude to well and barrier, and high friction  $\tau_m/\tau_D = 10^{-4}$ . For both subplots, we consider two representative parameters for the well-friction time  $\tau_W/\tau_D$ . The results for  $\tau_W/\tau_D = 10^{-4}$ , shown as light green circles in Fig. 5, correspond to the Markovian high-well-friction regime, for which the dynamics are predicted by the GH theory. The dark blue squares in the figure correspond to  $\tau_{MFP}$  for well-friction time  $\tau_W/\tau_D = 1$ , which corresponds to the long-well-memory regime where  $\tau_{MFP}$  is predicted by the PGH theory, evaluated using the memory kernel parameters at the potential well. As Fig. 5(b) demonstrates, the ‘‘Markovian-barrier acceleration’’ regime discussed in detail in the main text also exists for larger barrier heights.

Overall, Fig. 5 shows that the predictions from the main text are consistent with the numerical data for all barrier heights  $\beta U_0 \in [2, 7]$  considered here. In fact the predictions seem to improve for higher barriers. The exponential dependence of  $\tau_{MFP}$  on the barrier-height, known since Arrhenius [59], is also well visible in our semilogarithmic representation of the data.

## 3. Variation of inertial timescale

In Fig. 3 we consider barrier crossing for the high-friction regime  $\tau_m/\tau_D = 10^{-4}$ , while the friction magnitudes are equal  $\gamma_B/\gamma = \gamma_W/\gamma = 0.5$  and the friction memory times in the well  $\tau_W/\tau_D$  and on the barrier  $\tau_B/\tau_D$  are varied. In Fig. 6 we show additional numerical and analytical  $\tau_{MFP}$  for larger inertial times. We consider the inertial times  $\tau_m/\tau_D = 10^{-4}$  [Figs. 6(a)–6(c)],  $10^{-2}$  [Figs. 6(d)–6(f)], and 1 [Figs. 6(g)–6(i)]. While the first column of Fig. 6 shows the rescaled  $\tau_{MFP}$  as a function of the barrier-friction time  $\tau_B/\tau_D$  for various

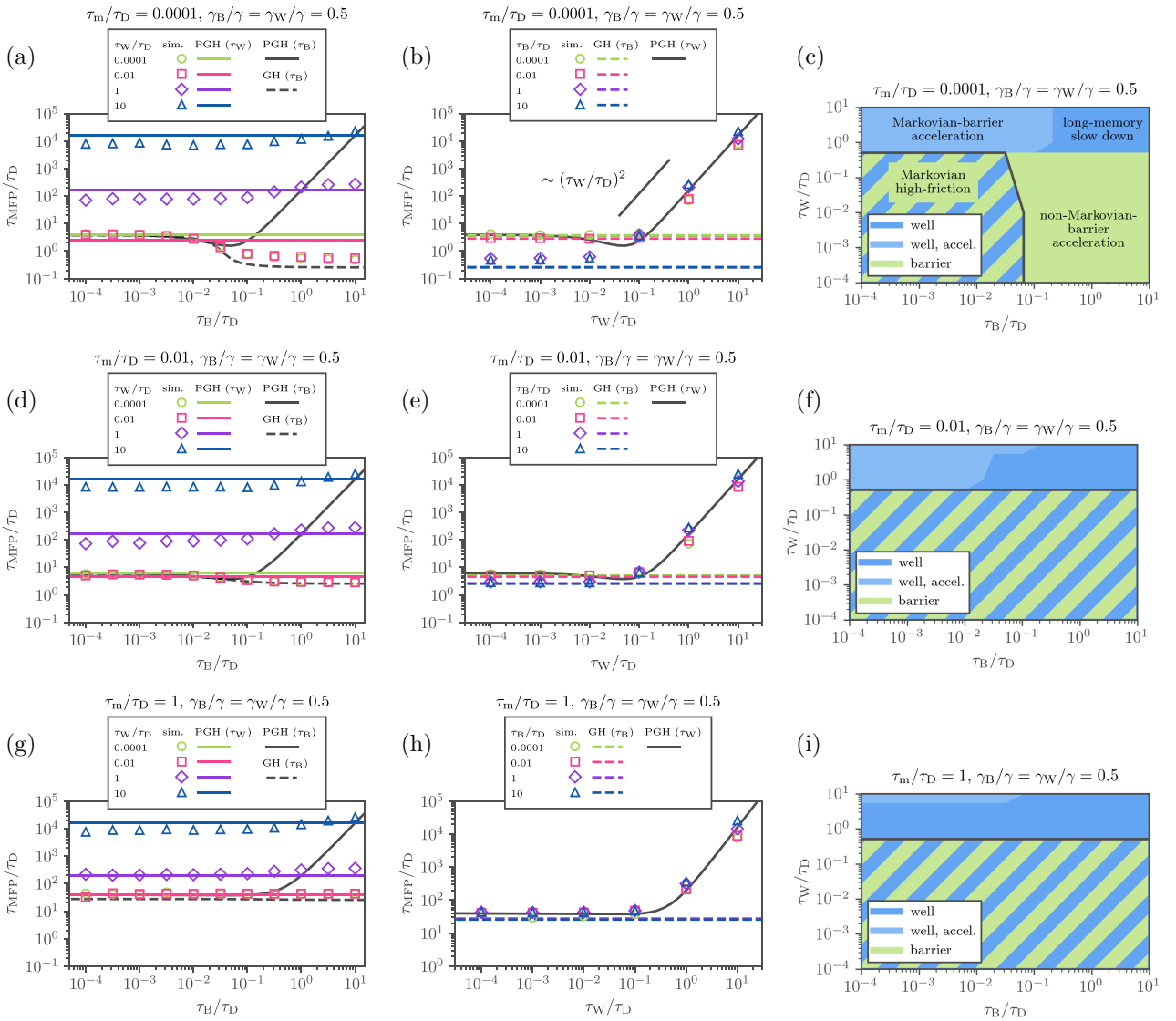


FIG. 6. MFPT,  $\tau_{\text{MFPT}}/\tau_D$ , for different barrier memory friction, and well memory friction, obtained from numerical simulations (data points) and compared with analytic predictions given by Grote and Hynes [13] (GH, broken lines) and Pollak *et al.* [34] (PGH, solid lines, evaluated using the heuristic formula [21]). The data are shown for various barrier-friction  $\tau_B/\tau_D$  and well-friction times  $\tau_W/\tau_D$  and equal friction magnitudes  $\gamma_B/\gamma = \gamma_W/\gamma = 0.5$ . The inertial timescale is constant and different in each row (a–c:  $\tau_m/\tau_D = 10^{-4}$ , d–f:  $\tau_m/\tau_D = 10^{-2}$ , g–i:  $\tau_m/\tau_D = 1$ ). (a, d, g)  $\tau_{\text{MFPT}}$  plotted over the barrier-friction time  $\tau_B/\tau_D$ . The theories are shown for the respective barrier-friction time in black and in the case of the PGH theory for the well-friction time as colored solid lines. (b, e, h)  $\tau_{\text{MFPT}}$  plotted over the well-friction time  $\tau_W/\tau_D$ . The theories are shown for the respective well-friction time in black and in the case of the GH theory for the barrier-friction time as colored broken lines. (c, f, i) Contour plots of agreement of the simulation results with the theoretical predictions. The color denotes whether the simulated  $\tau_{\text{MFPT}} \in [1/3 \tau_{\text{theo}}, 3 \tau_{\text{theo}}]$ , where  $\tau_{\text{theo}}$  is calculated using either the GH theory with the barrier-friction parameters or the PGH theory with the well-friction parameters. The hatching indicates that both theoretical predictions agree with the simulated data. The light blue area denotes the “Markovian-barrier acceleration” of the PGH prediction for which we define  $\tau_{\text{theo,MBA}} = 0.2 \tau_{\text{theo,PGH}}$ .

values of the well-friction time  $\tau_W/\tau_D$ , in the second column we vary the well-friction time for several constant values of the barrier-friction time. In both the first and second columns, the appropriate analytic predictions including memory effects are given either by the GH theory, which is evaluated for the effective barrier-friction parameters, determined by  $\tau_B$  (broken lines) or by the PGH theory (solid lines), which is evaluated for the effective well-friction parameters, given by  $\tau_W$ . The third column of Fig. 6 depicts phase diagrams that sum-

marize for which parameters  $(\tau_B/\tau_D, \tau_W/\tau_D)$  the numerical data agree with the predictions of the GH theory or PGH theory. Note that [Figs. 6(a)–6(c)] are replots of Figs. 3(a), 3(d), and 3(e).

Figure 6 shows that all conclusions drawn in the main text also hold true as  $\tau_m/\tau_D$  is varied, i.e., away from the high-friction limit. In particular, for larger inertial timescales  $\tau_m/\tau_D$ , the predictions for the  $\tau_{\text{MFPT}}$  are described globally by the PGH theory for the well-friction parameters.

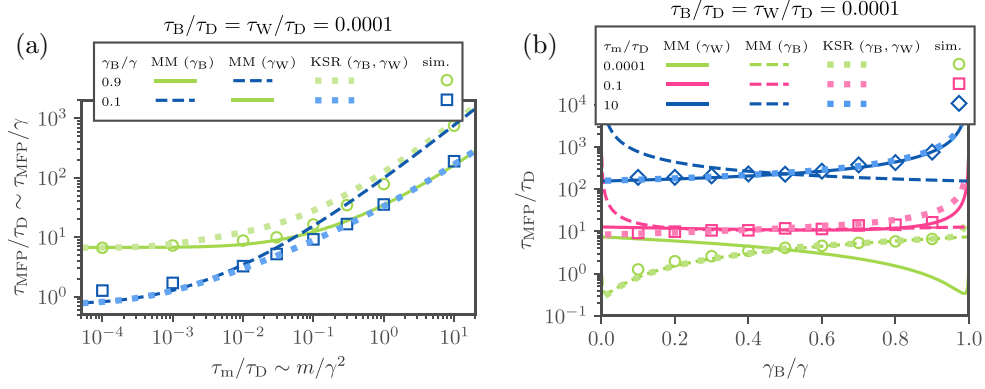


FIG. 7. MFPT,  $\tau_{MFP}/\tau_D$ , for different barrier memory friction,  $\Gamma_B(t) = \gamma_B/\tau_B e^{-t/\tau_B}$  and well memory friction,  $\Gamma_W(t) = \gamma_W/\tau_W e^{-t/\tau_W}$ , obtained from numerical simulations (data points) and compared with analytic predictions given by Mel'nikov and Meshkov [15] (MM) as well as the predictions by Krishnan *et al.* [48] (KSR, dotted lines), equivalent to Figs. 2(a) and 2(d). The data are shown for equal memory times in the Markovian limit with  $\tau_B/\tau_D = \tau_W/\tau_D = 10^{-4}$ . (a)  $\tau_{MFP}$  plotted over the inertial timescale  $\tau_m/\tau_D$  for different ratios of the barrier friction constant to total friction  $\gamma_B/\gamma$ . (b)  $\tau_{MFP}$  plotted over  $\gamma_B/\gamma$  for various  $\tau_m/\tau_D$ . The predictions by MM are shown for the effective barrier-friction parameters, given by  $\gamma_B$ , as broken lines and for the effective well-friction parameters, given by  $\gamma_W$ , as solid lines.

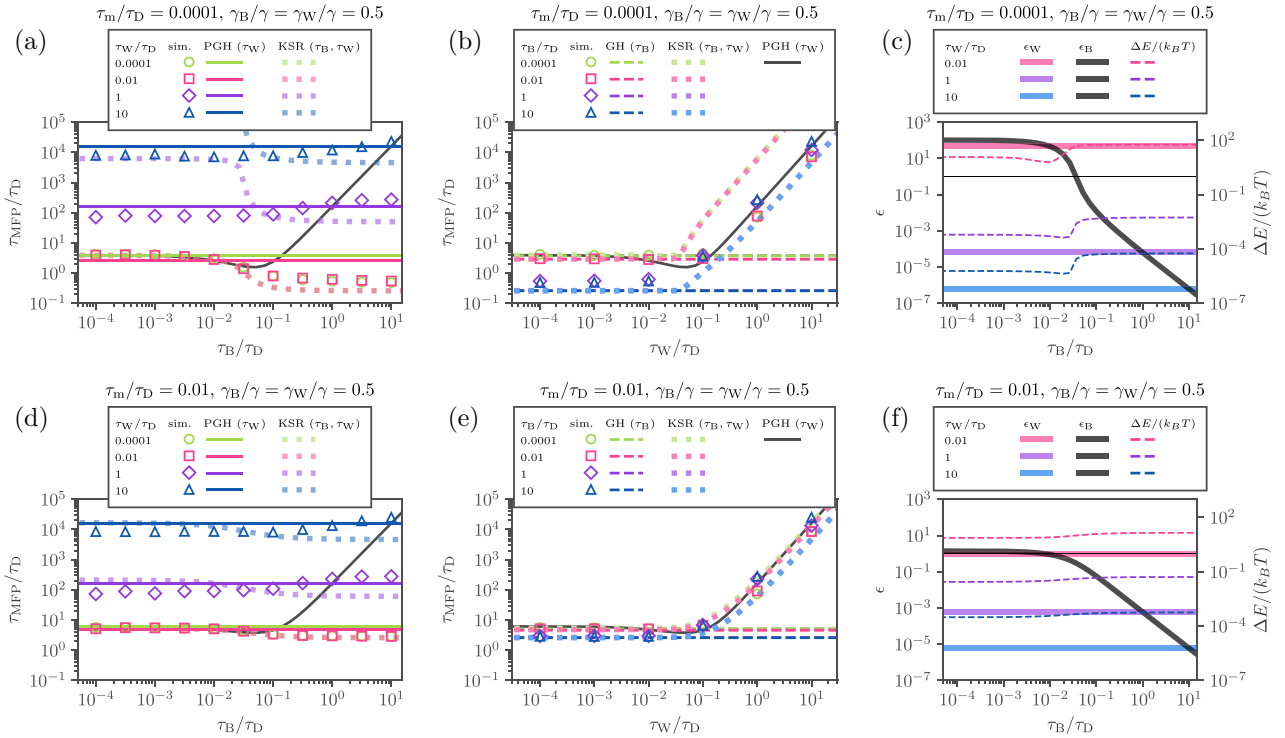


FIG. 8. MFPT,  $\tau_{MFP}/\tau_D$ , for different barrier memory friction and well memory friction, obtained from numerical simulations (data points) and compared with analytic predictions given by Grote and Hynes [13] (GH, broken lines) and by Pollak *et al.* [34] (PGH, solid lines), evaluated using the heuristic formula [21]), as well as predictions by Krishnan *et al.* [48] (KSR, dotted lines). The data are shown for various barrier-friction  $\tau_B/\tau_D$  and well-friction times  $\tau_W/\tau_D$  and equal friction constants  $\gamma_B/\gamma = \gamma_W/\gamma = 1/2$ . The inertial timescale is constant and different in each row (a–c:  $\tau_m/\tau_D = 10^{-4}$ , d–f:  $\tau_m/\tau_D = 10^{-2}$ ). (a, d)  $\tau_{MFP}$  plotted over the barrier-friction time  $\tau_B/\tau_D$ . The prediction by the PGH theory are shown for the respective barrier-friction time as black and for the well-friction time as colored solid lines. (b, e)  $\tau_{MFP}$  plotted over the well-friction time  $\tau_W/\tau_D$ . The prediction by the PGH theory is shown for the respective well-friction time in black and in the case of GH theory for the barrier-friction time as colored broken lines. (c, f) Perturbation parameters  $\epsilon_B$  for the barrier region and  $\epsilon_W$  for the well region and energy loss  $\Delta E/(k_B T)$ , both relevant for stability of the KSR theory. The thin black horizontal line denotes the value 1.

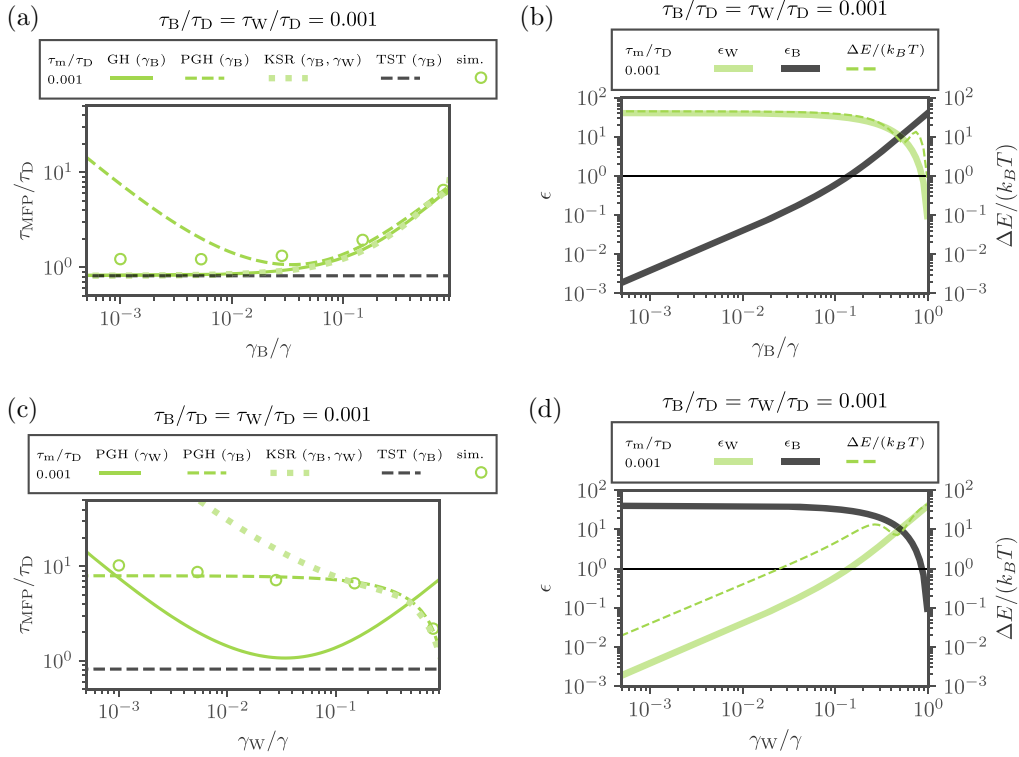


FIG. 9. MFPT,  $\tau_{\text{MFPT}}/\tau_D$ , for various single-exponential barrier- and well-friction parameters, obtained from numerical simulations (data points) and compared with analytic predictions given by Grote and Hynes [13] [GH, solid line in (a)], Pollak *et al.* [34] (PGH, evaluated using the heuristic formula [21]), transition-state theory (TST, black broken lines), as well as the predictions by Krishnan *et al.* [48] (KSR, dotted lines). The numerical data are shown for equal barrier and well-friction times,  $\tau_B/\tau_D = \tau_W/\tau_D = 10^{-3}$  and the inertial timescale is fixed in the high-friction regime  $\tau_m/\tau_D = 10^{-3}$ . (a) Results for the limit  $\gamma_B/\gamma \ll 1$ , the limit of Markovian low friction on the barrier. (c) Results for the limit  $\gamma_W/\gamma \ll 1$ , the limit of Markovian low friction in the well. (b, d) Perturbation parameters  $\epsilon_B$  for the barrier region and  $\epsilon_W$  for the well region and energy loss  $\Delta E/(k_B T)$ , both relevant for stability of the KSR theory. The thin black horizontal line denotes the value 1.

Furthermore, Figs. 6(d) and 6(g) show that the “Markovian-barrier acceleration” regime is also present for larger inertial times. On the other hand, the “non-Markovian-barrier acceleration” predicted by the GH theory vanishes.

#### 4. Comparison of numerical results to KSR theory

In the present section, we compare our numerical  $\tau_{\text{MFPT}}$  with the predictions of a theory for barrier crossing with space-inhomogeneous memory friction. Krishnan, Singh, and Robinson (KSR) [48] derived an analytic theory for  $\tau_{\text{MFPT}}$  in a piecewise harmonic potential with different well and barrier memory friction; this theory is based on the formalism by Pollak, Grabert, and Hänggi [34]. The analytical KSR predictions for  $\tau_{\text{MFPT}}$  had not been compared to numerical simulations in the literature.

The KSR model takes as input the memory-friction kernels for the well and barrier regions, for both of which we consider single exponentials, the particle mass  $m = \tau_m \gamma$ , the local angular frequencies of the potential for the well,  $\omega_0 = (\partial_x^2 U)(x = -L)/m$  and barrier  $\omega_b = -(\partial_x^2 U)(x = 0)/m$ , and the barrier height  $\beta U_0 = 3$ , where as before  $U(x)$  is the quartic potential (5).

We now compare the predictions of KSR theory with the same numerical data as considered in Figs. 2 and 3.

First, in Fig. 7 we consider the data from Fig. 2. For a detailed discussion of the data we refer to the main text, as this section focuses on evaluating the quality of the KSR theory with respect to the other theories. For the Markovian limit, i.e.,  $\tau_W/\tau_D = \tau_B/\tau_D \ll 1$ , we generally observe good agreement between numerical data and KSR theory throughout Fig. 7. However, the predictions by MM using effective local parameters perform slightly better in the whole parameter range. Of course, the true strength of the model by KSR here is the correct interpolation between barrier- and well-dominated dynamics, which needs to be chosen by hand in the evaluation of MM theory. This is most clearly seen in Fig. 2, where KSR theory switches between the barrier-dominated and well-dominated MM predictions as  $\tau_m/\tau_D$  is increased.

The data of Fig. 3(a) and 3(d) are discussed in this section in Figs. 8(a) and 8(b), where  $\tau_m/\tau_D = 10^{-4}$ . While the predictions by KSR again interpolate correctly between well- and barrier-dominated dynamics, in the regime where  $\tau_W/\tau_D \geq 0.1$  and  $\tau_B/\tau_D \leq 0.1$ , we observe significant deviations between the numerical  $\tau_{\text{MFPT}}$  and the corresponding KSR prediction. As can be seen clearly in the upper left corner of Fig. 3(a) and the right side of Fig. 3(b), the numerical and analytical data can deviate by several orders of magnitude. For larger inertial timescales, these deviations become smaller as shown in Figs. 8(c) and 8(d) where  $\tau_m/\tau_D = 10^{-2}$ . We

note that KSR throughout predicts a barrier crossing speedup as  $\tau_B/\tau_D$  is increased [see Figs. 8(a) and 8(d)], whereas the numerical data display the “Markovian-barrier acceleration” behavior for  $\tau_W/\tau_D \gtrsim 1$ , for which barrier crossing is in fact slower as  $\tau_B/\tau_D$  is increased. Possible explanations for the deviations observed in Figs. 7 and 8 are discussed in the following.

To rationalize the deviations between numerical and analytical predictions, we point out that KSR themselves state that their theory is not to be expected to be reliable if  $\epsilon_B \gtrsim 1$  in the barrier region or  $\epsilon_W \gtrsim 1$  in the well region (note that  $\epsilon$  and  $\epsilon'$  are used in the original work [48]). The perturbation parameters  $\epsilon_B$ ,  $\epsilon_W$  represent a measure for the strength of coupling between reaction coordinate and heat bath, and are defined as  $\epsilon_B = \gamma_B/[2m\lambda_B(1 + \tau_B\lambda_B)^2]$  and  $\epsilon_W = \gamma_W/[2m\lambda_W(1 + \tau_W\lambda_W)^2]$ , with  $\lambda_B$  and  $\lambda_W$  the GH frequencies which solve Eq. (B8) for the respective memory kernels (well or barrier). These conditions are easily violated in the case of small inertial timescales  $\tau_m = m/\gamma$ , as Fig. 8(c) shows. However, a similar perturbation parameter  $\epsilon$  is also relevant for the applicability of the PGH theory, and those authors note in their paper that the PGH theory remains valid even for large  $\epsilon$ , if at the same time the energy loss per cycle through the well region is large,  $\beta\Delta E > 1$  [34]. More so, the PGH predictions have been shown to globally agree well with numerical results obtained from a homogeneous memory kernel [35].

The clear deviations between KSR theory and the numerical results in Fig. 8(a), observed for small  $\tau_B/\tau_D$  and large  $\tau_W/\tau_D$  (dark purple and dark blue lines), can be rationalized by the simultaneous breakdown of both the conditions on the pair  $\epsilon_B$ ,  $\epsilon_W$ , and  $\beta\Delta E$ : as Fig. 8(c) shows, in the regime where deviations between theory and numerical data are observed,  $\epsilon_B \gtrsim 1$  while  $\beta\Delta E \ll 1$ . In contrast to that, Fig. 8(f) shows the perturbation parameters and energy loss per cycle for

slightly larger inertial times  $\tau_m/\tau_D = 0.01$ . Here the conditions  $\epsilon_B < 1$  and  $\epsilon_W < 1$  are met and the predictions agree with the simulation data in Figs. 8(c) and 8(e).

In Fig. 4 we consider  $\tau_{\text{MFP}}$  for the cases where  $\gamma_B/\gamma \ll 1$  and  $\gamma_W/\gamma \ll 1$ , i.e., the the scenario where the well- and barrier-friction magnitudes are very different. In Figs. 9(a) and 9(c) we compare the numerical results for  $\tau_{\text{MFP}}$  with KSR theory. As can be observed in Fig. 9(a), KSR theory (light green dotted line) correctly captures the limit  $\gamma_B/\gamma \ll 1$ , i.e., the limit of Markovian low friction on the barrier. However, Fig. 9(c) shows that KSR theory does not capture the opposite limit. For  $\gamma_W/\gamma \ll 1$ , KSR theory predicts a significant slow-down, which is not confirmed by simulation data. The breakdown of KSR theory is again understood by considering the perturbation parameters  $\epsilon_B$ ,  $\epsilon_W$  and the energy loss  $\Delta E/(k_B T)$ , which are plotted in Figs. 9(b) and 9(d) for the respective data. As previously discussed for the data in Fig. 8, KSR theory breaks down whenever the energy loss per cycle in the well region is small,  $\Delta E/(k_B T) \ll 1$ , while the coupling to the barrier heat bath is strong,  $\epsilon_B \gtrsim 1$ . This is again the case for the data in Fig. 9(c), as can be seen from the corresponding perturbation parameters in Fig. 9(d).

In summary, while KSR theory does capture the crossover from well-dominated to barrier-dominated  $\tau_{\text{MFP}}$ , the theory captures neither the “Markovian-barrier acceleration” regime, nor the limit  $\gamma_W/\gamma \ll 1$ . This can be explained by the assumptions underlying the KSR derivation, which are not fulfilled in these regimes: In both regimes, the energy exchange with the well heat bath is weak (small  $\beta\Delta E \ll 1$ ), while simultaneously the coupling to the barrier heat bath is strong ( $\epsilon_B \gtrsim 1$ ). While in the “Markovian-barrier acceleration” regime, the weak energy exchange in the well is due to long memory, in the regime  $\gamma_W/\gamma \ll 1$ , the weak energy exchange is because of the small well friction.

- 
- [1] R. Zwanzig, Memory effects in irreversible thermodynamics, *Phys. Rev.* **124**, 983 (1961).
- [2] H. Mori, Transport, collective motion, and Brownian motion, *Prog. Theor. Phys.* **33**, 423 (1965).
- [3] R. Zwanzig, Nonlinear generalized Langevin equations, *J. Stat. Phys.* **9**, 215 (1973).
- [4] R. Zwanzig, *Nonequilibrium Statistical Mechanics* (Oxford University Press, Oxford, 2001)
- [5] A. Berezhkovskii and A. Szabo, One-dimensional reaction coordinates for diffusive activated rate processes in many dimensions, *J. Chem. Phys.* **122**, 014503 (2005).
- [6] O. F. Lange and H. Grubmüller, Collective Langevin dynamics of conformational motions in proteins, *J. Chem. Phys.* **124**, 214903 (2006).
- [7] J. O. Daldrop, J. Kappler, F. N. Brüning, and R. R. Netz, Butane dihedral angle dynamics in water is dominated by internal friction, *Proc. Natl. Acad. Sci. USA* **115**, 5169 (2018).
- [8] J. Kappler, F. Noé, and R. R. Netz, Cyclization and Relaxation Dynamics of Finite-Length Collapsed Self-Avoiding Polymers, *Phys. Rev. Lett.* **122**, 067801 (2019).
- [9] R. Satija and D. E. Makarov, Generalized Langevin equation as a model for barrier crossing dynamics in biomolecular folding, *J. Phys. Chem. B* **123**, 802 (2019).
- [10] B. Lickert and G. Stock, Modeling non-Markovian data using Markov state and Langevin models, *J. Chem. Phys.* **153**, 244112 (2020).
- [11] H. Kramers, Brownian motion in a field of force and the diffusion model of chemical reactions, *Physica* **7**, 284 (1940).
- [12] D. Chandler, Statistical mechanics of isomerization dynamics in liquids and the transition state approximation, *J. Chem. Phys.* **68**, 2959 (1978).
- [13] R. F. Grote and J. T. Hynes, The stable states picture of chemical reactions. II. Rate constants for condensed and gas phase reaction models, *J. Chem. Phys.* **73**, 2715 (1980).
- [14] D. Chandler, Roles of classical dynamics and quantum dynamics on activated processes occurring in liquids, *J. Stat. Phys.* **42**, 49 (1986).

- [15] V. I. Mel'nikov and S. V. Meshkov, Theory of activated rate processes: Exact solution of the Kramers problem, *J. Chem. Phys.* **85**, 1018 (1986).
- [16] P. Hänggi, P. Talkner, and M. Borkovec, Reaction-rate theory: Fifty years after Kramers, *Rev. Mod. Phys.* **62**, 251 (1990).
- [17] V. I. Mel'nikov, The Kramers problem: Fifty years of development, *Phys. Rep.* **209**, 1 (1991).
- [18] R. B. Best and G. Hummer, Diffusive Model of Protein Folding Dynamics with Kramers Turnover in Rate, *Phys. Rev. Lett.* **96**, 228104 (2006).
- [19] G. Wilemski and M. Fixman, Diffusion-controlled intrachain reactions of polymers. II. Results for a pair of terminal reactive groups, *J. Chem. Phys.* **60**, 878 (1974).
- [20] A. Szabo, K. Schulten, and Z. Schulten, First passage time approach to diffusion controlled reactions, *J. Chem. Phys.* **72**, 4350 (1980).
- [21] J. Kappler, V. B. Hinrichsen, and R. R. Netz, Non-Markovian barrier crossing with two-time-scale memory is dominated by the faster memory component, *Eur. Phys. J. E* **42**, 119 (2019).
- [22] C. Ayaz, L. Tepper, F. N. Brünig, J. Kappler, J. O. Daldrop, and R. R. Netz, Non-Markovian modeling of protein folding, *Proc. Natl. Acad. Sci. USA* **118**, e2023856118 (2021).
- [23] J. E. Straub, M. Borkovec, and B. J. Berne, Calculation of dynamic friction on intramolecular degrees of freedom, *J. Phys. Chem.* **91**, 4995 (1987).
- [24] G. Ciccotti, M. Ferrario, J. T. Hynes, and R. Kapral, Dynamics of ion pair interconversion in a polar solvent, *J. Chem. Phys.* **93**, 7137 (1990).
- [25] I. Benjamin, L. L. Lee, Y. S. Li, A. Liu, and K. R. Wilson, Generalized Langevin model for molecular dynamics of an activated reaction in solution, *Chem. Phys.* **152**, 1 (1991).
- [26] R. Rey, E. Guàrdia, and J. A. Padró, Generalized Langevin dynamics simulation of activated processes in solution: Ion pair interconversion in water, *J. Chem. Phys.* **97**, 8276 (1992).
- [27] H. V. R. Annapureddy and L. X. Dang, Understanding the rates and molecular mechanism of water-exchange around aqueous ions using molecular simulations, *J. Phys. Chem. B* **118**, 8917 (2014).
- [28] H. Meyer, S. Wolf, G. Stock, and T. Schilling, A numerical procedure to evaluate memory effects in non-equilibrium coarse-grained models, *Adv. Theory Sim.* **4**, 2000197 (2021).
- [29] M. Tuckerman and B. J. Berne, Vibrational relaxation in simple fluids: Comparison of theory and simulation, *J. Chem. Phys.* **98**, 7301 (1993).
- [30] F. N. Brünig, O. Geburtig, A. von Canal, J. Kappler, and R. R. Netz, Time-dependent friction effects on vibrational infrared frequencies and line shapes of liquid water, *J. Phys. Chem. B* **126**, 1579 (2022).
- [31] R. Zwanzig, Ensemble method in the theory of irreversibility, *J. Chem. Phys.* **33**, 1338 (1960).
- [32] J. O. Daldrop, B. G. Kowalik, and R. R. Netz, External Potential Modifies Friction of Molecular Solutes in Water, *Phys. Rev. X* **7**, 041065 (2017).
- [33] B. Müller, J. Berner, C. Bechinger, and M. Krüger, Properties of a nonlinear bath: Experiments, theory, and a stochastic Prandtl-Tomlinson model, *New J. Phys.* **22**, 023014 (2020).
- [34] E. Pollak, H. Grabert, and P. Hänggi, Theory of activated rate processes for arbitrary frequency dependent friction: Solution of the turnover problem, *J. Chem. Phys.* **91**, 4073 (1989).
- [35] J. Kappler, J. O. Daldrop, F. N. Brünig, M. D. Boehle, and R. R. Netz, Memory-induced acceleration and slowdown of barrier crossing, *J. Chem. Phys.* **148**, 014903 (2018).
- [36] P. Talkner and H.-B. Braun, Transition rates of a non-Markovian Brownian particle in a double well potential, *J. Chem. Phys.* **88**, 7537 (1988).
- [37] J. E. Straub, M. Borkovec, and B. J. Berne, Non-Markovian activated rate processes: Comparison of current theories with numerical simulation data, *J. Chem. Phys.* **84**, 1788 (1986).
- [38] S. C. Tucker, M. E. Tuckerman, B. J. Berne, and E. Pollak, Comparison of rate theories for generalized Langevin dynamics, *J. Chem. Phys.* **95**, 5809 (1991).
- [39] R. Ianculescu and E. Pollak, A study of Kramers' turnover theory in the presence of exponential memory friction, *J. Chem. Phys.* **143**, 104104 (2015).
- [40] L. Lavacchi, J. Kappler, and R. R. Netz, Barrier crossing in the presence of multi-exponential memory functions with unequal friction amplitudes and memory times, *Europhys. Lett.* **131**, 40004 (2020).
- [41] A. Berezhkovskii and A. Szabo, Time scale separation leads to position-dependent diffusion along a slow coordinate, *J. Chem. Phys.* **135**, 074108 (2011).
- [42] G. Hummer, From transition paths to transition states and rate coefficients, *J. Chem. Phys.* **120**, 516 (2004).
- [43] M. Hinczewski, Y. von Hansen, J. Dzubiella, and R. R. Netz, How the diffusivity profile reduces the arbitrariness of protein folding free energies, *J. Chem. Phys.* **132**, 245103 (2010).
- [44] J. B. Straus, J. M. Gomez Llorente, and G. A. Voth, Manifestations of spatially dependent friction in classical activated rate processes, *J. Chem. Phys.* **98**, 4082 (1993).
- [45] E. Pollak and A. M. Berezhkovskii, Fokker-Planck equation for nonlinear stochastic dynamics in the presence of space and time dependent friction, *J. Chem. Phys.* **99**, 1344 (1993).
- [46] G. R. Haynes, G. A. Voth, and E. Pollak, A theory for the activated barrier crossing rate constant in systems influenced by space and time dependent friction, *J. Chem. Phys.* **101**, 7811 (1994).
- [47] S. Singh, R. Krishnan, and G. W. Robinson, Theory of activated rate processes with space-dependent friction, *Chem. Phys. Lett.* **175**, 338 (1990).
- [48] R. Krishnan, S. Singh, and G. W. Robinson, Space-dependent friction in the theory of activated rate processes: The Hamiltonian approach, *J. Chem. Phys.* **97**, 5516 (1992).
- [49] S. Singh and G. W. Robinson, Scaling in a model of chemical reaction rates with space-dependent friction, *J. Phys. Chem.* **98**, 7300 (1994).
- [50] J. O. Daldrop, W. K. Kim, and R. R. Netz, Transition paths are hot, *Europhys. Lett.* **113**, 18004 (2016).
- [51] A. F. Voter and J. D. Doll, Dynamical corrections to transition state theory for multistate systems: Surface self-diffusion in the rare-event regime, *J. Chem. Phys.* **82**, 80 (1985).
- [52] C. Ayaz, L. Scalfi, B. A. Dalton, and R. R. Netz, Generalized Langevin equation with a nonlinear potential of mean force and nonlinear memory friction from a hybrid projection scheme, *Phys. Rev. E* **105**, 054138 (2022).

- [53] H. Vroylandt, L. Goudenège, P. Monmarché, F. Pietrucci, and B. Rotenberg, Likelihood-based non-Markovian models from molecular dynamics, *Proc. Natl. Acad. Sci. USA* **119**, e2117586119 (2022).
- [54] S. A. M. Loos and S. H. L. Klapp, Irreversibility, heat and information flows induced by non-reciprocal interactions, *New J. Phys.* **22**, 123051 (2020).
- [55] S. Nakajima, On quantum theory of transport phenomena: Steady diffusion, *Prog. Theor. Phys.* **20**, 948 (1958).
- [56] G. W. Ford, J. T. Lewis, and R. F. O'Connell, Quantum Langevin equation, *Phys. Rev. A* **37**, 4419 (1988).
- [57] B. Carmeli and D. Chandler, Effective adiabatic approximation for a two level system coupled to a bath, *J. Chem. Phys.* **82**, 3400 (1985).
- [58] H. Eyring, The activated complex in chemical reactions, *J. Chem. Phys.* **3**, 107 (1935).
- [59] S. Arrhenius, Über die Reaktionsgeschwindigkeit bei der Inversion von Rohrzucker durch Säuren, *Z. Phys. Chem.* **4**, 226 (1889).





# Pair-Reaction Dynamics in Water: Competition of Memory Friction, Inertia and the Potential Shape

---

7

by Florian N. Brüinig, Jan O. Daldrop, and Roland R. Netz

**Contributions:** F.N.B., J.O.D. and R.R.N conceived the theory and designed the simulations. F.N.B. performed the simulations and analyzed the data. All authors discussed the results, analyses, and interpretations. F.N.B. and R.R.N. wrote the paper.

**Bibliographic information:** This chapter has previously been published as a perspective in the *Journal of Physical Chemistry B* by the American Chemical Society (ACS) as open access under the Creative Commons CC BY-NC-ND licence (<https://creativecommons.org/licenses/by-nc-nd/4.0/>) [5].

<https://doi.org/10.1021/acs.jpcb.2c05923>

# Pair-Reaction Dynamics in Water: Competition of Memory, Potential Shape, and Inertial Effects

Florian N. Brüning, Jan O. Daldrop, and Roland R. Netz\*



Cite This: *J. Phys. Chem. B* 2022, 126, 10295–10304



Read Online

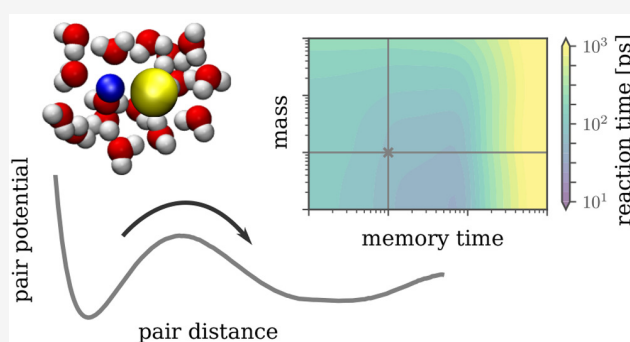
ACCESS |

Metrics & More

Article Recommendations

Supporting Information

**ABSTRACT:** When described by a one-dimensional reaction coordinate, pair-reaction rates in a solvent depend, in addition to the potential barrier height and the friction coefficient, on the potential shape, the effective mass, and the friction relaxation spectrum, but a rate theory that accurately accounts for all of these effects does not exist. After a review of classical reaction-rate theories, we show how to extract all parameters of the generalized Langevin equation (GLE) and, in particular, the friction memory function from molecular dynamics (MD) simulations of two prototypical pair reactions in water, the dissociation of NaCl and of two methane molecules. The memory exhibits multiple time scales and, for NaCl, pronounced oscillatory components. Simulations of the GLE by Markovian embedding techniques accurately reproduce the pair-reaction kinetics from MD simulations without any fitting parameters, which confirms the accuracy of the approximative form of the GLE and of the parameter extraction techniques. By modification of the GLE parameters, we investigate the relative importance of memory, mass, and potential shape effects. Neglect of memory slows down NaCl and methane dissociation by roughly a factor of 2; neglect of mass accelerates reactions by a similar factor, and the harmonic approximation of the potential shape gives rise to slight acceleration. This partial error cancellation explains why Kramers' theory, which neglects memory effects and treats the potential shape in harmonic approximation, describes reaction rates better than more sophisticated theories. In essence, all three effects, friction memory, inertia, and the potential shape nonharmonicity, are important to quantitatively describe pair-reaction kinetics in water.



## INTRODUCTION

Pair reactions in water, such as the association and dissociation of ions or hydrophobic molecules, are fundamental in biological and chemical processes and are commonly described by diffusive motion of the pair distance in a one-dimensional potential landscape.<sup>1–4</sup> The most important signatures of such reactions are the rates at which a pair dissociates or is created, which determine the turnover of complex biological reaction networks and the efficiency of large-scale chemical applications. Reaction-rate theory has a long history and dates back to Arrhenius,<sup>5</sup> who discovered the exponential dependence of reaction time on the free-energy or potential barrier height that separates reactants and products along a suitably chosen reaction coordinate. In a solvent, the reacting solutes experience friction,<sup>1–4,6–8</sup> which determines the pre-exponential factor of the Arrhenius law. But the mass of the reactants also influences the rate of a reaction. In fact, in his landmark paper, Kramers showed that reaction times exhibit a minimum at an intermediate value of the ratio of the effective friction and mass of a given reaction coordinate, a phenomenon that is called Kramers' turnover.<sup>1,9</sup>

However, the assumption of instantaneous friction, employed in early theories, breaks down whenever there is

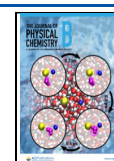
no pronounced separation between time scales of fast solvent relaxation and slow diffusion along the reaction coordinate, which is the case even for the simplest pair reactions in water.<sup>10,11</sup> One strategy is to circumvent such non-Markovian effects and to reduce friction memory by using suitable multidimensional reaction coordinates that explicitly account for solvent degrees of freedom.<sup>12–15</sup> Alternatively, the generalized Langevin equation (GLE),<sup>16,17</sup> which explicitly accounts for time-dependent friction due to solvent relaxation, can be used to model reaction rates<sup>18–34</sup> and transition-path times.<sup>35–37</sup>

Different analytical rate theories based on the GLE have been developed but necessarily rely on various approximations, the effects of which are difficult to disentangle.<sup>22,32,38,39</sup> This is where numerical solutions of accurately parametrized GLEs

Received: August 18, 2022

Revised: November 11, 2022

Published: December 6, 2022



become instrumental. The extraction of memory kernels from general time series data is an active field of research,<sup>33,40–45</sup> in particular in the context of reaction kinetics.<sup>10,30,46–49</sup> With recent methodological advances, it is possible to extract memory kernels from trajectories in the presence of arbitrary, not necessarily harmonic, potentials and to numerically solve the resulting GLE by Markovian embedding techniques.<sup>23,31,50,51</sup> While the one-dimensional GLE may in principle contain nonlinear friction contributions, the approximate linear friction GLE, which only includes a linear coupling of the velocity to a friction kernel with no further dependencies on position or velocity, becomes valid for a broad class of systems under well-defined conditions;<sup>52</sup> this explains why it accurately describes the dynamics of very different physical systems.<sup>31,51</sup> In this connection, it is important to note that most existing reaction-rate theories are in fact based on the approximate linear friction GLE.

As simple model systems, we consider the dissociation and association kinetics of two different pair reactions in water, NaCl and methane, which exhibit drastically different hydration properties. Ions are favorably dissolved in water by the formation of a strongly ordered hydration shell,<sup>53–55</sup> whereas nonpolar small objects such as methane are repelled from water and induce strong water–water hydrogen bonding in their hydration shell.<sup>56–58</sup> In fact, NaCl ion-pair dissociation in water has been widely studied,<sup>12–14,30,46,49,54,59–64</sup> and the failure of a Markovian kinetic model along a one-dimensional reaction coordinate,<sup>12,13,62,65</sup> the relevance of inertial<sup>62</sup> and memory effects,<sup>30,46,49,61</sup> has been demonstrated. In contrast, the reaction dynamics of hydrophobic molecules has received less attention. We analyze the reaction dynamics of these two systems based on extensive MD simulation trajectories of single reactant pairs in explicit water, from which we extract all parameters of the one-dimensional linear friction GLE in terms of the natural reaction coordinate, namely, the distance between the two reactants: These are the potential (or free-energy) landscape, the reduced mass, and the memory friction kernel that in general exhibits multiple time scales and oscillatory components.

As a crucial first step, we demonstrate by simulations of the GLE that it accurately reproduces the kinetics of the underlying MD simulations, which is nontrivial since the GLE could in principle also contain nonlinear friction contributions.<sup>52,66</sup> In a second step, we investigate how the pair-dissociation kinetics change when we independently vary the memory times and the effective mass, encompassing the Markovian limit of vanishing memory time and the overdamped limit of vanishing mass.

Throughout this paper, we determine reaction rates from mean first-passage times,  $\tau_{\text{MFP}}$ , which can be conveniently extracted from long simulation trajectories and which accurately reproduce barrier escape times, as we have shown previously.<sup>22</sup> We find that for both NaCl and methane, the neglect of memory slows down dissociation by roughly a factor of 2, while the neglect of mass accelerates dissociation by a similar factor. When neglecting both memory and mass, partial error cancellation takes place, but dissociation still slows down considerably. Approximating the free-energy landscape by a harmonic barrier also introduces significant errors. Thus, it transpires that for the quantitative prediction of reaction times, memory, finite mass, and nonharmonic potential effects must be simultaneously taken into account, and the GLE is the

appropriate tool to disentangle the effects of these different contributions on reaction times.

The free-energy barriers for the dissociation of NaCl and methane are about  $4 k_{\text{B}}T$  and  $2 k_{\text{B}}T$ , respectively; these are typical barrier heights not only of molecular association and dissociation reactions in water but also of dihedral stereoisomerization<sup>23</sup> as well as fast protein folding transitions.<sup>67</sup> Most reaction-rate theories rest on assumptions that become only valid in the limit of high free-energy barriers. Since many transitions in biophysical chemistry are in fact characterized by rather low barrier heights of the order of only a few  $k_{\text{B}}T$  and experimental transition rates are customarily interpreted in terms of reaction-rate theories, we therefore also compare the results from our simulations with reaction-rate-theory predictions. Interestingly, it turns out that, due to partial error compensation, Kramers' theory,<sup>1</sup> which neglects memory as well as nonharmonic potential effects, predicts the NaCl dissociation time better than Grote/Hynes (GH) theory,<sup>38</sup> which only neglects nonharmonic potential effects. It follows that agreement between the predictions of a particular reaction-rate theory and experimental or simulation results does not necessarily mean that the approximations made in deriving the reaction-rate theory are valid for the specific system.

## ■ SIMULATION MODEL AND THEORETICAL FRAMEWORK

We analyze the dynamics of single NaCl and methane pairs from MD simulations in SPC/E water at 300 K as described in the [Methods](#) section. The distance between the two reactants is used as the reaction coordinate  $x$ , along which a weak harmonic confining potential  $U_{\text{con}}(x) = kx^2/2$  is applied to prevent the reactants from diffusing apart and thereby to increase the number of association and dissociation events. The potential or free energy of a NaCl ion pair,  $U(x) = -k_{\text{B}}T \log(p(x))$ , obtained from the distribution function  $p(x)$ , is shown in [Figure 1A](#) as a solid line. The contact pair (CP) state is separated by a barrier of  $4.37 k_{\text{B}}T$ , located at the transition state (TS), from the solvent-separated pair (SSP) state. Snapshots from the MD simulation illustrate the different states in [Figure 1A](#). In fact, the TS in this one-dimensional projection corresponds to an ensemble of disparate states that do not single out well the actual TS in an enlarged multidimensional description.<sup>12,15</sup> This however is not a problem for our kinetic description using the GLE, since non-Markovian effects, caused by dimensional reduction, are fully accounted for. Note that the confinement potential  $U_{\text{con}}(x)$  changes the barrier height from the CP to the TS state slightly, as seen by comparing  $U(x)$  (solid line) and  $U(x) - U_{\text{con}}(x)$  (broken line) in [Figure 1A](#). Thus, the presence of a confining potential influences the reaction times, and it in fact also influences the shape of the extracted memory kernel, in agreement with previous results for confined molecules<sup>68</sup> (see [Supporting Information \(SI\)](#) section I for details); this, however, does not affect our general conclusions that memory, inertial, and potential-shape effects influence barrier-crossing times. The actual NaCl interaction potential, obtained by subtracting the centrifugal contribution and the confinement potential,  $U_{\text{int}}(x) = U(x) - U_{\text{con}}(x) + 2k_{\text{B}}T \log(x)$  (dotted line in [Figure 1A](#)), goes for large separations  $x$  to a constant. Note that in order to describe the simulated NaCl pair dynamics along  $x$ , the potential  $U(x)$  has to be used within the GLE.

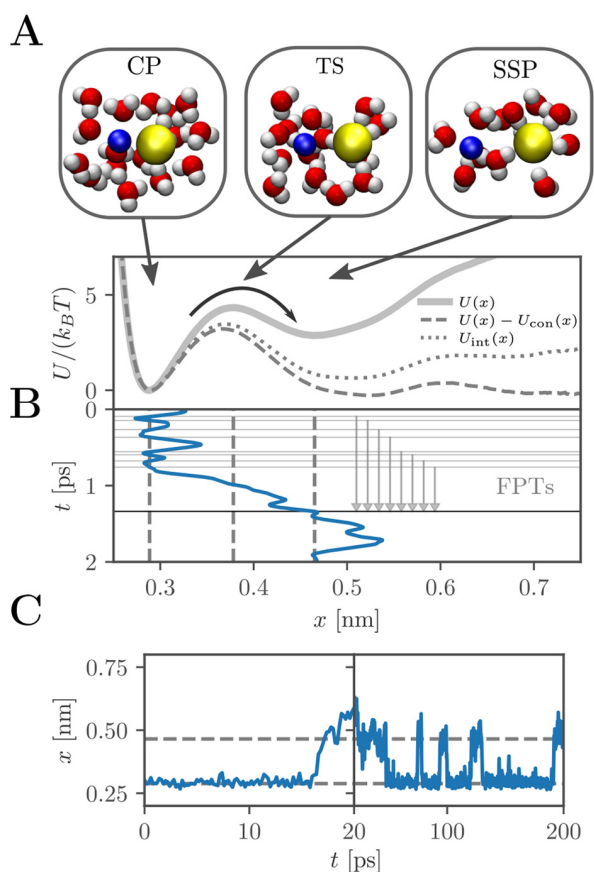


**Figure 1.** (A) Effective potential  $U(x)$  of a single NaCl ion pair in SPC/E water as a function of the ion separation  $x$  as obtained from molecular dynamics (MD) simulations in the presence of a weak harmonic confining potential  $U_{con}(x)$  (solid line). The broken line denotes  $U(x) - U_{con}(x)$ , and the dotted line denotes the interaction potential  $U_{int}(x)$  for which also the centrifugal potential contribution has been subtracted. Snapshots from the MD simulations illustrate the contact pair (CP), the solvent-separated pair (SSP) (both at the potential minima), and the transition state (TS) at the potential maximum. (B,C) Example trajectories of the interionic distance  $x$  on three different time scales, 2, 20, and 200 ps. The mean first-passage time  $\tau_{MFP}$  between the initial CP state and the final SSP state is calculated from the average of all first-passage times (FPTs); see main text for details.

In the following, we concentrate on the dissociation kinetics starting from the CP state, which we characterize by the mean first-passage time,  $\tau_{MFP}$ .<sup>22</sup> For this, we obtain from a single long MD trajectory first-passage times (FPTs), defined as the time span between passing through the initial position  $x_i$  and reaching the final position  $x_f$  for the first time. In Figure 1B, a few FPTs for the passage from the CP to the SSP state from an actual MD trajectory are shown, the average of all FPTs gives  $\tau_{MFP}$ . In Figures 1B,C, the dynamics of the NaCl ion-pair separation is shown on three different time scales, which illustrates the stochastic nature of the barrier-crossing dynamics that is characterized by the waiting time in the CP state on the order of  $\tau_{MFP} \approx 70$  ps.

In order to reveal the mechanisms that control the pair-reaction dynamics, we use the GLE that includes a general nonlinear potential  $U(x)$  and a memory friction kernel  $\Gamma(t)$ :

$$m\ddot{x}(t) = -\int_0^t \Gamma(t-t')\dot{x}(t')dt' - \nabla U[x(t)] + \eta(t) \quad (1)$$

Here,  $m$  is the effective mass and  $\eta(t)$  is a Gaussian random force with vanishing mean  $\langle \eta(t) \rangle = 0$  and correlations  $\langle \eta(t)\eta(t') \rangle = k_B T \Gamma(t-t')$ . The GLE in eq 1 neglects nonlinear friction effects, which is valid when correlations between velocities and random forces are independent of  $x$ <sup>52</sup> and has been successfully used to model the dynamics of protein folding and molecular vibrations.<sup>31,51</sup> We will further below validate the linear friction GLE in eq 1 by comparison with MD data. All parameters in eq 1 are extracted from simulation trajectories: The mass is obtained from the equipartition theorem  $m = k_B T / \langle \dot{x}^2(t) \rangle$  and is demonstrated to be independent of  $x$  in SI section II, as indeed expected for a linear distance coordinate.<sup>52</sup> The potential follows from the distribution  $p(x)$  via  $U(x) = -k_B T \log(p(x))$ , and the memory friction kernel  $\Gamma(t)$  is extracted from the simulation trajectory by numerical inversion of eq 1.<sup>31,51</sup>

In order to validate the linear friction GLE and its parametrization, we need to compare predictions of the GLE with the MD simulation results. For this, the GLE is numerically solved using Markovian embedding, for which the memory kernel is parametrized as a sum of exponentially decaying and oscillating components according to<sup>51,69–71</sup>

$$\Gamma(t) = \sum_{i=0}^n \frac{\gamma_i^e}{\tau_i^e} e^{-t/\tau_i^e} + \sum_{i=0}^l \frac{\gamma_i^o e^{-t/\tau_i^o}}{2\tau_i^o(1 + (\omega_i \tau_i^o)^2)^{-1}} \left[ \cos(\omega_i t) + \frac{\sin(\omega_i t)}{\tau_i^o \omega_i} \right] \quad (2)$$

where  $\tau_i^e$  and  $\tau_i^o$  denote the memory times of the non-oscillating and oscillating memory components,  $\omega_i$  denotes the oscillation frequency, and  $\gamma_i^e$  and  $\gamma_i^o$  denote the amplitudes of the memory components. The parametrization of the memory kernel is done in a way such that the long-time friction coefficient  $\gamma$ , defined by the integral  $\gamma = \int_0^\infty \Gamma(t)dt$ , is given by  $\gamma = \sum_i \gamma_i^e + \sum_i \gamma_i^o$  and thus is independent of the memory time scales.

In the Markovian limit, i.e., when all memory times go to zero, the memory kernel takes the form  $\Gamma(t) \rightarrow 2\gamma\delta(t)$ . In this limit, the GLE eq 1 reduces to the ordinary Langevin equation (LE)<sup>72</sup>

$$m\ddot{x}(t) = -\gamma\dot{x}(t) - \nabla U[x(t)] + \xi(t) \quad (3)$$

where the random force  $\xi(t)$  has zero mean and is correlated according to  $\langle \xi(t)\xi(t') \rangle = 2\gamma k_B T \delta(t-t')$ . In the limit  $m \rightarrow 0$ , the overdamped LE is obtained from eq 3, which neglects memory as well as inertial effects. The numerical effort of simulating the GLE in eq 1 is linear in the number of fit functions in eq 2 and thus amounts to  $n + l + 1$  times the effort of simulating the LE in eq 3. Additionally, the simulation effort scales as the inverse of the discretization time step, which has to be on the order of the shortest time scale of the system, which can be either the shortest memory time scale in eq 2 or the inertial time scale  $m/\gamma$ .

Most analytical rate theories are on the harmonic level and approximate the potential quadratically around the barrier top and the potential well. We investigate the accuracy of this approximation, which becomes exact only in the infinite-barrier height limit, in SI section III by a perturbation analysis in terms

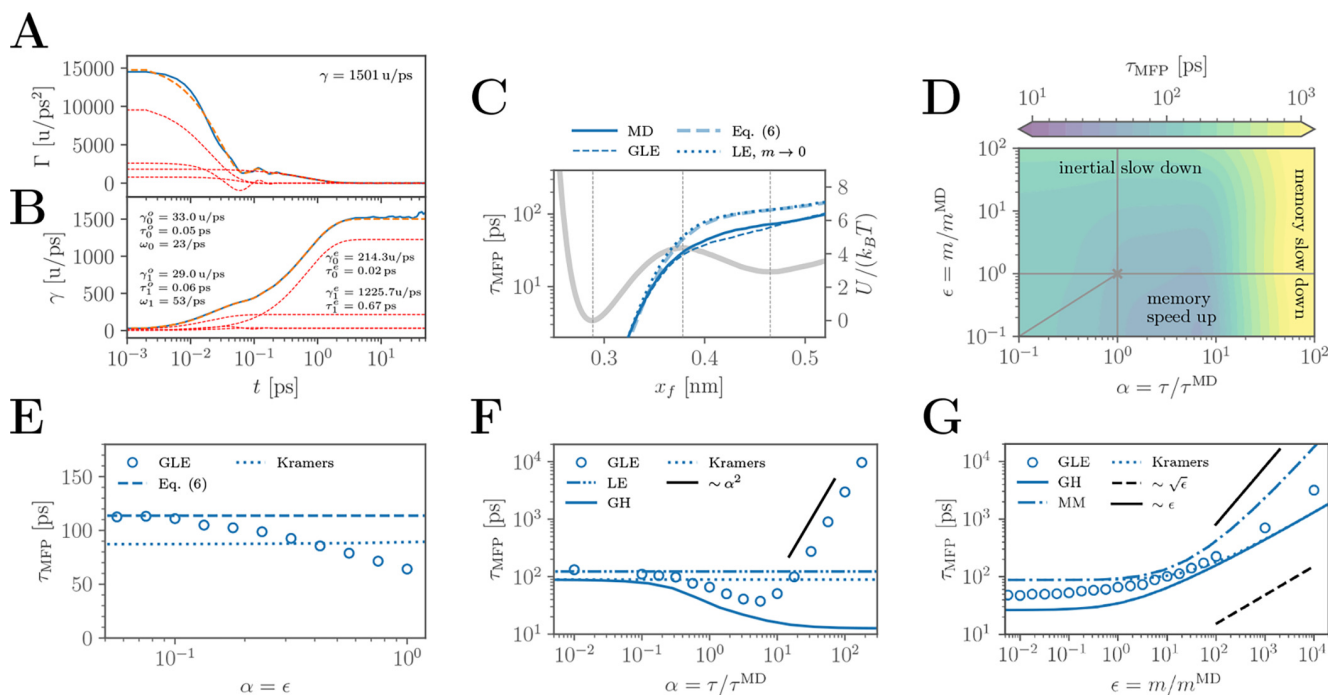


**Figure 2.** Analysis of NaCl dissociation dynamics in water. (A,B) Memory friction kernel (A) and its integral (B) from MD simulations (blue solid lines) compared with a fit according to eq 2 (yellow broken lines) which is a sum of two exponential and two oscillatory components (red broken lines). The fit parameters are given in the legend. (C) Potential  $U(x)$  is shown as a gray solid line (right scale) with the extrema indicated by vertical gray dotted lines. Profiles of  $\tau_{\text{MFP}}(x_f)$  (left scale) starting from the CP state are shown from MD simulations (blue solid line), from simulations of the GLE eq 1 (blue short-dashed line), from the theory in the overdamped Markovian limit eq 6 (blue long-dashed line), and from simulations of the LE eq 3 in the zero-mass limit (blue dotted line). (D) Contour plot of the CP-SSP dissociation  $\tau_{\text{MFP}}$  from GLE simulations as a function of the mass and memory-time scaling parameters  $\epsilon$  and  $\alpha$ . The gray solid lines illustrate the paths shown in (E–G). (E–G)  $\tau_{\text{MFP}}$  for the CP-SSP dissociation reaction as a function of  $\epsilon = \alpha$  (E),  $\alpha$  for  $\epsilon = 1$  (F), and  $\epsilon$  for  $\alpha = 1$  (G). Predictions according to Kramers' theory eq 4 (dotted lines), GH theory eq 5 (solid lines), MM theory (dashed-dotted line), and the overdamped Markovian theory eq 6 (broken lines) are shown for comparison. Simulations of the LE according to eq 3 are shown as a dash-double-dotted line in F. The error bars of the GLE simulation results in E–G are smaller than the symbol size.

of cubic and quartic potential corrections. The classical Kramers' expression for the escape of a massive particle over a barrier that is subject to memoryless friction, as described by LE eq 3, valid in the medium-to-high friction regime, reads<sup>1</sup>

$$\tau_{\text{Kr}} = \left[ \left( \frac{\gamma^2}{4m^2} + \omega_{\text{max}}^2 \right)^{1/2} - \frac{\gamma}{2m} \right]^{-1} \omega_{\text{max}} \tau_{\text{TST}} \quad (4)$$

where the barrier frequency  $\omega_{\text{max}} = \sqrt{-U''_{\text{max}}/m}$  depends on the potential curvature  $U''_{\text{max}} = U''(x_{\text{max}})$  at the barrier top located at  $x_{\text{max}}$ . For low friction  $\gamma/m \rightarrow 0$ , this expression reproduces the transition-state theory limit  $\tau_{\text{Kr}} \rightarrow \tau_{\text{TST}} = 2\pi\omega_{\text{min}}^{-1}e^{\beta U_0}$ , where  $\beta^{-1} = k_{\text{B}}T$  is the thermal energy,  $U_0$  denotes the barrier height, and  $\omega_{\text{min}} = \sqrt{U''_{\text{min}}/m}$  is the oscillation frequency at the minimum  $x_{\text{min}}$  with  $U''_{\text{min}} = U''(x_{\text{min}})$ .<sup>73</sup> In the high-friction limit,  $\gamma/m \rightarrow \infty$ , eq 4 reduces to  $\tau_{\text{Kr}} \rightarrow \frac{\gamma}{m\omega_{\text{max}}} \tau_{\text{TST}} = 2\pi\gamma e^{\beta U_0} / \sqrt{-U''_{\text{max}}U''_{\text{min}}}$  which is linear in the friction coefficient  $\gamma$ . Note that eq 4 misses the correct scaling in the low-friction or high-mass limit,  $\tau_{\text{MFP}} \sim \frac{m}{\gamma\beta U_0} e^{\beta U_0}$ , where  $\tau_{\text{MFP}}$  scales inversely proportional to  $\gamma$ , which was also derived by Kramers.<sup>1</sup> An exact expression for  $\tau_{\text{MFP}}$  in the Markovian limit, valid for arbitrary mass and friction and using the quadratic potential approximation, was

derived by Mel'nikov and Meshkov (MM)<sup>74</sup> (see SI section IV).

The GH prediction for  $\tau_{\text{MFP}}$  in the presence of memory acting at a harmonic barrier reads<sup>38</sup>

$$\tau_{\text{GH}} = \frac{\omega_{\text{max}}}{\lambda} \tau_{\text{TST}} \quad (5)$$

where the frequency  $\lambda$  is determined by the solution of the equation  $\lambda = \omega_{\text{max}}^2 / (\lambda + \tilde{\Gamma}(\lambda)/m)$  and  $\tilde{\Gamma}(\lambda)$  denotes the Laplace-transformed memory friction kernel  $\Gamma(t)$  acting at the barrier. In the Markovian limit, i.e., for short memory time, one has  $\tilde{\Gamma}(\lambda) = \gamma$  and the GH expression reduces to the Kramers' medium-to-high-friction result in eq 4. Note that in the limit of high mass or long memory time, GH theory reproduces the transition-state theory result,  $\tau_{\text{GH}} = \tau_{\text{TST}}$ , which means that it misses both the correct high-mass limit, characterized by  $\tau_{\text{MFP}} \sim \frac{m}{\gamma\beta U_0} e^{\beta U_0}$ ,<sup>1,74</sup> as well as the correct long-memory-time limit, where  $\tau_{\text{MFP}}$  scales as  $\tau_{\text{MFP}} \sim \tau^2 e^{\beta U_0}$ .<sup>22,39</sup>

In the overdamped Markovian limit, nonharmonic potential effects can be analytically treated and  $\tau_{\text{MFP}}$  between initial and final positions,  $x_i$  and  $x_f$  is given as<sup>75</sup>

$$\tau_{\text{MFP}}(x_i, x_f) = \beta \int_{x_i}^{x_f} dx' \gamma(x') e^{\beta U(x')} \int_{x_{\text{min}}}^{x'} dx e^{-\beta U(x)} \quad (6)$$

Here,  $\gamma(x)$  denotes a general position-dependent friction profile and  $x_{\min}$  a reflecting boundary. Equation 6 can be inverted and thereby used to determine  $\gamma(x)$  from measured profiles of  $\tau_{\text{MFP}}(x_i, x_f)$ .<sup>76,77</sup> In fact, position-dependent friction, determined by a different approach, has been shown to reproduce NaCl dissociation dynamics from simulations.<sup>63</sup> However, memory effects give rise to spurious spatially dependent friction profiles when analyzed on the Markovian level.<sup>31</sup> Furthermore, spatially dependent friction cannot simultaneously describe dissociation and association kinetics, which demonstrates the presence and importance of memory, as shown in SI section V. In fact, the assumption of a friction memory kernel that is independent of position is in this paper shown to be very accurate; the Markovian assumption, i.e., the neglect of memory effects, on the contrary is shown not to be accurate. As we demonstrate in SI section III, using a harmonic approximation for the free energy  $U(x)$  around its minimum and its barrier and in the high-barrier limit, the  $\tau_{\text{MFP}}$  between arbitrary initial and final positions to the left and right of a barrier predicted by eq 6 equals the Kramers' prediction eq 4 in the high-friction limit. In fact, the Kramers', MM, and GH rate theories do not depend on the precise locations of the initial and final positions of  $\tau_{\text{MFP}}$ , which is a consequence of the high-barrier assumption inherent in their derivations, but the dependence of  $\tau_{\text{MFP}}$  on the final position is not very pronounced (the dependence of  $\tau_{\text{MFP}}$  on the initial position is even weaker and displayed in SI section VI). It therefore is instructive to compare analytical rate-theory results for  $\tau_{\text{MFP}}$  with MD and GLE simulation results. We show in SI section III by a perturbative analysis beyond the harmonic approximation that deviations between the Kramers' high-friction approximation and eq 6 are for not too low barrier height mostly due to the harmonic approximation and not so much due to the high-barrier assumption, which opens up routes to systematically improve upon literature rate theories.

## RESULTS AND DISCUSSION

The memory kernel  $\Gamma(t)$  for NaCl extracted from MD simulations is shown in Figure 2A (blue line), and its running integral in Figure 2B (blue line) starts to increase at a few fs and plateaus at about 4 ps. The shape of  $\Gamma(t)$  is rather similar to previous results for single anions and cations in water,<sup>78</sup> which demonstrates that memory is caused not only by ion-ion interactions but also by hydration effects. A fit using the sum of two exponentially decaying and two oscillating components according to eq 2, shown in Figure 2A,B as a yellow broken line, is in near perfect agreement with the extracted data and will be used for all further GLE modeling. The individual memory components are shown as red broken lines, and their parameters are given in the legend.

In Figure 2C, the potential  $U(x)$  is shown (gray line) together with the  $\tau_{\text{MFP}}(x_f)$  profile from MD (blue solid line) for an initial position  $x_i$  at the minimum of  $U(x)$  as a function of the final positions  $x_f$  which corresponds to dissociation from the CP state (corresponding results for the inverse association reaction are reported in SI section VII). The dependence of  $\tau_{\text{MFP}}$  on the initial position  $x_i$  is very weak, as demonstrated and analytically explained in SI section VI. The  $\tau_{\text{MFP}}(x_f)$  profile from the GLE eq 1 with all parameters extracted from MD simulations (blue short-dashed line) agrees very well with the MD data (blue solid line). This presents a crucial validation of the linear friction GLE eq 1 and of the extracted parameters.

The GLE is not only able to reproduce the MD data, it also allows us to analyze the effects of varying mass and memory times on the dissociation kinetics in a nonharmonic potential landscape, which is not possible with MD simulations and also not with analytical rate theories. For this, we scale the mass  $m$  in the GLE by a factor  $\epsilon$  according to  $m = \epsilon m^{\text{MD}}$ . Likewise, we scale all memory times by a second factor  $\alpha$  according to  $\tau_i = \alpha \tau_i^{\text{MD}}$  and  $\omega_i = \alpha^{-1} \omega_i^{\text{MD}}$ , which ensures a smooth crossover to the Markovian limit as  $\alpha \rightarrow 0$ . Since the friction coefficient  $\gamma$  is independent of  $\alpha$ , by changing the value of  $\alpha$  we are able to disentangle the effects of memory times and memory amplitudes, the latter being characterized by the friction coefficient  $\gamma$ , on the reaction kinetics. In the overdamped Markovian limit, i.e. for  $\alpha, \epsilon \rightarrow 0$ ,  $\tau_{\text{MFP}}$  is given by eq 6, shown as a long-dashed line in Figure 2C and compared with simulations of the LE eq 3 in the  $m \rightarrow 0$  limit (dotted line). Both results agree nicely with each other, validating the numerical procedures used, but exhibit significantly longer  $\tau_{\text{MFP}}$  than the MD data by a factor of almost two to the right of the free-energy barrier, which clearly demonstrates the significance of inertia and memory effects for reaction dynamics.

The effect of gradually and simultaneously reducing inertial and memory effects is demonstrated in Figure 2E, where  $\tau_{\text{MFP}}$  from the CP to the SSP state obtained using the GLE is shown as a function of  $\alpha = \epsilon$  (circles). The overdamped Markovian limit from eq 6 (broken horizontal line) is approached by the GLE data in the limit  $\alpha = \epsilon \rightarrow 0$ , as expected. The Kramers' prediction eq 4 (dotted line) is evaluated using the friction coefficient  $\gamma$  and mass  $m$  extracted from the MD data and using the fitted potential curvatures  $U''_{\min}$  and  $U''_{\max}$  in the well and at the barrier top (see SI section VIII for details of the fitting procedure). It exhibits an almost negligible dependence on  $\epsilon$ , which shows that in the Markovian limit there are no discernible inertial effects. The significant difference between the broken and dotted lines is due to the harmonic-potential and high-barrier approximation in Kramers' theory. Interestingly, the Kramers' prediction (dotted line) is for  $\alpha = \epsilon = 1$  closer to the GLE result than the more accurate numerical solution of eq 6 (broken horizontal line) which does not use the harmonic-potential nor the high-barrier approximation; this is due to a subtle error compensation between the harmonic-potential/high-barrier and Markovian approximations, as we will discuss in more detail further below. As mentioned before, due to the high-barrier approximation, the Kramers' prediction does not depend on the locations of the initial and final positions used in the definition of  $\tau_{\text{MFP}}$  (as is the case for the MM and GH reaction-rate theories), while the MD and GLE simulation results obviously do, as demonstrated in Figure 2C and in SI Section VI. This is a general shortcoming of the high-barrier approximation employed in analytical theories and should be kept in mind when comparing with MD or GLE simulation results.

To disentangle inertial and memory effects, we in Figure 2F show  $\tau_{\text{MFP}}$  for NaCl dissociation from the CP to the SSP state using the GLE eq 1 as a function of the memory scaling parameter  $\alpha$  for original mass  $\epsilon = 1$  (circles).  $\tau_{\text{MFP}}$  exhibits a pronounced minimum close to the original memory time  $\alpha = 1$ , which demonstrates that memory accelerates barrier crossing for short and intermediate memory times but slows down barrier crossing for very long memory times. The barrier-crossing speed up for intermediate memory times, including

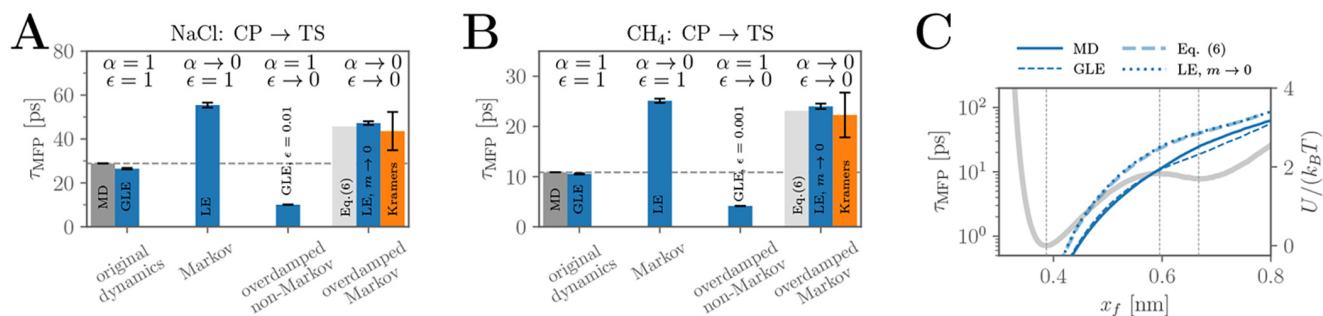


**Figure 3.** (A,B) Summary of memory friction and mass effects on the pair dissociation dynamics of NaCl and methane in water at 300 K. The bars denote  $\tau_{\text{MFP}}$  from the CP to the TS state from MD (gray bars and horizontal broken lines) and from simulations of the GLE eq 1 (blue bars) in the different limits of the memory and mass scaling parameters,  $\alpha$  and  $\epsilon$ . The theoretical overdamped Markovian limit eq 6 is shown as light-gray bars, and Kramers' theory eq 4 for high friction is shown as yellow bars. Error bars for the simulations denote the standard deviation of block averages, and error bars of Kramers' theory are estimated from the dominant errors in the harmonic fits to the potentials, as shown in SI section VIII. (C) Dissociation profiles  $\tau_{\text{MFP}}(x_f)$  for two methane molecules in water starting from the CP state from MD (blue solid line), from simulation of the GLE eq 1 (blue short-dashed line), from the overdamped Markovian theory eq 6 (blue long-dashed line), and from simulation of the LE eq 3 in the zero-mass limit (blue dotted line). The potential  $U(x)$  is shown as a gray solid line (right scale), vertical lines denote the CP, TS, and SSP states.

the original memory time  $\alpha = 1$ , can be intuitively understood by a simplified picture: Memory friction pushes against the direction of the previous velocity and thereby supports barrier crossing for a certain time after an unsuccessful barrier-crossing attempt.<sup>22</sup> In the Markov limit  $\alpha \rightarrow 0$ , the GLE data converge to the result obtained by simulations of the LE with finite mass eq 3 (dash-double-dotted horizontal line), as expected. The Kramers' prediction eq 4 (dotted horizontal line) is shifted down relative to the LE result eq 3 due to the harmonic potential approximation, as discussed before. Except an overall shift to shorter times, GH theory eq 5 (solid line) nicely reproduces the GLE data for not too large  $\alpha$  values and converges to the Kramers' prediction in the Markovian limit  $\alpha \rightarrow 0$ , which reflects that GH theory can be viewed as a correction to the Kramers' theory. In the long memory-time limit,  $\alpha \rightarrow \infty$ , GH theory converges to the transition-state theory time and therefore misses the quadratic scaling with the memory time indicated by the black solid line.<sup>22,39,79</sup> We again observe that Kramers' theory (dotted horizontal line), which neglects memory effects as well as nonharmonic potential effects, agrees better with the GLE data for original memory time, i.e., for  $\alpha = 1$ , than GH theory, which includes memory effects, and the LE eq 3, which includes the full potential shape.

In Figure 2G, the NaCl dissociation time,  $\tau_{\text{MFP}}$ , from the CP to the SSP state, using the GLE is shown as a function of the mass scaling parameter  $\epsilon$  for the original memory times, i.e., for  $\alpha = 1$  (circles). The dissociation time monotonically increases with growing mass. For the original mass,  $\epsilon = 1$ ,  $\tau_{\text{MFP}}$  is considerably larger than in the overdamped limit,  $\epsilon \rightarrow 0$ , an effect that is underestimated by Kramers' theory (dotted line), MM theory (dash-dotted line), and to a certain degree also by GH theory (solid line). So we see that inertial effects are more important for non-Markovian than for Markovian systems. GH theory and Kramers' theory converge to transition-state theory for large mass with a characteristic  $\tau_{\text{MFP}} \sim \sqrt{m}$  scaling (straight broken line), which deviates from the  $\tau_{\text{MFP}} \sim m$  scaling (straight solid line) for Markovian systems in the large-mass limit, as predicted by MM theory. In the low mass limit, on the other hand, Kramers' and MM theories converge. The GLE data show a slow crossover to the  $\tau_{\text{MFP}} \sim m$  scaling for large mass. Again, we see that due to error cancellation,

Kramers' theory agrees almost perfectly with the GLE data for original mass ( $\epsilon = 1$ ) but also for slightly enhanced mass, as would be relevant for heavier reactants.

The dependence of the NaCl dissociation time  $\tau_{\text{MFP}}$  on mass and memory time as obtained from the GLE is illustrated in Figure 2D in a contour plot as a function of  $\alpha$  and  $\epsilon$ , where three regimes can be broadly distinguished: the memory-speed-up regime (for low mass and intermediate memory time), the inertial slow-down regime (for large mass), and the memory-slow-down regime (for long memory time). The gray square indicates  $\alpha = \epsilon = 1$ , i.e., the original system parameters, and the gray solid lines indicate the one-dimensional cuts shown in Figure 2E–G.

In Figure 3A, we compare the NaCl dissociation time from the CP to the TS at the barrier top for the four different relevant limiting scenarios, namely (from left to right), the case with original mass and memory, the Markovian limit with original mass, the overdamped limit (using  $\epsilon = 0.01$  in the GLE) with original memory, and the overdamped Markovian limit. Note that the comparison of the various limits with the original MD simulations for the transition from the CP state to the barrier top in Figure 3A is slightly different than that for the transition from the CP to the SSP state in Figure 2E–G. The blue bars denote simulation results using the GLE, eq 1, and the LE, eq 3, with the latter being used in the limit  $\alpha, \epsilon \rightarrow 0$ , employing the full nonharmonic potential  $U(x)$ . We see that the MD and GLE results for original memory and mass agree very nicely with each other. The dissociation time in the Markovian limit with original mass is roughly doubled, and in the overdamped limit with original memory, it is roughly half, compared to the MD result (denoted by a broken horizontal line). In the overdamped Markovian limit, we see that the LE simulations (blue bar) and the exact integral formula eq 6 (gray bar) agree nicely with each other, as expected, and that their agreement with the MD result is slightly better than that for the GLE results when either the original mass or memory is used. This reflects partial error compensation of the neglect of mass and memory, as amply discussed above. Kramers' theory eq 4 (yellow bar), which in addition employs a harmonic potential-shape and high-barrier approximation, slightly lowers the dissociation time and thus further improves the agreement with the MD data, another manifestation of error cancellation



(note that the Kramers' formula eq 4 is divided by 2 for the comparison since the final state is the barrier top). Interestingly, the well-to-barrier-top dissociation shows reduced nonharmonic potential corrections in comparison with the well-to-well dissociation discussed in Figure 2, meaning that the Kramers' result in Figure 3A (yellow bar) agrees rather well with the prediction from the integral formula eq 6 (gray bar), as will be explained in detail further below.

To demonstrate that our findings are not specific to ion dissociation, we show in Figure 3B,C results for the dissociation dynamics of a pair of methane molecules in water at 300 K (the detailed analysis is presented in SI section IX). In Figure 3C, we show the free energy from the MD simulations (gray line) together with  $\tau_{\text{MFP}}$  profiles starting from the free-energy minimum, corresponding to the CP state, for varying final position  $x_f$ . We compare results from MD simulations (blue solid line) and corresponding GLE simulations (blue short-dashed line) and find, as for NaCl, good agreement. The  $\tau_{\text{MFP}}$  profiles for the overdamped Markovian limit from eq 6 (blue long-dashed line) and from simulations of the LE eq 3 in the overdamped limit (blue dotted line) agree nicely with each other and are significantly higher than the MD results. The comparison of methane dissociation times from the CP to the TS at the barrier top using different approximations in Figure 3B is similar to the NaCl results in Figure 3A and demonstrates significant and compensating memory and mass effects.

All analytical rate theories we compare with, namely MM, GH and Kramers' theory, use the harmonic approximation for the well and barrier regions of the pair potentials, which becomes accurate only in the high-barrier limit. The comparison of Kramers' theory eq 4 with eq 6 in Figure 2E demonstrates that the harmonic approximation is not very good for NaCl dissociation from well to well, and it becomes better for the NaCl dissociation from well to barrier top in Figure 3A. To shed light on that, in Figure 4, we compare the  $\tau_{\text{MFP}}$  from Kramers' theory eq 4 in the high-friction limit (colored solid lines) with the exact integral formula eq 6 (gray

solid lines) as a function of barrier height  $U_0$ , using the potential  $U(x)$  with a linearly scaled amplitude and the friction coefficient  $\gamma$  for NaCl from MD simulations. Data are shown for going from the CP to the TS, i.e., to the barrier top (blue and thin gray lines), and from the CP to the SSP, i.e., over the barrier from well to well (yellow and thick gray lines). The exponential scaling for  $U_0 \rightarrow \infty$  is clearly seen. The relative difference between the two predictions, given in the inset, decreases with  $U_0$ , as expected. The decrease however is quite slow and scales to leading order as  $U_0^{-1}$  for the CP-SSP and as  $U_0^{-1/2}$  for the CP-TS transitions, which is accurately predicted by a perturbative analysis (gray lines), see SI section III for details. The effect of the harmonic approximation is considerable for the CP-SSP transition and decreases the dissociation time by about 25% for a barrier height of  $U_0 \approx 5 k_B T$ , as also seen in Figure 2D. The effect of the harmonic approximation is much less drastic for the CP-TS reaction, contrary to what would be expected based on the leading-order perturbation results, which is due to a subtle compensation of cubic and quartic potential effects at the barrier top, as explained in SI section III. Therefore, while for high barriers the harmonic-potential approximation, employed in all analytical rate theories, is valid, nonharmonic potential effects are significant at moderate barrier heights as encountered for dissociation reactions in water and many other reactions in biophysical chemistry and cannot be disregarded.

## CONCLUSIONS

The dissociation dynamics of a NaCl and a methane–methane pair from MD simulations is accurately reproduced using the GLE when mass, memory function and pair potential are used as extracted from MD simulations. This is a nontrivial test of the accuracy of the approximate linear friction GLE, the friction-kernel extraction techniques, and the GLE simulation methods employed by us and allows us to use the GLE as a diagnostic tool to quantitatively study how friction memory and inertial effects influence reaction kinetics. By varying the mass and the memory times in the GLE, which is not possible within MD simulations, the impact of these fundamental system properties on the reaction dynamics is quantified. It turns out that mass, memory as well as nonharmonic potential effects are important for the quantitative prediction of reaction rates of NaCl and methane in water. Due to error cancellation, Kramers' theory, that neglects memory as well as nonharmonic potential effects, performs better than GH theory, that neglects nonharmonic potential effects but approximately accounts for mass and memory effects. This in particular means that good comparison of Kramers' theory with experimental or simulated reaction times does not mean that memory effects are negligible. Our results are obtained for specific pair reactions in water, but our conclusions presumably are valid for a much wider class of systems because the GLE employed by us makes no reference to system specificities except for the mass, the memory function and the free-energy profile.

As we show in this paper, neglecting mass or memory changes the dissociation time of NaCl roughly by a factor of 2, an equivalent change of reaction time is obtained when shifting the free-energy barrier by  $k_B T \ln 2 \approx 0.7 k_B T$ . So the effects we are discussing are in some sense comparable to typical experimental or theoretical uncertainties in the free-energy barriers. Nevertheless, for the quantitative prediction of reaction times and the thorough understanding of the

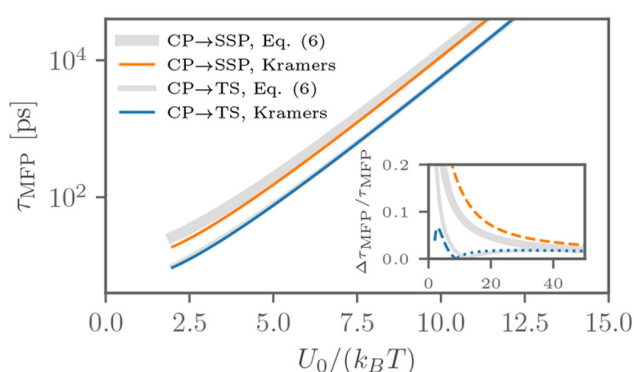


**Figure 4.** Effect of nonharmonic potential contributions on the NaCl dissociation dynamics in the overdamped Markovian limit. We compare  $\tau_{\text{MFP}}$  given by Kramers' theory eq 4 in the high-friction limit (colored solid lines) with the integral formula eq 6 (gray solid lines) for dissociation from the CP to the TS state (blue and thin gray lines) and from the CP to the SSP state (yellow and thick gray lines) as a function of barrier height  $U_0$ . In the inset, the relative difference between the two predictions is shown as blue and yellow broken lines (dotted lines denote negative values) and compared with the perturbative prediction (gray lines); see main text for details.

mechanisms controlling reaction times in complex systems, it is important to know how memory, mass and potential-shape effects modify reaction rates.

We extract all GLE parameters from force-field MD simulations. In the future it would be interesting to use ab initio simulations instead<sup>80,81</sup> and to investigate in more detail the role of the water model<sup>81,82</sup> for ion pair-reaction dynamics in water.

## METHODS

MD simulations are performed in explicit water at 300 K, using GROMACS version 2020.6,<sup>83</sup> the SPC/E water force field,<sup>84</sup> force-field parameters for the NaCl ion pair as reported previously,<sup>85</sup> which are similar to recently optimized values,<sup>86</sup> and Lennard-Jones parameters for the methane beads from the GROMOS 53A6 force field.<sup>87</sup> A weak confinement potential along the connecting vector of the reactants is applied,  $U_{\text{con}}(x) = kx^2/2$ , with  $k = 100 \text{ kJ mol}^{-1} \text{ nm}^{-2}$  for NaCl and  $k = 30 \text{ kJ mol}^{-1} \text{ nm}^{-2}$  for methane. The cubic simulation box with side length 4 nm is completely filled with water molecules and periodic boundary conditions are applied. Before production the systems are equilibrated under NPT conditions with atmospheric pressure for 400 ps using a Berendsen barostat with a time constant of 0.5 ps and subsequently under NVT conditions for 1 ns. Production runs are performed for 200 ns under NVT conditions using the velocity rescaling thermostat with a time constant of 0.5 ps only acting on water. The simulation time step is 2 fs and correlation functions are extracted at full time resolution. The center-of-mass motion of the entire system is removed at each simulation time step. The memory kernel is extracted from correlation functions as detailed previously.<sup>23,31</sup> The potential,  $U(x) = -k_{\text{B}}T \log(p(x))$ , is calculated directly from the distribution function  $p(x)$  with a bin size of 0.0025 nm for the ion and 0.005 nm for the methane pair.

Simulations of the GLE eq 1 using parametrized memory kernels with a sum of  $n$  exponential and  $l$  oscillating components, as given in eq 2, are performed by Markovian embedding using a fourth-order Runge–Kutta scheme.<sup>51</sup> The integration time step is 2 fs, equivalent to the MD simulation. When changing the mass and memory times, in particular for  $\alpha, \epsilon < 1$ , the simulation time step is suitably adapted. Errors of  $\tau_{\text{MFP}}$ , estimated from block averages, are smaller than the symbol size. The memoryless LE eq 3 is also simulated using a fourth-order Runge–Kutta scheme. Further details on the simulation techniques is given in SI section X.

## ASSOCIATED CONTENT

### Data Availability Statement

The custom computer codes and input files for the simulations are available from the corresponding author upon request.

### Supporting Information

The Supporting Information is available free of charge at <https://pubs.acs.org/doi/10.1021/acs.jpbc.2c05923>.

Detailed derivations, analysis procedures, additional data and discussion (PDF)

## AUTHOR INFORMATION

### Corresponding Author

Roland R. Netz – *Fachbereich Physik, Freie Universität Berlin, 14195 Berlin, Germany*; [orcid.org/0000-0003-0147-0162](https://orcid.org/0000-0003-0147-0162); Email: [rnetz@physik.fu-berlin.de](mailto:rnetz@physik.fu-berlin.de)

## Authors

Florian N. Brüning – *Fachbereich Physik, Freie Universität Berlin, 14195 Berlin, Germany*; [orcid.org/0000-0001-8583-6488](https://orcid.org/0000-0001-8583-6488)

Jan O. Daldrop – *Fachbereich Physik, Freie Universität Berlin, 14195 Berlin, Germany*

Complete contact information is available at: <https://pubs.acs.org/10.1021/acs.jpbc.2c05923>

## Notes

The authors declare no competing financial interest.

## Biographies



Florian Brüning studied physics at the Freie Universität Berlin, Germany, where he is currently pursuing a Ph.D. degree with Prof. Roland Netz. His research interests are vibrational spectroscopy, proton dynamics, and modeling of non-Markovian effects using the generalized Langevin equation, atomistic and quantum simulations, as well as theoretical calculations.



Roland Netz studied physics at the Technical University of Berlin and at MIT and received his Ph.D. in 1994 from the University of Cologne. After postdoctoral positions at Tel-Aviv University, UC Santa Barbara, Seattle, Institute Charles Sadron in Strasbourg, CEA in Paris, and the Max-Planck Institute for Colloids and Interfaces in Potsdam, he was appointed associate professor of physics at the LMU Munich in 2002 and full professor of physics at the TU Munich in 2004. Since 2011 he has held a chair in theoretical biosoft-matter physics at the Freie Universität Berlin. His research focuses on the structure, dynamics and spectroscopy of water, proteins, polymers and charged systems using quantum, atomistic, and coarse-grained simulations as well as theoretical approaches.

## ACKNOWLEDGMENTS

We gratefully acknowledge support by the Deutsche Forschungsgemeinschaft (DFG) Grants SFB 1078 project ID 221545957 and SFB 1114 project ID 235221301, the European Research Council (ERC) Advanced Grant NoMa-Memo Grant No. 835117, and computing time on the HPC clusters at ZEDAT and at the physics department, FU Berlin.

## REFERENCES

- (1) Kramers, H. A. Brownian motion in a field of force and the diffusion model of chemical reactions. *Physica* **1940**, *7*, 284–304.
- (2) Visscher, P. B. Escape rate for a Brownian particle in a potential Well. *Phys. Rev. B* **1976**, *13*, 3272–3275.
- (3) Chandler, D. Statistical mechanics of isomerization dynamics in liquids and the transition state approximation. *J. Chem. Phys.* **1978**, *68*, 2959.
- (4) Skinner, J. L.; Wolynes, P. G. Relaxation processes and chemical kinetics. *J. Chem. Phys.* **1978**, *69*, 2143–2150.
- (5) Arrhenius, S. Über die Reaktionsgeschwindigkeit bei der Inversion von Rohrzucker durch Säuren. *Zeit. Phys. Chem.* **1889**, *4*, 226–248.
- (6) Allen, M. P. Brownian dynamics simulation of a chemical reaction in solution. *Mol. Phys.* **1980**, *40*, 1073–1087.
- (7) Trullàs, J.; Giró, A.; Padró, J. A. Langevin dynamics study of NaCl electrolyte solutions at different concentrations. *J. Chem. Phys.* **1990**, *93*, 5177–5181.
- (8) Lickert, B.; Stock, G. Modeling non-Markovian data using Markov state and Langevin models. *J. Chem. Phys.* **2020**, *153*, 244112.
- (9) Best, R. B.; Hummer, G. Diffusive Model of Protein Folding Dynamics with Kramers Turnover in Rate. *Phys. Rev. Lett.* **2006**, *96*, 228104.
- (10) Straub, J. E.; Borkovec, M.; Berne, B. J. Calculation of dynamic friction on intramolecular degrees of freedom. *J. Phys. Chem.* **1987**, *91*, 4995–4998.
- (11) Hänggi, P.; Talkner, P.; Borkovec, M. Reaction-rate theory: Fifty years after Kramers. *Rev. Mod. Phys.* **1990**, *62*, 251–341.
- (12) Geissler, P. L.; Dellago, C.; Chandler, D. Kinetic pathways of ion pair dissociation in water. *J. Phys. Chem. B* **1999**, *103*, 3706–3710.
- (13) Mullen, R. G.; Shea, J.-E. E.; Peters, B. Transmission coefficients, committers, and solvent coordinates in ion-pair dissociation. *J. Chem. Theory Comput.* **2014**, *10*, 659–667.
- (14) Roy, S.; Baer, M. D.; Mundy, C. J.; Schenter, G. K. Reaction Rate Theory in Coordination Number Space: An Application to Ion Solvation. *J. Phys. Chem. C* **2016**, *120*, 7597–7605.
- (15) Takayanagi, T.; Nakatomi, T.; Yonetani, Y. On the ion-pair dissociation mechanisms in the small NaCl·(H<sub>2</sub>O)<sub>6</sub> cluster: A perspective from reaction path search calculations. *J. Comput. Chem.* **2018**, *39*, 1835–1842.
- (16) Zwanzig, R. Ensemble Method in the Theory of Irreversibility. *J. Chem. Phys.* **1960**, *33*, 1338–1341.
- (17) Mori, H. Transport, collective motion, and Brownian motion. *Prog. Theor. Phys.* **1965**, *33*, 423–455.
- (18) Adelman, S. A. Generalized Langevin theory for many-body problems in chemical dynamics: Reactions in liquids. *J. Chem. Phys.* **1980**, *73*, 3145–3158.
- (19) Ciccotti, G.; Ryckaert, J. P. On the derivation of the generalized Langevin equation for interacting Brownian particles. *J. Stat. Phys.* **1981**, *26*, 73–82.
- (20) Guàrdia, E.; Padró, J. A. Generalized Langevin dynamics simulation of interacting particles. *J. Chem. Phys.* **1985**, *83*, 1917–1920.
- (21) Canales, M.; Sesé, G. Generalized Langevin dynamics simulations of NaCl electrolyte solutions. *J. Chem. Phys.* **1998**, *109*, 6004–6011.
- (22) Kappler, J.; Daldrop, J. O.; Brüning, F. N.; Boehle, M. D.; Netz, R. R. Memory-induced acceleration and slowdown of barrier crossing. *J. Chem. Phys.* **2018**, *148*, 014903.
- (23) Daldrop, J. O.; Kappler, J.; Brüning, F. N.; Netz, R. R. Butane dihedral angle dynamics in water is dominated by internal friction. *Proc. Natl. Acad. Sci. U. S. A.* **2018**, *115*, S169–S174.
- (24) Satija, R.; Makarov, D. E. Generalized Langevin Equation as a Model for Barrier Crossing Dynamics in Biomolecular Folding. *J. Phys. Chem. B* **2019**, *123*, 802–810.
- (25) Wolf, S.; Lickert, B.; Bray, S.; Stock, G. Multisecond ligand dissociation dynamics from atomistic simulations. *Nat. Commun.* **2020**, *11*, 2918.
- (26) Seyler, S. L.; Pressé, S. Surmounting potential barriers: Hydrodynamic memory hedges against thermal fluctuations in particle transport. *J. Chem. Phys.* **2020**, *153*, 041102.
- (27) Singh, V.; Biswas, P. A generalized Langevin equation approach for barrier crossing dynamics in conformational transitions of proteins. *J. Stat. Mech. Theory Exp.* **2021**, *2021*, 063502.
- (28) Cherayil, B. J. Particle dynamics in viscoelastic media: Effects of non-thermal white noise on barrier crossing rates. *J. Chem. Phys.* **2021**, *155*, 244903.
- (29) Ferrer, B. R.; Gomez-Solano, J. R.; Arzola, A. V. Fluid Viscoelasticity Triggers Fast Transitions of a Brownian Particle in a Double Well Optical Potential. *Phys. Rev. Lett.* **2021**, *126*, 108001.
- (30) Meyer, H.; Wolf, S.; Stock, G.; Schilling, T. A Numerical Procedure to Evaluate Memory Effects in Non-Equilibrium Coarse-Grained Models. *Adv. Theory Simulations* **2021**, *4*, 2000197.
- (31) Ayaz, C.; Tepper, L.; Brüning, F. N.; Kappler, J.; Daldrop, J. O.; Netz, R. R. Non-Markovian modeling of protein folding. *Proc. Natl. Acad. Sci. U. S. A.* **2021**, *118*, No. e2023856118.
- (32) Acharya, S.; Bagchi, B. Non-Markovian rate theory on a multidimensional reaction surface: Complex interplay between enhanced configuration space and memory. *J. Chem. Phys.* **2022**, *156*, 134101.
- (33) Mukherjee, S.; Mondal, S.; Acharya, S.; Bagchi, B. Tug-of-War between Internal and External Frictions and Viscosity Dependence of Rate in Biological Reactions. *Phys. Rev. Lett.* **2022**, *128*, 108101.
- (34) Cherayil, B. J. Effects of Hydrodynamic Backflow on the Transmission Coefficient of a Barrier-Crossing Brownian Particle. *J. Phys. Chem. B* **2022**, *126*, S629–S636.
- (35) Satija, R.; Das, A.; Makarov, D. E. Transition path times reveal memory effects and anomalous diffusion in the dynamics of protein folding. *J. Chem. Phys.* **2017**, *147*, 152707.
- (36) Carlon, E.; Orland, H.; Sakaue, T.; Vanderzande, C. Effect of Memory and Active Forces on Transition Path Time Distributions. *J. Phys. Chem. B* **2018**, *122*, 11186–11194.
- (37) Singh, D.; Mondal, K.; Chaudhury, S. Effect of Memory and Inertial Contribution on Transition-Time Distributions: Theory and Simulations. *J. Phys. Chem. B* **2021**, *125*, 4536–4545.
- (38) Grote, R. F.; Hynes, J. T. The stable states picture of chemical reactions. II. Rate constants for condensed and gas phase reaction models. *J. Chem. Phys.* **1980**, *73*, 2715–2732.
- (39) Pollak, E.; Grabert, H.; Hänggi, P. Theory of activated rate processes for arbitrary frequency dependent friction: solution of the turnover problem. *J. Chem. Phys.* **1989**, *91*, 4073–4087.
- (40) Fricks, J.; Yao, L.; Elston, T. C.; Forest, M. G. Time-Domain Methods for Diffusive Transport in Soft Matter. *SIAM J. Appl. Math.* **2009**, *69*, 1277–1308.
- (41) Lei, H.; Baker, N. A.; Li, X. Data-driven parameterization of the generalized Langevin equation. *Proc. Natl. Acad. Sci. U. S. A.* **2016**, *113*, 14183–14188.
- (42) Jung, G.; Hanke, M.; Schmid, F. Iterative Reconstruction of Memory Kernels. *J. Chem. Theory Comput.* **2017**, *13*, 2481–2488.
- (43) Grogan, F.; Lei, H.; Li, X.; Baker, N. A. Data-driven molecular modeling with the generalized Langevin equation. *J. Comput. Phys.* **2020**, *418*, 109633.
- (44) Vroylandt, H.; Goudenège, L.; Monmarché, P.; Pietrucci, F.; Rotenberg, B. Likelihood-based non-Markovian models from molecular dynamics. *Proc. Natl. Acad. Sci. U. S. A.* **2022**, *119*, No. e2117586119.

- (45) Vroylandt, H.; Monmarché, P. Position-dependent memory kernel in generalized Langevin equations: Theory and numerical estimation. *J. Chem. Phys.* **2022**, *156*, 244105.
- (46) Ciccotti, G.; Ferrario, M.; Hynes, J. T.; Kapral, R. Dynamics of ion pair interconversion in a polar solvent. *J. Chem. Phys.* **1990**, *93*, 7137–7147.
- (47) Benjamin, I.; Lee, L. L.; Li, Y. S.; Liu, A.; Wilson, K. R. Generalized Langevin model for molecular dynamics of an activated reaction in solution. *Chem. Phys.* **1991**, *152*, 1–12.
- (48) Rey, R.; Guàrdia, E.; Padró, J. A. Generalized Langevin dynamics simulation of activated processes in solution: Ion pair interconversion in water. *J. Chem. Phys.* **1992**, *97*, 8276–8284.
- (49) Annapureddy, H. V. R.; Dang, L. X. Understanding the Rates and Molecular Mechanism of Water-Exchange around Aqueous Ions Using Molecular Simulations. *J. Phys. Chem. B* **2014**, *118*, 8917–8927.
- (50) Klippenstein, V.; Tripathy, M.; Jung, G.; Schmid, F.; Van Der Vegt, N. F. Introducing Memory in Coarse-Grained Molecular Simulations. *J. Phys. Chem. B* **2021**, *125*, 4931–4954.
- (51) Brünig, F. N.; Geburtig, O.; von Canal, A.; Kappler, J.; Netz, R. R. Time-Dependent Friction Effects on Vibrational Infrared Frequencies and Line Shapes of Liquid Water. *J. Phys. Chem. B* **2022**, *126*, 1579–1589.
- (52) Ayaz, C.; Scalfi, L.; Dalton, B. A.; Netz, R. R. Generalized Langevin equation with a nonlinear potential of mean force and nonlinear memory friction from a hybrid projection scheme. *Phys. Rev. E* **2022**, *105*, 054138.
- (53) Sedlmeier, F.; Netz, R. R. Solvation thermodynamics and heat capacity of polar and charged solutes in water. *J. Chem. Phys.* **2013**, *138*, 115101.
- (54) Van Der Vegt, N. F.; Haldrup, K.; Roke, S.; Zheng, J.; Lund, M.; Bakker, H. J. Water-Mediated Ion Pairing: Occurrence and Relevance. *Chem. Rev.* **2016**, *116*, 7626–7641.
- (55) Schwierz, N. Kinetic pathways of water exchange in the first hydration shell of magnesium. *J. Chem. Phys.* **2020**, *152*, 224106.
- (56) Lum, K.; Chandler, D.; Weeks, J. D. Hydrophobicity at Small and Large Length Scales. *J. Phys. Chem. B* **1999**, *103*, 4570–4577.
- (57) Ashbaugh, H. S.; Pratt, L. R. Colloquium: Scaled particle theory and the length scales of hydrophobicity. *Rev. Mod. Phys.* **2006**, *78*, 159–178.
- (58) Sedlmeier, F.; Netz, R. R. The spontaneous curvature of the water-hydrophobe interface. *J. Chem. Phys.* **2012**, *137*, 135102.
- (59) Ohtaki, H.; Radnai, T. Structure and dynamics of hydrated ions. *Chem. Rev.* **1993**, *93*, 1157–1204.
- (60) Karim, O. A.; McCammon, J. A. Dynamics of a Sodium Chloride Ion Pair in Water. *J. Am. Chem. Soc.* **1986**, *108*, 1762–1766.
- (61) Rey, R.; Guardia, E. Dynamical Aspects of the Na<sup>+</sup>-Cl<sup>-</sup> Ion Pair Association in Water. *J. Phys. Chem.* **1992**, *96*, 4712–4718.
- (62) Ballard, A. J.; Dellago, C. Toward the Mechanism of Ionic Dissociation in Water. *J. Phys. Chem. B* **2012**, *116*, 13490.
- (63) Wolf, S.; Stock, G. Targeted Molecular Dynamics Calculations of Free Energy Profiles Using a Nonequilibrium Friction Correction. *J. Chem. Theory Comput.* **2018**, *14*, 6175–6182.
- (64) Post, M.; Wolf, S.; Stock, G. Molecular Origin of Driving-Dependent Friction in Fluids. *J. Chem. Theory Comput.* **2022**, *18*, 2816–2825.
- (65) Roy, S.; Baer, M. D.; Mundy, C. J.; Schenter, G. K. Marcus Theory of Ion-Pairing. *J. Chem. Theory Comput.* **2017**, *13*, 3470–3477.
- (66) Brünig, F. N.; Netz, R. R.; Kappler, J. Barrier-crossing times for different non-Markovian friction in well and barrier: A numerical study. *Phys. Rev. E* **2022**, *106*, 44133.
- (67) Dalton, B. A.; Ayaz, C.; Tepper, L.; Netz, R. R. Fast protein folding is governed by memory-dependent friction. *arXiv* **2022**; <https://arxiv.org/abs/2208.13842>.
- (68) Daldrop, J. O.; Kowalik, B. G.; Netz, R. R. External Potential Modifies Friction of Molecular Solutes in Water. *Phys. Rev. X* **2017**, *7*, 041065.
- (69) Marchesoni, F.; Grigolini, P. On the extension of the Kramers theory of chemical relaxation to the case of nonwhite noise. *J. Chem. Phys.* **1983**, *78*, 6287–6298.
- (70) Morrone, J. A.; Markland, T. E.; Ceriotti, M.; Berne, B. J. Efficient multiple time scale molecular dynamics: Using colored noise thermostats to stabilize resonances. *J. Chem. Phys.* **2011**, *134*, 014103.
- (71) Lee, H. S.; Ahn, S. H.; Darve, E. F. The multi-dimensional generalized Langevin equation for conformational motion of proteins. *J. Chem. Phys.* **2019**, *150*, 174113.
- (72) Risken, H. *The Fokker–Planck Equation*, 2nd ed.; Springer: Berlin, 1996.
- (73) Eyring, H. The Activated Complex in Chemical Reactions. *J. Chem. Phys.* **1935**, *3*, 107–115.
- (74) Mel'nikov, V. I.; Meshkov, S. V. Theory of activated rate processes: Exact solution of the Kramers problem. *J. Chem. Phys.* **1986**, *85*, 1018–1027.
- (75) Weiss, G. H. First Passage Time Problems in Chemical Physics. *Adv. Chem. Phys.* **1967**, *13*, 1–18.
- (76) Hinczewski, M.; von Hansen, Y.; Dzubiella, J.; Netz, R. R. How the diffusivity profile reduces the arbitrariness of protein folding free energies. *J. Chem. Phys.* **2010**, *132*, 245103.
- (77) Von Hansen, Y.; Sedlmeier, F.; Hinczewski, M.; Netz, R. R. Friction contribution to water-bond breakage kinetics. *Phys. Rev. E - Stat. Nonlinear, Soft Matter Phys.* **2011**, *84*, 051501.
- (78) Kowalik, B.; Daldrop, J. O.; Kappler, J.; Schulz, J. C.; Schlaich, A.; Netz, R. R. Memory-kernel extraction for different molecular solutes in solvents of varying viscosity in confinement. *Phys. Rev. E* **2019**, *100*, 012126.
- (79) Kappler, J.; Hinrichsen, V. B.; Netz, R. R. Non-Markovian barrier crossing with two-time-scale memory is dominated by the faster memory component. *Eur. Phys. J. E* **2019**, *42*, 119.
- (80) Timko, J.; Bucher, D.; Kuyucak, S. Dissociation of NaCl in water from ab initio molecular dynamics simulations. *J. Chem. Phys.* **2010**, *132*, 114510.
- (81) Zhang, C.; Giberti, F.; Sevgen, E.; de Pablo, J. J.; Gygi, F.; Galli, G. Dissociation of salts in water under pressure. *Nat. Commun.* **2020**, *11*, 3037.
- (82) Wills, A.; Fernández-Serra, M. Role of water model on ion dissociation at ambient conditions. *J. Chem. Phys.* **2021**, *154*, 194502.
- (83) Abraham, M. J.; Murtola, T.; Schulz, R.; Páll, S.; Smith, J. C.; Hess, B.; Lindahl, E. GROMACS: High performance molecular simulations through multi-level parallelism from laptops to supercomputers. *SoftwareX* **2015**, *1–2*, 19–25.
- (84) Berendsen, H. J. C.; Grigera, J. R.; Straatsma, T. P. The missing term in effective pair potentials. *J. Phys. Chem.* **1987**, *91*, 6269–6271.
- (85) Dang, L. X. Mechanism and Thermodynamics of Ion Selectivity in Aqueous Solutions of 18-Crown-6 Ether: A Molecular Dynamics Study. *J. Am. Chem. Soc.* **1995**, *117*, 6954–6960.
- (86) Loche, P.; Steinbrunner, P.; Friedowitz, S.; Netz, R. R.; Bonthuis, D. J. Transferable Ion Force Fields in Water from a Simultaneous Optimization of Ion Solvation and Ion-Ion Interaction. *J. Phys. Chem. B* **2021**, *125*, 8581–8587.
- (87) Oostenbrink, C.; Villa, A.; Mark, A. E.; Van Gunsteren, W. F. A biomolecular force field based on the free enthalpy of hydration and solvation: The GROMOS force-field parameter sets 53A5 and 53A6. *J. Comput. Chem.* **2004**, *25*, 1656–1676.



Supplementary Information:  
Proton-Transfer Spectroscopy Beyond  
the Normal-Mode Scenario

---

A

A. *Supplementary Information:*  
*Proton-Transfer Spectroscopy Beyond the Normal-Mode Scenario*

---

**Supplementary information:**  
**Proton-transfer spectroscopy beyond the normal-mode scenario**

Florian N. Brünig,<sup>1</sup> Paul Hillmann,<sup>1</sup> Won Kyu Kim,<sup>2</sup> Jan O. Daldrop,<sup>1</sup> and Roland R. Netz<sup>1, a)</sup>

<sup>1)</sup>*Freie Universität Berlin, Department of Physics, 14195 Berlin, Germany*

<sup>2)</sup>*Korea Institute for Advanced Study, School of Computational Sciences, Seoul 02455, Republic of Korea*

(Dated: October 23, 2022)

---

<sup>a)</sup>rnetz@physik.fu-berlin.de

## I. QUANTUM ZERO-POINT MOTION EFFECTS

Quantum zero-point motion is known to smear out particle distributions and thereby to increase the particle density at barriers. Therefore in this section, we estimate the potential barrier height of a double-well potential for which the ground-state probability density develops a minimum at the barrier.

The one-dimensional stationary Schrödinger equation

$$-\frac{\hbar^2}{2m} \frac{\partial^2}{\partial d^2} \phi(d) = (U(d) - E) \phi(d) \quad (\text{S1})$$

is solved numerically for the quartic double-well potential

$$U(d) = U_0 \left( \left( \frac{d}{d_{\text{TW}}^*} \right)^2 - 1 \right)^2, \quad (\text{S2})$$

which is shown in fig. S1A to approximate the effective potential describing the excess proton distribution obtained from our ab initio molecular-dynamics (AIMD) simulations very well.

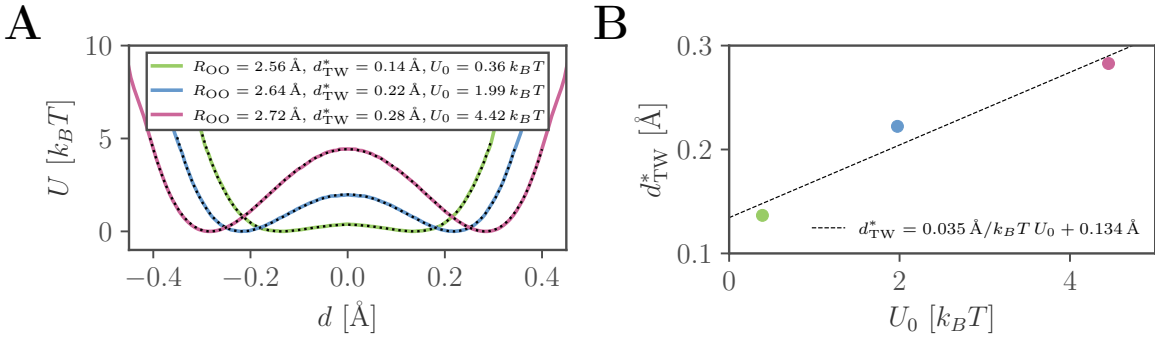


Figure S1. **A** Free-energy profiles  $U(d)$  for fixed  $R_{\text{OO}}$ , extracted from constrained ab initio molecular-dynamics (AIMD) simulations of the  $\text{H}_5\text{O}_2^+$  cation, are shown as colored lines. Fits according to eq. (S2) are shown as black dotted lines with fit parameters given in the legend. **B** Dependence of  $d_{\text{TW}}^*$  on  $U_0$ . Here a linear fit is shown as a black dashed line.

The equations are rescaled as

$$\frac{\partial^2}{\partial \tilde{x}^2} \phi(\tilde{x}) = (\tilde{U}(\tilde{x}) - \tilde{E}) \phi(\tilde{x}), \quad (\text{S3})$$

$$\tilde{U}(\tilde{x}) = \tilde{U}_0 (\tilde{x}^2 - 1)^2, \quad (\text{S4})$$

with  $\tilde{x} = d/d_{\text{TW}}^*$ ,  $\tilde{U}_0 = 2mU_0 d_{\text{TW}}^{*2}/\hbar^2$  and  $\tilde{E} = 2mE d_{\text{TW}}^{*2}/\hbar^2$ . Using the proton mass  $m = 1.7 \times 10^{-27}$  kg,  $\hbar = 1.1 \times 10^{-34}$  Js and  $d_{\text{TW}}^* = 0.22$  Å for the system with  $R_{\text{OO}} = 2.64$  Å, the rescaling factor for the energies is  $\hbar^2/(2m d_{\text{TW}}^{*2}) = 7.4 \times 10^{-21}$  J =  $1.8 k_B T$  at 300 K. Note that this scaling factor implicitly depends on  $U_0$  due to the dependence of  $d_{\text{TW}}^*$  on  $U_0$  shown in fig. S1B.

Dimensionless ground state energies  $\tilde{E}$  are numerically computed for  $\tilde{U}_0 \in [1, 2]$  using bisection to find the eigenvalues of the dimensionless Schrödinger equation eq. (S3). The ground state energy  $\tilde{E}$  shows approximately linear dependence on  $\tilde{U}_0 \in [1, 2]$  (see green dots in fig. S2A). A minimum of the ground-state density at the barrier is defined by a positive curvature at the origin,  $\frac{\partial^2}{\partial \tilde{x}^2} \phi^2(\tilde{x} = 0) > 0$ . From the Schrödinger equation eq. (S3) it becomes clear that the wave function of the ground state develops a minimum at the origin for  $\tilde{E} < \tilde{U}_0$ . It follows for the curvature of the probability density by inserting eq. (S3)

$$\frac{\partial^2}{\partial \tilde{x}^2} \phi^2(\tilde{x}) = 2 \left[ \left( \frac{\partial \phi(\tilde{x})}{\partial \tilde{x}} \right)^2 + (\tilde{U}(\tilde{x}) - \tilde{E}) \phi^2(\tilde{x}) \right]. \quad (\text{S5})$$



A. Supplementary Information:  
Proton-Transfer Spectroscopy Beyond the Normal-Mode Scenario

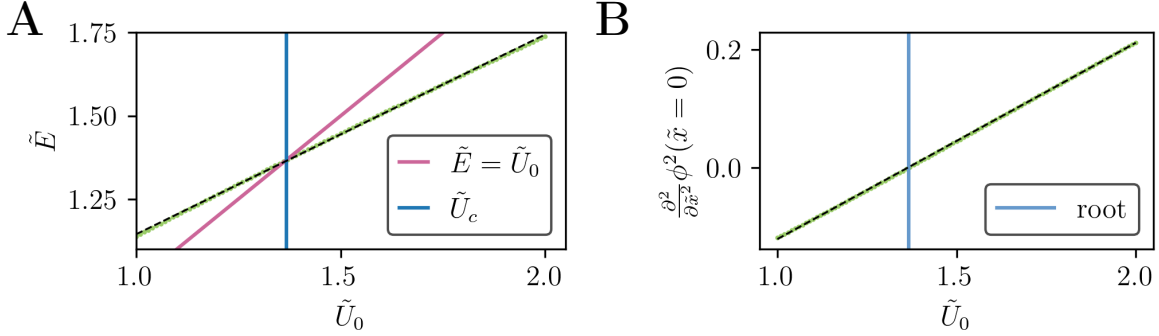


Figure S2. **A** Dimensionless ground state energy  $\tilde{E}$  as a function of the barrier height  $\tilde{U}_0$  (green dots). A linear fit according to  $\tilde{E}(U_0) = 0.601\tilde{U}_0 + 0.542$  is shown as a black dashed line. The crossing between the ground-state energy  $\tilde{E}$  and  $\tilde{E} = \tilde{U}_0$  (red line) is marked as a vertical blue line at  $\tilde{U}_c := \tilde{U}_0(\tilde{E} = \tilde{U}_0) = 1.36$ . **B** Curvature of the ground state probability density at the origin as a function of  $\tilde{U}_0$ . A linear fit according to  $\partial^2\phi^2/\partial\tilde{x}^2(\tilde{x}=0) = 0.334\tilde{U}_0 - 0.455$  is shown as a black dashed line. The point where the curvature vanishes is marked as a vertical blue line, which is given by  $\tilde{U}_c = 1.36$ .

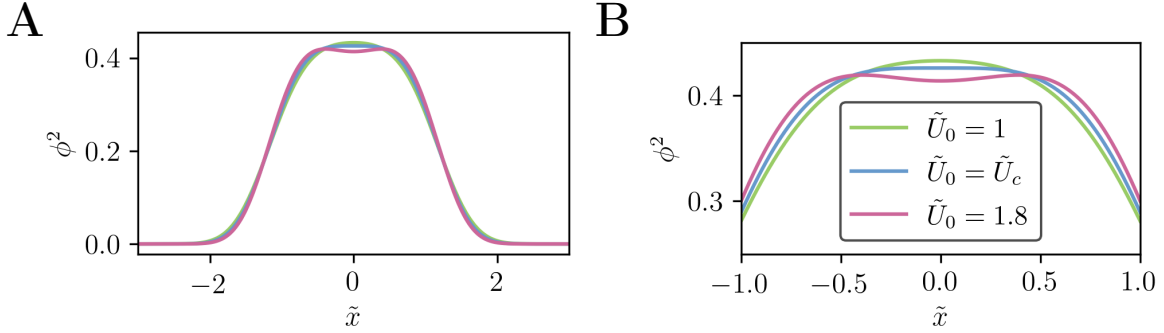


Figure S3. **A** Ground state probability densities for  $\tilde{U}_0 = 1$ ,  $\tilde{U}_0 = \tilde{U}_c$  and  $\tilde{U}_0 = 1.8$ . **B** Ground state probability densities around the origin.

Since the ground state is symmetric around the origin this becomes at the origin

$$\frac{\partial^2}{\partial\tilde{x}^2}\phi^2 = 2(\tilde{U}_0 - \tilde{E})\phi^2. \quad (\text{S6})$$

Fig. S2B shows the curvature at the origin  $\frac{\partial^2}{\partial\tilde{x}^2}\phi^2(\tilde{x}=0)$  as a function of  $\tilde{U}_0$  (green dots). A linear fit is used to determine the critical potential strength at which the curvature vanishes as  $\tilde{U}_c = 1.36$ . Fig. S3 shows a comparison of the ground state density distributions for  $\tilde{U}_0 = \{1, \tilde{U}_c, 1.8\}$ .

From this analysis we conclude that when treating the excess proton quantum-mechanically, a minimum in the ground state probability density, reflecting the effect of the barrier, appears for barrier heights of the double-well potential

$$U_0 > \frac{\hbar^2}{2m [d_{\text{TW}}^*(U_0)]^2} \tilde{U}_c k_B T, \quad (\text{S7})$$

which holds for  $U_0 > 2.5 k_B T$ , as can be read off from fig. S4. Therefore, using the naive assumption that a minimum in the probability density at the barrier top indicates the presence of an effective quantum-mechanical barrier, which is far from obvious, one could speculate that the presented results for the spectroscopic signatures of proton barrier-crossing are expected to survive quantum-mechanical zero-point motion effects for high enough potential barriers.

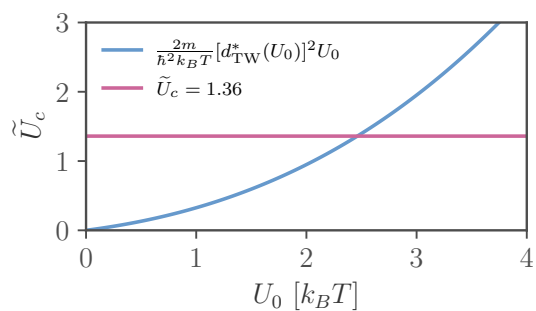


Figure S4. A minimum in the ground state probability density appears for  $\frac{2m}{\hbar^2 k_B T} [d_{\text{TW}}^*(U_0)]^2 U_0 > \tilde{U}_c$ , obtained by rearrangement of eq. (S7), where  $U_0$  is the barrier height of the double-well potential,  $\tilde{U}_c = 1.36$  is taken from fig. S2B and  $d_{\text{TW}}^*(U_0)$  is taken from the linear fit in fig. S1B.

## II. SUMMARY OF PREVIOUS EXPERIMENTAL AND THEORETICAL STUDIES ON INFRARED SPECTRA OF THE $\text{H}_5\text{O}_2^+$ CATION

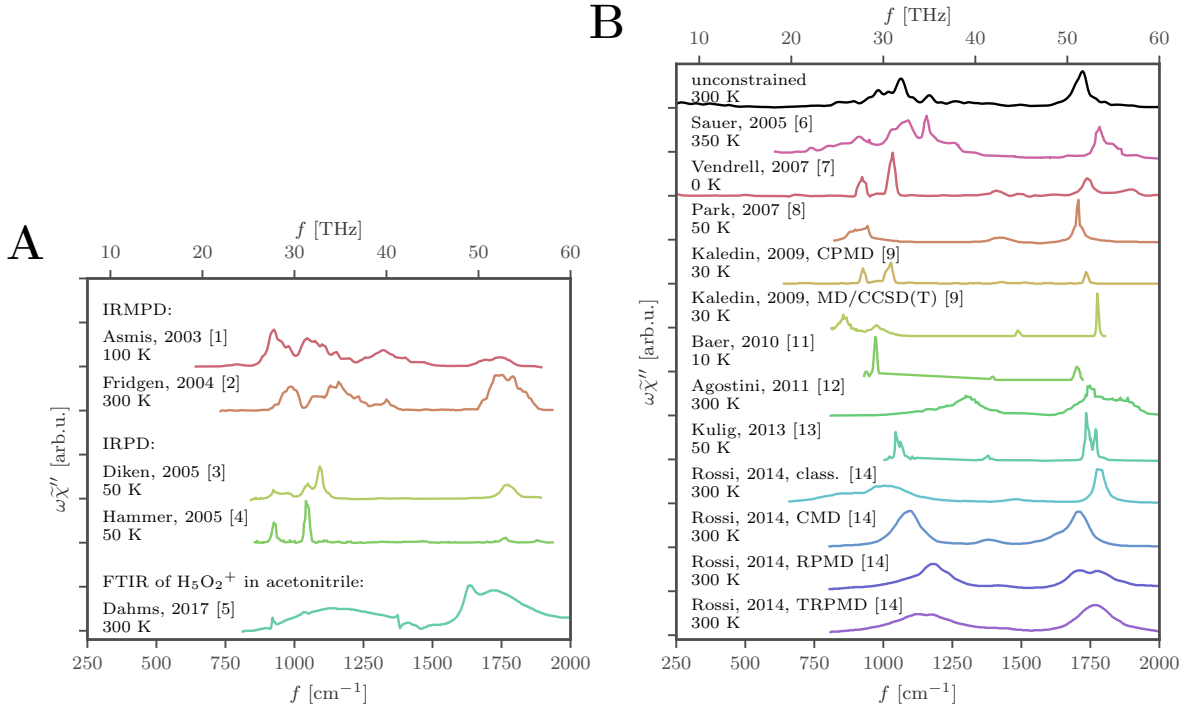


Figure S5. Collection of experimental (A) and theoretical (B) IR spectra of the  $\text{H}_5\text{O}_2^+$  cation in the proton-transfer regime (colored lines), compared to the IR spectrum obtained from AIMD simulations in this study, shown in black. **A** The experimental spectra were recorded using infrared multiple-photon-dissociation (IRMPD) spectroscopy<sup>1,2</sup>, infrared predissociation (IRPD) spectroscopy in Argon<sup>3</sup> and Neon<sup>4</sup> and Fourier-transform IR (FTIR) spectroscopy of  $\text{H}_5\text{O}_2^+$  cations solvated in acetonitrile<sup>5</sup>. **B** Theoretical spectra were obtained using AIMD simulations on the MP2/cc-pVTZ level<sup>6</sup>, the multiconfiguration time-dependent Hartree (MCTDH) method<sup>7</sup>, CPMD simulations using the BLYP functional<sup>8</sup>, CPMD simulations using the BLYP functional<sup>9</sup>, MD simulations on the CCSD(T) potential energy surface using MP2 dipole moment functions (based on<sup>10</sup>)<sup>9</sup>, AIMD simulations on the BLYP-D3 TZV2P level<sup>11</sup>, MD simulations using the multistate-empirical-valence-bond (MS-EVB) method<sup>12</sup>, AIMD simulations on the DZVP-BLYP level<sup>13</sup>, classical MD, centroid MD (CMD), as well as ring polymer MD simulations (RPMD, TRPMD)<sup>14</sup> on the CCSD(T) potential energy surface<sup>10</sup>. For comparison, the spectrum of the unconstrained  $\text{H}_5\text{O}_2^+$  cation obtained from AIMD simulations in this study (obtained on the BLYP-D3 TZV2P level) is shown as the black line at the top. All theoretical spectra report on isolated  $\text{H}_5\text{O}_2^+$ .

A collection of IR spectra of the  $\text{H}_5\text{O}_2^+$  cation in the so-called proton-transfer regime, 600 cm $^{-1}$  to 1500 cm $^{-1}$ , obtained from experiments is given in fig. S5A and from theoretical calculations in fig. S5B. The spectra vary greatly among different experimental studies, highlighting the subtle differences between experimental techniques and setups and also pointing to a pronounced temperature dependence of the spectra. Importantly, there are systematic differences between the gas-phase spectra obtained for isolated  $\text{H}_5\text{O}_2^+$  cations from theoretical calculations and experimental spectra, which rely on different model systems and employ different techniques, one experimental study reports on  $\text{H}_5\text{O}_2^+$  cations in acetonitrile solution.

Regarding the experimental infrared multiple-photon-dissociation (IRMPD) spectra, the authors themselves raise the question whether their data can be directly compared to linear absorption spectra<sup>1,2</sup>. For the infrared predissociation (IRPD) spectra<sup>3,4</sup> on the other hand, messenger-induced artifacts are known and have been studied theoretically<sup>8,11</sup>. For the case of  $\text{H}_5\text{O}_2^+$  cations solvated in acetonitrile solution, it is clear that the fluctuating electric fields created by the solvent strongly influence the resulting spectra<sup>5</sup>. Thus, differences between the different experimental spectra do not reflect inaccuracies in the measurements but rather subtle differences in the studied experimental systems.

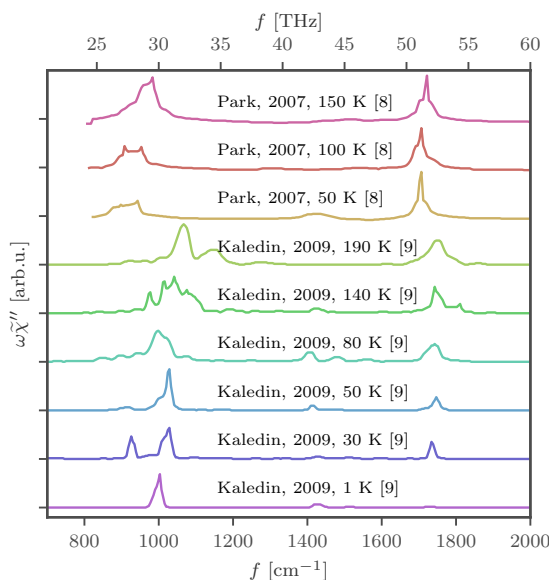


Figure S6. Comparison of theoretical IR spectra of the  $\text{H}_5\text{O}_2^+$  cation in the proton-transfer regime at various temperatures obtained from Car-Parinello MD (CPMD) simulations on BLYP level<sup>8,9</sup>.

The following collection of comments from the literature report on the discrepancies between the IRMPD and IRPD experimental spectra of isolated  $\text{H}_5\text{O}_2^+$  cations. Fridgen *et al.*<sup>2</sup> say that “at this point, we are unable to determine the source of the discrepancy between the present infrared spectrum and that obtained by Asmis *et al.*<sup>1</sup>”. Hammer *et al.*<sup>4</sup> state “the IR profiles obtained in these two measurements<sup>1,2</sup> were markedly different, perhaps reflecting the different ion sources used in the two experiments and/or the specific fluence characteristics of the laser sources”. Sauer and Döbler<sup>6</sup> discuss “that differences between the IRMPD spectrum<sup>1</sup> and the IRPD spectrum<sup>3</sup> should be due to the different excitation mechanisms and/or different temperatures”. Vendrell, Gatti, and Meyer<sup>7</sup> state that “spectra could not be consistently assigned in terms of fundamental frequencies and overtones of harmonic vibrational modes due to large amplitude anharmonic displacements and couplings of the cluster<sup>1,2,4,15</sup>” and conclude their study by pointing out that their “reported calculations are in excellent agreement to the experimental measurements of Refs.<sup>4,15</sup> on the predissociation spectrum of  $\text{H}_5\text{O}_2^+\text{-Ne}$ ”, which is the most widely accepted low-temperature spectrum of the isolated cation to date.

Furthermore, in theoretical studies, the temperature dependence was analyzed by Park *et al.*<sup>8</sup> and Kaledin *et al.*<sup>9</sup> in Car-Parinello MD (CPMD) simulations, presented in fig. S6, and by classical MD simulations on the CCSD(T) potential energy surface using MP2 dipole moment functions (based on<sup>10</sup>), leading to the conclusion that “classical MD simulations at a temperature of 30 K qualitatively reproduce many of the key features in the experimental vibrational [Ar-] predissociation”. Nuclear quantum effects were studied in detail by Rossi, Ceriotti, and Manolopoulos<sup>14</sup>, who compared spectra from different ring polymer MD simulations. The messenger-induced changes of spectra apparent in IRPD techniques were investigated by Park *et al.*<sup>8</sup> and Baer, Marx, and Mathias<sup>11</sup>.

More recent studies have focused on the  $\text{H}_5\text{O}_2^+$  cation in larger water clusters or in bulk water or other solvents and at room temperature<sup>5,12,13,16–18</sup>. Importantly, the electric fields of the environment heavily influence the spectra. These studies identify remarkably broad IR features in the  $1000\text{ cm}^{-1}$  to  $1200\text{ cm}^{-1}$  regime, associated with “proton shuttling”<sup>16</sup>, the “proton-transfer mode (PTM)”<sup>5,13,17</sup> or the “shared proton stretch”<sup>18</sup>.

The review of the published experimental and theoretical data shows that the data produced in this study is in qualitative agreement with previous results on  $\text{H}_5\text{O}_2^+$  cations in gas phase. However, especially in the region of  $800\text{ cm}^{-1}$  to  $1200\text{ cm}^{-1}$  associated with the proton-transfer motion, large temperature and system-dependent differences between the previously published results are observed and reflect the incomplete understanding of proton-transfer dynamics.

### III. NORMAL-MODE ANALYSIS OF THE $\text{H}_5\text{O}_2^+$ CATION

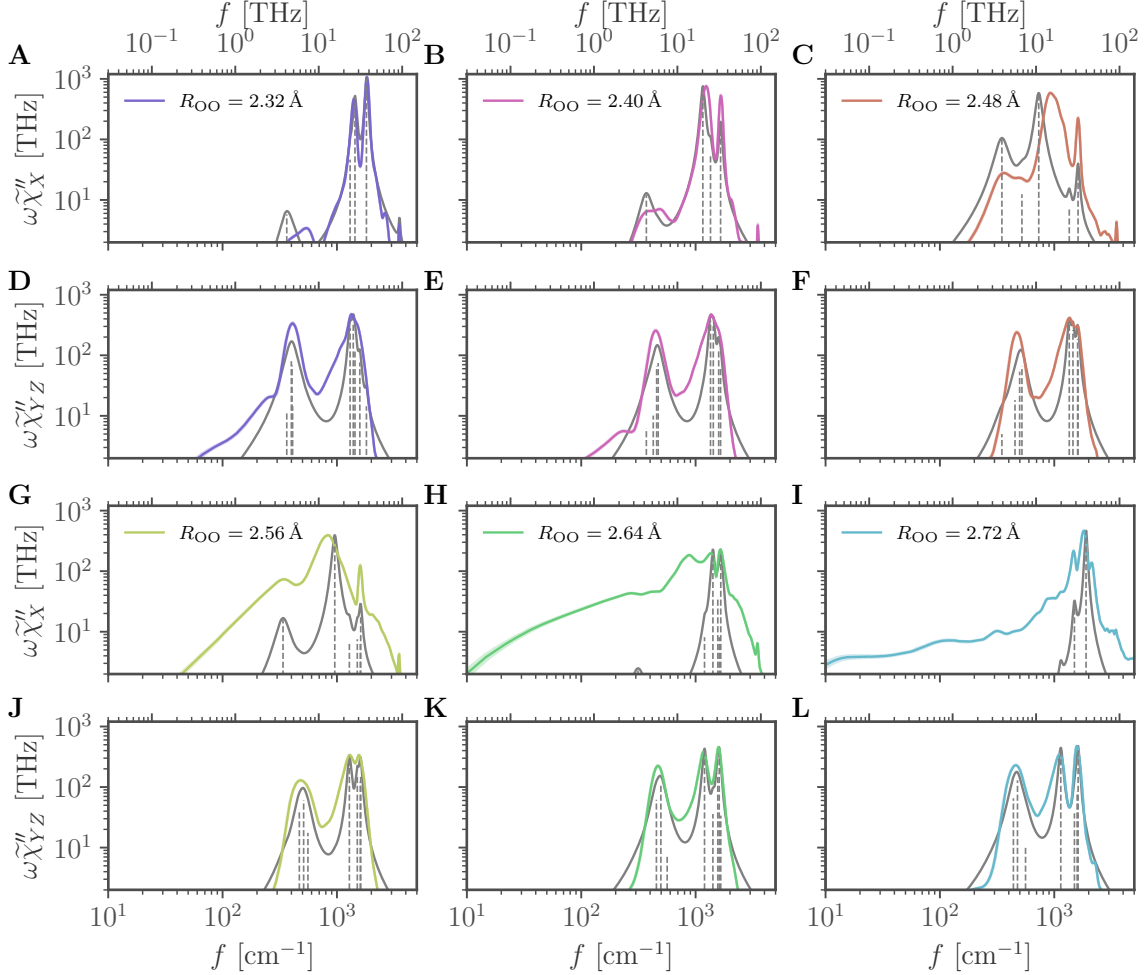


Figure S7. IR spectra of the excess proton (colored lines) in the  $\text{H}_5\text{O}_2^+$  cation for different constraint oxygen distances  $R_{\text{OO}}$  compared to normal-mode spectra calculated from energetically optimized structures and projected on the proton coordinate (grey dashed sticks). The discrete normal modes sum to smooth spectra (grey lines) by including line-broadening at finite temperature obtained from damped harmonic oscillations of the normal modes according to eq. S36 in section X and assuming a friction coefficient of  $\gamma = 16$  u/ps. The spectra are shown for different orientations (**A–C**, **G–I**:  $x$ -axis connecting the two oxygens, **D–F**, **J–L**:  $yz$ -plane).

The normal modes are obtained as the Eigenvectors of the Hessian of the optimal structure in a chosen coordinate system, the corresponding Eigenvalues determine the vibrational frequencies. The normal-mode analysis of the different  $\text{H}_5\text{O}_2^+$  systems was performed for energetically optimized structures using the same set of parameters as for the AIMD simulation.

A projection of the Eigenvectors on the proton coordinate allows to obtain the relative magnitudes of the excess-proton spectra predicted from the normal-mode analysis. These are scaled to the magnitudes of the excess-proton spectra obtained directly from the AIMD simulations for various  $R_{\text{OO}}$  and orientations in fig. S7. To improve the normal-mode spectra, line-broadening of the normal modes at finite temperature is modeled by damped harmonic oscillations (see SI section X). For vibrational motion in the  $yz$ -plane the agreement is very good for all barrier heights indicating, that

the method is well suited for modeling the excess-proton dynamics without a barrier. Along  $x$  the normal mode spectra serve to explain the major peaks of the spectra at high frequencies, which are thereby identified as the normal-mode contributions. The broad low-frequency shoulder, which is related to the barrier-crossing effects, can obviously not be modeled using normal modes.

The system with  $R_{OO} = 2.40 \text{ \AA}$  represents the global unconstrained minimum of the free-energy landscape, shown in fig. 1D in the main text, and can therefore be used to compare qualitatively to published data on the unconstrained  $\text{H}_5\text{O}_2^+$  cation, as done in tab. S1 for the range  $100 \text{ cm}^{-1}$  to  $2000 \text{ cm}^{-1}$ . The normal-modes can be grouped to rocking and wagging modes in the range  $300 \text{ cm}^{-1}$  to  $600 \text{ cm}^{-1}$ , the water-water stretch at around  $550 \text{ cm}^{-1}$  to  $650 \text{ cm}^{-1}$ , which is missing in the constrained case, the widely discussed proton-transfer mode along  $x$ , which varies greatly between  $800 \text{ cm}^{-1}$  to  $1200 \text{ cm}^{-1}$ , a pair of modes between  $1300 \text{ cm}^{-1}$  to  $1600 \text{ cm}^{-1}$ , associated with perpendicular excess-proton motion in the  $yz$ -plane, and the two water-bending modes at  $1600 \text{ cm}^{-1}$  to  $1800 \text{ cm}^{-1}$ , for which the lower one shows excess-proton motion in the  $yz$ -plane (named in-phase or gerade) and the higher one shows excess-proton motion along  $x$  (named out-of-phase or ungerade).

Illustrations of the normal modes in the range  $100 \text{ cm}^{-1}$  to  $2000 \text{ cm}^{-1}$  of  $\text{H}_5\text{O}_2^+$  cations with various constrained  $R_{OO}$  are shown in fig. S8, where the colored frames indicate similar normal modes for different values of  $R_{OO}$ . Fig. S9 summarizes the frequencies of the normal modes for all values of  $R_{OO}$  and highlights the associated relative excess-proton-motion intensities either along  $x$  or in the  $yz$ -plane. Most modes shift only weakly, including the wagging and rocking modes in the range  $300 \text{ cm}^{-1}$  to  $600 \text{ cm}^{-1}$  and the pair of modes between  $1300 \text{ cm}^{-1}$  to  $1600 \text{ cm}^{-1}$ , associated with perpendicular excess-proton motion in the  $yz$ -plane. However, the proton-transfer mode ( $1157 \text{ cm}^{-1}$  for  $R_{OO} = 2.40 \text{ \AA}$ ) strongly increases for values of  $R_{OO} \geq 2.40 \text{ \AA}$ , as shown previously by Wolke *et al.*<sup>19</sup> for the  $\text{D}_5\text{O}_2^+$  cation, which possibly explains why the proton-transfer mode in bulk is suggested to reside at much higher wavenumbers compared to the gas-phase spectra<sup>13</sup>. The in-phase water bending mode shows no shifting but the out-of-phase water bending mode, associated with excess-proton motion along  $x$ , strongly shifts. Generally, modes associated with proton motion along  $x$  are shown to be highly sensitive on the value of  $R_{OO}$ , while modes that are associated with proton motion in the  $yz$ -plane are not.

A. Supplementary Information:  
Proton-Transfer Spectroscopy Beyond the Normal-Mode Scenario

Table S1. Collection of previous identifications of normal modes in the  $\text{H}_5\text{O}_2^+$  cation in the range  $100\text{ cm}^{-1}$  to  $2000\text{ cm}^{-1}$ , compared to data obtained in this study with constrained  $R_{\text{OO}} = 2.40\text{ \AA}$  in the first row. Bold fonts indicate significant motion of the excess proton (if reported).

BLYP-D3, TZV2P, $R_{\text{OO}} = 2.40\text{ \AA}$	wagging, rocking	320, 426, <b>456</b> , <b>470</b>	p. trans. (x)	<b>1157</b>	proton perp. (yz)	<b>1350</b> , <b>1428</b>	water bend	<b>1501</b> , <b>1653</b>	
MP2, aug-cc-pVTZ <sup>b</sup>	H <sub>2</sub> O wag, H <sub>2</sub> O rock	362, 461, 532, 535	sym. OHO str.	627	asym. OHO str.	884	OHO bend (y, z)	1484, 1557	
MP2, cc-pVTZ <sup>b</sup>		367, 461, 522, 529		631		901		1493, 1572	
MP2, cc-pVTZ(aug-O) <sup>b</sup>		347, 456, 525, 532		626		904		1473, 1551	
CCSD(T), cc-pVTZ <sup>b</sup>		350, 457, 531, 535		633		896		1493, 1572	
CCSD(T), MP2, aug-cc-pVTZ <sup>b</sup>		339, 471, 532, 554		630		861		1494, 1574	
MP2, aug-cc-pVTZ <sup>4</sup>			OHO stretch	808				1720, 1770	
MCTDH <sup>7</sup>	wagging rocking	106, 108, 232, 254, 374, 422 481, 915, 930, 943	wat-wat str.	550	p. trans. doub.	<b>918</b> , <b>1033</b>	proton perp. p. trans. + wat. str.	<b>1391</b> <b>1411</b>	water bend water bend (gerade, unger.)
BLYP, aug-cc-pVTZ <sup>8</sup>			asym. OHO str.	938		938	OHO bend (y, z)	1408, 1478	
B3LYP, aug-cc-pVTZ <sup>8</sup>				891		891		1397, 1455	
MP2, aug-cc-pVTZ <sup>8</sup>				868		868		1405, 1478	
BLYP-D3, TZV2P, AIMD <sup>11</sup>	wagging, rocking	370, 431, 498, 514	OO stretch	571	p. trans. (v <sub>g</sub> )	<b>971</b>	proton <sub>yz</sub> (v <sub>p</sub> , v <sub>p</sub> ') water bend (δ <sub>s</sub> , δ <sub>e</sub> )	<b>1396</b> , <b>1477</b> <b>1636</b> , <b>1700</b>	
MS-EVB, EMA <sup>12</sup>				1032				1311, 1560	
B3LYP, aug-cc-pVTZ <sup>13</sup>		358		926				1638, 1769	

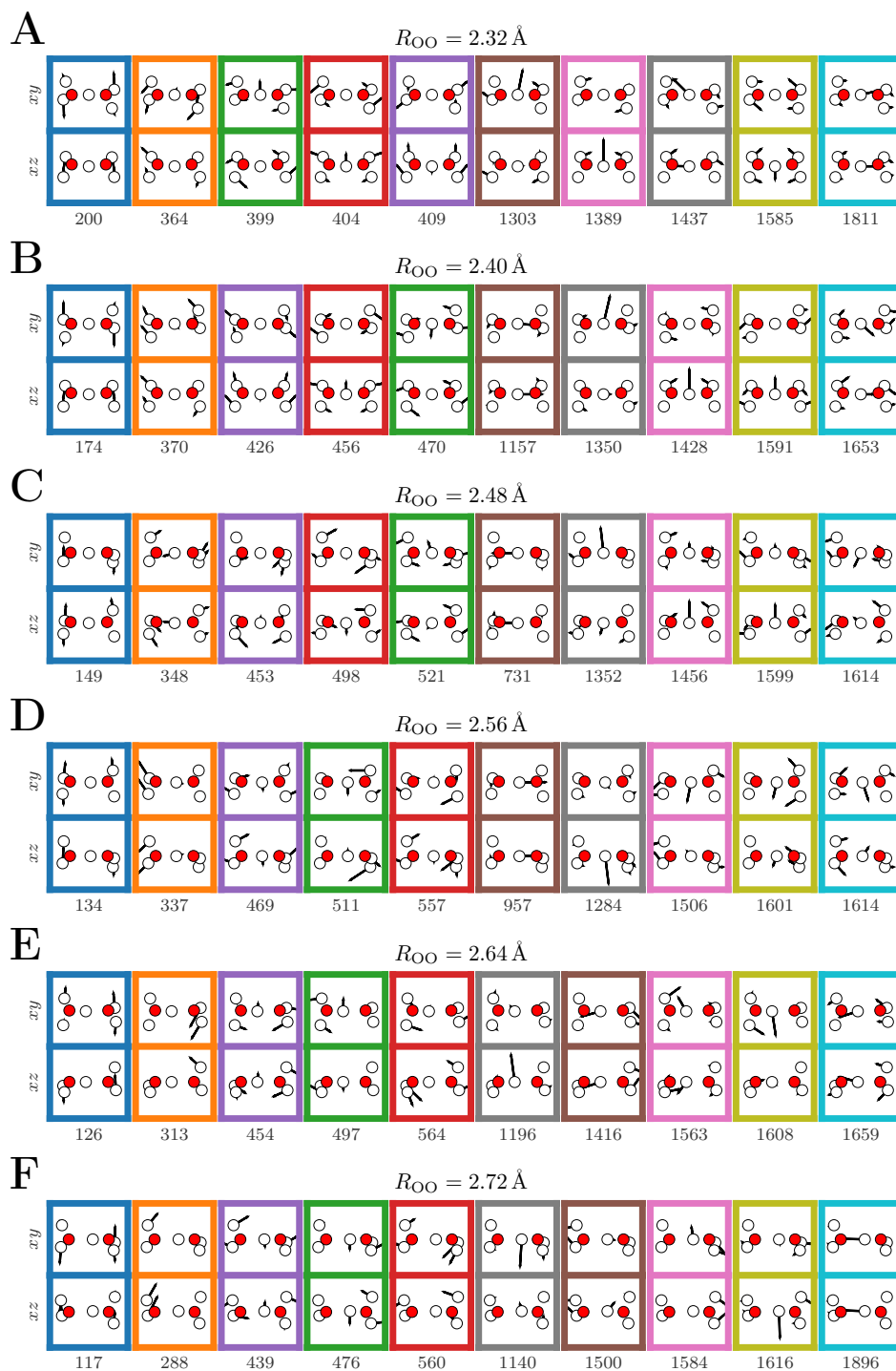


Figure S8. Illustrations of the normal modes of the  $\text{H}_5\text{O}_2^+$  cation for various constrained  $R_{OO}$ , projected on the  $xy$  and  $xz$  planes. The colored frames guide the eye through the shifting of a respective normal mode through A-F.



A. Supplementary Information:  
 Proton-Transfer Spectroscopy Beyond the Normal-Mode Scenario

---

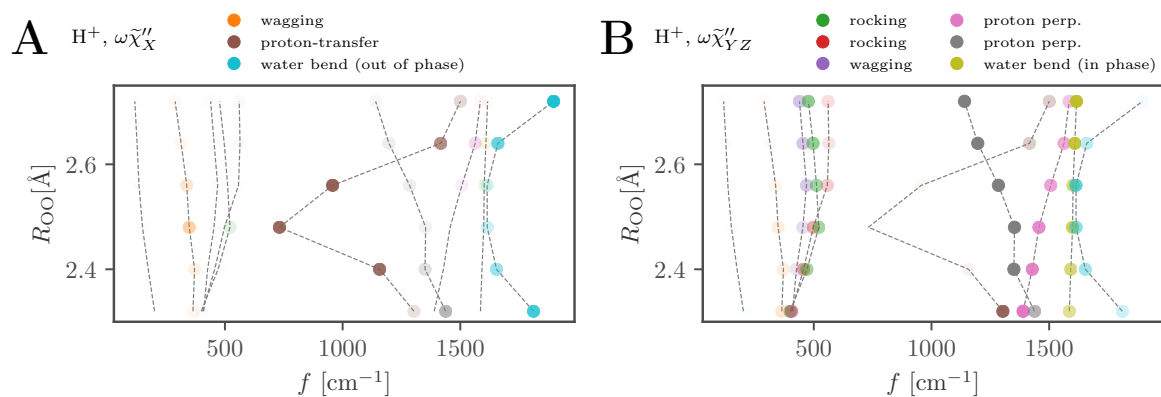


Figure S9. Normal mode frequencies of the excess-proton dynamics in the  $H_5O_2^+$  cation for various constrained  $R_{OO}$  as shown in fig. S7. The shading indicates the relative amplitudes of the respective normal modes, normalized to the maximal amplitude for each value of  $R_{OO}$ . The colors and grey dashed lines guide the eye through the shifting of a respective normal mode, as also shown in fig. S8.

#### IV. DECOMPOSITION OF THE $\text{H}_5\text{O}_2^+$ IR SPECTRA INTO EXCESS-PROTON AND WATER CONTRIBUTIONS

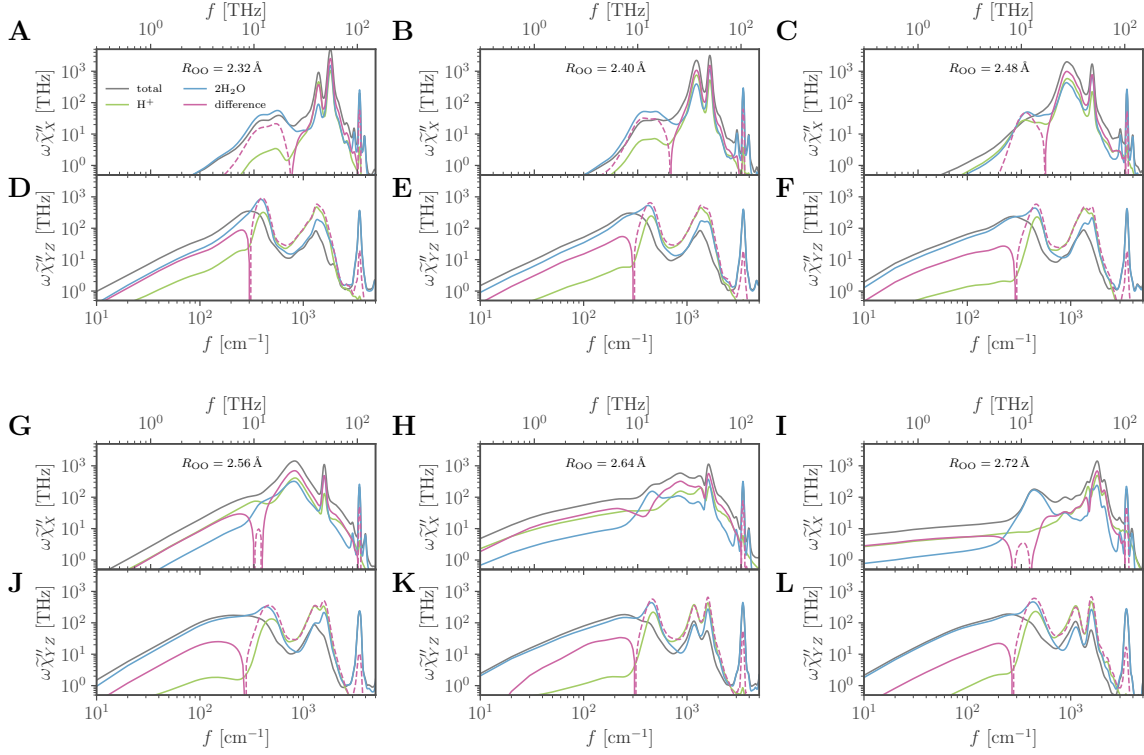


Figure S10. Decomposition of the IR spectra of the  $\text{H}_5\text{O}_2^+$  cation with two constrained oxygens at a given distance  $R_{\text{OO}}$  in different directions (**A–C**, **G–I**: along the  $x$ -axis connecting the two oxygens, **D–F**, **J–L**: along the  $yz$ -plane) into water and excess-proton contributions. The total IR spectra are shown in grey, the spectra of the excess proton in green and the spectra of the two water molecules in blue. The cross-correlation spectrum defined as  $\tilde{\chi}_{\text{H}^+, \text{H}_2\text{O}}'' = \tilde{\chi}_{\text{tot}}'' - \tilde{\chi}_{\text{H}^+}'' - \tilde{\chi}_{\text{H}_2\text{O}}''$  is shown in red. The dashed red line denotes negative values of the cross-correlation spectrum.

By using Wannier centers for charge localization, the total dipole moment of the simulation systems can be exactly decomposed into proton and water contributions  $\mathbf{p}_{\text{tot}}(t) = \mathbf{p}_{\text{H}^+}(t) + \mathbf{p}_{\text{H}_2\text{O}}(t)$ . A comparison of the IR spectra of the total dipole moment  $\omega\tilde{\chi}_{\text{tot}}''$  of the  $\text{H}_5\text{O}_2^+$  cation for various constrained oxygen positions to the power spectra of only the excess proton  $\omega\tilde{\chi}_{\text{H}^+}''$  and the power spectra of the dipole moments of the two flanking water molecules  $\omega\tilde{\chi}_{\text{H}_2\text{O}}''$  is shown in fig. S10A–L in different directions. As discussed in SI section VII, the cross-correlation spectra  $\omega\tilde{\chi}_{\text{H}^+, \text{H}_2\text{O}}''$ , shown in red in fig. S10A–L, are proportional to the cross-correlations of water-dipole-moment and excess-proton dynamics. Along  $x$ , the cross-correlation spectra of the six systems shown here, are nearly entirely positive as well as nearly proportional to the power spectrum of the proton itself, indicating constructive coupling of the proton motion to the water dipole moments along this axis, as previously shown<sup>6</sup>. An apparent exception to this is the rocking and wagging regime at  $300\text{ cm}^{-1}$  to  $600\text{ cm}^{-1}$  and the split OH-stretching mode at around  $3500\text{ cm}^{-1}$ , which show a strong negative cross-correlation spectrum in both  $x$  direction and  $yz$ -plane. Adjacent to this band all systems show two weak OH-stretching vibrations along  $x$ , likely a Stark effect of the mean excess-proton field on the water dipole moments. In the  $yz$ -plane the cross-correlation spectra are nearly entirely negative, indicating mainly out-of-phase motion of the excess-proton and the water dipole moments, producing generally weaker spectra in  $yz$  compared to  $x$ . It can be concluded that the IR spectrum of the  $\text{H}_5\text{O}_2^+$  cation along the axis connecting the two water oxygens reflects the excess-proton dynamics. This justifies the IR signal to be used as a reporter of the excess-proton dynamics, as well as the focus on its dynamics.

V. COMPARISON OF CONSTRAINED AND UNCONSTRAINED DICHROIC IR SPECTRA OF THE  $\text{H}_5\text{O}_2^+$  CATION

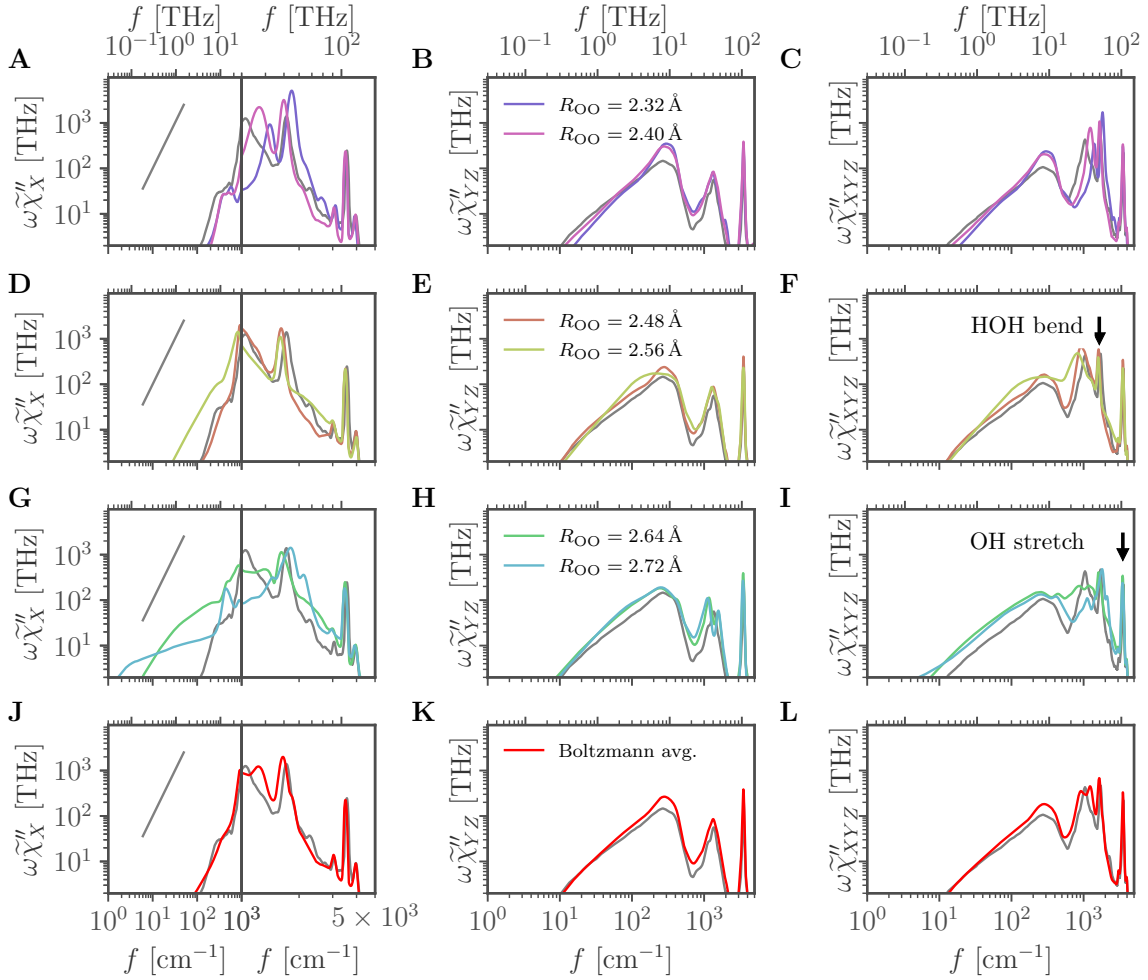


Figure S11. IR spectra of the  $\text{H}_5\text{O}_2^+$  cation in different directions (**A**, **D**, **G**, **J**: along the  $x$ -axis connecting the two oxygens, **B**, **E**, **H**, **K**: along the  $yz$ -plane **C**, **F**, **I**, **L**: isotropic spectrum). **A–I** The colors correspond to systems with different fixed oxygen-oxygen separation  $R_{\text{OO}}$ , grey lines denote the unconstrained system. **J–L** Comparison of the IR spectra of the unconstrained system (grey lines) to a Boltzmann average (red lines) according to eq. (S8) of the spectra in A-I. The HOH-bending mode and OH-stretching mode of the water molecules are indicated in F and I. The short straight grey lines in A, D, G and J indicate the  $\omega^2$ -scaling associated with the low-frequency shoulder of the power spectra.

IR spectra of the unconstrained  $\text{H}_5\text{O}_2^+$  cation and various systems with constrained  $R_{\text{OO}}$  are shown in fig. S11 in different directions. The  $x$ -axis corresponds to the direction connecting the two oxygens, while the  $yz$ -plane is orthogonal to that axis, as illustrated in fig. 1A in the main text. Interestingly, the spectra in  $x$ -direction strongly depend on the value of the constrained oxygen separation  $R_{\text{OO}}$  for frequencies lower than  $2500\text{ cm}^{-1}$  (figs. S11A, S11D, S11G and S11J). The HOH-bending mode is shifted to almost  $2000\text{ cm}^{-1}$  for  $R_{\text{OO}} = 2.32\text{ \AA}$  (fig. S11A) and to slightly lower frequencies than the unconstrained system for  $R_{\text{OO}} \geq 2.40\text{ \AA}$  (figs. S11D and S11G), whereas the frequency of the OH-stretching mode is not affected by fixing  $R_{\text{OO}}$ . The various spectra for the  $yz$ -plane in figs. S11B, S11E, S11H and S11K are indistinguishable on the other hand.

Here, the dominant features are the librations of the water molecules at  $300\text{ cm}^{-1}$  and the OH-stretching mode at around  $3500\text{ cm}^{-1}$ . While the OH-stretching mode appears in both directions, the HOH-bending mode is mainly visible along the  $x$ -axis. Note that in the  $yz$ -plane the HOH-bending mode contributions of the outer hydrogens of each water molecule cancel out due to symmetric motion with respect to the  $x$ -axis.

The isotropic spectra in figs. S11C, S11F, S11I and S11L depend on  $R_{\text{OO}}$  only in the regime  $400\text{ cm}^{-1}$  to  $1700\text{ cm}^{-1}$  since for lower frequencies, between  $10\text{ cm}^{-1}$  to  $400\text{ cm}^{-1}$ , the  $yz$ -contributions to the isotropic spectrum are dominant. In particular, this motivates the analysis of dynamics along  $x$ -direction, which shows the dominant contribution to the isotropic spectrum except for very low frequencies.

Interestingly, the spectra of the unconstrained systems are well recovered by a Boltzmann average of the spectra of the systems with fixed  $R_{\text{OO}}$  according to

$$\omega \tilde{\chi}''(\omega)_{\langle R_{\text{OO}} \rangle} = \frac{\sum_i \omega \tilde{\chi}''(\omega)_{R_{\text{OO}_i}} e^{-U(R_{\text{OO}_i})/k_B T}}{\sum_i e^{-U(R_{\text{OO}_i})/k_B T}}, \quad (\text{S8})$$

using the free energy along  $R_{\text{OO}}$  of the unconstrained system,  $U(R_{\text{OO}})$ , shown in fig. 1D in the main text. As shown in figs. S11J, fig. S11K and fig. S11L, the agreement is very good along all directions, which indicates a sufficient dynamic decoupling of the slow oxygen coordinate  $R_{\text{OO}}$  from the proton coordinate  $d$  with respect to IR spectra and allows observations for the constrained systems to be generalized to the unconstrained system.

## VI. RECROSSING TRANSFER PATHS OF THE EXCESS PROTON IN THE $\text{H}_5\text{O}_2^+$ CATION

After crossing the barrier once, the excess proton often immediately recrosses the barrier. In order to quantify this effect, the transfer paths are grouped into transfer events. A transfer event is defined by subsequently occurring transfer paths without recrossing of the same minimum and is sorted by the number of these crossings. An example for this definition is given in fig. S12A. The normalized distribution of the transfer events by the number of recrossings, in the following called the recrossing-number distribution  $p_{\text{RN}}(n)$ , is given in fig. S12B. For low barriers up to 40 subsequent recrossings are observed. For higher barriers the distribution is shifted to lower numbers of recrossings. Nevertheless, for all barrier heights a significant fraction of transfer events consist of multiple recrossings,  $\sum_{i=1}^{\infty} p_{\text{RN}}(n) = 0.47$  for  $R_{\text{OO}} = 2.56\text{ \AA}$ ,  $0.32$  for  $R_{\text{OO}} = 2.64\text{ \AA}$  and  $0.14$  for  $R_{\text{OO}} = 2.72\text{ \AA}$ . The mean number of recrossings is  $\sum_{i=0}^{\infty} n p_{\text{RN}}(n) = 1.84$  for  $R_{\text{OO}} = 2.56\text{ \AA}$ ,  $0.70$  for  $R_{\text{OO}} = 2.64\text{ \AA}$  and  $0.41$  for  $R_{\text{OO}} = 2.72\text{ \AA}$ .

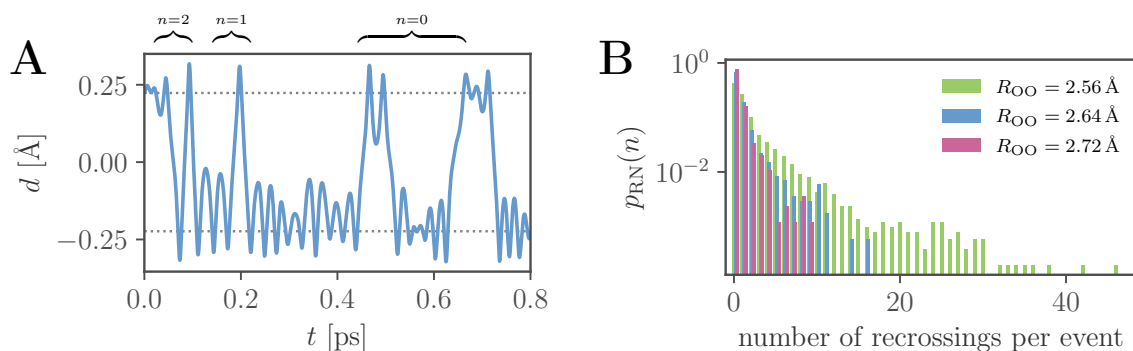


Figure S12. **A** Example trajectory of the excess-proton coordinate  $d(t)$  in the  $\text{H}_5\text{O}_2^+$  cation with constrained  $R_{\text{OO}}=2.64\text{ \AA}$ , showing nine transfer paths between the minima of the free energy denoted as grey dotted lines. The first three transfer paths belong to a single transfer event (with two recrossings). The subsequent two transfer paths also belong to a single transfer event (with one recrossing). The remaining four transfer paths according to our definition show no recrossing. It follows  $p_{\text{RN}}(0) = 4/6$ ,  $p_{\text{RN}}(1) = 1/6$  and  $p_{\text{RN}}(2) = 1/6$ . **B** Recrossing-number probability distributions  $p_{\text{RN}}(n)$  normalized such that  $\sum_{n=0}^{\infty} p_{\text{RN}}(n) = 1$ , for different  $R_{\text{OO}}$ .

## VII. IR POWER SPECTRA FROM LINEAR-RESPONSE THEORY

Assuming linear response of an observable  $x(t)$  with respect to a force that couples to an observable  $y(t)$ , the response function  $\chi_{xy}(t)$  is related to the correlation function  $C_{xy}(t') = \langle x(t+t')y(t) \rangle$  for  $t \geq 0$ <sup>20</sup>

$$\chi_{xy}(t) = -\frac{1}{k_B T} \frac{d}{dt} C_{xy}(t), \quad (\text{S9})$$

where  $k_B T$  is the thermal energy. Realizing that  $\chi(t)$  is single-sided, i.e.  $\chi(t) = 0$  for  $t < 0$ , the Fourier transform is calculated as

$$\begin{aligned} \tilde{\chi}_{xy}(\omega) &= -\frac{1}{k_B T} \int_0^\infty dt e^{i\omega t} \frac{d}{dt} C_{xy}(t) \\ &= -\frac{1}{k_B T} \left( C_{xy}(0) - i\omega \int_0^\infty dt e^{i\omega t} C_{xy}(t) \right) \\ &= -\frac{1}{k_B T} \left( C_{xy}(0) - i\omega \tilde{C}_{xy}^+(\omega) \right), \end{aligned} \quad (\text{S10})$$

where the superscript  $+$  denotes a single-sided Fourier transform. In case of  $x = y$ ,  $C_{xx}(t)$  is an autocorrelation function, which is real and symmetric, therefore it follows for the imaginary part of the response function in Fourier space

$$\tilde{\chi}_{xx}''(\omega) = \frac{1}{k_B T} \omega \operatorname{Re}(\tilde{C}_{xx}^+(\omega)) \quad (\text{S11})$$

$$= \frac{1}{k_B T} \frac{\omega}{2} \tilde{C}_{xx}(\omega). \quad (\text{S12})$$

When computing the power spectra of a stochastic process  $x(t)$ , limited to the time domain  $[0, L_t]$ , the Wiener-Kintchine theorem, eq. (S65) in section XVI, can be used to express  $\tilde{C}_{xx}(\omega)$  in terms of  $\tilde{x}(\omega)$ , turning eq. (S12) into

$$\tilde{\chi}_{xx}''(\omega) = \frac{\omega}{2k_B T L_t} |\tilde{x}(\omega)|^2. \quad (\text{S13})$$

In case of  $x(t)$  being the polarization  $\mathbf{p}(t)$  of the system, which is coupling to an external electric field  $\mathbf{E}(t)$ , the dimensionless dielectric susceptibility  $\chi(t)$  is given by

$$\tilde{\chi}(\omega) = \frac{1}{V \epsilon_0 l} \langle \tilde{\chi}_{\mathbf{p}\mathbf{p}}(\omega) \rangle, \quad (\text{S14})$$

where  $\epsilon_0$  is the vacuum permittivity,  $V$  is the system volume and an average is performed over the  $l$  dimensions of  $\mathbf{p}$ .

### VIII. SPECTRAL CROSS CONTRIBUTIONS OF EXCESS-PROTON DYNAMICS IN THE $\text{H}_5\text{O}_2^+$ CATION

A decomposition of a trajectory  $x(t)$  into two parts  $x(t) = x_1(t) + x_2(t)$  gives rise to three contributions in the total power spectrum

$$\begin{aligned}\omega\tilde{\chi}_{xx}''(\omega) &= \frac{\omega^2}{2k_B T} [\tilde{C}_1(\omega) + \tilde{C}_2(\omega) + 2\tilde{C}_{1,2}(\omega)] \\ &= \omega [\tilde{\chi}_1''(\omega) + \tilde{\chi}_2''(\omega) + \tilde{\chi}_{1,2}''(\omega)],\end{aligned}\quad (\text{S15})$$

where the cross-correlation contribution  $\tilde{\chi}_{1,2}''(\omega)$  is defined such that it equals the difference spectrum

$$\begin{aligned}\tilde{\chi}_{\text{diff}}''(\omega) &= \tilde{\chi}_{xx}'' - \tilde{\chi}_1''(\omega) - \tilde{\chi}_2''(\omega) = \tilde{\chi}_{1,2}''(\omega) \\ &= \frac{\omega}{k_B T} \tilde{C}_{1,2}(\omega).\end{aligned}\quad (\text{S16})$$

A positive cross-correlation spectrum hints to in-phase motion, a negative cross-correlation spectrum to out-of-phase motion of  $x_1(t + t')$  and  $x_2(t)$  at a given frequency. Therefore the decomposition of the excess-proton dynamics in the time domain according to  $d(t) = d_{\text{TW}}(t) + d_{\text{TP}}(t) + d_{\text{NM}}(t)$  into a transfer-waiting  $d_{\text{TW}}(t)$ , a transfer-path  $d_{\text{TP}}(t)$  and a normal-mode contribution  $d_{\text{NM}}(t)$ , as introduced in fig. 2 in the main text, produces spectral cross contributions. The spectral contributions  $\omega\tilde{\chi}_{\text{TW}}''$ ,  $\omega\tilde{\chi}_{\text{TP}}''$  and  $\omega\tilde{\chi}_{\text{NM}}''$  as well as the spectral cross contributions  $\omega\tilde{\chi}_{\text{TW,NM}}''$ ,  $\omega\tilde{\chi}_{\text{TP,TW}}''$  and  $\omega\tilde{\chi}_{\text{NM,TP}}''$  resulting from this decomposition are shown in fig. S13.

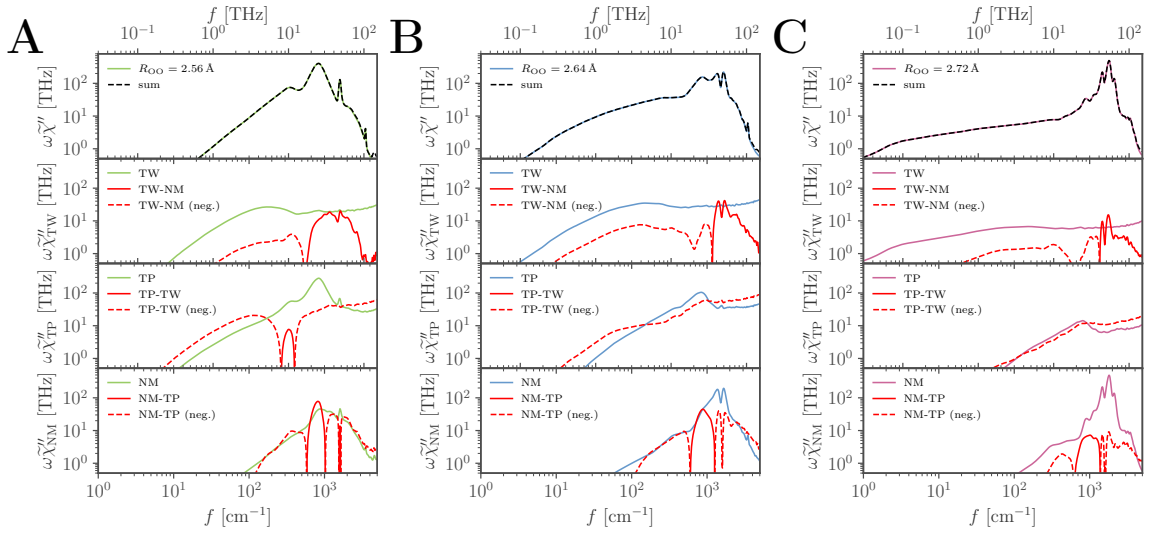


Figure S13. Spectral decomposition of the excess-proton dynamics in the  $\text{H}_5\text{O}_2^+$  cation for different constrained  $R_{\text{OO}}$  (**A**:  $R_{\text{OO}} = 2.56 \text{ \AA}$ , **B**:  $R_{\text{OO}} = 2.64 \text{ \AA}$ , **C**:  $R_{\text{OO}} = 2.72 \text{ \AA}$ ), similar to the results in fig. 2B in the main text (colored lines). The different cross-contributions are shown in red and negative cross-contributions as red broken lines.

## IX. DYNAMICS OF A TWO-STATE PROCESS

Consider an arbitrary two-state process  $d(t)$  characterized by a jump distance  $D$ , a jump-time probability distribution, which is the transfer-waiting-time probability distribution  $p_{\text{TW}}(t)$  with  $\int_0^\infty p_{\text{TW}}(t)dt = 1$ , and a survival probability  $q_{\text{TW}}(t) = \int_t^\infty p_{\text{TW}}(t')dt'$ . The conditional expectation values  $\langle d(t) \rangle|_{d(0)}$  for the process starting at time  $t = 0$  at either  $d(0) = 0$  or  $d(0) = D$  are thus given as

$$\langle d(t) \rangle|_{d(0)=0} = \cancel{0 p_{00}(t)} + D p_{0D}(t), \quad (\text{S17})$$

$$\langle d(t) \rangle|_{d(0)=D} = \cancel{0 p_{D0}(t)} + D p_{DD}(t), \quad (\text{S18})$$

where  $p_{xy}(t)$  denotes the probability to be at  $d(t) = y$  when starting at  $d(0) = x$ . In the long-time limit each state has equal probability. The autocorrelation function,  $C(t) = \langle d(t)d(0) \rangle$ , is therefore given as

$$\langle d(t)d(0) \rangle = \frac{1}{2} (\cancel{0 \langle d(t) \rangle|_{d(0)=0}} + D \langle d(t) \rangle|_{d(0)=D}) \quad (\text{S19})$$

$$= \frac{D^2}{2} p_{DD}(t). \quad (\text{S20})$$

In order to express the probability  $p_{DD}(t)$  in terms of the first-passage-time distribution  $p_{\text{TW}}(t)$  and survival probability  $q_{\text{TW}}(t)$ , all possible jumps within time  $t$  have to be considered, as illustrated in fig. S14

$$p_{DD}(t) = \int_0^\infty dt_D q_{\text{TW}}(t_D) \sum_{N=0}^\infty \prod_{j=1}^N \int_0^\infty dt_j^D p_{\text{TW}}(t_j^D) \int_0^\infty dt_j^0 p_{\text{TW}}(t_j^0) \delta \left[ t - t_D - \sum_{j=1}^N (t_j^D + t_j^0) \right]. \quad (\text{S21})$$

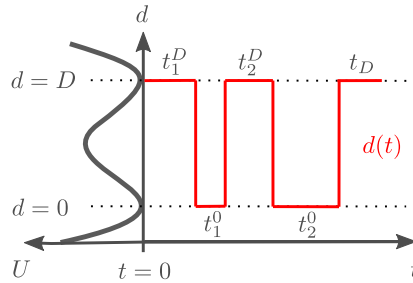


Figure S14. Schematic of a binary jump process  $d(t)$  with jumps separated by residence times  $t_j^0$  and  $t_j^D$  following the notation considered in eq. (S21). A doublewell potential,  $U(d)$ , is shown to highlight the relation of the binary jump process to the barrier-crossing dynamics.

Since  $p_{\text{TW}}(t)$  and  $q_{\text{TW}}(t)$  are single-sided, a single-sided Fourier transform is performed,

$$\begin{aligned} \tilde{p}_{\text{DD}}^+(\omega) &= \int_0^\infty dt e^{i\omega t} \int_0^\infty dt_D q_{\text{TW}}(t_D) \sum_{N=0}^\infty \prod_{j=1}^N \int_0^\infty dt_j^D p_{\text{TW}}(t_j^D) \\ &\quad \int_0^\infty dt_j^0 p_{\text{TW}}(t_j^0) \delta \left[ t - t_D - \sum_{j=1}^N (t_j^D + t_j^0) \right] \end{aligned} \quad (\text{S22})$$

$$= \int_0^\infty dt_D q_{\text{TW}}(t_D) \sum_{N=0}^\infty \prod_{j=1}^N \int_0^\infty dt_j^D p_{\text{TW}}(t_j^D) \quad (\text{S23})$$

$$\begin{aligned} &\int_0^\infty dt_j^0 p_{\text{TW}}(t_j^0) e^{i\omega [t_D + \sum_{j=1}^N (t_j^D + t_j^0)]} \\ &= \tilde{q}_{\text{TW}}(\omega) \sum_{N=0}^\infty \tilde{p}_{\text{TW}}(\omega)^{2N} \end{aligned} \quad (\text{S24})$$

$$= \frac{\tilde{q}_{\text{TW}}(\omega)}{1 - \tilde{p}_{\text{TW}}(\omega)^2}, \quad (\text{S25})$$

and it follows for the single-sided Fourier-transformed autocorrelation, eq. (S20),

$$\tilde{C}^+(\omega) = \frac{D^2}{2} \frac{\tilde{q}_{\text{TW}}(\omega)}{1 - \tilde{p}_{\text{TW}}(\omega)^2}. \quad (\text{S26})$$

From eqs. (S10) and (S26) we obtain our expression for the response function of the binary jump process

$$\tilde{\chi}_{DD}(\omega) = -\frac{D^2}{2k_B T} \left( 1 - \frac{i\omega \tilde{q}_{\text{TW}}(\omega)}{1 - \tilde{p}_{\text{TW}}(\omega)^2} \right). \quad (\text{S27})$$

In case of the jumping variable  $d(t)$  being a polarization with polarization jump  $2qd_{\text{TW}}^*$ , where  $q$  is the charge and  $d_{\text{TW}}^*$  a length scale, the dielectric susceptibility of the binary polarization jump process reads

$$\tilde{\chi}(\omega) = -\frac{2q^2 d_{\text{TW}}^{*2}}{V\epsilon_0 k_B T} \left( 1 - \frac{i\omega \tilde{q}_{\text{TW}}(\omega)}{1 - \tilde{p}_{\text{TW}}(\omega)^2} \right), \quad (\text{S28})$$

and eventually its power spectrum, proportional to the imaginary part of the dielectric susceptibility, is obtained as

$$\omega \tilde{\chi}''(\omega) = \frac{2q^2 d_{\text{TW}}^{*2}}{V\epsilon_0 k_B T} \text{Re} \left( \frac{\omega^2 \tilde{q}_{\text{TW}}(\omega)}{1 - \tilde{p}_{\text{TW}}(\omega)^2} \right). \quad (\text{S29})$$



## X. POWER SPECTRUM OF THE DAMPED HARMONIC OSCILLATOR

The absorbed power  $\omega \tilde{\chi}_{xx}''(\omega)$  of the damped harmonic oscillator described by the differential equation

$$m\ddot{x}(t) = -\gamma\dot{x}(t) - kx(t) + F_{\text{ext}}(t), \quad (\text{S30})$$

is computed from the linear response in Fourier space

$$\tilde{\chi}_{xx}(\omega) = \frac{\tilde{x}(\omega)}{\tilde{F}_{\text{ext}}(\omega)} \quad (\text{S31})$$

$$= (k - m\omega^2 - i\gamma\omega)^{-1} \quad (\text{S32})$$

$$= \frac{k - m\omega^2 + i\gamma\omega}{(k - m\omega^2)^2 + \gamma^2\omega^2}, \quad (\text{S33})$$

where  $\tilde{x}(\omega)$  is the oscillating variable,  $m$  the mass,  $\gamma$  the friction coefficient,  $k$  the spring constant of the harmonic potential and  $\tilde{F}_{\text{ext}}(\omega)$  an external force. For the power spectrum follows

$$\omega \tilde{\chi}_{xx}''(\omega) = \frac{\gamma\omega^2}{(k - m\omega^2)^2 + \gamma^2\omega^2}, \quad (\text{S34})$$

which by introducing the time scales  $\tau = 2\gamma/k$ ,  $\tau_m = \sqrt{m/k}$  and length scale  $D$  with  $D^2 = k_B T/k$  converts to

$$\omega \tilde{\chi}_{xx}''(\omega) = \frac{2D^2}{k_B T} \frac{\tau\omega^2}{4(1 - \tau_m^2\omega^2)^2 + \tau^2\omega^2}. \quad (\text{S35})$$

In case of the oscillating variable  $x(t)$  being a polarization with polarization jump  $qD$ , where  $q$  is the charge, the dielectric susceptibility reads

$$\omega \tilde{\chi}''(\omega) = \frac{2q^2 D^2}{V\epsilon_0 k_B T} \frac{\tau\omega^2}{4(1 - \tau_m^2\omega^2)^2 + \tau^2\omega^2}. \quad (\text{S36})$$

In spectroscopy this is known as a Lorentz band shape, which in the overdamped case,  $\tau_m \rightarrow 0$ , reads

$$\omega \tilde{\chi}''(\omega) = \frac{2q^2 D^2}{V\epsilon_0 k_B T} \frac{\tau\omega^2}{4 + \tau^2\omega^2}, \quad (\text{S37})$$

known as the Debye band shape<sup>21</sup>.

## XI. TRANSFER-PATH SHAPE

Kim and Netz<sup>22</sup> derived the transfer-path-time shape  $t(d_{\text{TP}})$  over a harmonic barrier by an exact calculation, valid for arbitrary barrier height, as

$$t(d_{\text{TP}}) = \tau - \frac{2\gamma d_{\text{TW}}^*{}^2}{k_B T U} \int_{\sqrt{U}}^{\sqrt{U}(d_{\text{TP}}/d_{\text{TW}}^*-1)} dy \left( \frac{\text{erf}(y) - \text{erf}(\sqrt{U})}{\text{erf}(\sqrt{U}(d_{\text{TP}}/d_{\text{TW}}^*-1)) - \text{erf}(\sqrt{U})} - \frac{1}{2} \right) D_+(y), \quad (\text{S38})$$

where  $D_+(x) = e^{-x^2} \int_0^x dt e^{t^2}$  is the Dawson integral function,  $\gamma$  is the friction constant,  $U = U_0/k_B T$  is the dimensionless barrier height,  $d_{\text{TW}}^*$  a length scale and  $\tau$  the time of the complete transition path across  $2d_{\text{TW}}^*$ . Note that the shape function is expressed at time  $t$  as a function of position  $d$ . The second term in eq. (S38) vanishes for  $d_{\text{TP}} = 2d_{\text{TW}}^*$  and reduces to  $-\tau$  for  $d_{\text{TP}} = 0$  (derived in<sup>22</sup>) and therefore  $t(d_{\text{TP}} = 0) = 0$  and  $t(d_{\text{TP}} = 2d_{\text{TW}}^*) = \tau$ . For a variable  $s = y/\sqrt{U}$ , eq. (S38) is rewritten as

$$t(d_{\text{TP}}) = \tau - \frac{2\gamma d_{\text{TW}}^*{}^2}{k_B T \sqrt{U}} \int_1^{d_{\text{TP}}/d_{\text{TW}}^*-1} ds \left( \frac{\text{erf}(\sqrt{U}s) - \text{erf}(\sqrt{U})}{\text{erf}(\sqrt{U}(d_{\text{TP}}/d_{\text{TW}}^*-1)) - \text{erf}(\sqrt{U})} - \frac{1}{2} \right) D_+(\sqrt{U}s). \quad (\text{S39})$$

For large  $U \gg 1$  and  $d_{\text{TW}}^* < d_{\text{TP}} < 2d_{\text{TW}}^*$ , eq. (S39) reduces to the asymptotic expression

$$\begin{aligned} t(d_{\text{TP}}) &\approx \tau + \frac{\gamma d_{\text{TW}}^*{}^2}{k_B T} \int_1^{d_{\text{TP}}/d_{\text{TW}}^*-1} ds \frac{D_+(\sqrt{U}s)}{\sqrt{U}} \\ &= \tau + \frac{\gamma d_{\text{TW}}^*{}^2}{2k_B T U} \ln(d_{\text{TP}}/d_{\text{TW}}^* - 1), \end{aligned} \quad (\text{S40})$$

where we use  $D_+(\sqrt{U}t)/\sqrt{U} \approx 1/(2Us)$ .

Therefore, further using the symmetric nature of  $t(d_{\text{TP}})$  in the limit  $U \rightarrow \infty$ , we obtain the asymptotic expression for  $t(d_{\text{TP}})$  as

$$t(d_{\text{TP}}) = \begin{cases} -\frac{\gamma d_{\text{TW}}^*{}^2}{2k_B T U} \ln(1 - d_{\text{TP}}/d_{\text{TW}}^*), & \text{for } 0 < d_{\text{TP}} < d_{\text{TW}}^* \\ \tau + \frac{\gamma d_{\text{TW}}^*{}^2}{2k_B T U} \ln(d_{\text{TP}}/d_{\text{TW}}^* - 1), & \text{for } d_{\text{TW}}^* < d_{\text{TP}} < 2d_{\text{TW}}^*. \end{cases} \quad (\text{S41})$$

It is straightforward to invert eq. (S41), yielding

$$d_{\text{TP}}(t) = \begin{cases} -d_{\text{TW}}^* \left( e^{-\frac{2k_B T U t}{\gamma d_{\text{TW}}^*{}^2}} - 1 \right), & \text{for } 0 < t < \tau/2 \\ d_{\text{TW}}^* \left( e^{\frac{2k_B T U (t-\tau)}{\gamma d_{\text{TW}}^*{}^2}} + 1 \right), & \text{for } \tau/2 < t < \tau. \end{cases} \quad (\text{S42})$$

Using the curvature parameter  $\kappa = \gamma d_{\text{TW}}^*{}^2 / (2k_B T U)$ , and shifting the variables  $t \rightarrow t + \tau/2$  and  $d_{\text{TP}} \rightarrow d_{\text{TP}} + d_{\text{TW}}^*$  to fulfill  $d_{\text{TP}}(t = 0) = 0$ , we arrive at the leading order expression as the sum of the above two functions

$$\begin{aligned} d_{\text{TP}}(t) &= d_{\text{TW}}^* \left[ e^{-\frac{\tau-2t}{2\kappa}} - e^{-\frac{\tau+2t}{2\kappa}} \right] \\ &= d_{\text{TW}}^* \left[ e^{t/\kappa} - e^{-t/\kappa} \right] / e^{\frac{\tau}{2\kappa}}. \end{aligned} \quad (\text{S43})$$

This expression is easily compared to the transfer-path shape (in the presence of a harmonic potential) derived from the path-integral approach (equivalent to eq. 3 in the main text)<sup>23,24</sup>

$$d_{\text{TP}}(t) = d_{\text{TW}}^* \left[ e^{t/\kappa} - e^{-t/\kappa} \right] / \mathcal{N}, \quad (\text{S44})$$

with a slightly different normalization factor  $\mathcal{N} = e^{\frac{\tau}{2\kappa}} - e^{-\frac{\tau}{2\kappa}}$ . Note that the difference vanishes in the high-barrier limit  $U \rightarrow \infty$ , i.e.  $\kappa \rightarrow 0$ , in which limit eq. (S43) derived from reference<sup>22</sup> becomes equivalent to eq. (S44) derived from the path-integral approach.

## XII. SPECTRAL SIGNATURES OF TRANSFER PATHS

The IR spectral signature of transfer paths is derived by modeling the Fourier-transformed transfer-path contribution  $\tilde{d}_{\text{TP}}(\omega)$  based on the transfer-path time  $\tau_{\text{TP}}$  and the recrossing-number probability distribution  $p_{\text{RN}}(n)$ . Recall that the power spectrum  $\omega\tilde{\chi}''(\omega)$  of a stochastic process  $x(t)$  limited to the time domain  $[0, L_t]$  is computed from the Fourier-transformed expressions  $\tilde{x}(\omega)$  as presented in section VII. In the following an expression for  $\tilde{d}_{\text{TP}}(\omega)$  is derived, based on the model for  $d_{\text{TP}}(t)$  illustrated in fig. S15A. The mean transfer path is expected to repeat on average with period  $\tau_{\text{TW}}$ . The model is therefore constrained to  $[0, \tau_{\text{TW}}]$ ; using eq. (S13), the IR power spectrum of the transfer-path contribution can then be written as

$$\omega\tilde{\chi}''_{\text{TP}}(\omega) = \omega^2 \frac{q^2}{V\epsilon_0 k_B T \tau_{\text{TW}}} \tilde{d}_{\text{TP}}(\omega) \tilde{d}_{\text{TP}}^*(\omega), \quad (\text{S45})$$

where  $q$  is the displaced charge.  $d_{\text{TP}}(t)$  is modeled by a single mean transfer path with shape  $d_{\text{TP}}^0(t)$  that is followed by a subsequent number of recrossing transfer paths, according to the recrossing-number probability distribution  $p_{\text{RN}}(n)$

$$d_{\text{TP}}(t) = \sum_{n=0}^{\infty} p_{\text{RN}}(n) \sum_{m=0}^n (-1)^m d_{\text{TP}}^0(t - m\tau_{\text{TP}}), \quad (\text{S46})$$

where the factor  $(-1)^m$  accounts for the alternation of recrossing transfer paths that are going up and down. A Fourier transform with respect to  $t$  turns eq. (S46) into

$$\begin{aligned} \tilde{d}_{\text{TP}}(\omega) &= \sum_{n=0}^{\infty} p_{\text{RN}}(n) \sum_{m=0}^n (-1)^m \int_{-\infty}^{\infty} dt e^{i\omega t} d_{\text{TP}}^0(t - m\tau_{\text{TP}}) \\ &= \tilde{d}_{\text{TP}}^0(\omega) \sum_{n=0}^{\infty} p_{\text{RN}}(n) \sum_{m=0}^n (-1)^m e^{-i\omega m\tau_{\text{TP}}}. \end{aligned} \quad (\text{S47})$$

An expression for the mean transfer-path shape  $d_{\text{TP}}^0(t)$  is obtained by regarding ensembles of rescaled transfer paths, shown in fig. S16 for various  $R_{\text{OO}}$ , along with the mean transfer paths, obtained from space-averaging the ensembles of rescaled transfer paths at each rescaled time between the respective turning points of the trajectory. The mean value at the turning points defines the length scale  $d_{\text{TP}}^*$ . The single mean transfer path  $d_{\text{TP}}^0(t)$  reaching between the turning points is then modeled by a truncated straight line

$$d_{\text{TP}}^0(t) = d_{\text{TP}}^* \left( \frac{2t}{\tau_{\text{TP}}} - 1 \right) (\theta(t) - \theta(t - \tau_{\text{TP}})), \quad (\text{S48})$$

$$(\text{S49})$$

with the Fourier transform

$$\tilde{d}_{\text{TP}}^0(\omega) = d_{\text{TP}}^* \frac{e^{i\omega\tau_{\text{TP}}} (2 - i\omega\tau_{\text{TP}}) - 2 - i\omega\tau_{\text{TP}}}{\omega^2 \tau_{\text{TP}}}. \quad (\text{S50})$$

The time scale  $\tau_{\text{TP}}$  in eq. (S47) is estimated directly from the simulation data, using the distributions shown in fig. S15B–D. The distributions of transfer-path times considering only multiple transfers in fig. S15B–D are sharply peaked at roughly the same value  $\tau_{\text{TP}} = 0.023$  ps for all systems.

To account for subsequent recrossings, the expression eq. (S47) is evaluated for an exponential decay of the recrossing-number probability distribution,  $p_{\text{RN}}(n) = (1 - e^{-\alpha})e^{-\alpha n}$ , with decay parameter  $\alpha$  and shown in fig. S17 for the given systems. Using this fit function the final expression for the transfer-path spectral contribution evaluates to

$$\omega\tilde{\chi}''_{\text{TP}}(\omega) = \frac{2d_{\text{TP}}^*{}^2 q^2}{V\epsilon_0 k_B T \tau_{\text{TW}}} \frac{e^{\alpha} (\omega\tau_{\text{TP}} \cos(\frac{\omega\tau_{\text{TP}}}{2}) - 2 \sin(\frac{\omega\tau_{\text{TP}}}{2}))^2}{\omega^2 \tau_{\text{TP}}^2 (\cosh(\alpha) + \cos(\omega\tau_{\text{TP}}))}. \quad (\text{S51})$$

An approximate expression for eq. (S51) is derived by factorizing  $\omega\tilde{\chi}''_{\text{TP}}(\omega)$  into the recrossing contribution  $X_{\text{rec}}(\omega, \alpha, \tau_{\text{TP}})$  and the shape contribution  $|\tilde{d}_{\text{TP}}^0(\omega, \tau_{\text{TP}})|^2$

$$|\tilde{d}_{\text{TP}}^0(\omega, \tau_{\text{TP}})|^2 = d_{\text{TP}}^*{}^2 \frac{2^4 (\omega\tau_{\text{TP}} \cos(\frac{\omega\tau_{\text{TP}}}{2}) - 2 \sin(\frac{\omega\tau_{\text{TP}}}{2}))^2}{\omega^4 \tau_{\text{TP}}^4}, \quad (\text{S52})$$

$$X_{\text{rec}}(\omega, \alpha, \tau_{\text{TP}}) = \frac{e^{\alpha} \omega^2 \tau_{\text{TP}}^2}{2 (\cosh(\alpha) + \cos(\omega\tau_{\text{TP}}))}, \quad (\text{S53})$$

$$\omega\tilde{\chi}''_{\text{TP}}(\omega) = \frac{q^2}{V\epsilon_0 k_B T \tau_{\text{TW}}} X_{\text{rec}}(\omega, \alpha, \tau_{\text{TP}}) |\tilde{d}_{\text{TP}}^0(\omega, \tau_{\text{TP}})|^2. \quad (\text{S54})$$

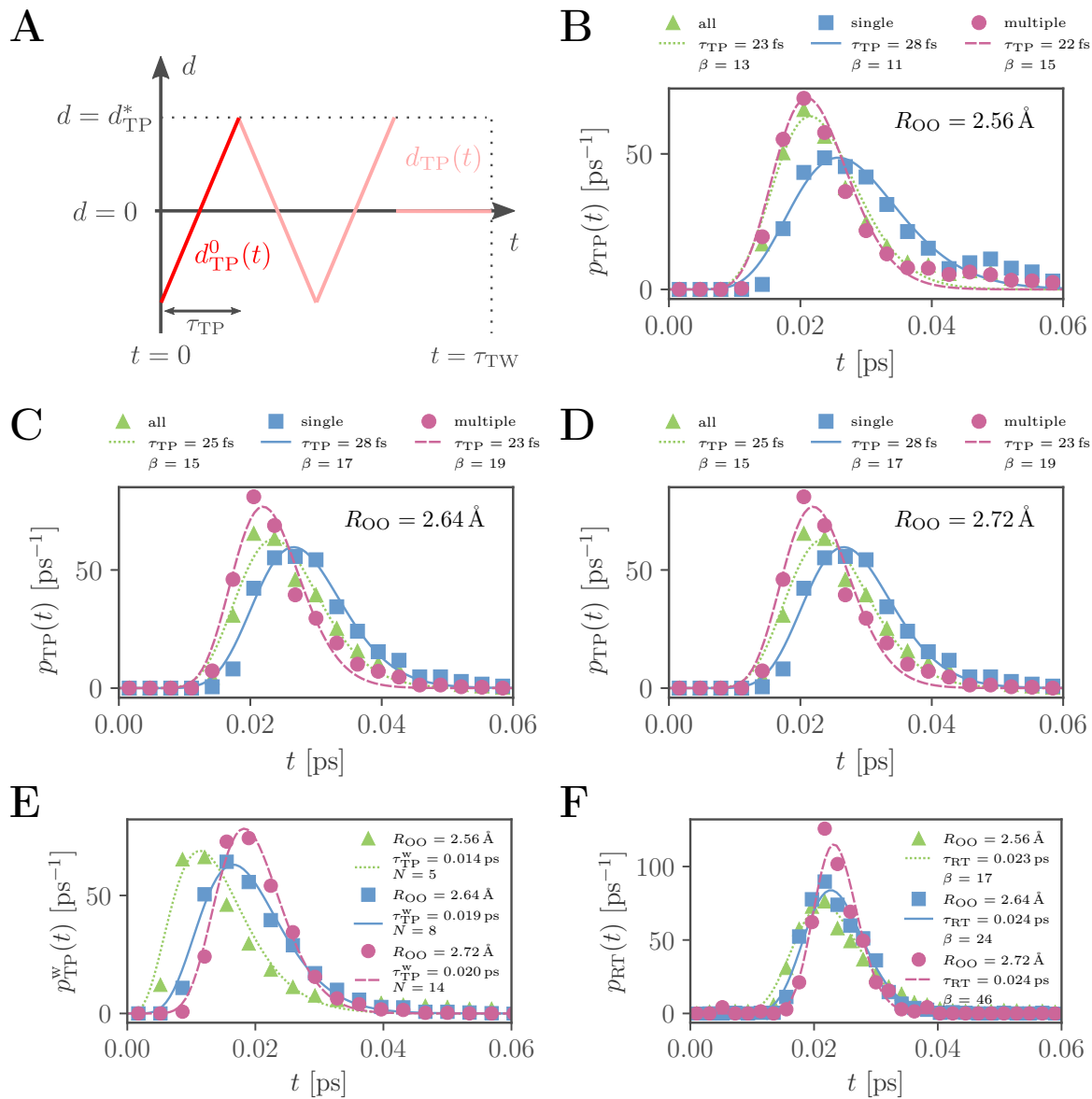


Figure S15. **A** Model for the transfer-path trajectory  $d_{\text{TP}}(t)$  with length  $\tau_{\text{TW}}$ . In this example the initial transfer path  $d_{\text{TP}}^0(t)$  with duration  $\tau_{\text{TP}}$  starts at  $t = 0$  and is followed by  $N = 2$  recrossing transfer paths, where  $N$  is drawn from the recrossing-number probability distribution  $p_{\text{RN}}(N)$ . The recrossing transfer paths are alternating and shifted relative to each other by the recrossing time  $\tau_{\text{RT}} \approx \tau_{\text{TP}}$ . **B–F** Transfer-path-time probability distributions measured between the turning points ( $p_{\text{TP}}(t)$ , B–D), between the minima of the free-energy landscape, ( $p_{\text{TP}}^w(t)$ , E) and recrossing-time distributions measured between recrossings of  $d = 0$  ( $p_{\text{RT}}(t)$ , F). The distributions (data points) are fitted to  $p_{\text{TP}}(t) = \frac{t^{\beta-1}}{(\beta-1)!} \left(\frac{\beta}{\tau}\right)^\beta e^{-\beta t/\tau}$  (solid, broken or dotted lines). Note that only the red curves in B–D are considered in the calculation of the TP spectral signature.

A. Supplementary Information:  
Proton-Transfer Spectroscopy Beyond the Normal-Mode Scenario

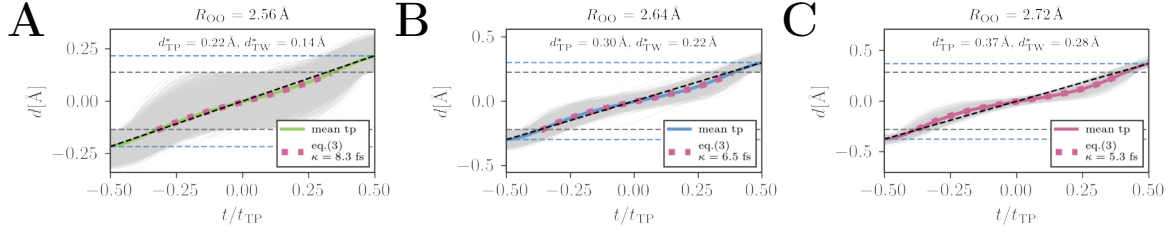


Figure S16. Ensembles of transfer paths sampled from the trajectories of the excess proton in the  $\text{H}_5\text{O}_2^+$  cation for different constrained oxygen distances  $R_{\text{OO}}$  (**A**:  $R_{\text{OO}} = 2.56 \text{ \AA}$ , **B**:  $R_{\text{OO}} = 2.64 \text{ \AA}$ , **C**:  $R_{\text{OO}} = 2.72 \text{ \AA}$ ), scaled to their individual transfer-path times  $t_{\text{TP}}$  between the respective turning points. The blue dashed lines indicate the mean initial and final values, which are used to estimate the parameter  $d_{\text{TP}}^*$ , the mean transfer-path distance along  $d$ . The horizontal grey dashed lines indicate the minima of the free energy, which are used to estimate the parameter  $d_{\text{TW}}^*$ . Mean transfer paths averaged over  $d$  (colored lines) are fitted between the minima of the free energy using eq. (3). The fits are shown as red dotted lines. Fit parameters are given in the legend.

The relevant maximum of  $X_{\text{rec}}(\omega, \alpha, \tau_{\text{TP}})$  resides at  $\omega = \pi/\tau_{\text{TP}}$ , which minimizes the denominator in eq.(S53). A Taylor expansion of the cos function in eq.(S53) to second order in  $\omega$  around  $\pi/\tau_{\text{TP}}$  leads to

$$X_{\text{rec}}(\omega, \alpha, \tau_{\text{TP}}) = \frac{e^{\alpha} \omega^2 \tau_{\text{TP}}^2}{2 \cosh(\alpha) - 2 + (\pi - \omega \tau_{\text{TP}})^2}. \quad (\text{S55})$$

Furthermore the shape contribution  $|\tilde{d}_{\text{TP}}^0(\omega, \tau_{\text{TP}})|^2$  can be estimated around  $\omega = \pi/\tau_{\text{TP}}$  by the following expression, which is in good agreement with the local series expansion

$$|\tilde{d}_{\text{TP}}^0(\omega, \tau_{\text{TP}})|^2 = d_{\text{TP}}^{*2} \frac{64 \omega^2 \tau_{\text{TP}}^2}{\pi^4 (\pi + \omega \tau_{\text{TP}})^2}, \quad (\text{S56})$$

$$\omega \tilde{\chi}_{\text{TP}}''(\omega) = \frac{d_{\text{TP}}^{*2} q^2}{V \epsilon_0 k_B T \tau_{\text{TW}}} \frac{64 e^{\alpha} \omega^4 \tau_{\text{TP}}^4}{\pi^4 (\pi + \omega \tau_{\text{TP}})^2 (2 \cosh(\alpha) - 2 + (\pi - \omega \tau_{\text{TP}})^2)}. \quad (\text{S57})$$

Note that eq. (S57) is a multiplication of a Debye-type function with the shoulder frequency  $\omega = \pi/\tau_{\text{TP}}$ , stemming from the shape contribution eq. (S56), and a Lorentz-type function with the resonance frequency  $\omega = \pi/\tau_{\text{TP}}$ , stemming from the recrossing contribution eq. (S55).

If the transfer-path shape  $d_{\text{TP}}^0(t)$  is alternatively modeled by a truncated cosine wave with period  $2\tau_{\text{TP}}$  according to

$$d_{\text{TP},\text{cos}}^0(t) = d_{\text{TP}}^* \cos\left(\frac{\pi t}{\tau_{\text{TP}}}\right) (\theta(t) - \theta(t - \tau_{\text{TP}})), \quad (\text{S58})$$

with the Fourier transform

$$\tilde{d}_{\text{TP},\text{cos}}^0(\omega) = d_{\text{TP}}^* \frac{i\omega \tau_{\text{TP}}^2 (1 + e^{i\omega \tau_{\text{TP}}})}{\pi^2 - \omega^2 \tau_{\text{TP}}^2}, \quad (\text{S59})$$

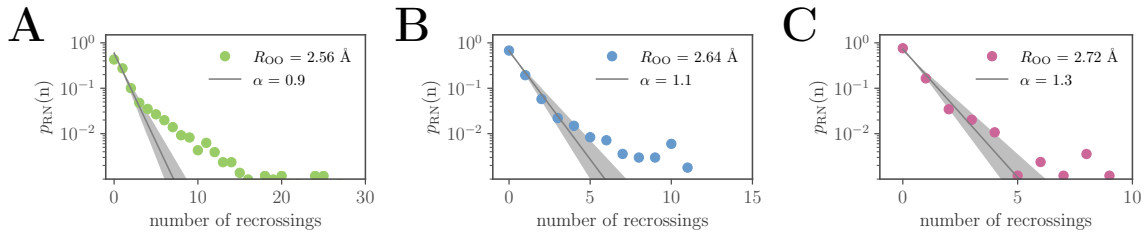


Figure S17. Recrossing-number probability distributions  $p_{\text{RN}}(n)$  for different constrained oxygen distances  $R_{\text{OO}}$  (**A**:  $R_{\text{OO}} = 2.56 \text{ \AA}$ , **B**:  $R_{\text{OO}} = 2.64 \text{ \AA}$ , **C**:  $R_{\text{OO}} = 2.72 \text{ \AA}$ ), normalized to  $\sum_{n=0}^{\infty} p_{\text{RN}} = 1$  and fits according to  $p_{\text{RN}}(n) = (1 - e^{-\alpha}) e^{-\alpha n}$ . The grey shaded areas show the variation of  $\alpha \pm 20\%$ .

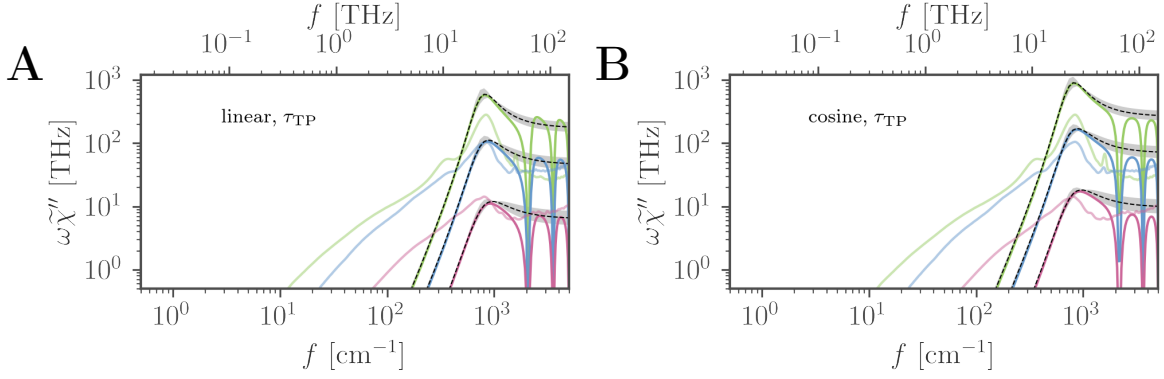


Figure S18. Models for the transfer-path spectral contribution given by eq. (S51) for the linear transfer-path shape (A) and eq. (S60) for the cosine transfer-path shape (B). The approximations are given by eqs. (S57) and (S61) and are shown as black dashed lines in A and B. The grey shaded areas show the variation of  $\alpha \pm 20\%$ .

a slightly different result is obtained.  
The resulting final expression

$$\omega \tilde{\chi}_{\text{TP,cos}}''(\omega) = \frac{d_{\text{TP}}^*{}^2 q^2}{V \epsilon_0 k_B T \tau_{\text{TW}}} \frac{e^\alpha \omega^4 \tau_{\text{TP}}^4 (\cos(\omega \tau_{\text{TP}}) + 1)}{(\pi^2 - \omega^2 \tau_{\text{TP}}^2)^2 (\cosh(\alpha) + \cos(\omega \tau_{\text{TP}}))}, \quad (\text{S60})$$

is Taylor-approximated as above to give

$$\omega \tilde{\chi}_{\text{TP,cos}}''(\omega) = \frac{d_{\text{TP}}^*{}^2 q^2}{V \epsilon_0 k_B T \tau_{\text{TW}}} \frac{e^\alpha \omega^4 \tau_{\text{TP}}^4}{(\pi + \omega \tau_{\text{TP}})^2 (2 \cosh(\alpha) - 2 + (\pi - \omega \tau_{\text{TP}})^2)}, \quad (\text{S61})$$

which are both shown in fig. S18B. In fact both approximate equations differ only by a factor of  $64/\pi^4 \approx 2/3$ . The linear shape was chosen for the presentation in the main text because of the good qualitative agreement of the mean TP shape in fig. S16 and quantitative agreement of the spectral shape in fig. S18A.

### XIII. IR SPECTRAL DECOMPOSITION OF THE EXCESS-PROTON DYNAMICS IN THE CONSTRAINED $\text{H}_5\text{O}_2^+$ CATION

Spectral decompositions of the excess-proton dynamics in the  $\text{H}_5\text{O}_2^+$  cation for different constrained  $R_{\text{OO}}$  are shown in fig. S19. Theoretical spectra are shown for the barrier-crossing model derived in section IX (respective eq. (1) in the main text) and the transfer-path model derived in section XII (respective eq. (5) in the main text), using the distance between the minima of the free energy in fig. 4B in the main text and fits applied to the distributions in fig. 4C in the main text and in section XII.

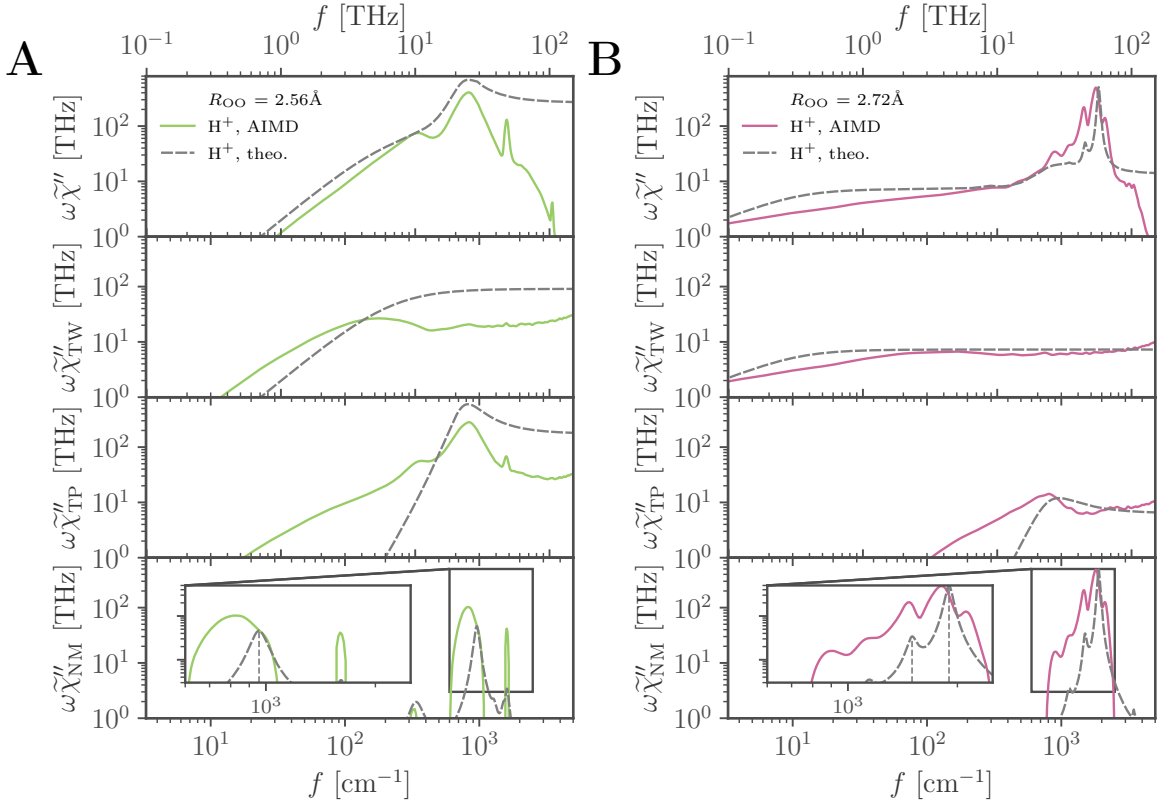


Figure S19. Spectral decomposition of the excess-proton dynamics in the  $\text{H}_5\text{O}_2^+$  cation for different constrained  $R_{\text{OO}}$  (**A**:  $R_{\text{OO}} = 2.56 \text{ \AA}$ , **B**:  $R_{\text{OO}} = 2.72 \text{ \AA}$ ) in analogy to the results in fig. 2B in the main text (colored lines). Theoretical spectra for the models discussed in the previous sections are shown as grey broken lines.

#### XIV. IR SPECTRA OF THE DEUTERATED $\text{H}_5\text{O}_2^+$ CATION

In order to test isotope effects, simulations were performed with the excess proton replaced by an excess deuteron. The resulting IR spectra for various  $R_{\text{OO}}$  and directions are shown in fig. S20 and compared to the excess-proton data. The regime between  $400\text{ cm}^{-1}$  to  $2000\text{ cm}^{-1}$  shows various shifts to lower frequencies and also splittings. This H/D isotope effect is expected since this region is linked to the excess-proton motion. As expected, the OH-stretching vibrations are not affected. These vibrations are associated with the flanking water molecules, that are not deuterated. Fig. S21 compares the H/D isotope effect for the decomposed spectra analog to fig. 2 in the main text. In contrast to the normal-modes involving the excess-proton as well as the transfer-path signature, which are all shifted by deuteration, the low-frequency transfer-waiting shoulder does not shift.

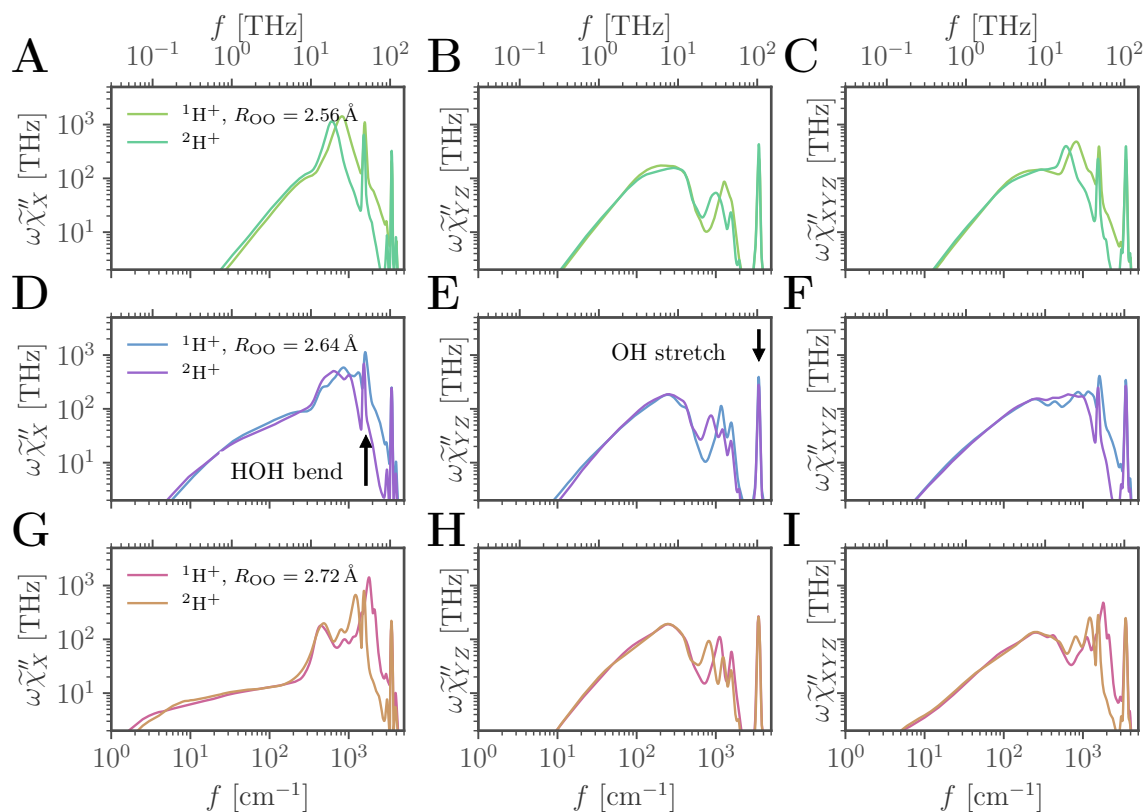


Figure S20. Comparison of the IR spectra of the  $\text{H}_5\text{O}_2^+$  cation with an excess proton ( $^1\text{H}^+$ ) or an excess deuteron ( $^2\text{H}^+$ ) in different directions. **A**, **D**, **G**: along the  $x$ -axis connecting the two oxygens, **B**, **E**, **H**: along the  $yz$ -plane, **C**, **F**, **I**: isotropic spectra. Each row corresponds to a system with a distinct constrained oxygen distance  $R_{\text{OO}}$  given in the first legend. The HOH-bending mode and OH-stretching mode of the water molecules are indicated in **D** and **E**.



A. Supplementary Information:  
Proton-Transfer Spectroscopy Beyond the Normal-Mode Scenario

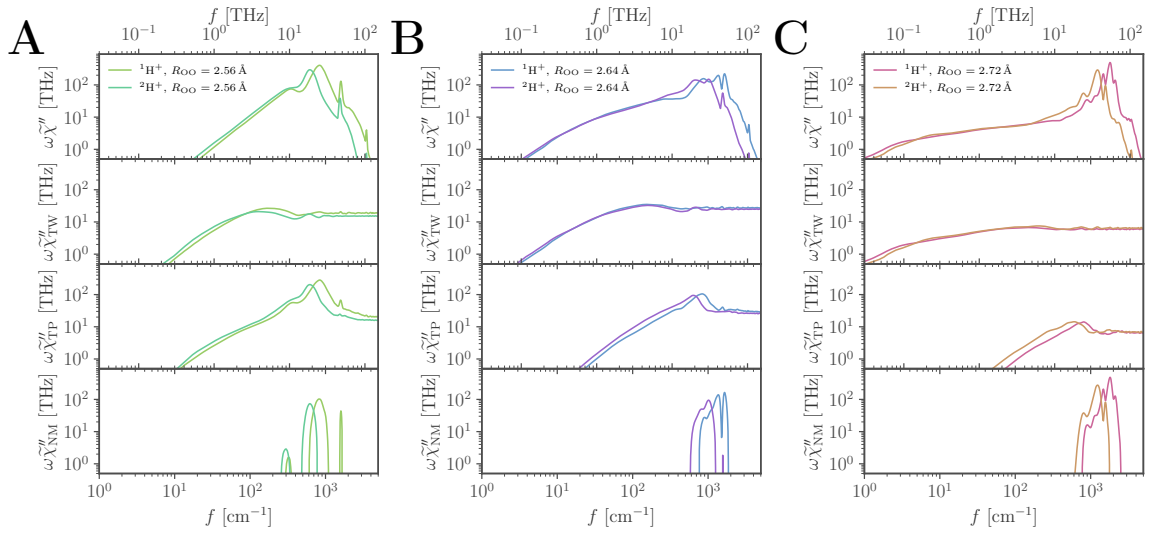


Figure S21. Comparison of the IR spectra of the  $\text{H}_5\text{O}_2^+$  cation with an excess proton ( $^1\text{H}^+$ ) or an excess deuteron ( $^2\text{H}^+$ ) for different  $R_{\text{OO}}$  (**A**:  $R_{\text{OO}} = 2.56 \text{ \AA}$ , **B**:  $R_{\text{OO}} = 2.64 \text{ \AA}$ , **C**:  $R_{\text{OO}} = 2.72 \text{ \AA}$ ), decomposed as described in fig. 2 in the main text.

## XV. DEUTERON TRANSFER-WAITING TIMES

As discussed in the previous section, no isotope effect is found for the low-frequency transfer-waiting shoulder of the IR spectrum, i.e. the mean transfer-waiting time  $\tau_{\text{TW}}$  does not depend on the mass of the reaction coordinate, but solely on friction constant  $\gamma$ , which is expected to be the same for the system with either an excess proton or an excess deuteron. Unfortunately, the determination of the friction constant  $\gamma$  is not straight-forward. In fig. S22 the mean transfer-waiting times  $\tau_{\text{TW}}$  measured from the simulations are compared to the heuristic formula<sup>25</sup>

$$\tau_{\text{TW}} = e^{\frac{U_0}{k_B T}} \left[ \frac{m k_B T}{\gamma U_0} + \frac{\pi}{2\sqrt{2}} \frac{\gamma d_{\text{TW}}^{*2}}{U_0} + 2\sqrt{\frac{m d_{\text{TW}}^{*2}}{U_0}} \right]. \quad (\text{S62})$$

Since the mass  $m$ , barrier height  $U_0$  and widths of the barrier  $2d_{\text{TW}}^*$  are known (given in fig. S22), estimates for the friction constant  $\gamma$  are obtained by comparing the simulation data to the heuristic formula. Note, that the theoretical predictions are only valid for  $U_0 > 2k_B T$ , and can therefore not be used for interpretation of the data for the lowest barrier considered here<sup>25</sup>. The obtained values,  $\gamma \approx 400$  u/ps for  $R_{\text{OO}} = 2.64$  Å and  $\gamma \approx 900$  u/ps for  $R_{\text{OO}} = 2.72$  Å, vary greatly and also deviate from the friction constants fitted to the line-broadening of the normal-modes,  $\gamma = 16$  u/ps. This discrepancy highlights the complex frequency dependence of dielectric friction, as previously discussed by Sedlmeier *et al.*<sup>26</sup> and Brünig *et al.*<sup>27</sup>. Indeed, fig. S22 validates the observation of the negligible isotope effect on the mean transfer-waiting time, since the heuristic formula of eq. (S62) shows little mass dependence in the predicted regime of  $\gamma$ , as seen in figs. S22B and S22C (the systems with a substantial barrier) from the negligible difference between the heuristic predictions for  $m = 1$  u (solid lines) and  $m = 2$  u (dashed lines) in the regime of the measured mean transfer-waiting time (horizontal dotted lines).

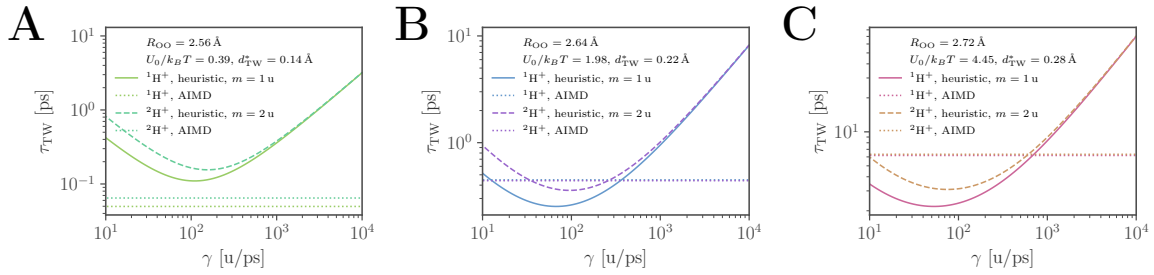


Figure S22. The transfer-waiting times  $\tau_{\text{TW}}$  of the excess proton ( $^1\text{H}^+$ ) and the excess deuteron ( $^2\text{H}^+$ ) of the  $\text{H}_5\text{O}_2^+$  cation, horizontal dotted lines, for different constrained oxygen distances  $R_{\text{OO}}$  (A:  $R_{\text{OO}} = 2.56$  Å, B:  $R_{\text{OO}} = 2.64$  Å, C:  $R_{\text{OO}} = 2.72$  Å), compared to the heuristic formula eq. (S62), solid and broken lines, as a function of the friction constant  $\gamma$ . Parameters entering the heuristic formula are given in the legends.

## XVI. WIENER-KINTCHINE THEOREM

The correlation function  $C_{xy}(t)$  of two stochastic processes  $x(t)$  and  $y(t)$  limited to the interval  $[0, L_t]$  is efficiently computed from the Fourier-transformed expressions  $\tilde{x}(\omega)$  and  $\tilde{y}(\omega)$  according to

$$C_{xy}(t) = \frac{1}{2\pi(L_t - t)} \int_{-\infty}^{\infty} d\omega e^{-i\omega t} \tilde{x}(\omega) \tilde{y}^*(\omega), \quad (\text{S63})$$

where the asterisk denotes the complex conjugate. This is known as the Wiener-Kintchine theorem<sup>28</sup>. Both sides of eq. (S63) are Fourier-transformed to give

$$\int_{-\infty}^{\infty} dt e^{i\omega t} L_t \left(1 - \frac{t}{L_t}\right) C_{xy}(t) = \tilde{x}(\omega) \tilde{y}^*(\omega), \quad (\text{S64})$$

which in the limit of large  $L_t$  reduces to

$$\tilde{C}_{xy}(\omega) = L_t^{-1} \tilde{x}(\omega) \tilde{y}^*(\omega). \quad (\text{S65})$$

Eq. (S63) can be derived starting off with the definition of the correlation function

$$C_{xy}(t) = \frac{1}{L_t - t} \int_0^{L_t - t} dt' x(t' + t) y(t'). \quad (\text{S66})$$

Defining  $x(t), y(t) = 0$  for  $t \notin [0, L_t]$ , the integral bounds can formally be extended

$$C_{xy}(t) = \frac{1}{L_t - t} \int_{-\infty}^{\infty} dt' x(t' + t) y(t'), \quad (\text{S67})$$

and making use of the convolution theorem

$$\begin{aligned} C_{xy}(t) &= \frac{1}{4\pi^2(L_t - t)} \int_{-\infty}^{\infty} dt' \int_{-\infty}^{\infty} d\omega e^{-i\omega(t+t')} \tilde{x}(\omega) \int_{-\infty}^{\infty} d\omega' e^{-i\omega't'} \tilde{y}(\omega') \\ &= \frac{1}{4\pi^2(L_t - t)} \int_{-\infty}^{\infty} d\omega e^{-i\omega t} \tilde{x}(\omega) \int_{-\infty}^{\infty} d\omega' \tilde{y}(\omega') \int_{-\infty}^{\infty} dt' e^{-it'(\omega+\omega')} \\ &= \frac{1}{4\pi^2(L_t - t)} \int_{-\infty}^{\infty} d\omega e^{-i\omega t} \tilde{x}(\omega) \int_{-\infty}^{\infty} d\omega' \tilde{y}(\omega') 2\pi \delta(\omega + \omega') \\ &= \frac{1}{2\pi(L_t - t)} \int_{-\infty}^{\infty} d\omega e^{-i\omega t} \tilde{x}(\omega) \tilde{y}(-\omega), \end{aligned} \quad (\text{S68})$$

noting that  $\tilde{y}(-\omega) = \tilde{y}^*(\omega)$  for a real function  $y(t)$  in order to obtain eq. (S63).

## REFERENCES

- <sup>1</sup>K. R. Asmis, N. L. Pivonka, G. Santambrogio, M. Brümmer, C. Kaposta, D. M. Neumark, and L. Wöste, *Science* **299**, 1375 (2003).
- <sup>2</sup>T. D. Fridgen, T. B. McMahon, L. MacAleese, J. Lemaire, and P. Maitre, *J. Phys. Chem. A* **108**, 9008 (2004).
- <sup>3</sup>E. G. Diken, J. M. Headrick, J. R. Roscioli, J. C. Bopp, M. A. Johnson, and A. B. McCoy, *J. Phys. Chem. A* **109**, 1487 (2005).
- <sup>4</sup>N. I. Hammer, E. G. Diken, J. R. Roscioli, M. A. Johnson, E. M. Myshakin, K. D. Jordan, A. B. McCoy, X. Huang, J. M. Bowman, and S. Carter, *J. Chem. Phys.* **122**, 244301 (2005).
- <sup>5</sup>F. Dahms, B. P. Fingerhut, E. T. J. Nibbering, E. Pines, and T. Elsaesser, *Science* **357**, 491 (2017).
- <sup>6</sup>J. Sauer and J. Döbler, *ChemPhysChem* **6**, 1706 (2005).
- <sup>7</sup>O. Vendrell, F. Gatti, and H. D. Meyer, *J. Chem. Phys.* **127**, 184303 (2007).
- <sup>8</sup>M. Park, I. Shin, N. J. Singh, and K. S. Kim, *J. Phys. Chem. A* **111**, 10692 (2007).
- <sup>9</sup>M. Kaledin, A. L. Kaledin, J. M. Bowman, J. Ding, and K. D. Jordan, *J. Phys. Chem. A* **113**, 7671 (2009).
- <sup>10</sup>X. Huang, B. J. Braams, and J. M. Bowman, *J. Chem. Phys.* **122**, 044308 (2005).
- <sup>11</sup>M. Baer, D. Marx, and G. Mathias, *Angew. Chemie - Int. Ed.* **49**, 7346 (2010).
- <sup>12</sup>F. Agostini, R. Vuilleumier, and G. Ciccotti, *J. Chem. Phys.* **134**, 084302 (2011).
- <sup>13</sup>W. Kulig and N. Agmon, *Nat. Chem.* **5**, 29 (2013).
- <sup>14</sup>M. Rossi, M. Ceriotti, and D. E. Manolopoulos, *J. Chem. Phys.* **140**, 234116 (2014).
- <sup>15</sup>J. M. Headrick, J. C. Bopp, and M. A. Johnson, *J. Chem. Phys.* **121**, 11523 (2004).
- <sup>16</sup>M. Thämer, L. De Marco, K. Ramasesha, A. Mandal, and A. Tokmakoff, *Science* **350**, 78 (2015).
- <sup>17</sup>R. Biswas, W. Carpenter, J. A. Fournier, G. A. Voth, and A. Tokmakoff, *J. Chem. Phys.* **146**, 154507 (2017).
- <sup>18</sup>J. A. Fournier, W. B. Carpenter, N. H. C. Lewis, and A. Tokmakoff, *Nat. Chem.* **10**, 932 (2018).
- <sup>19</sup>C. T. Wolke, J. A. Fournier, L. C. Dzugan, M. R. Fagiani, T. T. Odbadrakh, H. Knorke, K. D. Jordan, A. B. McCoy, K. R. Asmis, and M. A. Johnson, *Science* **354**, 1131 (2016).
- <sup>20</sup>F. Kohler, G. Findenegg, J. Fischer, and H. Posch, *The liquid state* (Verlag Chemie Weinheim, 1972).
- <sup>21</sup>P. Debye, *Chem. Cat. Company, Inc.* (Chemical Catalog Company, Incorporated, 1929).
- <sup>22</sup>W. K. Kim and R. R. Netz, *J. Chem. Phys.* **143**, 224108 (2015).
- <sup>23</sup>P. Faccioli, M. Sega, F. Pederiva, and H. Orland, *Phys. Rev. Lett.* **97**, 108101 (2006).
- <sup>24</sup>P. Cossio, G. Hummer, and A. Szabo, *J. Chem. Phys.* **148**, 123309 (2018).
- <sup>25</sup>J. Kappler, V. B. Hinrichsen, and R. R. Netz, *Eur. Phys. J. E* **42**, 119 (2019).
- <sup>26</sup>F. Sedlmeier, S. Shadkhoo, R. Bruinsma, and R. R. Netz, *J. Chem. Phys.* **140**, 054512 (2014).
- <sup>27</sup>F. N. Brünig, O. Geburtig, A. von Canal, J. Kappler, and R. R. Netz, *J. Phys. Chem. B* **126**, 1579 (2022).
- <sup>28</sup>N. Wiener, *Acta Math.* **55**, 117 (1930).



Supplementary Information:  
Spectral Signatures of Excess-Proton  
Waiting and Transfer-Path Dynamics in  
Aqueous Hydrochloric Acid Solutions

---

*B*

## Supplementary Information

### Spectral signatures of excess-proton waiting and transfer-path dynamics in aqueous hydrochloric acid solutions

Florian N. Brünig,<sup>1</sup> Manuel Rammner,<sup>1</sup> Ellen M.

Adams,<sup>2</sup> Martina Havenith,<sup>2</sup> and Roland R. Netz<sup>1</sup>

<sup>1</sup>*Freie Universität Berlin, Department of Physics, 14195 Berlin, Germany*

<sup>2</sup>*Ruhr-Universität Bochum, Department of Physical Chemistry II, 44780 Bochum, Germany*

## Supplementary Methods

### Supplementary Methods 1:

#### Kramers-Kronig estimate of complex index of refraction

Our THz spectroscopic experiments measure the frequency dependent extinction coefficient,  $\alpha_{\text{solution}}(\omega)$ , defined by the Beer-Lambert law

$$\alpha_{\text{solution}}(\omega) = \frac{1}{d} \ln \left( \frac{I_{\text{water}}(\omega)}{I_{\text{solution}}(\omega)} \right) + \alpha_{\text{water}}(\omega), \quad (1)$$

where  $d$  is the sample thickness,  $I_{\text{water}}(\omega)$  and  $I_{\text{solution}}(\omega)$  are the experimental transmitted intensities of the water reference and the sample.  $\alpha_{\text{water}}(\omega)$  is the extinction coefficient of bulk water and is taken from literature [1]. For comparison to the simulated data the power loss, i.e. the absorption spectrum, proportional to the imaginary part of the dielectric susceptibility  $\chi''(\omega)$ , has to be computed from the experimental extinction coefficient.

The extinction coefficient  $\alpha(\omega)$  is related to  $n''(\omega)$ , the imaginary part of the index of refraction, via

$$\alpha(\omega) = \frac{2\omega n''(\omega)}{c}, \quad (2)$$

where  $c$  is the speed of light in vacuum.

The complex dielectric susceptibility  $\chi(\omega)$  is related to the complex index of refraction  $n(\omega)$  as [2]

$$n^2(\omega) = [n'(\omega) + i n''(\omega)]^2 \quad (3)$$

$$= 1 + \chi(\omega) = 1 + \chi'(\omega) + i\chi''(\omega), \quad (4)$$

from which follows

$$\chi'(\omega) = n'^2(\omega) - n''^2(\omega) - 1 \quad (5)$$

$$\chi''(\omega) = 2n'(\omega)n''(\omega). \quad (6)$$

The missing real part of the index of refraction  $n'(\omega)$  is related to the imaginary part  $n''(\omega)$  by the Kramers-Kronig relation [3]

$$n'(\Omega) = n'(\infty) + \frac{2}{\pi} \text{p.v.} \int_0^{\infty} \frac{\omega n''(\omega)}{\omega^2 - \Omega^2} d\omega, \quad (7)$$



*B. Supplementary Information:*

*Spectral Signatures of Excess-Proton Waiting and Transfer-Path Dynamics in Aqueous Hydrochloric Acid Solutions*

---

where p.v. denotes the Cauchy principal value and  $n'(\infty)$  is the real index of refraction at the upper boundary of the integral. In practice, since experimental data is only available in a limited frequency range, extrapolation beyond the data range may improve the Kramers-Kronig inversion and a so-called ‘anchor point’, obtained from an independent measurement, can be used to replace  $n'(\infty)$  [4]. For measurements in the infrared (IR) regime, a good estimate for  $n'(\infty)$  is obtained by using the real index of refraction measured in the visible [5].

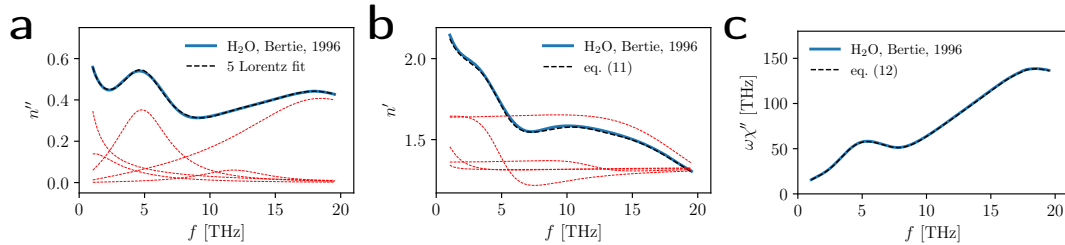
We perform the Kramers-Kronig transform using a set of Ansatz functions for the index of refraction, each consisting of a real part  $l'_i(\omega)$  and an imaginary part  $l''_i(\omega)$ , which follow approximately from a Lorentz oscillator model for the dielectric susceptibility [5]

$$l''_i(\omega) = \frac{A_i^2 \beta_i \omega}{(\omega_{0,i}^2 - \omega^2)^2 + \beta_i^2 \omega^2} \quad (8)$$

$$l'_i(\omega) = \frac{A_i^2 (\omega_{0,i}^2 - \omega^2)}{(\omega_{0,i}^2 - \omega^2)^2 + \beta_i^2 \omega^2}, \quad (9)$$

and extrapolate beyond the range of the available experimental data. We fit the imaginary index of refraction obtained from the experimental extinction coefficient  $\alpha(\omega)$  via eq. (2) as

$$n''(\omega) = \sum_i l''_i(\omega), \quad (10)$$



Supplementary Figure 1. Example of the calculation of the absorption spectrum  $\omega\chi''$  from refractive index data. The blue solid lines show literature data of water [1]. **a:** Imaginary part of the index of refraction  $n''$  and a fit (black broken line) as a sum of five Lorentz-type fit functions eq. (8) (red broken lines). **b:** Real part of the index of refraction  $n'$  and the estimate (black broken line) obtained from the Kramers-Kronig transform eq. (11) of the fit in a. The real parts of the individual fit functions according to eq. (9) are shown as red broken lines, shifted by the offset  $n'_{\text{lit.}} = 1.33$ . **c:** Absorption spectrum  $\omega\chi''$  and the estimate (black broken line) that is computed from the original data for  $n''$  in a and the estimate for  $n'$  in b.

where the  $l_i''(\omega)$  contain fit parameters  $A_i$ ,  $\omega_{0,i}$  and  $\beta_i$ . The real index of refraction is then given by

$$n'(\omega) = n'_{\text{lit.}} + \sum_i l_i'(\omega), \quad (11)$$

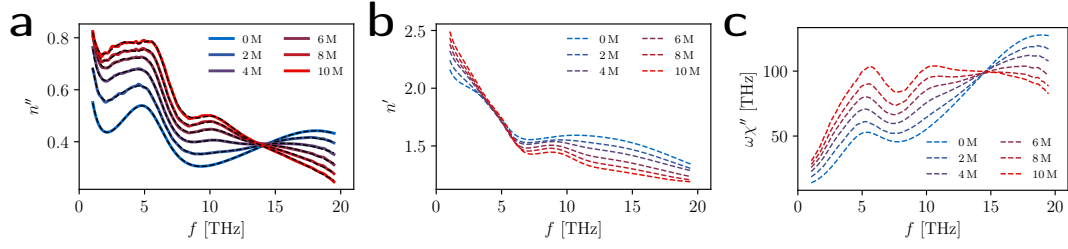
where the constant real index of refraction in the visible  $n'_{\text{lit.}} = 1.33$  is taken from the literature, which has been shown to be in general a good approximation for biological matter [5]. The absorption spectrum,  $\omega\chi''(\omega)$ , which is eventually used to compare to the simulation data, is computed using eqs. (2) and (6) [6] as

$$\omega\chi''(\omega) = c\alpha(\omega)n'(\omega), \quad (12)$$

where  $\alpha(\omega)$  is the original data and  $n'(\omega)$  is parametrized according to eq. (11). As a benchmark example, Supplementary Fig. 1 illustrates the result of this procedure applied to literature data of water [1] in the regime  $10\text{ cm}^{-1}$  to  $600\text{ cm}^{-1}$ , for which the experimental THz spectra are obtained. In Supplementary Fig. 2a the fits to the experimental THz data of aqueous hydrochloric acid (HCl) solutions in the range 2 M to 10 M (colored solid lines) are shown as black broken lines, that are used to estimate the real part of the refractive index, shown in Supplementary Fig. 2b as broken colored lines. The fit parameters are reported in Supplementary Tab. I. Eventually the resulting absorption spectra, shown in Supplementary Fig. 2c, are used to compare to simulation data in the main text.

*B. Supplementary Information:  
Spectral Signatures of Excess-Proton Waiting and Transfer-Path Dynamics in Aqueous Hydrochloric Acid Solutions*

---



Supplementary Figure 2. Calculation of the absorption spectra  $\omega\chi''$  from experimental THz extinction coefficient spectra of aqueous HCl solutions at various concentrations. **a:** Imaginary part of the index of refraction  $n''$  computed directly from the experimental absorption spectra (colored solid lines) and fits (black broken lines). The pure water data (blue solid line, 0 M) is taken from literature [1]. Each fit is a sum of five Lorentz-type fit functions eq. (8) with fit parameters reported in Supplementary Tab. I. **b:** Estimates of the real part of the index of refraction  $n'$  (colored broken lines) obtained from the fits in a according to eq. (11). **c:** Absorption spectra  $\omega\chi''$  (colored broken lines) that are computed from the original data for  $n''$  in a and the estimates for  $n'$  in b.

Supplementary Table I. Fit parameters of the five Lorentz-type fit functions eq. (8), that are used to fit the imaginary part of the index of refraction  $n''$  of aqueous HCl solutions at various concentrations in Supplementary Fig. 2A.

	$A_i$ [THz]	$\omega_{0,i}/(2\pi)$ [THz]	$\beta_i$ [THz]		$A_i$ [THz]	$\omega_{0,i}/(2\pi)$ [THz]	$\beta_i$ [THz]
0 M	0.679	1.749	53.66	6 M	0.9225	2.048	81.82
	0.3628	4.298	30.04		0.5483	4.082	32.04
	0.4378	5.653	26.39		0.4036	5.7	20.58
	0.1594	11.81	41.97		0.3602	10.55	33.78
	1.206	20.59	120.3		1.04	18.67	118.9
2 M	1.008	2.552	141.7	8 M	0.7904	1.703	51.2
	0.4925	4.314	34.67		0.5899	4.124	32.88
	0.3729	5.58	22.37		0.4266	5.845	20.53
	0.2535	11.01	40.95		0.414	10.55	34.43
	1.121	20.16	117.5		0.9807	17.85	112
4 M	0.7589	1.301	41.06	10 M	0.85	2.035	72.92
	0.5611	4.178	35.08		0.6844	4.483	39.35
	0.3975	5.616	21.92		0.3892	6.035	19.1
	0.2813	10.49	32.56		0.3797	10.6	31.25
	1.175	19.82	137.2		0.9387	17.08	109.7

## **Supplementary Methods 2:**

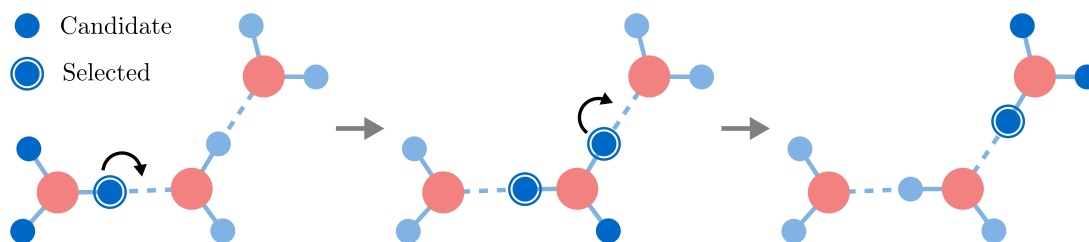
### **Excess-proton identification**

The identification of excess protons from trajectory data is a non-trivial task since the notion of an excess proton itself is subtle. While for the idealized structure of a Zundel cation it is possible to identify one proton that is qualitatively different from the others, in that it is symmetrically shared between two oxygen atoms, such a discrimination is impossible for an ideal symmetric Eigen cation from a configuration at a single time. Certainly it is possible to simply determine the protons that are the least closely associated to any oxygen atom in the simulation at each time step and call them excess protons. This is a perfectly reasonable choice when examining static properties of excess protons, as for example the radial distribution functions (RDFs) in Supplementary Note 4. Marx et al. [7] used a similar definition for the calculation of excess proton probability distributions in ab initio molecular dynamics (MD) simulations of protonated water.

In this work, however, we are interested in dynamical properties of excess protons. Since we aim to track and examine protons during their transfer between water molecules, including when they stay close to an oxygen atom, a selection based on a static geometric criterion would not suffice. Due to fluctuations of protons inside a hydronium molecule, also called ‘special pair dance’ [8, 9], a criterion based on instantaneous interatomic distances would lead to the disruption of otherwise continuous proton-transfer trajectories. Instead, similar to Calio et al. [9], we record the trajectories of protons that could potentially transfer from one water to a neighboring one and later discard those that did not. In fact, we are selecting *protons that transfer from one water molecule to another* and call them excess protons for simplicity.

#### **Selection of transfer candidates**

Ignoring the possibility of spontaneous autoionization of water molecules, proton transfer can only occur from one water molecule to another if the former has an extra proton associated to it, i.e. if it is a hydronium molecule. For the identification of hydronium molecules we use a geometric criterion: Each oxygen atom gets assigned its closest two protons which together form water molecules. The remaining protons are then assigned to the water molecule with



Supplementary Figure 3. Illustration of three consecutive snapshots during a proton transfer process. Transfer candidates and selected protons are highlighted. It becomes apparent why two of the protons belonging to one hydronium molecule are selected at the same time as transfer protons (see second snapshot). Such overlapping trajectories lead to the fact that our conditions select more protons than there are excess protons in the simulation.

the closest oxygen atom and together make up a hydronium molecule. All protons that belong to such a hydronium molecule are considered *candidates* for proton transfer. Furthermore, we exclude those candidates whose distance to their closest chloride ion is smaller than that to their second closest oxygen atom. These protons reside between a chloride ion and an oxygen atom (as opposed to residing between two oxygen atoms as most hydrogen atoms do) and do not exhibit proton transfer between water molecules.

5.5%, 11.1% and 16.4% of all protons fulfill these conditions in the 2 M, 4 M and 6 M simulation, respectively. This means that on average 28.9, 56.4 and 78.4 protons, respectively, are being selected as transfer candidates at each time step, which is a little less than three times the number of excess protons  $N_{\text{H}^+} = 10, 20$  and  $30$  in each simulation. This is to be expected, since each excess proton corresponds to one hydronium molecule which in turn holds three protons that are *part of*  $\text{H}_3\text{O}^+$ . The difference to  $3N_{\text{H}^+}$  is due to the excluded protons that are located between an oxygen atom and a chloride ion.

### Elimination of trajectories without transfer

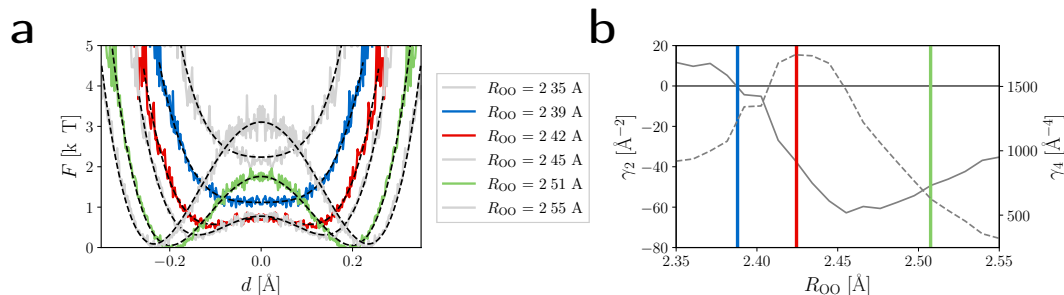
The conditions explained above define proton trajectories that potentially contain proton transfers between two water molecules. In order to further reduce the number of protons to those that actually contribute to proton transfer, the trajectories are filtered by another - dynamical - condition that selects only those trajectories which contain a transfer, defined

by a change of the proton's closest oxygen atom (the same criterion was used by Calio et al. [9]). This last condition leaves  $\sim 50\%$  of the previously selected protons in each simulation that actually contribute to the analysis, which is still more than  $N_{\text{H}^+}$  selected protons per time step because some trajectories overlap. This is the case since during the lifetime of a hydronium molecule, two of its protons might be tracked at the same time. One proton which transfers to initially create the respective hydronium molecule and one that transfers away from it later on. Figure 3 illustrates such a situation.

### Supplementary Methods 3:

#### Fits of the free-energy landscape

The two-dimensional (2D) free energy landscape spanned by  $R_{OO}$  and  $d$  shown in Fig. 4a in the main text, is fitted for cuts through the free energy along  $d$ . As in the main text in Fig. 4, here in Supplementary Fig. 4a, cuts along  $d$  are shown for  $R_{OO} = 2.39 \text{ \AA}$ , where the barrier just vanishes (blue solid line),  $R_{OO} = 2.42 \text{ \AA}$ , where the absolute barrier height is minimal (red solid line), and  $R_{OO} = 2.51 \text{ \AA}$ , for which the global minima of the 2D free energy are obtained (green solid line). Additionally, some results for other values of  $R_{OO}$  are shown as gray solid lines. The data is fitted by the quartic expression  $F(d) = F_{d=0}(1 + \gamma_2 d^2 + \gamma_4 d^4)$ , shown as black broken lines in Supplementary Fig. 4a with the fit parameters reported in Supplementary Tab. II. In Supplementary Fig. 4b the fit parameters  $\gamma_2$  (gray solid line) and  $\gamma_4$  (gray broken line) are plotted over  $R_{OO}$ . The vertical colored lines indicated the respective values of  $R_{OO}$  shown in Supplementary Fig. 4a. The barrier vanishes for  $\gamma_2 > 0$ , which defines the blue solid line. At the position where the absolute barrier height is minimal, indicated by the red solid line, the quartic fit parameter  $\gamma_4$  is maximal.



Supplementary Figure 4. Cuts along  $d$  through the two-dimensional free energy shown in the main text in Fig. 4a and fitted to  $F(d) = F_{d=0}(1 + \gamma_2 d^2 + \gamma_4 d^4)$ . (a) Cuts at various values of  $R_{OO}$  are shown as solid lines and fits as black broken lines with fit parameters reported in Supplementary Tab. II. (b) The fit parameters  $\gamma_2$ , shown as a gray solid line, and  $\gamma_4$ , shown as a gray broken line, are given over  $R_{OO}$ .



*B. Supplementary Information:  
Spectral Signatures of Excess-Proton Waiting and Transfer-Path Dynamics in Aqueous Hydrochloric Acid Solutions*

---

Supplementary Table II. Fit parameters for the fits shown in Supplementary Fig. 4a using the quartic expression  $F(d) = F_{d=0}(1 + \gamma_2 d^2 + \gamma_4 d^4)$ .

$R_{OO}$ [Å]	$F_{d=0}$ [ $k_B T$ ]	$\gamma_2$ [Å <sup>-2</sup> ]	$\gamma_4$ [Å <sup>-4</sup> ]
2.35	2.24	11.63	919.7
2.39	1.12	7.78	1099
2.42	0.73	-38.29	1747
2.45	0.78	-62.25	1625
2.51	1.76	-49.17	623.5
2.55	3.11	-35.24	319.6

## Supplementary Methods 4:

### Wiener-Kintchine theorem

The correlation function  $C_{xy}(t)$  of two stochastic processes  $x(t)$  and  $y(t)$  limited to the time interval  $[0, L_t]$  is efficiently computed from the Fourier-transformed expressions  $\tilde{x}(\omega)$  and  $\tilde{y}(\omega)$  according to

$$C_{xy}(t) = \frac{1}{2\pi(L_t - t)} \int_{-\infty}^{\infty} d\omega e^{-i\omega t} \tilde{x}(\omega) \tilde{y}^*(\omega), \quad (13)$$

where the asterix denotes the complex conjugate. This is known as the Wiener-Kintchine theorem [10]. Both sides of eq. (13) are Fourier-transformed to give

$$\int_{-\infty}^{\infty} dt e^{i\omega t} L_t \left(1 - \frac{t}{L_t}\right) C_{xy}(t) = \tilde{x}(\omega) \tilde{y}^*(\omega), \quad (14)$$

which in the limit of large  $L_t$  reduces to

$$\tilde{C}_{xy}(\omega) = L_t^{-1} \tilde{x}(\omega) \tilde{y}^*(\omega). \quad (15)$$

Eq. (13) can be derived starting off with the definition of the correlation function

$$C_{xy}(t) = \frac{1}{L_t - t} \int_0^{L_t - t} dt' x(t' + t) y(t'). \quad (16)$$

Defining  $x(t), y(t) = 0$  for  $t \notin [0, L_t]$ , the integral bounds can formally be extended

$$C_{xy}(t) = \frac{1}{L_t - t} \int_{-\infty}^{\infty} dt' x(t' + t) y(t'), \quad (17)$$

and making use of the convolution theorem

$$\begin{aligned} C_{xy}(t) &= \frac{1}{4\pi^2(L_t - t)} \int_{-\infty}^{\infty} dt' \int_{-\infty}^{\infty} d\omega e^{-i\omega(t+t')} \tilde{x}(\omega) \int_{-\infty}^{\infty} d\omega' e^{-i\omega't'} \tilde{y}(\omega') \\ &= \frac{1}{4\pi^2(L_t - t)} \int_{-\infty}^{\infty} d\omega e^{-i\omega t} \tilde{x}(\omega) \int_{-\infty}^{\infty} d\omega' \tilde{y}(\omega') \int_{-\infty}^{\infty} dt' e^{-it'(\omega+\omega')} \\ &= \frac{1}{4\pi^2(L_t - t)} \int_{-\infty}^{\infty} d\omega e^{-i\omega t} \tilde{x}(\omega) \int_{-\infty}^{\infty} d\omega' \tilde{y}(\omega') 2\pi\delta(\omega + \omega') \\ &= \frac{1}{2\pi(L_t - t)} \int_{-\infty}^{\infty} d\omega e^{-i\omega t} \tilde{x}(\omega) \tilde{y}(-\omega), \end{aligned} \quad (18)$$

noting that  $\tilde{y}(-\omega) = \tilde{y}^*(\omega)$  for a real function  $y(t)$  in order to obtain eq. (13).

## Supplementary Notes

### Supplementary Note 1:

#### **Alternative methods for simulation and characterization of excess-proton dynamics**

It is known that nuclear quantum effects (NQEs), specifically zero-point effects, significantly influence distributions of excess protons in water [7, 9, 11]. While the techniques for simulating NQEs have significantly advanced in recent years, the accurate calculation of dynamical properties, which is the focus of this study, remains an active field of research [12]. There are some subtle questions how the time-dependent polarization correlation functions of decomposed excess-proton trajectories, which form the basis of our spectroscopic analysis, would be extracted from simulation data encompassing NQEs, in particular, it is unclear whether the common approaches taken by centroid or ring-polymer MD are directly applicable. Most of all, it is noteworthy that previous studies found no significant differences between IR spectra computed from simulations with and without NQEs below  $3000\text{ cm}^{-1}$  [11, 13], which could mean that the neglect of NQEs might have less severe consequences for time-dependent correlation functions than it has for spatial distributions of excess protons. We therefore interpret the good agreement between simulated and experimental spectra in the THz regime in fig. 2c and in the mid-IR regime in fig. 1c as a validation of our chosen simulation techniques. Besides, our neglect of NQEs allows us to generate long trajectories that improve statistics and therefore the quality of our spectra, particularly down in the THz regime.

In Supplementary Note 4 we extract radial distribution functions involving excess protons and chloride ions from our simulation trajectories and obtain good agreement with previous simulations and experimental data [14–18].

In Supplementary Note 7 we show that our transfer-waiting time distributions in fig. 5f correspond quite closely to hydronium-oxygen continuous-identity auto-correlation functions [19], which were previously introduced to characterize proton-transfer time scales. The same correlation functions, but with the fast back-and-forth excess-proton transfer events between the same two water molecules of the transient  $\text{H}_5\text{O}_2^+$  complexes removed, have

been used to interpret the long time scales of uni-directional proton transfer, which reflects signatures observed in 2D IR experiments at time scales of 1 ps to 2 ps [19–21]. We note that back-and-forth proton-transfer events that occur within transient  $\text{H}_5\text{O}_2^+$  complexes are spectroscopically relevant and therefore must be included in the prediction of spectra. The longer time scale of uni-directional proton transfer at 1 ps to 2 ps contributes in linear absorption spectra at frequencies below 1 THz.

In Supplementary Note 8 we determine the diffusivities of excess protons and water molecules and obtain similar results as previous simulations [13, 16–19, 22]. Compared to the experimental data, the absolute diffusivities of excess protons  $D_{\text{H}^+}$  and water oxygens  $D_{\text{O}}$  are smaller by a factor of about three, but their ratios, given by  $D_{\text{H}^+}/D_{\text{O}} = (3.0 \pm 0.8), (4.3 \pm 1.3), (3.8 \pm 0.8)$  for 6 M, 4 M, 2 M HCl, respectively, are albeit large errors in satisfactory agreement with the experimental ratios of about  $D_{\text{H}^+}/D_{\text{O}} = 1.5, 2.3, 3.0$  for similar concentrations [23].

It has been shown that proton-transfer events are caused by subtle structural changes in the excess-proton solvation environment, for example the hydrogen-bond structure in the second solvation shell [11, 13, 18, 22]. Based on our simulations, we confirm that the suggested hydrogen-bond asymmetry coordinate can indeed be used to predict the excess proton that is most likely to transfer to a neighboring water among the three transfer candidates within a hydronium ion [11]. Along these lines, the presence of a fourth water molecule that forms a hydrogen-bond to a hydronium ion weakly correlates with back-and-forth transfer behavior [13, 18, 22]. These findings are presented in detail in Supplementary Note 9.

## Supplementary Note 2:

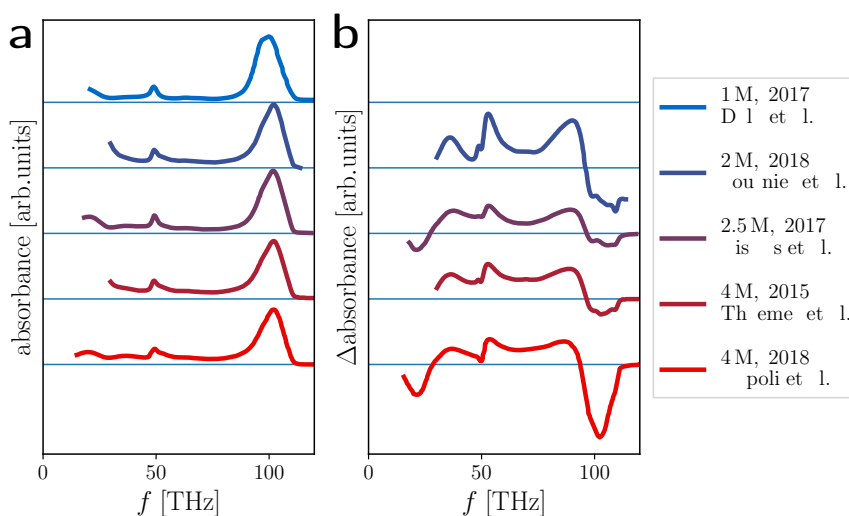
### Experimental infrared spectra of aqueous hydrochloric acid solutions

Supplementary Fig. 5a shows experimental IR absorption spectra and Supplementary Fig. 5b shows difference spectra of aqueous HCl solutions at various concentrations. All data is taken directly as published in the literature. The proton continuum band is clearly visible in all difference spectra, albeit with slight differences in shape. In comparison to our calculated difference spectra in Fig. 1b in the main text, the features at 40 THz, 50 THz and 90 THz are more pronounced.

Indeed difference spectra depend on the normalization applied to the underlying HCl solution

*B. Supplementary Information:  
Spectral Signatures of Excess-Proton Waiting and Transfer-Path Dynamics in Aqueous Hydrochloric Acid Solutions*

---



Supplementary Figure 5. Experimental IR absorption spectra (a) and corresponding difference spectra (b) of aqueous HCl at various concentrations, taken from [11, 24–27]. The data was not published with an absolute scale and is thus scaled arbitrarily. No difference spectrum was published for the spectrum at 1 M [24].

and pure water spectra which is further elucidated in Supplementary Note 3. Normalizations commonly used for spectra calculated from simulations employ sample volume or concentration of water molecules. In experimental setups, however, these parameters are often not reported. Of the four publications we took difference spectra from, only Napoli et al. explained the applied normalization scheme as normalization “to a unit area over the range shown”[11]. In light of these subtleties, comparisons between difference spectra from different sources should be considered with care.

### Supplementary Note 3:

## Normalization of infrared difference spectra of aqueous hydrochloric acid solutions

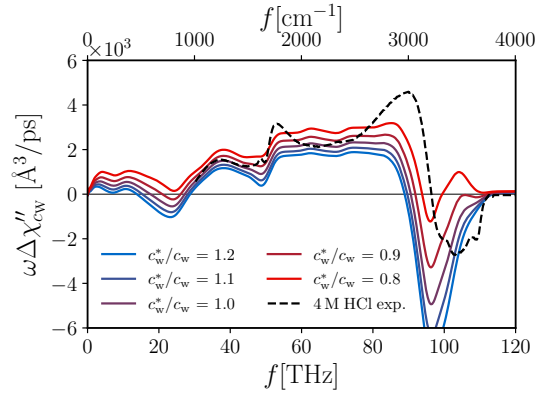
The normalization of the difference spectra is subtle and in many studies not well documented as discussed in the previous Supplementary Note 2. In Supplementary Fig. 6, we illustrate how small deviations in the normalization constants can lead to drastic variations among the difference spectra. Throughout this work difference spectra  $\omega\Delta\chi''_{c_w}(\omega)$  are defined as normalized by the water concentration  $c_w$  of the aqueous HCl solutions and by the concentration  $c_w^0$  of the reference water spectrum

$$\omega\Delta\chi''_{c_w}(\omega) = \frac{1}{c_w}\omega\chi''_{\text{solution}}(\omega) - \frac{1}{c_w^0}\omega\chi''_{\text{water}}(\omega), \quad (19)$$

according to eq. (8) from the methods section. In Supplementary Fig. 6, the difference spectra of the 4 M HCl solution, obtained from ab initio MD simulations in this study, are shown as a blue solid line and compared to difference spectra, that are obtained if instead slightly varied water concentrations for the acid solution  $c_w^*$  are used in the normalization. The data illustrates, that even in the moderate range of  $c_w^*/c_w = 0.8$  to  $1.2$ , some features of the difference spectra, like the dip at the position of the water bend around  $1650\text{ cm}^{-1}$  (50 THz), or the features in the OH stretch above  $3000\text{ cm}^{-1}$  (90 THz), are significantly changed. These features therefore have to be considered with great care. However, the dominant spectroscopic features, like the continuum band between  $2000\text{ cm}^{-1}$  to  $3000\text{ cm}^{-1}$  and the peak around  $1200\text{ cm}^{-1}$  (35 THz), that are associated with the excess proton dynamics and are at the focus of this study, are modified in height but not in shape and seem therefore very robust with respect to the normalization protocol.

*B. Supplementary Information:  
Spectral Signatures of Excess-Proton Waiting and Transfer-Path Dynamics in Aqueous Hydrochloric Acid Solutions*

---



Supplementary Figure 6. Illustration of the effect of variations of the normalization protocol used for difference spectra of the 4M HCl solution, obtained from ab initio MD simulations. The difference spectra are defined according to eq. (19) and the water concentrations for the acid solution  $c_w^*$  are varied (colored solid lines) with ratios reported in the legend. For comparison experimental data for a 4M HCl solution is shown as a black broken line [27].

## Supplementary Note 4:

### Spatial correlations

Spatial correlations in liquids can be quantified with radial distribution functions (RDFs),  $g_{ab}(r)$ , which denote the average density of particles of type  $a$  at a relative distance  $r$  around particles of type  $b$ . The local average density of  $a$  relative to  $b$  at distance  $r$  is given as  $\rho_a g_{ab}(r)$  where  $\rho_a = N_a/V$  is the global density of  $a$ . The RDF is computed from simulation data of two particle species with numbers  $N_a$  and  $N_b$  that are located at positions  $\vec{r}_i$  and  $\vec{r}_j$  [28]

$$g_{ab}(r) = \frac{V}{4\pi r^2 N_a N_b} \sum_{i=1}^{N_a} \sum_{j=1}^{N_b} \langle \delta(|\vec{r}_i - \vec{r}_j| - r) \rangle. \quad (20)$$

Average coordination numbers of species  $a$  within distance  $r$  of particles of species  $b$  are obtained by integration over  $g_{ab}(r)$

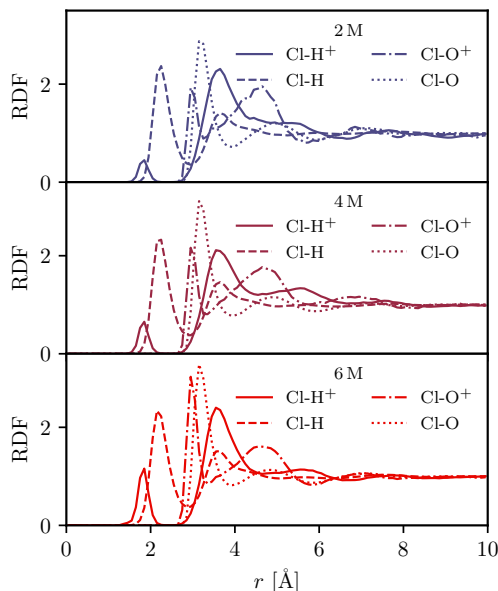
$$N_{ab}(r) = \rho_a \int_0^r dr' 4\pi r'^2 g_{ab}(r'). \quad (21)$$

In this Supplementary Note, the spatial correlations of the excess protons in the HCl solutions are analyzed using RDFs, specifically also the correlations with the chloride ions. Excess protons are identified in the simulation data as the remaining protons after the water molecules are assembled for each oxygen atom with the closest two hydrogen atoms at each time step of the simulation. Here and in Supplementary Note 8 we are not excluding protons close to the chloride ions, in contrast to the analysis of the proton-transfer statistics in the main text, which is described in Supplementary Methods 2. Hydronium ions are defined for each excess proton together with the water molecule of the closest oxygen atom.

#### 4.1. Correlations with the chloride ions

In Supplementary Fig. 7 the RDFs of the chloride ions are shown for the three HCl concentrations with respect to the excess protons as solid lines, all hydrogen nuclei, including excess protons, as broken lines, the oxygen nuclei of the water molecules as dotted lines and the oxygen nuclei of the hydronium ions as dash-dotted lines. For all HCl concentrations, the general features of the RDFs are comparable. But, there are a few concentration-dependent





Supplementary Figure 7. Spatial correlations between the chloride ions and other nuclei in terms of radial distribution functions (RDFs) as obtained from ab initio MD simulations of HCl solutions at various concentrations. RDFs are shown for the excess protons ( $\text{H}^+$ ) as solid lines, all hydrogen nuclei (H), including excess protons, as broken lines, the oxygen nuclei of the water molecules (O) as dotted lines and the oxygen nuclei of the hydronium ions ( $\text{O}^+$ ) as dash-dotted lines.

trends. The RDFs of the excess protons around the chloride ions (solid lines) show two dominant peaks, a small one that is located at around  $d_{\text{Cl-H}^+} = 1.8 \text{ \AA}$  and thereby left of the major peak of the hydrogen nuclei RDFs (broken lines) at around  $d_{\text{Cl-H}} = 2.2 \text{ \AA}$ . This peak is important as it corresponds to excess protons coordinated directly with the chloride ion, i.e. the excess proton sits in between the chloride ion and the oxygen atom of the respective hydronium ion. This contact ion pair is considered an important intermediate in the solvation of HCl [14]. Yet, the excess protons are still part of the hydronium ion, since an even smaller distance of around  $1.4 \text{ \AA}$  would be expected for the covalent bond to the chloride atom, which appears at much higher concentrations than 6 M [14]. The peak height at  $d_{\text{Cl-H}^+} = 1.8 \text{ \AA}$  (solid lines) clearly increases with HCl concentration in Supplementary Fig. 7, but even for the largest concentration of 6 M it remains smaller than the second and largest peak in the RDFs at about  $3.5 \text{ \AA}$ . This peak is located to the right of the first and

dominant peak in the RDFs of the oxygen nuclei of the hydronium ions (dash-dotted lines) at around  $d_{\text{Cl-O}^+} = 3.0 \text{ \AA}$ , which occurs at a slightly smaller distance than the respective peak of all oxygen nuclei at around  $d_{\text{Cl-O}} = 3.1 \text{ \AA}$ .

All of the presented data is in good agreement with results by Baer et al. [14] from comparable ab initio simulations, who additionally show data for much higher concentrations up to 16 m (16 mol/kg  $\simeq$  11.7 M) and successfully reproduced extended X-ray absorption fine structure (EXAFS) experimental measurements [15]. Specifically, they report  $d_{\text{Cl-O}^+} = 2.96 \text{ \AA}$  and  $d_{\text{Cl-O}} = 3.14 \text{ \AA}$  in excellent agreement with experimental EXAFS data [15]. Data comparing various exchange-correlation functionals used in the ab initio simulation also consistently reproduced the results presented in Supplementary Fig. 7 with no significant dependence on the type of functional (except for the PBE functional), albeit with large statistical uncertainties in some data [18].

When interpreting the RDFs, the actual densities of the species need to be put into perspective. The global densities of chloride ions, excess protons and hydronium ions are equal by definition. However, for the 2 M HCl solution data set, the ratio of water molecules to chloride ions or respectively excess protons is about 24.8 and drops to 11.2 for the 4 M and 6.5 for the 6 M data sets. These numbers would have to be divided by two, assuming that water molecules are equally and exclusively solvating all chloride ions and excess protons. It is therefore evident, that for the 6 M solution, hydronium ions are necessarily residing already in the first hydration shell of the chloride ions. More precisely, the average coordination numbers around the chloride ions are obtained by integration over the first peak of each RDF in Supplementary Fig. 7 and use of eq. (21). The obtained coordination numbers are reported in Supplementary Tab. III and are generally in good agreement with previous simulation and experimental results [14, 15]. The average number of hydronium ions in the first hydration shell of any chloride ion increases from 0.13 for 2 M to 0.52 for 6 M, see third column in Supplementary Tab. III. Previously, Baer et al. [14] interpreted this significant increase in the coordination number as an increase of contact ion pairs, where the excess proton is shared between the hydronium oxygen and the chloride ion. However, the coordination number of the excess protons around chloride ions does not increase as much, only from 0.007 for 2 M to 0.054 for 6 M, see first column in Supplementary Tab. III. Therefore, the excess protons of the hydronium ions in the first solvation shell of the chloride ions mostly point away from chloride ions and are predominantly coordinated with other water molecules, rather than

*B. Supplementary Information:  
Spectral Signatures of Excess-Proton Waiting and Transfer-Path Dynamics in Aqueous Hydrochloric Acid Solutions*

---

Supplementary Table III. Average coordination numbers  $N_{ab}$  around the chloride ions as obtained from the first peak of the RDFs in Supplementary Fig. 7 and eq. (21). Errors of the simulation data are estimated from the resolution of the RDFs.

	Cl-H <sup>+</sup> ( $r < 2.5 \text{ \AA}$ )	Cl-H ( $r < 3.0 \text{ \AA}$ )	Cl-O <sup>+</sup> ( $r < 3.5 \text{ \AA}$ )	Cl-O ( $r < 3.5 \text{ \AA}$ )
2 M	$0.007 \pm 0.001$	$5.64 \pm 0.07$	$0.13 \pm 0.01$	$4.8 \pm 0.1$
4 M	$0.020 \pm 0.001$	$5.42 \pm 0.07$	$0.26 \pm 0.01$	$4.6 \pm 0.1$
6 M	$0.054 \pm 0.001$	$5.12 \pm 0.07$	$0.51 \pm 0.01$	$4.2 \pm 0.1$
6 M, MOLOPT	$0.091 \pm 0.001$	$5.0 \pm 0.1$	$0.56 \pm 0.02$	$4.0 \pm 0.2$
6 M, TZV2P	$0.115 \pm 0.001$	$5.0 \pm 0.2$	$0.63 \pm 0.02$	$4.0 \pm 0.2$
2.5 m [14]			0.17	5.82
6 m [14]			0.42	5.21
10 m [14]			0.71	4.67
16 m [14]			1.05	3.99
6 m [14, 15]			$0.7 \pm 0.2$	$5.1 \pm 0.5$
10 m [14, 15]			$1.0 \pm 0.3$	$4.8 \pm 0.5$
16 m [14, 15]			$1.6 \pm 0.3$	$4.2 \pm 0.5$

with chloride ions. However, it is noteworthy that the chloride-excess-proton coordination is affected, when a different basis set is considered in the simulations, which is shown below in subsection 4.3 for simulations at 6 M. In particular, an increase of the coordination of the excess protons with the chloride ions is observed when considering the MOLOPT or TZV2P basis sets. Therefore, while the above results have to be considered with care when comparing to experimental data and additional analysis with more elaborate basis sets may be useful, the analysis performed in this study is self-consistent for the MOLOPT-SR basis set.

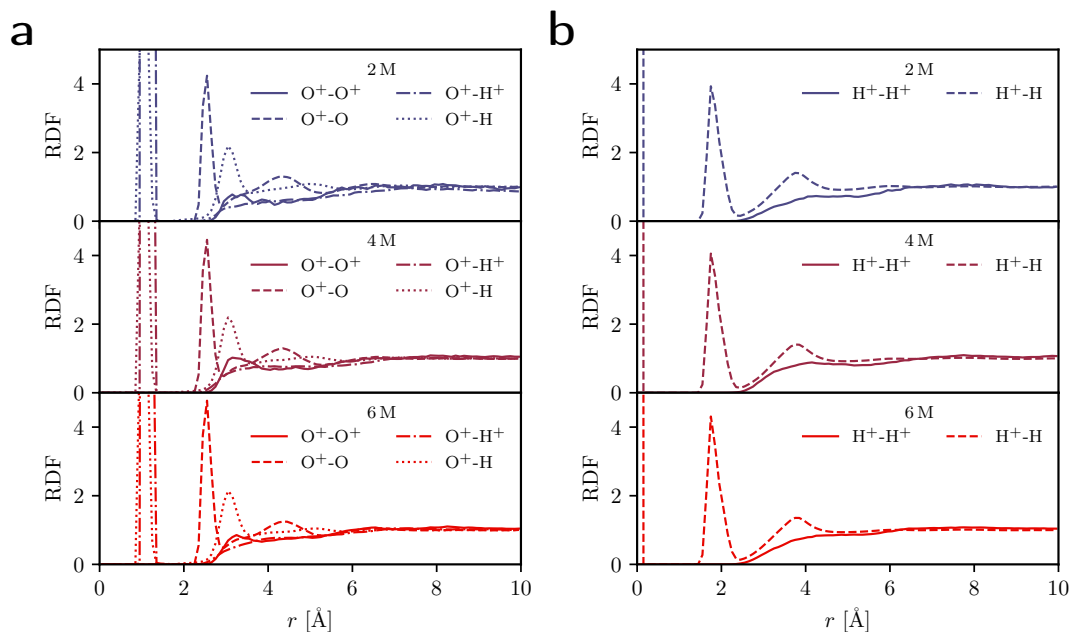
Taken together, this data indicates that the excess protons in aqueous HCl solutions mostly reside inside hydronium ions within our definition, and additionally stay away from the chloride ions, i.e. are located between two oxygen atoms and not between a chloride and an oxygen atom. This holds true even for moderately high concentrations up to 6 M considered in this study, but necessarily breaks down at very high concentrations when the water becomes saturated with HCl [14]. The data confirms the high solubility of excess protons in water, due

to energetic but also entropic effects [17, 29]. Furthermore, it justifies the focus on proton transfer between water molecules and the excess-proton selection and identification scheme in Supplementary Methods 2 to analyze the excess-proton spectral signatures of the HCl solutions. Note, that already the linear trend of the HCl difference spectra with concentration shown in Fig. 1d in the main text indicates that in the range up to 6 M considered in the ab initio MD simulations in this study, the effect of the chloride ions on the excess-proton spectra and dynamics is negligible. Similarly, Napoli et al. [11] previously showed that IR spectra of excess protons coordinated with chloride ions show much weaker spectral signatures as compared to the average spectra of all the excess protons.

#### 4.2. Correlations between oxygen and hydrogen atoms

In Supplementary Fig. 8a the spatial correlations of the hydronium ions and in Supplementary Fig. 8b of the excess protons themselves are discussed. Comparable results for aqueous HCl solutions were previously shown for various exchange-correlation functionals used in ab initio simulations [18] and for different self-consistent iterative multistate empirical valence bond (SCI-MS-EVB) simulations [16, 17].

In Supplementary Fig. 8a the RDFs of the oxygen nuclei of the hydronium ions are shown with respect to the oxygen nuclei of other hydronium ions ( $O^+$ ) as solid lines, for the oxygen nuclei of the water molecules (O) as broken lines, for the the excess protons ( $H^+$ ) as dash-dotted lines and all hydrogen nuclei (H), including excess protons, as dotted lines. Next to the trivial peaks of the dash-dotted as well as the dotted lines at below  $1.0 \text{ \AA}$ , belonging to the hydrogen nuclei which are part of the hydronium ions itself, a clear peak of the broken lines at  $d_{O^+-O} = 2.5 \text{ \AA}$  indicates the water oxygen nuclei in the first hydration shell, each of which are candidates to form a transient  $H_5O_2^+$  complex, i.e. the special pair, together with the hydronium ion. This peak is roughly consistent with the most probable oxygen-oxygen distance of the transient  $H_5O_2^+$  complex, that is seen in the free energy in Fig. 4a in the main text. A second, much smaller, peak at about  $4.2 \text{ \AA}$  indicates the water molecules in the second hydration shell of the hydronium ion. Boths peaks at about  $d_{O^+-O} = 2.5 \text{ \AA}$  and at  $4.2 \text{ \AA}$  are clearly shown in data for various exchange-correlation functionals [18], as well as for SCI-MS-EVB simulations [16, 17]. Beyond that, a decomposition of the first peak into three components was used to support the picture of an asymmetric Eigen state [9].



Supplementary Figure 8. Spatial correlations between the oxygen atoms of hydronium ions (a) and excess protons (b) with respect to other nuclei in terms of radial distribution functions (RDFs) as obtained from ab initio MD simulations of HCl solutions at various concentrations. **a**: RDFs are shown for the oxygen nuclei of the hydronium ions ( $O^+$ ) as solid lines, for the oxygen nuclei of the water molecules (O) as broken lines, for the the excess protons ( $H^+$ ) as dash-dotted lines and all hydrogen nuclei (H), including excess protons, as dotted lines. **b**: RDFs are shown for the excess protons ( $H^+$ ) as solid lines and all hydrogen nuclei (H), including excess protons, as broken lines.

Each peak is accompanied by peaks of the dotted lines at slightly larger distances, which indicate the hydrogen atoms belonging to the water molecules in the respective hydration shells. Additionally, the dotted lines show a weak and broad shoulder below roughly  $2.5 \text{ \AA}$ , the origin of which is further discussed in Supplementary Note 9. A slight relative maximum of the solid lines at  $d_{O^+-O^+} = 3.00 \text{ \AA}$  but with a magnitude below one indicates a metastable structure between two hydronium ions. However, note that there is no such signature in the dash-dotted lines, i.e. no apparent correlation with the excess proton of the nearest hydronium ion. The peak at  $d_{O^+-O^+} = 3.00 \text{ \AA}$  was also observed by Calio et al. [17] and at  $d_{O^+-O^+} = 3.20 \text{ \AA}$  by Xu et al. [16].

In Supplementary Fig. 8b the RDFs of the excess protons are shown with respect to the

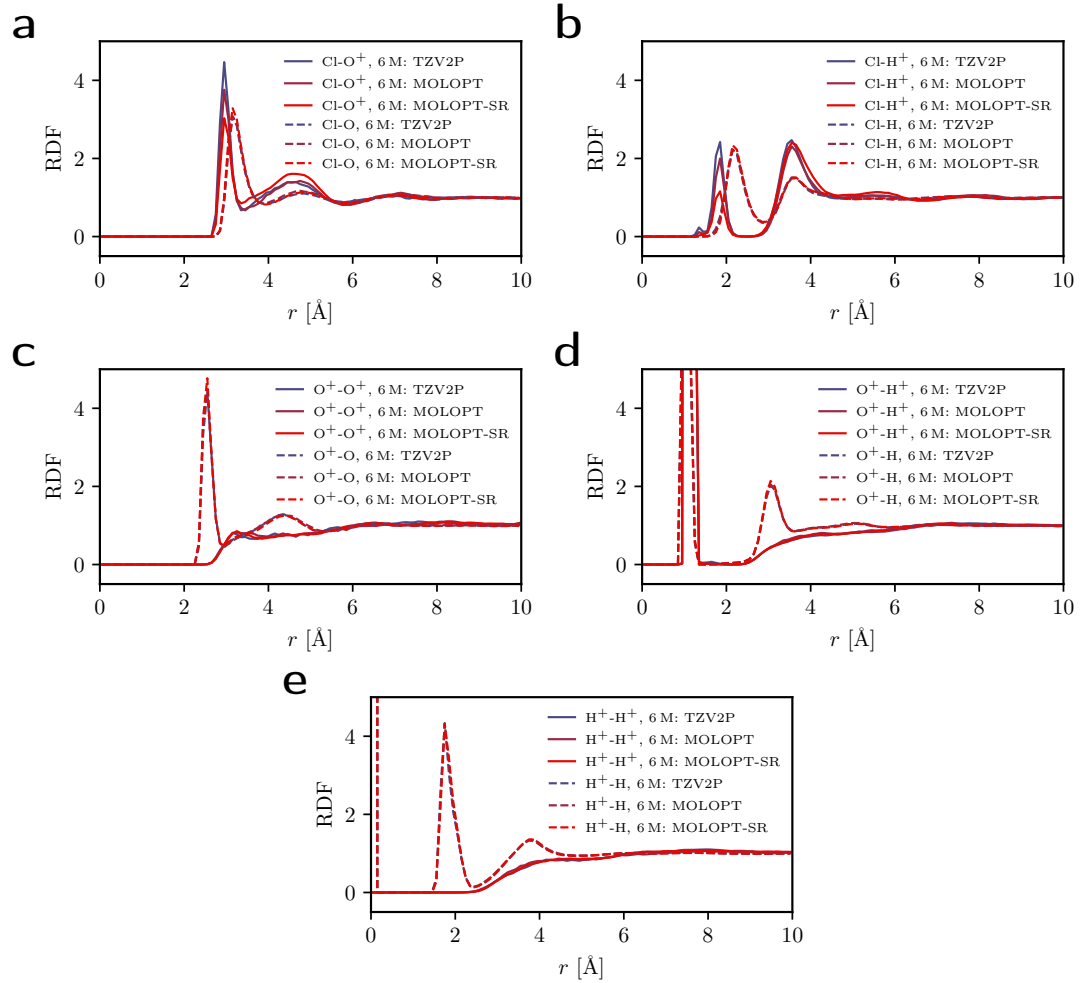
other excess protons ( $\text{H}^+$ ) as solid lines and all hydrogen nuclei (H), including excess protons, as broken lines. The main peak of the broken lines at  $d_{\text{H}^+-\text{H}} = 1.8 \text{ \AA}$  indicates the mean distances between hydrogen atoms within the same hydronium ion. The peak shows a shoulder at around  $2.1 \text{ \AA}$  possibly related to spatial correlations between the excess proton and two hydrogen atoms in the neighboring water molecule of the transient  $\text{H}_5\text{O}_2^+$  complex, i.e. of the special pair. The second peak of the broken lines at  $3.8 \text{ \AA}$  is related to other water molecules in the first hydration shell, that form hydrogen bonds (HBs) with the hydronium ion to which the excess proton is assigned. No spatial correlations are apparent in the RDFs between excess protons, shown as solid lines. In contrast to that, Xu et al. [16] observed a slight peak at  $d_{\text{H}^+-\text{H}^+} = 4.20 \text{ \AA}$ , indicative of spatial correlations between two excess protons. In summary, the RDFs of the hydronium ions as well as of the excess protons presented in Supplementary Figs. 8a and b indicate no spatial correlations between excess protons or hydronium ions and other excess protons. While there appears a slight relative maximum in the RDF between hydronium ions itself, this may simply be related to close-packing effects in the liquid.

### 4.3. Results for different basis sets

To address the quality of the simulations for the chosen MOLOPT-SR basis set, additional simulations of HCl solutions at 6 M with the DZVP-MOLOPT-GTH and TZV2P-GTH basis sets are performed [30, 31]. For both cases the chloride ions are modeled including diffuse functions by using the aug-DZVP-GTH and aug-TZV2P-GTH basis sets, respectively. Otherwise the setups are equivalent to the MOLOPT-SR simulations and each simulation is run for 28 ps under NVT condition. The spatial correlations in each data set are then compared by computing RDFs, the results of which are presented in Supplementary Figs. 9a–e. The correlations of the oxygen atoms and the hydrogen atoms among each other, that are most important for the solvation structure of the excess protons and therefore the focus of this study as discussed above, show no significant dependence on the choice of basis set as is seen from the near-perfect agreement of the RDF curves throughout Supplementary Figs. 9c–e. Regarding the chloride ions, some differences in the RDFs in Supplementary Figs. 9a and b are clearly discernible though. Most importantly, the first major peaks in the RDFs between chloride ions and oxygen atoms of hydronium ions (solid lines in Supplementary Fig. 9a) as

B. Supplementary Information:

Spectral Signatures of Excess-Proton Waiting and Transfer-Path Dynamics in Aqueous Hydrochloric Acid Solutions



Supplementary Figure 9. Spatial correlations between the chloride ions and oxygen atoms (a), chloride ions and hydrogen atoms (b), oxygen atoms of hydronium ions and oxygen atoms (c) or hydrogen atoms (d), and excess protons (e) with respect to other nuclei in terms of radial distribution functions (RDFs) as obtained from ab initio MD simulations of HCl solutions at 6 M for various basis sets considered in the simulation. Data obtained for the TZV2P basis set is shown in blue, for the MOLOPT basis set in purple and for the MOLOPT-SR basis set in red. **a,c:** RDFs are shown for the oxygen nuclei of the hydronium ions (O<sup>+</sup>) as solid lines, for the oxygen nuclei of the water molecules (O) as broken lines. **b,d,e:** RDFs are shown for the excess protons (H<sup>+</sup>) as solid lines and all hydrogen nuclei (H), including excess protons, as broken lines.

---

well as between chloride ions and excess protons (solid lines in Supplementary Fig. 9b) increase when the MOLOPT or TZV2P basis sets are used. Additionally, a second much smaller peak is visible at a closer distance for both simulations with the MOLOPT and TZV2P basis sets (solid blue and purple lines in Supplementary Fig. 9b), indicating that contact pairs between chloride ions and excess protons appear rarely throughout the simulations. This means that the role of the chloride spectator, that is argued in Supplementary Note 4.1 to be of minor importance, may be underestimated in simulations using the MOLOPT-SR basis set. In Supplementary Note 4.1 the coordination number of the excess protons around chloride ions at 6 M was found to be 0.054 from integration over the first major peak of the RDF up to 2.5 Å (solid red line in Supplementary Fig. 9b and first column in Supplementary Tab. 4.1). When considering the MOLOPT basis set, this value increases to 0.091 and for the TZV2P basis set to 0.115, meaning that on average each excess proton is for 9% or respectively 12% of the time coordinated with a chloride ion as the second nearest neighbour (or rarely even as the nearest neighbor) in a configuration that is not well described by a transient  $\text{H}_5\text{O}_2^+$  complex which forms the basis of the analysis performed in the main text.



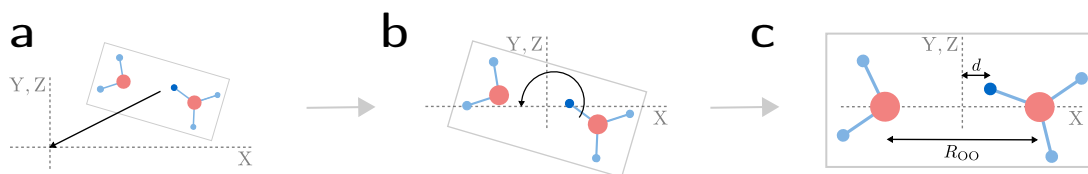
## Supplementary Note 5:

### Decomposition of infrared spectra of transient $\text{H}_5\text{O}_2^+$ complexes

To allow for a decomposition of IR spectra of transient  $\text{H}_5\text{O}_2^+$  complexes into contributions perpendicular and parallel to the connecting axis of the water oxygens, the dynamics of the transient  $\text{H}_5\text{O}_2^+$  complexes are described in a comoving internal coordinate system as introduced in the main text and shown in Supplementary Fig. 10c. The x-axis is defined as the axis connecting both oxygen atoms (in the following referred to as O-O axis), the coordinate origin being located in the middle between the oxygens. The yz-plane lies perpendicular to that axis. A transformation to this coordinate system thus involves a time-dependent translation and rotation of the trajectory  $\mathbf{r}_i(t)$  in the laboratory frame of each atom inside a  $\text{H}_5\text{O}_2^+$  complex and can be described by

$$\mathbf{r}'_i(t) = \mathbf{M}_{\phi(t),\theta(t)} [\mathbf{r}_i(t) - \mathbf{r}_0(t)], \quad (22)$$

where  $\mathbf{r}_0(t)$  is the trajectory of the oxygen-oxygen midpoint and  $\mathbf{M}_{\phi(t),\theta(t)}$  is a rotation matrix setting both oxygen atoms on the x-axis. The coordinate transform is illustrated in Supplementary Fig. 10. These operations do of course have an influence on the resulting spectra, which is discussed in Supplementary Note 6.



Supplementary Figure 10. Illustration of the coordinate transform eq. (22) from the laboratory frame to the internal coordinate system of the transient  $\text{H}_5\text{O}_2^+$  complexes, allowing for a distinction of movements perpendicular and parallel to the connecting axis between the water oxygens (referred to as O-O axis). **a:** First the oxygen-oxygen midpoint  $\mathbf{r}_0(t)$  is subtracted from the coordinates of the atoms of the transient subsystem  $\mathbf{r}_i(t)$ . **b:** Then the atoms are rotated, such that both oxygen atoms lie on the x-axis. **c:** In the resulting internal coordinate system the variable  $d$  is defined as the projection of the excess proton location onto the x-axis.  $R_{\text{OO}}$  is the distance between the two oxygen atoms.

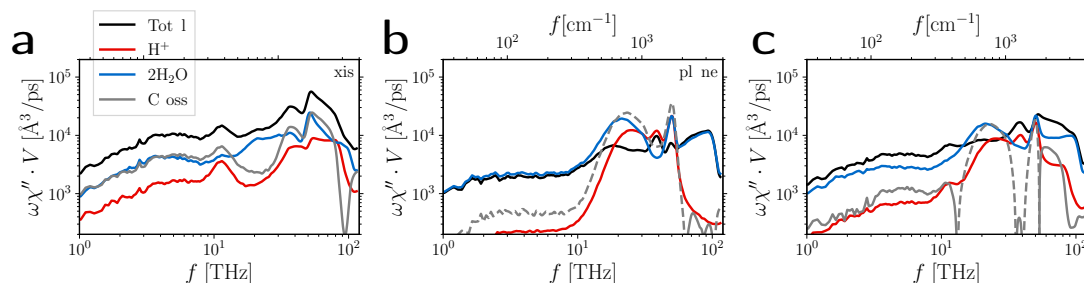
The internal coordinate system further defines  $d$ , the projection of the excess proton location onto the O-O axis, and  $R_{\text{OO}}$ , the distance between the two oxygen atoms according to

$$R_{\text{OO}}(t) = |x'_{\text{O}_1}(t) - x'_{\text{O}_2}(t)|$$

$$d(t) = x'_{\text{H}^+}(t).$$

Using such an internal coordinate system, we can decompose the spectra of protons and water molecules inside the transient  $\text{H}_5\text{O}_2^+$  complexes as well as their cross-correlation spectra into their contribution along and perpendicular to the O-O axis, respectively.

For that purpose, we extract the trajectories of the closest two water molecules to each previously extracted excess-proton trajectory (see Supplementary Methods 2), resulting in trajectories of transient  $\text{H}_5\text{O}_2^+$  complexes. Since the water molecules involve valence electrons, we use the localized-Wannier-center trajectory data for this, resulting in trajectories with a slightly lower time resolution of 4 fs than for the nuclei-only data. In order to be able to decompose the trajectories into parts perpendicular and parallel to the O-O axis, we describe the multidimensional  $\text{H}_5\text{O}_2^+$  trajectories using the internal coordinate system introduced above and calculate spectra accordingly.



Supplementary Figure 11. Absorption spectra including nuclei and electrons of transient  $\text{H}_5\text{O}_2^+$  complexes consisting of their excess protons ( $\text{H}^+$ , red solid lines), their closest two water molecules ( $2 \text{H}_2\text{O}$ , blue solid lines) and cross correlations (Cross, gray solid and broken lines) parallel to the O-O axis (a) and perpendicular to it, i.e. in the  $yz$ -plane of the local coordinate system (b). The isotropic spectrum is shown in c. Broken lines indicate negative values. Note that the spectra are averaged over the spatial dimensions.

In Supplementary Fig. 11 the resulting spectra are shown, separated into the contributions along (Supplementary Fig. 11A) and perpendicular to the O-O axis (Supplementary Fig. 11b)

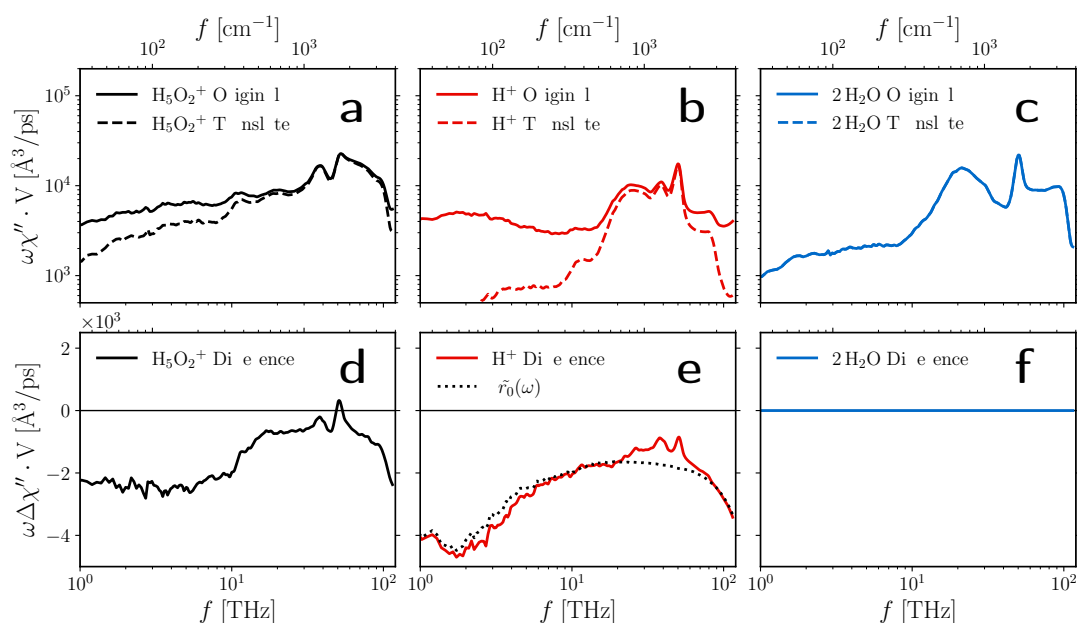
and each averaged over their spatial dimensions. The excess-proton spectrum perpendicular to the O-O axis (Supplementary Fig. 11b, red solid lines) clearly dominates the isotropic excess-proton spectrum (Supplementary Fig. 11c, red solid line). Including cross correlations, defined as the difference between the total spectrum and the sum of the proton and water contributions, a different picture emerges. In Supplementary Fig. 11a and b the cross correlations between the excess proton and its two closest water molecules are plotted in gray. The cross correlations between proton and water molecules are of the same order of magnitude and of similar shape as the proton spectrum itself and almost entirely positive along the x-axis and negative along the yz-plane, meaning that the water polarization is to some degree amplifying the proton's polarization dynamics along the O-O axis, whereas they cancel perpendicular to the O-O axis. This phenomenon was similarly observed for isolated  $\text{H}_5\text{O}_2^+$  complexes [32]. Also, Sauer and Döbler [33] found in an MD study of  $\text{H}_5\text{O}_2^+$  that “[...] the O-H<sup>+</sup>-O<sub>Y,Z</sub> bends (perpendicular to the O-O axis) have vanishing IR intensities and should not be seen in the spectra [...]”.

The analysis presented in this Supplementary Note shows, that the IR spectra of  $\text{H}_5\text{O}_2^+$  complexes in HCl solutions dominantly represent the motion of the excess proton along the O-O axis. This motivates the projection of the protons' movement onto the O-O axis,  $d$ , that is used for the decomposition in the main text.

## Supplementary Note 6:

### Spectral signature resulting from change of coordinate system

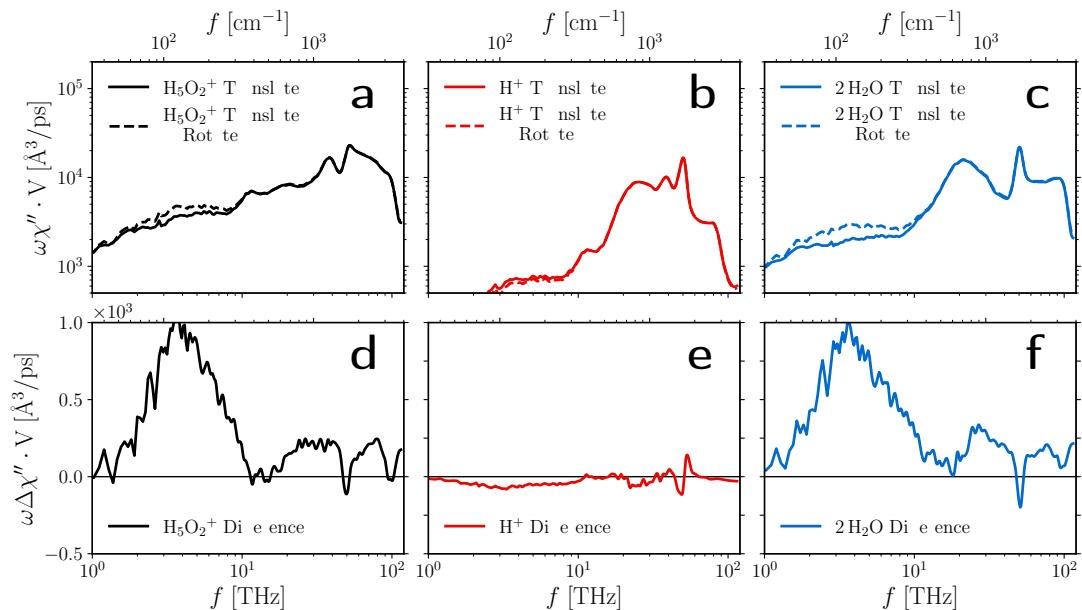
As presented in Supplementary Note 5, the dynamics of the transient  $\text{H}_5\text{O}_2^+$  complexes, including the excess protons, is described in the comoving internal coordinate systems. To estimate the effect of this coordinate transformation on the spectrum of protons and water molecules in the  $\text{H}_5\text{O}_2^+$  complexes, we compare the decomposed spectra of these complexes in the original coordinate system to those after translation and subsequent rotation, respectively. Figure 12 shows a comparison between the spectrum of  $\text{H}_5\text{O}_2^+$  complexes in their original coordinate system and translated according to  $\mathbf{r}_{i,\text{trans}}(t) = \mathbf{r}_i(t) - \mathbf{r}_0(t)$  (compare eq. (22)). The translation does not have any effect on the spectrum of the two water molecules because they are not charged and the dipole moment of a neutral system does not change



Supplementary Figure 12. **a–c**: Averaged non-normalized absorption spectra including nuclei and electrons of transient  $\text{H}_5\text{O}_2^+$  complexes in their original coordinate system (solid) and translated such that the coordinate origin is the midpoint between the oxygens (broken). **d–f**: The differences between the spectra above. A dotted line in e shows the spectrum of the movement of the oxygen midpoint  $\mathbf{r}_0(t)$ .

*B. Supplementary Information:*

*Spectral Signatures of Excess-Proton Waiting and Transfer-Path Dynamics in Aqueous Hydrochloric Acid Solutions*



Supplementary Figure 13. **a–c**: Non-normalized absorption spectra including nuclei and electrons of transient  $\text{H}_5\text{O}_2^+$  complexes that are translated but in their original orientation (solid) and additionally rotated such that the oxygen atoms lie on the O-O axis (broken). **d–f**: The differences between the spectra above.

upon translation. The excess proton, however, has a charge. Thus, its dipole moment is affected by this translation. The effect can be approximated by the spectrum of all oxygen midpoint trajectories  $\mathbf{r}_0(t)$  of the  $\text{H}_5\text{O}_2^+$  complexes using a charge of 1 e, which is shown in Supplementary Fig. 12e as a dotted line. While the translation leads to significant change in the proton spectrum at low and high frequencies, in the frequency range between 20 THz to 80 THz the effect of the translation is mostly negligible. Obviously, the error in the projected spectrum in Supplementary Fig. 12b is not transferred to the single-proton spectrum projected along the oxygen-oxygen distance coordinate  $d$ , that we show in Fig. 3c in the main text.

In contrast to the translation, the rotation mostly affects the water spectrum, because the translation due to rotation is larger for atoms further away from the rotation center. This can be seen in Supplementary Fig. 13 which shows a comparison between the spectrum of  $\text{H}_5\text{O}_2^+$  complexes that were translated as shown in Supplementary Fig. 12 and those that

were additionally rotated according to  $\mathbf{r}'_i(t) = \mathbf{M}_{\phi(t),\theta(t)} \mathbf{r}_{i,\text{trans}}(t)$  (compare eq. (22)). The proton spectrum is barely affected and the effect on the water spectrum is limited to low frequencies.

Since both translation and rotation have at most a minor effect on the transient  $\text{H}_5\text{O}_2^+$  spectrum in the relevant frequency range, our findings from the decomposition into x- and yz-contribution in Supplementary Note 5 for transient  $\text{H}_5\text{O}_2^+$  complexes also apply to the lab frame.

## **Supplementary Note 7:**

### **Distribution of proton-transfer waiting times**

The mean proton-transfer rate is at the heart of research on excess protons solvated in water, as it is the relevant microscopic time scale that determines the macroscopic large diffusion obtained by the Grotthuss process. As outlined in the main text, the mean transfer rate corresponds to the waiting time of a stochastic barrier-crossing process, that is not to be confused with the transfer-path time of the actual transition over the barrier. The waiting-time distributions that are also shown in Fig. 5c in the main text are discussed in this Supplementary Note and are compared to previous results from literature.

Agmon [34] gives a summary of early experimental results, suggesting a mean proton-transfer time of 1.5 ps obtained in NMR studies [35], which is believed to be correlated with the hydrogen bond rearrangement and water reorientation dynamics on the time scales of 1 ps to 2 ps determined from a number of other experiments. These time scales seem to contrast more recent experimental results from 2D IR spectroscopy, that report interconversion between different proton hydration structures, i.e. Eigen and Zundel-like structures, on time scales of around 100 fs and less [20, 36, 37]. On the other hand, Carpenter et al. [38] write, “the hydrated proton bend displays fast vibrational relaxation and spectral diffusion timescales of 200 – 300 fs, however, the transient absorption anisotropy decays on a remarkably long 2.5 ps timescale, which matches the timescale for hydrogen bond reorganization in liquid water”. Arguing that the latter would be an upper bound, they infer “the transfer of excess protons in water [...] is an activated process with a timescale of 1 – 2 ps.” Kundu et al. [20] confirm that “during the lifetime of the  $\text{H}_5\text{O}_2^+$  motif, that is on the order of 1 ps, the proton undergoes fluctuating large-amplitude motions exploring essentially all possible positions between the flanking water molecules”. Yuan et al. [39] measure a concentration-dependent ‘proton hopping time’ in HCl solutions using 2D IR chemical exchange spectroscopy with a methyl thiocyanate probe and extrapolate a time of 1.6 ps for the dilute limit.

It transpires, that two time scales determine the distribution of proton-transfer waiting times, which was confirmed in various simulation studies and interpreted as stemming from either back-and-forth or uni-directional proton transfer, respectively, in the literature sometimes referred to as ‘reversible’ and ‘irreversible’ proton transfer. Napoli et al. [11] point out that

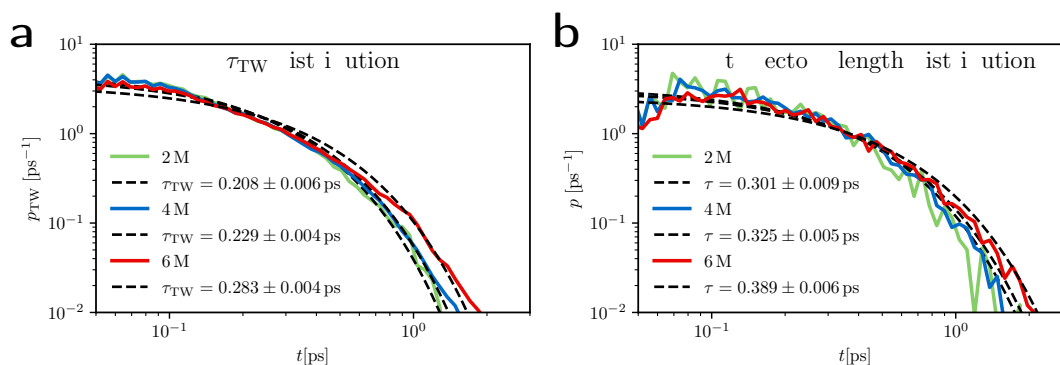
Supplementary Table IV. Collection of proton-transfer time scales reported in the literature.

	method	conc. [M]	T [K]		time
Meiboom [35]	NMR exp.				1.5 ps
Woutersen and Bakker [36]	2D IR exp.	5	300		<0.1 ps
Dahms et al. [37]	2D IR exp.	<1	300		<0.1 ps
Thämer et al. [27]	2D IR exp.	4	300		>0.48 ps
Carpenter et al. [38]	2D IR exp.	2	300		<2.5 ps
Kundu et al. [20]	2D IR exp.	1	300		<0.1 ps
					1 ps
Yuan et al. [39]	2D IR chemical exchange exp.	dillute limit	300		1.6 ps
Fischer et al. [40]	DFT CPMD	1.7	300	bi-directional	0.5 ps
Fischer and Gunlycke [18]	DFT CPMD	1.7	300	uni-directional	2.5 ps
Calio et al. [17]	MS-EVB	0.43 – 3.26	300		0.4 – 0.5 ps
					1.2 – 2.3 ps
Calio et al. [9]	MS-EVB, DFT BOMD	0.22 – 0.43	300		10 – 17 fs
					0.3 – 0.5 ps
					2.3 – 3.2 ps
	+ nuc.-quantum effects				12 – 15 fs
					0.83 – 0.27 ps
					1.4 ps
Arntsen et al. [19]	DFT BOMD		300	bi-directional	0.184 ps
				uni-directional	1.69 ps
Roy et al. [41]	DFT BOMD	2	300		1 – 2 ps
	DFT BOMD	8	300		2 – 4 ps



while they find a frequency-correlation time of  $(1.4 \pm 0.3)$  ps “corresponding to the pump ( $3150\text{ cm}^{-1}$ ) and probe ( $1760\text{ cm}^{-1}$ ) frequencies used in [27]”, the auto-correlation of the proton asymmetry actually decays on time scales of less than 100 fs with a second slower component of  $(0.8 \pm 0.1)$  ps. Fischer et al. [40] find the time scale of proton ‘hopping’ to be around 0.5 ps, including back-and-forth events, and deduce a time scale of 2.5 ps for uni-directional events in a later study [18]. Calio et al. [17] extract two timescales of about 400 fs to 500 fs and 1.3 ps to 2.3 ps for the concentrations 0.43 M to 3.26 M from fits to the long-lived anisotropy decays, which the authors argue “can correlate experimental time constants to irreversible proton transfer”. In a follow-up study Calio et al. [9] report three timescales of about 10 – 17 fs, 320 – 490 fs and 2.3 – 3.2 ps for the concentrations 0.22 M to 0.43 M from fits to the anisotropy decay of the excess-proton dynamics projected on the axis of the two closest oxygen atoms, with a slight acceleration to the values 12 – 15 fs, 83 – 270 fs and 1.4 ps when nuclear-quantum effects are considered. Roy et al. [41] find a time scale of 1 – 2 ps for uni-directional proton transfer between two water molecules in 2 M HCl solutions employing two-dimensional transition state theory and Marcus theory of ion pairing. This number increases significantly to 2 – 4 ps in 8 M HCl solutions. Arntsen et al. [19] report time constants of the excess-proton identity auto-correlation function, which is elaborated on further below. They find a values of 184 fs, but after eliminating back-and-forth events from the data the time scale increases to 1.69 ps. Furthermore, a couple of studies point out that the long time scale of proton transport increases significantly with concentration [29, 41]. A summary of the reported values is given in Supplementary Tab. IV. It transpires that the separation in back-and-forth and uni-directional events is important to distinguish two time scales in the broad distributions of proton-transfer times. For stochastic barrier-crossing processes of highly inertial or non-Markovian coordinates and furthermore for low energy barriers, it is well established that barrier-crossing events exhibit large numbers of subsequent back-and-forth events, due to the slow dissipation of the energy required for the initial barrier-crossing event [32, 41–45]. Such events appear especially important with regard to proton-transfer processes and their spectral signatures.

The proton-transfer waiting time distributions of the excess-protons in aqueous HCl solutions at various concentrations, reported in the main text in Fig. 5c, are plotted in Supplementary Fig. 14a on a double logarithmic scale in order to investigate the long time behavior. The distributions do decay in the picosecond range with a clear concentration dependence, i.e.



Supplementary Figure 14. Distributions of proton-transfer waiting times (a) and of the life times of the transient  $\text{H}_5\text{O}_2^+$  clusters, i.e. the trajectory lengths, (b) in HCl solutions at various concentrations as obtained from ab initio MD simulations. The same data as in a is also shown in Fig. 5c in the main text. For comparison, single exponential decays,  $p(t) = \exp(-t/\tau)/\tau$ , using the mean of the distributions  $\tau$  reported in the legend, are plotted as black broken lines.

the distributions have a longer tail for higher concentrations. Still, a single exponential fit using the mean of the distribution  $\tau_{\text{TW}}$  as the decay time scale,  $p_{\text{TW}}(t) = \exp(-t/\tau_{\text{TW}})/\tau_{\text{TW}}$ , is sufficient to describe the long time tail of the distributions. However, since the excess protons are tracked only in the transient  $\text{H}_5\text{O}_2^+$  cluster, the transfer-waiting times can only capture proton transfer during the life times of these  $\text{H}_5\text{O}_2^+$  clusters, i.e. the lengths of the trajectories, that are defined according to the procedure that is detailed in Supplementary Methods 2. The distributions of trajectory lengths are given in Supplementary Fig. 14b. They are again compared to single exponential functions,  $p(t) = \exp(-t/\tau)/\tau$ , shown as black broken lines, with the mean values of the distributions as the decay constants  $\tau$ . For all three concentrations the mean values are about 1.5 times larger than the respective waiting-times reported in Supplementary Fig. 14a, indicating that on average one to two transfers occur during the life time of a transient  $\text{H}_5\text{O}_2^+$  cluster.

### Identity auto-correlation functions

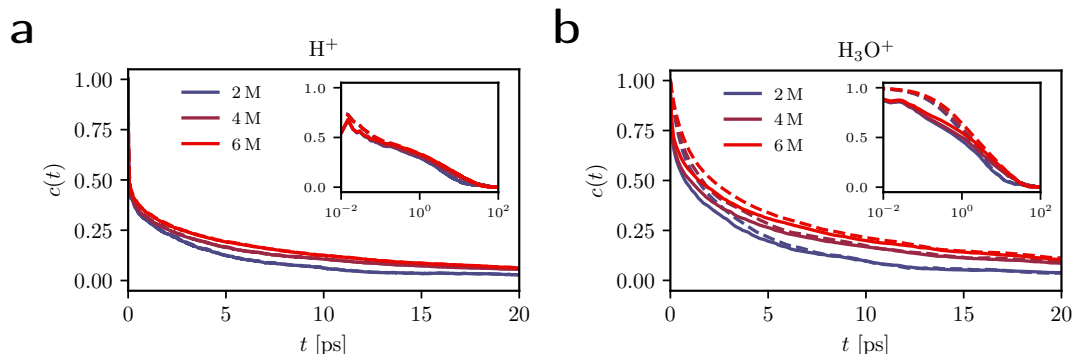
To describe the long time scales of excess-proton diffusion observed in the anisotropy decay of 2D IR experiments [27, 38], correlation times of the excess-proton identity have proven useful. Inspired by previous work [9, 19, 46], we computed auto-correlation functions of

the excess-proton and hydronium-oxygen identities from joint trajectories of the excess protons as also prepared for the analysis of the long-time diffusion properties described in Supplementary Note 8. Following this protocol, the excess protons are given as the remaining protons after the water molecules are assembled for each oxygen atom with the closest two hydrogen atoms at each time step of the simulation. Hydronium ions are defined by an excess proton together with the water molecule of the closest oxygen atom. Therefore, at each time step a total number of excess protons  $N_{\text{H}^+}$ , as well as hydronium ions, equivalent to the number of chloride ions in the simulation, is obtained. The trajectories are then stitched together to give  $N_{\text{H}^+}$  trajectories, each of the length of the whole simulation, for the excess protons and hydronium oxygens, respectively. Following Arntsen et al. [19], rapid back-and-forth fluctuation of hydronium-oxygen identities is ‘filtered’ from the trajectories by the following procedure. Whenever along a trajectory the identity changes from one oxygen atom to another, we check whether the identity returns to the original nucleus within 0.5 ps. If it returns without passing to a third nucleus in between, the identity remains with the original nucleus as if the identity did not change throughout this time. For the excess-proton identities this criterion does not suffice since the identity often fluctuates between three candidates within one hydronium ion. Rather the same procedure as also detailed in Supplementary Note 8 and similar to Calio et al. [9] is used to ‘filter’ the rapid back-and-forth fluctuation of excess-proton identities, i.e. the ‘special pair dance’: The candidate proton that either performs the next transfer to another water molecule or is the next to be identified as an excess proton while neighboring a chloride atom, remains the excess proton. These procedures define sets of trajectories from which the fast identity fluctuations are ‘filtered’. The identity auto-correlation functions are then calculated for excess-proton and hydronium-oxygen identities on both sets of trajectories, ‘filtered’ and ‘unfiltered’.

We define the identity auto-correlation function as

$$c(t) = \frac{\langle h(t)h(0) \rangle - \langle h \rangle^2}{\langle h \rangle - \langle h \rangle^2}, \quad (23)$$

where  $h(t)$  is one if an excess proton or hydronium oxygen atom has the same identity, i.e. is the same nucleus, as at  $t = 0$ , otherwise  $h(t)$  is zero. In our definition the identity auto-correlation function is designed to reach unity for  $t = 0$  and to decay to zero for long times and is thereby slightly different compared to previous work [19, 46, 47]. Additionally,



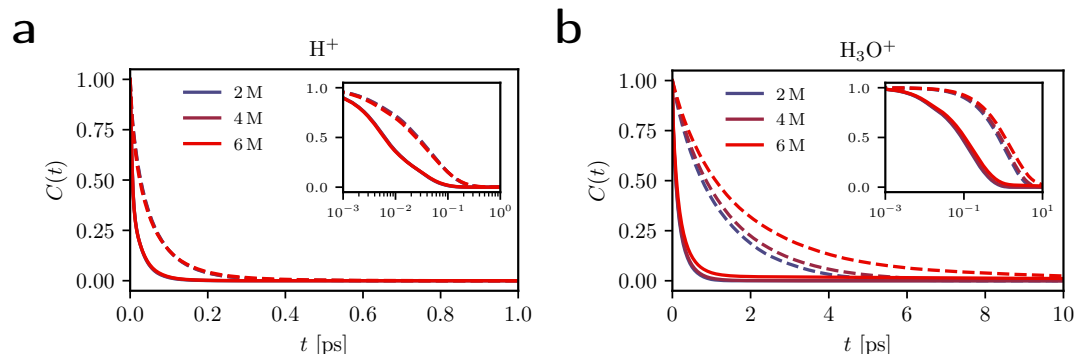
Supplementary Figure 15. Identity auto-correlation functions eq. (23) of the excess protons (a) and hydronium oxygens (b) obtained from ab initio MD simulations of HCl solutions at various concentrations. The correlations functions are computed from unfiltered (solid colored lines) and filtered trajectories (broken colored lines), see text for details. The data is shown on a logarithmic time axis in the insets.

the continuous identity auto-correlation function is given as [9, 19]

$$C(t) = \frac{\langle H(t)H(0) \rangle}{\langle H \rangle}, \quad (24)$$

where  $H(t)$  is one as long as an excess proton or hydronium oxygen atom continuously has the same identity for the entire time interval  $[0, t]$  and zero otherwise.

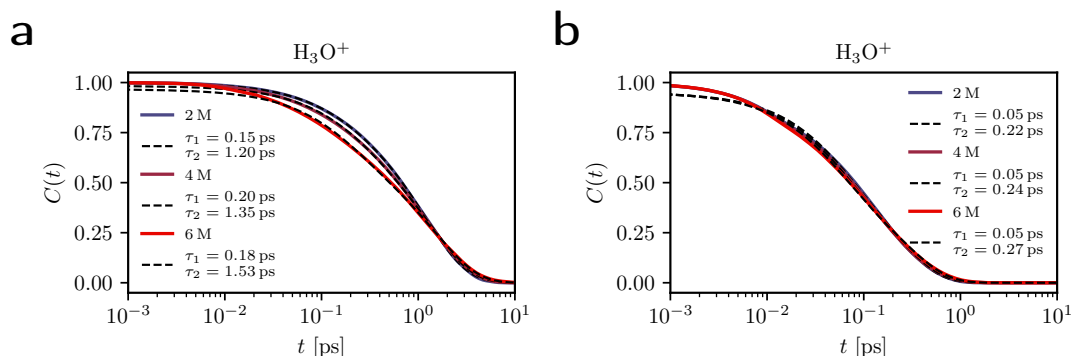
The excess-proton and hydronium-oxygen identity auto correlations obtained from our data according to eq. (23) are given in Supplementary Figs. 15a and b with the same data shown on a logarithmic time axis in the insets. Auto-correlation functions of the filtered trajectories are shown as broken colored lines for the three HCl solutions at various concentrations while the auto-correlation functions of the unfiltered trajectories are shown as solid colored lines. The curves decay on multiple time scales. All show remarkable long-time behavior beyond several picoseconds, indicating that proton as well as hydronium identity is correlated over very long times scales, which occurs from looping of identities over several different nuclei [46]. As expected, the two types of data from filtered or unfiltered trajectories converge in these long time regimes. Both, the excess-proton identity auto correlations in Supplementary Fig. 15a and the hydronium identities in Supplementary Fig. 15b show a clear concentration dependence, with longer decay times for higher concentrations. On short time scales the excess-proton identity auto correlations largely decay within 0.1 ps to a value of 0.5, whereas



Supplementary Figure 16. Continuous identity auto-correlation functions eq. (24) of the excess protons (a) and hydronium oxygens (b) obtained from ab initio MD simulations of HCl solutions at various concentrations. The correlations functions are computed from filtered (solid colored lines) and unfiltered trajectories (broken colored lines), see text for details. The data is shown on a logarithmic time axis in the insets.

the hydronium identity auto correlations decay to a value of 0.5 only after about 1 ps to 2 ps. Furthermore, a slight peak in the hydronium identity auto-correlation of the unfiltered trajectories (solid colored lines in Supplementary Fig. 15b) at about 0.025 ps indicates back-and-forth transfer of the excess proton in the transient  $\text{H}_5\text{O}_2^+$  cluster occurring at about twice the transfer-path time,  $\tau_{\text{TP}} = 12.6$  fs to 14.3 fs reported in the main text. Similarly, a peak in the excess-proton identity auto correlations of the unfiltered trajectories (solid colored lines in Supplementary Fig. 15a) at about 0.010 ps indicates the time scale of excess-proton rattling within a single hydronium ion, referred to as ‘special pair dance’ in the literature [8, 9].

Next, to focus on the fast time scales of the correlations, the continuous identity auto-correlation functions according to eq. (24) of the excess protons and of the hydronium oxygens are given in Supplementary Figs. 16a and b with the same data shown on logarithmic time axes in the insets. Again, the data is shown in each plot as computed from filtered (broken colored lines) and unfiltered trajectories (solid colored lines). Note, that for the computation of these continuous identity auto correlations, configurations where the excess-proton is located between the oxygen atom and a chloride ion are excluded. These configurations obviously produce spurious long-time auto correlations but have been analyzed to make up only 5% of the total trajectory lengths of all excess protons even at the highest concentration of 6 M,



Supplementary Figure 17. Continuous identity auto-correlation functions eq. (24) of the hydronium oxygens obtained from ab initio MD simulations of HCl solutions at various concentrations (already shown in Supplementary Fig. 16b). The correlation functions are computed from filtered (a) and unfiltered trajectories (b), see text for details. Each curve is fitted to a sum of two decaying exponentials with the time scales reported in the legends and shown as black broken lines.

which is discussed in detail in Supplementary Note 4. The excess-proton continuous identity auto correlations decay fully within 0.3 ps and the hydronium-oxygen identity continuous auto-correlations within 10 ps. In contrast to the data presented in Supplementary Fig. 15a and b, while the hydronium identity auto correlations in Supplementary Fig. 16b show again a clear concentration dependence, with longer decay times for higher concentrations, such a dependence is not visible for the excess-proton identity auto correlations in Supplementary Fig. 16a.

The time scales of the hydronium continuous identity auto correlations have been interpreted to be consistent with the time scales of the anisotropy decay observed in 2D IR experiments [19, 38]. Fits to these auto correlations with the sum of two decaying exponentials are therefore given as broken black lines, together with the original data from Supplementary Fig. 16b repeated as solid colored lines in Supplementary Fig. 17a (for the filtered trajectories) and b (for the unfiltered trajectories). The long time-scales of the bi-exponential fits to the correlations of the filtered trajectories, shown in 17a, reach from 1.2 ps to 1.53 ps, increasing with concentration. These time scales match the time scales reported for uni-directional proton transfer rather well (see Supplementary Tab. IV). With regard to the results reported in Supplementary Note 8, where the long-time diffusion constants are found to be too small by a factor of about four when compared to experiment, one would expect the time scales

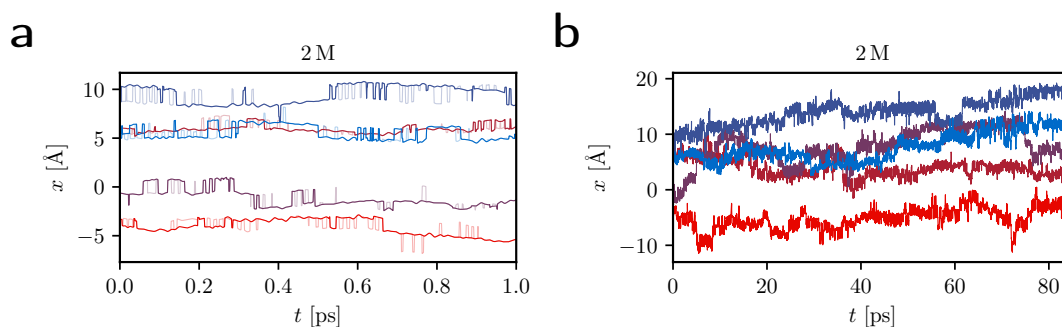
for uni-directional proton transfer to be longer by the same factor. However, the present analysis excludes configurations involving chloride ions, which presumably are characterized by longer decay times. The diffusion constants on the other hand would have to be split in vehicular diffusion, due to translation of hydronium ions, and the jump diffusion, due to uni-directional proton transfer, to allow for a better comparison to the time scales of the auto correlations.

When regarding the long time-scales of the bi-exponential fits to the correlations of the unfiltered trajectories, shown in Supplementary Fig. 17b, which reach from 0.22 ps to 0.27 ps, increasing with concentration, we find them to match perfectly the mean proton-transfer waiting times reported in the main text and in Supplementary Fig. 14. The continuous hydronium identity auto correlation therefore presents an alternative and intuitive interpretation for the proton-transfer waiting times that we discuss in the main text. In case that back-and-forth fluctuations of the excess-protons between two oxygen atoms within 0.5 ps are filtered from the trajectories, the continuous hydronium identity auto correlation in Supplementary Fig. 17a decays on time scales that match experimental spectroscopic anisotropy decays and have been interpreted as uni-directional proton transfer.

## Supplementary Note 8:

### Large-scale excess-proton diffusion

For the analysis of diffusion of the excess protons on long time scales, the principle excess-proton identification and selection scheme detailed in Supplementary Methods 2 needs to be augmented to identify joint excess-proton trajectories throughout the whole simulation trajectory. For this, excess protons are first identified based on a geometric criterion: after assembling at each time step the water molecules for each oxygen atom with the closest two hydrogen atoms, the remaining least associated protons form hydronium ions with their respective closest water molecules. We thereby obtain at each time step a total number of excess protons  $N_{\text{H}^+}$  equivalent to the number of chloride ions in the simulations. The trajectories of the excess protons are then stitched together to a total of  $N_{\text{H}^+}$  trajectories, each of the length of the whole simulation. In contrast to Supplementary Methods 2, protons that reside between an oxygen and a chloride atom are included in this analysis. The procedure obviously introduces jumps in the joint trajectories whenever an excess proton changes identity, which is a manifestation of the Grotthuss' process. However, rapid spurious jumps within the same hydronium ion, the 'special pair dance' [8, 9], are filtered from the trajectories by the following procedure: within each hydronium ion, the candidate proton that either performs the next transfer to another water molecule or is the next to be identified as an excess proton while neighboring a chloride atom, remains the excess proton (a procedure

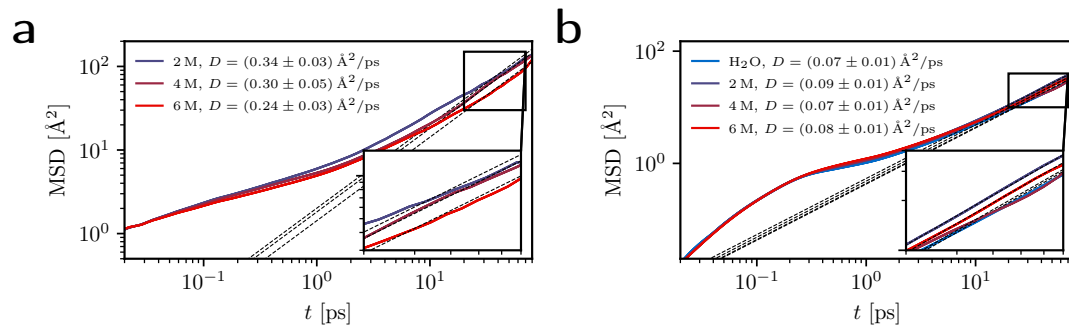


Supplementary Figure 18. Examples of five joint trajectories of excess protons in 2M HCl solution on short (a) and long time scales (b). In a, the pale colored lines indicate the spurious jumps, resulting from the 'special pair dance', that are removed from the trajectories (see text for details).



*B. Supplementary Information:*

*Spectral Signatures of Excess-Proton Waiting and Transfer-Path Dynamics in Aqueous Hydrochloric Acid Solutions*



Supplementary Figure 19. MSDs (mean squared displacements) in the lab frame,  $\langle |\mathbf{r}(t) - \mathbf{r}(0)|^2 \rangle$ , of the excess protons (a) and the oxygen atoms (b) computed from the simulation trajectories of HCl solutions at three concentrations. In b, the MSD of the oxygen atoms in the pure-water simulations is shown as well. Errors of the mean are indicated by the line widths and taken from standard deviations computed over the individual excess-proton and oxygen-atom joint trajectories. Linear fits are shown as black broken lines, which are fitted in the long time regimes, 20 ps to 80 ps, which is the range that is also shown enlarged in the insets.

that was also used by Calio et al. [9]). Lastly, the trajectories are unwrapped over the periodic boundary conditions. Some trajectories of excess protons produced by this protocol are illustrated in Supplementary Fig. 18a and b along a single Cartesian coordinate and on two different time scales. Additionally in Supplementary Fig. 18a, the pale colored lines show the trajectories before removal of the ‘special pair dance’.

Subsequently, the joint trajectories are used to calculate mean squared displacements (MSDs),  $\langle |\mathbf{r}(t) - \mathbf{r}(0)|^2 \rangle$ , of the excess protons in the lab frame. The MSDs averaged over all excess protons are shown in Supplementary Fig. 19a for simulations of HCl solutions at three different concentrations and compared to the MSDs computed for the oxygen atoms representative of the water molecules in Supplementary Fig. 19b. In general, the MSD is expected to show inertial scaling,  $\text{MSD} \sim t^2$ , for short time scales and diffusive scaling,  $\text{MSD} \sim t$ , for long time scales. Both regimes are well visible in Supplementary Fig. 19b for the oxygen atoms. For the excess protons the inertial regime is perturbed by the jumps in the joint trajectories, caused by changes of the excess-proton identities.

The diffusion constant  $D$ , which is an experimentally observed quantity, is related to the

MSD by

$$D = \frac{1}{6t} \langle |\mathbf{r}(t) - \mathbf{r}(0)|^2 \rangle, \quad (25)$$

and computed by a least-squares fit of the slopes in the diffusive regime between 20 ps to 80 ps. The diffusion constants are reported in the legends of Supplementary Figs. 19a and b with statistical errors from the linear fits.

To access the accuracy of these diffusion constants, we first focus on the values for the oxygen atoms. Within the error the same diffusion constant of about  $D_{\text{O}} = 0.08 \text{ \AA}^2/\text{ps}$  was obtained in all four simulations. While this value is significantly smaller than the experimental value of  $D_{\text{O}} = 0.23 \text{ \AA}^2/\text{ps}$  [48, 49], it is well known that specifically the BLYP exchange-correlation functional in our simulation approach produces too small diffusion constants. In agreement with our results, various studies of water utilizing ab initio MD together with the BLYP exchange-correlation functional, reported diffusion constants in the range of  $0.04 \text{ \AA}^2/\text{ps}$  to  $0.11 \text{ \AA}^2/\text{ps}$  for comparable setups to ours, as reviewed recently [50].

When regarding the excess proton diffusion constant, it has to be noted that it is known to be heavily concentration and temperature dependent in experiments [23]. In the dilute limit, the experimental diffusion constant of the excess proton,  $D_{\text{H}^+} = 0.94 \text{ \AA}^2/\text{ps}$ , is much higher than the experimental diffusion constant of water by a factor of  $D_{\text{H}^+}/D_{\text{O}} = 4.1$ , an observation that corroborates Grotthuss' hypothesis [51]. However, this factor drops to about 3.0 at 2 M and 1.5 at 6 M [23]. This trend was qualitatively captured in self-consistent iterative multistate empirical valence bond (SCI-MS-EVB) simulations of HCl [16, 17]. Both studies obtained values between  $D_{\text{H}^+} = 0.2 \text{ \AA}^2/\text{ps}$  to  $0.3 \text{ \AA}^2/\text{ps}$  around 1 M and  $D_{\text{H}^+} = 0.15 \text{ \AA}^2/\text{ps}$  to  $0.20 \text{ \AA}^2/\text{ps}$  around 3 M, compared to a value of  $D_{\text{H}^+} = 0.37 \text{ \AA}^2/\text{ps}$  in the dilute limit (one excess proton in 256 waters) [13]. While a similar trend is also indicated by our simulation data, the errors are too large to draw definite conclusions. The obtained diffusion constants for the excess protons,  $D_{\text{H}^+} = 0.24 \text{ \AA}^2/\text{ps}$  to  $0.34 \text{ \AA}^2/\text{ps}$ , are smaller than the experimental value. However, the ratios  $D_{\text{H}^+}/D_{\text{O}} = 0.34/0.09 = 3.8 \pm 0.8$  for 2 M,  $D_{\text{H}^+}/D_{\text{O}} = 0.30/0.07 = 4.3 \pm 1.3$  for 4 M and  $D_{\text{H}^+}/D_{\text{O}} = 0.24/0.08 = 3.0 \pm 0.8$  for 6 M, that are observed in our simulations, seem in satisfactory agreement with experiments. Similar ab initio simulation setups to ours but using a single excess proton in a box of water molecules obtained diffusion constants of  $D_{\text{H}^+} = 0.3 \text{ \AA}^2/\text{ps}$  to  $0.6 \text{ \AA}^2/\text{ps}$  [22] and of  $D_{\text{H}^+} = 0.3 \text{ \AA}^2/\text{ps}$  to  $0.8 \text{ \AA}^2/\text{ps}$  [19]. A study employing Car-Parrinello molecular-dynamics (CPMD) simulations

of 1.7 M HCl solutions and the PBE exchange-correlation functional found  $D_{\text{H}^+} = 0.9 \text{ \AA}^2/\text{ps}$  to  $1.1 \text{ \AA}^2/\text{ps}$  compared to  $D_{\text{O}} = 0.04 \text{ \AA}^2/\text{ps}$  to  $0.07 \text{ \AA}^2/\text{ps}$  for the water molecules [18]. An older study of a single excess proton in a box of 64 water molecules using CPMD with the BLYP functional obtained  $D_{\text{H}^+} = 0.05 \text{ \AA}^2/\text{ps}$  to  $0.08 \text{ \AA}^2/\text{ps}$  compared to  $D_{\text{O}} = 0.02 \text{ \AA}^2/\text{ps}$  to  $0.06 \text{ \AA}^2/\text{ps}$  for the water molecules [52]. The inclusion of nuclear quantum effects in simulations has been shown to significantly increase the obtained excess-proton diffusion constants [13].

We conclude that the accurate estimation of diffusion constants for the excess proton remains challenging, which is seen from the wide spread of results obtained in previous studies. Our results for the diffusion constants appear reasonable when compared to previously reported values and specifically the ratios  $D_{\text{H}^+}/D_{\text{O}} = 3.0$  to  $4.3$  are in good agreement with experiment.

## Supplementary Note 9:

### Hydrogen-bond structure

The hydrogen bond (HB) structure of the water molecules in the first hydration shell of the excess proton has been shown to play an important role for when and where the excess proton moves [11, 13, 18, 22]. In this Supplementary Note the HB structure around the excess protons in HCl solutions obtained in our ab initio simulations is discussed using some previously established methods. We follow the standard criterion and define HBs to be present when the distance between two oxygens, i.e. the donor and the acceptor of the HB, is  $< 3.5 \text{ \AA}$ , and the angle between the vector connecting the two oxygens and the vector connecting the donor oxygen with the hydrogen atom is  $< 30^\circ$  [47].

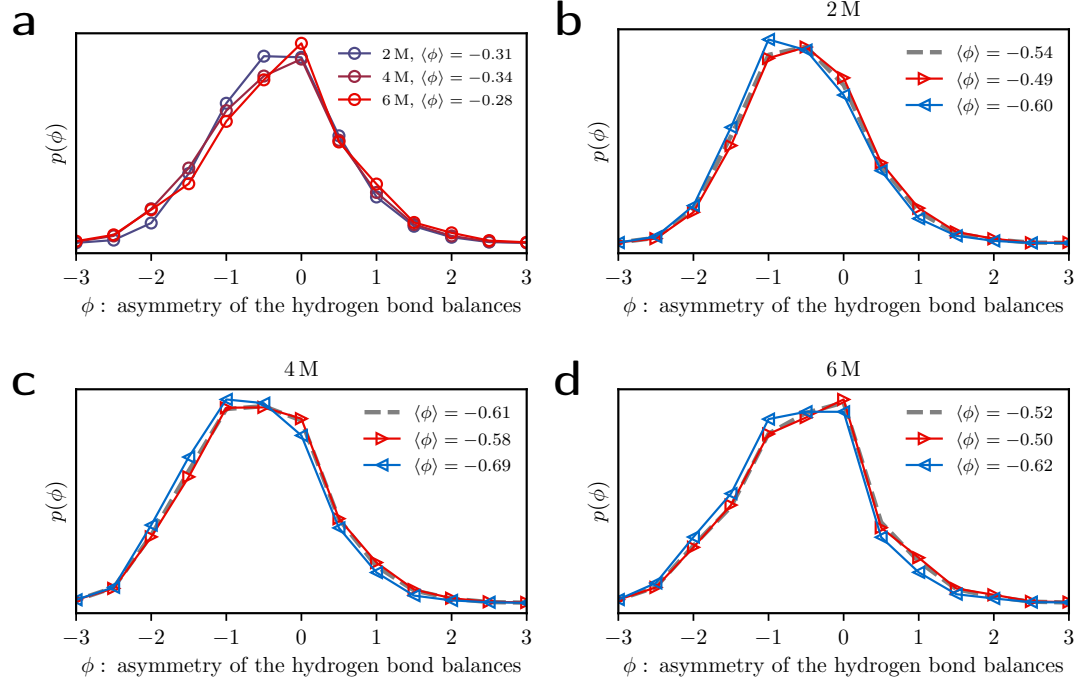
### Hydrogen-bond asymmetry

Napoli et al. [11] introduced the HB asymmetry  $\phi$  as a measure to identify the excess proton among the candidate protons in a hydronium ion. First, each water molecule is assigned a coordination number as the difference of the number of acceptor HBs minus the number of donor HBs. Then  $\phi$  is defined for each candidate proton at each time step as the coordination number of the closest neighboring water molecule minus the average of the coordination numbers of the closest water molecules of the other candidate protons of the same hydronium ion. By construction, the sum of  $\phi$  within a hydronium ion is zero. Napoli et al. [11] found that protons with strongly negative values of  $\phi$  show the typical spectral signatures associated with excess protons. We applied this measure to our simulation data, specifically to the joint trajectories of the excess protons that were prepared for the analysis of the long time diffusion in Supplementary Note 8 and from which the spurious ‘special pair dance’ was removed.

Normalized distributions of  $\phi$  over the whole simulations are shown in Supplementary Fig. 20a with mean values given in the legend. The mean values are clearly negative and we therefore conclude that this criterion agrees with our excess-proton identification scheme. To study the relation of HB structure with proton transfer, we filter the trajectories in time and regard the normalized distributions of  $\phi$  values around the transfer events, when an excess proton changes its closest oxygen. Distributions of  $\phi$  during 20 fs (40 time steps) before and after

*B. Supplementary Information:  
Spectral Signatures of Excess-Proton Waiting and Transfer-Path Dynamics in Aqueous Hydrochloric Acid Solutions*

---



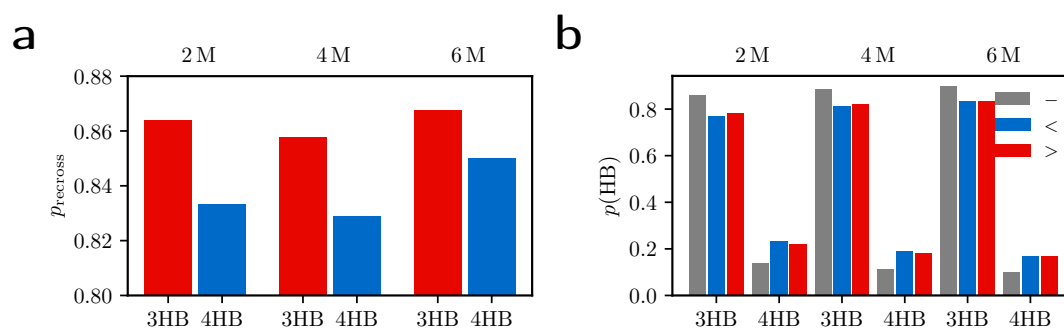
Supplementary Figure 20. Normalized distributions of the hydrogen bond asymmetries, denoted as  $\phi$ , of the excess proton trajectories from ab initio MD simulations of HCl solutions at various concentrations. See text for definition and details. Mean values of the distributions are reported in the legends. **a**: Distributions over the whole trajectories. **b–d**: Distributions of  $\phi$  during 20 fs before and after any transfer event (grey broken lines), i.e. when the excess proton changes the closest oxygen, and distributions of  $\phi$  around each uni-directional transfer event, which are split into the 20 fs before, corresponding to the donor oxygen of the proton transfer event (blue and left pointing triangles) and the 20 fs after, corresponding to the acceptor oxygen (red and right pointing triangles).

a transfer event are given in Supplementary Fig. 20b–d as grey broken lines with mean values reported in the legends. To further elucidate the data, we applied the same filter before and after each uni-directional transfer event. Uni-directional here refers to transfer events, that are not followed by a fast return back to the original oxygen atom within the following 50 fs (100 time steps). By only regarding these uni-directional events, we can discriminate different HB configurations around the donor oxygen of the proton-transfer

event, i.e. before the uni-directional transfer (shown in blue with left pointing triangles), and the acceptor oxygen, i.e. after the uni-directional transfer (shown in red with right pointing triangles), which show distinct distributions in Supplementary Fig. 20b–d. The mean values of the distributions before a transfer are more negative than the corresponding averages in Supplementary Fig. 20a, indicating that on average a more negative value of  $\phi$  precedes an imminent transfer event. Therefore,  $\phi$  actually seems to be a useful predictor for proton transfer.

### The fourth hydrogen bond

Inspired by Tse et al. [22], Biswas et al. [13] and Fischer and Gunlycke [18] investigated the role of a fourth water molecule hydrogen-bonded to the hydronium ion. Presumably, its presence determines whether an excess proton would transfer to a different oxygen atom [13] and in particular whether it is likely to return to the original oxygen atom, i.e. to perform back-and-forth transfers, or not [18]. In their simulations of 1.7 M HCl solutions, Fischer and Gunlycke [18] observed a higher return probability (67 %) if the hydronium ion was



Supplementary Figure 21. Correlations between the existence of a fourth hydrogen bond of a hydronium ion (4HB) and the return probability of the excess proton, as observed in ab initio MD simulations of HCl solutions at various concentrations. **a**: Probability of the excess proton to return across the mid plane between the oxygens within the following 50 fs. **b**: Time-averaged probabilities of all hydronium ions for the fourth hydrogen bond to exist (4HB) or not (3HB), as obtained from the whole simulation (grey, no hatching) and during the 20 fs before (blue) and after (red) each uni-directional transfer event.

coordinated with only three donor HBs as compared to four HBs (53 %), the additional one being an accepted HB from a fourth water molecule. In accordance with previous works, the fourth HB is defined to be present if the vector connecting the hydronium oxygen and the hydrogen atom of the fourth water molecule has a length of less than 2.6 Å and points at an angle of less than 35° with respect to the normal of the plane spanned by the three hydrogen nuclei of the hydronium ion [18, 22]. The probability of a return within the following 50 fs (100 time steps) upon any transfer across the mid plane between the oxygens obtained in our simulations is illustrated in Supplementary Fig. 21a depending on whether the donor hydrogen ion is accepting a HB from a fourth water molecule (4HB, shown in blue with hatching) or not (3HB, shown in red without hatching). The data shows the clear trend that the return probability is reduced if a fourth HB is present, in agreement with previous studies [18]. However, even though this correlation is discernible in our data, the mechanism does not appear to be a dominant driver for proton transfer in HCl solutions. This follows from Supplementary Fig. 21b, where the probability of observing the fourth HB is plotted for three different time averages; the averages over the whole simulations of all hydronium ions are given in grey, the averages over the 20 fs (40 time steps) before and after each uni-directional transfer event, i.e. without return, are given in blue and red respectively. Throughout the data, the time-averaged probability of a fourth HB is only about 10–20%. Before and after uni-directional transfer events this probability is significantly increased but it is still smaller than the probability of a uni-directional transfer event happening without the presence of a fourth HB.

We confirm that HB structure is highly correlated with the excess-proton transfer dynamics and the presented comparison with previous studies strengthens the existing hypotheses, that the HB asymmetry  $\phi$  or the fourth water molecule are useful descriptors.

---

## Supplementary References

- [1] Bertie, J. E. & Lan, Z. Infrared intensities of liquids XX: The intensity of the OH stretching band of liquid water revisited, and the best current values of the optical constants of H<sub>2</sub>O(l) at 25°C between 15,000 and 1 cm<sup>-1</sup>. *Appl. Spectrosc.* **50**, 1047 (1996).
- [2] Jackson, J. D., *Classical electrodynamics* (John Wiley & Sons, Inc., 1999).
- [3] Lucarini, V., Saarinen, J. J., Peiponen, K.-E. & Vartiainen, E. M., *Kramers-Kronig relations in optical materials research*, vol. 110 (Springer Science & Business Media, 2005).
- [4] Goplen, T. G., Cameron, D. G. & Jones, R. N. The Control of Errors in Infrared Spectrophotometry. VI. The Evaluation of Optical Constants by Combined Transmission and Attenuated Total Reflection Measurements. *Appl. Spectrosc.* **34**, 652 (1980).
- [5] Mayerhöfer, T. G. & Popp, J. Quantitative Evaluation of Infrared Absorbance Spectra – Lorentz Profile versus Lorentz Oscillator. *ChemPhysChem* **20**, 31 (2019).
- [6] Schienbein, P., Schwaab, G., Forbert, H., Havenith, M. & Marx, D. Correlations in the solute-solvent dynamics reach beyond the first hydration shell of ions. *J. Phys. Chem. Lett.* **8**, 2373 (2017).
- [7] Marx, D., Tuckerman, M. E., Hutter, J. & Parrinello, M. The nature of the hydrated excess proton in water. *Nature* **397**, 601 (1999).
- [8] Markovitch, O. *et al.* Special pair dance and partner selection: Elementary steps in proton transport in liquid water. *J. Phys. Chem. B* **112**, 9456 (2008).
- [9] Calio, P. B., Li, C. & Voth, G. A. Resolving the Structural Debate for the Hydrated Excess Proton in Water. *J. Am. Chem. Soc.* **143**, 18672 (2021).
- [10] Wiener, N. Generalized harmonic analysis. *Acta Math.* **55**, 117 (1930).
- [11] Napoli, J. A., Marsalek, O. & Markland, T. E. Decoding the spectroscopic features and time scales of aqueous proton defects. *J. Chem. Phys.* **148**, 222833 (2018).
- [12] Markland, T. E. & Ceriotti, M. Nuclear quantum effects enter the mainstream. *Nat. Rev. Chem.* **2**, 0109 (2018).
- [13] Biswas, R., Tse, Y. L. S., Tokmakoff, A. & Voth, G. A. Role of Presolvation and Anharmonicity in Aqueous Phase Hydrated Proton Solvation and Transport. *J. Phys. Chem. B* **120**, 1793



- (2016).
- [14] Baer, M. D., Fulton, J. L., Balasubramanian, M., Schenter, G. K. & Mundy, C. J. Persistent ion pairing in aqueous hydrochloric acid. *J. Phys. Chem. B* **118**, 7211 (2014).
- [15] Fulton, J. L. & Balasubramanian, M. Structure of Hydronium ( $\text{H}_3\text{O}^+$ )/ Chloride ( $\text{Cl}^-$ ) Contact Ion Pairs in Aqueous Hydrochloric Acid Solution : A Zundel-like. *J. Am. Chem. Soc.* **132**, 12597 (2010).
- [16] Xu, J., Izvekov, S. & Voth, G. A. Structure and dynamics of concentrated hydrochloric acid solutions. *J. Phys. Chem. B* **114**, 9555 (2010).
- [17] Calio, P. B., Li, C. & Voth, G. A. Molecular Origins of the Barriers to Proton Transport in Acidic Aqueous Solutions. *J. Phys. Chem. B* **124**, 8868 (2020).
- [18] Fischer, S. A. & Gunlycke, D. Analysis of Correlated Dynamics in the Grotthuss Mechanism of Proton Diffusion. *J. Phys. Chem. B* **123**, 5536 (2019).
- [19] Arntsen, C., Chen, C., Calio, P. B., Li, C. & Voth, G. A. The hopping mechanism of the hydrated excess proton and its contribution to proton diffusion in water. *J. Chem. Phys.* **154**, 194506 (2021).
- [20] Kundu, A. *et al.* Hydrated Excess Protons in Acetonitrile/Water Mixtures: Solvation Species and Ultrafast Proton Motions. *J. Phys. Chem. Lett.* **10**, 2287 (2019).
- [21] Carpenter, W. B. *et al.* Decoding the 2D IR spectrum of the aqueous proton with high-level VSCF/VCI calculations. *J. Chem. Phys.* **153**, 124506 (2020).
- [22] Tse, Y. L. S., Knight, C. & Voth, G. A. An analysis of hydrated proton diffusion in ab initio molecular dynamics. *J. Chem. Phys.* **142**, 014104 (2015).
- [23] Dippel, T. & Kreuer, K. D. Proton transport mechanism in concentrated aqueous solutions and solid hydrates of acids. *Solid State Ionics* **46**, 3 (1991).
- [24] Daly, C. A. *et al.* Decomposition of the Experimental Raman and Infrared Spectra of Acidic Water into Proton, Special Pair, and Counterion Contributions. *J. Phys. Chem. Lett.* **8**, 5246 (2017).
- [25] Fournier, J. A., Carpenter, W. B., Lewis, N. H. & Tokmakoff, A. Broadband 2D IR spectroscopy reveals dominant asymmetric  $\text{H}_5\text{O}_2^+$  proton hydration structures in acid solutions. *Nat. Chem.* **10**, 932 (2018).
- [26] Biswas, R., Carpenter, W., Fournier, J. A., Voth, G. A. & Tokmakoff, A. IR spectral assignments for the hydrated excess proton in liquid water. *J. Chem. Phys.* **146**, 154507 (2017).

- 
- [27] Thämer, M., De Marco, L., Ramasesha, K., Mandal, A. & Tokmakoff, A. Ultrafast 2D IR spectroscopy of the excess proton in liquid water. *Science* **350**, 78 (2015).
- [28] Hansen, J.-P. & McDonald, I. R., *Theory of simple liquids: with applications to soft matter* (Academic press, 2013).
- [29] Carpenter, W. B., Lewis, N. H., Fournier, J. A. & Tokmakoff, A. Entropic barriers in the kinetics of aqueous proton transfer. *J. Chem. Phys.* **151**, 034501 (2019).
- [30] VandeVondele, J. & Hutter, J. Gaussian basis sets for accurate calculations on molecular systems in gas and condensed phases. *J. Chem. Phys.* **127**, 114105 (2007).
- [31] VandeVondele, J. *et al.* Quickstep: Fast and accurate density functional calculations using a mixed Gaussian and plane waves approach. *Comput. Phys. Commun.* **167**, 103 (2005).
- [32] Brüning, F. N., Hillmann, P., Kim, W. K., Daldrop, J. O. & Netz, R. R., Proton-transfer spectroscopy beyond the normal-mode scenario (2021), Preprint at arXiv:2109.08514.
- [33] Sauer, J. & Döbler, J. Gas-phase infrared spectrum of the protonated water dimer: Molecular dynamics simulation and accuracy of the potential energy surface. *ChemPhysChem* **6**, 1706 (2005).
- [34] Agmon, N. The Grotthuss mechanism. *Chem. Phys. Lett.* **244**, 456 (1995).
- [35] Meiboom, S. Nuclear magnetic resonance study of the proton transfer in water. *J. Chem. Phys.* **34**, 375 (1961).
- [36] Woutersen, S. & Bakker, H. J. Ultrafast vibrational and structural dynamics of the proton in liquid water. *Phys. Rev. Lett.* **96**, 138305 (2006).
- [37] Dahms, F., Fingerhut, B. P., Nibbering, E. T., Pines, E. & Elsaesser, T. Large-amplitude transfer motion of hydrated excess protons mapped by ultrafast 2D IR spectroscopy. *Science* **357**, 491 (2017).
- [38] Carpenter, W. B., Fournier, J. A., Lewis, N. H. & Tokmakoff, A. Picosecond Proton Transfer Kinetics in Water Revealed with Ultrafast IR Spectroscopy. *J. Phys. Chem. B* **122**, 2792 (2018).
- [39] Yuan, R. *et al.* Tracking Aqueous Proton Transfer by Two-Dimensional Infrared Spectroscopy and ab Initio Molecular Dynamics Simulations. *ACS Cent. Sci.* **5**, 1269 (2019).
- [40] Fischer, S. A., Dunlap, B. I. & Gunlycke, D. Correlated dynamics in aqueous proton diffusion. *Chem. Sci.* **9**, 7126 (2018).
- [41] Roy, S. *et al.* Resolving Heterogeneous Dynamics of Excess Protons in Aqueous Solution with

- Rate Theory. *J. Phys. Chem. B* **124**, 5665 (2020).
- [42] Hänggi, P., Talkner, P. & Borkovec, M. Reaction-rate theory: Fifty years after Kramers. *Rev. Mod. Phys.* **62**, 251 (1990).
- [43] Ciccotti, G., Ferrario, M., Hynes, J. T. & Kapral, R. Dynamics of ion pair interconversion in a polar solvent. *J. Chem. Phys.* **93**, 7137 (1990).
- [44] Roy, S., Baer, M. D., Mundy, C. J. & Schenter, G. K. Reaction Rate Theory in Coordination Number Space: An Application to Ion Solvation. *J. Phys. Chem. C* **120**, 7597 (2016).
- [45] Kappler, J., Daldrop, J. O., Brünig, F. N., Boehle, M. D. & Netz, R. R. Memory-induced acceleration and slowdown of barrier crossing. *J. Chem. Phys.* **148**, 014903 (2018).
- [46] Hassanali, A., Giberti, F., Cuny, J., Kühne, T. D. & Parrinello, M. Proton transfer through the water gossamer. *Proc. Natl. Acad. Sci. U. S. A.* **110**, 13723 (2013).
- [47] Luzar, A. & Chandler, D. Hydrogen-bond kinetics in liquid water. *Nature* **379**, 55 (1996).
- [48] Mills, R. Self-diffusion in normal and heavy water in the range 1-45°. *J. Phys. Chem.* **77**, 685 (1973).
- [49] Harris, K. R. & Woolf, L. A. Pressure and temperature dependence of the self diffusion coefficient of water and oxygen-18 water. *J. Chem. Soc. Faraday Trans. 1* **76**, 377 (1980).
- [50] Gillan, M. J., Alfè, D. & Michaelides, A. Perspective: How good is DFT for water? *J. Chem. Phys.* **144**, 130901 (2016).
- [51] Roberts, N. & Northey, H. L. Hydrogen Ion Mobility in Aqueous Electrolyte Solutions. *J. Chem. Soc. Faraday Trans. 1* **68**, 1528 (1972).
- [52] Izvekov, S. & Voth, G. A. Ab initio molecular-dynamics simulation of aqueous proton solvation and transport revisited. *J. Chem. Phys.* **123**, 044505 (2005).

Supporting Information:  
Time-Dependent Friction Effects on  
Vibrational Infrared Frequencies and Line  
Shapes of Liquid Water

---

*C*

**Supporting Information:  
Time-Dependent Friction Effects on  
Vibrational Infrared Frequencies and Line  
Shapes of Liquid Water**

Florian N. Brüning, Otto Geburtig, Alexander von Canal, Julian Kappler, and Roland  
R. Netz\*

*Freie Universität Berlin, Germany*

E-mail: rnetz@physik.fu-berlin.de

## I Infrared power spectra from linear-response theory

Assuming linear response of an observable  $x(t)$  with respect to a force that couples to an observable  $y(t)$ , the response function  $\chi_{xy}(t)$  is related to the correlation function  $C_{xy}(t') = \langle x(t+t')y(t) \rangle$  for  $t \geq 0$ <sup>S1</sup>

$$\chi_{xy}(t) = -\frac{1}{k_B T} \frac{d}{dt} C_{xy}(t), \quad (\text{S1})$$

where  $k_B T$  is the thermal energy. Realizing that  $\chi(t)$  is single-sided, i.e.  $\chi(t) = 0$  for  $t < 0$ , the Fourier transform is calculated as

$$\begin{aligned} \tilde{\chi}_{xy}(\omega) &= -\frac{1}{k_B T} \int_{-\infty}^{\infty} dt e^{i\omega t} \frac{d}{dt} C_{xy}(t) \\ \tilde{\chi}_{xy}(\omega) &= -\frac{1}{k_B T} \left( C_{xy}(0) - i\omega \int_0^{\infty} dt e^{i\omega t} C_{xy}(t) \right) \\ \tilde{\chi}_{xy}(\omega) &= -\frac{1}{k_B T} \left( C_{xy}(0) - i\omega \tilde{C}_{xy}^+(\omega) \right), \end{aligned} \quad (\text{S2})$$

where the superscript  $+$  denotes a single-sided Fourier transform. In case of  $x = y$ ,  $C_{xx}(t)$  is an autocorrelation function, which is real and symmetric, therefore it follows for the imaginary part of the response function in Fourier space

$$\tilde{\chi}_{xx}''(\omega) = \frac{1}{k_B T} \omega \operatorname{Re}(\tilde{C}_{xx}^+(\omega)) \quad (\text{S3})$$

$$= \frac{1}{k_B T} \frac{\omega}{2} \tilde{C}_{xx}(\omega). \quad (\text{S4})$$

When computing the power spectrum of a stochastic process  $x(t)$ , limited to the time domain  $[0, L_t]$ , the Wiener-Khintchine theorem, eq. (S96) in section XII, can be used to express  $\tilde{C}_{xx}(\omega)$  in terms of  $\tilde{x}(\omega)$ , turning eq. (S4) into

$$\tilde{\chi}_{xx}''(\omega) = \frac{\omega}{2k_B T L_t} |\tilde{x}(\omega)|^2. \quad (\text{S5})$$

When computing the power spectrum of the observable  $x(t)$  from the ensemble average of equilibrium trajectories, a decomposition of  $x(t)$  into two parts  $x(t) = x_1(t) + x_2(t)$  gives rise to three contributions in the total power spectrum

$$\begin{aligned}\omega \tilde{\chi}_{xx}''(\omega) &= \frac{\omega^2}{2k_B T} \left[ \tilde{C}_1(\omega) + \tilde{C}_2(\omega) + 2\tilde{C}_{1,2}(\omega) \right] \\ &= \omega \left[ \tilde{\chi}_1''(\omega) + \tilde{\chi}_2''(\omega) + \tilde{\chi}_{1,2}''(\omega) \right],\end{aligned}\tag{S6}$$

where the cross-correlation contribution  $\tilde{\chi}_{1,2}''(\omega)$  is defined such that it equals the difference spectrum

$$\begin{aligned}\tilde{\chi}_{\text{diff}}''(\omega) &= \tilde{\chi}_{xx}'' - \tilde{\chi}_1''(\omega) - \tilde{\chi}_2''(\omega) = \tilde{\chi}_{1,2}''(\omega) \\ &= \frac{\omega}{k_B T} \tilde{C}_{1,2}(\omega).\end{aligned}\tag{S7}$$

A positive cross-correlation spectrum hints to in-phase motion, a negative cross-correlation spectrum to out-of-phase motion of  $x_1(t+t')$  and  $x_2(t)$  at a given frequency.

In case of  $x(t)$  being the polarization  $\mathbf{p}(t)$  of the system, coupling to an external electric field  $\mathbf{E}(t)$ , the dimensionless dielectric susceptibility  $\chi(t)$  is given by

$$\tilde{\chi}(\omega) = \frac{1}{V\epsilon_0 D} \langle \tilde{\chi}_{\mathbf{p}\mathbf{p}}(\omega) \rangle,\tag{S8}$$

where  $\epsilon_0$  is the vacuum permittivity,  $V$  is the system volume and an average is performed over the  $D$  dimensions of  $\mathbf{p}$ .

## II Decomposition of water infrared spectra into single-molecular and collective components

Fig. S1A and B show a complete decomposition of the total (A, nuclear and electronic) and the nuclei-only (B, further discussed in section III) IR spectra obtained from aiMD simulations of 256 H<sub>2</sub>O molecules (gray solid lines), as introduced in the main text, into self (blue solid lines) and collective cross components (purple solid lines), which follow from the molecular dipole moments  $\mathbf{p}_i(t)$  of all the molecules in the bulk as<sup>S2</sup>

$$\tilde{\chi}''(\omega) = \tilde{\chi}_{\text{self}}''(\omega) + \tilde{\chi}_{\text{cross}}''(\omega) \quad (\text{S9})$$

$$\sim \left\langle \sum_i \mathbf{p}_i(0) \sum_j \mathbf{p}_j(t) \right\rangle = \sum_i \langle \mathbf{p}_i(0) \mathbf{p}_i(t) \rangle + \sum_i \langle \mathbf{p}_i(0) \sum_{j \neq i} \mathbf{p}_j(t) \rangle. \quad (\text{S10})$$

The data in fig. S1A clearly shows, that whereas in the OH stretching regime the collective cross-component effects are constructive and lead to an amplification of the total infrared spectrum with respect to the self spectrum, in the HOH bending regime the collective cross-component effects are destructive and lead to a slight decrease of the amplitude of the total IR spectrum with respect to the self spectrum. In the regime of the librations between 300 cm<sup>-1</sup> to 800 cm<sup>-1</sup> the collective effects contribute constructively as well as destructively. At the small signature around 200 cm<sup>-1</sup>, associated with translational vibrations of water molecules against each other, the collective cross-component effects contribute constructively.



C. Supporting Information:

Time-Dependent Friction Effects on Vibrational Infrared Frequencies and Line Shapes of Liquid Water

---

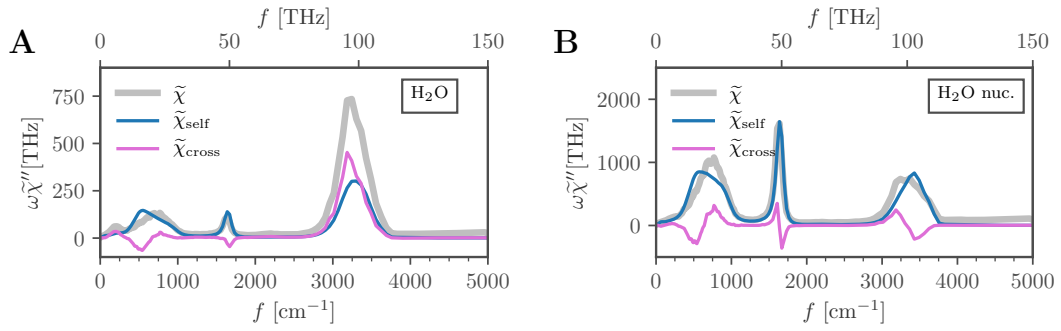


Figure S1: Decomposition of the infrared (IR) spectra (gray solid lines) into self (blue solid lines) and collective cross contributions (purple solid lines), obtained from the total dipole-moment trajectory from the ab initio Molecular Dynamics (aiMD) simulation of 256 H<sub>2</sub>O molecules including nuclear and electronic charges after Wannier localization (**A**) and an approximation using partial charges on the nuclear dynamics of the same aiMD simulation (**B**, see the following section III for details).

### III Infrared spectra from nuclear coordinates

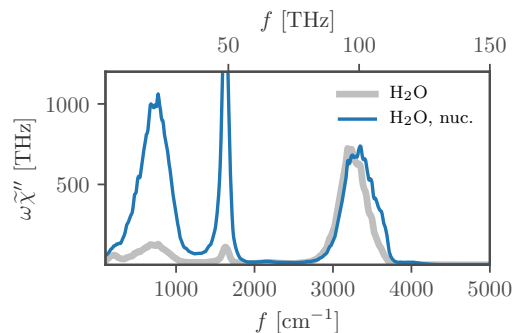


Figure S2: Comparison of IR spectra obtained from the total dipole-moment trajectory including nuclear and electronic charges from the aiMD simulation (gray solid line) and an approximation using partial charges on the nuclear dynamics of the same aiMD simulation (blue solid line).

Fig. S2 shows a comparison of the IR spectrum of the aiMD simulation, using the total dipole moment including nuclear and electronic charges and a nuclei-only power spectrum, which is obtained by assigning the partial charges  $1e$  to the hydrogen atoms and  $-2e$  to the oxygen atoms of the aiMD simulation in post processing. Both spectra are qualitatively similar but the nuclei-only spectrum is significantly increased at lower frequencies, due to the neglect of electronic polarization effects. In the OH-stretching regime at around  $3300\text{ cm}^{-1}$  both spectra coincidentally have a similar amplitude. Interestingly the nuclei-only spectrum in the OH-stretching regime is blue-shifted with respect to the spectrum from nuclear and electronic charges, indicating a slow down of the total dipole-moment dynamics in this regime due to the electronic degrees of freedom.

## IV Extraction and parametrization of the potentials

From the entire set of trajectories of a vibrational coordinate a histogram is created with 50 equidistant bins centered at  $x_i$ . From this histogram  $h(x_i)$  the potential (or free energy) is calculated as

$$U(x_i) = -\log(h(x_i))k_B T, \quad (\text{S11})$$

where the potential is shifted vertically so that  $\min(U[x_i]) = 0$ . The largest and smallest value of  $x_i$  where  $U(x_i) < 8k_B T$  are the edges for a new histogram with 99 equidistant bins. From this histogram the potential is again calculated as shown above. This potential is then fitted to a 4th-order polynomial,  $U(x) = a + bx + cx^2 + dx^3 + ex^4$ , using the Levenberg-Marquardt algorithm. The position of the minimum of the fit function,  $x_0$ , is subsequently obtained using Newton's method, both implemented in `scipy v1.5`. Eventually,  $U(x)$  is rewritten as

$$U(x) = k_0 + \frac{k}{2}(x - x_0)^2 + \frac{k_3}{3}(x - x_0)^3 + \frac{k_4}{4}(x - x_0)^4 \quad (\text{S12})$$

$$k_4 = 4e \quad (\text{S13})$$

$$k_3 = 3(d + k_4 x_0) \quad (\text{S14})$$

$$k = 2(c + k_3 x_0 - \frac{6}{4}k_4 x_0^2) \quad (\text{S15})$$

$$k_0 = a - \frac{k_2}{2}x_0^2 + \frac{k_3}{3}x_0^3 - \frac{k_4}{4}x_0^4. \quad (\text{S16})$$

Note that  $k_0$  is small but can be non-zero because of discretization effects. The results of the fits for the different vibrational coordinates are presented in fig. S3A–D, by comparing the second derivatives of the fit functions,  $U''(x) = k + 2k_3(x - x_0) + 3k_4(x - x_0)^2$ , (blue broken lines) with second derivatives obtained numerically from the data,  $U''(x_i) = (U(x_{i+1}) - 2U(x_i) + U(x_{i-1})) / (x_i - x_{i-1})^2$ , using histograms with 300 equidistant bins. The numerically obtained derivatives are smoothed (gray and purple dots) by iterative convolution with a flat window function, which has a width of three bins. The plots illustrate that for all

vibrational coordinates the fit functions and particularly the harmonic fit parameter  $k$  (shown as horizontal gray dotted lines) match well the numerically obtained curvature of the potential around the position of the minima at  $x_0$  (shown as vertical gray dotted lines).

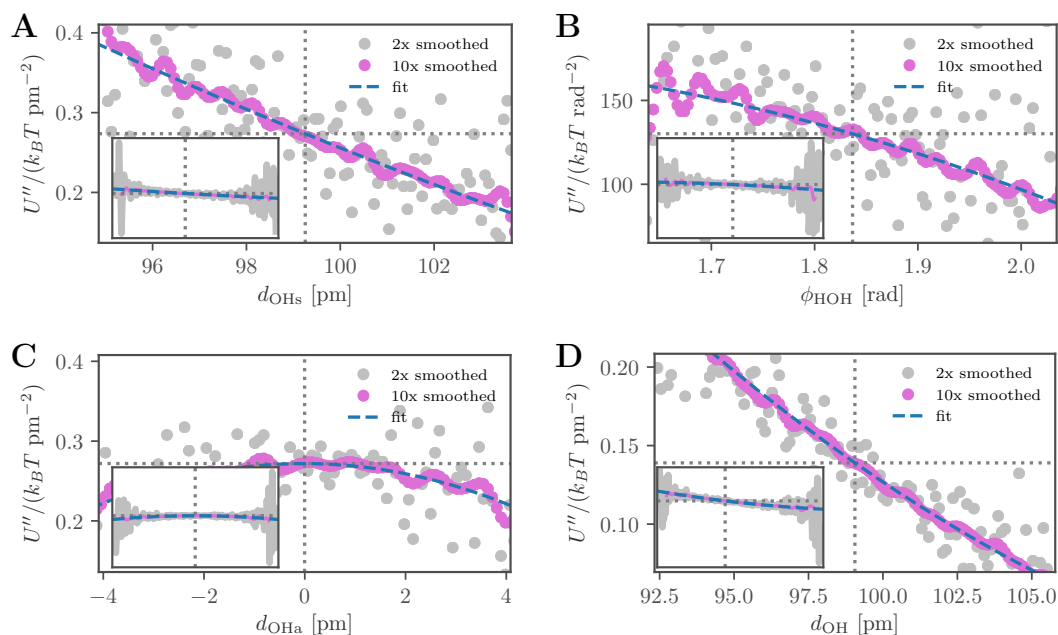


Figure S3: Second derivatives of the potential, obtained numerically and iteratively smoothed (gray and purple dots), of the various vibrational coordinates (**A**:  $d_{\text{OHs}}$  coordinate, **B**:  $\phi_{\text{HOH}}$  coordinate, **C**:  $d_{\text{OHa}}$  coordinate and **D**:  $d_{\text{OH}}$  coordinate.). The second derivatives of the fit functions are shown as blue broken lines. The vertical gray dotted lines denote the position of the minima at  $x_0$  and the horizontal gray dotted lines denote the values of the harmonic fit parameters  $k$ . The insets show a wider range of data, for which  $U(x_i) < 8 k_B T$ .

## V Extraction of the time-dependent friction kernels

The extraction of time-dependent friction kernels from trajectories with an anharmonic potential is performed using a modification of a recently published approach<sup>S3</sup> and is based on previous work by Harp and Berne<sup>S4</sup>. The derivation starts from the generalized Langevin

*C. Supporting Information:*

*Time-Dependent Friction Effects on Vibrational Infrared Frequencies and Line Shapes of Liquid Water*

---

equation (GLE)

$$m\ddot{x}(t) = - \int_0^t \Gamma(t-t')\dot{x}(t')dt' - \nabla U[x(t)] + F_R(t), \quad (\text{S17})$$

which is multiplied by the initial velocity  $\dot{x}(0)$  and ensemble averaged

$$m \langle \dot{x}(0)\ddot{x}(t) \rangle = - \int_0^t dt' \Gamma(t') \langle \dot{x}(0)\dot{x}(t-t') \rangle - \langle \dot{x}(0)\nabla U[x(t)] \rangle, \quad (\text{S18})$$

assuming the random force  $F_R(t)$  to be uncorrelated with  $\dot{x}(0)$ . Defining the correlation functions as

$$C_{vv}(t) = \langle \dot{x}(0)\dot{x}(t) \rangle, \quad (\text{S19})$$

$$C_{v\nabla U}(t) = \langle \dot{x}(0)\nabla U[x(t)] \rangle, \quad (\text{S20})$$

$$C_{x\nabla U}(t) = \langle x(0)\nabla U[x(t)] \rangle, \quad (\text{S21})$$

eq. (S18) is written as

$$m \frac{d}{dt} C_{vv}(t) = - \int_0^t dt' \Gamma(t') C_{vv}(t-t') - C_{v\nabla U}(t) \quad (\text{S22})$$

and integrated over time

$$mC_{vv}(t) - mC_{vv}(0) = - \int_0^t dt'' \int_0^{t''} dt' \Gamma(t') C_{vv}(t''-t') - \int_0^t dt'' C_{v\nabla U}(t''). \quad (\text{S23})$$

For the terms on the right hand side, one finds

$$\begin{aligned}
\int_0^t dt'' C_{v\nabla U}(t'') &= \int_0^t dt'' \langle \dot{x}(0) \nabla U[x(t'')] \rangle \\
&= \int_0^t dt'' \langle \dot{x}(-t'') \nabla U[x(0)] \rangle \\
&= \left\langle \nabla U[x(0)] \int_0^t dt'' \dot{x}(-t'') \right\rangle \\
&= \left\langle \nabla U[x(0)] \int_{-t}^0 dt'' \dot{x}(t'') \right\rangle \\
&= \langle \nabla U[x(0)]x(0) \rangle - \langle \nabla U[x(0)]x(-t) \rangle \\
&= C_{x\nabla U}(0) - C_{x\nabla U}(t)
\end{aligned} \tag{S24}$$

and

$$\begin{aligned}
\int_0^t dt'' \int_0^{t''} dt' \Gamma(t') C_{vv}(t'' - t') &= \int_0^t dt'' \int_0^{t''} dt''' \Gamma(t'' - t''') C_{vv}(t''') \\
&= \int_0^t dt''' C_{vv}(t''') \int_{t'''}^t dt'' \Gamma(t'' - t''') \\
&= \int_0^t dt''' C_{vv}(t''') \int_0^{t-t'''} dt'' \Gamma(t'') \\
&= \int_0^t dt''' C_{vv}(t''') G(t - t'''),
\end{aligned} \tag{S25}$$

where

$$G(t) = \int_0^t dt' \Gamma(t'), \tag{S26}$$

is the integral over the friction kernel. Inserting eq. (S24) and eq. (S25) into eq. (S23), one obtains

$$mC_{vv}(t) - mC_{vv}(0) = - \int_0^t dt' C_{vv}(t') G(t - t') - C_{x\nabla U}(0) + C_{x\nabla U}(t). \tag{S27}$$

*C. Supporting Information:*

*Time-Dependent Friction Effects on Vibrational Infrared Frequencies and Line Shapes of Liquid Water*

---

The mass is found to be

$$m = \frac{C_{x\nabla U}(0)}{C_{vv}(0)}, \quad (\text{S28})$$

which follows from multiplying the GLE eq. (S17) by the initial position  $x(0)$ , averaging over the ensemble and evaluating at  $t = 0$

$$m \langle x(0)\ddot{x}(0) \rangle = - \langle x(0)\nabla U[x(0)] \rangle \quad (\text{S29})$$

$$-m \langle \dot{x}(0)\dot{x}(0) \rangle = - \langle x(0)\nabla U[x(0)] \rangle. \quad (\text{S30})$$

Using eq. (S28) in eq. (S27), one finds

$$C_{vv}(t) \frac{C_{x\nabla U}(0)}{C_{vv}(0)} = - \int_0^t dt' C_{vv}(t') G(t-t') + C_{x\nabla U}(t). \quad (\text{S31})$$

Eq. (S31) is a Volterra equation of first kind which can be discretized in time,  $t = i\Delta t$ , and solved numerically,

$$C_{vv}^i \frac{C_{x\nabla U}^0}{C_{vv}^0} = - \sum_{j=0}^i w_{j,i} \Delta t C_{vv}^j G^{i-j} + C_{x\nabla U}^i \quad (\text{S32})$$

$$= -G^i w_{i,i} \Delta t C_{vv}^0 - \sum_{j=0}^{i-1} w_{j,i} \Delta t C_{vv}^j G^{i-j} + C_{x\nabla U}^i, \quad (\text{S33})$$

where  $w_{j,i}$  are integration weights and the corresponding iteration relation reads

$$G^i = - \frac{1}{\omega_{i,i} \Delta t C_{vv}^0} \left( \sum_{j=0}^{i-1} \omega_{j,i} \Delta t C_{vv}^j G^{i-j} + \frac{C_{x\nabla U}^0}{C_{vv}^0} C_{vv}^i - C_{x\nabla U}^i \right). \quad (\text{S34})$$

Thus by calculating the necessary correlation functions,  $C_{vv}^i = C_{vv}(i\Delta t)$  and  $C_{x\nabla U}^i = C_{x\nabla U}(i\Delta t)$ , from equilibrium trajectories, the integral of the time-dependent friction kernel,  $G^i = G(i\Delta t)$ , can be obtained by iteration from the initial value  $G^0 = 0$ . The friction kernel  $\Gamma^i = \Gamma(i\Delta t)$  is subsequently obtained by a numerical derivative.

## VI Power spectrum of the Generalized Langevin Equation

A random process  $x(t)$  with mass  $m$  and subject to time-dependent (or frequency-dependent) friction  $\Gamma(t)$  in a harmonic potential  $U(x) = \frac{k}{2}x^2$  can be described by the generalized Langevin equation

$$m\ddot{x}(t) = - \int_0^t dt' \Gamma(t-t')\dot{x}(t') - kx(t) + F_R(t), \quad (\text{S35})$$

obeying for the random force  $F_R(t)$  the fluctuation-dissipation relation  $\langle F_R(t)F_R(t') \rangle = k_B T \Gamma(t-t')$ . A Fourier transform gives

$$-\omega^2 m \tilde{x}(\omega) = i\omega \tilde{\Gamma}^+(\omega) \tilde{x}(\omega) - k \tilde{x}(\omega) + \tilde{F}_R(\omega), \quad (\text{S36})$$

as well as

$$\langle \tilde{F}_R(\omega) \tilde{F}_R(\omega') \rangle = k_B T \int_{-\infty}^{\infty} dt e^{i\omega t} \int_{-\infty}^{\infty} dt' e^{i\omega' t'} \Gamma(t-t') \quad (\text{S37})$$

$$\begin{aligned} &= k_B T \int_{-\infty}^{\infty} dt' e^{i(\omega'+\omega)t'} \int_{-\infty}^{\infty} dt e^{i\omega(t-t')} \Gamma(t-t') \\ &= 2\pi k_B T \delta(\omega' + \omega) \tilde{\Gamma}(\omega). \end{aligned} \quad (\text{S38})$$

The absorbed power  $\omega \tilde{\chi}''(\omega)$  is derived in Fourier space from linear response to an external force  $F_{\text{ext}}$ , which is calculated according to

$$\tilde{\chi}(\omega) = \frac{\langle \tilde{x}(\omega) \rangle}{\tilde{F}_{\text{ext}}(\omega)}. \quad (\text{S39})$$

$$= (k - m\omega^2 - i\tilde{\Gamma}^+(\omega)\omega)^{-1}, \quad (\text{S40})$$



C. Supporting Information:

Time-Dependent Friction Effects on Vibrational Infrared Frequencies and Line Shapes of Liquid Water

---

Using eqs. (S38) and (S40) the autocorrelation in Fourier space is given by

$$\tilde{C}_{xx}(\omega) = \int_{-\infty}^{\infty} dt e^{i\omega t} \langle x(t)x(0) \rangle \quad (\text{S41})$$

$$\begin{aligned} &= \frac{1}{4\pi^2} \int_{-\infty}^{\infty} dt e^{i\omega t} \int_{-\infty}^{\infty} d\omega' e^{-i\omega't} \int_{-\infty}^{\infty} d\omega'' e^{-i\omega''0} \langle \tilde{x}(\omega')\tilde{x}(\omega'') \rangle \\ &= \frac{1}{4\pi^2} \int_{-\infty}^{\infty} d\omega' 2\pi\delta(\omega - \omega') \int_{-\infty}^{\infty} d\omega'' \langle \tilde{x}(\omega')\tilde{x}(\omega'') \rangle \\ &= \frac{1}{2\pi} \int_{-\infty}^{\infty} d\omega'' \langle \tilde{x}(\omega)\tilde{x}(\omega'') \rangle \end{aligned} \quad (\text{S42})$$

$$\begin{aligned} &= \frac{1}{2\pi} \int_{-\infty}^{\infty} d\omega'' \langle \tilde{\chi}(\omega)\tilde{F}_R(\omega)\tilde{\chi}(\omega'')\tilde{F}_R(\omega'') \rangle \\ &= k_B T \int_{-\infty}^{\infty} d\omega'' \tilde{\chi}(\omega)\tilde{\chi}(\omega'')\delta(\omega'' + \omega)\tilde{\Gamma}(\omega) \\ &= k_B T \tilde{\chi}(\omega)\tilde{\chi}(-\omega)\tilde{\Gamma}(\omega), \end{aligned} \quad (\text{S43})$$

which is further simplified by realizing that the Fourier transform of the purely real function  $\chi(t)$  is even  $\tilde{\chi}(-\omega) = \tilde{\chi}^*(\omega)$

$$\begin{aligned} \tilde{C}_{xx}(\omega) &= k_B T \tilde{\chi}(\omega)\tilde{\chi}^*(\omega)\tilde{\Gamma}(\omega) \\ &= k_B T |\tilde{\chi}(\omega)|^2 \tilde{\Gamma}(\omega) \\ &= \frac{k_B T \tilde{\Gamma}(\omega)}{\left|k - m\omega^2 - i\tilde{\Gamma}^+(\omega)\omega\right|^2}. \end{aligned} \quad (\text{S44})$$

From eq. (S4) the power spectrum follows

$$\omega \tilde{\chi}''(\omega) = \frac{\omega^2 \text{Re}\tilde{\Gamma}^+(\omega)}{\left|k - m\omega^2 - i\tilde{\Gamma}^+(\omega)\omega\right|^2}. \quad (\text{S45})$$

## VII Power spectrum of the damped harmonic oscillator

The absorbed power  $\omega\tilde{\chi}''(\omega)$  of the damped harmonic oscillator described by memoryless Langevin equation

$$m\ddot{x}(t) = -\gamma\dot{x}(t) - kx(t) + F_{\text{ext}}(t), \quad (\text{S46})$$

is computed from the linear response in Fourier space

$$\tilde{\chi}(\omega) = \frac{\langle \tilde{x}(\omega) \rangle}{\tilde{F}_{\text{ext}}(\omega)} \quad (\text{S47})$$

$$= (k - m\omega^2 - i\gamma\omega)^{-1} \quad (\text{S48})$$

$$= \frac{k - m\omega^2 + i\gamma\omega}{(k - m\omega^2)^2 + \gamma^2\omega^2}, \quad (\text{S49})$$

where  $\tilde{x}(\omega)$  is the oscillating variable,  $m$  is the mass,  $\gamma$  the friction coefficient,  $k$  the spring constant of the harmonic potential and  $\tilde{F}_{\text{ext}}(\omega)$  an external force. For the power spectrum follows

$$\omega\tilde{\chi}''(\omega) = \frac{\gamma\omega^2}{(k - m\omega^2)^2 + \gamma^2\omega^2}, \quad (\text{S50})$$

which by introducing the time scales  $\tau = 2\gamma/k$ ,  $\tau_\omega = \sqrt{m/k}$  and length scale  $L$  with  $L^2 = 2k_B T/k$  converts to

$$\omega\tilde{\chi}''(\omega) = \frac{L^2}{k_B T} \frac{\tau\omega^2}{4(1 - \tau_\omega^2\omega^2)^2 + \tau^2\omega^2}. \quad (\text{S51})$$

In spectroscopy this is known as a Lorentzian line shape<sup>S5</sup>, which in the overdamped case,  $\tau_\omega \rightarrow 0$ , reads

$$\omega \tilde{\chi}''(\omega) = \frac{\gamma \omega^2}{k^2 + \gamma^2 \omega^2} \quad (\text{S52})$$

$$= \frac{L^2}{k_B T} \frac{\tau \omega^2}{4 + \tau^2 \omega^2}. \quad (\text{S53})$$

Eq. (S52) is also known as the Debye line shape.

## VIII Parametrization of the extracted memory kernels

The memory kernels  $\Gamma(t)$ , extracted from the aiMD simulation data as described in section V, are truncated at 50 ps, oversampled at a time resolution of  $\Delta t = 0.025$  fs and subsequently Fourier transformed using the FFT algorithm implemented in numpy v1.19. The real part of the Fourier-transformed memory kernel is then fitted to a combination of  $n$  exponential and  $l$  oscillating memory kernels according to eq. (5) in the main text. The Fourier-transformed expressions of the fundamental kernels are found to be

$$\tilde{\Gamma}_{\text{osc}}^+(\omega, a_i, \tau_i, \omega_i) = \frac{a_i}{2} \left( \frac{1 + \frac{i}{\omega_i \tau_i}}{\frac{1}{\tau_i} + i\omega_i - i\omega} + \frac{1 - \frac{i}{\omega_i \tau_i}}{\frac{1}{\tau_i} - i\omega_i - i\omega} \right), \quad (\text{S54})$$

$$\tilde{\Gamma}_{\text{exp}}^+(\omega, \gamma_i, \tau_i) = \gamma_i \frac{1}{1 - i\omega \tau_i}, \quad (\text{S55})$$

$$\tilde{\Gamma}^+(\omega) = \sum_{i=1}^n \tilde{\Gamma}_{\text{exp}}^+(\omega, \gamma_i, \tau_i^e) + \sum_{i=1}^l \tilde{\Gamma}_{\text{osc}}^+(\omega, a_i, \tau_i^o, \omega_i). \quad (\text{S56})$$

The real part of the Fourier-transformed memory kernel  $\tilde{\Gamma}'^+(\omega)$  is fitted in the  $(2n + 3l)$ -dimensional parameter space using the Levenberg-Marquardt algorithm implemented in scipy v1.5.  $n$  and  $l$  are iteratively increased until the fit quality does not improve significantly. The initial values for all  $\gamma_i$ ,  $\tau_i^e$ ,  $a_i$ ,  $\tau_i^o$  and  $\omega_i$  are chosen suitably. After fitting in Fourier space, another fit is performed in the time domain, by subtracting the  $l$  oscillating fit functions from the memory kernels in the time domain and again fitting the  $n$  exponential functions

to the remainder. This significantly improves the fits for the long-time tails of the memory kernels. The hereby obtained fit parameters for the friction memory kernels for the different vibrational coordinates in the bulk water system are summarized in tabs. S1–S4.

The effective masses of the vibrational coordinates that are used throughout this study are determined by the equipartition theorem  $m_{\text{OHs}} = k_B T / \langle \dot{d}_{\text{OHs}}^2 \rangle = 1.901\,04\text{ u}$ ,  $m_{\text{OHa}} = k_B T / \langle \dot{d}_{\text{OHa}}^2 \rangle = 1.845\,71\text{ u}$ ,  $m_{\text{OH}} = k_B T / \langle \dot{d}_{\text{OH}}^2 \rangle = 0.936\,477\text{ u}$  and  $m_{\text{HOH}} = k_B T / \langle \dot{\phi}_{\text{HOH}}^2 \rangle = 0.418\,17\text{ u}\text{\AA}^2$ . Comparable analytic estimates are given by the reduced mass of the  $d_{\text{OH}}$  coordinate  $m_{\text{OH}} = (m_{\text{O}}m_{\text{H}})/(m_{\text{O}} + m_{\text{H}}) = 0.947\,617\text{ u}$ . For the masses of the  $d_{\text{OHs}}$  and  $d_{\text{OHa}}$  coordinates it follows  $m_{\text{OHa}} = m_{\text{OHs}} = 2m_{\text{OH}} = 1.895\,23\text{ u}$ . Furthermore,  $m_{\text{HOH}} = m_{\text{H}}\langle \dot{d}_{\text{OH}} \rangle^2/2 = 0.503\,345\text{ u}\text{\AA}^2$  can be estimated.

**Table S1: Fit parameters according to eq. (5) in the main text of the friction memory kernel of the  $d_{\text{OHs}}$  coordinate.**

$\gamma_i$ [u/ps]	$\tau_i^e$ [ps]	
2758	0.115	
25941	1.28	
54005	5.72	
$a_i$ [u/ps <sup>2</sup> ]	$\tau_i^o$ [ps]	$\omega_i$ [THz]
8468	0.00944	170
3525	0.0146	1290
5985	0.0256	614
1095	0.0599	675
10560	0.0807	28.7
6318	0.122	313

**Table S2: Fit parameters according to eq. (5) in the main text of the friction memory kernel of the  $\phi_{\text{HOH}}$  coordinate.**

$\gamma_i$ [u/ps]	$\tau_i^e$ [ps]	
661	0.582	
5210	3.08	
$a_i$ [u/ps <sup>2</sup> ]	$\tau_i^o$ [ps]	$\omega_i$ [THz]
322	0.0257	1280
2139	0.0283	28.9
2577	0.0322	953
37	0.0323	1590
786	0.0394	110
4600	0.0396	643
374	0.0417	162
435	0.0465	136
4089	0.0532	612
69	0.056	252
471	0.0612	84.4
49	0.0839	284
40	0.12	311
2836	0.143	14.4

**Table S3: Fit parameters according to eq. (5) in the main text of the friction memory kernel of the  $d_{\text{OHa}}$  coordinate.**

$\gamma_i$ [u/ps]	$\tau_i^e$ [ps]	
5653	0.183	
32596	2.03	
$a_i$ [u/ps <sup>2</sup> ]	$\tau_i^o$ [ps]	$\omega_i$ [THz]
7584	0.0165	1280
3186	0.021	300
5051	0.0266	602
3208	0.0361	141
1320	0.0401	413
2810	0.0415	644
39665	0.0752	36.5
1353	0.0768	677
2010	0.0856	100

**Table S4: Fit parameters according to eq. (5) in the main text of the friction memory kernel of the  $d_{\text{OH}}$  coordinate.**

$\gamma_i$ [u/ps]	$\tau_i^e$ [ps]	
1212	0.109	
9005	1.06	
19399	4.52	
$a_i$ [u/ps <sup>2</sup> ]	$\tau_i^o$ [ps]	$\omega_i$ [THz]
1343	0.0174	249
1669	0.0264	616
1544	0.0301	145
420	0.0364	411
137	0.0688	673
845	0.0699	100
10641	0.081	35.5
1802	0.115	312

## IX Simulation of the generalized Langevin equation

The GLE

$$m\ddot{x}(t) = - \int_0^t \Gamma(t-t')\dot{x}(t')dt' - \nabla U[x(t)] + F_R(t), \quad (\text{S57})$$

with a sum of  $n$  exponential and  $l$  oscillating memory kernels, analogous to eq. (5) in the main text,

$$\Gamma(t) = \sum_{i=1}^n a_i e^{-t/\tau_i} + \sum_{i=1}^l a_i e^{-t/\tau_i} \left( \cos(\omega_i t) + \frac{1}{\tau_i \omega_i} \sin(\omega_i t) \right), \quad (\text{S58})$$

can be efficiently simulated using Markovian embedding (which for the oscillating components is derived in detail in section X)

$$\dot{x}(t) = v(t), \quad (\text{S59})$$

$$m_x \dot{v}(t) = -\nabla U[x(t)] + \sum_{i=1}^n a_i [y_i(t) - x(t)] + \sum_{i=1}^l a_i [z_i(t) - x(t)], \quad (\text{S60})$$

$$\gamma_i \dot{y}_i(t) = a_i [x(t) - y_i(t)] + F_i(t) \quad \text{for } n \text{ exp. components}, \quad (\text{S61})$$

$$\dot{z}_i(t) = w_i(t), \quad (\text{S62})$$

$$m_i \dot{w}_i(t) = -\gamma_i w_i(t) + a_i [x(t) - z_i(t)] + F_i(t) \quad \text{for } l \text{ osc. components}. \quad (\text{S63})$$

For the  $n$  exponential components we obtain  $a_i = \frac{\gamma_i}{\tau_i^e}$  from the fit parameters  $\gamma_i$  and  $\tau_i^e$ . To obtain  $m_i$  and  $\gamma_i$  for the  $l$  oscillating components from the fit parameters  $a_i$ ,  $\tau_i^o$  and  $\omega_i$  we use

$$m_i = a_i ((\tau_i^o)^{-2} + \omega_i^2)^{-1}, \quad (\text{S64})$$

$$\gamma_i = 2 \frac{m_i}{\tau_i^o}. \quad (\text{S65})$$

The random force  $F_i$  present in eqs. (S61) and (S63) is

$$F_i = \sqrt{2k_B T \gamma_i \delta t^{-1}} \Xi, \quad (\text{S66})$$

where  $\Xi$  is a Gaussian random distribution with zero mean and a standard deviation of one. In the numerical simulation we use the `numpy.random.normal` function to generate these random numbers. Eqs. (S60)–(S63) are numerically solved using a 4th-order Runge-Kutta scheme to obtain the trajectory of  $x$ . The timestep of the simulation is 0.001 fs and only every 500th value is stored. Thus the trajectory is evaluated at a time step of 0.5 fs. The trajectory contains  $2.5 \times 10^7$  values which corresponds to a simulation time of 12.5 ns. Each trajectory is divided into 50 parts of 250 ps and their spectra are calculated using the Wiener-Khintchine relation introduced in section XII. All 50 spectra are then averaged to give the final spectrum. Starting velocity and position are set to be zero.

The memoryless Langevin equation, with a friction constant  $\gamma$  replacing the integral over the memory kernel,

$$m\ddot{x}(t) = -\gamma\dot{x}(t) - \nabla U[x(t)] + F_R(t), \quad (\text{S67})$$

is likewise simulated using a 4th-order Runge-Kutta scheme. The timestep of these simulations is 0.1 fs for a total of  $10^7$  steps, which corresponds to a simulation time of 1 ns. Each trajectory is divided into 200 parts of 5 ps and their spectra are calculated using the Wiener-Khintchine relation introduced in section XII. All 200 spectra are then averaged to give the final spectrum.



## X Oscillating memory kernels

### X.1 Oscillating memory kernels from a Hamiltonian model

Oscillating memory kernels arise from inertial dynamics in orthogonal degrees of freedom at time scales of the order of the primary reaction coordinate. The relation of the time scales of the orthogonal coordinate and the memory kernel is understood from an explicit derivation of the dynamics of the primary coordinate  $x$  with velocity  $v$ , linearly coupled to an orthogonal coordinate  $y$  with velocity  $w$  and coupling constant  $k$ . The Hamiltonian of the system is given as

$$H = \frac{m}{2}v^2 + \frac{m_y}{2}w^2 + \frac{k}{2}(x - y)^2, \quad (\text{S68})$$

defining the Hamilton equations

$$\dot{x}(t) = v \quad (\text{S69})$$

$$m\dot{v}(t) = k[x(t) - y(t)] \quad (\text{S70})$$

$$\dot{y}(t) = w(t) \quad (\text{S71})$$

$$m_y\dot{w}(t) = -k[x(t) - y(t)]. \quad (\text{S72})$$

These Newtonian equations of motion can straight-forwardly be extended to Langevin equations by introducing random forces  $F_x(t)$ ,  $F_y(t)$  and friction terms with coefficients  $\gamma_x$ ,  $\gamma_y$

$$\dot{x}(t) = v \quad (\text{S73})$$

$$m\dot{v}(t) = -\gamma_x v(t) + k[x(t) - y(t)] + F_x(t) \quad (\text{S74})$$

$$\dot{y}(t) = w(t) \quad (\text{S75})$$

$$m_y\dot{w}(t) = -\gamma_y w(t) - k[x(t) - y(t)] + F_y(t). \quad (\text{S76})$$

The random forces have zero mean,  $\langle F_i(t) \rangle = 0$ , and strength  $\langle F_i(t)F_i(t') \rangle = 2\gamma_i k_B T \delta(t - t')$ , fulfilling the fluctuation-dissipation relation.

To obtain the GLE including the memory kernel, we will now find a solution for  $y$  using eq. (S76) and insert this solution in eq. (S74). Eq. (S76) is essentially a driven damped harmonic oscillator, which can be solved in a general fashion using matrix exponentials and introducing the inertial time scale  $\tau_{m_y} = m_y/\gamma_y$  and the memory time scale  $\tau_{k_y} = \gamma_y/k$ . First we write the coupled first order ordinary differential eqs. (S75) and (S76) in the matrix form

$$\dot{\vec{y}}(t) = A\vec{y}(t), \quad (\text{S77})$$

where

$$\vec{y}(t) = \begin{pmatrix} y \\ \dot{y} \end{pmatrix} \quad (\text{S78})$$

$$A = \begin{pmatrix} 0 & 1 \\ -(\tau_{m_y}\tau_{k_y})^{-1} & -\tau_{m_y}^{-1} \end{pmatrix}, \quad (\text{S79})$$

$$A^{-1} = \begin{pmatrix} -\tau_{m_y}^{-1} & (\tau_{m_y}\tau_{k_y})^{-1} \\ -1 & 0 \end{pmatrix}. \quad (\text{S80})$$

The solution is given as

$$\begin{aligned} \vec{y}(t) = & \exp(A[t - t_0])\vec{y}_0 \\ & + \int_{t_0}^t dt' \exp(A[t - t']) \begin{pmatrix} 0 \\ -(\tau_{m_y}\tau_{k_y})^{-1}x(t') + m_y^{-1}F_y(t') \end{pmatrix}. \end{aligned} \quad (\text{S81})$$

C. Supporting Information:

Time-Dependent Friction Effects on Vibrational Infrared Frequencies and Line Shapes of Liquid Water

---

Next a partial integration over the integral containing  $x(t)$  is performed

$$\begin{aligned}
\vec{y}(t) &= \exp(A[t - t_0])\vec{y}_0 \\
&- \left[ A^{-1} \exp(A[t - t']) \begin{pmatrix} 0 \\ -(\tau_{m_y} \tau_{k_y})^{-1} x(t) \end{pmatrix} \right]_{t_0}^t \\
&+ A^{-1} \int_{t_0}^t dt' \exp(A[t - t']) \begin{pmatrix} 0 \\ -(\tau_{m_y} \tau_{k_y})^{-1} v(t') \end{pmatrix} \\
&+ \int_{t_0}^t dt' \exp(A[t - t']) \begin{pmatrix} 0 \\ m_y^{-1} F_y(t') \end{pmatrix}.
\end{aligned} \tag{S82}$$

The matrix exponential can be evaluated by diagonalizing the matrix  $A$ . After introducing  $\omega_0 = \sqrt{(2\tau_{m_y})^{-2} - (\tau_{m_y} \tau_{k_y})^{-1}}$  the Eigenvalues  $\lambda_{1,2}$  of  $A$  are given as

$$\lambda_{1,2} = -(2\tau_{m_y})^{-1} \pm \omega_0, \tag{S83}$$

and the matrix exponential reads

$$\exp(At) = \frac{1}{\lambda_2 - \lambda_1} \begin{pmatrix} \lambda_2 e^{\lambda_1 t} - \lambda_1 e^{\lambda_2 t} & e^{\lambda_2 t} - e^{\lambda_1 t} \\ \lambda_1 \lambda_2 (e^{\lambda_1 t} - e^{\lambda_2 t}) & \lambda_2 e^{\lambda_2 t} - \lambda_1 e^{\lambda_1 t} \end{pmatrix} \tag{S84}$$

$$= e^{-t/(2\tau_{m_y})} \begin{pmatrix} \cosh(\omega_0 t) + \frac{\sinh(\omega_0 t)}{2\tau_{m_y} \omega_0} & -\frac{\sinh(\omega_0 t)}{\omega_0} \\ \frac{\sinh(\omega_0 t)}{\tau_{m_y} \tau_{k_y} \omega_0} & \cosh(\omega_0 t) - \frac{\sinh(\omega_0 t)}{2\tau_{m_y} \omega_0} \end{pmatrix}, \tag{S85}$$

giving

$$A^{-1} \exp(At) = \tau_{m_y} \tau_{k_y} e^{-t/(2\tau_{m_y})} \begin{pmatrix} -\frac{1}{\tau_{m_y}} \cosh(\omega_0 t) + \frac{1}{2\tau_{m_y}^2 \omega_0} \sinh(\omega_0 t) + \frac{1}{\tau_{m_y} \tau_{k_y} \omega_0} \sinh(\omega_0 t) & -\frac{1}{2\tau_{m_y} \omega_0} \sinh(\omega_0 t) - \cosh(\omega_0 t) \\ \frac{1}{\tau_{m_y} \tau_{k_y}} \cosh(\omega_0 t) + \frac{1}{\tau_{m_y} \tau_{k_y} \omega_0} \sinh(\omega_0 t) & \frac{1}{\tau_{m_y} \tau_{k_y} \omega_0} \sinh(\omega_0 t) \end{pmatrix}. \quad (\text{S86})$$

The solution for  $y(t) = \vec{y}_1(t)$  is now obtained from eqs. (S82)–(S86) and by sending  $t_0 \rightarrow -\infty$ , i.e. assuming an equilibrated system

$$y(t) = x(t) - \int_{-\infty}^t dt' v(t') e^{-(t-t')/(2\tau_{m_y})} \left[ \cosh(\omega_0(t-t')) + \frac{1}{2\tau_{m_y} \omega_0} \sinh(\omega_0(t-t')) \right] - \int_{-\infty}^t dt' F_y(t') e^{-(t-t')/(2\tau_{m_y})} \frac{1}{m_y \omega_0} \sinh(\omega_0(t-t')). \quad (\text{S87})$$

To obtain the generalized Langevin equation for  $x(t)$  containing the oscillating memory kernel

$$\Gamma(t) = k e^{-t/(2\tau_{m_y})} \left[ \cosh(\omega_0 t) + \frac{1}{2\tau_{m_y} \omega_0} \sinh(\omega_0 t) \right], \quad (\text{S88})$$

eq. (S87) is inserted in eq. (S74)

$$m\dot{v}(t) = -\gamma_x v(t) + F_x(t) + \int_{-\infty}^t dt' v(t') \Gamma(t-t') + F'_y(t), \quad (\text{S89})$$

where

$$F'_y(t) = k \int_{-\infty}^t dt' F_y(t') e^{-(t-t')/(2\tau_{m_y})} \frac{1}{m_y \omega_0} \sinh(\omega_0(t-t')). \quad (\text{S90})$$

## X.2 Underdamped limit: oscillating kernel

The kernel of eq. (S88) can be analysed for two limiting cases. For  $\text{Im}(\omega_0) > (2\tau_{m_y})^{-1}$ , which is equivalent to  $4\tau_{m_y} > \tau_{k_y}$ , the underdamped case,  $\omega_0$  is purely imaginary and the kernel is

$$\Gamma(t) = ke^{-t/(2\tau_{m_y})} \cos(\text{Im}(\omega_0)t) + \frac{1}{2\tau_{m_y}\text{Im}(\omega_0)} \sin(\text{Im}(\omega_0)t). \quad (\text{S91})$$

The integral is evaluated to

$$\gamma = \int_0^\infty dt\Gamma(t) = k \frac{4\tau_{m_y}}{1 - 4\tau_{m_y}^2 \text{Im}(\omega_0)^2} = k\tau_{k_y} = \gamma_y. \quad (\text{S92})$$

## X.3 Overdamped limit: exponential kernel

For  $\text{Re}(\omega_0) < (4\tau_{m_y})^{-1}$  and  $\tau_{k_y} > (4\tau_{m_y})$ , the overdamped case, it follows that  $\omega_0$  is purely real. The integral equally gives

$$\gamma = \int_0^\infty dt\Gamma(t) = k \frac{4\tau_{m_y}}{1 - 4\tau_{m_y}^2 \omega_0^2} = k\tau_{k_y} = \gamma_y. \quad (\text{S93})$$

## XI Simulations of single H<sub>2</sub>O molecule in the NVE ensemble

For the aiMD simulations of a single H<sub>2</sub>O molecule, representing the gas phase, 47 initial configurations are sampled from a 25 ps NVT simulation and subsequently simulated in the NVE ensemble. The NVT simulation is temperature-controlled using an individual thermostat with a time constant of 10 fs for each atom. The NVE simulations are each run for 10 ps with a time step of 0.25 fs. The distributions of their initial configurations are shown in fig. S4 to sample well the equilibrium distributions from the NVT trajectory.

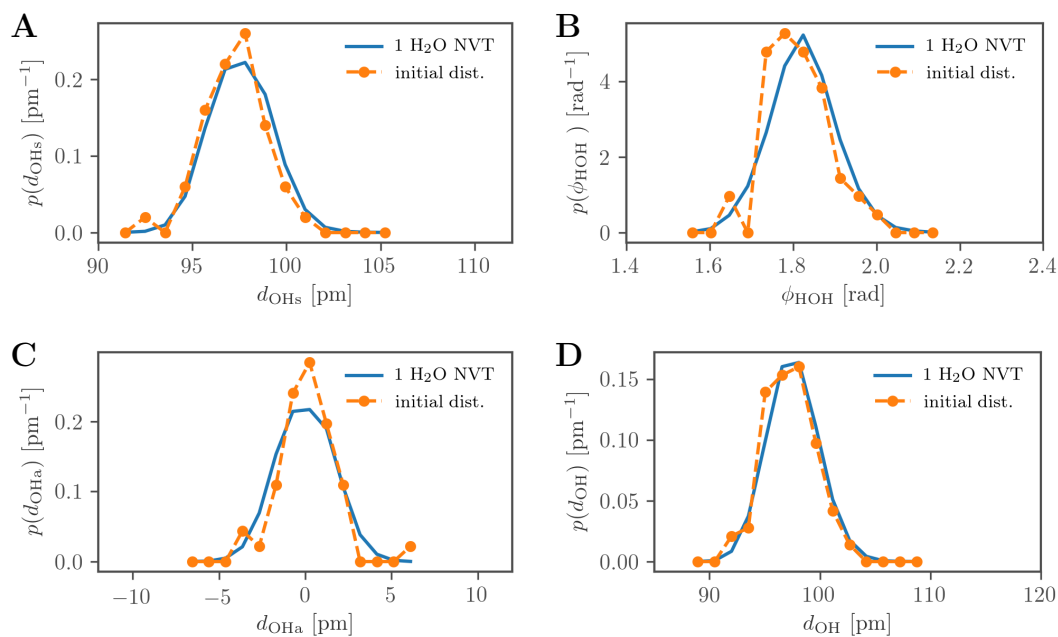


Figure S4: Comparison of the distributions for the different coordinates sampled from the aiMD simulations of a single H<sub>2</sub>O molecule under NVT conditions (blue solid lines) and 47 samples taken from the NVT trajectory as initial conditions for equivalent simulations under NVE conditions (orange dots). **A:**  $d_{\text{OHs}}$  coordinate, **B:**  $\phi_{\text{HOH}}$  coordinate, **C:**  $d_{\text{OHa}}$  coordinate and **D:**  $d_{\text{OH}}$  coordinate.

## XII Wiener-Khintchine theorem

The correlation function  $C_{xy}(t)$  of two stochastic processes  $x(t)$  and  $y(t)$  limited to the interval  $[0, L_t]$  is efficiently computed from the Fourier-transformed expressions  $\tilde{x}(\omega)$  and  $\tilde{y}(\omega)$  according to

$$C_{xy}(t) = \frac{1}{2\pi(L_t - t)} \int_{-\infty}^{\infty} d\omega e^{-i\omega t} \tilde{x}(\omega) \tilde{y}^*(\omega), \quad (\text{S94})$$

where the asterisk denotes the conjugate form. This is known as the Wiener-Khintchine theorem<sup>S7</sup>. Both sides of eq. (S94) are Fourier-transformed to give

$$\int_{-\infty}^{\infty} dt e^{i\omega t} 2\pi L_t \left(1 - \frac{t}{L_t}\right) C_{xy}(t) = \tilde{x}(\omega) \tilde{y}^*(\omega), \quad (\text{S95})$$

which in the limit of large  $L_t$  reduces to

$$\tilde{C}_{xy}(\omega) = L_t^{-1} \tilde{x}(\omega) \tilde{y}^*(\omega). \quad (\text{S96})$$

Eq. (S94) can be derived starting off with the definition of the correlation function

$$C_{xy}(t) = \frac{1}{L_t - t} \int_0^{L_t - t} dt' x(t' + t) y(t'), \quad (\text{S97})$$

and making use of the convolution theorem

$$\begin{aligned} C_{xy}(t) &= \frac{1}{4\pi^2(L_t - t)} \int_0^{L_t - t} dt' \int_{-\infty}^{\infty} d\omega e^{-i\omega(t+t')} \tilde{x}(\omega) \int_{-\infty}^{\infty} d\omega' e^{-i\omega't'} \tilde{y}(\omega') \\ &= \frac{1}{4\pi^2(L_t - t)} \int_{-\infty}^{\infty} d\omega e^{-i\omega t} \tilde{x}(\omega) \int_{-\infty}^{\infty} d\omega' \tilde{y}(\omega') \int_0^{L_t - t} dt' e^{-it'(\omega + \omega')} \\ &= \frac{1}{4\pi^2(L_t - t)} \int_{-\infty}^{\infty} d\omega e^{-i\omega t} \tilde{x}(\omega) \int_{-\infty}^{\infty} d\omega' \tilde{y}(\omega') 2\pi \delta(\omega + \omega') \\ &= \frac{1}{2\pi(L_t - t)} \int_{-\infty}^{\infty} d\omega e^{-i\omega t} \tilde{x}(\omega) \tilde{y}(-\omega), \end{aligned} \quad (\text{S98})$$

noting that  $\tilde{y}(-\omega) = \tilde{y}^*(\omega)$  for a real function  $y(t)$  in order to obtain eq. (S94).

### XIII Decomposition of the OH stretch mode

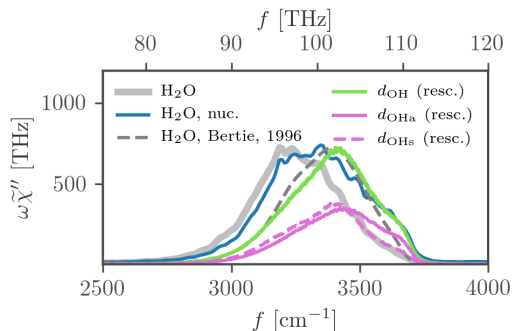


Figure S5: Comparison of IR spectra in the OH-stretching regime obtained from the total dipole-moment trajectory including nuclear and electronic charges from the aiMD simulation of 256 H<sub>2</sub>O molecules (gray solid line), an approximation using partial charges on the nuclear dynamics of the same aiMD simulation (blue solid line, introduced in section III), experimental Fourier-transform infrared spectroscopy (FTIR) data (gray broken line)<sup>S6</sup> and rescaled power spectra of the  $d_{\text{OH}}$  (green solid line),  $d_{\text{OH}_s}$  (purple solid line) and  $d_{\text{OH}_a}$  (purple broken line) vibrational coordinates.

As introduced in the main text, vibrational coordinates for the OH stretch mode are given by  $d_{\text{OH}_s} = (d_{\text{OH}_1} + d_{\text{OH}_2})/2$  for the symmetric stretching-vibration and  $d_{\text{OH}_a} = (d_{\text{OH}_1} - d_{\text{OH}_2})/2$  for the antisymmetric stretching vibration. Fig. S5 compares the power spectra of these coordinates, obtained from averaging over all 256 H<sub>2</sub>O molecules in the aiMD simulation, to power spectra of the  $d_{\text{OH}}$  coordinate, experimental FTIR data and the IR spectra obtained from the total dipole-moment trajectory including nuclear and electronic charges from the aiMD simulation and an approximation using partial charges on the nuclear dynamics of the aiMD simulation, as introduced in section III. The power spectrum of the  $d_{\text{OH}}$  coordinate is blue-shifted with respect to the power spectra considering the total dipole moment, indicating a slow down of the collective nuclear and electronic dynamics with respect to the single-molecule dynamics, as discussed in section II. This is similar to the effect of the slow down



observed in the IR spectra including electronic degrees of freedom compared to the nuclei-only IR spectra, discussed in section III. As expected for the decomposition, the power spectra of  $d_{\text{OHs}}$  and  $d_{\text{OHa}}$  exactly sum up to the  $d_{\text{OH}}$  power spectrum, there exists no remaining cross-correlation spectrum, so they form orthogonal coordinates.

The potentials, power spectra and analysis in terms of frequency-dependent friction of the  $d_{\text{OHs}}$  and  $\phi_{\text{HOH}}$  coordinates are shown in the main text. The remaining discussion is shown here for the  $d_{\text{OH}}$  coordinate in fig. S6 and for the  $d_{\text{OHa}}$  coordinate in fig. S7. The potential of the  $d_{\text{OH}}$  coordinate shows strong nonharmonic contributions in fig. S6A, seen from the reduced potential coefficients  $\tilde{k}_3 = k_3/k_B T (k/k_B T)^{-3/2} = -0.128$  and  $\tilde{k}_4 = k_4/k_B T (k/k_B T)^{-2} = 0.00503$ . The potential of the  $d_{\text{OHa}}$  coordinate is symmetric by definition and therefore has a negligible cubic and only a small quartic contribution  $\tilde{k}_4 = -0.0141$  in fig. S7A compared to the potential of the  $d_{\text{OHs}}$  coordinate, shown in fig. 3A in the main text, which has a significant cubic contribution. When compared to the potential of a single water molecule in figs. S6B and S7B, the  $d_{\text{OH}}$  coordinate shows a shift of the minimum from 97.37 pm to 99.06 pm, i.e. elongation of the bond length due to hydrogen bonding. As expected, the potential of the  $d_{\text{OHa}}$  coordinate is centered around zero for both systems. Both coordinates show a significant potential softening in the liquid phase, which follows from comparison of the dominant harmonic contributions of  $k/(k_B T) = 0.139 \text{ pm}^{-2}$  for  $d_{\text{OH}}$  and  $k/(k_B T) = 0.272 \text{ pm}^{-2}$  for  $d_{\text{OHa}}$  with the respective gas-phase values of  $k/(k_B T) = 0.183 \text{ pm}^{-2}$  for  $d_{\text{OH}}$  and  $k/(k_B T) = 0.352 \text{ pm}^{-2}$  for  $d_{\text{OHa}}$ .

The memory kernels in the time domain, shown in figs. S6C for the  $d_{\text{OH}}$  coordinate and S7C for the  $d_{\text{OHa}}$  coordinate, are discussed further below in fig. S8. The frequency-dependent friction, shown in figs. 3D in the main text for the  $d_{\text{OHs}}$  coordinate, S6D for the  $d_{\text{OH}}$  coordinate and S7D for the  $d_{\text{OHa}}$  coordinate show remarkable differences. The frequency-dependent friction of the  $d_{\text{OHs}}$  coordinate shows a much stronger contribution in the regime of the HOH bending band at around  $1650 \text{ cm}^{-1}$ , indicating that it couples more intensely to the HOH bending mode than the  $d_{\text{OHa}}$  mode.

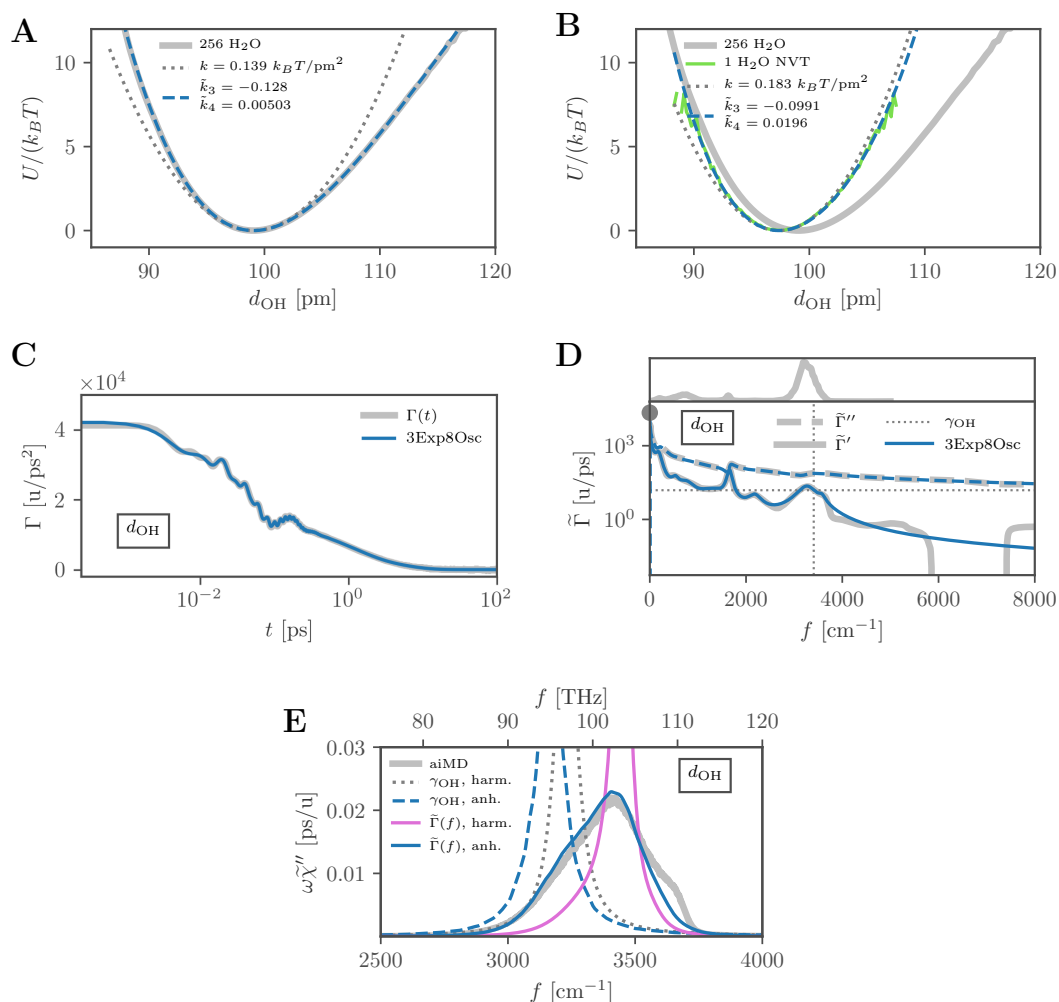


Figure S6: Results for the stretch coordinate  $d_{\text{OH}}$  from aiMD simulations. **A, B:** Potential  $U(d_{\text{OH}})$  for 256  $\text{H}_2\text{O}$  in the liquid phase (gray solid line) and for a single  $\text{H}_2\text{O}$  molecule (green solid line in B), both compared to the nonharmonic fit according to eq. (4) in the main text (blue broken line) and the harmonic part (gray dotted line). **C, D:** Friction as a function of time and frequency (gray lines) compared with the fit according to eq. (5) in the main text (blue lines). Real and imaginary parts in (D) are shown as solid and broken lines, the spectrum on top is the full absorption spectrum from aiMD. The dotted horizontal line in (D) shows the constant real friction  $\gamma_{\text{OH}} = \tilde{\Gamma}'(f_{\text{OH}})$  evaluated at the OH stretch vibrational frequency  $f_{\text{OH}} = 3400 \text{ cm}^{-1}$ . The gray circle denotes the static friction  $\tilde{\Gamma}'(0)$ . **E:** Power spectrum  $\omega\tilde{\chi}''$  (gray solid line) compared to models of varying complexity: Lorentzian with harmonic potential and constant friction  $\gamma_{\text{OH}}$  (gray dotted line), nonharmonic potential and constant friction  $\gamma_{\text{OHs}}$  (blue broken line), harmonic potential and frequency-dependent friction  $\tilde{\Gamma}(f)$  (purple solid line), nonharmonic potential and frequency-dependent friction  $\tilde{\Gamma}(f)$  (blue solid line).

C. Supporting Information:

Time-Dependent Friction Effects on Vibrational Infrared Frequencies and Line Shapes of Liquid Water

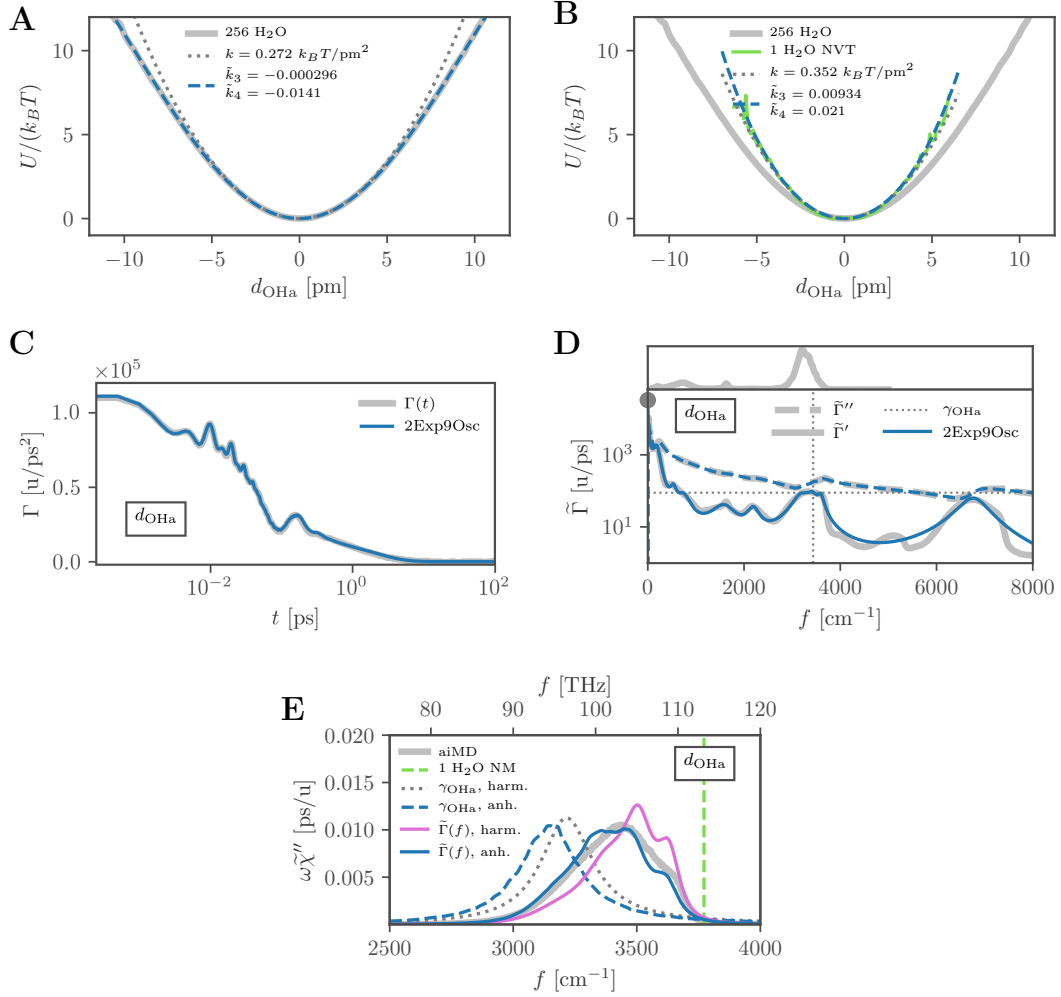


Figure S7: Results for the antisymmetric stretch coordinate  $d_{\text{OHa}}$  from aiMD simulations. **A, B:** Potential  $U(d_{\text{OHa}})$  for 256  $\text{H}_2\text{O}$  in the liquid phase (gray solid line) and for a single  $\text{H}_2\text{O}$  molecule (green solid line in B), both compared to the nonharmonic fit according to eq. (4) in the main text (blue broken line) and the harmonic part (gray dotted line). **C, D:** Friction as a function of time and frequency (gray lines) compared with the fit according to eq. (5) in the main text (blue lines). Real and imaginary parts in (D) are shown as solid and broken lines, the spectrum on top is the full absorption spectrum from aiMD. The dotted horizontal line in (D) shows the constant real friction  $\gamma_{\text{OHa}} = \tilde{\Gamma}'(f_{\text{OHa}})$  evaluated at the OH stretch vibrational frequency  $f_{\text{OHa}} = 3440 \text{ cm}^{-1}$ . The gray circle denotes the static friction  $\tilde{\Gamma}'(0)$ . **E:** Power spectrum  $\omega\tilde{\chi}''$  (gray solid line) compared to models of varying complexity: normal mode of single  $\text{H}_2\text{O}$  (broken vertical line), Lorentzian with harmonic potential and constant friction  $\gamma_{\text{OHa}}$  (gray dotted line), nonharmonic potential and constant friction  $\gamma_{\text{OHa}}$  (blue broken line), harmonic potential and frequency-dependent friction  $\tilde{\Gamma}(f)$  (purple solid line), nonharmonic potential and frequency-dependent friction  $\tilde{\Gamma}(f)$  (blue solid line).

Figs. S6E and S7E show the power spectra of the two coordinates, compared to the different GLE models. As shown in the main text for the  $d_{\text{OHs}}$  and  $\phi_{\text{HOH}}$  coordinates, the frequency-dependent-friction model including a nonharmonic potential outperforms the other models for all coordinates. In case of the  $d_{\text{OHa}}$  coordinate, shown in fig. S7E, the frequency-dependent-friction model with the harmonic potential also performs very well, due to the negligible nonharmonic contribution to the potential in fig. S7A.

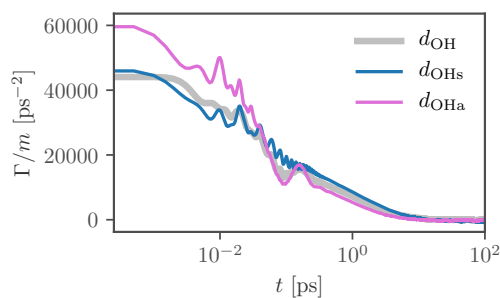


Figure S8: Comparison of time-dependent friction kernels extracted from the aiMD simulations for the  $d_{\text{OH}}$  (gray solid line),  $d_{\text{OHs}}$  (blue solid line) and  $d_{\text{OHa}}$  (purple solid line) coordinates.

The time-dependent friction kernels of the  $d_{\text{OH}}$ ,  $d_{\text{OHs}}$  and  $d_{\text{OHa}}$  coordinates are compared in fig. S8, scaled by the mass of the respective coordinate. The time-dependent friction kernel of the  $d_{\text{OHa}}$  coordinate differs significantly from the one of the  $d_{\text{OHs}}$  coordinate. However, all friction kernels show various oscillating decay time scales between 10 fs and 5 ps, which is discussed in detail in the main text for the example of  $d_{\text{OHs}}$ .

## XIV Constant-friction line shape

The dependence of the Lorentzian line shape function eq. (S51) on the friction coefficient  $\gamma$  for the  $d_{\text{OHs}}$  coordinate is illustrated in fig. S9A and for the  $\phi_{\text{HOH}}$  coordinate in fig. S9B. A variation of  $\gamma$  does not shift the peak position but significantly changes the width. This

C. Supporting Information:

Time-Dependent Friction Effects on Vibrational Infrared Frequencies and Line Shapes of Liquid Water

follows analytically from the maximum of eq. (S51)

$$\frac{\partial}{\partial \omega} [\omega \tilde{\chi}''(\omega)] = \frac{L^2}{k_B T} \left[ -\frac{8\tau\omega(\omega^4\tau^4 - 1)}{(\omega^2(\tau^2 - 8\tau_\omega^2) + 4\omega^4\tau_\omega^4 + 4)^2} \right] \quad (\text{S99})$$

$$\stackrel{!}{=} 0 \quad \text{for} \quad \omega = \tau_\omega^{-1}, \quad (\text{S100})$$

which does not depend on  $\gamma$ . When considering nonharmonic effects in the potential, simulated power spectra still show no significant shifts for variation of the friction coefficient, as shown in figs. S9C and D.

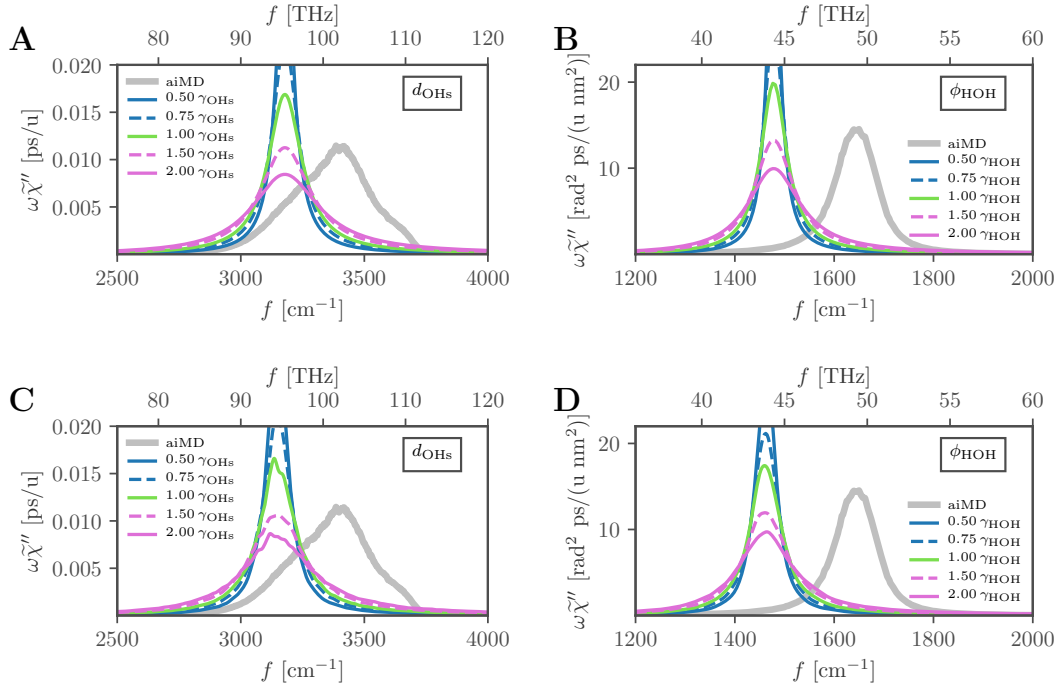


Figure S9: Power spectra, obtained from the aiMD simulations (gray solid lines) and compared to spectra from a constant friction model with the harmonic fit to the potential (A, B) and considering nonharmonic effects (C, D). The spectra are shown for variations of the friction coefficient  $\gamma_{\text{OHS}} = \Gamma'(f_{\text{OHS}})$  and  $\gamma_{\text{HOH}} = \Gamma'(f_{\text{OHS}})$ , where  $f_{\text{OHS}} = 3390 \text{ cm}^{-1}$  and  $f_{\text{HOH}} = 1650 \text{ cm}^{-1}$  are at the maxima of the respective power spectra from the simulations. **A, C:**  $d_{\text{OHS}}$  coordinate and **B, D:**  $\phi_{\text{HOH}}$  coordinate.

---

## References

- (S1) Kohler, F.; Findenegg, G.; Fischer, J.; Posch, H. *The liquid state*; Verlag Chemie Weinheim, 1972.
- (S2) Carlson, S.; Brünig, F. N.; Loche, P.; Bonthuis, D. J.; Netz, R. R. Exploring the absorption spectrum of simulated water from MHz to infrared. *J. Phys. Chem. A* **2020**, *124*, 5599–5605.
- (S3) Daldrop, J. O.; Kappler, J.; Brünig, F. N.; Netz, R. R. Butane dihedral angle dynamics in water is dominated by internal friction. *Proc. Natl. Acad. Sci.* **2018**, *115*, 5169–5174.
- (S4) Harp, G.; Berne, B. Time-correlation functions, memory functions, and molecular dynamics. *Phys. Rev. A* **1970**, *2*, 975–996.
- (S5) *Infrared Raman Spectroscopy: Methods and applications*; Schrader, B., Ed.; Wiley-VCH: New York, 1995.
- (S6) Bertie, J. E.; Lan, Z. Infrared intensities of liquids XX: The intensity of the OH stretching band of liquid water revisited, and the best current values of the optical constants of H<sub>2</sub>O(l) at 25°C between 15,000 and 1 cm<sup>-1</sup>. *Appl. Spectrosc.* **1996**, *50*, 1047–1057.
- (S7) Wiener, N. Generalized harmonic analysis. *Acta Math.* **1930**, *55*, 117–258.



Supporting Information:  
Pair-Reaction Dynamics in Water:  
Competition of Memory Friction, Inertia  
and the Potential Shape

---

*D*



**Supporting Information:  
Pair-Reaction Dynamics in Water:  
Competition of Memory, Potential-Shape and  
Inertial Effects**

Florian N. Brünig, Jan O. Daldrop, and Roland R. Netz\*

*Fachbereich Physik, Freie Universität Berlin, Arnimallee 14, 14195 Berlin, Germany*

E-mail: [rnetz@physik.fu-berlin.de](mailto:rnetz@physik.fu-berlin.de)

## I Effect of the confinement along the reaction coordinate

The harmonic confinement,  $kx^2/2$ , applied along the reaction coordinate  $x$ , the distance between the two reactants, has an impact on the equilibrium distributions and the reaction kinetics. In Fig. S1 this effect is illustrated by showing the effective pair potentials and  $\tau_{\text{MFP}}$  for the NaCl ion pair obtained from simulations with different confinement strengths  $k = 30, 50, 100 \text{ kJ mol}^{-1} \text{ nm}^{-2}$ ; the data for  $k = 100 \text{ kJ mol}^{-1} \text{ nm}^{-2}$  in blue is shown throughout the main text and the other sections of the supplement. In Fig. S1A the effective potential landscape is shown to be significantly broadened when the value for  $k$  is decreased. Also the barrier height from the contact-pair (CP) to solvent-separated-pair (SSP) states, i.e. for the dissociation reaction, decreases by about  $0.5 k_B T$  when going from  $k = 100 \text{ kJ mol}^{-1} \text{ nm}^{-2}$  to  $k = 30 \text{ kJ mol}^{-1} \text{ nm}^{-2}$ .

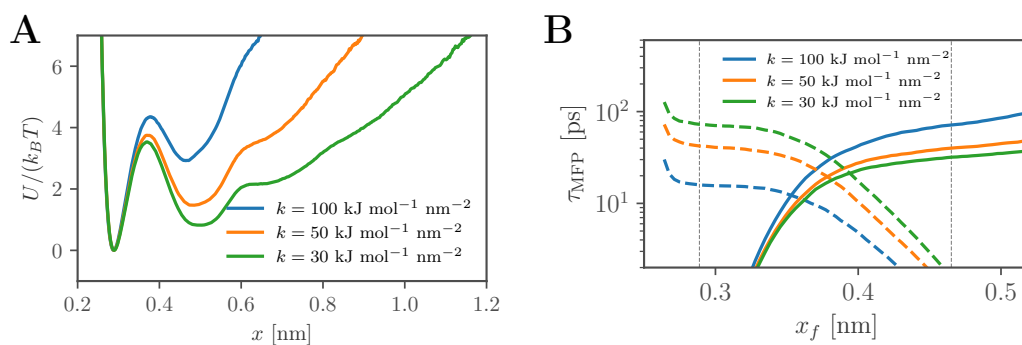


Figure S1: Effective pair potentials (A) and profiles of  $\tau_{\text{MFP}}(x_f)$  (B) for both the dissociation (solid lines) and association reactions (broken lines) along the reaction coordinate  $x$ , obtained from molecular dynamics (MD) simulations of the NaCl ion pair in water at different harmonic confinement strengths  $kx^2/2$ . In B the positions of the local minima of the pair potential for  $k = 100 \text{ kJ mol}^{-1} \text{ nm}^{-2}$  are indicated by vertical gray broken lines, which define the initial positions  $x_i$  for the profiles of  $\tau_{\text{MFP}}(x_f)$ .

In Fig. S1B profiles of  $\tau_{\text{MFP}}(x_f)$  are shown for both the dissociation (solid lines) and the association reactions (broken lines) from MD simulations. In accordance with the changes of the barrier height seen in Fig. S1A, the dissociation reaction becomes faster with decreasing confinement strength, while the association reaction becomes slower. Thus, to focus on

*D. Supporting Information:*

*Pair-Reaction Dynamics in Water: Competition of Memory Friction, Inertia and the Potential Shape*

---

the dissociation reaction in such equilibrium simulations, a high confinement is preferable, because the systems spends little time in the less favorable solvent-separated pair (SSP) state. In Fig. S2 it is demonstrated that also the extracted kernels are slightly modified when the confinement potential strength changes, which presumably reflects that the memory kernel is different for the CP and the SSP state.

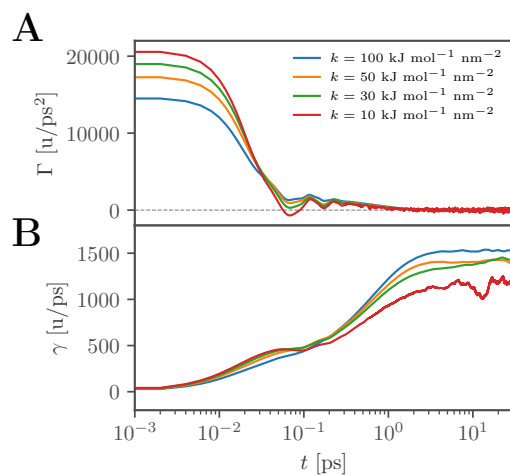


Figure S2: Memory friction kernel (**A**) and its running integral (**B**) for the NaCl ion pair in water from MD simulations at different harmonic confinement strengths  $kx^2/2$ .

## II Effective mass along the reaction coordinate

The effective mass of the reaction coordinate is estimated from the equipartition theorem,  $m = k_B T / \langle \dot{x}^2(t) \rangle$  and found to be 13.961 u for NaCl and 8.049 u for methane, which is in good agreement with the theoretical predictions of the reduced mass, 13.946 u for NaCl and 8.022 u for methane. As an important test of the form of the GLE, Eq. (1) in the main text, that uses a constant mass, the effective mass for the two systems considered in this study are shown in Figs. S3A and B as a function of the reaction coordinate  $X_i$  according to  $m_i = k_B T / \langle \dot{x}_i^2(t) \rangle|_{x_i(t) \in X_i}$ . The mass profiles are seen to be constant, as expected for atomic-distance coordinates based on exact arguments<sup>S1</sup>.

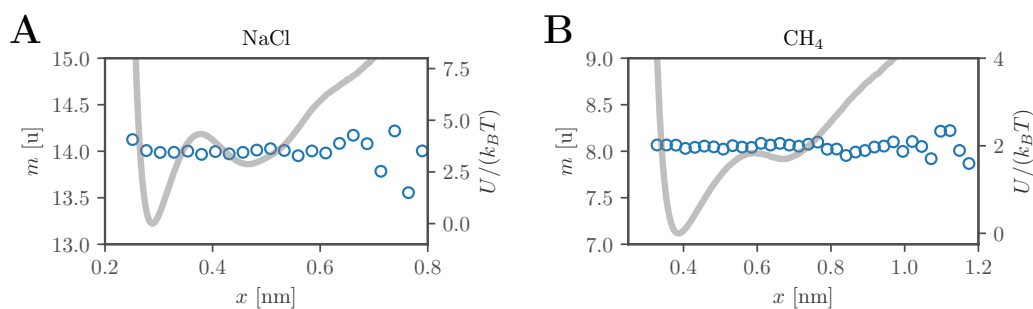


Figure S3: Effective mass profiles (blue circles) computed from the equipartition theorem along the reaction coordinate for the NaCl ion pair (A) and the methane pair separation coordinate (B) in water. For illustration the pair potentials are shown as thick gray lines on a second axis.

### III Nonharmonic-potential and barrier-height effects

The exponential scaling of reaction times with the potential barrier height  $U_0$  is known since Arrhenius<sup>S2</sup>. Our work focuses on the prefactor of the exponential scaling that is predicted by various analytical rate theories and depends on mass, memory friction and the potential shape. As also discussed in sections IV and VIII, the rate theories that are considered in this study, namely MM, GH and Kramers' medium-to-high-friction theories, use local harmonic approximations for the well and barrier regions of the nonharmonic pair potentials. This is often called a high-barrier approximation, since the local harmonic approximation becomes exact in the high-barrier limit. However, the harmonic approximation and the high-barrier approximation are distinct. In this section a perturbation analysis is presented in the overdamped Markovian limit that includes non-harmonic corrections and thereby allows us to improve the analytic prediction of reaction times for finite barrier height and to test the high-barrier approximation in dependence of the barrier height.

The exact prediction for the crossing time over a barrier in the overdamped Markovian limit given in Eq. (6) in the main text, which for constant friction  $\gamma$  reads

$$\tau_{\text{MFP}}(x_i, x_f) = \beta\gamma \int_{x_i}^{x_f} dx' e^{\beta U(x')} \int_{x_{\text{min}}}^{x'} dx e^{-\beta U(x)}, \quad (\text{S1})$$

is first compared to the Kramers' result for high friction, which follows via a harmonic approximations of the potential  $U(x)$  and is given by

$$\tau_{\text{Kr}}^{\text{hf}} = \frac{\gamma}{m\omega_{\text{max}}} \tau_{\text{TST}} \quad (\text{S2})$$

$$= \frac{2\pi\gamma}{m\omega_{\text{max}}\omega_{\text{min}}} e^{\beta U_0} \quad (\text{S3})$$

$$= \frac{2\pi\gamma}{\sqrt{U_{\text{min}}''|U_{\text{max}}''|}} e^{\beta U_0}. \quad (\text{S4})$$

The test is performed for a double-well (DW) potential,  $U(x) = U_0(1 - (x/L)^2)^2$  with length scale  $L$ , illustrated in Fig. S4A, as well as for the NaCl and methane pair potentials, which

are scaled by a constant factor in order to be able to vary the barrier height  $U_0$  from well to barrier top, i.e. from the contact pair (CP) to the transition state (TS).

The curvatures at the well bottom and at the barrier top, that enter the Kramers theory, are obtained from iterative smoothing of the pair potentials, as discussed in detail in section VIII. For consistency, the potential that is used for the evaluation of Eq. (S1) is obtained at the highest iteration of smoothing as presented in Fig. S10. Since different iteration levels are used around the well bottoms and the barrier top, the smoothed potential is constructed by combination of potentials with different numbers of smoothing iterations. The obtained smooth potentials are shown in Fig. S4D and G as blue solid lines and are compared to the raw data represented by gray solid lines. Subsequently, to accelerate the numerics, the smooth potential is represented by a fifth-order spline, for which the number of knots is determined such that the squared deviation between the spline and the smooth potential for values  $< 10 k_B T$  is below  $0.0002(k_B T)^{-2}$ . Afterwards, the spline is scaled linearly when investigating different barrier heights. The double integral in Eq. (S1) is then evaluated using the function ‘integrate.dblquad’, while for the spline representation the class ‘interpolate.UnivariateSpline’ is used, both implemented in `scipy 1.5.4`.

In Fig. S4B and C the results for the double-well potential are presented, scaled by the diffusion time scale  $\tau_D = \gamma L^2 / k_B T$ . In Fig. S4D–F the results for the NaCl and in Fig. S4G–I for the methane system are presented. Kramers’ theory (colored solid lines) slightly underestimates the exact analytical theory by up to 10%-20% in each system, but the relative difference,  $\tau_{\text{MFP}}^{\text{eq.}(6)} / \tau_{\text{MFP}}^{\text{Kramers}} - 1$ , which is shown in the insets in Figs. S4B,E,H, does decrease with barrier height, as expected, but the decrease is quite slow. Even at a barrier height of  $U_0 = 20 k_B T$  a relative difference of about 2% persists for the double-well and the NaCl systems and of about 6% for the methane system. Therefore, while for high barriers the quality of the local harmonic approximations of the potential used by the analytical rate theories does improve, even at moderately high barriers  $< 20 k_B T$ , nonharmonic-potential effects are significant and cannot be disregarded.

The error of the harmonic approximation can be estimated analytically from the exact solution, Eq. (S1), by deriving higher-order corrections to the Kramers' high-friction result Eq. (S2), which allows to predict the scaling of the relative error of the harmonic approximation with the barrier height. First, the inner integral of Eq. (S1) is approximated by Taylor expansion around the barrier top position  $x_B$  according to

$$I(x') = \int_{x_{\min}}^{x'} dx e^{-\tilde{U}(x)} = I(x_B) + (x' - x_B)I'(x_B) + (x' - x_B)^2 I''(x_B)/2 + \dots, \quad (\text{S5})$$

where  $\beta U(x) = \tilde{U}(x)$  is used. Since  $I'(x_B) = \exp(-\tilde{U}(x_B))$ , the first term in the expansion is exponentially dominant over the correction terms. By expanding the potential  $U(x)$  around the local minimum at  $x_A$ , i.e. the potential well, the inner integral thus can be written as

$$I(x') = \int_{x_{\min}}^{x'} dx e^{-\tilde{U}(x)} \approx I(x_B) \approx \int_{-\infty}^{\infty} dx e^{-\tilde{U}(x)} \quad (\text{S6})$$

$$\simeq \int_{-\infty}^{\infty} dx \exp\left(-\tilde{U}_A - \frac{1}{2}(x - x_A)^2 \tilde{U}_A^{II} - \frac{1}{6}(x - x_A)^3 \tilde{U}_A^{III} - \frac{1}{24}(x - x_A)^4 \tilde{U}_A^{IV} + \dots\right) \quad (\text{S7})$$

$$\simeq e^{-\tilde{U}_A} \int_{-\infty}^{\infty} dx \exp\left(-\frac{1}{2}(x - x_A)^2 \tilde{U}_A^{II}\right) \left(1 + \frac{1}{72}x^6 (\tilde{U}_A^{III})^2 - \frac{1}{24}x^4 \tilde{U}_A^{IV} + \dots\right) \quad (\text{S8})$$

$$= e^{-\tilde{U}_A} \left(\sqrt{\frac{2\pi}{\tilde{U}_A^{II}}} + \frac{(\tilde{U}_A^{III})^2}{72} \frac{15\sqrt{2\pi}}{(\tilde{U}_A^{II})^{7/2}} - \frac{\tilde{U}_A^{IV}}{24} \frac{3\sqrt{2\pi}}{(\tilde{U}_A^{II})^{5/2}} + \dots\right) \quad (\text{S9})$$

$$= e^{-\tilde{U}_A} \sqrt{\frac{2\pi}{\tilde{U}_A^{II}}} \left(1 + \frac{5(\tilde{U}_A^{III})^2}{24(\tilde{U}_A^{II})^3} - \frac{\tilde{U}_A^{IV}}{8(\tilde{U}_A^{II})^2} + \dots\right), \quad (\text{S10})$$

where Roman superscripts denote the order of derivatives,  $\tilde{U}_A^i = \partial^i \tilde{U}_A / \partial x^i|_{x=x_A}$ . In the derivation, the series expansion of the exponential function has been used  $\exp(x) = 1 + x + x^2/2 + \dots$  and the fact that odd powers in  $x$  do not contribute to the symmetric integral. The extension of the integral boundaries to infinity corresponds to a high-barrier approximation and leads to a correction that is exponentially small in the barrier height.

## MFPT to barrier top

Next, the outer integral of Eq. (S1) is approximated by a Taylor expansion of the potential around the barrier top at  $x_B$ . First, we consider the case in which the upper boundary of the integral, i.e. the final position of  $\tau_{\text{MFP}}$ , is located at the barrier top,

$$\tau_{\text{MFP}}(x_i, x_B) \simeq \beta\gamma I(x_B) \int_{x_i}^{x_B} dx' e^{\beta U(x')} \quad (\text{S11})$$

$$\simeq \beta\gamma I(x_B) \int_{-\infty}^{x_B} dx \exp\left(\tilde{U}_B + \frac{1}{2}(x - x_B)^2 \tilde{U}_B^{II} + \frac{1}{6}(x - x_B)^3 \tilde{U}_B^{III} + \frac{1}{24}(x - x_B)^4 \tilde{U}_B^{IV} + \dots\right) \quad (\text{S12})$$

$$\simeq \beta\gamma I(x_B) e^{\tilde{U}_B} \int_{-\infty}^{x_B} dx \exp\left(-\frac{1}{2}(x - x_B)^2 |\tilde{U}_B^{II}|\right) \left(1 + \frac{1}{6}x^3 \tilde{U}_B^{III} + \frac{1}{72}x^6 (\tilde{U}_B^{III})^2 + \frac{1}{24}x^4 \tilde{U}_B^{IV} + \dots\right) \quad (\text{S13})$$

$$\simeq \beta\gamma I(x_B) e^{\tilde{U}_B} \frac{1}{2} \sqrt{\frac{2\pi}{|\tilde{U}_B^{II}|}} \left(1 - \frac{2\tilde{U}_B^{III}}{3\sqrt{2\pi}|\tilde{U}_B^{II}|^{3/2}} + \frac{5(\tilde{U}_B^{III})^2}{24(\tilde{U}_B^{II})^3} + \frac{\tilde{U}_B^{IV}}{8|\tilde{U}_B^{II}|^2} + \dots\right). \quad (\text{S14})$$

The extension of the integral boundary to minus infinity leads to a correction that is exponentially small in the barrier height but also eliminates the dependence on the initial position  $x_i$ . The final expression for the MFPT is given as

$$\tau_{\text{MFP}}(x_i, x_B) \simeq \beta\gamma e^{\tilde{U}_B - \tilde{U}_A} \frac{1}{2} \sqrt{\frac{2\pi}{|\tilde{U}_B^{II}|}} \sqrt{\frac{2\pi}{\tilde{U}_A^{II}}} \left(1 + \frac{5(\tilde{U}_A^{III})^2}{24(\tilde{U}_A^{II})^3} - \frac{\tilde{U}_A^{IV}}{8(\tilde{U}_A^{II})^2} + \dots\right) \left(1 - \frac{2\tilde{U}_B^{III}}{3\sqrt{2\pi}|\tilde{U}_B^{II}|^{3/2}} + \frac{5(\tilde{U}_B^{III})^2}{24(\tilde{U}_B^{II})^3} + \frac{\tilde{U}_B^{IV}}{8|\tilde{U}_B^{II}|^2} + \dots\right) \quad (\text{S15})$$

$$\simeq e^{\tilde{U}_0} \frac{1}{2} \frac{2\pi\beta\gamma}{\sqrt{|\tilde{U}_B^{II}|\tilde{U}_A^{II}}} \left(1 - \frac{2\tilde{U}_B^{III}}{3\sqrt{2\pi}|\tilde{U}_B^{II}|^{3/2}} + \frac{5(\tilde{U}_A^{III})^2}{24(\tilde{U}_A^{II})^3} - \frac{\tilde{U}_A^{IV}}{8(\tilde{U}_A^{II})^2} + \frac{5(\tilde{U}_B^{III})^2}{24(\tilde{U}_B^{II})^3} + \frac{\tilde{U}_B^{IV}}{8|\tilde{U}_B^{II}|^2}\right) \quad (\text{S16})$$

$$= \frac{\tau_{\text{Kr}}^{\text{hf}}}{2} \left(1 - \frac{2\tilde{U}_B^{III}}{3\sqrt{2\pi}|\tilde{U}_B^{II}|^{3/2}} + \frac{5(\tilde{U}_A^{III})^2}{24(\tilde{U}_A^{II})^3} - \frac{\tilde{U}_A^{IV}}{8(\tilde{U}_A^{II})^2} + \frac{5(\tilde{U}_B^{III})^2}{24(\tilde{U}_B^{II})^3} + \frac{\tilde{U}_B^{IV}}{8|\tilde{U}_B^{II}|^2}\right). \quad (\text{S17})$$



## MFPT over barrier top

Here the outer integral of Eq. (S1) reaches over the barrier

$$\tau_{\text{MFP}}(x_i, x_f) \simeq \beta\gamma I(x_B) \int_{x_i}^{x_f} dx' e^{\beta U(x')} \quad (\text{S18})$$

$$\simeq \beta\gamma I(x_B) \int_{-\infty}^{\infty} dx \exp\left(\tilde{U}_B + \frac{1}{2}(x - x_B)^2 \tilde{U}_B^{II} + \frac{1}{6}(x - x_B)^3 \tilde{U}_B^{III} + \frac{1}{24}(x - x_B)^4 \tilde{U}_B^{IV} + \dots\right) \quad (\text{S19})$$

$$\simeq \beta\gamma I(x_B) e^{\tilde{U}_B} \int_{-\infty}^{\infty} dx \exp\left(-\frac{1}{2}(x - x_B)^2 |\tilde{U}_B^{II}|\right) \left(1 + \frac{1}{72}x^6 (\tilde{U}_B^{III})^2 + \frac{1}{24}x^4 \tilde{U}_B^{IV} + \dots\right) \quad (\text{S20})$$

$$\simeq \beta\gamma I(x_B) e^{\tilde{U}_B} \sqrt{\frac{2\pi}{|\tilde{U}_B^{II}|}} \left(1 + \frac{5(\tilde{U}_B^{III})^2}{24(\tilde{U}_B^{II})^3} + \frac{\tilde{U}_B^{IV}}{8|\tilde{U}_B^{II}|^2} + \dots\right), \quad (\text{S21})$$

where compared to the well-to-barrier-top case, Eq. (S14), the prefactor 1/2 and the  $-2\tilde{U}_B^{III}/(3\sqrt{2\pi}|\tilde{U}_B^{II}|^{3/2})$  term are missing. The final result is given as

$$\tau_{\text{MFP}}(x_i, x_f) \simeq \beta\gamma e^{\tilde{U}_B - \tilde{U}_A} \sqrt{\frac{2\pi}{|\tilde{U}_B^{II}|}} \sqrt{\frac{2\pi}{\tilde{U}_A^{II}}} \left(1 + \frac{5(\tilde{U}_A^{III})^2}{24(\tilde{U}_A^{II})^3} - \frac{\tilde{U}_A^{IV}}{8(\tilde{U}_A^{II})^2} + \dots\right) \left(1 + \frac{5(\tilde{U}_B^{III})^2}{24(\tilde{U}_B^{II})^3} + \frac{\tilde{U}_B^{IV}}{8|\tilde{U}_B^{II}|^2} + \dots\right) \quad (\text{S22})$$

$$\simeq e^{\tilde{U}_0} \frac{2\pi\beta\gamma}{\sqrt{|\tilde{U}_B^{II}|\tilde{U}_A^{II}}} \left(1 + \frac{5(\tilde{U}_A^{III})^2}{24(\tilde{U}_A^{II})^3} - \frac{\tilde{U}_A^{IV}}{8(\tilde{U}_A^{II})^2} + \frac{5(\tilde{U}_B^{III})^2}{24(\tilde{U}_B^{II})^3} + \frac{\tilde{U}_B^{IV}}{8|\tilde{U}_B^{II}|^2}\right) \quad (\text{S23})$$

$$= \tau_{\text{Kr}}^{\text{hf}} \left(1 + \frac{5(\tilde{U}_A^{III})^2}{24(\tilde{U}_A^{II})^3} - \frac{\tilde{U}_A^{IV}}{8(\tilde{U}_A^{II})^2} + \frac{5(\tilde{U}_B^{III})^2}{24(\tilde{U}_B^{II})^3} + \frac{\tilde{U}_B^{IV}}{8|\tilde{U}_B^{II}|^2}\right). \quad (\text{S24})$$

## Application to explicit potentials

The correction terms Eq. (S17) and Eq. (S24) can be evaluated analytically for the double-well model potential

$$U(x) = U_0 \left(1 - \frac{x^2}{L^2}\right)^2, \quad (\text{S25})$$

$$U^I(x) = -U_0 \left(\frac{4x}{L^2} - \frac{4x^3}{L^4}\right), \quad (\text{S26})$$

$$U^{II}(x) = -U_0 \left(\frac{4}{L^2} - \frac{12x^2}{L^4}\right) \quad \Longrightarrow \quad \tilde{U}_A^{II} = \tilde{U}_0 \frac{8}{L^2}, \tilde{U}_B^{II} = -\tilde{U}_0 \frac{4}{L^2}, \quad (\text{S27})$$

$$U^{III}(x) = U_0 \frac{24x}{L^4} \quad \Longrightarrow \quad \tilde{U}_A^{III} = -\tilde{U}_0 \frac{24}{L^4}, \tilde{U}_B^{III} = 0, \quad (\text{S28})$$

$$U^{IV}(x) = U_0 \frac{24}{L^4} \quad \Longrightarrow \quad \tilde{U}_A^{IV} = \tilde{U}_B^{IV} = \tilde{U}_0 \frac{24}{L^4}. \quad (\text{S29})$$

When inserting these values into Eq. (S17) and Eq. (S24), we obtain for the transition to the barrier top and over the barrier top the same result (except the prefactor of 1/2) since the third derivative at the barrier vanishes,  $\tilde{U}_B^{III} = 0$ , i.e. for  $x_f > x_B$  we obtain

$$\begin{aligned} \tau_{\text{MFP}}(x_i, x_f) &\simeq \tau_{\text{Kr}}^{\text{hf}} \left(1 + \frac{5(\tilde{U}_A^{III})^2}{24(\tilde{U}_A^{II})^3} - \frac{\tilde{U}_A^{IV}}{8(\tilde{U}_A^{II})^2} + \frac{\tilde{U}_B^{IV}}{8|\tilde{U}_B^{II}|^2}\right) \\ &= \tau_{\text{Kr}}^{\text{hf}} \left(1 + \frac{15}{64\tilde{U}_0} - \frac{3}{64\tilde{U}_0} + \frac{12}{64\tilde{U}_0}\right) \\ &= \tau_{\text{Kr}}^{\text{hf}} \left(1 + \frac{3}{8\tilde{U}_0}\right) \end{aligned} \quad (\text{S30})$$

$$\Longrightarrow \frac{\tau_{\text{MFP}}(x_i, x_f)}{\tau_{\text{Kr}}^{\text{hf}}} - 1 = \frac{3}{8\tilde{U}_0}. \quad (\text{S31})$$

This estimate is shown in Fig. S4C as a gray solid line and agrees well with the actual error, i.e. the relative difference between the Kramers' high friction prediction and the exact analytical result, that is plotted as a yellow broken line for the well-to-well case (CP to SSP) and as a blue broken line for the well-to-barrier-top case (CP to TS). Specifically the  $U_0^{-1}$  scaling is well visible.

For both the NaCl and methane systems, the correction terms for well-to-barrier-top and

D. Supporting Information:

Pair-Reaction Dynamics in Water: Competition of Memory Friction, Inertia and the Potential Shape

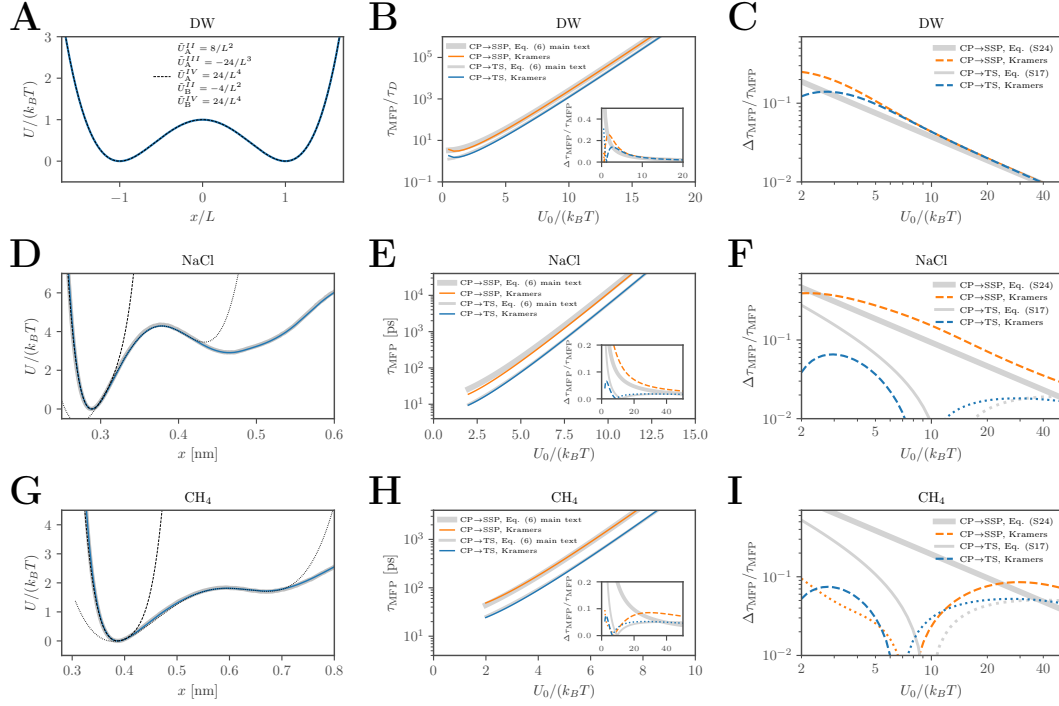


Figure S4: Comparison of the scaling of  $\tau_{\text{MFP}}$  with the barrier-height in the overdamped Markovian limit as given by Kramers' high friction theory Eq. (S2) (in B, E and H: blue solid line for going from the CP to the TS and yellow solid line for going from the CP to the SSP) and the exact analytical result of Eq. (6) (gray solid lines). The relative difference between the analytical theories, i.e.  $\tau_{\text{MFP}}^{\text{eq.(6)}}/\tau_{\text{MFP}}^{\text{Kramers}} - 1$  is given as broken lines in the respective colors in C, F and I (as well as in the insets in B, E and H), dotted colored lines denote negative values. Additionally, the analytical estimate of the relative difference, given by Eq. (S17) and Eq. (S24), is shown as lightgray solid lines in C, F and I and in the insets in B, E and H. See main text for details. **A–C**: Results for the double-well potential. **D–F**: Results for the NaCl pair potential. **F–G**: Results for the methane pair potential.

well-to-well cases, Eq. (S17) and Eq. (S24) respectively, are unequal. To evaluate these terms the local numerical derivatives are used as reported in Tab. S1 in section VIII. The local polynomial approximations of the potentials that follow from these parameters are also shown explicitly in Figs. S4D and G as broken black lines for the well bottom and dotted black lines for the barrier top.

We first discuss the well-to-barrier-top case (CP to TS), for which the estimated error, Eq. (S17), is given in Figs. S4F and I as thin gray solid lines. For both NaCl and methane it agrees well with the actual error, i.e. the relative difference between the Kramers' high friction prediction and the exact analytical result, that is plotted as blue broken lines, the dotted lines denote negative values. All curves show a crossing from positive to negative values at around  $U_0 = 10 k_B T$ , which reflects a complex competition of the various terms in Eq. (S17).

For the well-to-well case (CP to SSP) the estimated error, Eq. (S24), is given in Figs. S4F and I as thick gray solid lines and again compared to the actual error, that is plotted as yellow lines, dotted lines denote negative values. The estimated error is in both cases dominated by the  $U_0^{-1}$  scaling, that is also visible for the DW system discussed above and shown in Fig. S4C. For NaCl this scaling agrees well with the actual error (yellow broken line in Fig. S4F). For methane the actual error for the well-to-well case (yellow broken and yellow dotted lines in Fig. S4I) is much closer to the one of the well-to-barrier-top case (blue broken and blue dotted lines in Fig. S4I), than to the estimated one. This behavior is understood from the underlying potential in Fig. S4G, which shows that the two scenarios are actually very similar. Moreover, the barrier is highly asymmetric when compared to the potential of NaCl in Fig. S4D, which means that the cubic term at the barrier top,  $\tilde{U}_B^{III}$ , is important. However, the  $-2\tilde{U}_B^{III}/(3\sqrt{2\pi}|\tilde{U}_B^{II}|^{3/2})$  term drops out of the estimated error for the well-to-well case, Eq. (S24), due to the shift of the integration boundaries to infinity, which explains the deviation between the actual and the predicted error. Once again, these results confirm the complex interplay of potential effects beyond the harmonic approximation.

## IV Rate theories for barrier crossing

Theoretical predictions for barrier-crossing dynamics in a viscous environment reach back to Kramers<sup>S3</sup>, who derived different friction-dependent prefactors to the Arrhenius law in the opposing inertia dominated and overdamped regimes. The well-known Kramers turnover between these regimes was only later fully covered in a theory by Mel'nikov and Meshkov (MM)<sup>S4</sup>. A memory-induced barrier-crossing acceleration compared to the overdamped Kramers limit was first demonstrated by Grote and Hynes (GH)<sup>S5</sup>, which gives way to barrier-crossing slow down in the long memory-time limit<sup>S6,S7</sup>.

All these reaction-rate theories calculate a prefactor to transition-state theory, which, assuming a harmonic potential well for the reactant state, predicts the mean escape time of a particle over a frictionless barrier to be<sup>S8</sup>

$$\tau_{\text{TST}} = \frac{2\pi}{\omega_{\text{min}}} e^{\beta U_0}, \quad (\text{S32})$$

where  $U_0$  denotes the barrier height,  $\beta^{-1} = k_B T$  is the thermal energy, and the well frequency  $\omega_{\text{min}} = \sqrt{U''_{\text{min}}/m}$  depends on the curvature  $U''_{\text{min}} := U''(x_{\text{min}})$  at the minimum  $x_{\text{min}}$  of the potential well from which the particle escapes.

Kramers considered the escape from a harmonic potential well for a particle undergoing Brownian motion, as described by the Langevin equation (LE) Eq. (3) with position-independent friction  $\gamma$ , for both the limits of medium-to-high friction and low friction<sup>S3</sup>. For the medium-to-high friction regime, he obtained

$$\tau_{\text{Kr}}^{\text{mh}} = \left[ \left( \frac{\gamma^2}{4m^2} + \omega_{\text{max}}^2 \right)^{1/2} - \frac{\gamma}{2m} \right]^{-1} \omega_{\text{max}} \tau_{\text{TST}}, \quad (\text{S33})$$

from which follows in the high-friction limit,  $\gamma/m \rightarrow \infty$ ,

$$\tau_{\text{Kr}}^{\text{hf}} = \frac{\gamma}{m\omega_{\text{max}}} \tau_{\text{TST}}, \quad (\text{S34})$$

where the barrier frequency  $\omega_{\max} = \sqrt{-U''_{\max}/m}$  depends only on the curvature  $U''_{\max} := U''(x_{\max})$  at the barrier top  $x_{\max}$ , which reflects usage of the harmonic approximation for the barrier.

In the low-friction limit he derived

$$\tau_{\text{Kr}}^{\text{lf}} = \frac{m}{\gamma\beta U_0} e^{\beta U_0}. \quad (\text{S35})$$

Note the opposite scaling of the predictions with the friction constant  $\gamma$ : While for high friction  $\tau_{\text{Kr}}^{\text{hf}} \sim \gamma$ , for low friction  $\tau_{\text{Kr}}^{\text{lf}} \sim \gamma^{-1}$ .

Mel'nikov and Meshkov (MM)<sup>S4</sup> derived a solution to the Kramers' problem which is valid for all values of the friction and hence bridges the two asymptotic expressions Eq. (S33) and Eq. (S35). The Melnikov'/Meshkov (MM) result is given by

$$\tau_{\text{MM}} = A^{-1}(\Delta) \left[ \left( \frac{\gamma^2}{4m^2} + \omega_{\max}^2 \right)^{1/2} - \frac{\gamma}{2m} \right]^{-1} \omega_{\max} \tau_{\text{TST}}, \quad (\text{S36})$$

$$A(\Delta) = \exp \left[ \frac{2}{\pi} \int_0^{\frac{\pi}{2}} \ln \left[ 1 - e^{-\Delta/[4\cos^2(x)]} \right] dx \right], \quad (\text{S37})$$

$$\Delta = 2\sqrt{2} \frac{\gamma}{\sqrt{m}} \beta \int_{-\sqrt{2}L}^0 \sqrt{U_0 - U(x)} dx. \quad (\text{S38})$$

Importantly, while the prefactor  $A(\Delta)$ , which becomes relevant in the inertial regime,  $\gamma \rightarrow 0$ , considers the full nonharmonic potential,  $U(x)$ , Eq. (S36) still contains the harmonic approximations of the potential for both well and barrier and is therefore not exact for a general potential shape.

While both Kramers' and MM theory consider Markovian dynamics, Grote and Hynes (GH)<sup>S5</sup> developed a theory for the mean first-passage time including non-Markovian effects. Their expression for the case where the dynamics in a harmonic potential well relax fast and only memory effects on a harmonic barrier are relevant is given by

$$\tau_{\text{GH}} = \frac{\omega_{\max}}{\lambda} \tau_{\text{TST}}, \quad (\text{S39})$$

where  $\tilde{\Gamma}(\lambda)$  denotes the Laplace-transformed memory friction kernel  $\Gamma(t)$  at the barrier top, and the real reactive frequency,  $\lambda > 0$ , is the solution of the equation

$$\lambda = \frac{\omega_{\max}^2}{\lambda + \tilde{\Gamma}(\lambda)/m}. \quad (\text{S40})$$

Thus, for a single exponential kernel  $\Gamma(t) = \gamma e^{-t/\tau}/\tau$ ,  $\lambda$  is given as the single positive solution of the cubic equation

$$\lambda^3 + \frac{\lambda^2}{\tau} + \left( \frac{\gamma}{m\tau} - \omega_{\max}^2 \right) \lambda = \frac{\omega_{\max}^2}{\tau}. \quad (\text{S41})$$

In the Markovian limit, i.e. for delta-correlated friction,  $\Gamma(t) = 2\gamma\delta(t)$  and  $\tilde{\Gamma}(\lambda) = \gamma$ , it follows that  $\lambda = (\gamma^2/(4m^2) + \omega_{\max}^2)^{1/2} - \gamma/(2m)$  and thus  $\tau_{\text{GH}} = \tau_{\text{Kr}}^{\text{mh}}$ , the Kramers medium-to-high-friction result in Eq. (S33). Note that, either in the inertial,  $m \rightarrow \infty$ , or the long memory limit,  $\tau \rightarrow \infty$ , it follows that  $\lambda = \omega_{\max}$  and thus Grote/Hynes (GH) theory reduces to the transition-state theory result,  $\tau_{\text{GH}} = \tau_{\text{TST}}$ . It thereby misses both the Markovian low-friction limit, covered by Eq. (S35)<sup>S3,S4</sup> and the memory slow-down regime for long memory time that is obtained if memory effects in the barrier and well regions are equally important<sup>S6,S7</sup>. Evidently, it also misses nonharmonic-potential effects.

In the overdamped Markovian limit, the Fokker-Planck equation is most suitable for analytical calculations, for arbitrary potential shapes  $U(x)$  and position-dependent friction  $\gamma(x)$  it reads<sup>S9</sup>

$$\frac{\partial}{\partial t} P(x, t) = \frac{\partial}{\partial x} \left[ \frac{\beta^{-1}}{\gamma(x)} e^{-\beta U(x)} \frac{\partial}{\partial x} [P(x, t) e^{\beta U(x)}] \right] \quad (\text{S42})$$

and describes the time propagation of the distribution  $P(x, t)$ . From the Fokker-Planck equation, the exact expression for  $\tau_{\text{MFP}}$  between initial  $x_i$  and final positions  $x_f$ , shown as Eq. (6) in the main text, follows as<sup>S10</sup>

$$\tau_{\text{MFP}}(x_i, x_f) = \beta \int_{x_i}^{x_f} dx' \gamma(x') e^{\beta U(x')} \int_{x_{\min}}^{x'} dx e^{-\beta U(x)}. \quad (\text{S43})$$

Eq. (S43) can be inverted and thereby used to estimate a position-dependent friction profile

$\gamma(x)$  from measured values of  $\tau_{\text{MFP}}$ , which is presented in detail in section V.

## V Position-dependent friction effects

The dynamics of overdamped Markovian systems is often modeled with a position-dependent friction profile,  $\gamma(x)$ . Such a profile can be estimated from  $\tau_{\text{MFP}}(x)$  data and the Fokker-Planck solution Eq. (6) in the main text, that is repeated here

$$\tau_{\text{MFP}}(x_i, x_f) = \beta \int_{x_i}^{x_f} dx' \gamma(x') e^{\beta U(x')} \int_{x_{\min}}^{x'} dx e^{-\beta U(x)}, \quad (\text{S44})$$

where  $x_i$  is the starting position and  $x_f$  the final position of  $\tau_{\text{MFP}}$ ,  $\beta = (k_B T)^{-1}$  and  $x_{\min}$  is the lower reflecting boundary. Eq. (S44) holds for dissociation dynamics with  $x_f > x_i$ . The corresponding solution for association dynamics  $x_f < x_i$  is

$$\tau_{\text{MFP}}(x_i, x_f) = \beta \int_{x_f}^{x_i} dx' \gamma(x') e^{\beta U(x')} \int_{x'}^{x_{\max}} dx e^{-\beta U(x)}, \quad (\text{S45})$$

where  $x_{\max}$  is the upper reflecting boundary.

Eq. (S44) and Eq. (S45) can be inverted to give<sup>S11,S12</sup>

$$\gamma_{\rightarrow}(x_f) = k_B T \frac{\partial \tau_{\text{MFP}}(x_i, x_f)}{\partial x_f} e^{-\beta U(x_f)} \left[ \int_{x_{\min}}^{x_f} dx e^{-\beta U(x)} \right]^{-1}, \quad \text{for } x_f > x_i, \quad (\text{S46})$$

$$\gamma_{\leftarrow}(x_f) = -k_B T \frac{\partial \tau_{\text{MFP}}(x_i, x_f)}{\partial x_f} e^{-\beta U(x_f)} \left[ \int_{x_f}^{x_{\max}} dx e^{-\beta U(x)} \right]^{-1}, \quad \text{for } x_f < x_i, \quad (\text{S47})$$

or, alternatively, when instead taking the spatial derivative with respect to the initial position  $x_i$

$$\gamma_{\rightarrow}(x_i) = -k_B T \frac{\partial \tau_{\text{MFP}}(x_i, x_f)}{\partial x_i} e^{-\beta U(x_i)} \left[ \int_{x_{\min}}^{x_i} dx e^{-\beta U(x)} \right]^{-1}, \quad \text{for } x_f > x_i, \quad (\text{S48})$$

$$\gamma_{\leftarrow}(x_i) = k_B T \frac{\partial \tau_{\text{MFP}}(x_i, x_f)}{\partial x_i} e^{-\beta U(x_i)} \left[ \int_{x_i}^{x_{\max}} dx e^{-\beta U(x)} \right]^{-1}, \quad \text{for } x_f < x_i. \quad (\text{S49})$$



D. Supporting Information:

Pair-Reaction Dynamics in Water: Competition of Memory Friction, Inertia and the Potential Shape

---

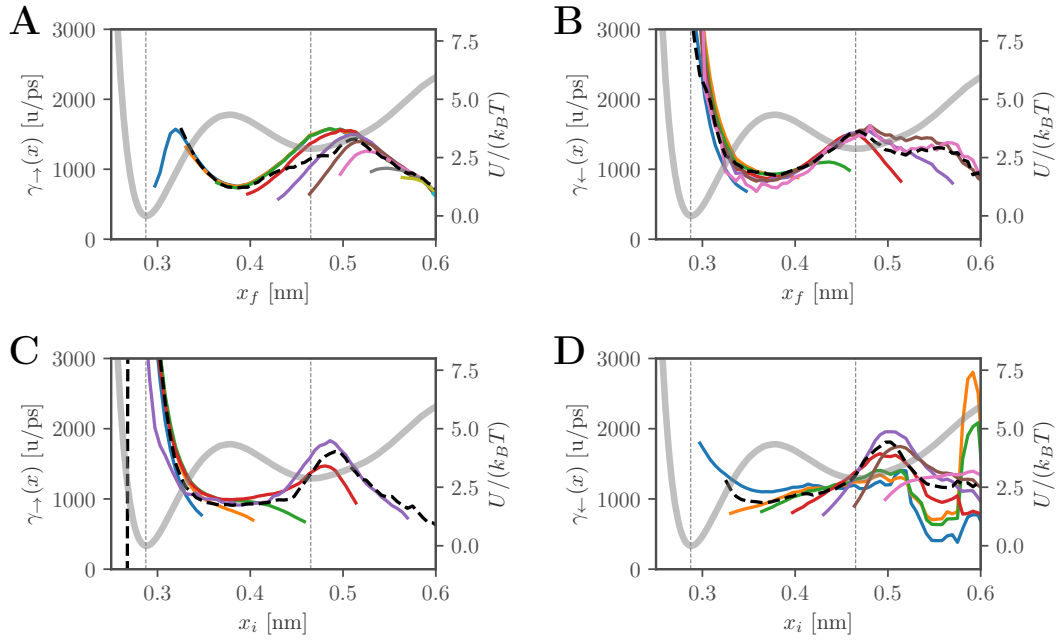


Figure S5: Position-dependent friction profiles estimated from  $\tau_{\text{MFP}}$  profiles obtained from MD simulations of the NaCl ion pair in water for either the dissociation dynamics,  $\gamma_{\rightarrow}(x)$ , (A, C) or the association dynamics,  $\gamma_{\leftarrow}(x)$  (B, D), using the respective Eq. (S46)–Eq. (S49). The overlap profiles are shown as black broken lines, see text for details. For illustration the pair potentials are shown as thick gray lines on a second axis. **A, B:** The profiles are shown as calculated from  $\tau_{\text{MFP}}$  for various fixed initial positions  $x_i$  and plotted over the final positions  $x_f$  as colored solid lines. **C, D:** The profiles are shown as calculated from  $\tau_{\text{MFP}}$  for various fixed final positions  $x_f$  and plotted over the initial positions  $x_i$  as colored solid lines.

From Eq. (S46) and the  $\tau_{\text{MFP}}(x_f)$  data for the dissociation dynamics of the NaCl ion pair shown in the main text in Fig. 2C, the friction profile  $\gamma_{\rightarrow}(x_f)$  is estimated, while from Eq. (S47) and the  $\tau_{\text{MFP}}(x_f)$  data for association dynamics shown in Fig. S8B, one obtains the friction profile  $\gamma_{\leftarrow}(x_f)$ .

In practice, the estimation of these profiles is not straight-forward. Importantly,  $x_i$  and  $x_f$  should not be too close to each other because otherwise inertial and memory effects lead to spurious artifacts<sup>S12,S13</sup>. It is therefore advisable to estimate the profiles for various combinations of  $x_i$  and  $x_f$  and take the mean in regions where the data overlap, as presented previously for water pair dynamics<sup>S12</sup>. Profiles  $\gamma_{\rightarrow}(x_f)$  along  $x_f$  for various fixed values of  $x_i$  are given in Fig. S5A and for  $\gamma_{\leftarrow}(x_f)$  in Fig. S5B as colored solid lines.

Corresponding profiles  $\gamma_{\rightarrow}(x_i)$  along  $x_i$  for various fixed values of  $x_f$  are given in Fig. S5C and for  $\gamma_{\leftarrow}(x_i)$  in Fig. S5D as colored solid lines. The overlap profiles are estimated from the mean of all profiles  $\gamma(x_f)|_{x_i}$  (or  $\gamma(x_i)|_{x_f}$ ) for which  $|x_f - x_i| \in [0.05, 0.1]$  nm and are shown in Fig. S5A–D as black broken lines and repeated in Fig. S6 as blue ( $\gamma_{\rightarrow}(x)$ ) and yellow ( $\gamma_{\leftarrow}(x)$ ) lines.

Comparison of the four position-dependent friction profiles in Fig. S6 demonstrates significant deviations among them. In fact, the result depends strongly on the direction of  $\tau_{\text{MFP}}$ , i.e. on whether one determines friction profiles from dissociation or association reactions, and also on details of the averaging procedure. We conclude that due to significant inertial and memory effects, strong variations between the friction profiles for association and dissociation reactions determined from variation of the initial and final positions are seen in Fig. S5<sup>S12,S13</sup> and therefore there is no unique friction profile that would describe the dynamics of the NaCl separation coordinate.

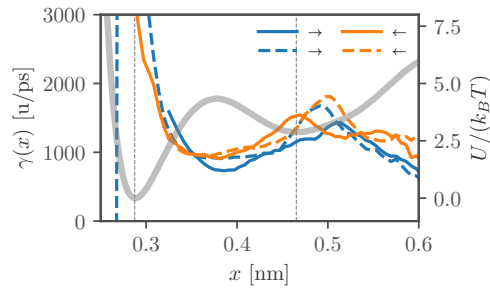


Figure S6: Comparison of the various position-dependent friction profiles estimated from  $\tau_{\text{MFP}}$  profiles obtained from MD simulations of the NaCl ion pair in water for either the dissociation dynamics,  $\gamma_{\rightarrow}(x)$ , (blue lines) or the association dynamics,  $\gamma_{\leftarrow}(x)$  (yellow lines), using the respective Eq. (S46)–Eq. (S49), shown in Fig. S5 as black broken lines. Profiles that are estimated for various fixed initial positions  $x_i$  and plotted over the final positions  $x_f$  are here shown as solid lines. The broken lines denote the opposite case, i.e. profiles that are estimated for various fixed final positions  $x_f$  and plotted over the initial positions  $x_i$ . For illustration the pair potential is shown as a thick gray line on a second axis.

## VI Dependence of the mean first-passage time on the initial position

In Fig. S7 the dependence of  $\tau_{\text{MFP}}(x_i, x_f)$  on the initial position  $x_i$  is illustrated for the NaCl ion pair (Fig. S7A) and the pair of methane beads (Fig. S7B). The data is shown both for the dissociation (blue solid lines) and association reactions (blue broken lines) and the final positions  $x_f$  are taken as the local minima (vertical thin gray broken lines) left and right of the potential barrier (gray solid lines). All profiles are very flat within the well regions from which they depart, even for the association reaction of methane where the barrier to the CP state is virtually non-existent. This means that the precise choice of  $x_i$  is rather unimportant when comparing with analytical rate theories, for which the predicted  $\tau_{\text{MFP}}$  does not depend on the choice of  $x_i$  due to the inherent high-barrier approximation, which is discussed in section III.

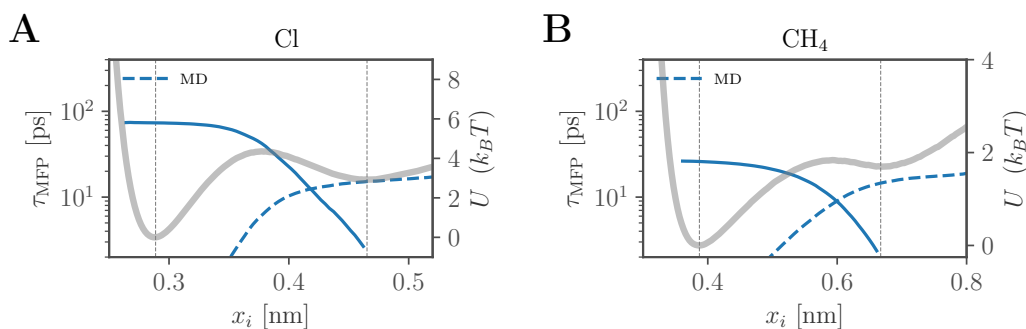


Figure S7: Profiles of  $\tau_{\text{MFP}}(x_i)$  for the dissociation (solid lines) and associations reactions (broken lines) along the reaction coordinate  $x$ , obtained from MD simulations of the NaCl ion pair (A) and a pair of methane beads (B) in water. For comparison the potentials are shown as a gray solid line with the scale on the right side of the plot. The positions of the minima are indicated as vertical gray dotted lines and determine the final positions of each  $\tau_{\text{MFP}}(x_i)$ .

The weak dependence of the MFPT on the initial position can be easily understood in the Markovian overdamped limit based on the exact expression Eq. (6) in the main text, from

which one derives

$$\frac{\partial\tau_{\text{MFP}}(x_i, x_f)/\partial x_i}{\partial\tau_{\text{MFP}}(x_i, x_f)/\partial x_f} = -\frac{e^{\beta U(x_i)} \int_{x_{\text{min}}}^{x_i} dx e^{-\beta U(x)}}{e^{\beta U(x_f)} \int_{x_{\text{min}}}^{x_f} dx e^{-\beta U(x)}}. \quad (\text{S50})$$

If the initial position  $x_i$  coincides with the potential minimum and if there is no second deeper minimum between  $x_i$  and  $x_f$ , one obtains in the high-barrier limit

$$\frac{\partial\tau_{\text{MFP}}(x_i, x_f)/\partial x_i}{\partial\tau_{\text{MFP}}(x_i, x_f)/\partial x_f} \approx -e^{\beta U(x_i) - \beta U(x_f)} / 2, \quad (\text{S51})$$

which means that the ratio of the dependence of the MFPT on the initial position and on the final position depends exponentially on the free energy difference of the initial and final positions. For dissociation reactions, the initial state has a lower free energy than the final state, which explains the very weak dependence of the dissociation MFPT on the initial position in Fig. S7 compared to the dependence on the final position shown in the main text.

## VII NaCl ion pair association reaction dynamics

In Fig. S8, the analysis of the association dynamics of the NaCl ion pair in water is presented, using the same methodology that is employed in the main text for the dissociation reaction. In Fig. S8A a summary of the results is presented similar to Fig. 3A in the main text and in Figs. S8B–E the data is shown in detail similar to Figs. 2C,E–G in the main text.

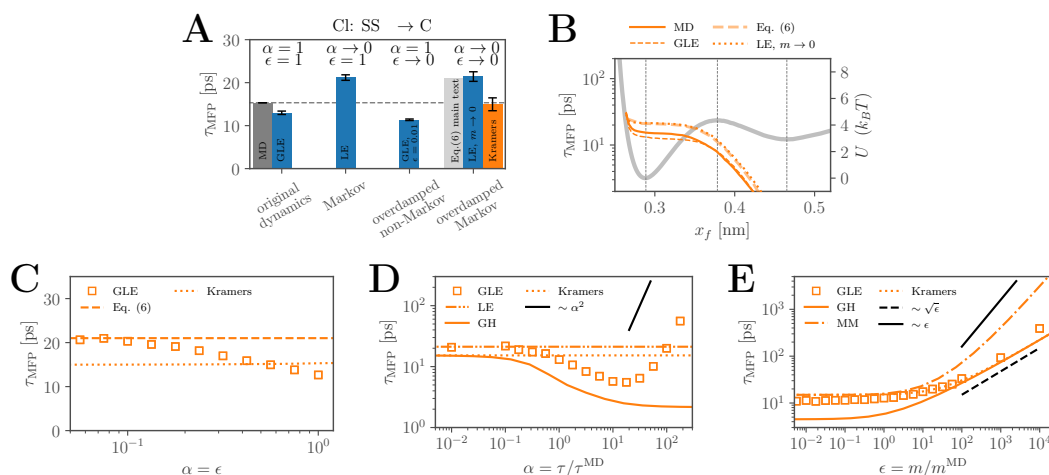


Figure S8: Analysis of the association dynamics along the separation coordinate of a single NaCl ion pair in water. **A**: Summary of the results, similar to Fig. 3A in the main text, in terms of  $\tau_{\text{MFP}}$  from the SSP to the CP of the pair potential, as obtained from MD (gray bar and horizontal gray broken line) and using the generalized Langevin equation (GLE) in different limits of the memory and inertial scaling parameters,  $\alpha$  and  $\epsilon$  (blue bars). The analytical result of Eq. (6) is shown for the overdamped Markovian limit as a lightgray bar. Additionally, Kramers' theory for high friction Eq. (S34) is shown as a yellow bar. Stochastic errors for the MD data are obtained as standard errors of the mean over ten fragments of the total trajectory. Stochastic errors for the various GLE and LE simulations (blue bars) are calculated from the standard error of the mean over ten independent runs. Errors for the rate theories (yellow bars) are estimated from the dominant errors in the harmonic fits to the potentials, as shown in SI section VIII. **B**: Profiles of  $\tau_{\text{MFP}}$  starting from the SSP state, obtained directly from MD simulations (yellow solid line), from simulation of the GLE Eq. (1) (yellow short-dashed line), from the theory for the overdamped Markovian limit Eq. (6) (yellow long-dashed line) and from simulations of the overdamped LE, Eq. (3) for  $m \rightarrow 0$  (yellow dotted line). For comparison the potential is shown as a gray solid line with the scale on the right side of the plot. The positions of the extrema are indicated as vertical gray dotted lines. **C–E**: Scaling of  $\tau_{\text{MFP}}$  of the association reactions from the SSP to the CP (yellow squares) with respect to changing both  $\alpha$  and  $\epsilon$  simultaneously (C), only memory effects (D) and only inertial effects (E) as obtained from GLE simulations. Theoretical predictions by Kramers for medium-to-high friction (dotted lines) and by GH (solid lines) are shown for comparison. The analytical result Eq. (6) is shown in C as a broken yellow line. Predictions by MM theory are shown in E as a dash-dotted line. Further numerical data are obtained for the Markovian limit using Eq. (3) in D (yellow dash-double-dotted line).

## VIII Harmonic approximations of the pair potentials

The rate theories that are considered in this study, namely MM, GH and Kramers' medium-to-high-friction theories, use local harmonic approximations for the well and barrier regions of the nonharmonic pair potentials. Thus, the pair potentials must be fitted quadratically,  $U(x) = U_i^{II}(x - x_i)^2/2$  around the extrema at  $x_i$ , the two well regions of the contact pair (CP) and solvent-separated pair (SSP) states, with  $U_A^{II}$  and  $U_C^{II}$  respectively, as well as the TS at the barrier top, with  $U_B^{II}$ . The parameters  $x_i$  and  $U_i^{II}$  are obtained from the numerical derivatives of the potentials. The potentials,  $U(x)/(k_B T) = -\log(h(x))$ , are obtained from histograms  $h(x)$  of the trajectory data with equidistant bins of width  $x_{j+1} - x_j = 0.5$  pm, that are smoothed by iterative convolution with a flat window function, which has a width of three bins. The numerical derivatives are then calculated by successive central differences, i.e.

$$U^I(x_j) = \frac{U(x_{j+1}) - U(x_{j-1}))}{(x_{j+1} - x_{j-1})}, \quad (\text{S52})$$

$$U^{II}(x_j) = \frac{U(x_{j+2}) - 2U(x_j) + U(x_{j-2}))}{(x_{j+1} - x_{j-1})^2}, \quad (\text{S53})$$

$$U^{III}(x_j) = \frac{U(x_{j+3}) - 3U(x_{j+1}) + 3U(x_{j-1}) - U(x_{j-3}))}{(x_{j+1} - x_{j-1})^3}, \quad (\text{S54})$$

$$U^{IV}(x_j) = \frac{U(x_{j+4}) - 4U(x_{j+2}) + 6U(x_j) - 4U(x_{j-2}) + U(x_{j-4}))}{(x_{j+1} - x_{j-1})^4}. \quad (\text{S55})$$

The first and second numerical derivatives obtained after different iterations of smoothing are shown in different shades of gray in Fig. S10. The curves are then linearly interpolated to obtain  $x_i$  from  $U^I(x_i) = 0$ , shown as vertical black broken lines throughout Fig. S10, and  $\kappa_i$  from  $U^{II}(x_i) = \kappa_i$  shown as horizontal black broken lines in the lower panels in Fig. S10. The convergence of the values of  $x_i$  and  $U_i^{II}$  with the number of iterations is reported in the insets in Fig. S10. A summary of the fit parameters together with higher derivatives is given in Tab. S1.

In Figs. S9A and B, the local harmonic fits are shown as black broken lines and compared to the potentials as thick solid lines. The fit parameters are reported in the legends. For

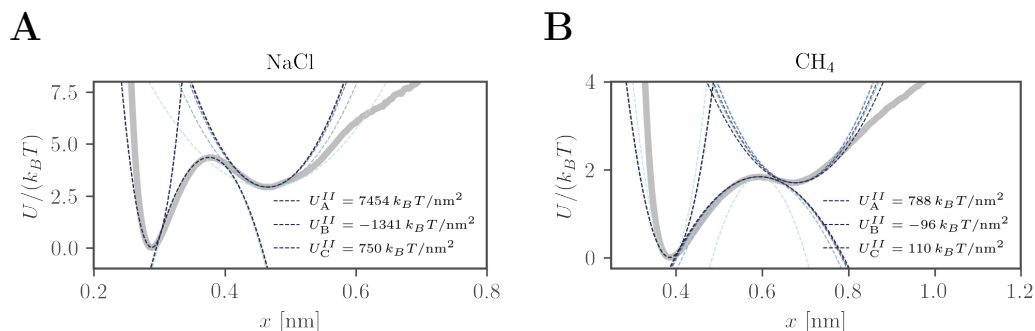


Figure S9: Asymptotic harmonic fits of the well and barrier regions, shown as black broken lines, of the effective pair potentials (gray solid lines) of the NaCl ion pair (A) and the methane pair (B) in water. The fitted curvatures  $U_i^{II}$  are reported in the legend with indices from A to C corresponding to the three extrema from left to right. Alternative local harmonic fits corresponding to curves for different levels of smoothing in Fig. S10, i.e. different numbers of smoothing iterations, are plotted as broken lines in different shades of gray corresponding to Fig. S10.

comparison, the parabolas corresponding to the other curves in Fig. S10, i.e. different numbers of iterations of the smoothing procedure, are plotted as broken lines in the corresponding shades of gray. It is seen that these alternative local harmonic fits are also good local approximations of the potential. Due to the wide spread of curvatures determined in Fig. S10 and confirmed graphically in Figs. S9A and B, relative error margins for  $U_i^{II}$  of  $\pm 10\%$  are assumed. These relative errors are propagated to errors of the rate theories that are evaluated based on these harmonic approximations, noting that  $\sqrt{U_{\max}^{II}}$  appears in the numerator and  $\sqrt{U_{\min}^{II}}$  in the denominator of the different rate theories. Therefore, a relative error of 10% in

**Table S1: Derivatives at the local extrema of the pair potentials, determined after iterative smoothing.**

NaCl	$x_i$ [nm]	$U^{II}$ [ $k_B T/\text{nm}^2$ ]	$U^{III}$ [ $k_B T/\text{nm}^3$ ]	$U^{IV}$ [ $k_B T/\text{nm}^4$ ]
	0.289	7453	$-5.18 \times 10^5$	$2.77 \times 10^7$
	0.378	-1341	$2.39 \times 10^4$	$1.38 \times 10^6$
	0.465	750	$3.68 \times 10^3$	$1.14 \times 10^6$
CH <sub>4</sub>				
	0.387	788	$-3.17 \times 10^4$	$2.34 \times 10^6$
	0.595	-95	$1.64 \times 10^3$	$3.49 \times 10^4$
	0.667	109	$1.71 \times 10^3$	$-1.37 \times 10^5$



### D. Supporting Information:

## Pair-Reaction Dynamics in Water: Competition of Memory Friction, Inertia and the Potential Shape

both curvatures directly propagates to the relative error of the predicted  $\tau_{\text{MFP}}$  and is assumed to be the dominant source of error.

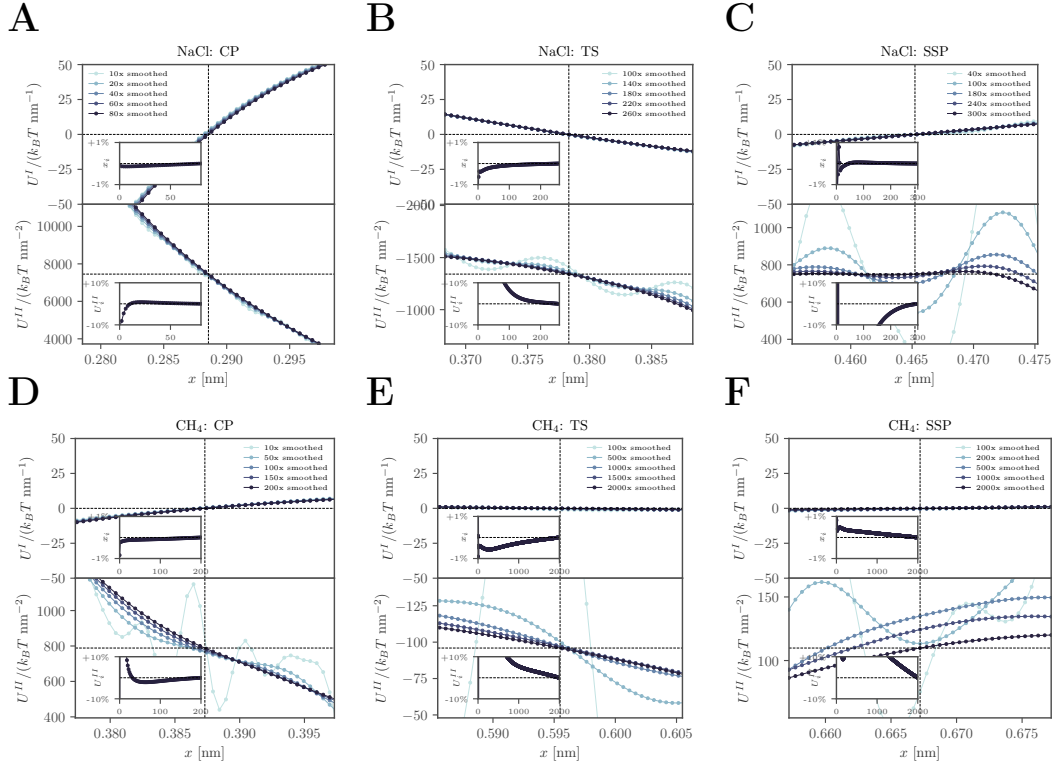


Figure S10: First (upper panels) and second derivatives (lower panels) of the effective pair potentials around the three local extrema corresponding to the CP (A, D), the TS (B, E) and the SSP states (C, F) for NaCl and methane. The derivatives are calculated numerically after consecutive iterations of smoothing of the potentials, that are obtained from the simulation data at a fixed bin width. The vertical black broken lines denote the position of the local extrema,  $x_i$ , determined from the first derivatives. In the lower panels the horizontal black broken lines denote the values of the harmonic fit parameters  $U_i^{II}$ , that are determined from the second derivatives at the highest iteration of smoothing. The convergence of the relative deviations of the values of  $x_i$  and  $U_i^{II}$  with the number of iterations is shown in the insets. **A–C:** Results for the NaCl pair potential. **D–F:** Results for the methane pair potential.

## IX Methane pair reaction dynamics

In Fig. S11, the analysis of the dissociation dynamics of a pair of unpolar methane beads in water is presented, using the same methodology that is employed in the main text for the NaCl ion pair. MD simulations were performed analogously to the MD simulations for NaCl as presented in the methods section. The reaction coordinate is the relative distance  $x$ , along which a weak harmonic potential with force constant  $k = 30 \text{ kJmol}^{-1}\text{nm}^{-2}$  is applied to increase the number of dissociation events. The memory kernel obtained from the MD simulation data is shown in Fig. S11A and its integral in Fig. S11B as blue solid lines. In contrast to the memory kernel of the NaCl ion pair shown in Fig. 2A, three exponentially decaying components, according to Eq. (2), suffice to fit the memory kernel satisfactorily (yellow broken lines in Fig. S11A and B). Furthermore, the integral value of  $\gamma = 790 \text{ u/ps}$  is only roughly half the value of that for the ion pair and is reached after about 20 ps.

In Fig. S11C the free energy obtained from the MD simulation is shown as a thick gray line around the barrier, that separates the CP and the SSP in the first hydration shell. In analogy to Fig. 2C in the main text, a profile for  $\tau_{\text{MFP}}$  is shown as a blue solid line, between the initial position  $x_i$  located at the minimum of the free energy, corresponding to the CP and varying final positions  $x_f$ , i.e. for the dissociation reaction of the methane beads. The association reaction is not considered here, since its barrier is very small. According profiles for  $\tau_{\text{MFP}}$  as obtained from a numerical simulation of the GLE Eq. (1) using the fit to the memory kernel, shown in Fig. S11A and the free energy shown in Fig. S11C, are shown in Fig. S11C as a blue short-dashed line and exhibit good agreement with the profiles obtained directly from the MD. Again, we compare to profiles for the overdamped Markovian limit, that are obtained from Eq. (6), shown as a blue long-dashed line, as well as from numerical simulation of the overdamped LE, Eq. (3) for  $m \rightarrow 0$ , shown as a blue dotted line. Similar to the NaCl ion pair, the  $\tau_{\text{MFP}}$  profiles of the methane dissociation dynamics of the MD data are significantly sped up when compared to the profiles in the overdamped Markovian limit. Therefore, also in this system the reaction dynamics are significantly dependent on both inertia and memory

friction, which is summarized in Fig. S11D, showing a contour plot of the dissociation times  $\tau_{\text{MFP}}$  as a function of  $\alpha$  and  $\epsilon$ , the scaling factors of the memory and inertial time scales.

In Fig. S11E  $\tau_{\text{MFP}}$  in the simultaneous limit of small inertia and small memory times,  $\alpha, \epsilon \rightarrow 0$ , is shown as blue circles. Again, in this overdamped Markovian limit the analytical result from Eq. (6),  $\tau_{\text{MFP}}^{\text{eq.(6)}} = 39.56$  ps shown as a blue broken line, is approached, which was already seen in Fig. S11C to be significantly slower than  $\tau_{\text{MFP}} = (19.4 \pm 0.4)$  ps for the original dynamics,  $\alpha = \epsilon = 1$ , which corresponds rather well to the MD data,  $\tau_{\text{MFP}} = (25.86 \pm 0.01)$  ps. This limit is reached only for  $\alpha, \epsilon < 0.02$ , which is in contrast to the respective data for the NaCl ion pair, presented in Fig. 2E, where the analytic limit is reached already for  $\alpha, \epsilon < 0.1$ . Therefore, when compared to the case of the NaCl ion pair, the dissociation dynamics of two methane beads in water is relatively further away from the overdamped Markovian limit. Also in the methane system there appears to be a significant cancellation of memory acceleration and slowing-down due to inertial effects, which is discussed in the following.

Fig. S11F shows how the dissociation dynamics of a pair of methane beads in water depends on the memory-time scaling parameter  $\alpha$ .  $\tau_{\text{MFP}}$  obtained from GLE simulations are shown as blue circles, that level to a constant value of  $\tau_{\text{MFP}}^{\text{Markov}} = (42.2 \pm 0.8)$  ps in the Markovian limit,  $\alpha \rightarrow 0$ , which is similar to the value of the overdamped Markovian limit  $\tau_{\text{MFP}}^{\text{eq.(6)}} = 39.56$  ps in Fig. S11C and likewise significantly slower than  $\tau_{\text{MFP}}$  for the original dynamics,  $\alpha = 1$ . This memory-induced acceleration is well predicted by GH theory, shown as a blue solid line in Fig. S11F. In the Markovian limit the GH theory converges to the constant value of Kramers' medium-to-high-friction theory (blue dotted line). In the long memory-time limit,  $\tau_{\text{MFP}}$  show a quadratic scaling with the memory time scale that is not captured by either theory, as discussed already for the NaCl ion pair data in the main text. Interestingly, GH theory for  $\alpha \leq 1$  (as well as Kramers' medium-to-high-friction theory in the Markovian limit,  $\alpha \rightarrow 0$ ) agrees well with the  $\tau_{\text{MFP}}$  data of the GLE simulations. This suggests that the harmonic approximations of the potential shape employed by both theories are rather good, which is in contrast to the results presented for NaCl in the main text. However, a detailed analysis of

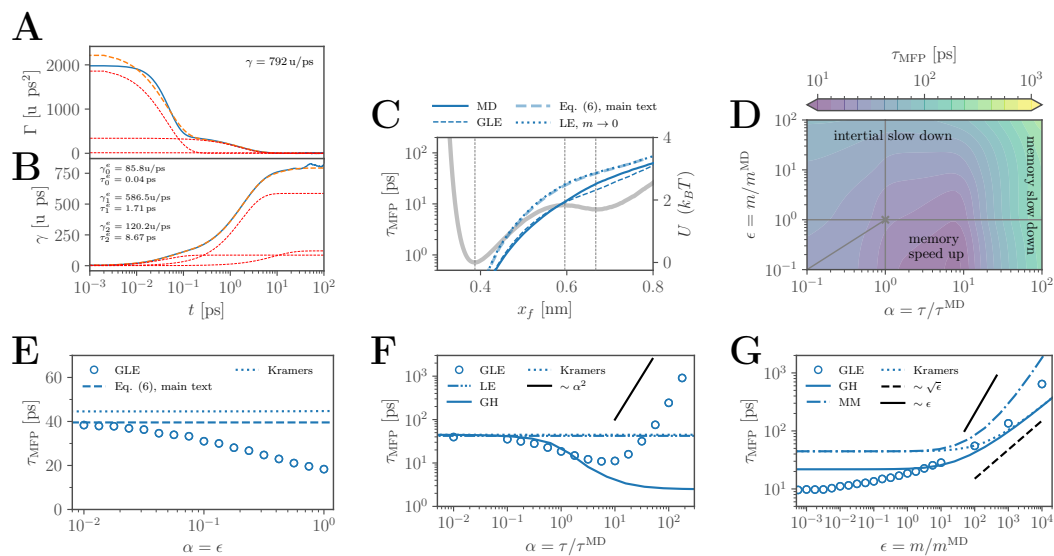


Figure S11: Analysis of the reaction dynamics for a single methane pair in water, similar to the analysis in the main text for a NaCl ion pair, using simulations of the GLE Eq. (1) and the LE Eq. (3). **A, B**: The memory friction kernel (A) and its integral (B) are shown as blue solid lines together with a fit according to Eq. (2), shown as yellow broken lines, which is a sum of three exponentially decaying components (red broken lines). The fit parameters are given in the legend. **C**: Profiles of  $\tau_{\text{MFP}}$  starting from the CP state, obtained directly from MD simulations (blue solid line), from simulation of the GLE Eq. (1) (blue short-dashed line), from the theory for the overdamped Markovian limit Eq. (6) (blue long-dashed line) and from simulations of the overdamped LE, Eq. (3) for  $m \rightarrow 0$ , (blue dotted line). For comparison the potential is shown as a gray solid line with the scale on the right side of the plot. The positions of the extrema are indicated as vertical gray dotted lines. **D**: Contour plot of  $\tau_{\text{MFP}}$  between the CP and the SSP states for rescaled inertial and memory times determined by the scaling parameters  $\epsilon$  and  $\alpha$ . The gray solid lines illustrate the parameter combinations shown in detail in E–G. **E–G**: Scaling of the  $\tau_{\text{MFP}}$  for dissociation as obtained from GLE simulations (blue circles) when changing memory times and mass simultaneously (E), when changing only memory times (F) and when changing only the mass (G). Theoretical predictions according to Kramers theory for medium-to-high friction (dotted lines) and by GH (solid lines) are shown for comparison. Predictions by MM theory are shown in G as a dash-dotted line. Further numerical data obtained for the overdamped Markovian limit using Eq. (6) for  $m \rightarrow 0$  is shown in E (blue broken line) and for the Markovian limit using Eq. (3) in F (blue dash-double-dotted line, which overlaps with the blue dotted line).

the harmonic approximation with respect to the barrier height given in section III shows that the good agreement is in fact fortuitous for the specific barrier height and due to cancellation of competing nonharmonic-potential effects.

Fig. S11G shows the dissociation dynamics of a pair of methane beads in water as a function of the particle mass, that is varied by the scaling parameter  $\epsilon$ . The  $\tau_{\text{MFP}}$  data (blue circles) only slowly saturates in the overdamped limit for  $\epsilon < 0.01$  to a value of about  $\tau_{\text{MFP}}^{\text{od.non-M.}} = 10$  ps, indicating that the original dynamics,  $\epsilon = 1$ , is in fact slowed-down by a factor of  $\tau_{\text{MFP}}^{\text{od.non-M.}}/\tau_{\text{MFP}} = 0.5$  due to inertial effects. The GH (solid blue line), Kramers' medium-to-high friction (dotted blue line) and MM theories (blue dash-dotted line) that are plotted here for comparison, do not model the data satisfactorily. In the inertial limit the MM theory shows a different scaling than the other theories,  $\tau_{\text{MFP}} \sim \epsilon$ , which appears in better agreement with the simulation data.

While for methane, nonharmonic potential effects appear less important, the competition of inertial and memory effects on the dissociation dynamics is clearly visible also for the methane data.

## X Simulation of the GLE

Simulations of the GLE, Eq. (1) in the main text,

$$m\ddot{x}(t) = - \int_0^t \Gamma(t-t')\dot{x}(t')dt' - \nabla U[x(t)] + \eta(t), \quad (\text{S56})$$

using parametrized memory kernels with a sum of  $n$  exponential and  $l$  oscillating components,

$$\Gamma(t) = \sum_{i=0}^n \frac{\gamma_i^e}{\tau_i^e} e^{-t/\tau_i^e} + \sum_{i=0}^l \frac{\gamma_i^o e^{-t/\tau_i^o}}{2\tau_i^o(1 + (\omega_i\tau_i^o)^2)^{-1}} \left[ \cos(\omega_i t) + \frac{\sin(\omega_i t)}{\tau_i^o \omega_i} \right], \quad (\text{S57})$$

are performed by Markovian embedding according to<sup>S14</sup>

$$\dot{x}(t) = v(t) \quad (\text{S58})$$

$$m\dot{v}(t) = -\nabla U[x(t)] + \sum_{i=1}^n a_i^e [y_i(t) - x(t)] + \sum_{i=1}^l a_i^o [z_i(t) - x(t)], \quad (\text{S59})$$

$$\gamma_i^e \dot{y}_i(t) = a_i^e [x(t) - y_i(t)] + F_i(t), \quad (\text{S60})$$

$$\dot{z}_i(t) = w_i(t) \quad (\text{S61})$$

$$m_i^o \dot{w}_i(t) = -\gamma_i^o w_i(t) + a_i^o [x(t) - z_i(t)] + F_i(t). \quad (\text{S62})$$

Eq. (S59)–Eq. (S62) are numerically solved using a 4th-order Runge-Kutta scheme in a custom C++ implementation to obtain the trajectory of  $x$ . For the  $n$  exponential components  $a_i^e = \gamma_i^e/\tau_i^e$  is obtained from the fit parameters  $\gamma_i^e$  and  $\tau_i^e$ .  $m_i^o$  and  $a_i^o$  for the  $l$  oscillating components are obtained from the fit parameters  $\gamma_i^o$ ,  $\tau_i^o$  and  $\omega_i$  by using

$$a_i^o = \frac{\gamma_i^o}{2\tau_i^o(1 + (\omega_i\tau_i^o)^2)^{-1}}, \quad (\text{S63})$$

$$m_i^o = \frac{\gamma_i^o \tau_i^o}{2}. \quad (\text{S64})$$

The random force  $F_i$  present in Eq. (S60) and Eq. (S62) is given by

$$F_i = \sqrt{2k_B T \gamma_i \delta t^{-1}} \Xi, \quad (\text{S65})$$

where  $\Xi$  is a Gaussian random distribution with zero mean and a standard deviation of one.

The memoryless LE, Eq. (3) in the main text,

$$m\ddot{x}(t) = -\gamma\dot{x}(t) - \nabla U[x(t)] + \xi(t), \quad (\text{S66})$$

with a constant homogeneous friction  $\gamma$  as well as its overdamped limit,  $m \rightarrow 0$ , are simulated using a 4th-order Runge-Kutta scheme in a custom C++ implementation. The corresponding equations for the LE Eq. (S66) are

$$\dot{x}(t) = v(t) \quad (\text{S67})$$

$$m\dot{v}(t) = -\gamma v(t) - \nabla U[x(t)] + F_R(t), \quad (\text{S68})$$

and for the overdamped limit

$$\gamma\dot{x}(t) = -\nabla U[x(t)] + F_R(t), \quad (\text{S69})$$

where  $F_R(t)$  are again random forces given by Eq. (S65).

The full nonharmonic potential used in the simulations of the GLE and LE,  $U(x) = -k_B T \log(p(x))$ , is calculated directly from the distribution function  $p(x)$  obtained in the MD simulations with a bin size of 0.0025 nm for the ion and 0.005 nm for the methane pair. Inside the range [0.27, 0.8] nm for the ion pair ([0.36, 1.0] nm for the methane pair), the gradient is computed with a local linear fit between the nearest data points of  $U(x)$ . Outside of this range the potentials are approximated using a least-square fit to a polynomial of third order. Most GLE simulations are performed with an integration timestep of  $dt = 2 \text{ fs} = dt^{\text{MD}}$ ,

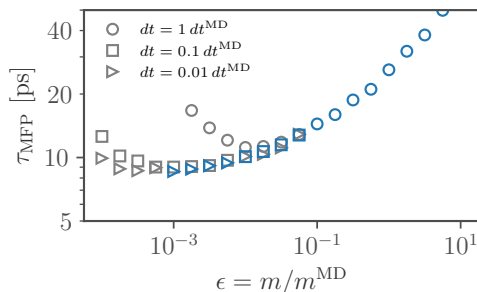


Figure S12: Scaling of  $\tau_{\text{MFP}}$  for the dissociation of NaCl in water from the CP state to the TS as a function of the mass scaling parameter  $\epsilon$  from simulations of the GLE. Different symbols illustrate different simulation time steps, the time step used for the analysis and the total simulation times are the same. Blue symbols denote data produced according to the criterion introduced in the text and used for all data shown in the main text.

equivalent to that of the MD simulation, and every value is stored for the computation of  $\tau_{\text{MFP}}$ . Usually, ten independent simulations, each of a length of 20 ns, are run. For the long-memory and inertial regimes, where  $\tau_{\text{MFP}}$  are significantly larger, each simulation was run instead for 200 ns. Errors of  $\tau_{\text{MFP}}$ , that are estimated from the standard error of the mean across the ten simulations, are smaller than the size of the plot symbols.

When modifying the original masses and memory times to explore the overdamped and Markovian limits, i.e for  $\alpha, \epsilon < 1$ , the simulation timestep is multiplied by a factor  $10^i$ , where  $i = \min(0, \lfloor 1 + \log_{10}[\min(\alpha, \epsilon)] \rfloor)$ , while only every  $10^{-i}$ -th step is stored for the analysis. The necessity for decreasing the simulation time step is illustrated in Fig. S12 for the dissociation dynamics of the NaCl ion pair in water by showing  $\tau_{\text{MFP}}$  as a function of the mass scaling parameter  $\epsilon < 1$ . Different symbols denote different integration time steps,  $dt$ , while the total length of the simulations and the time step used for the analysis is kept fixed. It is well visible that for  $\epsilon < 0.01$  the gray circles (corresponding to data for  $dt = dt^{\text{MD}}$ ) deviate from the data with smaller integration time steps, which clearly indicates discretization effects. Likewise, for  $\epsilon < 0.001$  the gray squares (corresponding to data for  $dt = 0.1 dt^{\text{MD}}$ ) deviate from the gray triangles. The criterion introduced above for choosing the integration time step based on the values of  $\epsilon$  and  $\alpha$  is used for the data shown in blue, these results are not



affected by discretization errors.

## References

- (S1) Ayaz, C.; Scalfi, L.; Dalton, B. A.; Netz, R. R. Generalized Langevin equation with a nonlinear potential of mean force and nonlinear memory friction from a hybrid projection scheme. *Phys. Rev. E* **2022**, *105*, 054138.
- (S2) Arrhenius, S. Über die Reaktionsgeschwindigkeit bei der Inversion von Rohrzucker durch Säuren. *Zeit. Phys. Chem.* **1889**, *4*, 226–248.
- (S3) Kramers, H. A. Brownian motion in a field of force and the diffusion model of chemical reactions. *Physica* **1940**, *7*, 284–304.
- (S4) Mel'nikov, V. I.; Meshkov, S. V. Theory of activated rate processes: Exact solution of the Kramers problem. *J. Chem. Phys.* **1986**, *85*, 1018–1027.
- (S5) Grote, R. F.; Hynes, J. T. The stable states picture of chemical reactions. II. Rate constants for condensed and gas phase reaction models. *J. Chem. Phys.* **1980**, *73*, 2715–2732.
- (S6) Pollak, E.; Grabert, H.; Hänggi, P. Theory of activated rate processes for arbitrary frequency dependent friction: solution of the turnover problem. *J. Chem. Phys.* **1989**, *91*, 4073–4087.
- (S7) Kappler, J.; Daldrop, J. O.; Brüning, F. N.; Boehle, M. D.; Netz, R. R. Memory-induced acceleration and slowdown of barrier crossing. *J. Chem. Phys.* **2018**, *148*, 014903.
- (S8) Eyring, H. The Activated Complex in Chemical Reactions. *J. Chem. Phys.* **1935**, *3*, 107–115.
- (S9) Risken, H. *The Fokker-Planck Equation*, 2nd ed.; Springer: Berlin, 1996.

- 
- (S10) Weiss, G. H. First Passage Time Problems in Chemical Physics. *Adv. Chem. Phys.* **1967**, *13*, 1–18.
- (S11) Hinczewski, M.; von Hansen, Y.; Dzubiella, J.; Netz, R. R. How the diffusivity profile reduces the arbitrariness of protein folding free energies. *J. Chem. Phys.* **2010**, *132*, 245103.
- (S12) Von Hansen, Y.; Sedlmeier, F.; Hinczewski, M.; Netz, R. R. Friction contribution to water-bond breakage kinetics. *Phys. Rev. E - Stat. Nonlinear, Soft Matter Phys.* **2011**, *84*, 051501.
- (S13) Ayaz, C.; Tepper, L.; Brünig, F. N.; Kappler, J.; Daldrop, J. O.; Netz, R. R. Non-Markovian modeling of protein folding. *Proc. Natl. Acad. Sci. U. S. A.* **2021**, *118*, e2023856118.
- (S14) Brünig, F. N.; Geburtig, O.; von Canal, A.; Kappler, J.; Netz, R. R. Time-Dependent Friction Effects on Vibrational Infrared Frequencies and Line Shapes of Liquid Water. *J. Phys. Chem. B* **2022**, *126*, 1579–1589.



## Fluctuation-Dissipation Theorem

---

Consider a Hamiltonian system under a perturbation by a time-dependent external force  $F(t)$  coupling directly to an observable  $A(q, p)$ , that is a function of positions  $q$  and momenta  $p$ , for example an external electric field  $E(t)$  coupling to the polarization  $P(q)$ . Then the total Hamiltonian  $H_{tot}$  will consist of an unperturbed part  $H_0$  and the time-dependent perturbation  $H'(t)$ ,

$$H_{tot} = H_0 + H'(t) \tag{E.1}$$

$$= H_0 - A(q, p)F(t). \tag{E.2}$$

The effect of the external force on any observable, expressed as the deviation  $\Delta B(t)$  from the unperturbed mean  $B_0$ , defines in the linear regime the single-sided linear response function  $\chi_{BA}(t - t')$ , i.e.  $\chi_{BA}(t) = 0$  for  $t < 0$ ,

$$\Delta B(t) = \int_{-\infty}^t \chi_{BA}(t - t')F(t')dt'. \tag{E.3}$$

Alternatively eq. (E.3) reads in Fourier space

$$\Delta \tilde{B}(\omega) = \tilde{\chi}_{BA}(\omega)\tilde{F}(\omega). \tag{E.4}$$

The Fourier-transformed expression  $\tilde{\chi}_{BA}(\omega)$  of the single-sided linear response function  $\chi_{BA}(t)$  is also called the generalized susceptibility, which is a complex function consisting of real  $\tilde{\chi}'_{BA}(\omega)$  and imaginary parts  $\tilde{\chi}''_{BA}(\omega)$

$$\tilde{\chi}_{BA}(\omega) = \tilde{\chi}'_{BA}(\omega) + i\tilde{\chi}''_{BA}(\omega). \tag{E.5}$$

In some works the imaginary part is defined with a minus sign. This is a matter of convention, related to the definition of the Fourier transform. In this work the forward and backward Fourier transforms are defined as

$$\tilde{f}(\omega) = \int_{-\infty}^{\infty} dt e^{i\omega t} f(t), \tag{E.6}$$

$$f(t) = \frac{1}{2\pi} \int_{-\infty}^{\infty} d\omega e^{-i\omega t} \tilde{f}(\omega). \tag{E.7}$$

$\tilde{\chi}'_{BA}(\omega)$  in eq. (E.5) is called the reactive part and  $\tilde{\chi}''_{BA}(\omega)$  is called the dissipative

part, which becomes clear in the following derivation.

The dissipated energy from the system per period of time  $T = 2\pi/\omega$  of the perturbing force  $F(t)$  is given by

$$\left\langle \frac{dH'(t)}{dt} \right\rangle = \frac{1}{T} \frac{d}{dt} \int_0^T \langle A(q, p) F(t) \rangle dt \quad (\text{E.8})$$

$$= \frac{1}{T} \int_0^T \langle A(q, p) \rangle \frac{\delta F(t)}{\delta t} dt \quad (\text{E.9})$$

The real force  $F(t)$  at the given frequency  $\omega$  is

$$F(t) = \frac{1}{2\pi} \text{Re} \int_{-\infty}^{\infty} \delta(\omega - \omega') \tilde{F}(\omega') e^{-i\omega' t} d\omega' \quad (\text{E.10})$$

$$= \frac{1}{2\pi} \text{Re} \tilde{F}(\omega) e^{-i\omega t} \quad (\text{E.11})$$

$$= \frac{1}{4\pi} \left( \tilde{F}(\omega) e^{-i\omega t} + \tilde{F}^*(\omega) e^{i\omega t} \right), \quad (\text{E.12})$$

where  $\tilde{F}^*(\omega)$  is the complex conjugate to  $\tilde{F}(\omega)$ . Analogously the real deviation  $\Delta A(t)$  from the unperturbed mean  $A_0$  contributes to the energy dissipation and is expressed through linear response as

$$\langle A(q, p) \rangle = \Delta A(t) \quad (\text{E.13})$$

$$= \int_{-\infty}^t \chi_{AA}(t-t') F(t') dt' \quad (\text{E.14})$$

$$= \frac{1}{2\pi} \text{Re} \int_{-\infty}^{\infty} \delta(\omega - \omega') \tilde{F}(\omega') e^{-i\omega' t} \tilde{\chi}_{AA}(\omega') d\omega' \quad (\text{E.15})$$

$$= \frac{1}{4\pi} \left( \tilde{\chi}_{AA}(\omega) \tilde{F}(\omega) e^{-i\omega t} + \tilde{\chi}_{AA}^*(\omega) \tilde{F}^*(\omega) e^{i\omega t} \right). \quad (\text{E.16})$$

Entering eqs. (E.12) and (E.16) into eq. (E.9) one obtains

$$\begin{aligned} \left\langle \frac{dH'(t)}{dt} \right\rangle &= \frac{1}{T} \int_0^T \frac{\omega}{(4\pi)^2} \langle -i\tilde{\chi}_{AA}(\omega) \tilde{F}(\omega) \tilde{F}^*(\omega) \\ &\quad + i\tilde{\chi}_{AA}^*(\omega) \tilde{F}^*(\omega) \tilde{F}(\omega) \\ &\quad + \text{terms containing } e^{\pm 2i\omega t} \rangle dt. \end{aligned} \quad (\text{E.17})$$

The  $e^{\pm 2i\omega t}$  terms are time-averaged out and the real remainder is

$$\left\langle \frac{dH'(t)}{dt} \right\rangle = \frac{\omega}{8\pi^2} \tilde{\chi}_{AA}''(\omega) \tilde{F}(\omega) \tilde{F}^*(\omega) \quad (\text{E.18})$$

$$= \frac{\omega}{8\pi^2} \tilde{\chi}_{AA}''(\omega) |\tilde{F}(\omega)|^2, \quad (\text{E.19})$$

which shows that the imaginary part of the susceptibility  $\tilde{\chi}_{AA}''(\omega)$  is related to the energy dissipation introduced by a force  $F(t)$  that is conjugate to  $A(q, p)$  in the Hamiltonian. In the following the generalized susceptibility  $\tilde{\chi}_{AB}(\omega)$  will be related to the correlation functions of the observables, which is the essence of the fluctuation-dissipation theorem. Consider the distribution function  $\rho(q, p, t)$  of an  $N$  particle system described by the perturbed Hamiltonian of eq. (E.2). Its time propagation is governed by the Liouville operator

$$L(q, p, t) = \sum_i^{3N} \left[ \frac{\delta H}{\delta p_i} \frac{\delta}{\delta q_i} - \frac{\delta H}{\delta q_i} \frac{\delta}{\delta p_i} \right] \quad (\text{E.20})$$

$$\begin{aligned} &= \sum_i^{3N} \left[ \frac{\delta H_0}{\delta p_i} \frac{\delta}{\delta q_i} - \frac{\delta H_0}{\delta q_i} \frac{\delta}{\delta p_i} \right] - F(t) \left[ \frac{\delta A}{\delta p_i} \frac{\delta}{\delta q_i} - \frac{\delta A}{\delta q_i} \frac{\delta}{\delta p_i} \right] \\ &= L_0(q, p) - F(t) \Delta L(q, p), \end{aligned} \quad (\text{E.21})$$

and

$$\frac{\delta}{\delta t} \rho(q, p, t) = -L(q, p, t) \rho(q, p, t). \quad (\text{E.22})$$

Again the function  $\rho(q, p, t)$  is split into unperturbed  $\rho_0(q, p)$  and perturbed parts  $\Delta\rho(q, p, t)$ , as well as using the Liouville operator as given in eq. (E.21)

$$\frac{\delta}{\delta t} [\rho_0 + \Delta\rho(t)] = -[L_0 - F(t)\Delta L] [\rho_0 + \Delta\rho(t)] \quad (\text{E.23})$$

$$\frac{\delta}{\delta t} [\Delta\rho(t)] = -L_0\Delta\rho(t) + F(t)\Delta L\rho_0 + [F(t)\Delta L\Delta\rho(t)] \quad (\text{E.24})$$

The last term is neglected as it is small and eq. (E.24) is formally solved

$$\Delta\rho(t) = \int_{-\infty}^t dt' e^{-(t-t')L_0} F(t') \Delta L \rho_0. \quad (\text{E.25})$$

Assuming a canonical distribution,  $\nabla\rho_0(H_0) = -\frac{\rho_0}{k_B T} \nabla H_0$ , the integrand is expressed as

$$\Delta L \rho_0 = -\frac{\rho_0}{k_B T} \Delta L H_0 \quad (\text{E.26})$$

$$= -\frac{\rho_0}{k_B T} \sum_i^{3N} \left[ \frac{\delta A}{\delta p_i} \frac{\delta}{\delta q_i} - \frac{\delta A}{\delta q_i} \frac{\delta}{\delta p_i} \right] H_0 \quad (\text{E.27})$$

$$= \frac{\rho_0}{k_B T} \dot{A}, \quad (\text{E.28})$$

where  $\dot{A}$  is defined for the unperturbed system  $H_0$  to be

$$\dot{A} = \sum_i^{3N} \left[ \frac{\delta A}{\delta q_i} \dot{q}_i + \frac{\delta A}{\delta p_i} \dot{p}_i \right] \quad (\text{E.29})$$

$$= - \sum_i^{3N} \left[ \frac{\delta A}{\delta p_i} \frac{\delta}{\delta q_i} - \frac{\delta A}{\delta q_i} \frac{\delta}{\delta p_i} \right] H_0. \quad (\text{E.30})$$

Eq. (E.28) is inserted into eq. (E.25)

$$\Delta\rho(t) = \frac{1}{k_B T} \int_{-\infty}^t dt' F(t') e^{-(t-t')L_0} \rho_0 \dot{A}. \quad (\text{E.31})$$

Next the perturbation of another arbitrary observable  $\Delta B(t)$  is expressed in terms of the perturbed distribution  $\Delta\rho(t)$

$$\Delta B(t) = \int dq^{3N} \int dp^{3N} B(q, p) \Delta\rho(t) \quad (\text{E.32})$$

$$= \frac{1}{k_B T} \int dq^{3N} \int dp^{3N} B \int_{-\infty}^t dt' F(t') e^{-(t-t')L_0} \rho_0 \dot{A} \quad (\text{E.33})$$

$$= \frac{1}{k_B T} \int_{-\infty}^t dt' F(t') \int dq^{3N} \int dp^{3N} B e^{-(t-t')L_0} \rho_0 \dot{A}, \quad (\text{E.34})$$

where the inner integrand is identified to be the correlation function in an unperturbed equilibrium ensemble

$$\langle B(t-t') \dot{A}(t) \rangle = \int dq^{3N} \int dp^{3N} B e^{-(t-t')L_0} \rho_0 \dot{A}, \quad (\text{E.35})$$

leaving us with the expression

$$\Delta B(t) = \frac{1}{k_B T} \int_{-\infty}^t dt' F(t') \langle B(t-t') \dot{A}(t) \rangle. \quad (\text{E.36})$$

Comparison of eq. (E.36) with eq. (E.3) allows to relate the linear response function  $\chi_{BA}(t-t')$  to the correlation function in an equilibrium ensemble

$$\chi_{BA}(t-t') = \frac{1}{k_B T} \langle B(t-t') \dot{A}(t) \rangle, \quad (\text{E.37})$$

or equivalently

$$\chi_{BA}(t) = \frac{1}{k_B T} \langle B(t) \dot{A}(0) \rangle. \quad (\text{E.38})$$

$$\chi_{BA}(t) = -\frac{1}{k_B T} \frac{d}{dt} \langle B(t) A(0) \rangle. \quad (\text{E.39})$$

# List of Figures

---

- 1.1. Illustration of the Grotthuss process of proton transport in water. An excess proton attaches to a water molecule, thereby forming a charged hydronium ion,  $\text{H}_3\text{O}^+$ . Whenever any of the three hydrogen atoms of the hydronium ion transfers to a hydrogen-bonded water molecule, a new hydronium ion is formed, while the original ion becomes again a neutral water molecule. Thus, an excess proton can transfer quickly across a chain of water molecules by exchanging identity with the hydrogen atoms of water itself during the formation of intermediate hydronium ions. . . . . 6
- 1.2. Illustration of the Eigen ( $\text{H}_9\text{O}_4^+$ , green on the left) [57] and Zundel states ( $\text{H}_5\text{O}_2^+$ , red in the middle) [48] as intermediate solvation structures of the excess proton in water. The figure shows the Eigen-Zundel-Eigen transition as a model for excess-proton transport. Alternatively, the transport can be regarded as a Zundel-Eigen-Zundel transition, depending on whether the Zundel or the Eigen states are assumed to be the dominant solvation species. . . . . 13
- 1.3. Spatial correlations between the oxygen atoms of hydronium ions (A) and excess protons (B) with respect to other nuclei in terms of radial distribution functions (RDFs) as obtained from ab initio MD simulations of hydrochloric acid solutions at various concentrations. **A:** RDFs are shown for the oxygen nuclei of the hydronium ions ( $\text{O}^+$ ) as solid lines, for the oxygen nuclei of the water molecules (O) as broken lines, for the the excess protons ( $\text{H}^+$ ) as dashed and dotted lines and all hydrogen nuclei (H), including excess protons, as dotted lines. **B:** RDFs are shown for the excess protons ( $\text{H}^+$ ) as solid lines and all hydrogen nuclei (H), including excess protons, as broken lines. . . . . 16
- 1.4. Spatial correlations between the chloride counterions and other nuclei in terms of radial distribution functions (RDFs) as obtained from ab initio MD simulations of hydrochloric acid solutions at various concentrations. RDFs are shown for the excess protons ( $\text{H}^+$ ) as solid lines, all hydrogen nuclei (H), including excess protons, as broken lines, the oxygen nuclei of the water molecules (O) as dotted lines and the oxygen nuclei of the hydronium ions ( $\text{O}^+$ ) as dashed and dotted lines. . . . . 17



1.5.	Normalized distributions of the hydrogen bond asymmetries, denoted as $\phi$ , of the excess proton trajectories from ab initio MD simulations of HCl solutions at various concentrations. See text for definition and details. Mean values of the distributions are reported in the legends. <b>A:</b> Distributions over the whole trajectories. <b>B–D:</b> Distributions of $\phi$ during 20 fs before and after any transfer event (gray broken lines), i.e. when the excess proton changes the closest oxygen, and distributions of $\phi$ around each uni-directional transfer event, which are split into the 20 fs before, corresponding to the donor oxygen of the proton transfer event (blue and left pointing triangles) and the 20 fs after, corresponding to the acceptor oxygen (red and right pointing triangles). . . . .	20
1.6.	Correlations between the existence of a fourth hydrogen bond of a hydronium ion (4HB) and the return probability of the excess proton, as observed in ab initio MD simulations of HCl solutions at various concentrations. <b>A:</b> Probability of the excess proton to return across the mid plane between the oxygens within the following 50 fs. <b>B:</b> Time-averaged probabilities of all hydronium ions for the fourth hydrogen bond to exist (4HB) or not (3HB), as obtained from the whole simulation (gray, no hatching) and during the 20 fs before (blue) and after (red) each uni-directional transfer event. . . . .	21
1.7.	<b>A:</b> IR absorption spectra obtained from ab initio MD simulations of pure water (blue solid line) and HCl solutions at various concentrations (dark purple: 2 M, purple: 4 M and red: 6 M). The spectra are divided by the water molecular number concentration $c_W$ . <b>B:</b> Difference spectra between the three HCl spectra and the water spectrum, obtained from the spectra in A. The red dotted line shows an experimental difference spectrum of HCl at 4 M [54], rescaled in height to match the simulation results. . . .	22
1.8.	Examples of five joint trajectories of excess protons in 2 M HCl solution on short ( <b>A</b> ) and long time scales ( <b>B</b> ). In A, the pale colored lines indicate the spurious jumps, resulting from the ‘special pair dance’, that are removed from the trajectories (see text for details). . . . .	23
1.9.	MSDs (mean squared displacements) in the lab frame, $\langle  \mathbf{r}(t) - \mathbf{r}(0) ^2 \rangle$ , of the excess protons ( <b>A</b> ) and the oxygen atoms ( <b>B</b> ) computed from the simulation trajectories of HCl solutions at three different concentrations. In B, the MSD of the oxygen atoms in the pure-water simulations is shown as well. Errors of the mean are indicated by the line widths and taken from standard deviations computed over the individual excess-proton and oxygen-atom joint trajectories. Linear fits are shown as black broken lines, which are fitted in the long time regimes, 20 ps to 80 ps, the range that is also shown enlarged in the insets. . . . .	24

- 
- 1.10. Identity auto-correlation functions Eq. (1.18) of the excess protons (**A**) and hydronium oxygens (**B**) obtained from ab initio MD simulations of HCl solutions at various concentrations. The correlation functions are computed from unfiltered (solid colored lines) and filtered trajectories (broken colored lines), see text for details. The data is shown on a logarithmic time axis in the insets. . . . . 29
- 1.11. Continuous identity auto-correlation functions Eq. (1.19) of the excess protons (a) and hydronium oxygens (b) obtained from ab initio MD simulations of HCl solutions at various concentrations. The correlations functions are computed from filtered (solid colored lines) and unfiltered trajectories (broken colored lines), see text for details. The data is shown on a logarithmic time axis in the insets. . . . . 30
- 1.12. Continuous identity auto-correlation functions Eq. (1.19) of the hydronium oxygens obtained from ab initio MD simulations of HCl solutions at various concentrations (already shown in Fig. 1.11B). The correlation functions are computed from filtered (**A**) and unfiltered trajectories (**B**), see text for details. Each curve is fitted to a sum of two decaying exponentials with the time scales reported in the legends and shown as black broken lines. . . . . 31
- 1.13. IR spectra for the Zundel cation in gas phase,  $\text{H}_5\text{O}_2^+$ , for various NQE simulation techniques (RPMD, CMD and TRPMD). Reprinted from Rossi, M., Ceriotti, M. & Manolopoulos, D. E. *J. Chem. Phys.* 140, 234116 (2014), with the permission of AIP Publishing. . . . . 32
- 1.14. IR and VDOS spectra and difference spectra for 4M HCl solution from experiment and ab initio molecular dynamics simulations with quantum and classical nuclei. Reprinted from Napoli, J. A., Marsalek, O. & Markland, T. E. *J. Chem. Phys.* 148, 222833 (2018), with the permission of AIP Publishing. . . . . 33
- 1.15. IR difference spectra obtained from classical and CMD trajectories of (a, left) aMS-EVB 3.2 and (b, right) MS-EVB 3.2 simulations of 1 HCl aqueous system along with the experimental ATR difference spectrum. Reprinted with permission from Biswas, R., Tse, Y. L. S., Tokmakoff, A. & Voth, G. A. *J. Phys. Chem. B* 120, 1793 (2016). Copyright 2016 American Chemical Society. . . . . 34

1.16. **A, B:** Illustration of the proposed active-site proton cage near the chromophore of bacteriorhodopsin. Reprinted from Ref. [13], used under Creative Commons CC-BY license (<http://creativecommons.org/licenses/by/4.0/>). **C:** Snapshot from the ab initio MD simulation of a water molecule and an excess proton in between two carboxylate molecules. The reaction coordinate for the proton transfer between the two carboxylates is the distance between carboxyl group and water oxygen  $R_{O_C O_W}$  and and the excess proton's relative asymmetry to these oxygens  $R_{O_C H} - R_{O_W H}$ . **D:** Example trajectories of the  $R_{O_C H}$  distances of the three central hydrogen atoms in the system. The proton transfer is well visible as a fast jump process by which protons 1 and 2 exchange **E:** The free energy of the asymmetry coordinate  $R_{O_C H} - R_{O_W H}$  shows an effective barrier height of about  $3 k_B T$  for proton transfer between the two carboxyl group via a Grotthus mechanism. . . . . 36

1.17. **A:** Snapshot from the ab initio MD simulation of an excess proton and two water molecules that are located in between a pair of carboxylate molecules. The pink cylinder illustrates the confining potential acting on the water oxygen nuclei, which is centered on the axis connecting the carbon atoms. The carbon atoms are fully constraint in the MD simulations. **B:** IR spectra of the model system shown in Figure S13a along different axes for different confining strengths ( $k$  in  $k_B T / \text{\AA}^2$ ) of the water molecules. For each figure, IR spectra along the X axis connecting the fully constrained carbon atoms of the carboxylates are shown in the upper panel and IR spectra in the YZ plane in the lower panel. Reprinted from Ref. [7], used under Creative Commons CC-BY license (<http://creativecommons.org/licenses/by/4.0/>). . . . . 37

- 1.18. **A:** Snapshots from the ab initio MD simulations of a proposed water cluster near the chromophore of Agp2, including one side of the chromophore with ring C and ring D, side chains H278 and Y165, that were each truncated at the ring, three water molecules TW1, TW2 and W6 (see Fig. 1 of Ref. [7]) and an excess proton, so that the total charge amounts to 1 e. The pink circle illustrates the location of the excess proton during the course of the non-equilibrium simulations. A number of constraints is applied to model the confining effect inside the protein. The heavy atoms of the chromophore and H278 are fully constrained, except for the carboxylic side chain at ring C. Furthermore the water oxygen atoms are constraint by a weak quadratic potential in all dimensions,  $k(x^2 + y^2 + z^2)$ , with  $k = 0.04 k_B T / \text{\AA}^2$ . Furthermore, for Y165, the oxygen atom of the hydroxyl group and the carbon atom of the phenyl ring that connects to the back bone of the protein are constrained by such a quadratic potential with  $k = 0.04 k_B T / \text{\AA}^2$ . A small number of simulations of this non-equilibrium system are performed for each, H<sub>2</sub>O and D<sub>2</sub>O, under NVT conditions at 300 K using a simulation time step of 0.5 fs. All show a transfer of the excess proton to Y165 as a Grotthus process within the first 5 ps, in some simulations the excess proton is further transferred to the nitrogen atom of the keto group at ring D. Interestingly, in some simulations, Y165 is protonated at the phenyl ring, before the proton from the hydroxyl group is released, which probably presents another meta-stable state. Each simulation is run for about 5 ps to 7.5 ps or until the keto group at ring D is protonated, which is considered the meta-stable reference configuration. The first 0.1 ps are truncated for initial fast equilibration. **B:** IR spectra of the model system shown in Figure S13b. The IR spectra are averaged over three non-equilibrium simulations for H<sub>2</sub>O, five non-equilibrium simulations for D<sub>2</sub>O and all dimensions. Reprinted from Ref. [7], used under Creative Commons CC-BY license (<http://creativecommons.org/licenses/by/4.0/>). . . . . 39
- 1.19. IR absorption spectra obtained from ab initio MD simulations of pure water (blue solid line, BLYP-D3 quality) and normal modes calculated from a single water molecule on the same level (vertical gray broken lines) [1]. The black broken line shows an experimental spectrum [198]. . . . . 43



# Bibliography

---

- [1] Brünig, F. N., Geburtig, O., von Canal, A., Kappler, J. & Netz, R. R. Time-Dependent Friction Effects on Vibrational Infrared Frequencies and Line Shapes of Liquid Water. *J. Phys. Chem. B* 126, 1579 (2022).
- [2] Brünig, F. N., Rammler, M., Adams, E. M., Havenith, M. & Netz, R. R. Spectral signatures of excess-proton waiting and transfer-path dynamics in aqueous hydrochloric acid solutions. *Nat. Commun.* 13, 4210 (2022).
- [3] Brünig, F. N., Netz, R. R. & Kappler, J. Barrier-crossing times for different non-Markovian friction in well and barrier: A numerical study. *Phys. Rev. E* 106, 44133 (2022).
- [4] Brünig, F. N., Hillmann, P., Kim, W. K., Daldrop, J. O. & Netz, R. R. Proton-transfer spectroscopy beyond the normal-mode scenario. *J. Chem. Phys.* 157, 174116 (2022).
- [5] Brünig, F. N., Daldrop, J. O. & Netz, R. R. Pair-Reaction Dynamics in Water: Competition of Memory, Potential Shape, and Inertial Effects. *J. Phys. Chem. B* 126, 10295 (2022).
- [6] Kundu, A., Mamatkulov, S. I., Brünig, F. N., Bonthuis, D. J., Netz, R. R., Elsaesser, T. & Fingerhut, B. P. Short-Range Cooperative Slow-down of Water Solvation Dynamics Around  $\text{SO}_4^{2-}$ — $\text{Mg}^{2+}$  Ion Pairs. *ACS Phys. Chem. Au* 2, 506 (2022).
- [7] Yang, Y., Stensitzki, T., Sauthof, L., Schmidt, A., Piwowarski, P., Velazquez Escobar, F., Michael, N., Nguyen, A. D., Szczepek, M., Brünig, F. N., Netz, R. R., Mroginski, M. A., Adam, S., Bartl, F., Schapiro, I., Hildebrandt, P., Scheerer, P. & Heyne, K. Ultrafast proton-coupled isomerization in the phototransformation of phytochrome. *Nat. Chem.* 14, 823 (2022).
- [8] Ayaz, C., Tepper, L., Brünig, F. N., Kappler, J., Daldrop, J. O. & Netz, R. R. Non-Markovian modeling of protein folding. *Proc. Natl. Acad. Sci. U. S. A.* 118, e2023856118 (2021).
- [9] Lindow, N., Brünig, F. N., Dercksen, V. J., Fabig, G., Kiewisz, R., Redemann, S., Müller-Reichert, T., Prohaska, S. & Baum, D. Semi-automatic stitching of filamentous structures in image stacks from serial-section electron tomography. *J. Microsc.* 284, 25 (2021).

- [10] Carlson, S., Becker, M., Brünig, F. N., Ataka, K., Cruz, R., Yu, L., Tang, P., Kanduč, M., Haag, R., Heberle, J., Makki, H. & Netz, R. R. Hydrophobicity of Self-Assembled Monolayers of Alkanes: Fluorination, Density, Roughness, and Lennard-Jones Cutoffs. *Langmuir* 37, 13846 (2021).
- [11] Schwarzl, R., Liese, S., Brünig, F. N., Laudisio, F. & Netz, R. R. Force Response of Polypeptide Chains from Water-Explicit MD Simulations. *Macromolecules* 53, 4618 (2020).
- [12] Carlson, S., Brünig, F. N., Loche, P., Bonthuis, D. J. & Netz, R. R. Exploring the absorption spectrum of simulated water from MHz to infrared. *J. Phys. Chem. A* 124, 5599 (2020).
- [13] Friedrich, D., Brünig, F. N., Nieuwkoop, A. J., Netz, R. R., Hegemann, P. & Oschkinat, H. Collective exchange processes reveal an active site proton cage in bacteriorhodopsin. *Commun. Biol.* 3, 4 (2020).
- [14] Lindow, N., Redemann, S., Brünig, F. N., Fabig, G., Müller-Reichert, T. & Prohaska, S., in *Mitosis Meiosis Part B*, edited by Maiato, H. & Schuh, M. (Academic Press, 2018), vol. 145 of *Methods in Cell Biology*, pp. 45–64.
- [15] Daldrop, J. O., Kappler, J., Brünig, F. N. & Netz, R. R. Butane dihedral angle dynamics in water is dominated by internal friction. *Proc. Natl. Acad. Sci. U. S. A.* 115, 5169 (2018).
- [16] Kappler, J., Daldrop, J. O., Brünig, F. N., Boehle, M. D. & Netz, R. R. Memory-induced acceleration and slowdown of barrier crossing. *J. Chem. Phys.* 148, 014903 (2018).
- [17] Kreuer, K. D. Proton conductivity: Materials and applications. *Chem. Mater.* 8, 610 (1996).
- [18] Armaroli, N. & Balzani, V. The Hydrogen Issue. *ChemSusChem* 4, 21 (2011).
- [19] Bell, R. P., *The proton in chemistry* (Springer Science & Business Media, 2013).
- [20] Agmon, N., Bakker, H. J., Campen, R. K., Henchman, R. H., Pohl, P., Roke, S., Thämer, M. & Hassanali, A. Protons and Hydroxide Ions in Aqueous Systems. *Chem. Rev.* 116, 7642 (2016).
- [21] Myers, R. J. One-Hundred Years of pH. *J. Chem. Educ.* 87, 2009 (2010).
- [22] Sazali, N. Emerging technologies by hydrogen: A review. *Int. J. Hydrogen Energy* 45, 18753 (2020).
- [23] Wraight, C. A. Chance and design—Proton transfer in water, channels and bioenergetic proteins. *Biochim. Biophys. Acta - Bioenerg.* 1757, 886 (2006).

- 
- [24] Heberle, J. Proton transfer reactions across bacteriorhodopsin and along the membrane. *Biochim. Biophys. Acta - Bioenerg.* 1458, 135 (2000).
- [25] Klauss, A., Haumann, M. & Dau, H. Alternating electron and proton transfer steps in photosynthetic water oxidation. *Proc. Natl. Acad. Sci.* 109, 16035 (2012).
- [26] Greife, P., Schönborn, M., Capone, M., Assunção, R., Narzi, D., Guidoni, L. & Dau, H. The electron–proton bottleneck of photosynthetic oxygen evolution. *Nature* 617, 623 (2023).
- [27] Saura, P., Riepl, D., Frey, D. M., Wikström, M. & Kaila, V. R. I. Electric fields control water-gated proton transfer in cytochrome c oxidase. *Proc. Natl. Acad. Sci.* 119, e2207761119 (2022).
- [28] Marx, D. Proton transfer 200 years after Von Grotthuss: Insights from ab initio simulations. *ChemPhysChem* 7, 1848 (2006).
- [29] Barth, A. Infrared spectroscopy of proteins. *Biochim. Biophys. Acta - Bioenerg.* 1767, 1073 (2007).
- [30] Schrader, B. (ed.), *Infrared and Raman spectroscopy: Methods and applications* (Wiley-VCH, New York, 1995).
- [31] Weiss, G. H. First Passage Time Problems in Chemical Physics. *Adv. Chem. Phys.* 13, 1 (1967).
- [32] Hummer, G. From transition paths to transition states and rate coefficients. *J. Chem. Phys.* 120, 516 (2004).
- [33] Kim, W. K. & Netz, R. R. The mean shape of transition and first-passage paths. *J. Chem. Phys.* 143, 224108 (2015).
- [34] Siegman, A. E., *Lasers* (University science books, 1986).
- [35] Hänggi, P., Talkner, P. & Borkovec, M. Reaction-rate theory: Fifty years after Kramers. *Rev. Mod. Phys.* 62, 251 (1990).
- [36] Eyring, H. The Activated Complex in Chemical Reactions. *J. Chem. Phys.* 3, 107 (1935).
- [37] Kramers, H. A. Brownian motion in a field of force and the diffusion model of chemical reactions. *Physica* 7, 284 (1940).
- [38] Zwanzig, R. Ensemble Method in the Theory of Irreversibility. *J. Chem. Phys.* 33, 1338 (1960).
- [39] Mori, H. Transport, collective motion, and Brownian motion. *Prog. Theor. Phys.* 33, 423 (1965).



- [40] de Grotthuss, C. Mémoire — Sur la décomposition de l'eau et des corps qu'elle tient en dissolution à l'aide de l'électricité galvanique. *Ann. Chim.* 58, 54 (1806).
- [41] Gierer, A. & Wirtz, K. Anomalous Mobility of H<sup>+</sup> and OH<sup>-</sup> Ions. *J. Chem. Phys.* 17, 745 (1949).
- [42] Eigen, M., De Maeyer, L. & Bernal, J. D. Self-dissociation and protonic charge transport in water and. *Proc. R. Soc. London. Ser. A. Math. Phys. Sci.* 247, 505 (1958).
- [43] Meiboom, S. Nuclear magnetic resonance study of the proton transfer in water. *J. Chem. Phys.* 34, 375 (1961).
- [44] Roberts, N. & Northey, H. L. Hydrogen Ion Mobility in Aqueous Electrolyte Solutions. *J. Chem. Soc. Faraday Trans. 1* 68, 1528 (1972).
- [45] Dippel, T. & Kreuer, K. D. Proton transport mechanism in concentrated aqueous solutions and solid hydrates of acids. *Solid State Ionics* 46, 3 (1991).
- [46] Agmon, N. The Grotthuss mechanism. *Chem. Phys. Lett.* 244, 456 (1995).
- [47] Suhrmann, R. & Breyer, F. I. Über den Einfluss gelöster Salze auf den Assoziationszustand des lösenden Wassers. *Zeit. Phys. Chem.* 20B, 17 (1933).
- [48] Zundel, G. & Metzger, H. Energiebänder der tunnelnden Überschuss-Protonen in flüssigen Säuren. Eine IR-spektroskopische Untersuchung der Natur der Gruppierungen H<sub>5</sub>O<sub>2</sub><sup>+</sup>. *Zeit. Phys. Chem.* 58, 225 (1968).
- [49] Coutre, J. L., Tittor, J., Oesterhelt, D. & Gerwert, K. Experimental evidence for hydrogen-bonded network proton transfer in bacteriorhodopsin shown by Fourier-transform infrared spectroscopy using azide as catalyst. *Proc. Natl. Acad. Sci. U. S. A.* 92, 4962 (1995).
- [50] Garczarek, F. & Gerwert, K. Functional waters in intraprotein proton transfer monitored by FTIR difference spectroscopy. *Nature* 439, 109 (2006).
- [51] Mathias, G. & Marx, D. Structures and spectral signatures of protonated water networks in bacteriorhodopsin. *Proc. Natl. Acad. Sci.* 104, 6980 (2007).
- [52] Daldrop, J. O., Saita, M., Heyden, M., Lorenz-Fonfria, V. A., Heberle, J. & Netz, R. R. Orientation of non-spherical protonated water clusters revealed by infrared absorption dichroism. *Nat. Commun.* 9, 311 (2018).
- [53] Kim, J., Schmitt, U. W., Gruetzmacher, J. A., Voth, G. A. & Scherer, N. E. The vibrational spectrum of the hydrated proton: Comparison of experiment, simulation, and normal mode analysis. *J. Chem. Phys.* 116, 737 (2002).
- [54] Thämer, M., De Marco, L., Ramasesha, K., Mandal, A. & Tokmakoff, A. Ultrafast 2D IR spectroscopy of the excess proton in liquid water. *Science* 350, 78 (2015).

- 
- [55] Dahms, F., Fingerhut, B. P., Nibbering, E. T. J., Pines, E. & Elsaesser, T. Large-amplitude transfer motion of hydrated excess protons mapped by ultrafast 2D IR spectroscopy. *Science* 357, 491 (2017).
- [56] Carpenter, W. B., Fournier, J. A., Lewis, N. H. C. & Tokmakoff, A. Picosecond Proton Transfer Kinetics in Water Revealed with Ultrafast IR Spectroscopy. *J. Phys. Chem. B* 122, 2792 (2018).
- [57] Wicke, E., Eigen, M. & Ackermann, T. Über den Zustand des Protons (Hydroniumions) in wässriger Lösung. *Zeit. Phys. Chem.* 1, 340 (1954).
- [58] Markland, T. E. & Ceriotti, M. Nuclear quantum effects enter the mainstream. *Nat. Rev. Chem.* 2, 0109 (2018).
- [59] Marx, D., Tuckerman, M. E., Hutter, J. & Parrinello, M. The nature of the hydrated excess proton in water. *Nature* 397, 601 (1999).
- [60] Rossi, M., Ceriotti, M. & Manolopoulos, D. E. How to remove the spurious resonances from ring polymer molecular dynamics. *J. Chem. Phys.* 140, 234116 (2014).
- [61] Napoli, J. A., Marsalek, O. & Markland, T. E. Decoding the spectroscopic features and time scales of aqueous proton defects. *J. Chem. Phys.* 148, 222833 (2018).
- [62] Calio, P. B., Li, C. & Voth, G. A. Resolving the Structural Debate for the Hydrated Excess Proton in Water. *J. Am. Chem. Soc.* 143, 18672 (2021).
- [63] Heberle, J., Riesle, J., Thiedemann, G., Oesterhelt, D. & Dencher, N. A. Proton migration along the membrane surface and retarded surface to bulk transfer. *Nature* 370, 379 (1994).
- [64] Wolf, S., Freier, E., Potschies, M., Hofmann, E. & Gerwert, K. Directional proton transfer in membrane proteins achieved through protonated protein-bound water molecules: A proton diode. *Angew. Chemie - Int. Ed.* 49, 6889 (2010).
- [65] Tripathi, R., Forbert, H. & Marx, D. Settling the Long-Standing Debate on the Proton Storage Site of the Prototype Light-Driven Proton Pump Bacteriorhodopsin. *J. Phys. Chem. B* 123, 9598 (2019).
- [66] Asmis, K. R., Pivonka, N. L., Santambrogio, G., Brümmer, M., Kaposta, C., Neumark, D. M. & Wöste, L. Gas-Phase Infrared Spectrum of the Protonated Water Dimer. *Science* 299, 1375 (2003).
- [67] Fridgen, T. D., McMahon, T. B., MacAleese, L., Lemaire, J. & Maitre, P. Infrared spectrum of the protonated water dimer in the gas phase. *J. Phys. Chem. A* 108, 9008 (2004).

- [68] Diken, E. G., Headrick, J. M., Roscioli, J. R., Bopp, J. C., Johnson, M. A. & McCoy, A. B. Fundamental excitations of the shared proton in the  $\text{H}_3\text{O}_2^-$  and  $\text{H}_5\text{O}_2^+$  complexes. *J. Phys. Chem. A* 109, 1487 (2005).
- [69] Hammer, N. I., Diken, E. G., Roscioli, J. R., Johnson, M. A., Myshakin, E. M., Jordan, K. D., McCoy, A. B., Huang, X., Bowman, J. M. & Carter, S. The vibrational predissociation spectra of the  $\text{H}_5\text{O}_2^+ \cdot \text{RG}_n$  ( $\text{RG}=\text{Ar, Ne}$ ) clusters: Correlation of the solvent perturbations in the free OH and shared proton transitions of the Zundel ion. *J. Chem. Phys.* 122, 244301 (2005).
- [70] Roberts, S. T., Petersen, P. B., Ramasesha, K., Tokmakoff, A., Ufimtsev, I. S. & Martinez, T. J. Observation of a Zundel-like transition state during proton transfer in aqueous hydroxide solutions. *Proc. Natl. Acad. Sci. U. S. A.* 106, 15154 (2009).
- [71] Decka, D., Schwaab, G. & Havenith, M. A THz/FTIR fingerprint of the solvated proton: Evidence for Eigen structure and Zundel dynamics. *Phys. Chem. Chem. Phys.* 17, 11898 (2015).
- [72] Wolke, C. T., Fournier, J. A., Dzugan, L. C., Fagiani, M. R., Odbadrakh, T. T., Knorke, H., Jordan, K. D., McCoy, A. B., Asmis, K. R. & Johnson, M. A. Spectroscopic snapshots of the proton-transfer mechanism in water. *Science* 354, 1131 (2016).
- [73] Fournier, J. A., Carpenter, W. B., Lewis, N. H. C. & Tokmakoff, A. Broadband 2D IR spectroscopy reveals dominant asymmetric  $\text{H}_5\text{O}_2^+$  proton hydration structures in acid solutions. *Nat. Chem.* 10, 932 (2018).
- [74] Kundu, A., Dahms, F., Fingerhut, B. P., Nibbering, E. T. J., Pines, E. & Elsaesser, T. Hydrated Excess Protons in Acetonitrile/Water Mixtures: Solvation Species and Ultrafast Proton Motions. *J. Phys. Chem. Lett.* 10, 2287 (2019).
- [75] Carpenter, W. B., Lewis, N. H. C., Fournier, J. A. & Tokmakoff, A. Entropic barriers in the kinetics of aqueous proton transfer. *J. Chem. Phys.* 151, 034501 (2019).
- [76] Carpenter, W. B., Yu, Q., Hack, J. H., Dereka, B., Bowman, J. M. & Tokmakoff, A. Decoding the 2D IR spectrum of the aqueous proton with high-level VSCF/VCI calculations. *J. Chem. Phys.* 153, 124506 (2020).
- [77] Richards, R. E. & Smith, J. A. S. Nuclear magnetic resonance spectra of some acid hydrates. *Trans. Faraday Soc.* 47, 1261 (1951).
- [78] Kakiuchi, Y., Shono, H., Komatsu, H. & Kigoshi, K. Proton Magnetic Resonance Absorption in Hydrogen Perchlorate Monohydrate and the Structure of Oxonium Ion. *J. Chem. Phys.* 19, 1069 (1951).

- 
- [79] Esser, T. K., Knorke, H., Asmis, K. R., Schöllkopf, W., Yu, Q., Qu, C., Bowman, J. M. & Kaledin, M. Deconstructing Prominent Bands in the Terahertz Spectra of  $\text{H}_7\text{O}_3^+$  and  $\text{H}_9\text{O}_4^+$ : Intermolecular Modes in Eigen Clusters. *J. Phys. Chem. Lett.* 9, 798 (2018).
- [80] Sauer, J. & Döbler, J. Gas-phase infrared spectrum of the protonated water dimer: Molecular dynamics simulation and accuracy of the potential energy surface. *ChemPhysChem* 6, 1706 (2005).
- [81] Vendrell, O., Gatti, F. & Meyer, H. D. Full dimensional (15-dimensional) quantum-dynamical simulation of the protonated water dimer. II. Infrared spectrum and vibrational dynamics. *J. Chem. Phys.* 127, 184303 (2007).
- [82] Agostini, F., Vuilleumier, R. & Ciccotti, G. Infrared spectroscopy of small protonated water clusters at room temperature: An effective modes analysis. *J. Chem. Phys.* 134, 084302 (2011).
- [83] Yu, Q. & Bowman, J. M. High-Level Quantum Calculations of the IR Spectra of the Eigen, Zundel, and Ring Isomers of  $\text{H}^+(\text{H}_2\text{O})_4$  Find a Single Match to Experiment. *J. Am. Chem. Soc.* 139, 10984 (2017).
- [84] Yu, Q. & Bowman, J. M. Classical, Thermostated Ring Polymer, and Quantum VSCF/VCI Calculations of IR Spectra of  $\text{H}_7\text{O}_3^+$  and  $\text{H}_9\text{O}_4^+$  (Eigen) and Comparison with Experiment. *J. Phys. Chem. A* 123, 1399 (2019).
- [85] Kulig, W. & Agmon, N. A 'clusters-in-liquid' method for calculating infrared spectra identifies the proton-transfer mode in acidic aqueous solutions. *Nat. Chem.* 5, 29 (2013).
- [86] Hassanali, A., Giberti, F., Cuny, J., Kühne, T. D. & Parrinello, M. Proton transfer through the water gossamer. *Proc. Natl. Acad. Sci. U. S. A.* 110, 13723 (2013).
- [87] Tse, Y. L. S., Knight, C. & Voth, G. A. An analysis of hydrated proton diffusion in ab initio molecular dynamics. *J. Chem. Phys.* 142, 014104 (2015).
- [88] Daly, C. A., Streacker, L. M., Sun, Y., Pattenaude, S. R., Hassanali, A. A., Petersen, P. B., Corcelli, S. A. & Ben-Amotz, D. Decomposition of the Experimental Raman and Infrared Spectra of Acidic Water into Proton, Special Pair, and Counterion Contributions. *J. Phys. Chem. Lett.* 8, 5246 (2017).
- [89] Wang, H. & Agmon, N. Reinvestigation of the Infrared Spectrum of the Gas-Phase Protonated Water Tetramer. *J. Phys. Chem. A* 121, 3056 (2017).
- [90] Yuan, R., Napoli, J. A., Yan, C., Marsalek, O., Markland, T. E. & Fayer, M. D. Tracking Aqueous Proton Transfer by Two-Dimensional Infrared Spectroscopy and ab Initio Molecular Dynamics Simulations. *ACS Cent. Sci.* 5, 1269 (2019).

- [91] Fischer, S. A. & Gunlycke, D. Analysis of Correlated Dynamics in the Grotthuss Mechanism of Proton Diffusion. *J. Phys. Chem. B* 123, 5536 (2019).
- [92] Roy, S., Schenter, G. K., Napoli, J. A., Baer, M. D., Markland, T. E. & Mundy, C. J. Resolving Heterogeneous Dynamics of Excess Protons in Aqueous Solution with Rate Theory. *J. Phys. Chem. B* 124, 5665 (2020).
- [93] Li, C. & Swanson, J. M. Understanding and Tracking the Excess Proton in Ab Initio Simulations; Insights from IR Spectra. *J. Phys. Chem. B* 124, 5696 (2020).
- [94] Arntsen, C., Chen, C., Calio, P. B., Li, C. & Voth, G. A. The hopping mechanism of the hydrated excess proton and its contribution to proton diffusion in water. *J. Chem. Phys.* 154, 194506 (2021).
- [95] Schmitt, U. W. & Voth, G. A. Multistate empirical valence bond model for proton transport in water. *J. Phys. Chem. B* 102, 5547 (1998).
- [96] Day, T. J., Soudackov, A. V., Čuma, M., Schmitt, U. W. & Voth, G. A. A second generation multistate empirical valence bond model for proton transport in aqueous systems. *J. Chem. Phys.* 117, 5839 (2002).
- [97] Biswas, R., Tse, Y. L. S., Tokmakoff, A. & Voth, G. A. Role of Presolvation and Anharmonicity in Aqueous Phase Hydrated Proton Solvation and Transport. *J. Phys. Chem. B* 120, 1793 (2016).
- [98] Biswas, R., Carpenter, W., Fournier, J. A., Voth, G. A. & Tokmakoff, A. IR spectral assignments for the hydrated excess proton in liquid water. *J. Chem. Phys.* 146, 154507 (2017).
- [99] Yu, Q., Carpenter, W. B., Lewis, N. H. C., Tokmakoff, A. & Bowman, J. M. High-Level VSCF/VCI Calculations Decode the Vibrational Spectrum of the Aqueous Proton. *J. Phys. Chem. B* 123, 7214 (2019).
- [100] Marx, D. & Hutter, J., *Ab initio molecular dynamics: basic theory and advanced methods* (Cambridge University Press, 2009).
- [101] Becke, A. D. Density-functional exchange-energy approximation with correct asymptotic behavior. *Phys. Rev. A* 38, 3098 (1988).
- [102] Lee, C., Yang, W. & Parr, R. G. Development of the Colle-Salvetti correlation-energy formula into a functional of the electron density. *Phys. Rev. B* 37, 785 (1988).
- [103] Grimme, S., Antony, J., Ehrlich, S. & Krieg, H. A consistent and accurate ab initio parametrization of density functional dispersion correction (DFT-D) for the 94 elements H-Pu. *J. Chem. Phys.* 132, 154104 (2010).
- [104] Goedecker, S., Teter, M. & Hutter, J. Separable dual-space Gaussian pseudopotentials. *Phys. Rev. B* 54, 1703 (1996).

- 
- [105] Kühne, T. D. *et al.* CP2K: An electronic structure and molecular dynamics software package - Quickstep: Efficient and accurate electronic structure calculations. *J. Chem. Phys.* 152, 194103 (2020).
- [106] VandeVondele, J. & Hutter, J. Gaussian basis sets for accurate calculations on molecular systems in gas and condensed phases. *J. Chem. Phys.* 127, 114105 (2007).
- [107] Markovitch, O., Chen, H., Izvekov, S., Paesani, F., Voth, G. A. & Agmon, N. Special pair dance and partner selection: Elementary steps in proton transport in liquid water. *J. Phys. Chem. B* 112, 9456 (2008).
- [108] Knight, C. & Voth, G. A. The curious case of the hydrated proton. *Acc. Chem. Res.* 45, 101 (2012).
- [109] Schran, C. & Marx, D. Quantum nature of the hydrogen bond from ambient conditions down to ultra-low temperatures. *Phys. Chem. Chem. Phys.* 21, 24967 (2019).
- [110] Baer, M., Marx, D. & Mathias, G. Theoretical messenger spectroscopy of microsolvated hydronium and Zundel cations. *Angew. Chemie - Int. Ed.* 49, 7346 (2010).
- [111] Eucken, A. Assoziation in Flüssigkeiten. *Zeitschrift für Elektrochemie und Angew. Phys. Chemie* 52, 255 (1948).
- [112] Cao, Z., Peng, Y., Yan, T., Li, S., Li, A. & Voth, G. A. Mechanism of fast proton transport along one-dimensional water chains confined in carbon nanotubes. *J. Am. Chem. Soc.* 132, 11395 (2010).
- [113] Fulton, J. L. & Balasubramanian, M. Structure of Hydronium ( $\text{H}_3\text{O}^+$ )/ Chloride ( $\text{Cl}^-$ ) Contact Ion Pairs in Aqueous Hydrochloric Acid Solution : A Zundel-like local configuration. *J. Am. Chem. Soc.* 132, 12597 (2010).
- [114] Baer, M. D., Fulton, J. L., Balasubramanian, M., Schenter, G. K. & Mundy, C. J. Persistent ion pairing in aqueous hydrochloric acid. *J. Phys. Chem. B* 118, 7211 (2014).
- [115] Xu, J., Izvekov, S. & Voth, G. A. Structure and dynamics of concentrated hydrochloric acid solutions. *J. Phys. Chem. B* 114, 9555 (2010).
- [116] Calio, P. B., Li, C. & Voth, G. A. Molecular Origins of the Barriers to Proton Transport in Acidic Aqueous Solutions. *J. Phys. Chem. B* 124, 8868 (2020).
- [117] Mills, R. Self-diffusion in normal and heavy water in the range 1-45°. *J. Phys. Chem.* 77, 685 (1973).
- [118] Harris, K. R. & Woolf, L. A. Pressure and temperature dependence of the self diffusion coefficient of water and oxygen-18 water. *J. Chem. Soc. Faraday Trans. 1* 76, 377 (1980).

- [119] Gillan, M. J., Alfè, D. & Michaelides, A. Perspective: How good is DFT for water? *J. Chem. Phys.* 144, 130901 (2016).
- [120] Izvekov, S. & Voth, G. A. Ab initio molecular-dynamics simulation of aqueous proton solvation and transport revisited. *J. Chem. Phys.* 123, 044505 (2005).
- [121] Cassone, G. Nuclear Quantum Effects Largely Influence Molecular Dissociation and Proton Transfer in Liquid Water under an Electric Field. *J. Phys. Chem. Lett.* 11, 8983 (2020).
- [122] Woutersen, S. & Bakker, H. J. Ultrafast vibrational and structural dynamics of the proton in liquid water. *Phys. Rev. Lett.* 96, 138305 (2006).
- [123] Fischer, S. A., Dunlap, B. I. & Gunlycke, D. Correlated dynamics in aqueous proton diffusion. *Chem. Sci.* 9, 7126 (2018).
- [124] Ciccotti, G., Ferrario, M., Hynes, J. T. & Kapral, R. Dynamics of ion pair interconversion in a polar solvent. *J. Chem. Phys.* 93, 7137 (1990).
- [125] Roy, S., Baer, M. D., Mundy, C. J. & Schenter, G. K. Reaction Rate Theory in Coordination Number Space: An Application to Ion Solvation. *J. Phys. Chem. C* 120, 7597 (2016).
- [126] Luzar, A. & Chandler, D. Hydrogen-bond kinetics in liquid water. *Nature* 379, 55 (1996).
- [127] Brzezinski, P. & Gennis, R. B. Cytochrome c oxidase: exciting progress and remaining mysteries. *J. Bioenerg. Biomembr.* 40, 521 (2008).
- [128] Wolf, A., Dragelj, J., Wonneberg, J., Stellmacher, J., Balke, J., Woelke, A. L., Hodoscek, M., Knapp, E. W. & Alexiev, U. The redox-coupled proton-channel opening in cytochrome c oxidase. *Chem. Sci.* 11, 3804 (2020).
- [129] Haumann, M., Liebisch, P., Müller, C., Barra, M., Grabolle, M. & Dau, H. Photosynthetic O<sub>2</sub> Formation Tracked by Time-Resolved X-ray Experiments. *Science* 310, 1019 (2005).
- [130] Klauss, A., Haumann, M. & Dau, H. Seven Steps of Alternating Electron and Proton Transfer in Photosystem II Water Oxidation Traced by Time-Resolved Photothermal Beam Deflection at Improved Sensitivity. *J. Phys. Chem. B* 119, 2677 (2015).
- [131] Fitzpatrick, A. E., Lincoln, C. N., van Wilderen, L. J. G. W. & van Thor, J. J. Pump–Dump–Probe and Pump–Repump–Probe Ultrafast Spectroscopy Resolves Cross Section of an Early Ground State Intermediate and Stimulated Emission in the Photoreactions of the Pr Ground State of the Cyanobacterial Phytochrome Cph1. *J. Phys. Chem. B* 116, 1077 (2012).

- 
- [132] Zienicke, B., Molina, I., Glenz, R., Singer, P., Ehmer, D., Escobar, F. V., Hildebrandt, P., Diller, R. & Lamparter, T. Unusual spectral properties of bacteriophytochrome Agp2 result from a deprotonation of the chromophore in the red-absorbing form Pr. *J. Biol. Chem.* 288, 31738 (2013).
- [133] Schmidt, A., Sauthof, L., Szczepek, M., Lopez, M. F., Escobar, F. V., Qureshi, B. M., Michael, N., Buhrke, D., Stevens, T., Kwiatkowski, D., von Stetten, D., Mroginski, M. A., Krauß, N., Lamparter, T., Hildebrandt, P. & Scheerer, P. Structural snapshot of a bacterial phytochrome in its functional intermediate state. *Nat. Commun.* 9, 4912 (2018).
- [134] Nieva, J. L., Madan, V. & Carrasco, L. Viroporins: structure and biological functions. *Nat. Rev. Microbiol.* 10, 563 (2012).
- [135] Andreas, L. B., Reese, M., Eddy, M. T., Gelev, V., Ni, Q. Z., Miller, E. A., Emsley, L., Pintacuda, G., Chou, J. J. & Griffin, R. G. Structure and Mechanism of the Influenza A M218–60 Dimer of Dimers. *J. Am. Chem. Soc.* 137, 14877 (2015).
- [136] Freier, E., Wolf, S. & Gerwert, K. Proton transfer via a transient linear water-molecule chain in a membrane protein. *Proc. Natl. Acad. Sci. U. S. A.* 108, 11435 (2011).
- [137] Kaila, V. R. & Hummer, G. Energetics and dynamics of proton transfer reactions along short water wires. *Phys. Chem. Chem. Phys.* 13, 13207 (2011).
- [138] Kohler, F., Findenegg, G., Fischer, J. & Posch, H., *The liquid state* (Verlag Chemie Weinheim, 1972).
- [139] Thomas, M., *Theoretical modeling of vibrational spectra in the liquid phase* (Springer, 2016).
- [140] Wiener, N. Generalized harmonic analysis. *Acta Math.* 55, 117 (1930).
- [141] Debye, P., *Polar Molecules* (Chemical Catalog Company, Incorporated, 1929).
- [142] Agmon, N. Tetrahedral Displacement : The Molecular Mechanism behind the Debye Relaxation in Water. *J. Phys. Chem.* 100, 1072 (1996).
- [143] Laage, D. & Hynes, J. T. A molecular jump mechanism of water reorientation. *Science* 311, 832 (2006).
- [144] Silvestrelli, P. L., Bernasconi, M. & Parrinello, M. Ab initio infrared spectrum of liquid water. *Chem. Phys. Lett.* 277, 478 (1997).
- [145] Heyden, M., Sun, J., Funkner, S., Mathias, G., Forbert, H., Havenith, M. & Marx, D. Dissecting the THz spectrum of liquid water from first principles via correlations in time and space. *Proc. Natl. Acad. Sci. U. S. A.* 107, 12068 (2010).



- [146] Sidler, D., Meuwly, M. & Hamm, P. An efficient water force field calibrated against intermolecular THz and Raman spectra. *J. Chem. Phys.* 148, 244504 (2018).
- [147] Badger, R. M. A relation between internuclear distances and bond force constants. *J. Chem. Phys.* 2, 128 (1934).
- [148] Mikenda, W. Stretching frequency versus bond distance correlation of O–D(H) ··· Y (Y = N, O, S, Se, Cl, Br, I) hydrogen bonds in solid hydrates. *J. Mol. Struct.* 147, 1 (1986).
- [149] Lawrence, C. P. & Skinner, J. L. Vibrational spectroscopy of HOD in liquid D<sub>2</sub>O. VI. Intramolecular and intermolecular vibrational energy flow. *J. Chem. Phys.* 119, 1623 (2003).
- [150] Møller, K. B., Rey, R. & Hynes, J. T. Hydrogen bond dynamics in water and ultrafast infrared spectroscopy: A theoretical study. *J. Phys. Chem. A* 108, 1275 (2004).
- [151] Bakker, H. J. & Skinner, J. L. Vibrational spectroscopy as a probe of structure and dynamics in liquid water. *Chem. Rev.* 110, 1498 (2010).
- [152] Ramasesha, K., De Marco, L., Mandal, A. & Tokmakoff, A. Water vibrations have strongly mixed intra- and intermolecular character. *Nat. Chem.* 5, 935 (2013).
- [153] Perakis, F., De Marco, L., Shalit, A., Tang, F., Kann, Z. R., Kühne, T. D., Torre, R., Bonn, M. & Nagata, Y. Vibrational spectroscopy and dynamics of water. *Chem. Rev.* 116, 7590 (2016).
- [154] Max, J. J., Larouche, P. & Chapados, C. Orthogonalized H<sub>2</sub>O and D<sub>2</sub>O species obtained from infrared spectra of liquid water at several temperatures. *J. Mol. Struct.* 1149, 457 (2017).
- [155] Matt, S. M. & Ben-Amotz, D. Influence of intermolecular coupling on the vibrational spectrum of water. *J. Phys. Chem. B* 122, 5375 (2018).
- [156] Ohno, K., Okimura, M., Akai, N. & Katsumoto, Y. The effect of cooperative hydrogen bonding on the OH stretching-band shift for water clusters studied by matrix-isolation infrared spectroscopy and density functional theory. *Phys. Chem. Chem. Phys.* 7, 3005 (2005).
- [157] Zhang, C., Guidoni, L. & Kühne, T. D. Competing factors on the frequency separation between the OH stretching modes in water. *J. Mol. Liq.* 205, 42 (2015).
- [158] Futera, Z. & English, N. J. Communication: Influence of external static and alternating electric fields on water from long-time non-equilibrium ab initio molecular dynamics. *J. Chem. Phys.* 147, 031102 (2017).
- [159] Ojha, D., Karhan, K. & Kühne, T. D. On the hydrogen bond strength and vibrational spectroscopy of liquid water. *Sci. Rep.* 8, 16888 (2018).

- 
- [160] Boyer, M. A., Marsalek, O., Heindel, J. P., Markland, T. E., McCoy, A. B. & Xantheas, S. S. Beyond Badger's rule: The origins and generality of the structure-spectra relationship of aqueous hydrogen bonds. *J. Phys. Chem. Lett.* 10, 918 (2019).
- [161] Cassone, G., Spomer, J., Trusso, S. & Saija, F. Ab initio spectroscopy of water under electric fields. *Phys. Chem. Chem. Phys.* 21, 21205 (2019).
- [162] Yu, C.-C. C., Chiang, K.-Y. Y., Okuno, M., Seki, T., Ohto, T., Yu, X., Korepanov, V., Hamaguchi, H.-o. o., Bonn, M., Hunger, J. & Nagata, Y. Vibrational couplings and energy transfer pathways of water's bending mode. *Nat. Commun.* 11, 5977 (2020).
- [163] Ren, P. & Ponder, J. W. Polarizable Atomic Multipole Water Model for Molecular Mechanics Simulation. *J. Phys. Chem. B* 107, 5933 (2003).
- [164] Fanourgakis, G. S. & Xantheas, S. S. Development of transferable interaction potentials for water. V. Extension of the flexible, polarizable, Thole-type model potential (TTM3-F, v. 3.0) to describe the vibrational spectra of water clusters and liquid water. *J. Chem. Phys.* 128, 074506 (2008).
- [165] González, M. A. & Abascal, J. L. A flexible model for water based on TIP4P/2005. *J. Chem. Phys.* 135, 224516 (2011).
- [166] Hasegawa, T. & Tanimura, Y. A Polarizable Water Model for Intramolecular and Intermolecular Vibrational Spectroscopies. *J. Phys. Chem. B* 115, 5545 (2011).
- [167] Bukowski, R., Szalewicz, K., Groenenboom, G. C. & van der Avoird, A. Predictions of the Properties of Water from First Principles. *Science* 315, 1249 (2007).
- [168] Wang, Y., Shepler, B. C., Braams, B. J. & Bowman, J. M. Full-dimensional, ab initio potential energy and dipole moment surfaces for water. *J. Chem. Phys.* 131, 54511 (2009).
- [169] Wang, Y., Huang, X., Shepler, B. C., Braams, B. J. & Bowman, J. M. Flexible, ab initio potential, and dipole moment surfaces for water. I. Tests and applications for clusters up to the 22-mer. *J. Chem. Phys.* 134, 94509 (2011).
- [170] Medders, G. R. & Paesani, F. Infrared and raman spectroscopy of liquid water through "first-principles" many-body molecular dynamics. *J. Chem. Theory Comput.* 11, 1145 (2015).
- [171] Paesani, F. Getting the Right Answers for the Right Reasons: Toward Predictive Molecular Simulations of Water with Many-Body Potential Energy Functions. *Acc. Chem. Res.* 49, 1844 (2016).

- [172] Reddy, S. K., Moberg, D. R., Straight, S. C. & Paesani, F. Temperature-dependent vibrational spectra and structure of liquid water from classical and quantum simulations with the MB-pol potential energy function. *J. Chem. Phys.* 147, 244504 (2017).
- [173] Torii, H. Time-domain calculations of the polarized Raman spectra, the transient infrared absorption anisotropy, and the extent of delocalization of the OH stretching mode of liquid water. *J. Phys. Chem. A* 110, 9469 (2006).
- [174] Auer, B. M. & Skinner, J. L. IR and Raman spectra of liquid water: Theory and interpretation. *J. Chem. Phys.* 128, 224511 (2008).
- [175] Yang, M. & Skinner, J. L. Signatures of coherent vibrational energy transfer in IR and Raman line shapes for liquid water. *Phys. Chem. Chem. Phys.* 12, 982 (2010).
- [176] Ni, Y. & Skinner, J. L. IR and SFG vibrational spectroscopy of the water bend in the bulk liquid and at the liquid-vapor interface, respectively. *J. Chem. Phys.* 143, 014502 (2015).
- [177] Schmidt, J. R. & Corcelli, S. A. Infrared absorption line shapes in the classical limit: A comparison of the classical dipole and fluctuating frequency approximations. *J. Chem. Phys.* 128, 184504 (2008).
- [178] Choi, J. H. & Cho, M. Computational IR spectroscopy of water: OH stretch frequencies, transition dipoles, and intermolecular vibrational coupling constants. *J. Chem. Phys.* 138, 174108 (2013).
- [179] Kananenka, A. A. & Skinner, J. L. Fermi resonance in OH-stretch vibrational spectroscopy of liquid water and the water hexamer. *J. Chem. Phys.* 148, 244107 (2018).
- [180] Ceriotti, M., Fang, W., Kusalik, P. G., McKenzie, R. H., Michaelides, A., Morales, M. A. & Markland, T. E. Nuclear Quantum Effects in Water and Aqueous Systems: Experiment, Theory, and Current Challenges. *Chem. Rev.* 116, 7529 (2016).
- [181] Marsalek, O. & Markland, T. E. Quantum dynamics and spectroscopy of ab Initio liquid water: The interplay of nuclear and electronic quantum effects. *J. Phys. Chem. Lett.* 8, 1545 (2017).
- [182] Metiu, H., Oxtoby, D. W. & Freed, K. F. Hydrodynamic theory for vibrational relaxation in liquids. *Phys. Rev. A* 15, 361 (1977).
- [183] Whitnell, R. M., Wilson, K. R. & Hynes, J. T. Vibrational relaxation of a dipolar molecule in water. *J. Chem. Phys.* 96, 5354 (1992).
- [184] Tuckerman, M. & Berne, B. J. Vibrational relaxation in simple fluids: Comparison of theory and simulation. *J. Chem. Phys.* 98, 7301 (1993).

- 
- [185] Joutsuka, T. & Ando, K. Vibrational spectroscopy and relaxation of an anharmonic oscillator coupled to harmonic bath. *J. Chem. Phys.* 134, 204511 (2011).
- [186] Morrone, J. A., Markland, T. E., Ceriotti, M. & Berne, B. J. Efficient multiple time scale molecular dynamics: Using colored noise thermostats to stabilize resonances. *J. Chem. Phys.* 134, 014103 (2011).
- [187] Gottwald, F., Ivanov, S. D. & Kühn, O. Applicability of the Caldeira-Leggett model to vibrational spectroscopy in solution. *J. Phys. Chem. Lett.* 6, 2722 (2015).
- [188] Gottwald, F., Ivanov, S. D. & Kühn, O. On computing spectral densities from classical, semiclassical, and quantum simulations. *J. Chem. Phys.* 150, 180901 (2019).
- [189] Woutersen, S. & Bakker, H. J. Resonant intermolecular transfer of vibrational energy in liquid water. *Nature* 402, 507 (1999).
- [190] Lock, A. J. & Bakker, H. J. Temperature dependence of vibrational relaxation in liquid H<sub>2</sub>O. *J. Chem. Phys.* 117, 1708 (2002).
- [191] Cowan, M. L., Bruner, B. D., Huse, N., Dwyer, J. R., Chugh, B., Nibbering, E. T., Elsaesser, T. & Miller, R. J. Ultrafast memory loss and energy redistribution in the hydrogen bond network of liquid H<sub>2</sub>O. *Nature* 434, 199 (2005).
- [192] Ashihara, S., Huse, N., Espagne, A., Nibbering, E. T. & Elsaesser, T. Vibrational couplings and ultrafast relaxation of the O-H bending mode in liquid H<sub>2</sub>O. *Chem. Phys. Lett.* 424, 66 (2006).
- [193] Ashihara, S., Huse, N., Espagne, A., Nibbering, E. T. & Elsaesser, T. Ultrafast structural dynamics of water induced by dissipation of vibrational energy. *J. Phys. Chem. A* 111, 743 (2007).
- [194] Rey, R., Ingrosso, F., Elsaesser, T. & Hynes, J. T. Pathways for H<sub>2</sub>O bend vibrational relaxation in liquid water. *J. Phys. Chem. A* 113, 8949 (2009).
- [195] Van Der Post, S. T., Hsieh, C.-S. S., Okuno, M., Nagata, Y., Bakker, H. J., Bonn, M. & Hunger, J. Strong frequency dependence of vibrational relaxation in bulk and surface water reveals sub-picosecond structural heterogeneity. *Nat. Commun.* 6, 8384 (2015).
- [196] De Marco, L., Carpenter, W., Liu, H., Biswas, R., Bowman, J. M. & Tokmakoff, A. Differences in the vibrational dynamics of H<sub>2</sub>O and D<sub>2</sub>O: Observation of symmetric and antisymmetric stretching vibrations in heavy water. *J. Phys. Chem. Lett.* 7, 1769 (2016).
- [197] Carpenter, W. B., Fournier, J. A., Biswas, R., Voth, G. A. & Tokmakoff, A. Delocalization and stretch-bend mixing of the HOH bend in liquid water. *J. Chem. Phys.* 147, 084503 (2017).

- [198] Bertie, J. E. & Lan, Z. Infrared intensities of liquids XX: The intensity of the OH stretching band of liquid water revisited, and the best current values of the optical constants of H<sub>2</sub>O(l) at 25°C between 15,000 and 1 cm<sup>-1</sup>. *Appl. Spectrosc.* 50, 1047 (1996).
- [199] Arrhenius, S. Über die Reaktionsgeschwindigkeit bei der Inversion von Rohrzucker durch Säuren. *Zeit. Phys. Chem.* 4, 226 (1889).
- [200] Brown, R. XXVII. A brief account of microscopical observations made in the months of June, July and August 1827, on the particles contained in the pollen of plants; and on the general existence of active molecules in organic and inorganic bodies. *Philos. Mag.* 4, 161 (1828).
- [201] Langevin, P. Sur la théorie du mouvement brownien. *Compt. Rendus* 146, 530 (1908).
- [202] Geissler, P. L., Dellago, C. & Chandler, D. Kinetic pathways of ion pair dissociation in water. *J. Phys. Chem. B* 103, 3706 (1999).
- [203] Mullen, R. G., Shea, J.-E. E. & Peters, B. Transmission coefficients, committors, and solvent coordinates in ion-pair dissociation. *J. Chem. Theory Comput.* 10, 659 (2014).
- [204] Fricks, J., Yao, L., Elston, T. C. & Forest, M. G. Time-Domain Methods for Diffusive Transport in Soft Matter. *SIAM J. Appl. Math.* 69, 1277 (2009).
- [205] Lei, H., Baker, N. A. & Li, X. Data-driven parameterization of the generalized Langevin equation. *Proc. Natl. Acad. Sci. U. S. A.* 113, 14183 (2016).
- [206] Jung, G., Hanke, M. & Schmid, F. Iterative Reconstruction of Memory Kernels. *J. Chem. Theory Comput.* 13, 2481 (2017).
- [207] Rey, R. & Guardia, E. Dynamical Aspects of the Na<sup>+</sup>-Cl<sup>-</sup> Ion Pair Association in Water. *J. Phys. Chem.* 96, 4712 (1992).
- [208] Annapureddy, H. V. R. & Dang, L. X. Understanding the Rates and Molecular Mechanism of Water-Exchange around Aqueous Ions Using Molecular Simulations. *J. Phys. Chem. B* 118, 8917 (2014).
- [209] Meyer, H., Pelagejcev, P. & Schilling, T. Non-Markovian out-of-equilibrium dynamics: A general numerical procedure to construct time-dependent memory kernels for coarse-grained observables. *Europhys. Lett.* 128, 40001 (2019).
- [210] Grote, R. F. & Hynes, J. T. The stable states picture of chemical reactions. II. Rate constants for condensed and gas phase reaction models. *J. Chem. Phys.* 73, 2715 (1980).

- 
- [211] Pollak, E., Grabert, H. & Hänggi, P. Theory of activated rate processes for arbitrary frequency dependent friction: solution of the turnover problem. *J. Chem. Phys.* 91, 4073 (1989).
- [212] Kappler, J., Hinrichsen, V. B. & Netz, R. R. Non-Markovian barrier crossing with two-time-scale memory is dominated by the faster memory component. *Eur. Phys. J. E* 42, 119 (2019).
- [213] Lavacchi, L., Kappler, J. & Netz, R. R. Barrier crossing in the presence of multi-exponential memory functions with unequal friction amplitudes and memory times. *EPL* 131, 40004 (2020).
- [214] Van Kampen, N. G. Elimination of fast variables. *Phys. Rep.* 124, 69 (1985).
- [215] Einstein, A. & Others. On the motion of small particles suspended in liquids at rest required by the molecular-kinetic theory of heat. *Ann. Phys.* 17, 208 (1905).
- [216] von Smoluchowski, M. Zur kinetischen Theorie der Brownschen Molekular Bewegung und der Suspensionen. *Ann. d. Phys.* 21, 756 (1906).
- [217] Zwanzig, R., *Nonequilibrium Statistical Mechanics* (Oxford University Press, 2001).
- [218] Schulz, R., Yamamoto, K., Klossek, A., Flesch, R., Hönzke, S., Rancan, F., Vogt, A., Blume-Peytavi, U., Hedtrich, S., Schäfer-Korting, M., Rühl, E. & Netz, R. R. Data-based modeling of drug penetration relates human skin barrier function to the interplay of diffusivity and free-energy profiles. *Proc. Natl. Acad. Sci. U. S. A.* 114, 3631 (2017).
- [219] Best, R. B. & Hummer, G. Coordinate-dependent diffusion in protein folding. *Proc. Natl. Acad. Sci. U. S. A.* 107, 1088 (2010).
- [220] Hinczewski, M., von Hansen, Y., Dzubiella, J. & Netz, R. R. How the diffusivity profile reduces the arbitrariness of protein folding free energies. *J. Chem. Phys.* 132, 245103 (2010).
- [221] Von Hansen, Y., Sedlmeier, F., Hinczewski, M. & Netz, R. R. Friction contribution to water-bond breakage kinetics. *Phys. Rev. E - Stat. Nonlinear, Soft Matter Phys.* 84, 051501 (2011).
- [222] Wolf, S. & Stock, G. Targeted Molecular Dynamics Calculations of Free Energy Profiles Using a Nonequilibrium Friction Correction. *J. Chem. Theory Comput.* 14, 6175 (2018).
- [223] Ayaz, C., Scalfi, L., Dalton, B. A. & Netz, R. R. Generalized Langevin equation with a nonlinear potential of mean force and nonlinear memory friction from a hybrid projection scheme. *Phys. Rev. E* 105, 054138 (2022).
- [224] Grogan, F., Lei, H., Li, X. & Baker, N. A. Data-driven molecular modeling with the generalized Langevin equation. *J. Comput. Phys.* 418, 109633 (2020).

- [225] Mukherjee, S., Mondal, S., Acharya, S. & Bagchi, B. Tug-of-War between Internal and External Frictions and Viscosity Dependence of Rate in Biological Reactions. *Phys. Rev. Lett.* 128, 108101 (2022).
- [226] Vroylandt, H., Goudenège, L., Monmarché, P., Pietrucci, F. & Rotenberg, B. Likelihood-based non-Markovian models from molecular dynamics. *Proc. Natl. Acad. Sci. U. S. A.* 119, e2117586119 (2022).
- [227] Vroylandt, H. & Monmarché, P. Position-dependent memory kernel in generalized Langevin equations: Theory and numerical estimation. *J. Chem. Phys.* 156, 244105 (2022).
- [228] Marchesoni, F. & Grigolini, P. On the extension of the Kramers theory of chemical relaxation to the case of nonwhite noise. *J. Chem. Phys.* 78, 6287 (1983).
- [229] Lee, H. S., Ahn, S. H. & Darve, E. F. The multi-dimensional generalized Langevin equation for conformational motion of proteins. *J. Chem. Phys.* 150, 174113 (2019).
- [230] Zwanzig, R. Nonlinear generalized Langevin equations. *J. Stat. Phys.* 9, 215 (1973).
- [231] Mel'nikov, V. I. & Meshkov, S. V. Theory of activated rate processes: Exact solution of the Kramers problem. *J. Chem. Phys.* 85, 1018 (1986).







# Erklärung

---

Hiermit erkläre ich, dass ich die vorliegende Dissertationsschrift mit dem Titel

Non-Markovian Dynamics and Vibrational Spectroscopy  
of Hydrated Protons and Water

selbständig angefertigt und ohne Benutzung anderer als der angegebenen Quellen und Hilfsmittel angefertigt habe. Diese Dissertation wurde in gleicher oder ähnlicher Form noch in keinem früheren Promotionsverfahren eingereicht.

Berlin, den 10. Januar 2023



# Danksagung

---

Ich bedanke mich herzlich bei Prof. Roland Netz für die Chance unter seiner lehrreichen Betreuung die Promotion anzutreten, für die spannenden Themen in Lehre und Forschung und die interessanten Diskussionen in zahlreichen Seminaren und Meetings. Ebenfalls bedanke ich mich bei Prof. Heberle für die Begutachtung und die Betreuung im Rahmen des Sonderforschungsbereichs 1078.

Mein besonderer Dank gilt Jan Daldrop und Julian Kappler, welche mich in den ersten Jahren der Promotion besonders unterstützt haben und von denen ich viele der theoretischen und computergestützten Methoden gelernt habe. Darüber hinaus danke ich der gesamten Arbeitsgruppe Netz mit den aktuellen und ehemaligen Mitgliedern für die schöne Zeit, insbesondere bei Julian Kappler, Cihan Ayaz, Alexander von Canal und Henrik Kiefer, mit denen ich die meiste Zeit das Büro geteilt habe, und Annette Schumann-Welde für die administrative Unterstützung.

Für die Beiträge zu den Publikationen, welche die Grundlage dieser kumulativen Arbeit bilden, bedanke ich mich bei meinem Koautoren Jan Daldrop, Julian Kappler, Manuel Rammler, Otto Geburtig, Alexander von Canal, Won Kyu Kim, Paul Hillmann, Ellen Adams und Prof. Martina Havenith.

Ich möchte mich auch bei den aktuellen und ehemaligen Mitgliedern des Sonderforschungsbereichs 1078 bedanken, welche meine Perspektive auf unterschiedliche Bereiche der Biophysik erweitert haben und mit deren Hilfe die Doktorarbeit finanziert wurde.

Des weiteren möchte ich mich bei Jens Dreger und Jörg Behrmann für die exzellente Betreuung der Computerressourcen am Fachbereich Physik bedanken, welche für die umfangreichen Berechnungen, die dieser Doktorarbeit zu Grunde liegen, genutzt wurden.

Ich bin dankbar für die andauernden Freundschaften mit Frederic Sulzmann, Jonas Sonnenschein, Jens Bollosch und Carli Freudenberg, die mit mir zusammen lange Abschnitte des Physikstudiums gegangen sind.

Darüber hinaus wäre die Dissertation nicht möglich gewesen ohne die Unterstützung vieler großartiger Menschen in meinem Leben außerhalb der Universität, bei denen ich mich an dieser Stelle auch bedanken möchte: zuerst bei meinem Eltern Heidemarie Brünig und Henning Haupt, welche mich immer bei fast allen Entscheidungen und vor allem während des Physikstudiums unterstützt haben, bei Laura Meichsner für die gemeinsame Zeit und den emotionalen Rückhalt, bei meinen Freunden Peter Pfeiderer, Samir Khoury, Moritz Kölbach, Kai Kruschel und Michael Landau für die Musik die uns gemeinsam erfüllt, bei meiner Wohngemeinschaft für ein aufregendes Leben in Berlin, und nicht zuletzt bei Peter Pfeiderer, Moritz Kölbach, Ash Willison und Laura Meichsner für die hilfreichen Kommentare und Korrekturen.

